Ministry of Education Republic of Azerbaijan,
Azerbaijan Technical University,
International Federation for the Promotion of Mechanism and Machine Science (IFToMM),
Azerbaijan Committee of International Federation for the Promotion of Mechanism and Machine Science (AzC IFToMM),
Izmir Institute of Technology

PROCEEDINGS

OF THE SECOND INTERNATIONAL SYMPOSIUM OF MECHANISM AND MACHINE SCIENCE (ISMMS-2017)

11-14 September 2017, AzTU, Baku, Azerbaijan

CONTENTS

Honorary Chairman of symposium:

Mikayil Jabbarov-Minister of Education of Azerbaijan Republic.

Simposium Chairmans:

Professor Khalig Yahudov-Acting Rector of Azerbaijan Technical University.
Professor Rasim Alizade-Chair of Azerbaijan Committee of International Federation for Promotion of of Mechanism and Machine Science.

Simposium Co-Chairmans:

Professor Ilham Pirmammadov- Vice-Rector for science and technology of Azerbaijan Technical University.
Professor Ayaz Abdullayev-Head of Mechanical Engineering Scientific Laboratory of Azerbaijan Technical University.
Professor Gokhan Kiper-İzmir Institute of Technology, Turkey.

Executive Secretary:

PhD Firuz Mammadov-Department of Theory Mechanism and Machine of Az. Technical University.

Scientific Secretary:

PhD Islam Islamov-Head of the department "Planning of scientific research and scientific-technical information" of Azerbaijan Technical University.

International Scientific Committee:

Alishir Alifov (Russia).
Bernard Roth (USA).
Daizhong Su (England).
Can Dede (Turkey).
Jorge Angeles (Canada).
Minir Yarullin (Russia).
Paulo Flores (Portugal).
Erkin Gezgin (Turkey).
Nazim Mir-Nasiri (Kazakhstan).
Chen I Minq (Singapore).
Erwin-Chistian Lovasz (Romania).
Glazunov Viktor Arkadievich (Russia).

Local Organizing Committee:

Mazakhir Farzaliyev (Azerbaijan).
Rafik Aliyev (Azerbaijan).
Alesker Aliyev (Azerbaijan).
Fazil Veliyev (Azerbaijan).
Ramiz Gurbanov (Azerbaijan).
Ali Sadikhov (Azerbaijan).
Ali Najafov (Azerbaijan).
Ziyafet Kerimov (Azerbaijan).
Vugar Mikayilov (Azerbaijan).
Rafig Jamalov (Azerbaijan).

Aim:

The main objective of the second **ISMMS-2017** is to attract scholars, researchers, teachers, students, professionals and other groups interested in the promotion of science of mechanisms and machines, to submit their scientific work in our Symposium.

ISMMS is well-known and the number of scientific works in the field of MMS grows in the world every year. Potential speakers are affered to submit offers on oral, poster or the vidio-presentations which offer new researchers and theoretical contributions of field of science about mechanisms and machines. All adopted articles will be published in the scientific journal Machine Science (ISSN 2227-6912), and also in scientific proceeding of the Symposium with ISBN, and also with the modified version the selected papers will be published in scientific journals **IFToMM.**

Topics:

Computational kinematics and synthesis of mechanisms; gear driver and transmissions; dynamic of machines; realiability of machines; tribology; mechatronics; manipulators and robots; oil-field machines and mechanisms; technological machines; transport vehicles.

Correspondence Address:
1. Professor Rasim Alizade, Charman of Department of Theory Mechanism and Machine, Azerbaijan Technical University, Baku, Azerbaijan
2. Profesor Gokhan Kiper, Department of Mechanical Engineering, Izmir Institute of Technology, Izmir, Turkey
www.aztu.edu.az
E-mail: alizada_rasim@hotmail.com; gokhankiper@iyte.edu.tr
Phone:(+994 12)538-94-03;(+994 50)679-59-65; (+994 50)856-00-09; (+994 51)664-50-25;
Fax: (+994 12)538-32-80
H.Javid ave 25, Baku, Azerbaijan, AZ1073, Azerbaijan Technical University

Foreword

IFToMM was found in 1969 in Poland at the second World congress as the International Federation for the Development of the Theory of Mechanisms and Machines. The main goal of the World Federation is the development of international cooperation in the field of Theory of Mechanisms and Machines - TMM.

Initially, IFToMM included scientific organizations from 13 countries. In 1995, the General Assembly of the Ninth World Congress of the International Federation of the Theory of Mechanisms and Machines - IFToMM (Italy, Milan) approved the Azerbaijan Committee of the International Federation of the Theory of Mechanisms and Machine (AzC IFToMM). The scientific organization was approved Azerbaijan Technical University and the Chair of AzC IFToMM was appointed Doctor of Technical Science, Professor Rasim Alizade.

AzC IFToMM has performed first International Symposium of Mechanism and Machine Science ISMMS-2010 in Izmir Institute of Technology, Izmir Turkey, on 5-8 October 2010. The Symposium ISMMS-2010 was organized by Azerbaijan National Aviation Academy (Rector, Academician, Dr. Sc., Professor Arif Pashayev), Izmir Institute of Technology (Rector, Dr., Professor Zafer Ilken) and the Azerbaijan Committee of International Federation Theory of Mechanism and Machine (Dr. Sc. Professor Rasim Alizade). The programs of the ISMMS-2010 covered following sections of relevance to MMS, Mechanism and Machine Science: Structural Synthesis and Kinematic Architecture; Linkages, Cams, Gearing and Transmissions; Control Systems; Mechanisms of Flying and Space Machinery; Mechatronics; Robotics; Dynamics and Vibrations of Machinery; Computational Kinematic Synthesis and Analysis; Nanotechnology and Micro: Manipulators, Robots, Mechanisms.

In 2011 year, at the 13-th World Congress of IFToMM noted that 48 countries of the world are members of the International Federation for promotion of development the Machine and Mechanism Science (MMS) with the keyboard IFToMM. The science of mechanisms and machines (MMS) consider the theory of geometry, motion, dynamics and control of machines and mechanisms with the transformation and transmission of energy and information using in industry, biomechanics, in space and the environment.

AzC IFToMM 2017 International Symposium of Mechanism and Machine Science ISMMS-2017 has taken place in Azerbaijan Technical University, Baku, Azerbaijan, on 11-14 September 2017.

The programs of ISMMS-2017 cover sections of relevant to Mechanism and Machine Science:

- Manipulators and Robots.
- Kinematics and Synthesis of Mechanisms.
- Dynamic of Machines.
- Transport Vehicles.

Key lectures

Oussama Khatib

PROFESSOR IN THE SCHOOL OF ENGINEERING

Robotic Laboratory, Department of Computer Science, Stanford University, Stanford, California, USA.

Oussama Khatib received his PhD from Sup'Aero, Toulouse, France, in 1980. He is Professor of Computer Science and Director of the Robotics Laboratory at Stanford University. His research focuses on methodologies and technologies in human-centered robotics including humanoid control architectures, human motion synthesis, interactive dynamic simulation, haptics, and human-friendly robot design. He is a Fellow of IEEE. He is Co-Editor of the Springer Tracts in Advanced Robotics (STAR) series and the Springer Handbook of Robotics, which received the PROSE Award for Excellence in Physical Sciences & Mathematics. Professor Khatib is the President of the International Foundation of Robotics Research (IFRR). He has been the recipient of numerous awards, including the IEEE RAS Pioneer Award in Robotics and Automation, the IEEE RAS George Saridis Leadership Award in Robotics and Automation, the IEEE RAS Distinguished Service Award, the Japan Robot Association (JARA) Award in Research and Development, and the IEEE Technical Field Award.

Ocean One: A Robotic Avatar for Oceanic Discovery

Oussama Khatib
Robotics Laboratory, Department of Computer Science
Stanford University, Stanford, California, USA
E-mail: ok@cs.stanford.edu

Abstract

The promise of oceanic discovery has intrigued scientists and explorers for centuries, whether to study underwater ecology and climate change, or to uncover natural resources and historic secrets buried deep at archaeological sites. The quest to explore the ocean requires skilled human access. Reaching these depth is imperative since factors such as pollution and deep-sea trawling increasingly threaten ecology and archaeological sites. These needs demand a system deploying human-level expertise at the depths, and yet remotely operated vehicles (ROVs) are inadequate for the task. A robotic avatar could go where humans cannot, while embodying human intelligence and intentions through immersive interfaces. To meet the challenge of dexterous operation at oceanic depths, in collaboration with KAUST's Red Sea Research Center and MEKA Robotics, we developed Ocean One, a bimanual force-controlled humanoid robot that brings immediate and intuitive haptic interaction to oceanic environments. Teaming with the French Ministry of Culture's Underwater Archaeology Research Department, we deployed Ocean One in an expedition in the Mediterranean to Louis XIV's flagship Lune, lying off the coast of Toulon at ninety-one meters. In the spring of 2016, Ocean One became the first robotic avatar to embody a human's presence at the seabed. This expedition demonstrated synergistic collaboration between a robot and a human operating over challenging manipulation tasks in an inhospitable environment. Tasks such as coralreef monitoring, underwater pipeline maintenance, and offshore and marine operations will greatly benefit from such robot capabilities. Ocean One's journey in the Mediterranean marks a new level of marine exploration: Much as past technological innovations have impacted society, Ocean One's ability to distance humans physically from dangerous and unreachable work spaces while connecting their skills, intuition, and experience to the task promises to fundamentally alter remote work. We foresee that robotic avatars will search for and acquire materials in hazardous and inhospitable settings, support equipment at remote sites, build infrastructure for monitoring the environment, and perform disaster prevention and recovery operations- be it deep in oceans and mines, at mountain tops, or in space.

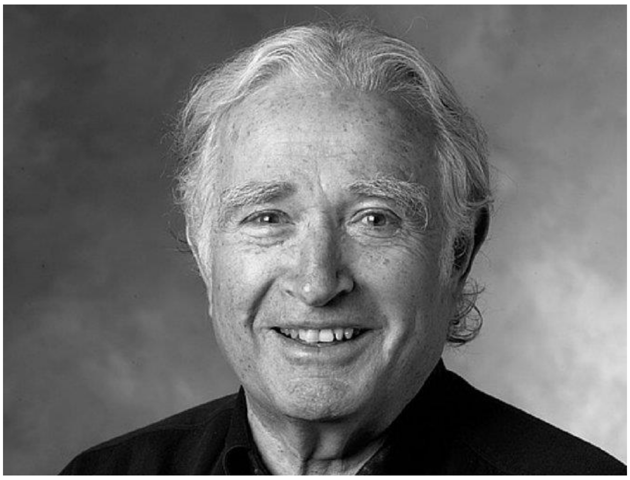

Bernard Roth
PROFESSOR IN THE SCHOOL OF ENGINEERING
Mechanical Engineering Department, Stanford University, USA.

Roth is one of the founders of the Hasso Plattner Institute of Design at Stanford (the d.school) and is active in its development: currently, he serves as Academic Director. His design interests include organizing and presenting workshops on creativity, group interactions, and the problem solving process. Formerly he researched the kinematics, dynamics, control, and design of computer controlled mechanical devices. In kinematics, he studied the mathematical theory of rigid body motions and its application to the design of machines. All publications – 2016: Books and book Chapters-26; Journal articles-113; Conference Procceding-77.

Teaching Courses in 2016-2017 academic years: Advanced Kinematics; Mechanical Engineering Design; The Designer in Society; Transformative Design.

Design Process as an Educational Tool

Bernard ROTH
Stanford, CA 94305, USA
E-mail: broth@stanford.edu

Abstract

The design thinking methodology is different in basic ways from traditional educational methodologies. It is learning by doing, i.e., problem based learning. The students learn by working on real-world problems. Our philosophy is that a lot of good learning can be obtained by doing something real while you are in still not "fully prepared." We put a lot of emphasis into problem definition. Getting a deep understanding of who the solution is for is a very important part of our process. We call this user a user centered approach. For the past thirteen years, we have been providing design thinking classes to graduate and undergraduate students, and been running workshops for professionals and organizations. This paper will present some examples that reveal the power of our methods to solve difficult problems in the university and in industry and to change people's lives.

Keywords: Design Thinking, Projects, User-centered, Auto-inject, Six-bar.

Introduction

Traditionally education is in the main content centric. Students are expected to learn a specific set of predetermined material using a predetermined curriculum and schedule. Most of this education is done in the framework of logical thinking that deals with predefined objectives that are realized using deductive or inductive thinking. The emphasis is on rationally defined approaches to obtain specific predetermined goals. The path to the goal may be difficult and my even lead to dead ends, yet the desired goal is always in mind and it is clear when the objective is obtained.

In contrast, in a true design thinking approach, the problem gets defined as part of the solution process. In other words, the problem definition is not clear in the beginning. Part of any true design thinking process is to define the design opportunity. In a true design thinking approach both the problem and the solution are not clearly defined in the beginning. Polynesian explorers refer to such a voyage as a cone of possibility, rather than a voyage with a specific predefined destination.

Design Thinking Mindsets

The design thinking methodologies we have developed at the Stanford d.school are different in basic ways from traditional educational methodologies. They fall under the heading of learning by doing, i.e., problem based learning. The students learn by working on real-world problems. Such ideas are not new to education. The modern roots of the learning-by-doing methodology go back to John Dewey, Maria Montessori and hosts of other educational innovators. It is obvious that giving students the opportunity to do something real can be inspirational and often more effective than abstract and seemingly useless learning. Design thinking has the potential to empower students. It can move students from being passive learners to powerful creators.

Many surveys of practicing professionals have shown that skills such as making presentations, cooperating with people from different backgrounds, expressing one's ideas, as well as being able to organize and meet deadlines, are far more widely used than the specific technical content of their expertise. Design thinking projects enhance these needed interpersonal skills. For students, such projects also have the positive effect of fostering creative confidence and empowering people to live more fully committed lives.

Traditionally education is about preparing students to do things after they graduate. The d.school philosophy is that a lot of good learning can be obtained by doing something real while you are school and still not "fully prepared." We call this: having a *bias toward action.* The bias toward action manifests itself in many ways. For example, in our Launchpad class students start businesses within a very short time. They need to have launched their business by the fifth week of a ten-week class, or drop the class. The idea is not to worry things to death. Nothing will ever be perfect. Often the best way to learn is from mistakes.

Alongside a bias toward action is the mindset to *learn from failure.* Nobody likes to fail. Our students have generally been very successful, and so failure is hard for them to accept. Yet, failure can be a great gift. If you learn from failure you often can move ahead to better result than is you succeeded. One important way to learn is to test out ideas in their early stages. So, we have a strong bias to *show rather than tell* (that is doing rather than talking about it) and to try out our ideas by making quick prototypes. We call this *embracing experimentation*.

Our methodology is heavily weighted to team based learning and team based teaching. Moreover, we depend heavily on diversity in both the teaching and student teams. We call our form of team teaching and team learning *radical collaboration*.

We put a lot of emphasis into problem definition. Getting a deep understanding of how to embody *human values* is a very important part of our process. We call this user centered approach *empathy*. This is one of the most crucial mindsets. In the past engineers and other professional problem solvers, tended to deal only with other professionals and ignored the end users and the human centered aspects of their work. The idea of co-design, where the users were directly involved in the design process seemed very radical, as was also the idea of being user centered. Fortunately, nowadays there is a trend toward involving users on many levels of the solution process.

Since our methods involve gather a lot of information it is important to have a mindset for creating *clarity from confusion*

Also, it is important for people to know where they are in the design process, what comes next and what specifically they are striving for. We call this being *mindful of process.* Professionals tend to do this subconsciously. For students and other inexperienced design thinkers, it is very useful to have in mind a step by step process that gives a default answer to the question of: what do I do next?

Design Thinking Process

The two most common design thinking processes we use involves involve five or six different steps. The five-step process is usually given as: empathize, define, ideate, prototype and test. The six-step process is usually given as: understand, observe, point-of-view, ideate, prototype and test. These are virtually the same, since understand and observe are part of the process of empathizing, and point-of-view is simply one form of defining a problem. Some people use these two forms interchangeably and others prefer one or the other. In both cases, it is important to realize that nobody is talking about a linear ordered set of steps. In practice, steps may come in any order and be repeated several times during any pert of the process. The process is best taken as a nominal guide, and a fallback position as to what to do when it is not clear what the best next step is.

For beginning students, the idea of a step-by-step process forms a good guide in how to approach a problem and move from problem definition through to a final solution. It is also a good pedagogical device to break the solution process into discrete steps. In that way, each step can be learned and practiced without the need to go through the entire design process. This is very useful in building student's skills. It is also useful for professionals seeking to develop special skills and in depth expertise in specific aspects of the process

We have found that the design thinking learning-by--doing teaching methodology is very appealing to students. It changes the classroom from a low energy, passive, learning environment into a highly charged fully participatory situation.

In traditional education, a professor "teaches" the students. The students "learn" the material. The goal is that after graduation the students will be able to apply their learned knowledge to real-world problems. Whereas in a design thinking educational setting the goal is for students to get engaged and confident in their innovation process at the current time. This goal is accomplished by project based learning, in which the students go through a design thinking process while practice radical collaboration in a culture of prototyping. The faculty's main role is to act as coaches that create situations where the students are the experts. The students get exposed to different faculty points of view due to the diversity of backgrounds within each teaching team.

Our learning by doing culture involves relatively little formal lecturing. We move students quickly to complete immersion in a problem by insisting that they incorporate a human centered viewpoint. After taking as much time as is necessary to make sure we have a good problem statement (we call it point-of-view), we move rapidly into the ideation phase by use of sketches, lists and prototypes.

Human Centered Design-Empathy

One of the strongest aspects of design thinking is that it is human centered. A human centered designer needs to be truly empathetic to the people being designed for. Most professionals are basically not empathic to the people they are supposed to be providing for. This may seem strange, yet it is frequently the case. For example, most professors believe they know better than students what the students need. Doctors feel they know better than patients what the patients' needs are. And so on in virtually every profession. In general professionals talk to their peers, who are other professionals. On those occasions when consumer interest is explicitly considered, it is done on a macro scale by using anonymous surveys or focus groups. In human centered design thinking, the emphasis is on finding implicit human needs by carefully observation and in depth engagement with individual people. Often instead of looking for "average" people, we are looking for the outliers, the so-called extreme users. These are the people that lead to insights that can yield truly new and amazing solutions.

A good example of human centered design is given by the development of an automatic injection mechanical system for people that take periodic injections of a given dose size. Such regular dose size treatments are often used by Rheumatoid Arthritis and Multiple Sclerosis patients. By doing extensive interviews and watching people's actual behaviors designers deduced several valuable guidelines for the mechanism synthesis phases of their designs. For example, they learned that people have lengthy routines as they target an injection and work up the resolve to insert the needle. A person with Rheumatoid Arthritis used the needle tip to probe around and identify an injection target. After she chose the spot, she took a couple practice swings for courage, then missed and inserted the needle close by. She would like to be able to aim better and to be able to compose herself before starting the injection, confident that the needle will go where she expects it to go.

A person with Multiple Sclerosis made a paper "clock" to help rotate through injection sites on her thigh. She lined the clock up with a freckle and then worked her way around the clock, targeting a different "hour" for each day's injection. She tried to build up her courage (sometimes with wine), took practice swings, closed her eyes, and then inserted the needle knowing that she would inevitably miss her target. She had built up a ritual around control and targeting, even though it was not achievable with the tools she was using.

The design team built prototypes to test the hypothesis that a stable base with site visibility and a needle that is retracted prior to injection would help people feel more confident. The prototypes began as syringe accessories, with the first being a two-part tool: literally a puck-like "site" or guide piece that interfaced with a separate "inject" piece.

The team observed the benefits of being able to move the prototype around freely, to then hold it stably in place while still having the option of changing your mind, and to then start the injection without disturbing the device from its targeted position. For people with compromised or unsteady hands, this design offers ergonomic advantages. For everyone, the anxiety that comes with inserting the needle can be deferred, as the stakes feel low while the injection part is being positioned and repositioned.

This approach works best when the act of placing the device on the skin is not what either unlocks or triggers the injector. From this the concept arose that auto injectors have clear bases to help target the injection. This allows for the auto injector to be repositioned on the skin and then held stably on an injection site while a user gets ready to trigger the injection.

The designers chose to work on populations that require injections on a weekly up to a monthly basis of fixed drug volumes from 0.2mL to 3mL delivered subcutaneously about 6mm deep. Furthermore, given the drug's refrigeration requirements, they restricted themselves to full dose injections.

The actual mechanism for automatic injection and needle retraction is quite complicated, as seen in the patent application figure bellow It turned out that only engineers are interested in seeing it. So, the final design had the mechanism covered by labels with product information.

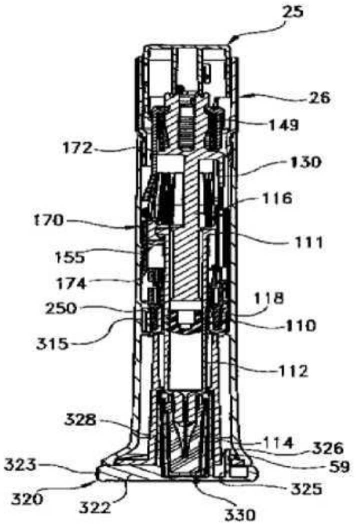

Fig. 1. Patent drawing of automatic injection device The patients are mainly interested in seeing the drug flow out and being assured it has all been injected. In the photo below, the auto-injector on the left shows the mechanism. It is purposely covered first as shown in the center and ultimately as shown on the right. So, that only the bottom part of the auto-injector is left transparent and the patient can see the piston pushing the drug out of the syringe

Learnings from watching patients deal with prototypes led to making it so the patient does not see the needle and does not need to apply force to actuate. The injections activate automatically after a short delay once the patient has rotated the top form the lock to the unlocked position. Since patients were concerned about wasting very expensive drugs, the bottom is left transparent so the patient can visual confirm that the actuation entirely empties all the medicine.

A classic example of both how a lack of empathy can lead to troublesome results, and how incorporating empathy can lead to amazing results comes from Doug Dietz, a senior designer at GE Medical. Doug's group designed an MRI machine to be used to examine children. The group worked in the usual professional way. They talked to other design engineers and scientists. They talked to customer engineers, and to doctors and hospital administrators. They talked to everyone but the patients!

They completed a very professional looking machine, and it was successfully marketed to hospitals and clinics. After some time, Doug decided to visit a local clinic and see the machine in operation. When he identified himself to the nurses they heaped praise on him about how well the machine worked. He felt elated. Then a child was dragged in screaming by his mother, and the nurse asked Doug to leave since they had to sedate the child to get him into the MRI machine. Doug soon learned that to use his machine approximately 85% of the children had to be sedated. It made him feel terrible.

Fig. 2. The injection mechanism fully visible, and partially and fully covered

Ultimately Doug realized he had not been practicing human centered design. Acting on his realization he formed an advisory group of children that were chronic patients. He also consulted children's museums, child psychologists and parents. The result was a reframing of the experience. Instead of a medical procedure he made the MRI machine the center of an adventure. He made comic books showing the idea of seeing inside your skin and sent them to the children in a knapsack two days before their examination. Mainly though he had the room and MRI machine repainted. One adventure had the room painted so that the machine was part of a pirate ship, and the child had to hold still lying on her back so the prates would not find her. Another adventure involved holding still looking up at the stars.

With the adventure series, the sedation rate dropped to less than 2%. Some children were heard saying: "mommy, can we come back tomorrow?" When you look at the original MRI machines with the eyes of a child, it becomes clear how getting into the machine could seem like crawling into the mouth of a metallic monster. Empathy for his users allowed Doug to see his design with the eyes of a child.

Culture of Prototyping

A useful way to check if you have a good POV is make small tests. Think of these tests as prototypes. People often use the term “mock-up” to indicate a quick prototype. I prefer the term “crap-up” to indicate an even simpler and quicker form of prototype. The noun “prototype” implies a formal model of some complete object. So, for our purposes, it is best to think in terms of the verb “to prototype.”

Useful simple prototypes quickly give you some important information. A classic example is the surgical tool configuration put together for doctors by IDEO. It is made from a clothes pin, a film container, a marker and some scotch tape.

Fig. 3. Prototype of surgical tool

Two less traditional prototype that were created by Stanford students are a simulated bicycle accident, used to get information about bike safety design, and the game of *musical chairs*, used to test ideas for the design of the airline *Jet Blue's* customer callback system. These are shown here:

Fig. 4. Prototype of bicycle accident

Courses and Workshops

The scale of our activity has grown each year. This year at the Hasso Plattner Institute of Design at Stanford we offered over 70 interdisciplinary courses of which half were regular 10 week long classes and half were shorter length “popup” courses. Over 1,000 Stanford students attended these classes, and over 900 Executives and Educators participated in special short term workshops and trainings.

Fig. 5. Prototype of call-waiting experience

Our classes are all project based. A few courses have been offered regularly. While many others tend to only be offered for several years. All our courses tend to change each time they are offered. Our longest standing class is the two-quarter sequence now called *Design for Extreme Affordability*. The class generally has forty students that are divided into 10 teams of four. As of 2017, the class has been offered for 13 years. There have been 120 projects for 21 Countries, of these 33 are still in the market. Two of the early projects have received a lot of publicity due to the social good they have bought. They the *d.light* and *Embrace* projects, described below.

d.light is a for profit company that makes affordable solar powered LED task lights. Since kerosene and candle lighting are dangerous, toxic and relatively expensive, the students felt there was a strong need to replace them with solar powered lighting in areas that do not have electricity. The success of their concept can be seen by the following cumulative results, as of May 31, 2017: 75 million lives empowered; 5.8 billion dollars US saved in consumer energy costs; 19 million school aged children serviced; 26 million tons of CO2 offset; 40 billion productive hours created from darkness.

Embrace is a not for profit company that manufactures and markets a lifesaving baby warmer. Premature and other low body weight babies need to be kept warm or they will die. The students realized that in rural areas the traditional hospital incubators are basically ineffective. Firstly, they are too expensive and require a dependable supply of electricity. Secondly, the incubators that do exist in poor countries are in cities and are too far for mother in rural areas to get their babies to the lifesaving incubators in time. The students invented an inexpensive sleeping-bag like device that relies on a removable bladder containing a wax like substances that melts under heat and maintains body temperature for at least 4 hours. The heat can be supplied from boiling water and does not rely on electricity. At this writing, over 250,000 babies in 22 countries have been kept warm by *Embrace*.

One Stanford student was so inspired by *Embrace*, that when he learned that babies die or have lifelong disabilities due the lack of a blue-light therapy for jaundice, he stopped out of school for a year to develop a blue-light LED based inexpensive device, he named Brilliance, which has now been sold to over 20 countries and been used to treat over 250, 000 babies.

This year there was a project that led to the development of a linkage for use in manually tamping dirt floors in Rwanda. The students found that homeowners who aspire for a more dignified, healthier living space need an accessible, affordable way to build a floor. Currently, the skilled labor required for the compacting process makes the installation price unaffordable and serves as a deterrent do-it-yourself construction. The floors are built by adding a top layer of sand and sealant to a gravel base that is compacted into a rigid subsurface by a hand-held ram that needs to be repeatedly smashed into each small section until the subsurface is rigid enough to support a thin layer of cement. This preparatory work is very labor intensive, and the most expensive part of the entire floor building process.

To accommodate the need to reduce the cost of the tamping process, the students developed a planar 6-bar linkage composed of a slightly offset slider-crank 4-bar and a dyad that drives the slider crank's coupler. The device is meant to be powered by the operator's foot, although hand operation is also possible. and Fig. 6. shows a skeleton diagram of the kinematic structure, and Fig. 7. shows a Solid Works sketch of the device. The crank for the slider crank is link EC. It is connected to the device's base with a turning joint at E. The slider-crank's coupler link is BC, which is extended to include point D. The slider is link BA. A is the impact part of the slider which drives an 8 inch by 8-inch square base (0.2m x 0.2m) into the dirt to create the compacting.

It has been shown that the resulting compacted floors are of high quality and can be produced by reasonable expenditures of time and effort. This device a viable alternative to hand compacting in the Rwandan environment. It is currently undergoing final development in the local area where it will be fabricated and brought to market as a $50, bicycle transportable, do-it-yourself compactor. It is estimated that over a million floors will be installed in the next few using the principles embodied in this device.

Creative Confidence

Looking at such results it is easy to understand how this type of experience can deeply affect students. For many their introduction to design thinking project based learning has been life changing.

With design thinking, there is a big addition to the universe of problem solving: Now people are center stage. So, in addition to artifacts we have experiences, in addition to physical prototypes we have stories.

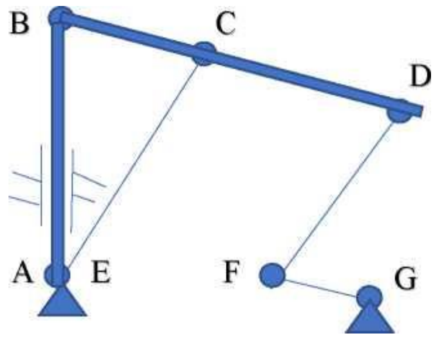

Fig. 6. Skeleton diagram of the kinematic structure action. The linkage could be hand driven by pushing on the coupler at point D. However, since foot power is more powerful than hand-cranking, the dyad composed of links DF and FG is attached to the coupler through a turning joint at D. The input torque is them obtained from stepping on a foot peddle rigidly attached to link FG next

Fig. 7. Solid Works sketch of tamping device

We say that students empowered by design thinking mindsets have increased their personal efficacy, to the point where they have creative confidence. They are imbued with a feeling of confidence that they can problem solve in a meaningful way that will improve the world around them. Traditional education, with its reliance on teachers and other experts, tends to give students a sense of inadequacy, regardless of how well they do academically. Whereas design thinking's project based experiences, with its reliance on coaches that assist students to find their own way, tend to empower students both in their outlook and their own estimation of their abilities. In this sense design thinking is a transformational educational reform.

Ali Najafov

Dr. Sc. Professor Head of Machine Design Department, Azerbaijan Technical Universty, Baku, Azerbaijan.

Professor Najafov Ali, botrn on 11.09.1961 in Tovuz, Azerbaijan. Head of departament for Machine Design of Azerbaijan Technical University. Author of more than 100 scientific works, incuding 8 patents and author's certificates. Since 1994 is chairman of the DAAD-Alumni in Azerbaijan

The scientic research of professor Najafov covers scientic areas such a strength calculations, scientific basis of design and construction, assessment of reliability and technical level of the machines, devices and equipment, the metods for the choice of the most appropriate materials for the machine parts and units providing technical requirements for their production and use, the search of selection methods of their shapes and sizes, the create and modernize of modern types of energy-efficient mechanical systems in accordance with environmental requirements and etc.

The results of some theoretical and experimental research of Professor A. Najafov were used in the oil-producing area "Absheronneft" of SOCAR. In 2013 his Eurasian patent "Three-stage double-flow cylindrical gear reducer" was awarded with the diploma of the 2nd degree in the first republican competition of the State Committee on Standardization, Metrology and Patent of Azerbaijan Republic

At the invitation of German Academic Exchange Service (DAAD), Professor A Najafov in different years worked as a researcher in some leading universities of Germany: in 1991-93 at the Ruhr-University Bochum, in 1996 and in 2005 at the Technical University of Karlsruhe, in 1999 at the Center for Nuclear Research in Karlsruhe. At the invitation of the Swiss Academy of Technical Sciences in 1996-97 he worked as a scientist-designer in MAAG Gear Co, in Zurich.

New Constructive Decision of a Mechanical Drive for Sucker-Rod Pumps for Oil Production

Ali NAJAFOV, Ayaz ABDULLAYEV,
Machine Design Department of Azerbaijan Technical University,
H.Javid ave 25, AZ1073 Baku, Azerbaijan.
E-mail: ali.najafov@rohe.az

Abstract
In this paper is new constructive decision of beamless pumping unit with new design of 3 stage package gear on only two shafts described.

Keywords: Sucker-Rod Pump, Beamless Pumping Unit, Package Gear.

Introduction

In oil-producing countries the sucker-rod pumps is one of the major aggregates for the mechanized way of an oil recovery on land.

The application of the method of oil pumping begins on the Baku oil fields since 1923. The history of development of pumping units is well recognized in stages to improve their standards. Without considering the first samples, which had a wooden rocker and outdoor gear, it can be said that their development as a serious engineering products, began with the creation of the design, the parameters of which were regulated by the standard of "pumping unit" (GOST 5866). Worldwide the parameters of pumping units are regulated by the standard of the American Petroleum Institute Specification for Pumping Units Spec HE API. At present in Azerbaijan is valid the last edition of Interstate Standard developed by the Azerbaijan Scientific-Research and Design Institute of petroleum engineering (AzINMASH) in 1998 and harmonized with Spec HE API.

But in split of almost 90-year history of pumping unit is a fairly conservative set of equipment, the basic design elements of which are not changed for the past many ten years.

As in the time of the Nobel Brothers activity in Azerbaijan, which despite resistance from the conservative oil companies and dealers have implemented many of his revolutionary ideas such as pipeline transportation of oil, oil storage in steel tanks and many others, without modern oil industry is impossible and now has to contend with the still ongoing conservatism of oil companies who do not want to change anything in the equipment for the oil extraction.

Now issue of standard sucker-rod pumps makes several ten thousand a year and provides security of maintenance of all funds of oil wells. However the low efficiency, the big expenditure of the electric power, an incomplete construction of driving gear and reformative mechanisms, impossibility of use in existing aggregates of electric motors with a rotation high frequency lead to research of more perfect construction of a mechanical drive of sucker-rod pumps-MDSRP [1, 2].

One of essential deficiencies of known MDSRP (beam pumping unit) is that at the big traverse stroke, except increase in a dimension of the machine tool; raise as well the sizes of a beam head. At the usual beam with application of an arc beam head the span arrow in any position of the mechanism is organized.

Operation of the deep pump at each movement plunger up and downwards is accompanied by change of a direction of movement of pump rods and transition through some positions (dead points) with zero speed that should vary during one cycle of operation of machine on magnitude and a direction. As a result the "bifurcation" - an exit of the linkwork from a dead point has important value at start-up and machine stopping. At that dynamic loads on rods depend on magnitude of speed and acceleration which are drastic shown at descent of pumps to the big depths. As rods are set in motion by sucker-rod pump, operation of the deep pump essentially depends on the law of movement of a suspension bracket polished rod. Thus laws of movement of a suspension point of rods for an ideal case are simple harmonic functions accordingly for a path - a cosinusoid, speeds - a sinusoid, accelerations - a cosinusoid with amplitudes r, $r\omega$, $r\omega^2$. However, in an existing construction of the sucker-rod pump the real law of change of a path, speed and acceleration of suspension point of rods considerably differs from the simple harmonic.

Execution of a driving gear of an existing MDSRP with use of a double-reduction gear unit of classical execution demands application of electric motors of the big power with the lowest rotational speed and efficiency. It essentially augments its overall dimensions, reduces reliability and efficiency.

Method of solution

Department of «Machine parts» of Azerbaijan Technical University is developed, made and tested essentially new constructive decision of a mechanical drive for sucker-rod pumps (fig.1). Thus execution of the reformative mechanism as slide-crank mechanism with the embedded planetary gear, which has the changing laws of a path, speed and acceleration of suspension point of rods closest to theoretical laws and a bifurcation, allows reducing of the beam in this mechanical system having rather difficult construction, [3].

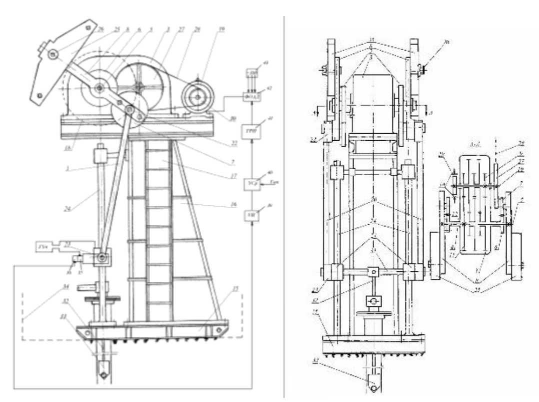

Fig. 1. The kinematic diagram of new constructive decision of a mechanical drive for sucker-rod pumps

It has been investigated the analytical kinematics of the geared linkage mechanism transforming a rotational motion of rod's suspension center of the new constructive decision of a mechanical drive for rod pumps into reciprocal , Fig.

2. It is made the estimation of deviation of the real maximum speeds and accelerations from the maximum speeds and accelerations of ideal harmonic motion of suspension center of rods of a mechanical drive for sucker-rod pumps.

By the kinematic calculation is determined a connection between displacement of an initial link - crank with the displacement, speed and acceleration of a driven link – suspension bracket of a rod of MDSRP [4, 5]. Here $s_c = s_0 / l,\ \lambda = r / l$ - are parameters of the transforming mechanism on which variable kinematic parameters of the given mechanical system depend. As an independent variable is set the rotation angle of the crank φ.

In the construction of modern beam-pumping units (fig. 2, a) the crank and the connecting rod on the both extreme positions lie on the straight line, that passes through the rotation center of the crank. However, the real displacement of the plunger of the deep-pump performed by the common pumping units, as a rule, does not correspond to the made demands. As a main cause for this are considered elastic deformations of the bars and rods, that are formed as a result of impose of variable in magnitude loads, influence of the inertial forces of flowing liquid masses and pumping bars, which substantially depend also on significant difference between laws of variations of way, velocity and acceleration of rod's suspension point in common beam-pumping units and simple harmonic laws.

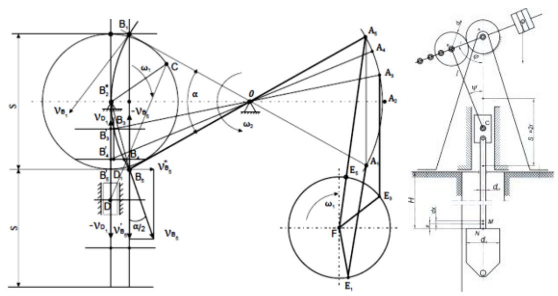

a) b)

Fig. 2. Kinematics of the normal pumping unit a) and of the new constructive decision of a mechanical drive for sucker-rod pumps b)

And the execution of the transforming mechanism as a slide-crank mechanism in new constructive design of sucker-rod pumps (fig. 2, b) with the embedded planetary gear possessing the laws that are particularly close to the theoretic laws of variation of way, velocity and acceleration of rod's suspension point, and bifurcation enables to eliminate the beam in the present mechanical system, that has a relatively compound construction and leads to increase of the overall dimensions of the system. This way friction losses in kinematic pairs decrease, and stroke of wellhead rod's bracket by oil extraction takes place in a wide range due to theoretically derived laws of motion of rod's suspension point respectively co sinusoid - for way, sinusoid - for velocity and co sinusoid - for acceleration with the amplitudes r, $r\omega$ and $r\omega^2$ of mechanical drive of well pumps.

Compared with beam-pumping units the developed beamless pumping unit has more reliability and infallibility, because it lacks such weak links as swivel beam head and its supporting nodes. The pumping unit equipped with the developed transforming geared linkage mechanism has better dynamic behavior because the crank rotates uniformly, there are not significant unbalanced masses and acting on the base horizontally directed alternating forces that are characteristic for beam-pumping units. Since the beam head with the beam is replaced by the fixed base with the positioned guide gear wheel, better centering with the wellhead is ensured.

It is established, that dynamic loads in rods depend not only on value and the variation law of acceleration, but also on motion speed of suspension center of rods at the moment of motion of plunger up. Therefore it is necessary to find deviation of the kinematic parameters characterizing qualities of the new constructive decision of a MDSRP. In this connection as qualitative parameters of state of this mechanical system are accepted the deviations of the real maximum speeds and accelerations from the maximum speeds and accelerations at ideal harmonic motion [4]:

$$\chi_v = \frac{(v_c)_{\max}}{(v_c)_u} = \frac{\sin(\varphi+\psi)}{\sin\varphi\cos\psi}, \quad (1)$$

$$\chi_a = \frac{(a_c)_{\max}}{(a_c)_u} = \frac{1}{\cos\varphi}\left[\frac{\cos(\varphi+\psi)}{\cos\psi} + \lambda\frac{\cos^2\varphi}{\cos^3\psi}\right] \quad (2)$$

here $(v_c)_u$, $(a_c)_u$ - are accordingly the maximum speed and the maximum acceleration at ideal harmonic motion of rod's suspension center of the given mechanical system.

For definition of rotation angle of the crank corresponding to the maximum values of speed and acceleration of a suspension center of rod the derivative of the expressions (1) and (2) is equated to zero. The change pattern of speed and acceleration of suspension center of rod of sucker-rod pumps depending on rotation angle of crank is presented in the Fig. 3 [4].

It is established, that by using of the new constructive decision of a MDSRP the deviation of the real maximum speeds and accelerations from the maximum speeds and accelerations at ideal harmonic motion depending on a parameter value λ makes 2-7 %. That testifies expediency of use of the new constructive decision of a mechanical drive (sucker-rod pumps) at an oil recovery.

Thereby, comparing with the proposed construction of the new construction decision of mechanical drive for sucker rod pumps, plunger of the deep-well pump of common pumping units is staying at the lower and upper dead points longer for the time *t**, that can lead to the anticipatory deterioration of pump's plunger because of the ingress of big amount of sand into the cavity of pump's cylinder or incomplete use of whole capacity of the cylinder because of the ingress of condensate gases and oil displacement [5].

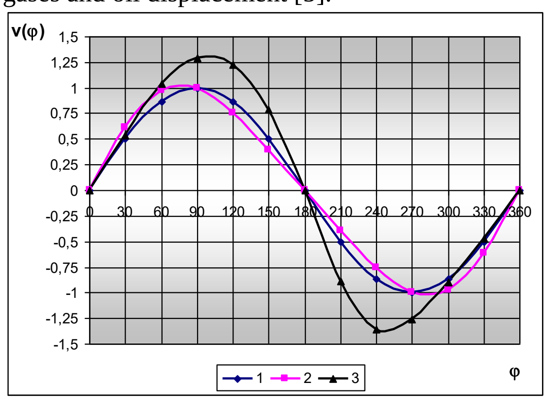

a)

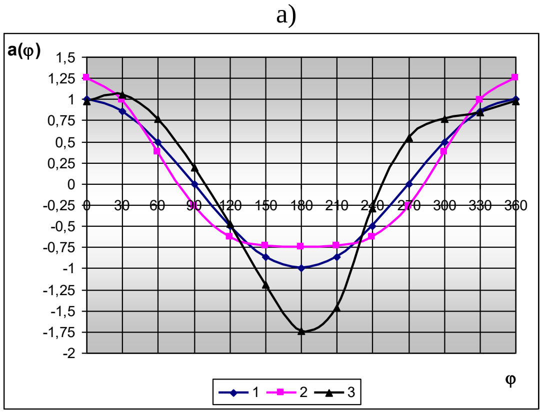

b)

Fig. 3. Change pattern of speed (**a**) and acceleration (**b**) of suspension center of rod of sucker-rod pumps depending on **φ** : 1, 2, 3 – respectively for ideal harmonic motion, for new constructive decision, for existing construction

Approaching of the laws of variation of way, velocity and acceleration of rod's suspension point of new constructive decision of MDSRP to the harmonic laws decreases additional dynamic load caused by rods' vibrations and also inertial loads on the rods, which undoubtedly will increase their durability [6].

Use in the new constructive decision of a mechanical drive for sucker-rod pumps as a driving gear of AN-reducer diminishes its overall dimensions, friction losses in kinematic pairs, and allows receiving practically any quantity motion of a suspension bracket of a rod at an oil recovery [7].

During the full cycle of operation of the deep pump, the rod suspension point is loaded unevenly, which is accompanied by uneven energy consumption during each cycle. When the plunger moves upwards, work is done to raise the bars and liquid, and when the plunger moves down the bars are lowered by their own weight and, thus, the engine is unloaded. Such a load fluctuation requires the use of high power engines in the drives of sucker-rod pumps with extremely low efficiency.

One of the basic requirements that the kinematic scheme of the sucker-rod pumps must satisfy is to maintain the same average speed when the rod suspension point moves up and down. In other words, the time taken to move up and down should be the same. For this purpose, a normal crank-slider mechanism is used as the transforming mechanism in the new design solution of the beamless sucker-rod pump. Obviously, in this case, the rate of change of speed is equal to one, that is, it is ensured that the average velocity is maintained when the rod suspension point moves up and down. At the same time, the kinematic height - the distance from the center of the crank's rotation to the lower boom suspension point of the new design of the mechanical drive of rod pumps, is equal to the sum of the lengths of the crank and connecting rod, which depend on the stroke length S and λ.

In the sucker-rod pumps for oil production, applying an additional load of dynamic nature to the static load associated with the beginning of the movement of the liquid column and the lower end of the rod string at the end of the deformation period during the upward motion leads to the appearance of elastic oscillations in the rod string. In this case, the additional dynamic loads arising in each of the sections of the rod column vary with time according to a certain periodic law, and, owing to the resistances, the amplitude of these oscillations gradually decreases. The lower end of the rods is driven by the finite speed of the rod suspension point with the end of the unloading period at the end of the deformation at the last downward stroke. There are elastic oscillations of the rod string. It is obvious that for a certain diameter of the pump and the depth of its descent, the maximum dynamic load depends on the speed and acceleration of the rod suspension point at the end of the initial rod deformation period for a certain pumping regime (stroke length and number of oscillations) dimensions of the crank and connecting rod.

The study and evaluation of the real values of the dynamic loads that take place under various operating conditions of a deep-well pump are of practical interest. A comparative evaluation of the output parameters of the SKD-7 rocking machine and the new design of the MDSRP is given in Table 1. In Fig. 4 shows the nomogram for determining the maximum dynamic load on the rods of borehole pumps, depending on the dimensionless parameters characterizing the ratio of the diameter of the plunger and the pipe to the diameter of the rod.

Table 1.

Name of the parameters	Name of the equipment	
	Sucker-rod pump SKD-7	New design of MDFSP
S_c, m	3	3
H, m	1345	1345
d_H, mm	56	56
F_{cT}, N	62000	62000
n, min^{-1}	12/9	12/9
υ_c, m/s	1.81/1.355	1.45/1.088
a_c, m/s^2	1.12/0.628	0.9116/0.5128
F_c^i, N	136,00	110,00
F_{vib}, N	1680,00	1085,00
F_g, N	1816,00	1195,00
F_{max}, N	8016,00	7395,00
F_g / F_{max}	0.227	0.1616

Currently the authors have designed sucker-rod pumps with transforming slide-crank mechanism with the embedded planetary gear (fig. 4), proposed various designs of beamless pumping units with toothed slide-crank transforming mechanism, carried out the industrial test of package gear in the oil fields of island “Pirallahy” near Baku (fig. 5).

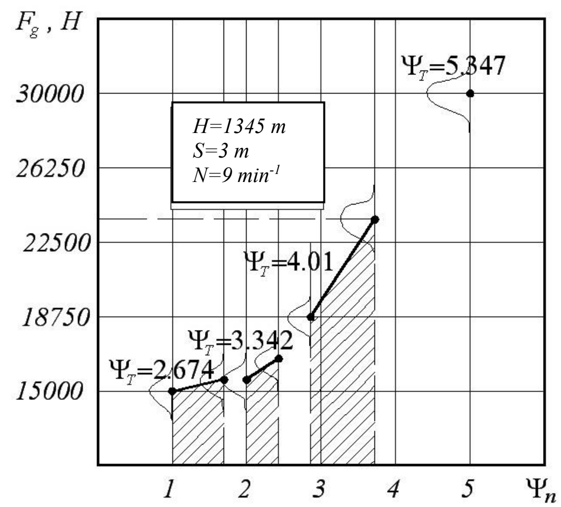

Fig. 4. Nomogram of determination of the maximum dynamic load on the rods of borehole pumps

Gear execution multistage, placed on two shafts practically with an unrestricted reduction ratio, gives the chance to diminish amount of belts, and also a reduction ratio of V-belt drive and by that overall dimensions, and consequently also metal consumption of plant at preservation of functionality of a mechanical drive rod pumps.

Fig. 4. A prototype of new constructive decision of a MDSRP with three stage package gear (U_Σ=64)

Fig. 5. Industrial test of sucker-rod pumps SKD 3-1.5-710 with three stage package gear (U_{Σ}=64) in the oil fields of island "Pirallahy" near Baku

Prominent feature of the last is that is ensured energy supply at the expense of use of electric motors of low power with the big rotational speed, the amount of constructive elements is diminished and by that reliability of the this mechanical system is augmented.

Comparing with classical multistage gears the AN-reducers have following specific advantages:

- possibility to getting very high gear-ratio;
- small dimensions;
- higher efficiency;
- high reliability and higher technical level;
- absence of countershafts;
- saving of energy supply.

As a basic kinematical schema of AN-reducer was chosen three- and fife-stage schemas where influence of rotation direction of double gear blocks are favorable for the loss of enhancements and increasing of efficiency of it [8].

Due to exclusion of countershafts on frictionless bearings the reliability level of AN-reducer in comparison with classical gears is higher up to 7.5 %.

Thanks to exclusion of pair of frictionless bearings the efficiency of AN-reducer increased up to 4.5 % [9].

Based on derived results was established, that the technical level of engineered AN-reducer is comply with the modern world gears models [10].

Conclusions and results

It is established, that by using of new design of beamless mechanical drive for sucker-rod pumps the deviation of the real maximum speeds and accelerations from the maximum speeds and accelerations at ideal harmonic motion makes 2-7 %.

With the use of a new design of beamless mechanical drive for sucker-rod pumps, the relative magnitude of the dynamic load (on average by 28.8%) and the maximum load at the suspension point of the rods are significantly reduced in comparison with the common beam-pumping units.

References

1. Aliverdizade K.S. Technology and technique of oil and gas recovery, Moscow/Russia, 1971, p.172.
2. Rohlin S.M., Ryzhenkov I.I., Fetisov A.A. Economy of rational use of oil resources of bowels. Moscow/Russia, Nedra, 1991, p.236.
3. Abdullayev A.H., Najafov A.M. Mechanical drive of sucker-rod pumps / Patent 012103, F04B 47/02, EAPO, Moscow/Russia, Bulletin 4, 2009, p.4.
4. Abdullayev A.H., Najafov A.M. Analytical kinematics of the geared linkwork of the new constructive decision of a mechanical drive for sucker-rod pumps // Azerbaijan oil industry, Baku/Azerbaijan, №4, 2006, p.52-56.
5. A.Najafov, A.Abdullayev, Y.Yaqubaliyev. Research of Velocity and Acceleration of Suspension Point of new Constructive Decision of a Mechanical Drive for Sucker-Rod Pumps // Int. Simp.of mech & Mach. Science 2010, AzCIFToMM-Izmir Inst. Of Tech. 5-8 Okt. 2010, Turkey.
6. Abdullayev A.H., A.Albers, Najafov A.M., Estimation of inertial load in new constructive decision of mechanical drive for sucker-rod pumps//Azerbaijan oil industry, Baku/Azerbaijan, № 9, 2006, pages 46-49.
7. Abdullayev A.H., Najafov A.M. Three-stage double-flow cilindrical gear / Patent № 017053 B1, F16H 1/20 ЕАПО, Moscow/Russia, Bulletin № 9, 2012, p-4.
8. Najafov A.M. The exploratiry designing of mechanical drive of succer-rod pumps. Saarbrücken/Germany, "Palmarium Academic Publishing", 2013, p-149.
9. Najafov A.M. The theoretical evaluation of influences of friction bearing to the efficiency of package gear // Herald of Machinery, Moscow/Russia, №3, 2010, p. 19-21.
10. Abdullayev A.H., Najafov A.M. The qualitative assessment of technical level of package gear // Herald of Machinery, Moscow/Russia, №12, 2008, p. 6-9.

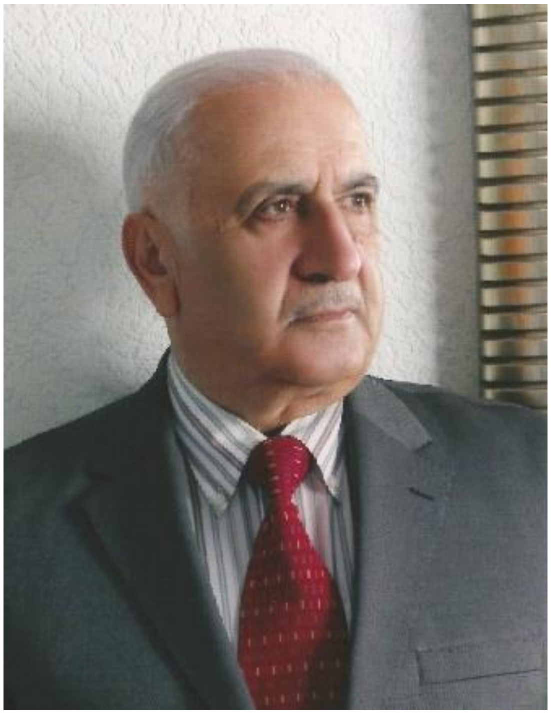

Rasim Alizade

Professor, Dr. Sc., Chair of AzC IFToMM, Head of Mechanism and Machine Theory Department, Azerbaijan Technical University, Baku, Azerbaijan.

Prof. Rasim ALIZADE is Chair of Azerbaijan Committee and Member of Technical Committee for Linkage Mechanisms and Mechanical control of the International Federation for the Promotion Mechanism and Machines Science, IFToMM, which regroup 47 countries. He devoted 50 years to the further promotion of theoretical base for the Structural and Kinematic Analysis and Synthesis of Spatial Linkages and Manipulators. He is a member of Editorial board IFToMM Journal APPLIED MECHANICS and deputy chief editor of International Journal Machines Science foundered by Ministry of Education of Azerbaijan Republic and was Chair of the International Symposium of Mechanism and Machines Science – AzCIFToMM October 2010, Izmir, Turkey. Under Prof. Rasim ALIZADE's leadership, there are scientific schools in the Theory of Mechanism and Machines in Azerbaijan and Turkey.

He studied Mechanical Engineering Sciences at Kharkov Transport Engineering Institute, Ukraine, then he was awarded Engineer Diploma – B.S. and M.S. degrees (1960-1965). His graduate study was carried out at the Mechanical Engineering Scientific Institute, Academy of Science USSR, Moscow, in the laboratory of Analysis and Synthesis of Mechanisms where he received the Ph.D degree in Theory of Mechanism and Machines Science (1968). R.ALIZADE was awarded IREX Foundation Postdoctoral Fellowship to conduct Kinematic Analysis and Synthesis studies in the Mechanical Engineering Departments at the Rensselaer Polytechnic Institute, Troy and at the Columbia University, New York, USA (1973 – 1974). He was also awarded by Fulbright Foundation and invited as Visiting Professor to the Department of Mechanical Engineering, Florida University, Gainsvilly, USA (1981). Then he was also invited as Visiting Professor to the Mechanical Engineering Department of Beijing Astronautic and Aeronautic University, China (1989 – 1990). His second scientific work "Kinematic Analysis and Synthesis of Spatial Linkages" was carried out at the Kazakhstan State University, Almaty (1992) for the Doctor of Technical Science degrees (Dr.Tech.Sc.) in the Theory of Mechanism and Machines Science.

Doctor Technical Science Rasim ALIZADE previously served as a Head of Textile and Food Machines Department (1970 – 1978), Dean of Mechanical Engineering Faculty, Dean of Robotic Engineering Faculty (1979 – 1990), Vice Rector (1991 - 1992), Head of Theory of Mechanism and Machines Department (1993 – 2001) at the Azerbaijan Technical University, Professor of Mechanical Engineering Department at the Izmir Technology Institute (2002 – 2013), Izmir, Turkey, Professor of Flying Apparatus and Aviation Engines Department at the Azerbaijan Aviation Academy (from 2014 still today) and Head of the Theory Mechanisms and Machines Department at the Azerbaijan Technical University (from November 2015 still to day). His research interests in this period were further development of Screw Theory, Structural and Kinematic Synthesis of Mechanisms, and Kinematic Analysis of Robot Manipulators.

In 2002 Prof. R.ALIZADE has been invited to the Mechanical Engineering Department of Izmir Institute of Technology, Turkey. He has taught courses in Engineering Design: Theory of Mechanism and Machines I-II; Kinematic Analysis of Mechanisms; Structural Design of Robot Manipulators; Kinematic Geometry of Robots; Synthesis Problems of Manipulators. The main research area in Robotics with the Ph.D graduate Turkish students are the application of the Screw Theory to the Structural and Kinematic Analysis and Synthesis of Overconstraint Robot Manipulators. Twelve scientific specialists from Turkey and Azerbaijan got degree of Ph.D under the guidance of Prof. R.ALIZADE. He is an author of eight inventions and more than 100 scientific papers.

Proceedings of the International Symposium of Mechanism and Machine Science, 2017
AzC IFToMM-Azerbaijan Technical University
11-14 September 2017, Baku, Azerbaijan

Structural synthesis of robot manipulators by using screw with variable pitch

Rasim Alizade
Mechanism and Machine Theory Department,
Azerbaijan Technical University,
AZ 1073, Baku, Azerbaijan.
E-mail: alizada_rasim@hotmail.com

Abstract
This paper focuses on the systematic type synthesis of parallel robot manipulators by using new structural formulas based on the screw theory. New structural formulas as a total number of screw in kinematic pairs (\$), number of screws with variable pitch $(\tilde{\$})$, total number of screws that represent the contact geometry of lower and higher joint elements (t), mobility equation for robot manipulators (M), dimension of the closed loop (λ), motion of end effector of parallel manipulator (m), number degree of freedom of kinematic pairs (f), refers to find the kinematic structure of robot manipulators realizing a specified motion requirement. Twenty kinematic pairs with structural parameters $(\$, \tilde{\$}, \mathrm{f}, \mathrm{t})$ are introduced. History of six structural formulas using for structural synthesis of parallel robot manipulators from space and different subspaces are presented as a table with equations, authors, years and some commentaries. The structural synthesis approach is based on the elementary notions of screw theory. Using the proposed of structural formulas approach, families of platform manipulators are constructed from a set of structural units. This paper is appropriate for engineers with interest in robotics, rovers, space docking parallel manipulators and screw theory.
Keywords: Kinematic pair screws; Motion of end effector; Screws with variable pitch; Dimension of closed loop.

Introduction

Structural synthesis of robot manipulators is the fundamental concept in robot design. The mobility of robotic mechanical system indicates the number of independent input parameters to solve the configuration of robots. If mobility of the kinematic chain is equal to zero $(M = 0)$ and can not be split into several structural groups, we will get a simple structural group. Combining the simple platform (with $n \geq 2$ kinematic pairs) type structural groups with given actuators, we can get parallel platform type robot manipulators needed to define the location (position and orientation) of end effectors. Serial platform manipulators control the motion of the platform, which are connected each others by hinges, branches, legs and other kinematic chains going from the platforms toward the frame. Complex robot manipulators consist of independent branches and legs loops with variable general constraints $\{\lambda_k\}_2^6$. Many platform type robot manipulators use legs with variable general constraints. Therefore structural formulas are used by engineers for design the parallel and serial platform Euclidean robot manipulators with variable general constraints. Structural synthesis of parallel Cartesian platform robot manipulators consists from connecting the simple structural groups constructed in the orthogonal planes to actuators and moving platform.

The history of formulas for structural analysis and synthesis of mechanisms and robotic mechanical systems during the second half of the 19th century, the first and second half of the 20th century and the beginning of 21st century had been investigated and illustrated in the Table by 38 equations, authors, years and commentaries in the fundamental investigations[1] and in a critical review [2]. Several investigations are described a systematic approach of structural synthesis and analysis of mechanisms by using screw theory. First investigation was given by Mueller [3] , where in equations for simple structural group and for kinematic chains were used the number of screw in kinematic pairs. Voinea and Atanasiu [4] and Waldron [5] introduced mobility equation of mechanisms with rank parameter equivalent to screw system of the closed loops. The scientific investigations of structural synthesis and analysis of robot manipulators by using screw theory were more dedicated in the beginning of 21st century. Huang and Li [6] proposed a type synthesis of parallel manipulators with mobility $\{M_i\}_3^5$ by using screw theory. Fang and Tsai [7] developed a problem of structural synthesis and analysis by applying screw theory. They enumerated limb structures for parallel manipulators according to reciprocity of limb twist system and wrench system. Jin et.al. [8] are proposed the structural synthesis and analysis of parallel manipulators by using screw algebra. The design of parallel manipulators based on Plücker coordinates is examined by Gao et.al. [9]. An analytical method of using equivalent screw groups for structural synthesis of over constrained parallel manipulators is described in the study of Zhoo et.al. [10]. Kong and Gosselin $[11-14]$ proposed a new way for the type synthesis of parallel manipulators with different type of end effector motions by using screw theory and virtual chain approach.

History of formulas for structural synthesis and analysis of robot manipulators given by author at.al. are presented as 6 several equations (formulas 1-6 in Table 1) with the unique key controlling parameters. In investigation [15] the mobility number, λ, is a characteristic of an independent loop of robot manipulator. In Table 1 (formulas $\#\,1$) we have been considered mobility equation which contain mixed independent loops with variable general constraint. The history of new formula [16] about the number of independent loops was done in Table 1(formulas $\#\,2$). The number of independent loops in platform manipulators is described by the number of mobile platforms (B), the total number of joints on the mobile platforms (j_b) and the total number of branches between mobile platforms (c_b). In the paper [17] and in the Table 1.1 (formulas $\#\,3$) the number of independent loops is described as $L=C-B$, where $C=c_l+c_b$ is sum of legs and branches. A classification of parallel manipulators based on the number of mobile platforms, number of joints on the mobile platforms, number of legs and branches, and types of kinematic pairs are also presented. A new structural formulas for robots (formulas $\#\,4$ in the Table 1), working in Cartesian space, having three legs in orthogonal planes, introducing simple structural groups in space $\lambda=6$ and in subspaces $\{\lambda\}_3^5$, and connected to actuators and to the end effector are introduced. Simple serial platform type structural groups in $\lambda=3$ and $\lambda=6$ are presented also in [1]. In the study [18] new structural formulas (formulas $\#\,5\ in\ the\ Table 1$) for parallel and serial platform Euclidean robot manipulators with variable general constraints of branch loops and legs were presented. Selecting the legs of the robot manipulators as moving dyads on Euclidean planes the direct and inverse task will become easier to solve. The new proposed Euclidean manipulators have several legs, which create Euclidean motions on their own Euclidean planes. The motion of the platform is defined by three independent curves of three platform points moving on three Euclidean reference planes. The general formula for motion of platforms is given also. To create new robot manipulators, simple platform structural groups with variable general constraints were considered.

This study enunciates screw system with variable pitch for the prismatic and cylindrical joints. Applying concepts the number of independent screw, number of screw with variable pitch, number of screws and motions for lower and higher kinematic pairs (Table 1.6.1) become possible to provide the structural characteristics of 20 kinematic pairs (Table 2). Two new general mobility equations for robot manipulator with mixed and the same dimension of closed loop are presented in the work (Table1.6.2 and 1.6.3).

Applying above mobility equations for structural synthesis problem the new wheeled robot that are called as “Rover” had been designed. This rover consists from moving platform and two suspensions with six wheels connected to the platform. Each suspension consist from paired two Chebyshev lambda mechanisms called bogie and one dyad called rocker. Two parallel suspensions are connected by a differential gear mechanism (Fig.2).

The problem of structural synthesis of parallel wheeled rover was solved by using structural formulas 3 and 5 from Table 1.6. In current study, new structural formulas are introduced for parallel Euclidean plaform robot manipulators (Table1.6) with variable and fixed general constraints. Structural synthesis task of four new design Eucilidean docking parallel manipulators with three, four, five and six legs were solved for spacecraft (Table 3). Furthermore, new 6DoF Euclidean docking manipulators of Spacecraft and their structural classification with the same general constraints of each legs are presented. Also, in the Table 3 were depicted the structural parameters, kinematic structures, motion of platform, number of legs and 3D drawing of new docking parallel manipulator of Spacecraft. It is clear that the 6DoF Euclidean parallel manipulator with different number of legs will better generate the given position and orientation of moving platform.

Table 1. Structural formulas for synthesis and analysis of robot manipulators

№	Equations	Authors	Commentary
1	2	3	4
1.	1. $M = \sum_{i=1}^{j} f_i - \sum_{k=1}^{L} \lambda_k$ 2. $M = \sum_{i=1}^{j} f_i - \lambda L$ 3. $d = 6 - \lambda$ $\{d\}_0^4$ – general constraint for motion of rigid body in space; L – the number of independent loops; λ – the loop motion parameters; f_i – the DoF of kinematic pairs; j – the number of joints.	F. Freudenstain and R.I.Alizade [15] 1975	1. Mobility equation for mechanisms which contain mixed independent loops with variable general constraint. 2. Mobility equation of mechanisms with the same number of independent, scalar loop closure equations in each independent loop. M is the mobility of mechanisms. λ_k is the dimension of the active motion space.
2.	1. $L = j_b - B - C_B$ 2. $M = \sum_{i=1}^{j} f_i - \lambda(j_B - B - C_B) + q - j_p$ 3. $\sum_{i=1}^{j} f_i = \lambda(j_B - B - C_b)$ B – the number of mobile platforms; j_B – the total number of joints on the mobile platforms; C_b – the total number of branches between mobile platforms.	R.I.Alizade [16] 1988	1. L is the number of independent loops. 2. M is mobility of mechanisms and platform manipulators. 3. Equation for simple structural groups $\{\lambda\}_2^6$, q is excessive over closing constraints, j_p is number of passive DoF in kinematic pairs.
3.	1. $L = C - B$ 2. $M = \sum_{i=1}^{j} f_i - \lambda(C - B)$ 3. $\sum_{i=1}^{j} f_i = \lambda(C - B)$ $C = C_l + C_b$, parameter C is the sum of legs and branches. $C_l = j_B - 2C_b$ C_l – the total number of legs.	R.I.Alizade and C.Bayram [17] 2003	1. New formula for the number of independent loops. 2. Mobility equation of platform robot manipulators. 3. Equation for simple structural groups.

Table 1. Continue

1	2	3	4
4.	1. $M = (B - C)\lambda + \sum_{i=1}^{j} f_i + q - j_p$ 2. $M = (\lambda + 3) + \sum_{l=1}^{C_l}(d_l - D) + \sum_{l=1}^{C_l}(f_l - \lambda_l) + q - j_p$ $C = C_l + C_b + C_h$ C_h – the number of hinges; $\lambda = 6 - d$; λ – the number of independent location parameters of rigid body in the independent loop; d_l – the number of dimensions of vectors in subspaces of legs. f_l – DoF of the kinetic pairs on the leg.	R.I.Alizade, C.Bayram and E. Gezgin [1] 2007	1. Mobility equation for robotic systems. 2. A structural formula of mobility loop–legs equation for parallel Cartesian platform manipulators. d is the constraint parameter of independent loop. D is the number of dimensions of vectors in Cartesian space.
5.	1. $M = \lambda + j_h + \sum_{L=1}^{n}(f_L - \lambda_L) + \sum_{l=1}^{C_l}(f_l - \lambda_l) + q - j_p$ 2. $m = \lambda + c_l + j_h + \sum_{l=1}^{C_l}(d_l - D) + \sum_{L=1}^{n}(f_L - \lambda_L)$ j_h – the number of hinges between platforms; f_L – DoF of kinematic pair on the branch-loop. λ_L – the motion of rigid body in branch-loop.	Rasim Alizade, Fatih Cemal Can, Erkin Gezgin [18] 2008	1. The general structural formula of serial-parallel Euclidean robot manipulators with variable general constraints. 2. The general formula for motion of platforms. D – dimensions of vectors ($D = 3$ for space R^3, $d = 2$ for plane R^2)
6.	1. $\$ = f - \tilde{\$} + t$ 2. $M = \sum_{f=1}^{\lambda-1} fP_f - \sum_{k=1}^{L} \lambda_k + q$ 3. $M = \sum_{f=1}^{\lambda-1} fP_f - \lambda(C - B) + q$ 4. $M = \lambda + \sum_{l=1}^{c_l}\left(\sum_{f=1}^{\lambda-1} fP_f - \lambda_l\right) + \sum_{b=1}^{L_b}\left(\sum_{f=1}^{\lambda-1} fP_f - \lambda_b\right) + j_h$ 5. $m = \lambda + c_l + j_h + \sum_{l=1}^{c_l}(d_l - D) + \sum_{b=1}^{L_b}\left(\sum_{f=1}^{\lambda-1} fP_f - \lambda_b\right)$ 6. $M = \lambda + \left(\sum_{f=1}^{\lambda-1} fP_f - \lambda_l\right)c_l + \sum_{f=1}^{\lambda-1}(fP_f - \lambda_b)\,L_b + j_h$ 7. $m = \lambda + c_l + j_h + (d_l - D)c_l + \left(\sum_{f=1}^{\lambda-1} fP_f - \lambda_b\right)L_b$ t – represents the number of screws that describe the contact geometry of joint elements. $t = 2$ – contact elements on surface; $t = 3$ – contact elements on line; $t = 4$ – contact elements on points;	Rasim Alizade 2017	1. Total screws in kinematic pair. 2. Mobility equation for robot manipulators with variable loop motion parameters. 3. Mobility equation with the same dimension in each independent loop. 4. Structural formula for Euclidean platform type robot manipulators with variable general constraints. 5. Structural formula that describe the motions of end effector on the parallel robot manipulators. 6. Mobility equation for Euclidean manipulators with constant general constraint. 7. Motion of end effector of Euclidean manipulator with constant general constraint.

Introduction to screw with variable pitch

The structural and kinematic analysis and synthesis problem have been studying with the goal of identified new methods for composing robot manipulators capable of performing various prescribed positions and orientations of the end effectors. Screw with variable pitch can represent the prismatic joint, P, with the variable pitch parameter $\mu_P = \infty$, and also the cylindrical joint $C(RP)$ with variable pitch $\mu_C = (\infty; 0)$ that describe a rotation motion $(\mu_R = 0)$ and translation motion $\mu_P = \infty$.

As shown in Fig. 1, the location of a rigid body (RB) of the cylindrical joint can be described by the three parameters for position (x, y, z) and three independent parameters (d, α, θ) for orientation. Let coordinate system A and was then translated parallel to the point B_1 (Fig. 1a). The position of point B_1 is described by vector $\bar{r}(x, y, z)$. Next, the system B_2 that is initially aligned with system B_1 is rotated by the twist angle α about the x_{B_1} axis. Following this the coordinate system B_2 of rigid body is translated along the z_{B_2} axis by a distance d. Lastly the coordinate system B that was firstly aligned with the system B_2 is rotated by the angle θ around z_B, so we will get orientation of the coordinate system $Bx_By_Bz_B$.

Transformation of one coordinate system B to a reference coordinate system A correspond to the transformation of screw \$, when the relative position and orientation of the pair of screws are known (Fig. 1a). By using homogeneous coordinates the transformation of the system will be represented by 4×4 matrix as:

$$
{}_B^AT = \begin{bmatrix} 1 & 0 & 0 & x \\ 0 & 1 & 0 & y \\ 0 & 0 & 1 & z \\ 0 & 0 & 0 & 1 \end{bmatrix} \begin{bmatrix} 1 & 0 & 0 & 0 \\ 0 & c\alpha & -s\alpha & 0 \\ 0 & s\alpha & c\alpha & 0 \\ 0 & 0 & 0 & 1 \end{bmatrix} \begin{bmatrix} 1 & 0 & 0 & 0 \\ 0 & 1 & 0 & 0 \\ 0 & 0 & 1 & \tilde{d} \\ 0 & 0 & 0 & 1 \end{bmatrix}
\begin{bmatrix} c\tilde{\theta} & -s\tilde{\theta} & 0 & 0 \\ s\tilde{\theta} & c\tilde{\theta} & 0 & 0 \\ 0 & 0 & 1 & 0 \\ 0 & 0 & 0 & 1 \end{bmatrix} = \begin{bmatrix} c\tilde{\theta} & -s\tilde{\theta} & 0 & x \\ s\tilde{\theta}c\alpha & c\tilde{\theta}c\alpha & -s\alpha & y - \tilde{d}s\alpha \\ s\tilde{\theta}s\alpha & 0 & c\alpha & z + \tilde{d}c\alpha \\ 0 & 0 & 0 & 1 \end{bmatrix} \quad (1)
$$

where: $S\theta$ and $C\theta$ represent the sine and cosine of θ, and $S\alpha$ and $C\alpha$ represent the sine and cosine of α.

Knowledge of these six parameters $(x, y, z, \alpha, d, \theta)$ completely defines the position and orientation of the B coordinate system attached to the rigid body of the cylindrical joint and measured with respect to the A coordinate system as shown in Eq.(1). The location of rigid body reduce a single vector $\bar{S}//\bar{Z}_B$ and a couple moment $\bar{U}//Z_{B_1}$ at point B_1 with a twist angle α (Fig. 1b). The couple moment $\bar{U} = \bar{r} \times \bar{S}$ may be resolved into two components: one $\bar{U}_{//}$collinear with joint vector $\bar{S}$ in the direction by twist angle α. The perpendicular component $\bar{U}_{\perp}$ will rotate rigid body around cylindrical joint vector $\bar{S}$ by rotation angle θ, so $\bar{\theta} = \theta\bar{S}$.

The twist angel α was defined between vectors $\bar{S}$ and $\bar{U}$ (Fig. 1b) mesured in a right-hand sense about $\bar{x}_{B_1}$. The rotation angle θ was defined between $\bar{x}_{B_2}$ and $\bar{x}_B$ measured in a right hand sense about $\bar{S}$ (Fig. 1a). It is known that, there are two distinct angles between 0 and 2π that will have the same cosine value. So, the expressed for the cosine and sine of α and θ can be expressed by Eqs. (2):

$$
\begin{cases} \cos\alpha = \bar{U} \cdot \bar{S} \\ \sin\alpha = (\bar{U} \times \bar{S}) \cdot \bar{x}_{B_1} \end{cases}
\begin{cases} \cos\theta = \bar{x}_B \cdot \bar{x}_{B_2} \\ \sin\theta = (\bar{x}_B \times \bar{x}_{B_2}) \cdot \bar{Z}_B \end{cases} \quad (2)
$$

As show in Fig. 1, the axes of the cylindrical joint $\bar{S}$ and a couple moment $\bar{U}_{//}$ has the same line. Thus the combination of a collinear vector $\bar{S}$ and a couple moment $\bar{U}_{//}$ is called a screw or wrench.

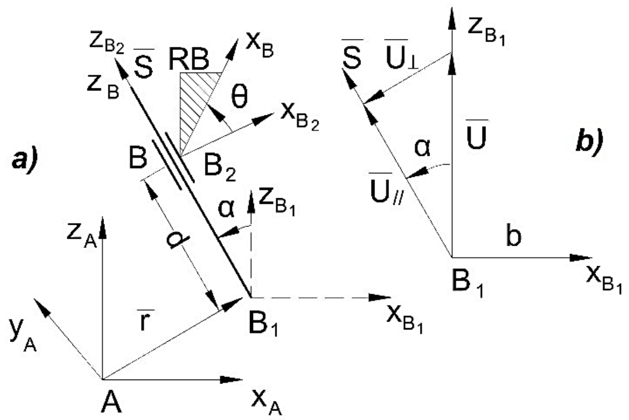

Fig. 1. Kinematic model of cylindrical joint

So, the screw with variable pitch has both a translation d and rotation θ about the axis $\bar{S}$ described by twist angle α. Parameters d, θ and α are independent parameters of rigid body motion respect to screw $\tilde{\$}$ with variable pitch.

Two collinear vectors $\bar{S}$ and $\bar{U}_{//}$ uniqually determine the position and orientation of the screw with variable pitch. $\bar{S}$ is an axis vector and $\bar{U}_{//}$ is moment of screw $\tilde{S}$, where $\bar{S}$ defines the direction of motion of screw $\tilde{\$}$ and moment $\bar{U}_{//}$ determines the rotation around the axis. Unit vector $\bar{S}$ and moment $\bar{U}_{//}$ can be introduced as dual vector that is called a screw with variable pitch:

$$\tilde{\$} = \bar{S} + \varepsilon\left(\bar{U}_{//} + \tilde{\mu}\bar{S}\right) \qquad (3)$$

where $\varepsilon^2 = 0$ is operator of Clifford.

The ratio of joint position d and joint rotation θ in cylindrical joint reduce to the following variable pitch:

$$\tilde{\mu} = \frac{d}{\theta} \qquad (4)$$

As shown in Fig. 1b the rotation moment in cylindrical joint reduce to expression as follow:

$$\bar{U}_{//} = \bar{U} \cdot \cos\alpha = (\bar{r} \times \bar{S}) \cos\alpha \qquad (5)$$

Hence, using Eqs. $(3 \div 5)$ the vectors $\bar{S}$ and resultant couple moment $\bar{U}$ describing location of a rigid body with cylindrical joint can be descried as a screw with variable pitch:

$$\tilde{\$} = \begin{bmatrix} \bar{S} \\ (\bar{r} \times \bar{S}) \cos\alpha + \tilde{\mu}\bar{S} \end{bmatrix} \qquad (6)$$

So, as shown in Eq. (6), six independent components $(x, y, z, \alpha, d, \theta)$ describe the location of screw with variable pitch. As shown in Eq. (7) the couple moment $\bar{U}$ of the screw with variable pitch is:

$$\bar{U} = (\bar{r} \times \bar{S}) \cos\alpha + \tilde{\mu}\bar{S} \qquad (7)$$

Since the screw axis and its moment are in orthogonal planes and unit of screw with variable pitch $|\tilde{\$}| = 1$, so

$$\bar{S} \cdot (\bar{r} \times \bar{S}) = 0 \quad \text{and} \quad \bar{S} \cdot \bar{S} = 1 \qquad (8)$$

Multiplying both side of Eq.(7) to the vector $\bar{S}$ we get the following equation:

$$\bar{S} \cdot \bar{U} = (\bar{r} \times \bar{S}) \cdot \bar{S} \cos\alpha + \tilde{\mu}\bar{S} \cdot \bar{S} \quad or \quad \tilde{\mu} = \frac{\bar{S} \cdot \bar{U}}{\bar{S} \cdot \bar{S}} \qquad (9)$$

For revolute, prismatic, screw and cylindrical joints the parameters of pitch to Eq.(8) can be described as follows:

$$\mu_R = 0, \qquad \mu_{\$} = \frac{d}{\theta}, \qquad \tilde{\mu}_p = \infty, \quad \tilde{\mu}_C = \{0, \infty\}.$$

Structural formulas for robot manipulators by using screw theory.

The design problem of robot manipulators are a valuable task for structural synthesis. It is known that over constraint robot manipulator must satisfy the geometry of angular and linear constraints that correspond to the geometry of kinematic pairs moving in subspaces. The goal of structural synthesis by using screw theory are identified new methods for composing robot manipulators capable of performing various prescribed functions, position and orientations of end effectors. It is required to form a new structural formula for robot manipulators by using screw theory allows to solve the structural synthesis with variable general constraints including platforms, hinges, legs and branch loops with different ranks, that is introduced from different subspaces and spaces.

It is known that two rigid bodies attached to each other by surfaces are formed lower kinematic pairs, otherwise if contact geometry of two rigid bodies is line or a point are formed higher kinematic pairs. Due to the fact that the unconstraint space has dimension $\lambda = 6$ with independent motions 3R3P, but dimension of over constraint subspaces is $\lambda = 2 \div 5$ with different angular and linear or just angular conditions in the loops of robot manipulators. Usually kinematic pairs need constraints $c = 1 \div 5$ in order to be defined properly degree of freedom $f = \lambda - c$. Each kinematic pair has input and output link screws and joint independent screws $\$$ with constant pitch μ, however some joints with translation motions has additional variable screws $\tilde{\$}$ with variable pitch $\tilde{\mu}$.

The simple planar surface can be represented by two parallel screws $\underline{\$_1\$_2}$ or two orthogonal screws $\$_1^{\perp}\$_2$, so for lower kinematic pairs number of screws $t = 2$. The intersection of two planar surfaces $\underline{\$_1\$_2}$ and $\underline{\$_2\$_3}$ will be result in a line represented by $\underline{\$_1\overline{\$_2}}\overline{\$_3}$ or as $\$_1^{\perp}\$_2^{\perp}\$_3$ so for higher kinematic pair with line contact of elements the number of screws $t = 3$. The intersection of three planar surfaces that will be result in a point can be represented by four screws $\underline{\$_1\overline{\$_2}}\overline{\$_3} \to \$_2^{\perp}\$_4$ or as $\$_1^{\perp}\$_2^{\perp}\$_3^{\perp}\$_4$, so for higher kinematic pair with point contact of elements the number of screws $t = 4$. Elements of the structural bonds can be illustrated as "__" describe the parallel of screws and "⊥" describe the perpendicular of screws.

Table 2. Joints kinematic parameters

№	Name	Symbol	Kinematic parameters				Diagram
			t	f	$\tilde{\$}$	$\$$	
1	2	3	4	5	6	7	8
1	Revolute	R	2	1	0	3	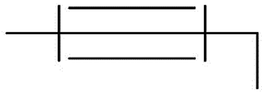
2	Prismatic	P	3	1	1	3	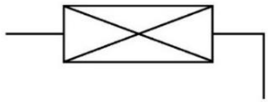
3	Screw	H	2	1	0	3	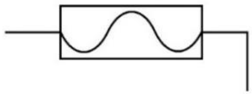
4	Cylindrical	C	2	2	1	3	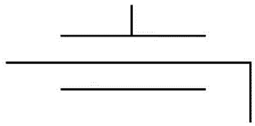
5	Sphere with finger	S_f	2	2	0	4	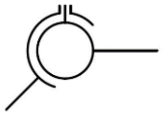
6	Spherical	S	2	3	0	5	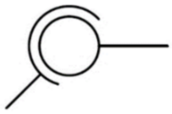
7	Sphere in cylinder slot	S_{cs}	3	4	1	6	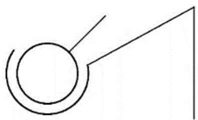
8	Sphere in torus slot	S_{ts}	3	4	0	7	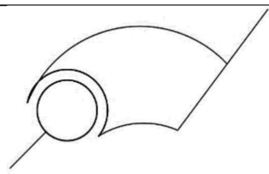
9	Plane to slope line	$F_{/L}$	4	4	1	7	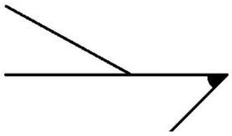
10	Plane to perpendicular line	$F_{\perp L}$	4	3	1	6	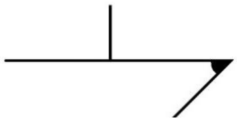

Table 2. Continue

1	2	3	4	5	6	7	8
11	Plane to parallel lines	$F_{//L}$	3	4	2	5	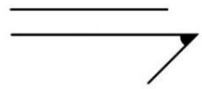
12	Line to Sphere	L_S	4	4	1	7	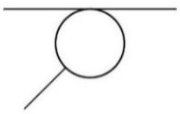
13	Cylinder to plane	C_F	3	4	2	5	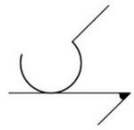
14	Cylinder to torus	C_t	4	4	1	7	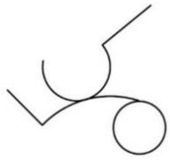
15	Sphere to plane	S_F	4	5	2	7	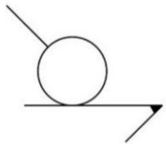
16	Hyperboloid to Sphere	H_s	4	5	2	7	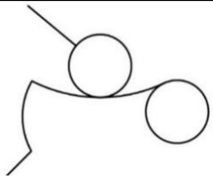
17	Sphere to Torus	S_t	4	5	2	7	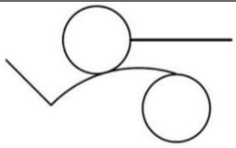
18	Torus to plane	T_F	4	5	2	7	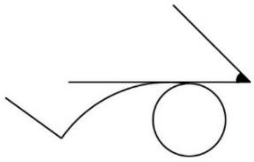
19	Torus to torus	T_t	4	5	2	7	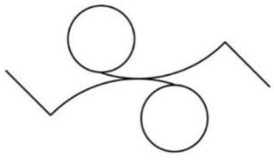
20	Sphere to sphere	S_s	4	5	2	7	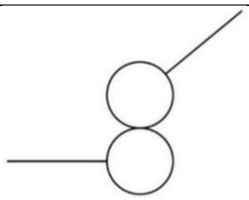

The usage of recurrent screws in the study of kinematic pairs can clarify the motion concept easily. From this point of view the number of independent screws in kinematic pairs can be introduced as follow:

$$\$ = f - \tilde{\$} + t \tag{9}$$

where:

$\tilde{\$}$ = number of screws with variable pitch;

t = number of screws of lower ($t = 2$) or higher kinematic pairs ($t = 3$ for line and $t = 4$ for point contact of elements);

f = degrees of freedom of relative motion permitted at joint.

The twenty kinematic pairs of robot manipulators in all types, symbols, kinematic parameters and their diagrams are shown in Table 2. Using Eq.(9) and (1.1) from Table 1 we can introduce a new general mobility equation for mechanisms with mixed dimensions of closed loops as:

$$M = \sum_{f=1}^{\lambda-1} fP_f - \sum_{k=1}^{L} \lambda_k + q \tag{10}$$

where $\lambda_k -$ number of independent, scalar, loop closure equations associated with k-th independent loop;

P_f is the number of f mobility joints. $f = \$ + \tilde{\$} - t$ is DoF at joint;

q = number of depended constraint equations.

As show in Table 1, the number of independent loops $L = c - B$, so mobility Eq. (10) can be introduced as mobility equation for robot manipulators with the same number of independent, scalar loop closure equation in each independent loop:

$$M = \sum_{f=1}^{\lambda-1} fP_f - \lambda(C - B) + q \tag{11}$$

where $C = c_l + c_b$ is the sum of legs and branches; B = number of mobile platforms.

The overall performance of robots and rovers are usually constructed from the multiple platforms, hinges leg and branch loops with variable general constraint parameters, describing the location of rigid body. These robots and rovers can be affected by the topology of their possible mechanical structures. The motions (rotation and translation) of rigid links and platforms of the manipulators could be described in space R^3 and in plane R^2 with dimensions of vectors $D = 3$ and $D = 2$ in reference frame respectively. The location of rigid body in the three dimensional space R^3 can be obtain by Euclidean motions of the two dimensional subspaces R^2. It is known that the location of rigid body in space R^3 can be determined minimum by three independent curves of the three points of moving rigid body. Let there are dyads kinematic chains on each Euclidean "$3 \leq planes \leq 6$". If these kinematic chains of Euclidean planes are joined to the moving rigid body by spherical or spherical-torus kinematic pairs, so we will attain location of the rigid body in the three dimensional space R^3.

The general structural formula for parallel-serial Euclidean platform type manipulators with variable general constraints [18] including hinges (j_h), leg (l) and branch (L_b) loops can be also formulated in the form as (Table 1):

$$M = \lambda + \sum_{l=1}^{c_l}\left(\sum_{f=1}^{\lambda-1} fP_f - \lambda_l\right) + \sum_{b=1}^{L_b}\left(\sum_{f=1}^{\lambda-1} fP_f - \lambda_b\right) + j_h \tag{12}$$

where λ is the dimension parameter of moving platform; λ_l and λ_b are dimension parameters of leg and branch loops; j_h is the number of hinges between platforms.

The structural formula for motion [18] of platforms that are created by mechanical system from different Euclidean planes can be introduced in the following form (table 1):

$$m = \lambda + c_l + j_h + \sum_{l=1}^{c_l}(d_l - D) + \sum_{b=1}^{L_b}\left(\sum_{f=1}^{\lambda-1} fP_f - \lambda_b\right) \tag{13}$$

where d_l is the number of dimensions of vectors of the legs in Euclidean planes;

D is the number of dimensions of vectors in the reference frame.

If the number of independent scalar leg-closure equations identical in each Euclidean planes and identical in each branch loops, the general structural formula (12) for Euclidian manipulators can be defined as

$$M = \lambda + \left(\sum_{f=1}^{\lambda-1} fP_f - \lambda_l\right)c_l + \sum_{f=1}^{\lambda-1}\left(fP_f - \lambda_b\right)L_b + j_h \tag{14}$$

The general formula for motion of end effector of manipulator (13) with the same dimensions of Euclidean manipulator legs and branch-loops can be given in the following from:

$$m = \lambda + c_l + j_h + (d_l - D)c_l + \left(\sum_{f=1}^{\lambda-1} fP_f - \lambda_b\right)L_b \tag{15}$$

Structural Synthesis of 6DoF Parallel Docking Manipulator of Spacecraft.

In space flights the orbital docking system is used. The use of an orbital station with two docking units ensures a rigid connection with the formation of a hermetically sealed tunnel. A large number of interacting mechanisms are concentrated in the docking aggregates. The multi-functionality of the working bodies requires the solution of the problem of the structural synthesis of spatial manipulators of coupling aggregates. Since the mechanisms operate in open space, it is therefore necessary to develop new manipulators, nodes and elements of kinematic pairs. Structural parameters, kinematic structure, motion of platform and 3D drawing of the spaces docking manipulators $6RRS_t$ is depicted in Table 3. Controllable space vehicles are brought to a touch with a certain speed and position, after which the process of docking with a spatial manipulator of a parallel structure begins, which ends with a rigid connection of two docking units. After the end of the flight, an undocking takes place by releasing the mechanical connections of the docking device of the platform manipulator from the orbital station (Table 3.1).

When docking it is required that the coaxial position of the docking assemblies and the zero linear and angular velocities be maintained. The possible values of the relative coordinates and their first derivatives in the case of mechanical contact are called the initial conditions of the docking. Deviations from the co-axial position (Table 3.2) are determined by the linear coordinates δ_y, δ_z and planar angles δ_ψ, δ_φ, δ_θ. The total deviations of the docking units from the co-axial position are added from the errors: unit settings, measurements and control dynamics. Electromechanical docking devices have been created to reduce errors based on electromechanical dampers. With the damping, the brake robot can accelerate in a unit of millisecond to a speed of several thousand revolutions per minute.

The new four proposed Euclidean docking manipulators have identical legs as plane dyads RR as shown in Table 3.3a. Each end of dyads connect to the moving platform by spherical-tours pairs. Kinematic pair with 4DoF is introduced as sphere in torus slot pair S_{ts} that perform three rotations and one circular translation (Table 3.3 b). Note that, end points of each dyads respect to the fixed reference frame (Table 3.3 c) define the curve of one point of the platform in the reference Euclidean plane. Three legs RRS_{ts} of the moving platform defines the three reference Euclidean planes (Table 3.3 c) that are located under an angle of 120°. It is known that the location of the moving rigid body in space can be defined by minimum three independent curves of three rigid body points moving on three Euclidean reference planes.

Since the Euclidean parallel docking manipulator consist of a movable platform and legs, then the number of branch-loops $L_b = 0$, hinges $j_h = 0$ and $\lambda_l = const$, so Eq. (14) takes the form:

$$M = \lambda + \left(\sum_{f=1}^{\lambda-1} fP_f - \lambda_l \right) c_l \tag{16}$$

In the same way when $L_b = 0$, $j_h = 0$ and $d_l = const$, then the formula (15) for motion of platform of Euclidean docking manipulator can be written in the form

$$m = \lambda + (1 + d_l - D)c_l \tag{17}$$

Example 1.

Design a parallel Euclidean docking robot manipulator with $\lambda = 6$, $\lambda_l = 6$, $c_l = 6$, $M = 6$. Find both the number and kind of kinematic pairs on each leg. Also, find the motion of docking platform.

By using Eq.(16) total DoF and kind of kinematic pairs of the legs can be calculated as

$$(M - \lambda)c_l^{-1} + \lambda_l = \sum_{f=1}^{5} fP_f \quad or$$

$$6 = P_1 + 4P_4, \quad or \quad P_1 = 2 \; and \; P_4 = 1$$

so that, in the designed docking manipulator, each leg will consist of two kinematic pairs with one degrees of freedom (revolute pairs RR) and one kinematic pair with four degrees of freedom (sphere in torus slot pair S_{ts}). By using Eq.(17), the motion of the docking platform will be $m = 6$, it means motion of platform will R_x, R_y, R_z, P_x, P_y, P_z.

Kinematic structure with different structural parameters of Euclidean docking robot manipulator with six legs is shown in Table 3.1.

The above procedure can be used for Euclidean docking robot manipulators with three, four and five legs.

The result of the new Euclidean docking robot manipulators are shown in Table 4. Elements of the structural bonds can be illustrated as: Restangle (▭): describes moving platform with spherical-torus pairs S_t.

Platform leg $(-, \llcorner)$: connection of the spherical-torus pairs on the moving platform with pairs of the legs.

$\overline{\underset{m}{R}}$: input joint on fixed frame.

$\overline{R}$: input joint on moving frame.

Table 3. Parallel Euclidean Platform Spacecraft Docking Manipulator

<table>
<tr><td>№</td><td colspan="9">The new Spatial Docking Manipulator of Spacecraft</td></tr>
<tr><td rowspan="3">1</td><td colspan="9">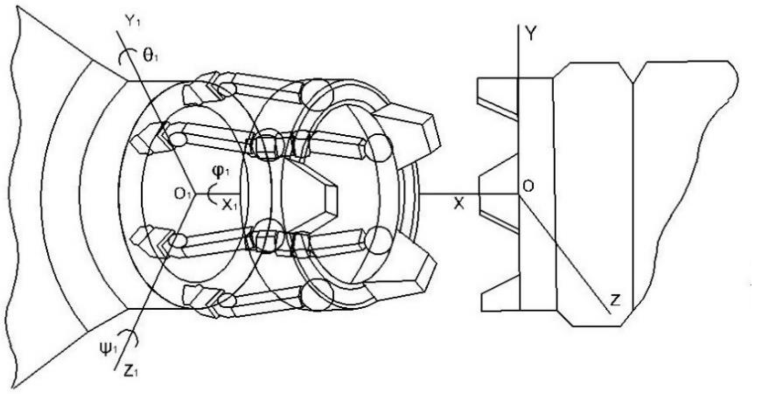
</td></tr>
<tr><td>$R\underline{\overline{R}}$
$\underline{\overline{R}}R$ – [$S_t\ S_t\ S_t\ S_t\ S_t\ S_t$] – $R\underline{\overline{R}}$
$\underline{\overline{R}}R$ – $\underline{\overline{R}}R$ – $R\underline{\overline{R}}$</td><td>$R_x$, R_y, R_z,
P_x, P_y, P_z</td><td>α
60°</td><td>λ_l
6</td><td>c_l
6</td><td>leg.
$P_1 = 2$
$P_4 = 1$</td><td>d_l
2,2,2
2,2,2</td><td>m_p
6</td><td>M
6</td></tr>
<tr><td>1</td><td>2</td><td>3</td><td>4</td><td>5</td><td>6</td><td>7</td><td>8</td><td>9</td></tr>
<tr><td></td><td colspan="9">The Deviations of the Docking Units.</td></tr>
<tr><td>2</td><td colspan="9">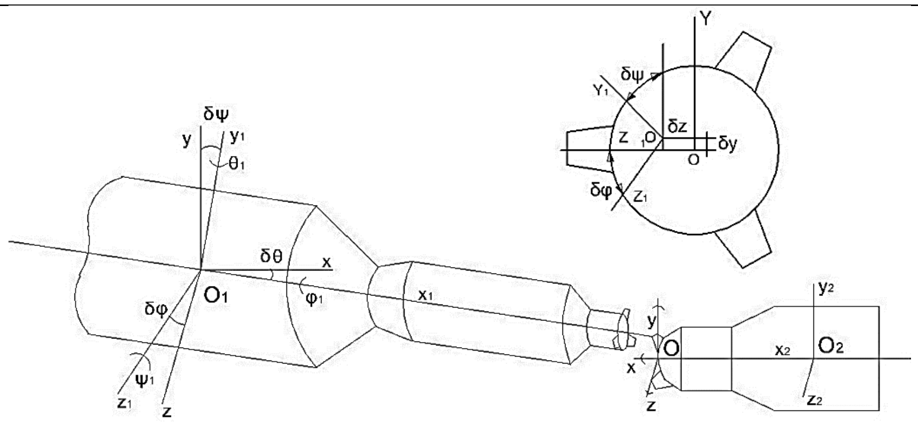
</td></tr>
<tr><td></td><td>a</td><td>Dyad in reference Euclidean plane.</td><td>b</td><td colspan="3">Sphere in torus slot pair</td><td>c</td><td colspan="2">The three platform points on three Euclidean planes.</td></tr>
<tr><td>3</td><td colspan="2">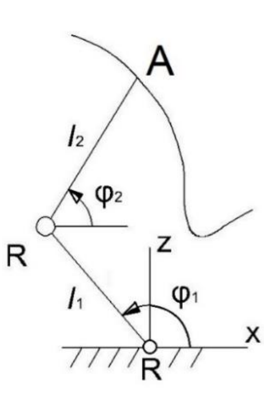

RR</td><td colspan="4">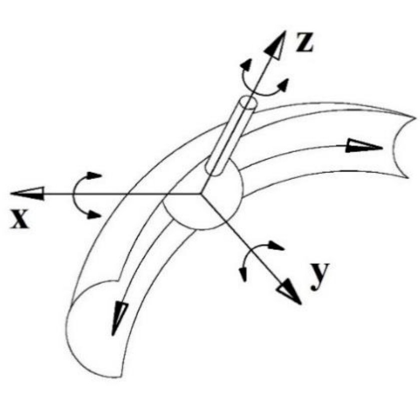

S_t</td><td colspan="3">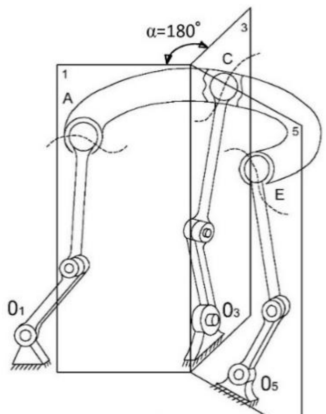

3RRS$_t$</td></tr>
</table>

Table 4. New 6DoF Parallel Docking Manipulators of Spacecraft

Structural bonding	Illustration: Motion of platform	Angle between Euclidean planes	λ_l	c_l	leg. $\sum f P_f$	d_l	m_p	M
1	2	3	4	5	6	7	8	9
$\overline{R}\overline{R}-\boxed{S_{ts}S_{ts}S_{ts}}-\overline{R}\underline{R}$ $\overline{R}\,\underline{R}$	$R_x, R_y, R_z, P_x, P_y, P_z$	$120°$	6	3	$P_1 = 2$ $P_4 = 1$	2,2,2	6	6
1	2	3	4	5	6	7	8	9
1	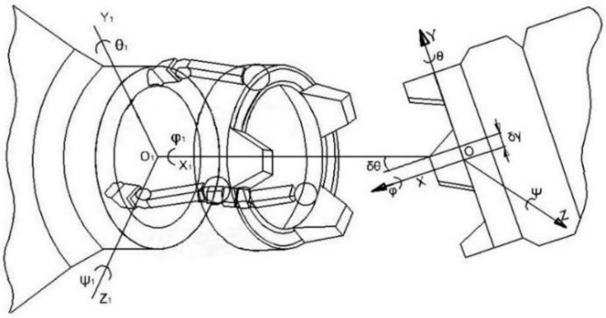							
1	2	3	4	5	6	7	8	9
$\overline{R}R$ $\overline{R}R-\boxed{S_{ts}S_{ts}S_{ts}S_{ts}}-\overline{R}\underline{R}$ $R\underline{R}$	$R_x, R_y, R_z, P_x, P_y, P_z$	$90°$	6	4	$P_1 = 2$ $P_4 = 1$	2,2,2, 2	6	6
2	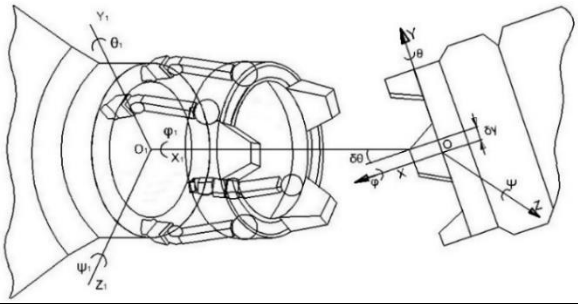							
1	2	3	4	5	6	7	8	9
$\overline{R}R$ $\overline{R}R-\boxed{S_{ts}S_{ts}S_{ts}S_{ts}S_{ts}}-\overline{R}\underline{R}$ $\overline{R}R$ $R\underline{R}$	$R_x, R_y, R_z, P_x, P_y, P_z$	$72°$	6	5	$P_1 = 2$ $P_4 = 1$	2,2,2, 2,2	6	6
3	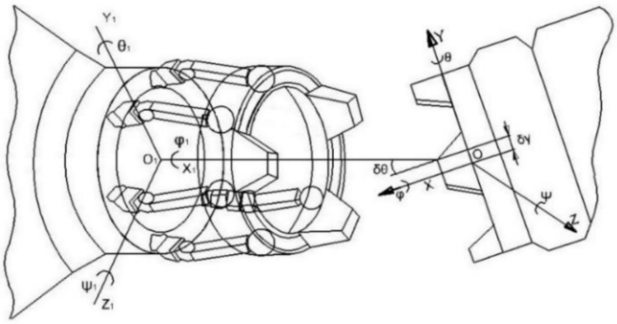							

Structural Synthesis of Wheeled Robots.

It is obvious that wheeled robot have been developed for Mars and Moon surface. First we consider the definition of wheeled robot: "A wheeled robot is an autonomous system capable of traveling a terrain with natural or artificial obstacles". As shown in Fig. 2.1 kinematic structure of wheeled robot has six wheels with symmetric structure for both sides. Each side has three wheels which are connected to each other by the main linkage and two loops kinematic chain. Main linkage called rocker that has two joints, where first joint connected to back wheel and second joint assembled to platform. The rocker is kinematic chain where the second path of link connected rigidly to another linkage system with two wheels. The second linkage system is called bogie (Fig. 2.2). So, rocker-bogie kinematic chain is called suspension system. Wheeled rough terrain mobile robots are called as "Rover". Rovers can carry more weight with high-speed, easy novigation and more precisely can be calculated position and orientation. First rover was "Lunakhod" and second rover was six wheeled syspension system, which connects the wheels to the platform. This connection are linkage mechanisms, damping and complex spring.

The new bogie mechanism consists of two Chebyshev lambda mechanisms which are connected symmetrically. Paired two lambda mechanisms are used as motion generation mechanisms, where couplers are input links. To move the coupler points M_1 and M_2 along a line sufficiently and necessary to fulfil the design relation: $3d - a = 2b$. The length of parametre d can be changed according to relation $1{,}55a \leq d \leq 3a$ (Fig. 2.1). The same second suspension kinematic chains are assembled in opposite side of moving platform. Right and left suspensions are connected to each other by a differential gear mechanism (Fig. 2). When one side climbing over obstacle, this mechanism rotates the platform around the rocker joints by average angle of two sides (Fig. 2.1). So, the wheeled robot is equipped with six wheels and possibly a manipulator setup mounted on the platform for handling of work pieces, tools or special devices. On inclined surface the moving rover can hold the main plarform horizontal. Navigation gets easier by this feature of rover. Rovers are driven by commands which are sent from ground operators after tested in *3*□ computer simulation. Some of the critical motions such as climbing high slope, new rover designs are needed to more flexible duaring field operation.

Example 2.

Design a parallel wheeld rover with six legs $c_l = 6$, three branch $c_b = 3$ and one moving platform $B = 1$ (Fig. 2.1). The dimension parameter of each independent loops on the left and right suspensions $\{\lambda_k\}_1^8 = 3$ (Fig. 2.2). The number of kinematic pairs with one DoF in the left and right suspensions $P_1 = 30$. Two suspensions kinematic chains are connected by differential gear mechanism. Find the number of motors for parallel whelled rover. Also, find the motion of the rover's platform.

First, we define the number of independent loops (Table 1.3):

$$L = C - B = c_l + c_b - B = 6 + 3 - 1 = 8.$$

Using Eq. (11) total DoF of parallel wheeled rover can be calculated as

$$M = \sum_{f=1}^{5} f P_f - \lambda(C - B) = P_1 - \lambda(c_l + c_b - B) =$$
$$= 30 - 3(6 + 3 - 1) = 6.$$

By using Eq.(17), the motion of the moving rover's platform can be defined as

$$m = \lambda + (1 + d_l - D)c_l = 6 + (1 + 2 - 3) = 6.$$

Thus, the problem of the structural synthesis of the wheeled rocker-bogie mechanism is solved and it is introduced in Fig.2. Spring and damper application to double lambda bogie good solution for high-speed off-road vehicles.

Rocker-Bogie suspensions can be used also for vehicles with a larger number of wheels. An example of a layout for an 8-wheeler each suspension will consist from four motion generation Chebyshev lamda mechanisms with the four given wheels. İn this case the vehicle may be summetrical and it can run in both direction without any difference.

№

1

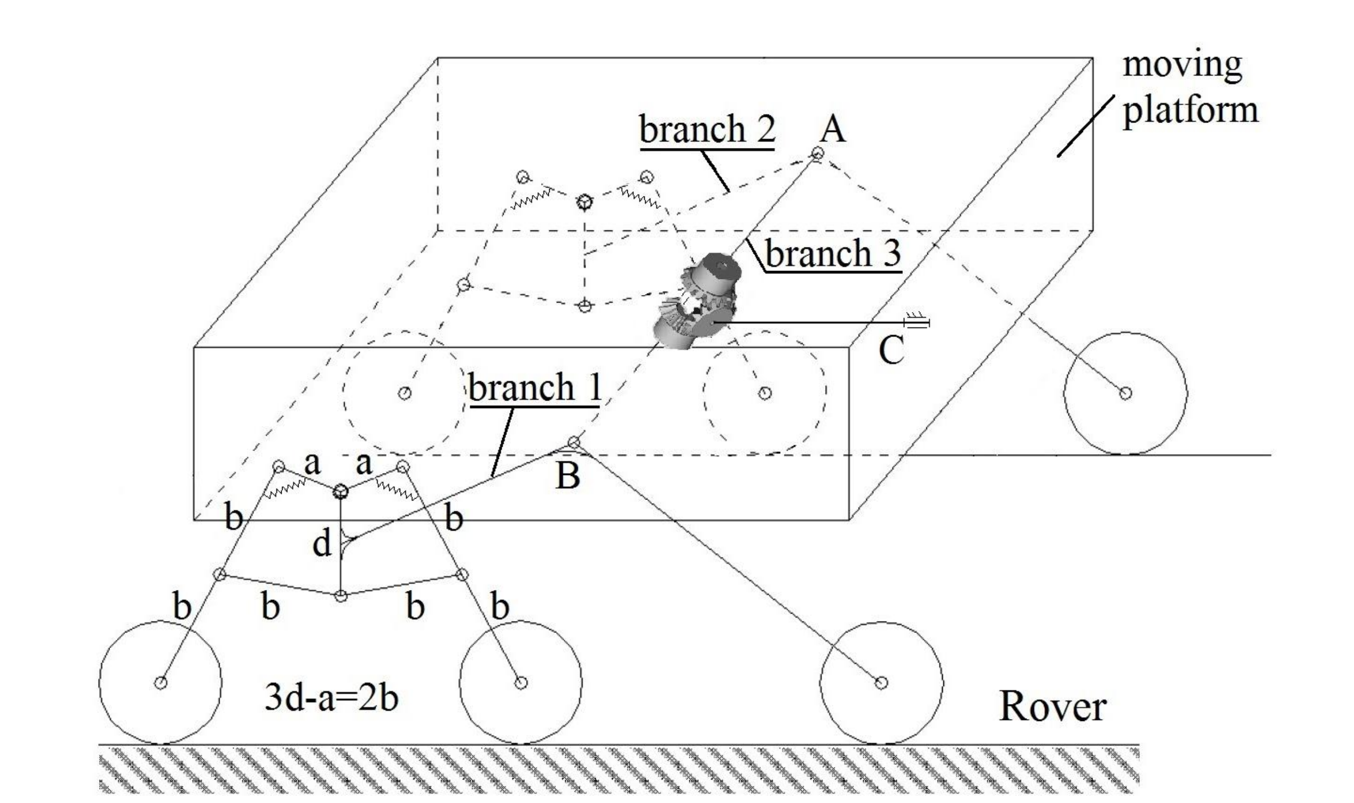

2

1

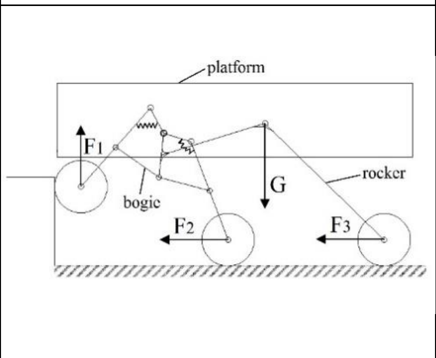

2

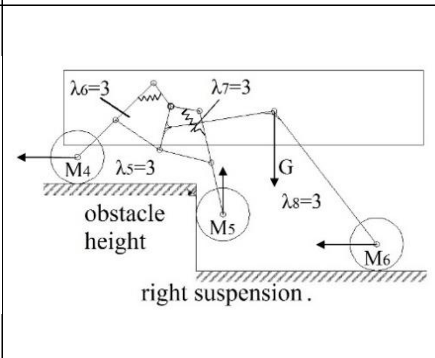

3

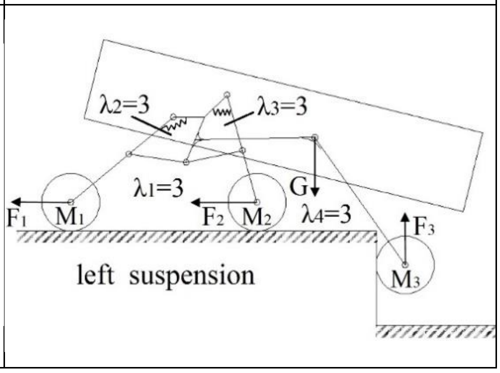

Fig. 2. Kinematic model of rocker-bogey mechanism

Conclusion

The problem of structural synthesis of the robot manipulators with variable general constraint of the legs and closed loops can be difficult and complex task depends on the DoF and motion of an end-effector concept. It is described a new structural formula of kinematic pairs for robot manipulators by using screw with variable pitch. From this point the twenty kinematic pairs are shown with types, simbols, kinematic screw parameters and their diagrams. It were introduced two new general mobility equations for mechanisms with mixed or fixed dimensions of close loops. The general structural formula for Euclidean manipulators with variable or identical general constraints are introduced. The new structural formula for motion of end effector of robot with legs from different Euclidean planes were considered. Four new Euclidean 6DoF parallel docking manipulators of Spacecraft were reviewed and synthesized. Funally, by using sistematic process of structural synthesis by using for mobility of robot and motion of moving platform were developed to create new structure of wheeled robot-rover for Mars and Moon surface.

References

[1]. Rasim Alizade, Cagdas Bayram, Erkin Gezgin, Structural Synthesis of serial platform manipulators, IFToMM J., Mechanism and Machine Theory 42 (2007) 580-599.

[2]. G.Gogu, Mobility of mechanisms: a critical review, IFToMM J.Mech. Mach. Theory 40 (2005) 1068-1097.

[3]. R.Muller, Die zwanglanfigkeit kinematische ketten, Unpublished dissertation (1920), as quoted in K. Federhofer: Graphische Kinematic and Kinetostatic, Springer, Berlin, 1932.

[4]. R.Voinea, M. Atanasiu, Contributions a la theorie geometrigue des vis, Bull. Inst. Politech. Bucuresti XXI (3) (1959).

[5]. K.J.Waldron, The constraint analysis of mechanisms, J. Mech. 1 (1966) 101-114.

[6]. Z.Huang, Q.C.Li, General methodology for type synthesis of symmetrical lower-mobility parallel manipulators and several novel manipulators, Int. J. Robot. Res. 21 (2002) 131-145.

[7]. Yuefa Fang, Lung-Wen Tsai, Structure synthesis of a class of 4-DoF and 5-DoF parallel manipulators with identical limb structures, Int. J. Robot. Res. 21 (2002) 799-810.

[8]. Y.Jin, I. M.Chen, G.Yang, Structure synthesis and singularity analysis of a parallel manipulator based on selective actuation. Proceeding of the International Conference on Robotics and automation (2004) 4533-4538.

[9]. F.Gao, W. Li, X.Zhao, Z.Jin, H. Zhao, New Kinematic structures for 2-5 DoF parallel manipulator designs, IFToMM J, Mechanism and Machine Theory 37 (2002) 1395-1411.

[10]. T.S.Zhao, J.S.Dai, Z.Huang, Geometric analysis of over constrained parallel manipulators with 3-4 DoF, ASME Journal Series C, Vol. 45, No. 3, (2002) 730-740.

[11]. X.Kong, C.M.Gosselin, Type Synthesis of 3T1R 4-DoF parallel manipulators based on screw theory, IEEE Transactions on Robotics and Automation, Vol. 20, No. 2, April (2004) 181-190.

[12]. X.Kong, C.M.Gosselin, Type synthesis of 4-DoF SP-equivalent parallel manipulators: A virtual chain approach, IFToMM J., Mechanism and Machine Theory, 41 (2006) 1306-1329.

[13]. X.Kong, C.M.Gosselin, Generation of parallel manipulators with three translational degrees of freedom based on screw theory, Proceedings of Symposium on Mechanisms, Machines and Mechatronics, Montreal, Canada (2001).

[14]. X.Kong, C.M.Gosselin, Type synthesis of parallel mechanisms, Springer (2007).

[15]. F.Freudenstein, R.Alizade, On the degree of freedom of mechanisms with variable general constraint, IV World IFToMM Congress, England,(1975) 51-56.

[16]. R.I.Alizade, On the degree of freedom of kinematic chain, Az. Pol. Inst., Automation design of mechanisms, manipulator and robots, Baku (1988) 3-14.

[17]. Rasim Alizade, Cagdaş Bayram, Structural synthesis of parallel manipulators, IFToMM J. Mech. Mach. Theory 39 (2004) 857-870.

[18]. R.I.Alizade, F. C. Can, E. Gezgin, Structural synthesis of Euclidean platform robot manipulators with variable general constraints, IFToMM J. Mech. Mach. Theory 43 (2008) 1431-1449.

Proceedings of the International Symposium of Mechanism and Machine Science, 2017
AzCIFToMM – Azerbaijan Technical University
11-14 September 2017, Baku, Azerbaijan

Topics 1. Manipulators and robots

Analysis and Manufacturing of 6 DoF Hybrid Robot Manipulator for Teleoperation in Medical Applications

Erkin GEZGİN
Izmir Katip Celebi University
Department of Mechatronics Engineering, Turkey
E-mail: erkin.gezgin@ikc.edu.tr

Abstract
Parallel to the rapidly developing technology, robot manipulators, whose areas of usage have continuously been expanded from the last periods of past century, have been took part in many different successful applications. Thanks to its increasing significance, nowadays medical science is one of the primary areas of those applications. Thus, this study targets mainly the field of medical science. Within the scope of this paper, six degrees of freedom hybrid robot manipulator with large workspace and adequate precision was introduced and equipped with dual actuators in its two Cartesian axes for possible haptic integration for the future. Target hybrid manipulator was designed in such a way that it can be used in various related medical applications such as teleoperations in robotic surgery, surgical navigation, dental and laparoscopic simulations. After the structural design part was completed, direct and inverse kinematic analysis procedures were carried out and by using rapid prototyping techniques the manipulator was manufactured.
Keywords: Hybrid Robot Manipulators, Teleoperation, Kinematic Analysis.

1. Introduction

By the help of robot manipulators, wide ranges of robotic applications that are capable of haptic feedback from virtual or distant environments are continuously increasing in many areas for various user profiles. While utilizing novel algorithms in haptic control provide life like feedbacks, new manipulator designs offer larger workspaces and increased manipulation precision. Although related studies in the literature are mostly focused on control parts of the issue, design of a capable robot manipulator with sufficient degrees of freedom for predefined workspaces with respect to the given tasks and constraints should not be left unattended as it constitutes the most important part in this research area.

Wayne et al. [1] surveyed three different control algorithms that are related to the haptic manipulators in terms of interactions between humans and robotic devices and introduced their comparisons with each other. In their study authors created a bridge between the old and current developing control algorithms to emphasize the rapid development in the related literature. Hyung et al. [2] started their study by considering the negative effects of singularities in parallel manipulators on the haptic systems. In the light of their research, they proposed four task based and redundant control algorithms for the singularity problems of six degrees of freedom parallel haptic manipulator with four sub chains that was also designed by them. Also they compared the results of their algorithms in a simulation environment. Erwin et al. [3] designed force controlled haptic planar manipulator for the movement control analysis of human arm. In their study they reduced the contact instability problem by using servo based control system on the lightweight but stiff manipulator. Their manipulator and the controller design were tried on a subject that performs a position based task and the results were introduced. Schouten et al. [4] designed a torque controlled manipulator with haptic controller to specify the dynamics of human wrist joint. In their study the dynamics of the human wrist joint and effects due to neurological dysfunctions were measured under virtual conditions. Dede et al. [5] designed six degrees of freedom haptic hybrid robot manipulator that is capable of displaying point type contact. Authors reconfigured the R-Cube manipulator for the translational part of the system in terms of dimensions and orientations in order to comply with the requirements of the haptic system design criteria. The most important merits of the system are introduced as its compactness and high stiffness. In their study authors also presented the integration of the hybrid manipulator mechanism with control interface. Ryu et al. [6] designed six degrees of freedom modular manipulator in order to control a mobile system by means of teleoperation. Their introduced design has dual parallel manipulators with individual three degrees of freedom that are attached each other to form six degrees of freedom modular manipulator system. The system is capable to be used in the control of both planar and spatial tasks in various applications by utilizing only the necessary actuators and the manipulator section to reduce the CPU loads during calculations. Pinskier et al. [7] proposed a flexure based haptic enabled modular manipulator for micromanipulation tasks. In their study they investigated and verified the performance of an experimental 2 degrees of freedom configuration. Tian et al. [8] introduced the design of six degrees of freedom precision positioning system that was formed by the assembly of dual three degrees of freedom individual systems operated by piezoelectric actuators. In their study motion with high precision capability was obtained.

After the investigation of brief literature survey, it can be easily seen that, usage of robot manipulators for various fields are increasing. Throughout the literature, each study has tried to overcome the mechanical and software constraints by proposing new manipulator designs along with new control schemes to achieve precise, comfortable and efficient manipulation. Considering the advances in the field, this study tries to introduce six degrees of freedom new hybrid manipulator design that is formed by the assembly of three degrees of freedom serial spherical and three degrees of freedom parallel Cartesian manipulators for the medical applications. Cartesian part of the manipulator is modified by considering R-Cube [9] Cartesian parallel manipulator design in order to decrease the total number of dyads to achieve small footprint and comfortable manipulation in its workspace. While the semi-decoupled nature of the manipulator renders kinematic analysis problems to be solved easier, it also provides easy solutions to control problems. Although the study does not cover haptic feedback control, the manipulator is equipped with two actuators for future haptic integration. Throughout the study, structural design of the manipulator was introduced along with its direct and inverse kinematic analysis tasks. Also the manufacturing steps were shown along with the first manipulator prototype.

2. Structural Design and Synthesis

As mentioned in previous section the main aim of this study is to design a robot manipulator that will be used for the teleoperation tasks in medical applications such as robotic surgery, surgical navigation, dental and laparoscopic simulations. In the light of this aim, prior to the structural synthesis, design constraints of the task were specified as below.

- The end effector of the robot manipulator should be capable of mimicking all of the rigid body motions in space to ensure adequate teleoperation control.
- In order to utilize the robot manipulator for various different tasks, its overall workspace should be large and singularity free.
- Kinematic structure of the robot manipulator should be able to adapt various different applications without any modifications.
- Structure of the manipulator should be as simple as possible to render the kinematic analysis and control tasks easier.
- As the manipulator will be utilized for medical applications, it should have a structure that provides an adequate precision.

Considering the criterions above, structure of the manipulator was determined to be hybrid. The overall system was decided to be designed in a way that three degrees of freedom Cartesian parallel manipulator section is responsible for translations while its three degrees of freedom serial spherical manipulator section is responsible for orientations. Thus the overall degrees of freedom become six. In order to fulfil the design constraints in Cartesian space, structure of the R-Cube parallel manipulator was modified so that Cartesian part of the final manipulator has two dyads instead of three. Although removing the dyad that is responsible for the z translation from the manipulator cancelled its decoupled motion in z axis, the hybrid manipulator gained a larger workspace and a smaller footprint (Figure 1-2). In accordance with the possible haptic integration for future, the manipulator was equipped with dual actuators that are responsible for decoupled x and y translations. Moreover to be able to inspect z translation, single encoder was attached to one of the dyads.

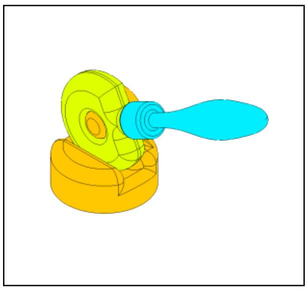

While it is clear that, the serial part of the hybrid manipulator is three degrees of freedom, the mobility of the Cartesian section can be calculated by using the formulation [10] introduced below for the Cartesian manipulators.

$$M = (\lambda + 3) + \sum_{i=1}^{c_l}(d_i - D) + \sum_{i=1}^{c_l}(f_i - \lambda_i) + q - j_p \quad (1)$$

Where in equation 1, λ is the space or subspace number, D is the dimension of the vectors in Cartesian space, d_i represents the dimensions of the vectors on the subspaces of the structural groups on the related leg, f_i is the total degrees of freedom of all joints in related leg, q is the number of excessive links, j_p is the number of passive degrees of freedoms, and c_l is the total number of legs. If the variables of this mobility equation are evaluated with respect to the designed manipulators Cartesian section, the mobility will be calculated as three.

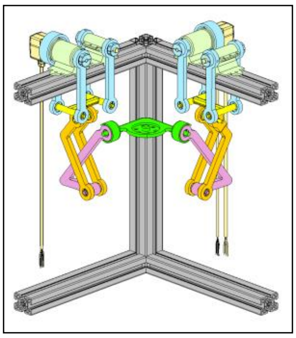

Fig. 1. a) Three Degrees of Freedom Serial Spherical Manipulator Responsible for Orientations, b) Three Degrees of Freedom Cartesian Manipulator Responsible for Orientations

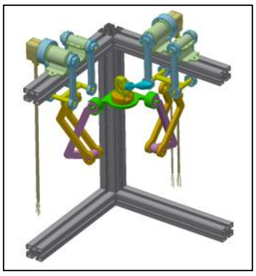

Fig. 2. Designed Six Degrees of Freedom Hybrid Robot Manipulator

$$M = (4+3)+(2-3)+(2-3)+(7-5)+(7-5)+0-6=3$$

When the overall hybrid manipulator is considered, it can easily be seen that the kinematic structure of the manipulator consists of three closed loops, 17 revolute joints, and 15 links including the ground (Figure 3).

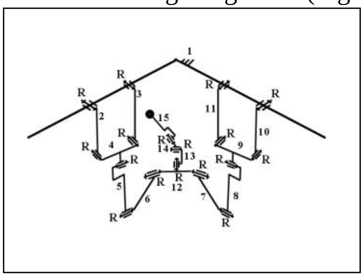

Fig. 3. Simple Kinematic Structure of Designed Hybrid Manipulator

3. Kinematic Analysis

This section is devoted to the direct and inverse kinematic analysis of the proposed hybrid manipulator. As the kinematic analysis of serial spherical section is straight forward and known, only Cartesian part of the manipulator will be considered.

3.1. Direct Task

Section view of the Cartesian part of the hybrid manipulator from the x-z plane is shown in figure 4 by revealing all its construction parameters and variables. Point P on the platform is taken so that it locates at the intersection of the three revolute axis of the serial spherical manipulator section.

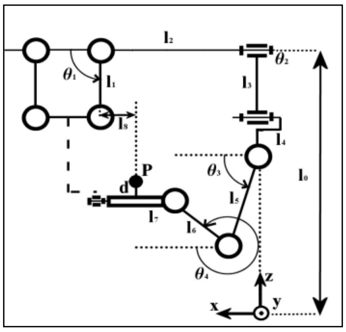

Fig. 4. Section View of the Cartesian Part of The Hybrid Manipulator from the x-z Plane

As the translations on x and y axes are decoupled, the x and y coordinates of the P point on the platform can be easily calculated by the equations below.

$$P_x = l_2 + l_1 \cos\theta_1 - l_8$$
$$P_y = l_2 - l_3 \cos\theta_2 - l_8 \qquad (2)$$

It can be easily seen from the equation 2 that x and y coordinates of the point P on the platform depends only the variable angles θ_1 and θ_2 respectively. However, due to the modified Cartesian part, z coordinate of point P should be calculated in a more complex manner.

$$P_z = l_0 - (l_3 \sin\theta_2 + l_4 + l_5 \sin\theta_3 + l_6 \sin\theta_4 - d) \qquad (3)$$

As seen in equation 3, z coordinate of the point P on the platform depends on four individual variable angles ($\theta_1, \theta_2, \theta_3, \theta_4$), yet as the Cartesian section of the manipulator has three degrees of freedom, one of the dependent variables should be eliminated from the equation. From this point of view in order to eliminate the selected parameter θ_4 from the equation 3, x coordinate of the point P will be written in another form.

$$P_x = l_5 \cos\theta_3 + l_6 \cos\theta_4 + l_7 \quad (4)$$

When the x coordinates of point P in equation 2 and 4 are equalized,

$$\cos\theta_4 = K_1,\ K_1 = \frac{(l_2 + l_1\cos\theta_1 - l_8 - l_5\cos\theta_3 - l_7)}{l_6} \quad (5)$$

equation 5 will be obtained. Also by using equation 3,

$$\sin\theta_4 = A_1 - K_2,\ A_1 = -\frac{P_z}{l_6},$$
$$K_2 = \frac{(-l_0 + l_3\sin\theta_2 + l_4 + l_5\sin\theta_3 - d)}{l_6} \quad (6)$$

equation 6 can be written as above. If the squares of the equation 5 and 6 are taken and added together side by side,

$$A_1^2 - 2K_2A_1 + K_3 = 0, K_3 = K_1^2 + K_2^2 - 1 \quad (7)$$

equation 7 without the dependent variable θ_4 will be obtained. If the quadratic equation is solved for the parameter A_1,

$$A_{1.1}, A_{1.2} = \frac{2K_2 \pm \sqrt{4K_2^2 - 4K_3}}{2} \quad (8)$$

two solutions will be found. Using these solutions, two distinct solutions for the z coordinate of point P can be calculated.

$$P_{z1} = -l_6 A_{1.1}$$
$$P_{z2} = -l_6 A_{1.2} \quad (9)$$

At this point it should be noted that, if the system is being used in the upper section of the workspace, the z coordinate of point P should be taken from the solutions that has the larger value and if the system is being used in the lower section of the workspace, the z coordinate of point P should be taken from the solution that has the smaller value.

3.2. Inverse Task

Similar to the direct task as the translations on x and y axes are decoupled, variable angles θ_1 and θ_2 can be easily calculated by using the given values of x and y coordinates of point P.

$$\theta_1 = \cos^{-1}\frac{P_x - l_2 + l_8}{l_1}$$
$$\theta_2 = \cos^{-1}\frac{P_y - l_2 + l_8}{l_3} \quad (11)$$

In order to find the variable angle θ_3 by using the given value of z coordinate of point P, θ_4 should be eliminated by utilizing the equations 3 and 4.

$$l_6\sin\theta_4 = R_1 - l_5\sin\theta_3,\ R_1 = l_0 + d - l_3\sin\theta_2 - l_4 - P_z \quad (12)$$

$$l_6\cos\theta_4 = R_2 - l_5\cos\theta_3,\ R_2 = P_x - l_7 \quad (13)$$

When the squares of equation 12 and 13 are taken and added side by side, a single equation is obtained that is dependent on the variable θ_3.

$$R_1\sin\theta_3 + R_2\cos\theta_3 = R_3,\ R_3 = \frac{R_1^2 + R_2^2 + l_5^2 - l_6^2}{2l_5} \quad (14)$$

If $\cos\theta_3$ is replaced with $\sqrt{1-\sin^2\theta_3}$ in equation 14, equation below will be formed.

$$(R_1^2 + R_2^2)\sin^2\theta_3 - 2R_1R_3\sin\theta_3 + (R_3^2 - R_2^2) = 0 \quad (15)$$

Utilizing equation 15, value of $\sin\theta_3$ can be calculated easily.

$$(\sin\theta_3)_{1,2} = \frac{2R_1R_3 \pm \sqrt{4R_1^2R_3^2 - 4(R_1^2 + R_2^2)(R_3^2 - R_2^2)}}{2(R_1^2 + R_2^2)} \quad (16)$$

Finally using equation 16, θ_3 can be calculated.

$$(\theta_3)_{1,2} = \sin^{-1}\frac{2R_1R_3 \pm \sqrt{4R_1^2R_3^2 - 4(R_1^2 + R_2^2)(R_3^2 - R_2^2)}}{2(R_1^2 + R_2^2)} \quad (17)$$

4. Prototype Manufacturing

After the completion of the kinematic analysis and simulation runs, manufacturing of the hybrid robot manipulator was carried out. All of the links of the designed manipulator was printed by using rapid prototyper that utilizes ABS-Plus material. Also the manipulator frame was constructed by aluminum profiles to reduce the overall weight of the system (Figure 6).

Fig. 6. Manipulator Links that are Printed oh Rapid Prototyper and the Aluminum Manipulator Frame

As mentioned before due to possible haptic feedback integration to the manipulator for future, two of its translation axes were equipped with brushless maxon actuators with hall effect sensors and encoders (Figure 7).

Fig. 7. Brushless Maxon Actuators and the Detail of the Passive Revolute Joint

In order to be able to inspect the z translation of the system single Maxon HEDL-5540 encoder was attached to a joint located on one of the dyads of the manipulator (Figure 8) to measure the variable θ_3 (Figure 4).

Fig. 8. Maxon HEDL-5540 encoder

Overall prototyped hybrid manipulator can be seen in Figure 9 with its Cartesian Part and the attached serial part on the platform.

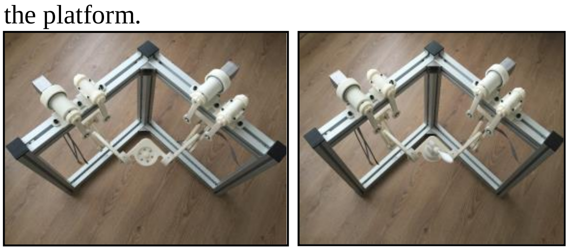

Fig. 9. Prototype of the Hybrid Manipulator

5. Conclusions

Throughout this paper six degrees of freedom hybrid manipulator with large workspace and low footprint was proposed and manufactured for medical applications. Hybrid structure was formed by using three degrees of freedom modified R-Cube Cartesian manipulator for translations and attached on its platform, three degrees of freedom serial spherical manipulator for orientations. The direct and inverse tasks of the Cartesian part of the proposed manipulator were introduced along with the equations. As the manipulator was equipped with dual brushless actuators in its Cartesian part, possible haptic integration will be considered in future studies.

6. Acknowledgements

This work was supported by the Research Fund of the İzmir Katip Celebi University Project Number: 2013-2-FMBP-08

References

[1]. Wayne J. Book, Davin K. Swanson, Reach out and touch someone: controlling haptic manipulators near and far, Annual Reviews in Control 28 (2004) 87-95.

[2]. Hyung Wook Kim, Jae Hoon Lee, Il Hong Suh,Byung-Ju Yi, Comparative study and experimental verification of singular-free algorithms for a 6 DOF parallel haptic device, Mechatronics 15 (2005) 403-422.

[3]. Erwin de Vlugt, Alfred C. Schouten, Frans C.T. van der Helm, Piet C. Teerhuis, Guido G. Brouwn, A force-controlled planar haptic device for movement control analysis of the human arm, Journal of Neuroscience Methods 129 (2003) 151-168.

[4]. Alfred C. Schouten, Erwin de Vlugt, J.J. Bob van Hilten, Frans C.T. van der Helma, Design of a torque-controlled manipulator to analyse the admittance of the wrist joint, Journal of Neuroscience Methods 154 (2006) 134–141.

[5]. Bilgincan T, Gezgin E., and Dede M.I.C. "Integration of the hybrid-structure haptic interface: HIPHAD v1.0." In Proceedings of the International Symposium of Mechanism and Machine Theory, (2010) 267-284.

[6]. Dongseok Ryu, Jae-Bok Song, Changhyun Cho, Sungchul Kang, Munsang Kim, Development of a six DOF haptic master for teleoperation of a mobile manipulator, Mechatronics 20 (2010) 181-191.

[7]. Joshua Pinskier, Bijan Shirinzadeh, Leon Clark, Yanding Qin, Sergej Fatikow, Design, development and analysis of a haptic-enabled modular flexure-based manipulator, Mechatronics, http://dx.doi.org/10.1016/j.mechatronics.2016.10.004.

[8]. Cai, Kunhai, Yanling Tian, Fujun Wang, Dawei Zhang, Xianping Liu, and Bijan Shirinzadeh. "Design and control of a 6-degree-of-freedom precision positioning system." Robotics and Computer-Integrated Manufacturing 44 (2017) 77-96.

[9]. Li, Weimin, Feng Gao, and Jianjun Zhang, R-CUBE, a decoupled parallel manipulator only with revolute joints, Mechanism and Machine theory 40.4 (2005) 467-473.

[10]. Alizade, Rasim, Cagdas Bayram, and Erkin Gezgin, Structural synthesis of serial platform manipulators, Mechanism and Machine Theory 42.5 (2007) 580-599.

Proceedings of the International Symposium of Mechanism and Machine Science, 2017
AzC IFToMM – Azerbaijan Technical University
11-14 September 2017, Baku, Azerbaijan

Energy Efficient Autonomous Lower Limb Exoskeleton for Human Motion Enhancement

Nazim Mir-Nasiri, Hudyjaya Siswoyo Jo
Electrical and Electronic Engineering Department,
Nazarbayev University, Astana, Republic of Kazakhstan,
E-mail: nazim.mir-nasiri@nu.edu.kz, hsiswoyo@swinburne.edu.my

Abstract
The paper describes conceptual design, control strategies and partial simulation for a new fully autonomous lower limb wearable exoskeleton system for human motion enhancement that can support its weight and increase strength and endurance. During the last decade, researchers have focused on the development of lower limb exoskeletons for power augmentation for military or medical assistance. Various problems remain to be solved where the most important is the creation of a power and cost efficient system that will allow an exoskeleton to operate for extended periods without being frequently recharged. The designed exoskeleton is enabling to decouple the weight/mass carrying function of the system from the forward motion function which reduces the power and size of propulsion motors and thus the overall weight, cost of the system. The decoupling takes place by blocking the motion at knee joint by placing passive air cylinder across the joint. The cylinder is actuated when the knee angle has reached the minimum allowed value to bend. The value of the minimum bending angle depends on usual walk style of the subject. The mechanism of the exoskeleton features a seat to rest the subject's body weight at the moment of blocking the knee joint motion. The mechanical structure of each leg has six degrees of freedom: four at the hip, one at the knee and one at the ankle. Exoskeleton legs are attached to subject legs using flexible cuffs. The operation of all actuators depends on the amount of pressure felt by the feet pressure sensors and knee angle sensor. The sensor readings depend on actual posture of the subject and can be classified in three distinct cases: subject stands on one leg, subject stands still on both legs and subject stands on both legs but transit its weight from one leg to other. This exoskeleton is power efficient because electrical motors are smaller in size and did not participate in supporting the weight like in all other existing exoskeleton designs.
Keywords: Energy efficient system, exoskeleton, motion enhancement, robotics.

1. Introduction

EXOSKELETON for human performance enhancement are wearable devices that can support and assist the user besides increasing their strength and endurance. The lower limb exoskeletons are now applied to several fields, including power augmentation for the military [1] or medical assistance [2], and rehabilitation [3-5]. In such devices human provides control signals while the exoskeleton actuators provide required power for performing the task. A distinctive characteristic of exoskeletons compared to other robotic interfaces with haptic feedback is their close physical and cognitive coupling between the robot and the user [6]. In such design, the physical human-robot interfaces were developed, i.e. the mechanical and sensory components that mediate the transfer of physical interaction between the user and the exoskeleton [7].

On lower extremity exoskeletons, most previous researchers paid their attention in developing walking aid systems for gait disorder persons or aged people [8, 9]. One of those systems is HAL (Hybrid Assistive Leg) developed by Yoshiyuki Sankai of University of Tsukuba was aimed at assisting human leg muscles during walking [10].The system was based on electromyography (EMG) sensing of human muscles as the primary drive signals. The development resulted in several versions of HAL with the latest HAL-5 in 2009 [11]. The exoskeleton was motor powered on the hip and knee joints, leaving other joints free. The significance of their design is the implementation of EMG sensing which detects muscle activities before actual limb movement. Motor driven joints approach was taken by other researches as well [12]. The developed Berkeley Lower Extremity Exoskeleton (BLEEX) was aimed at enhancing human strength and endurance for payload transport [13,14]. The exoskeleton incorporates hydraulic actuation on all three sagittal joints and two coronal joints on the hip with all others joints free. The overall control design of BLEEX was to minimize interface between human and machine. Therefore, there was no sensor in direct measurement of human leg but includes all required sensors for determining the dynamics of the exoskeleton. The control system monitors the dynamics of the exoskeleton to determine operator's intention of motion. The significance of BLEEX is of the complex control network distributed throughout the exoskeleton and a custom designed onboard engine to power the hydraulic actuation system.

Hydraulic actuation was implemented by various researchers. The ECUST Leg Exoskeleton Robot (ELEBOT) designed at East China University of Science and Technology (ECUST) shares the similar design goal as BLEEX but with a simplified system [15]. ELEBOT has the same approach of using hydraulic system as joint actuation. However, it was identified that only the knee joints would require substantial actuation support and therefore leaving all other joints free. The control of ELEBOT also came close to that of BLEEX by only monitoring stance phase and torque generated on the hydraulic actuators.

While the above exoskeleton designs requires substantial power for operation on low efficiency, an exoskeleton design at Massachusetts Institute of Technology (MIT) attempted to lower the power requirement for load carrying [16]. The exoskeleton has only series elastic actuation at hip sagittal joints, variable damper at the knee joints and spring at ankle sagittal joints. The control is based on a state machine and monitors forces and orientation of the exoskeleton to determine the states. The Walking Assist Device designed at Honda Research and Development aims at increasing the lower extremity endurance of the elderly and those with weak legs [17]. By partially supporting the upper body weight, the user bears less weight on the lower limbs and requires less energy for motion. The device was a pair of non-anthropomorphic mechanical limbs attached to a seat. The whole device was fixed between the user’s legs during operation. The walking assist device was only powered by electric motor at each of the knee joints and incorporates only pressure sensors beneath the shoes of the device. The control monitors user’s weight applied on the pressure sensors and provides required force on both knees to achieve the predetermined weight reduction on both of the user’s legs.

Various problems remain to be solved, the most daunting being the creation of a power and cost efficient system that will allow an exoskeleton to operate for extended periods without being frequently plugged into external power. The paper presents a conceptual design and partial simulation of a new exoskeleton that will enable to decouple the weight/mass carrying function of the system from the forward motion control which will reduce the power and size of propulsion motors and thus reduce the overall weight, cost and required electrical power for the system. Such lighter and cheaper devices are currently important engineering research area in medicine and military [18].

II. Mechanical Structure of the Exoskeleton

Fig. 1 shows the conceptual sketch of the proposed exoskeleton structure in Solid Works. In the figures seat 1 is there to rest subject’s body and support its weight. Each exoskeleton leg has four degrees of freedom: two at the hip 2, one at the knee 3 and one at the ankle 4 to allow legs forward and lateral motions. Cushioned seat 1 in between subject crotch is connected to two parallel rigid pipes 5 at the back the object. A back panel 6 mounted onto the rigid pipes serves as a platform for control and power supply mounting. At hip level, the two parallel rigid pipes extend out to the two hip coronal joints. The link then continues to both sides of the hip 2 where sagittal and transverse joints are located, subsequently to the knee joints 3 and through the ankle joints 4 to the ground. Both exoskeleton legs are attached to subject legs using flexible cuffs 7. Single degree four-bar linkage mechanism 8 with rotary joints at the hip level provides hip-centered lateral rotation of the exoskeleton leg around vertical axis. The remaining three single-degree parallel axes rotary joints at the hip 2, knee 3 and ankle 4 provide freedom of flexion at the joints. Pneumatic cylinders 9 are used to block the motion at the knee joints 3 when necessary to support the weight.

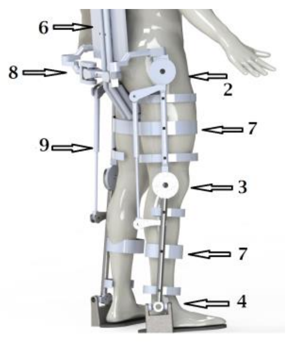

Fig. 1. Components of the exoskeleton

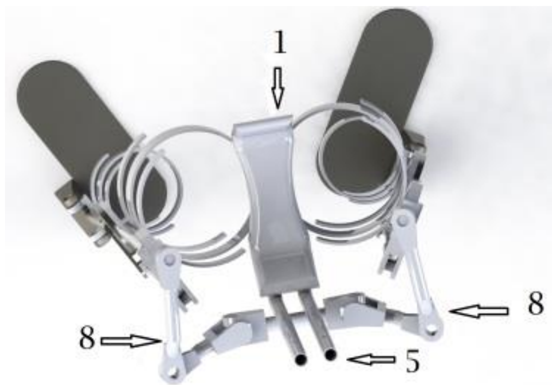

Fig. 2. Shows schematic diagrams of the exoskeleton

In these figures 1 are adjustable telescopic members of the exoskeleton; 2 are dummy pneumatic cylinders that are able to inhibit the motion at the knee joints; 3 and 4 are the sensors to detect motion of subject thigh and shank; 5 are springs to support feet 6 of the exoskeleton; 7 and 8 are flexible belts to fasten exoskeleton to the subject thigh and shank. In the figures M_1 and M_2 are motors driving the hip and knee joints of each leg; C_1 and C_2 are solenoid valves of the pneumatic cylinders 2 that are able to inhibit motions at the knee joints; S_1 and S_2 are flexible strips 3 and 4 with bonded strain gages that are able to sense the tiny motions of subject limbs; F_1 and F_2 are foot pressure sensors to sense the amount of pressure applied by the ground on the exoskeleton sole 6 during the walk. The pressure at the exoskeleton sole is generated due to the transmission of the weight forces via mechanical structure to the ground while the subject is resting on the seat.

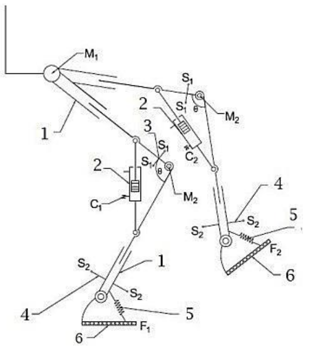

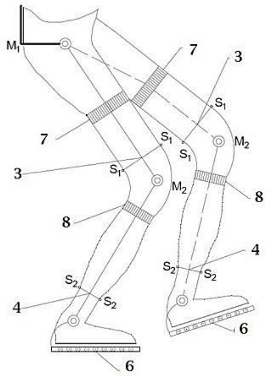

III. Human-Machine Interfacing and Control

The operation of all actuators, i.e. hip joint motors M1, Knee joint motors M2 the knee motion inhibiting cylinders solenoid valves C1 and C2, depends on the amount of pressure felt by the feet pressure sensors F1 and F2 (Fig. 2). The pressure on the feet depends on actual posture of the subject and can be classified in three distinct cases. If (case 1, Fig.3b) the subject is standing on one leg and the knee motion is inhibited, then the total subject body weight P_b is resting on the seat 1 (Fig.1) and the weight is fully transmitted via stationary leg structure to the ground. The expected pressure reading from the corresponding foot sensors F (Fig. 4) will be at its maximum possible value $P=P_b$. However, the reading from other foot pressure sensor will be at zero value because it is not in touch with the ground. If (case 2, Fig. 3a) the subject stands still on both legs then the total subject body weight is almost equally shared by both leg structures and the expected pressure reading from both feet sensors will be about half of the maximum possible value $P=P_b/2$. If (case 3, Fig. 3c, d) the subject is in the stage of transiting the weight from, e.g. leg 1 to leg 2 while standing on both legs, then the reading from sensor F_1 will gradually reduce from its half value $P_b/2$ to zero while the reading from sensor F_2 will gradually increase from its half value $P_b/2$ to its maximum possible value P_b. The pressure reading P at the shoe-ground sensor F is due to both object's and exoskeleton's weights.

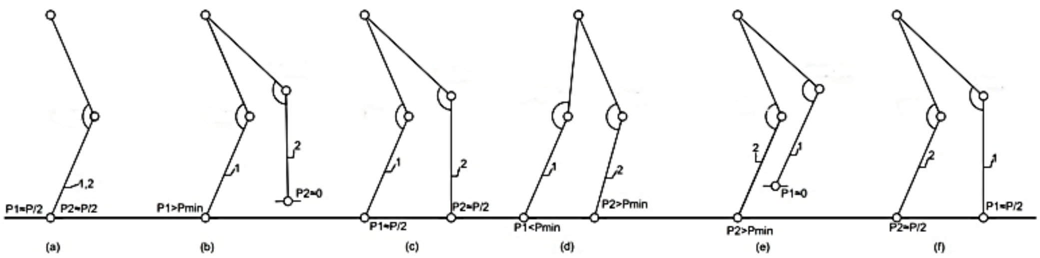

Fig. 3. Gaits of the exoskeleton

Several rules have been established to control the operation of the actuators during the subject walk. The first rule establishes a condition when the knee joint motion has to be inhibited, i.e. should be blocked by cylinder. Simultaneously, the hip and knee motors M_1 and M_2 have to be deactivated. At this condition the object puts its one foot on the ground and prepares to move the body in forward direction (leg 2 in Fig.3c). It is exactly the case when the exoskeleton is ready to carry the weight with no assistance from the leg muscles and the deactivated motors. The signal to initiate this action comes from the respective foot sensor, i.e. when the reading from the sensor is $P>0$ and it is growing. The cylinder is actuated and the motors deactivates when the contact with the ground is confirmed. This condition implies a stilt type of walk when the object's weight rests on the "rigid" leg while the object takes a step forward with another leg.

The second rule establishes a condition when the knee motion is unblocked, i.e. cylinder is deactivated and respective hip and knee motors M_1 and M_2 have to be reactivated instead. Obviously, it is the case when the reading of pressure sensors P=0, i.e. the foot is not in touch with the ground. Alternatively, if the foot is in touch with the ground it depends on gradually decreasing pressure signal from the foot sensors and the minimum allowed pressure value P_{min} that should initiate this action. At this condition the exoskeleton leg mechanism is ready to follow the intended motion of the object leg and to take a new step without hindering the leg motion (leg 1 in Fig.3d). Motors M_1, M_2 and flexible sensors S_1 and S_2 are used to execute this action (Fig. 2).

Based on the rules discussed above, the following control strategy for the walk is proposed:

- Motors M_1 and M_2 of each leg are actuated only and only if the pressure reading from the corresponding pressure sensors at the foot either zero or keeps decreasing until $P \leq P_{min}$ (second rule) in order to pick up the leg from the ground and take a step
- Cylinders solenoid valves C_1 and C_2 are actuated only and only if the pressure reading from the corresponding pressure sensors at the foot become be P>0 and keeps increasing (i.e. confirm the ground touch, first rule).

The control strategy for the motors M_1 and M_2 is aimed to make sure that the exoskeleton structure will follow the subject's leg physical motion without hindering it. The set of sensors S_1 and S_2 (flexible strips with bonded strain gages) are attached to the links of the exoskeleton (Fig. 2). When the subject limbs commence the motion the limbs will touch and bend the strips. The sensors will detect in real time any intended tiny motions of the subject's limbs and send the signals to the PID controller. The controller will react immediately by activating hip and knee motors M_1 and M_2 in order to move the links of the exoskeleton away from the object limbs and thus to restore the original shape of the strips. The set point of the PID controller is zero signals from the sensors. The PID controller can provide fast system response and accurate positioning of the exoskeleton links with respect to subject's limps. As a result object limp can move free with no obstruction from the exoskeleton.

The system operational or logic flow chart is shown in Fig. 4. If the common switch is on then the system start receiving data from pressure F sensors (Fig. 2). If P >0 that means that the foot is in contact with the ground. If the value of P is growing that means the subject is stepping of that foot and the motors have to be deactivated and the cylinder has to be activated. This is weight supporting condition for the exoskeleton. If instead P is decreasing that means the subject is transmitting the weight from this leg to another one and if $P \geq P_{\min}$ then motors should kept deactivated and the cylinder is activated to support the weight. If $P \leq P_{min}$ that means the limit is reached and the subject is ready to move this leg one step forward. Therefore, the cylinder valve is deactivated to allow the motion of the exoskeleton components. In this condition the reading of strain gages S_1, S_1', and S_2, S_2' and operation of both motors M_1 and M_2 are initiated. By comparing the reading from the pair of sensors S_1, S_1', and S_2, S_2' the sense of motors rotation can be established. For example, if the reading $S_1 > S_1'$ the rotation of M_1 can be set in clockwise direction. Conversely, if $S_1 < S_1'$ then the rotation of M1 can be set in counterclockwise direction. Same is true for the data received from sensors S_2, S_2' that control the sense of rotation of motor M_2. The speed of motor rotation is controlled by the motor driver and PWM signal received from the microcontroller. PWM is selected to be proportional to the absolute difference between the readings of the pair of sensors, i.e. $| S_1 - S_1' \| S_2 - S_2'|$. It is very effective way of monitoring the speed of the motor response to the object intention to move a limb. The higher is the pressure applied by the user to the strip the higher is the acceleration of the motor to restore the shape of the strip with attached strain gages. It is in a way implementation of proportional control strategy for the motor speed control. The microcontroller operates in loop continuously checking status of all sensors, making decision and actuating either cylinder valves or the motors as long as the common switch is on (Fig. 4).

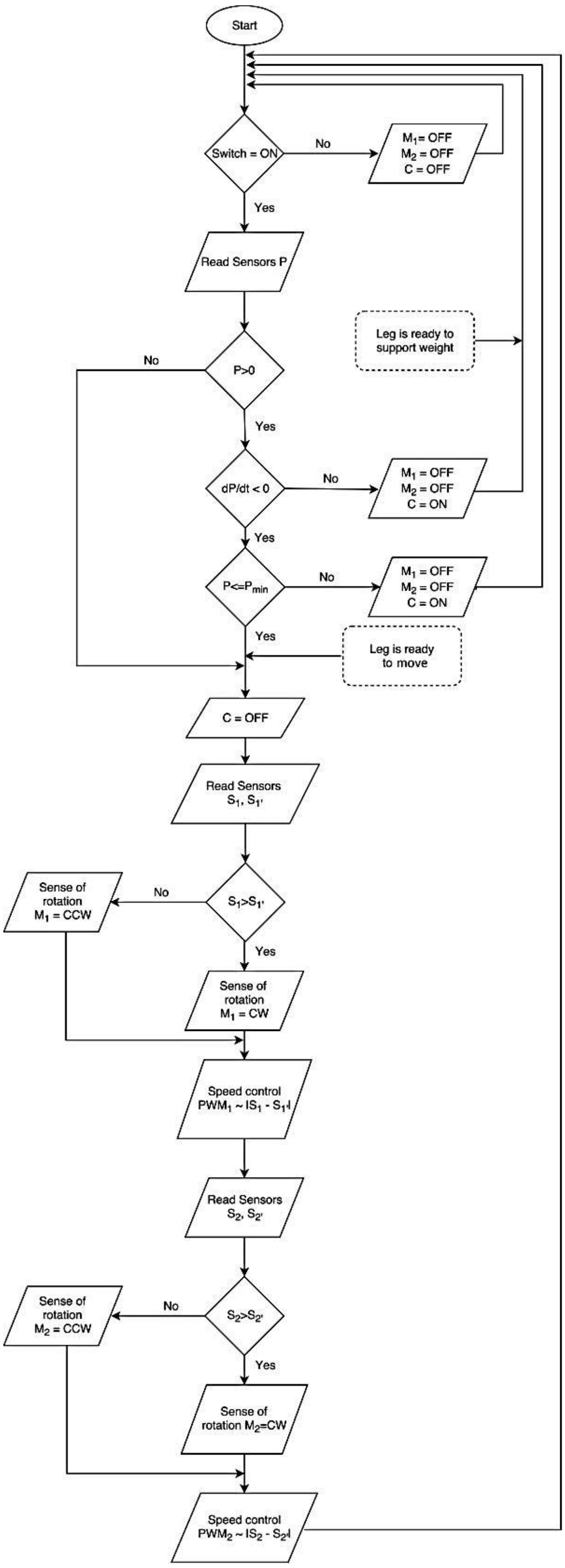

Fig. 4. Flow chart of controller operation

IV. Computer Simulation of Human-Machine Interface with MATLAB Simulink

The main control system for the exoskeleton is divided into four subsystems where each subsystem is responsible for the sensing and actuation of each joint. For simulation purpose, the subject movement is taken from the recorded data of typical human lower limb movement during walking. Figure 5 shows the top layer of the program that controls the overall logic of the exoskeleton motion.

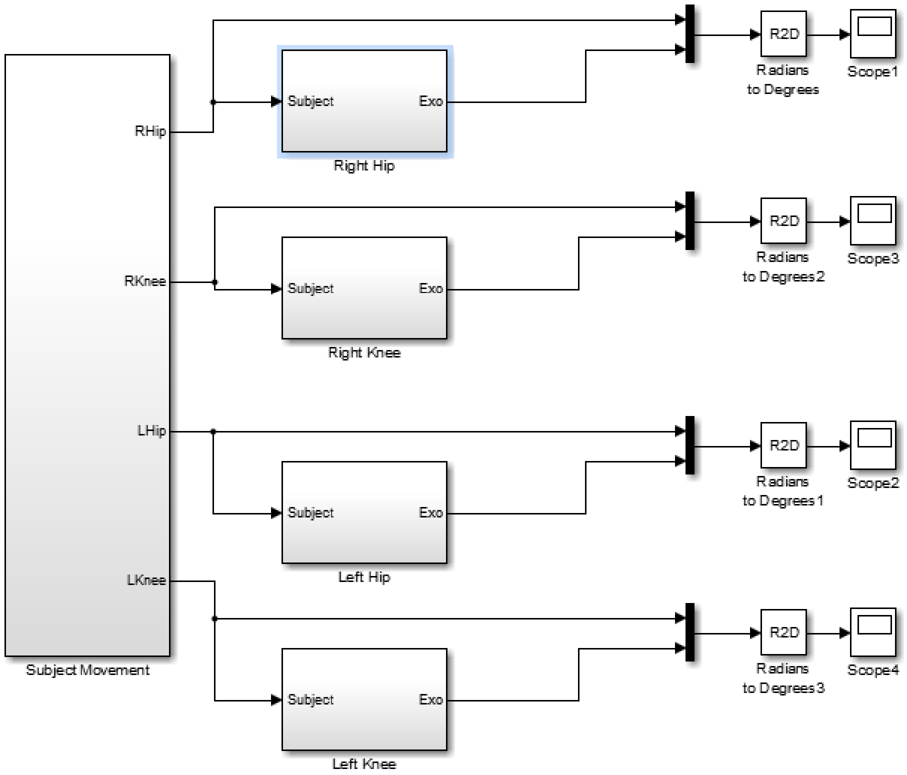

Fig. 5. Top layer of exoskeleton simulation program

The “Subject Movement” block provides the data to simulate the subject movement input to the individual joint controller which runs a closed-loop control algorithm to control the movement of its actuator

Fig. 6 and Fig. 7 show the second layer of the simulation program for hip and knee joint respectively where the closed-loop controller is implemented. The controller setup is identical for both hip and knee joint except for the addition of inhibition logic for knee joint. The controller consists of a “PID” block, “DC Motor” block, “Load Torque” block and “Sensor” block. The “PID” block calculates the desired output to be applied to the actuator, “DC Motor” block simulates the response of the DC motor towards the voltage applied, “Load Torque” block calculates the static and dynamic loads acting on the joint actuator and “Sensor” block simulate the electrical signal given by the sensing system in response to the subject movement. The DC motor model is constructed based on classical DC motor equivalent circuit as well as on the closed loop simulation technique based on the motor torque-current and speed-voltage relations. The load for the joints are constructed and calculated based on the dynamic model derived based on classical Lagrangian mechanics [19]. To simplify the code management, each torque component is grouped into a separate function block.

Fig. 8 shows the detail of the “Sensor” block. The “Cantilever Beam” block is constructed from the mathematical model of strain gauges responses to the deflection of cantilever beam that is to which it is bonded. The thigh or shank movement of the human object will result in the displacement of the deformable material (beams) which will further result in the deformation of the strain gauges. Foil type strain gauge can be attached to the deformable materials such as Low Density Polyethylene (LDPE) sheet to achieve the measurement with maximum sensitivity. The block receives the input from the movement of the thigh or shank which will create the deflection of the cantilever beam. Depending on the beams length and thickness, materials properties of the material and the position of strain gauge on the cantilever beam, the amount of strain of each gauge can be calculated as a result of this deflection. Once the strain is calculated it can be converted to output voltage by means of Wheatstone bridge circuit. In order to follow closely the subjects leg motion the output voltage from Wheatstone bridge is then compared to the zero voltage reference to generate the error for the PID controller. The PID controller then instantly applies the output to the joint DC motor to actuate and drive the exoskeleton link in order to follow the subject movement with accuracy and fast response.

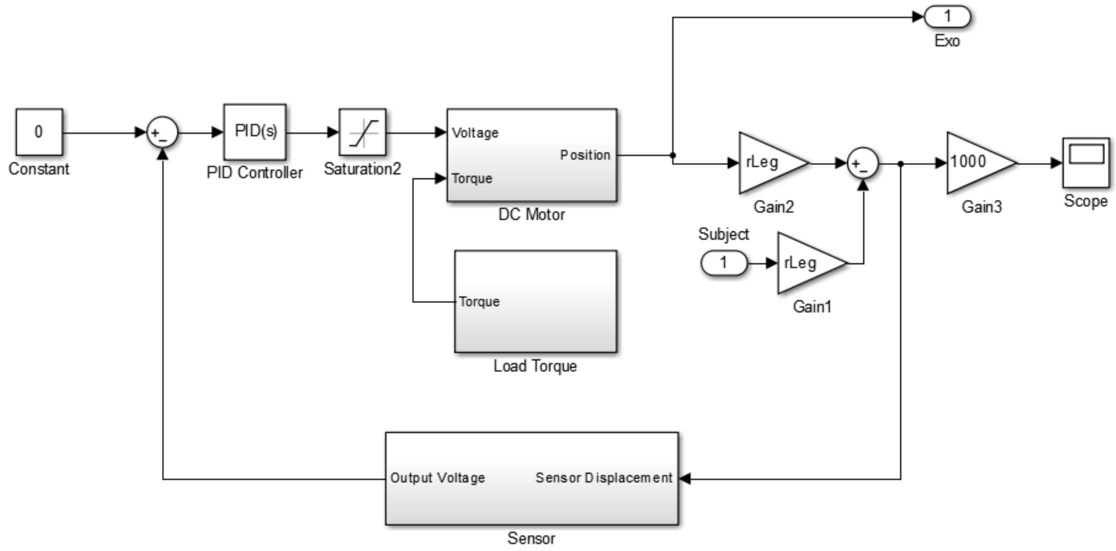

Fig. 6. Closed-loop controller for hip joint

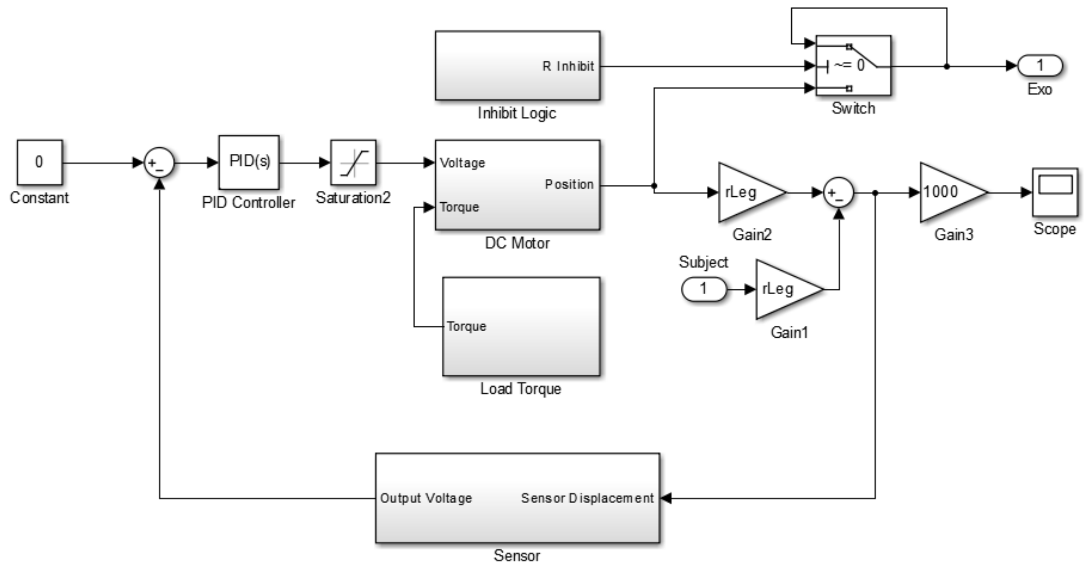

Fig. 7. Closed-loop controller for knee joint

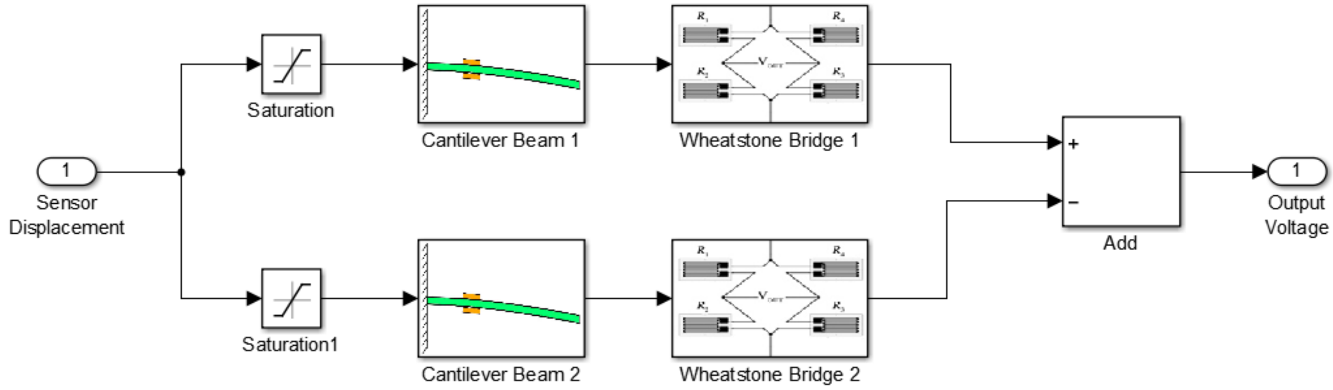

Fig. 8. Simulink model of the sensing subsystem

The parameters used in the simulation work are shown in Table 1.

TABLE I
SIMULATION PARAMETERS

Symbol	Quantity	Value
	Mechanical Parameters	
r_{leg}	Length of leg (thigh and shank)	0.4 m
m_{thigh}	Mass of thigh	4 kg
m_{shank}	Mass of shank	3 kg
m_{knee}	Mass of knee	1 kg
m_{ankle}	Mass of ankle	0.5 kg
	Motor Parameters (Maxon DCX32L 24V)	
K_t	Torque constant	27.3 mNm/A
R	Terminal resistance	0.331 Ω
L	Terminal inductance	0.103 mH
J	Rotor inertia	72.8 gcm^2
b	Viscous friction	5.17x10^{-3} mNm/rad/s
	Sensor Parameters	
h	Thickness of cantilever beam	5 mm
x	Strain gauge distance	35 mm
l	Length of cantilever beam	70 mm
G	Gauge factor	31

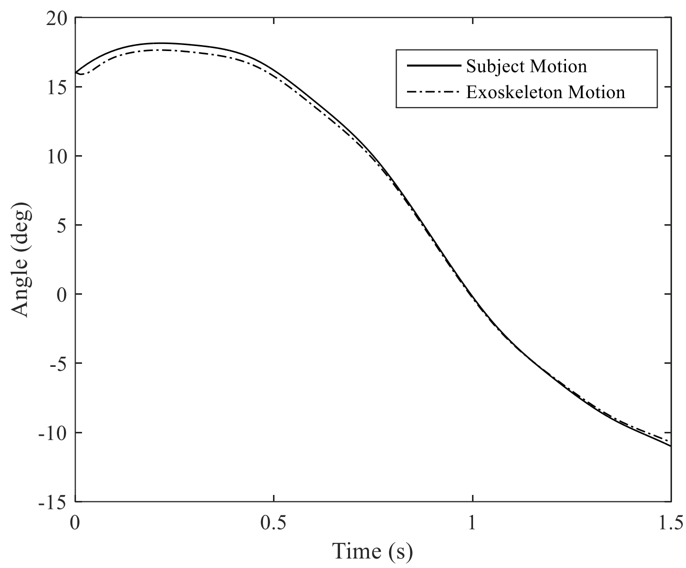

Fig. 9. Hip joint angle during leg swinging motion

Fig. 9 and Fig. 10 show the hip and knee joint angles variation of one leg during part of walking cycle (free swing of the leg). In these figures the angle of the subject's leg is shown in solid line and the angle of the exoskeleton is shown in dashed line. As it can be seen from the figures the dynamic motion of the exoskeleton leg very closely traces the motion of subject leg during its free swing in space. It proves the efficiency of the developed control system and its subcomponents.

V. Conclusion

The paper describes the methodology of mechanical design and effective control of a new exoskeleton system to enhance walk capabilities of people. It also can be used for rehabilitation of people with leg injuries. The core idea is to use exoskeleton to decouple weight carrying capabilities of the legs from its body advancing capabilities. This has been done by special logic and intelligent management of electrical motors and motion inhibiting passive pneumatic cylinders operation. The operation is managed and controlled by the microcontroller which receives the necessary data from the strain gauge sensors located at the subject's thighs and shanks and the pressure sensors located at the feet. The paper also demonstrates the MATLAB Simulink modelling of the exoskeleton leg dynamic behavior that proves fast and precise response to the human motion intentions. This approach in exoskeleton design enables the user to focus on just forward motion that takes much less muscle tension and leave to the exoskeleton to carry the heavy body weight. This makes the exoskeleton more power efficient because electrical motors are smaller in size and did not participate in supporting the weight like in all other existing exoskeleton designs. The motors just provide a synchronous fast motion of the exoskeleton leg in response to human intention to take a step.

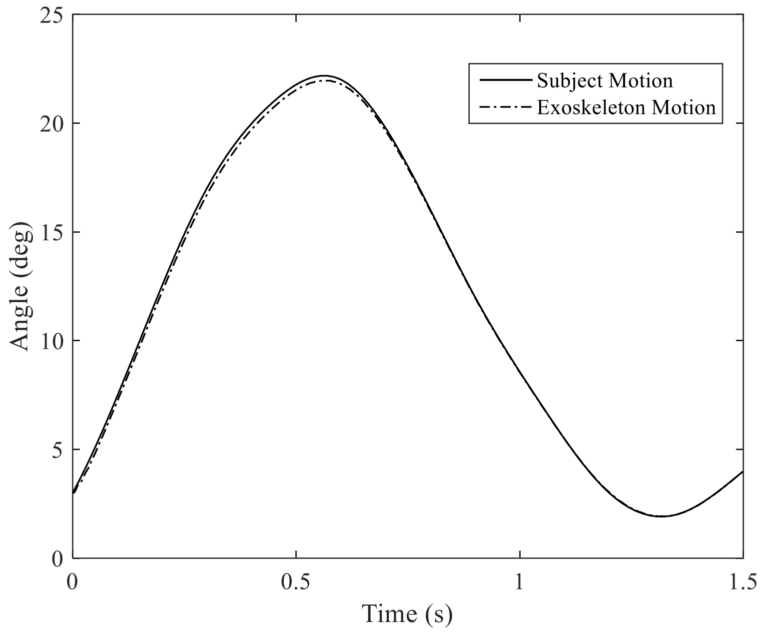

Fig.10. Knee joint angle during leg swinging motion

References

[1] Zoss, A.B., Kazerooni, H. & Chu, A., "Biomechanical design of the Berkeley lower extremity exoskeleton (BLEEX)," IEEE/ASME Transactions on Mechatronics, 11(2), pp. 128–138. 2006.
[2] K. Suzuki, G. Mito, H. Kawamoto, Y. Hasegawa, Y. Sankai, "Intention-based walking support for paraplegia patients with robot suit HAL," Journal of Advanced Robotics, 21, pp. 1441-1469, 2007.
[3] Y. Mao, S. K. Agrawal, "Design of a Cable Driven Arm Exoskeleton (CAREX) for Neural Rehabilitation", IEEE Transactions on Robotics, vol. 28, no. 4, pp. 922-931, 2012.
[4] P. K. Jamwal, Q. X. Sheng, H. Shahid, G. P. John, "An adaptive wearable parallel robot for the treatment of ankle injuries," IEEE/ASME Transactions on Mechatronics, 19(1), pp. 64-75, 2014.
[5] J. Iqbal, K. Baizid, "Stroke rehabilitation using exoskeleton-based robotic exercisers," Mini Review, Biomedical Research, 26 (1), pp. 197-201, 2015.
[6] J. L. Pons, Wearable Robots: Bio-mechatronic Exoskeletons, Wiley & Sons, Ltd.: Hoboken, NJ, USA. 2008.
[7] De Santis, B. Siciliano, A. De Luca, A. Bicchi, "An atlas of physical human-robot interaction,"

Mechanisms and Machines Theory," vol. 43, pp. 253-270, 2008.
[8] J. F. Veneman, R. Kruidhof, E. E. Hekman, R. Ekkelenkamp, E. H. Van Asseldonk, H. van der Kooij, "Design and evaluation of the LOPES exoskeleton robot for interactive gait rehabilitation," IEEE Trans. on Neural Systems and Rehabilitation Engineering, vol. 15, pp. 379-86, 2007.
[9] S. Banala, S. Agrawal, J. Scholz, "Robot assisted gait training with active leg exoskeleton (ALEX)," IEEE Trans. Neural Syst. Rehabilitation Engineering., vol. 17, pp. 2-8, 2009.
[10] H. Kawamoto, Y. Sankai, "Power assists method based on phase sequence and muscle force condition for HAL," Journal of Advanced Robotics, 19(7), pp. 717–734, 2005.
[11] T. Kawabata, H. Satoh, Y. Sankai, "Working posture control of robot suit HAL for reducing structural stress," in Proc. of IEEE International Conference on Robotics and Biomimetics (ROBIO), , Guilin, 2009, pp. 2013–2018.
[12] P. Kao, D. P. Ferris, "Motor adaptation during dorsiflexion-assisted walking with a powered orthosis," Journal of Gait Posture., vol. 29, pp. 230-236, 2009.
[13] H. Kazerooni, R. Steger, L. Huang, "Hybrid control of the Berkeley lower extremity exoskeleton (bleex)," The International Journal of Robotics Research, 25(5-6), pp. 561–573, 2006.
[14] J. Ghan, H. Kazerooni, "System identification for the Berkeley lower extremity exoskeleton (BLEEX)," In Proc. of IEEE International Conference on Robotics and Automation (ICRA), Florida, 2006, pp. 3477–3484.
[15] C. Heng, Z. Jun, X. Chunming, Z. Hong, C. Xiao, W. Yu, "Design and Control of a Hydraulic-Actuated Leg Exoskeleton for Load-Carrying Augmentation," in Proc. Of IEEE International Conference on Intelligent Robotics and Automation (ICIRA), Part I, vol. 6424, Shanghai, 2010, pp. 590–599.
[16] C. J. Walsh, D. Paluska, "Development of a lightweight, underactuated exoskeleton for load-carrying augmentation," in Proc. of IEEE International Conference on Robotics and Automation (ICRA), Florida, 2006, pp. 3485–3491.
[17] Y. Ikeuchi, J. Ashihara, Y. Hiki, H. Kudoh, T. Noda, "Walking assist device with bodyweight support system," in Proc. of IEEE/RSJ International Conference on Intelligent Robots and Systems, St. Louis, 2009, pp. 4073–4079.
[18] M. Leslie, "The next generation of exoskeletons," A Magazine of the IEEE Engineering in Medicine and Biology Society, vol. 3, no. 4, pp. 56-61, 2012.
[19] H. B. Tawakal, M. Adnan, I. Javaid, I. Umer, S. K. Umer, "Kinematic and dynamic Analysis of Lower Limb Exoskeleton," WASET International Journal of Mechanical, Aerospace, Industrial, Mechatronic and Manufacturing Engineering, , vol.6, no.9, pp. 1945-1949, 2012.

Real time controlled two dof five bar robot manipulator

Fatih Cemal CAN, Hayrettin ŞEN
Izmir Katip Çelebi University
Faculty of Engineering and Architecture
Mechatronics Engineering Department
E-mail: fatihcemal.can@ikc.edu.tr

Abstract
In this research, computer controlled two DoF five bar robot manipulator is investigated. In order to control manipulator, a human machine interface program is developed in Visual C# after completing inverse kinematic analysis of robot manipulator. By the help of inverse kinematics, this program calculates two joint variables for given positions of end point. Then the program sends a data package containing these joint variables to Arduino microcontroller. Arduino microcontroller set the positions of two servos according to calculated joint angles. Also using standard geometries, robot can follow trajectory a line, a circle and a rectangle. Furthermore, a lot of patterns can be generated using function with variable radius and angle of rotation.

Keywords: Two Dof Robot, Five bar, Arduino, Visual C#

1. Introduction

The five-bar linkage mechanism applications have been used in different engineering fields. Researcher working in mechatronics, biomedical, mechanical and electrical and electronics engineering fields designed and implemented the five bar mechanism in their published investigations. Inverse kinematics, link design, medical application, dynamic simulation, calibration and performance were topics of research interest on the five-bar linkage mechanism. Some studies about these topics are presented as follows.

As a biomedical engineering application, a laparoscopic robotic camera system based on five-bar linkage was designed and tested by Kobayashi and et al. [1]. Thisrobotic system reduce the process time for different surgical operations if human assisted camera system is compared to robot assisted the camera system.

Hybrid five-bar mechanism was investigated by researchers [2, 3]. A dynamic simulation and control of these kinds of mechanism was carried out in Simmechanics of Matlab by Zi and et al. [3]. The five-bar was driven by a constant velocity motor and servo motor in this study. The aim of the study was to control tracking trajectory of the end point of the mechanism via Traditional PD control and closed loop PD-type iterative learning control.

Inverse kinematics analysis of six different five-bar planar parallel manipulators which were RRRRR, RRRRP, PRRRP, RPRPR, RRRPR and RPRRP was presented by Alıcı[4]. Sylvester elimination method was used to solve the set of nonlinear equations in his study.
Villarreal-Cervantesand et al. [5] optimized design parameters of a five-bar parallel robot by using a novel mechatronic design approach. They designed kinematic and dynamic parameters of the five-bar's links with respect to desired trajectories [5, 6].

A position accuracy calibration of a five-bar planar parallel robot (DexTAR) was established by Joubair and et al. [7]. Experimental validation setup was constructed and the position error reduced to 0.08 mm with in the entire robot workspace of 600x600 mm.

A real-time control of a five-bar parallel robot (DexTAR) was studied using dynamic model of the robot to implement minimum time trajectory planning by Bourbonnais and et al. [8]. They used working mode region to reach points of pick and place operations. Several working modes are considered to reach same pick and place points in their study.

In this study, a five-bar linkage was designed and two links of the mechanism were produced by using 3D printer. In section 2, the inverse kinematics analysis of five-bar manipulator will be presented. In the next section human machine interface design and control algorithm will be explained. In section four electronic hardware and circuit are illustrated along with figures. Then, experimental test results will be presented in section five. Finally, a conclusion will be drawn at the end of the study.

2. Inverse Kinematic Analysis of the Robot Manipulator

Five bar mechanism has two degrees of freedom according to Grubler formulation. In inverse kinematics, end point location (P) is known in Fig. 1. Using this location, two input angles θ_1 and θ_2 must be calculated. This problem can be solved by dividing manipulator into two serial RR manipulators.

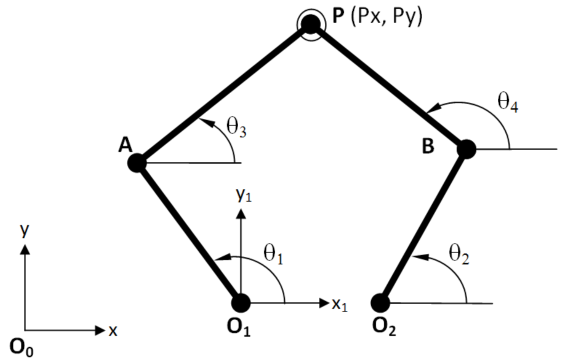

Fig. 1. Two DoF Five Bar Robot

From the first serial kinematic chain, vector loop closure equation (1) is as follows,

$$\mathrm{O_0O_1 + O_1A + AP = O_0P} \quad (1)$$

Second, the second serial kinematic chain, vector loop closure equation (2) is as follows,

$$\mathrm{O_0O_2 + O_2B + BP = O_0P} \quad (2)$$

In this study, user of the robot manipulator changes O_0P vector in human machine interface. However these equations are dependent on each joint angle related to kinematic chain. In order to compute input angles, other joint variables must be eliminated.

$$d_{x1} + i\, d_{y1} + L_1 e^{i\,\theta_1} + L_3 e^{i\,\theta_3} = P_x + i\, P_y \quad (3)$$

$$d_{x2} + i\, d_{y2} + L_2 e^{i\,\theta_2} + L_4 e^{i\,\theta_4} = P_x + i\, P_y \quad (4)$$

Rearranging equation (3), angle which is need to be eliminated is kept alone,

$$L_3 e^{i\,\theta_3} = P_x + i\, P_y - d_{x1} - i\, d_{y1} - L_1 e^{i\,\theta_1} \quad (5)$$

The offset distances in equation (5) can be combined with the end coordinates as follows,

$$L_3 e^{i\theta_3} = (P_x - d_{x1}) + i(P_y - d_{y1}) - L_1 e^{i\theta_1} \quad (6)$$

Conjugate of the equation (6) is written as follows,

$$L_3 e^{-i\theta_3} = (P_x - d_{x1}) - i(P_y - d_{y1}) - L_1 e^{-i\theta_1} \quad (7)$$

Multiplying equations (6) and (7), angle θ_3 is able to be eliminated.

$$\begin{aligned} L_3^2 = (P_x - d_{x1})^2 + (P_y - d_{y1})^2 + L_1^2 \\ - (P_x - d_{x1}) L_1 (e^{i\theta_1} + e^{-i\theta_1}) \\ + (P_y - d_{y1}) L_1\, i\, (e^{i\theta_1} - e^{-i\theta_1}) \end{aligned} \quad (8)$$

Remember that $(e^{i\theta_1} + e^{-i\theta_1})$equals to $2\cos(\theta_1)$ and $i(e^{i\theta_1} - e^{-i\theta_1})$ equals to $2\sin(\theta_1)$ in equation (8). The equation can be simplified using these equalities as follows,

$$A\cos(\theta_1) + B\sin(\theta_1) + C = 0 \quad (9)$$

where $A = -2\,(P_x - d_{x1})L_1$, $B = -2\,(P_y - d_{y1})L_1$ and $C = (P_x - d_{x1})^2 + (P_y - d_{y1})^2 + L_1^2 - L_3^2$. Half-tangent rule can be used for this equation in order to solve one unknown $(\cos(\theta_1) = \frac{1-t_1^2}{1+t_1^2}, \sin(\theta_1) = \frac{2\,t_1}{1+t_1^2}$ and $t_1 = \operatorname{atan}(\frac{\theta_1}{2}))$.

$$(C - A)t_1^2 + 2\,B\,t_1 + (C + A) = 0 \quad (10)$$

Two different roots are able to be obtained from the equation. Discriminant must be real for physically realizable result.

$$dis1 = \sqrt{4B^2 - 4(C^2 - A^2)} \quad (11)$$

One unknown t_1 is calculated using discriminant.

$$t_1 = \frac{(-4\,B \mp dis1)}{2(C - A)} \quad (12)$$

One can compute the angle using half tangent value.

$$\theta_1 = 2\tan(t_1) \quad (13)$$

Once θ_1 is known, other angle of kinematic chain is calculated as follows,

$$\begin{aligned} \theta_3 = atan2(P_x - d_{x1} - L_1\cos(\theta_1), P_y - d_{y1} \\ - L_1\sin(\theta_1)) \end{aligned} \quad (14)$$

Similarly, applying same process to the second kinematic chain, we can obtain the discriminant as follows,

$$dis2 = \sqrt{4E^2 - 4(F^2 - D^2)} \quad (15)$$

where $D = -2\,(P_x - d_{x2})L_2$, $E = -2\,(P_y - d_{y2})L_2$ and $F = (P_x - d_{x2})^2 + (P_y - d_{y2})^2 + L_2^2 - L_4^2$.

Similar to pervious solution, unknown of the second kinematic chain is now known using equation as follows,

$$t_2 = \frac{(-4\,E \mp dis2)}{2(F - D)} \quad (15)$$

$$\theta_2 = 2\tan(t_2) \quad (16)$$

$$\begin{aligned} \theta_4 = atan2(P_x - d_{x2} - L_2\cos(\theta_2), P_y - d_{y2} \\ - L_2\sin(\theta_2)) \end{aligned} \quad (17)$$

Two solutions are obtained for each angle. Totally four modes can be found for the robot. But, the robot is working on just one mode which is shown in Fig. 1.

3. Visual C# Interface Design and Program for Human - Machine Interaction

The program of the robot is constructed on kinematic analysis of the robot. Two coordinates of the end point location are inputs for this program. User is able to use mouse cursor in order to define end point location of the robot. User must click mouse left button on the Form then he must move cursor wherever he wants. Program solves angles according to end points and redraws lines of the robot.

Human machine interface consists of two parts. The first part is the interface design of the program. This part is related to graphical drawing of the robot, angles in text boxes and control buttons and output of the program. The design of the program is illustrated in Fig. 2.

The second part is algorithm or coding. Follow chart of the visual program is depicted in Fig. 3. This code is written using events of graphical objects such as buttons, lines, form and buttons. This kind of programming is named event based programming. We use load, mouse down, mouse move and mouse up events for our code.

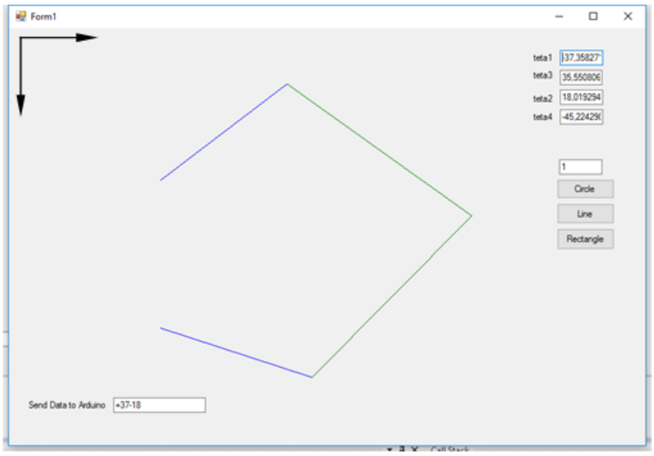

Fig. 2. Human Machine Interface in Visual C#

Start: Form1_Load event is working. In this event, link lengths and other constant parameters are defined.

Input: Form1_Mousedown, Form1_MouseMove and Form1_MouseUp events are working.

Calculate: dis1 and dis2 are calculated according to inverse kinematic analysis of the robot.

Are roots of dis1 and dis2 real? Program must decide that the results are physically realizable or not. Non real results cannot be used in real environment. Therefore, they are unnecessary.

Calculate:If roots are real, angles are calculated using Equations (13, 14, 16 and 17).

Prepare and send data packages to Arduino: When two angles are calculated, they are packaged in order for sending. The data package includes plus and minus symbols which show the direction of the rotation, and two digit numbers which indicate magnitude of the rotation.

One Data Package

+	9	0	-	4	5

Is Arduino serial connection OK?: In order to send packages to Arduino, COM port number of Arduino must be valid and connected. Baud rate of the connection must be selected correctly.

Is close of Form clicked?: The program runs until close of form is clicked. The program ends if it is clicked.

The flow chart of Arduino program is illustrated in Figure 4. This code waits for the input from interface program, separate according to data package format and sends these to servo motors.

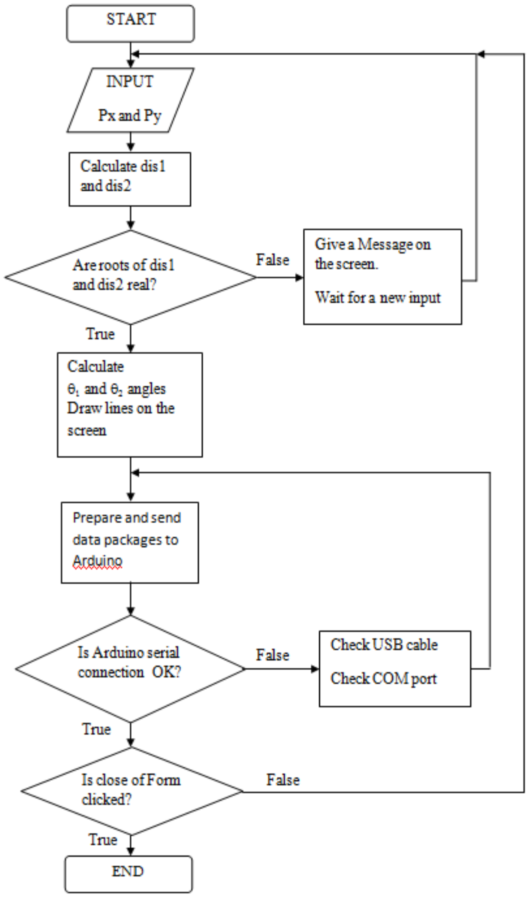

Fig. 3. Flow Chart of Visual C# Human Machine Interface (HMI) Program

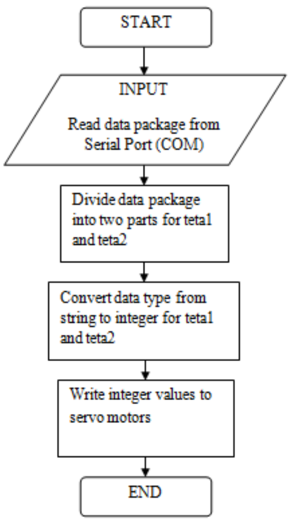

Fig. 4. Flow Chart of Arduino Program

4. Electronic Hardware and Circuit

Arduino Mega 1280 Micro Controller is used to control the robot. The robot has two servos connected to digital pins 9 and 10 which are used as PWM (pulse width modulation) ports of Arduino. The electronic circuit of the robot is seen in Figure 5. This circuit is created in Autodesk Circuit Online Software. Arduino Uno is used in the circuit because Arduino mega is not available in this software. One 5V DC power source must be used to supply required power to servo motors. The Arduino code can be simulated in the program. Simulation can be seen in Figure 6.

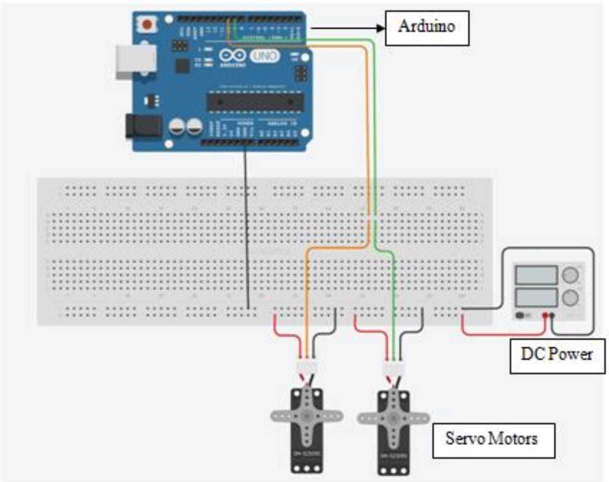

Fig. 5. Electronic Circuit in Autodesk Circuits

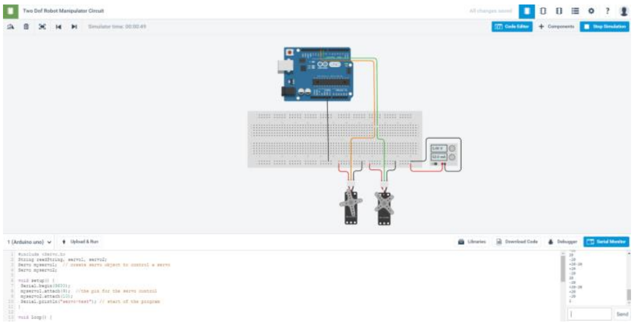

Fig. 6. Simulation in Autodesk Circuits

5. The robot construction and Test Results

The robot is constructed using two Emax ES 3005 water proof servo motors and 3-D printed parts. Two link lengths $L_1$and L_2 are chosen same (20 mm) because they are servo links packaged in servo motor box. Other two link lengths L_3 and L_4 are selected to be same (30 mm). Distance between shafts of two servo motors is 19 mm.

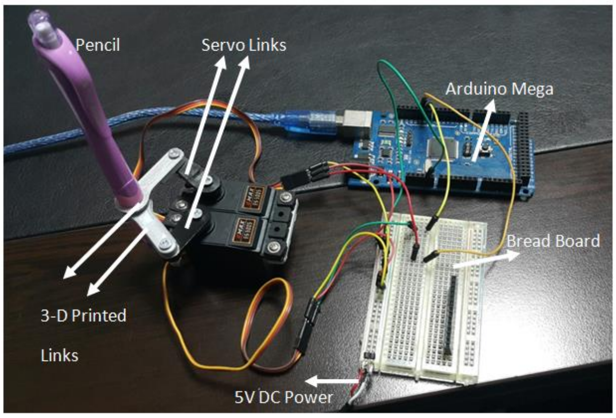

Fig. 7. Electrical connection and whole setup

5.1. Drawing a line and a rectangle

These two shapes are the most basic task to test our robot. Simply, pencil translates forward and backward between two points to draw a line and four lines are used to draw a rectangle (Fig. 8.). We defined the length of the line as 20 mm in the program. The straightness of the line was good but the length of the line was nearly 19.20 mm. This dimension error depends on joint clearances and friction at the joints. Next, the rectangle was drawn. Fillets are created by our robot at the corner. This rectangle was not perfect dimensioned similar to the line. But straightness and appearance of the rectangle is acceptable.

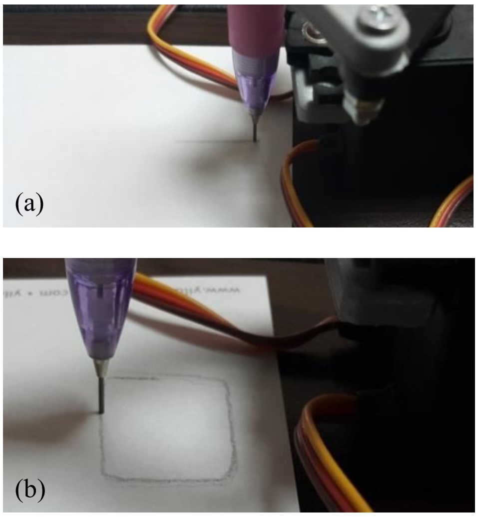

Fig. 8. Drawing Test (a) Line Drawing (b) Rectangle drawing

5.2. Computer Aided Free Hand Drawing

We tried to test our robot manipulator using human machine interface (HMI). User entered required points from HMI, points were sent to microcontroller and microcontroller set angles of two servo motors. Acceptable outputs were obtained as seen from Figures 9 and 10. We firstly tried to draw a letter and then a spiral. The letter and the shape are very close to original shape which is drawn on HMI.

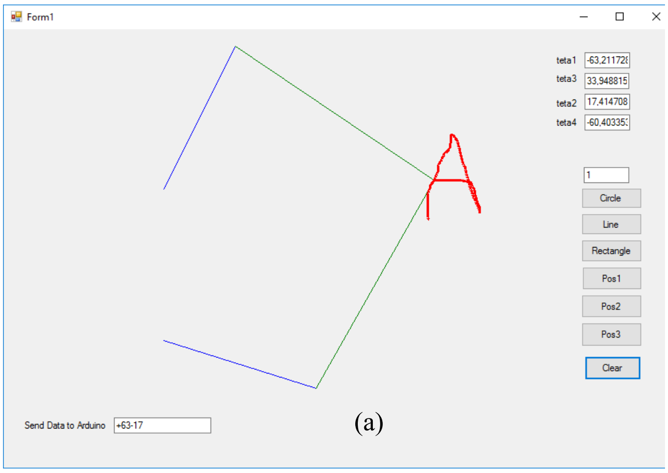

(a)

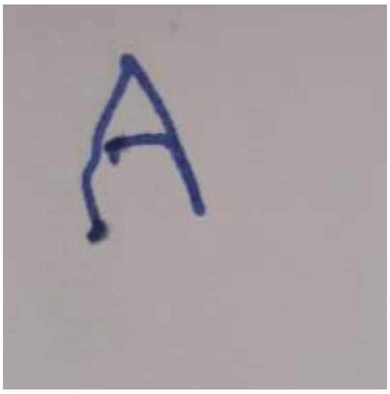

(b)

Fig. 9. Free hand drawing of letter A (a) Input from Human-Machine Interface (b) Output on the paper

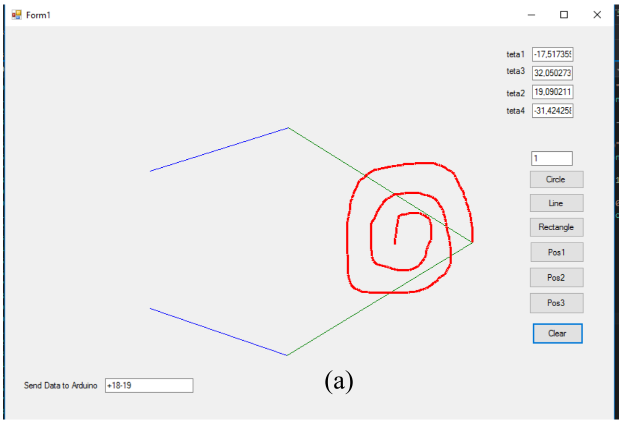

(a)

(b)

Fig. 10. Free hand drawing of a spiral (a) Input from Human-Machine Interface (b) Output on the paper

5.3. Drawing a pattern

In this section, a circular pattern drawing will be explained along with examples. We created the pattern by using Equations as follows,

$$P_x = 60 + r\cos\left(\beta\frac{\pi}{180}\right) \tag{15}$$

$$P_y = 60 + r\sin\left(\beta\frac{\pi}{180}\right) \tag{16}$$

Where Px and Py are coordinates of the end point of the robot, r is radius of circle, β is angle of the rotation of radius. If radius is constant and β angle is changing uniformly, we will get a circle. However, if radius is changed according to a linear function (r=r+a*k, if r>90 then k=-1, if r<1 then k=+1) and also changing rotation of angle ($\beta = \beta$ +dt), the patterns can be drawn. According to this pattern configuration and formulation, the end-effector of five-bar robot drew the patterns shown in Fig. 11.

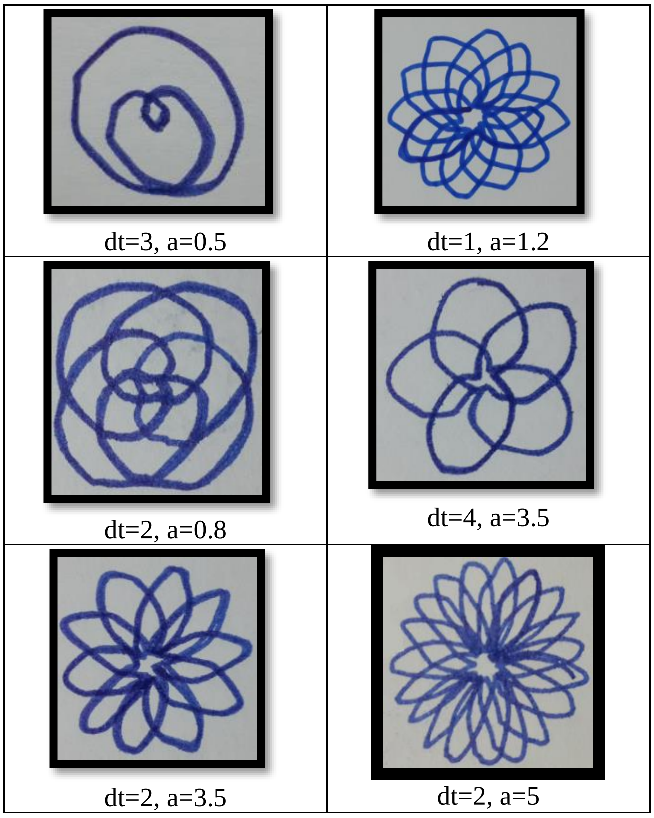

Fig. 11. Some pattern drawings for different dt and a values

6. Conclusion

The five-bar robot manipulator was constructed and tested in this study. Two servo motors of the robot were controlled using HMI program through Arduino microcontroller. Test results were shown for a line, a rectangle, free hand drawing and patterns. Cost of our robot manipulator is very low (it is nearly 50$) compared to other robot manipulators. Readability and appearance of the test shapes are good. However, accuracy and repeatability are not very well. Therefore, they must be improved. Due to its cost, this robot manipulator will be useful to explain the working principle of the five-bar robot manipulator and application of the robot to engineering students.

References

[1]. Kobayashi, E., Masamune, K., Sakuma, I., Dohi, T., & Hashimoto, D., *A new safe laparoscopic manipulator system with a five-bar linkage mechanism and an optical zoom,* Computer Aided Surgery, 4(4), pages 182-192, 1999.

[2]. Cheng, L., Lin, Y., Hou, Z. G., Tan, M., Huang, J., & Zhang, W. J., *Adaptive tracking control of hybrid machines: a closed-chain five-bar mechanism case,* IEEE/ASME Transactions on Mechatronics, 16(6), pages 1155-1163, 2011.

[3]. Zi, B., J. Cao, and Z. Zhu, *Dynamic simulation of hybrid-driven planar five-bar parallel mechanism based on simmechanics and tracking control,* International Journal of Advanced Robotic Systems, 8(4), pages 28-33, 2011.

[4]. Alici, G., *An inverse position analysis of five-bar planar parallel manipulators,* Robotica, 20(02), pages 195-201, 2002.

[5]. Villarreal-Cervantes, M.G., Cruz-Villar, C. A., Alvarez-Gallegos, J., & Portilla-Flores, E. A., *Differential evolution techniques for the structure-control design of a five-bar parallel robot,* Engineering Optimization, 42(6), pages 535-565, 2010.

[6]. Kim, J., *Task based kinematic design of a two DOF manipulator with a parallelogram five-bar link mechanism,* Mechatronics, 16(6), pages 323-329, 2006.

[7]. Joubair, A., M. Slamani, and I.A. Bonev, *Kinematic calibration of a five-bar planar parallel robot using all working modes,* Robotics and Computer-Integrated Manufacturing, 29(4), pages 15-25, 2013.

[8]. Bourbonnais, F., P. Bigras, and I.A. Bonev, *Minimum-time trajectory planning and control of a pick-and-place five-bar parallel robot,* IEEE/ASME Transactions on Mechatronics, 20(2), pages 740-749, 2015.

Proceedings of the International Symposium of Mechanism and Machine Science, 2017
AzCIFToMM – Azerbaijan Technical University
11-14 September 2017, Baku, Azerbaijan

Experimental Verification of Quasi-Static Equilibrium Analysis of a Haptic Device

Ibrahimcan GÖRGÜLÜ[1], Omar W. MAAROOF[1], Barış Taner[1], Mehmet İsmet Can DEDE[1], Marco CECCARELLI[2],

[1]Izmir Institute of Technology
IzTech Robotics Laboratory, Gülbahçe Mah., Urla, Izmir, Turkey
E-mail: candede@iyte.edu.tr
[2] University of Cassino and South Latium,
LARM Laboratory of Robotics and Mechatronics, Cassino, Italy
E-mail: ceccarelli@unicas.it

Abstract

HIPHAD v1.0 is a kinesthetic haptic device which was designed and manufactured in IzTech Robotics Laboratory. In this work, the quasi-static equilibrium analysis is carried out by including the gravitational effects. The calculations are verified through an experimental procedure and the results are presented to characterize the device performance

Keywords: R-CUBE, HIPHAD v1.0, Haptic Device, Quasi-Static Equilibrium Analysis, Parallel Mechanism.

1. Introduction

Kinesthetic haptic devices target at stimulating the human sensory systems responsible for acquiring the sense of location/configuration, motion, force and compliance. These sensory capabilities are generally located at the muscles, tendons and joints. In order to cope with the required stimulation activities, kinesthetic devices are designed to cover the workspace of the targeted body part and their force display capabilities are designated to be in the range of the human capabilities.

A variety of solutions exist as kinesthetic haptic devices that can be categorized with respect to the energy source they use: pneumatics [1], hydraulics [2], electrodynamics [3], electromagnetics [4]; their control structure: open-loop impedance [5], closed-loop impedance [6], closed-loop admittance [7]; the human body part they target: hand [8], arm [9] and the entire body [10]; being grounded or not: wearables [11,12], ground fixed [13,14]; mechanism type: serial [13], parallel [9], hybrid [3]; being biomechanical (using human bones/ joints) [15] or standalone [12]. HIPHAD v1.0 is a kinesthetic haptic device that uses electrical energy to run motors, has open-loop impedance type control structure, which targets the hand motion of the human while the human is seated on a chair working on a desk.

The mechanism of HIPHAD v1.0 is a hybrid combination of a spatial 3 degree-of-freedom (DoF) translational parallel mechanism and a 3 DoF serial spherical orientation mechanism [16]. The parallel mechanism is based on the R-CUBE design [17].

In a previous work on the dynamic analysis of the HIPHAD v1.0 haptic device, the R-CUBE mechanism orientation was changed from its original orientation to a new orientation in which the gravitational effects are equally shared among the actuators. The dynamic equation of motion for the R-CUBE mechanism was developed analytically and verified via simulation studies.

In this paper, the analytical equations of motions are experimentally tested on a manufactured R-CUBE mechanism prototype. However, the R-CUBE mechanism is re-oriented for better operator ergonomics so that the operator can work seated. The next section provides brief introduction of the HIPHAD device kinematics in its new orientation. The quasi-static force analysis is reformulated with respect to the new orientation. Finally, experimental set-up to validate the quasi-static force analysis is described and the test results are presented to verify the gravity compensation calculation and to characterize the device performance.

2. Kinematics of HIPHAD

In the operation procedure of the HIPHAD device, motion demands of the user are based the wrist point position with respect to the base frame by utilizing the real-time measurements from the position sensors in direct kinematics equations. S parameter in Fig. 1 is the distance from the origin to the related actuation axis along related base frame axis and it is constant for all axes. This parameter defines the workspace location with respect to the origin, O. Homing position of the mechanism is defined to be in the middle of its workspace.

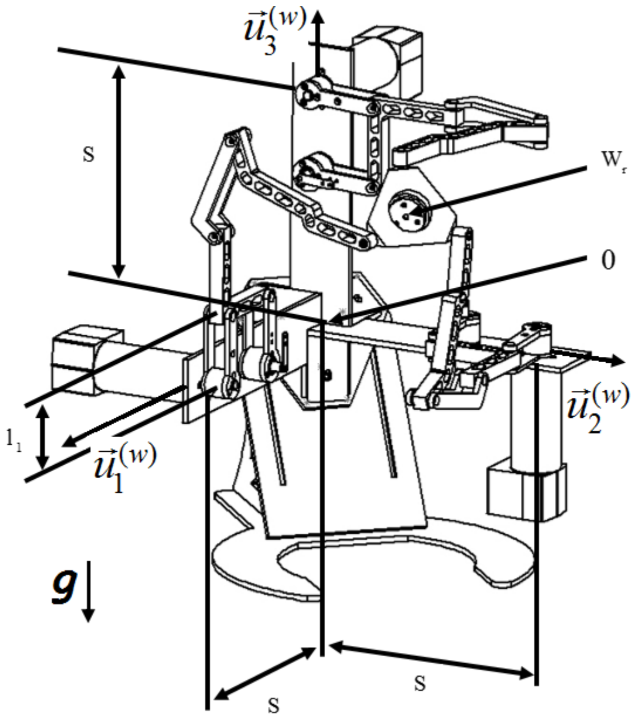

Fig. 1. A sketch of the translational parallel mechanism with its main parameters

Translational parallel mechanism of HIPHAD is an R-Cube mechanism, which has decoupled motion along base frame axes shown in Fig. 1 as $\vec{u}_i^{(w)}; i = 1,2,3$. Hence, motion along any base frame axis is generated by the actuator that has its rotation axis located on the respective base frame axis. In Equation (1), calculation of the position vector of the wrist point $\overrightarrow{OW_r}$ with respect to the base frame, $\mathcal{F} = \mathcal{F}\left\{O; \vec{u}_1^{(w)}, \vec{u}_2^{(w)}, \vec{u}_3^{(w)}\right\}$, is described.

$$\overrightarrow{W}_r = \sum_{i=1}^{3} W_{ri}\vec{u}_i^{(w)} \qquad (1)$$
$$W_{ri} = S + l_1 \cdot \sin(\theta_{i1})$$

The initial position of actuators that define the initial position of the wrist point are represented with a solid red line arrow and the angle limits are given in the Fig. 2.

Inverse kinematics of HIPHAD is provided for the whole kinematic chain including the calculation of passive joint positions on three legs. The actuated and passive joint angles in the kinematic chain of the leg i are given by θ_{i1}, θ_{i2}, θ_{i3} and θ_{i4}. These joint angles are provided in Fig. 2 and Fig. 3.

The mechanical structure of HIPHAD constrains the first link rotation to ±68º [16], and therefore, the solution for θ_{i1} is unique as formulated with σ equal to 1 in Equation (3).

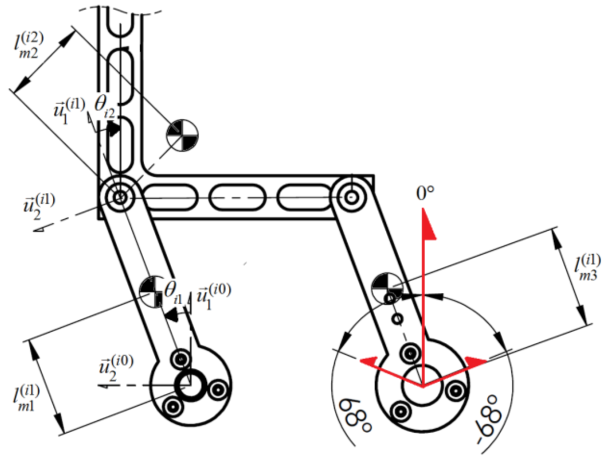

Fig. 2. Active and passive joint angles with mass center locations of parallelogram i

$$\mathbf{\sin(\theta_{i1}) = \frac{W_{ri} - S}{l_1}} \qquad (2)$$

$$\cos(\theta_{i1}) = \sigma\sqrt{1 - \sin^2(\theta_{i1})} \qquad (3)$$

The solution for θ_{i1} using Equation (2) and (3) is given by

$$\theta_{i1} = \operatorname{atan2}(\sin(\theta_{i1}); \cos(\theta_{i1})) \qquad (4)$$

The second joint angle can be calculated by using the information of θ_{i1} as $\theta_{i2} = -\theta_{i1}$. The other joint angles are defined relative to the previous links as indicated in Fig. 3 and are calculated as these angles are calculated as

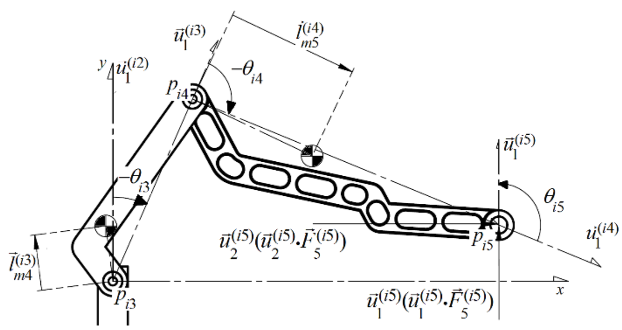

Fig. 3. Passive joint angles, mass center locations and

frame unit vector of limb i.

$$\theta_{i4} = \operatorname{atan2}\left(-\sqrt{1-\left(\frac{x_i^2+y_i^2-l_4^2-l_5^2}{2l_4l_5}\right)^2}\,;\frac{x_i^2+y_i^2-l_4^2-l_5^2}{2l_4l_5}\right) \quad (5)$$

$$\theta_{i3} = \operatorname{atan2}\begin{pmatrix}-\sqrt{1-\left(\frac{x_i(l_4l_5\cos(\theta_{i4}))+y_i(l_5\sin(\theta_{i4}))}{x_i^2+y_i^2}\right)^2} \\ \frac{x_i(l_4l_5\cos(\theta_{i4}))+y_i(l_5\sin(\theta_{i4}))}{x_i^2+y_i^2}\end{pmatrix} \quad (6)$$

In Equations (5) and (6), x_i and y_i denotes the joint position P_{i5} with respect to P_{i3} with respect to the plane defined by $x-y$ axes in Fig. 3. Here the x_i and y_i location of P_{i5} is determined by the location of the other two limbs of HIPHAD. It is possible to identify the location of P_{i5} with the notation in Fig. 4, where Cp platform dimension constant, Cx is a constant shift and Cy is the location of P_{i3} along the y direction by solving the following expressions

$$\begin{aligned} x_1 &= W_{r2} - C_x - C_p \\ y_1 &= W_{r3} - {C_y}^1 - C_p \\ x_2 &= W_{r3} - C_x - C_p \\ y_2 &= W_{r1} - {C_y}^2 - C_p \\ x_3 &= W_{r1} - C_x - C_p \\ y_3 &= W_{r2} - {C_y}^3 - C_p \end{aligned} \quad (7)$$

$${C_y}^i = \vec{u}_1^{(i0)} \cdot \left(l_1\vec{u}_1^{(i1)} + l_2\vec{u}_1^{(i2)}\right)$$

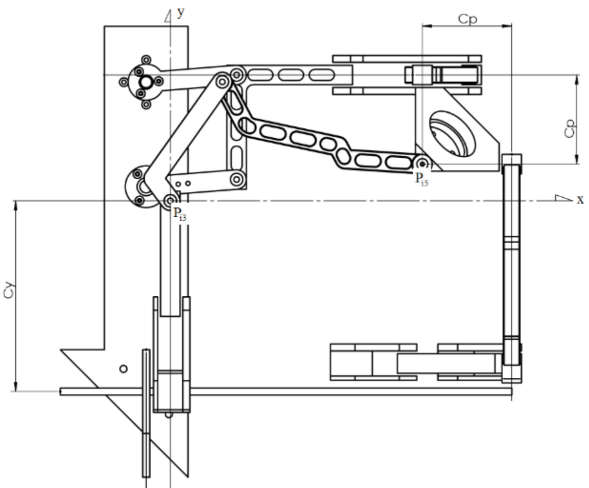

Fig. 4. Top view of HIPHAD

The positions of mass centers and edge points of the links are required for quasi-static equilibrium analysis and this needs the calculation of orientation and translation of each link's frame. The transformation matrices between the frames are given in Equation set (8) and these matrices will be used in dynamic calculation in next section. The frames are indicated in Fig. 5 and i is an index for one of the three limbs of HIPHAD.

In order to have a common matrix notations, in this work, for the same parameter u, if it is a column matrix, it is shown as $\bar{u}$; if it is a non-colum matrix, it is shown as $\hat{u}$; if it is a skew-symmetric matrix, it is shown as $\tilde{u}$.

$$\begin{aligned} \hat{C}^{(i0,i1)} &= e^{\tilde{u}_3\theta_{i1}} \\ \hat{C}^{(i1,i2)} &= e^{-\tilde{u}_3\theta_{i1}}e^{-\tilde{u}_1\pi/2} \\ \hat{C}^{(i2,i3)} &= e^{-\tilde{u}_3\theta_{i3}} \\ \hat{C}^{(i3,i4)} &= e^{-\tilde{u}_3\theta_{i4}} \\ \hat{C}^{(i4,i5)} &= e^{\tilde{u}_3\theta_{i5}} \end{aligned} \quad (8)$$

Using the above transformation matrices, overall transformation matrix for limb i can be calculated as

$$\begin{aligned} \hat{C}^{(i0,i5)} &= \hat{C}^{(i0,i1)}\hat{C}^{(i1,i2)}\hat{C}^{(i2,i3)}\hat{C}^{(i3,i4)}\hat{C}^{(i4,i5)} \\ \hat{C}^{(i0,i5)} &= e^{-\tilde{u}_1\pi/2}e^{-\tilde{u}_3(\theta_{i3}+\theta_{i4}-\theta_{i5})} \end{aligned} \quad (9)$$

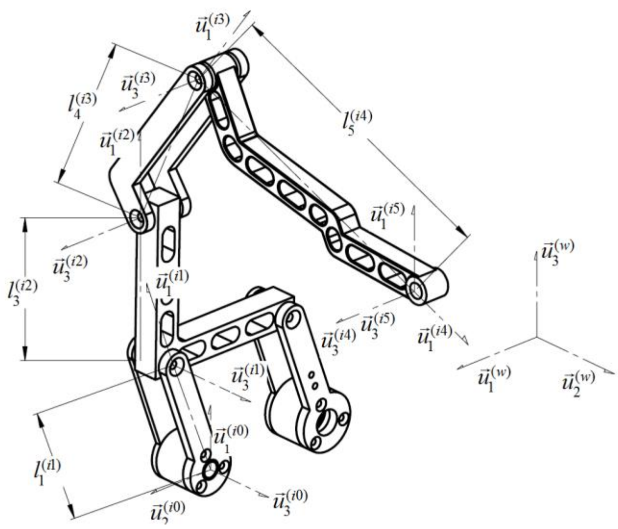

Fig. 5. A schematic representation with link frames of one of the limbs of HIPHAD

It should be noted that θ_{i5} basically equal to the summation of θ_{i4} and θ_{i3}. Therefore, rotation matrix for the last frame can be simplified as

$$\hat{C}^{(i0,i5)} = e^{-\tilde{u}_1\pi/2} \quad (10)$$

The orientations of each limb are calculated with respect to the frames of their first link. The corresponding rotations in world frame formulations are expressed as

$$\hat{C}^{(w,10)} = e^{-\tilde{u}_3\pi/2}e^{-\tilde{u}_2\pi/2}$$
$$\hat{C}^{(w,20)} = \hat{I} \tag{11}$$
$$\hat{C}^{(w,30)} = e^{\tilde{u}_2\pi/2}e^{\tilde{u}_3\pi/2}$$

3. Quasi-Static Equilibrium Analysis of HIPHAD

HIPHAD is a kinesthetic haptic device which makes the user to feel forces at the handle of the device. This force is generated by torque input to the actuators of the haptic interface. In order to generate a desired force at the end effector, an analytic relationship must be established between the actuator torque and end effector force by making use of quasi-static analysis.

Newton-Euler method is used for the quasi-static equilibrium analysis. The reason for choosing this method is due to the fact that resultant calculated forces includes the information of reaction forces and torques in addition to the actuation force and torques for every joint. Quasi-static equilibrium analysis should start with the calculation of the torques and forces of the 4th and 5th links caused by the gravitational acceleration. With that, $\vec{F}_5^{(i5)}$ force at the P_{i5} point on $\vec{u}_1^{(i5)}$- $\vec{u}_2^{(i5)}$ plane can be determined and recursive calculations can initiate from p_{i5} point to the 0th frame. This force can be calculated by using

$$\begin{aligned}
\vec{M}_2^{(i2)} &= \left(\vec{l}_4^{(i3)} + \vec{l}_{m5}^{(i4)}\right)\times\vec{g}^{(w)}m_5 \\
&\quad + \left(\vec{l}_{m4}^{(i3)}\right)\times\vec{g}^{(w)}m_4 \\
&\quad + \left(\vec{l}_4^{(i3)} + \vec{l}_5^{(i4)}\right) \\
&\quad \times\vec{F}_5^{(i5)} = 0 \\
\vec{M}_3^{(i3)} &= \left(\vec{l}_{m5}^{(i3)}\right)\times\vec{g}^{(w)}m_5 \\
&\quad + \left(\vec{l}_5^{(i4)}\right)\times\vec{F}_5^{(i5)} \\
&= 0
\end{aligned} \tag{12}$$

where $\vec{M}_2^{(i2)}$ and $\vec{M}_3^{(i3)}$ are the moments at the corresponding frames, $\vec{g}$ is the gravitational acceleration, $\vec{l}_4^{(i3)}$ and $\vec{l}_5^{(i4)}$ are the link lengths in vector form, $\vec{l}_{m4}^{(i3)}$ and $\vec{l}_{m5}^{(i4)}$ are the mass center position vectors and m_4 and m_5 are the masses of 4th and 5th links, respectively.

It should be noted that, since $\vec{F}_5^{(i5)}$ is calculated in $\vec{u}_1^{(i5)}$-$\vec{u}_2^{(i5)}$ plane, the $\vec{u}_3^{(i5)}$ component of $\vec{F}_5^{(i5)}$ will always be 0. The other components of $\vec{F}_5^{(i5)}$ are compensated by the actuators that are connected the other limbs. In this concept, although the forces within the ith serial chain (limb) are summed up recursively, the components of $\vec{F}_5^{(i5)}$ force should be subtracted from the ith limb and added to the corresponding neighboring limbs along with the external forces generated by the human acting on P_{i5}.

The total force equilibrium at the 4th frame of each limb system including the externally applied force to the platform $\bar{F}_{5ext}^{(w)}$ can be written in the matrix form as

$$\begin{aligned}
\bar{F}_{34}^{(14)} &= \bar{u}_3^{(14)}\left(\bar{u}_3^{(14)}\right)^T\hat{C}^{(14,w)}\bar{F}_{5ext}^{(w)} \\
&\quad + \hat{C}^{(14,w)}\bar{g}^{(w)}m_5 \\
&\quad - \hat{C}^{(14,15)}\bar{F}_5^{(15)} \\
&\quad + \bar{u}_3^{(14)}\left(\left(\bar{u}_1^{(25)}\right)^T\cdot\bar{F}_5^{(25)}\right) \\
\bar{F}_{34}^{(24)} &= \bar{u}_3^{(24)}\left(\bar{u}_3^{(24)}\right)^T\hat{C}^{(24,w)}\bar{F}_{5ext}^{(w)} \\
&\quad + \hat{C}^{(24,w)}\bar{g}^{(w)}m_5 \\
&\quad - \hat{C}^{(24,25)}\bar{F}_5^{(25)} \\
&\quad + \bar{u}_3^{(24)}\left(\left(\bar{u}_2^{(15)}\right)^T\cdot\bar{F}_5^{(15)}\right) \\
\bar{F}_{34}^{(34)} &= \bar{u}_3^{(34)}\left(\bar{u}_3^{(34)}\right)^T\hat{C}^{(34,w)}\bar{F}_{5ext}^{(w)} \\
&\quad + \hat{C}^{(34,w)}\bar{g}^{(w)}m_5 \\
&\quad + \bar{u}_3^{(34)}\left(\left(\bar{u}_2^{(25)}\right)^T\cdot\bar{F}_5^{(25)}\right. \\
&\quad \left. + \left(\bar{u}_1^{(15)}\right)^T\cdot\bar{F}_5^{(15)}\right)
\end{aligned} \tag{13}$$

It should be noted that $\bar{F}_5^{(35)}$ does not appear in the equation for $\bar{F}_{34}^{(34)}$. The reason for this is that since the gravitational force acts along the $-\vec{u}_3^{(35)}$-axis, this force does not generate any moment that cause a motion of the 4th and 5th links.

General representation can be used for remaining recursive force calculations as

$$\begin{aligned}
\bar{F}_{23}^{(i3)} &= \hat{C}^{(i3,i4)}\bar{F}_{34}^{(i4)} + \hat{C}^{(i3,w)}\bar{g}^{(w)}m_4 \\
\bar{F}_{12}^{(i2)} &= \hat{C}^{(i2,i3)}\bar{F}_{23}^{(i3)} + \hat{C}^{(i2,w)}\bar{g}^{(w)}m_2
\end{aligned} \tag{14}$$

where m_4 and m_2 are the masses of the links, and $\bar{F}_{23}^{(i3)}$ and $\bar{F}_{12}^{(i2)}$ are the resultant forces on the 2nd and 1st frames, respectively.

It should be noted that $\bar{F}_{01}^{(i1)}$ force is not calculated since this force acts on the actuator shaft which is carried by the bearing and does not result in any motion of any movable parts.

Finally, by making use of above equations, resultant torque on the actuators can be calculated as

$$\begin{aligned}
&\bar{T}_1^{(10)} \\
&= \mathrm{smm}\left(l_1\hat{C}^{(10,11)}\bar{u}_1^{(11)}\right)\hat{C}^{(10,12)}\bar{F}_{12}^{(12)} \\
&+ \mathrm{smm}\left(\bar{l}_{m1}^{(10)}\right)\hat{C}^{(10,w)}\bar{g}^{(w)}m_1 \\
&+ \mathrm{smm}\left(\bar{l}_{m3}^{(10)}\right)\hat{C}^{(10,w)}\bar{g}^{(w)}m_3
\end{aligned} \tag{15}$$

$$\begin{aligned}\overline{T}_2^{(20)} &= \mathrm{smm}\left(l_1\hat{C}^{(20,21)}\overline{u}_1^{(21)}\right)\hat{C}^{(20,22)}\overline{F}_{12}^{(22)} \\ &+ \mathrm{smm}\left(\overline{l}_{m1}^{(20)}\right)\hat{C}^{(20,w)}\overline{g}^{(w)}m_1 \\ &+ \mathrm{smm}\left(\overline{l}_{m3}^{(20)}\right)\hat{C}^{(20,w)}\overline{g}^{(w)}m_3\end{aligned}$$

$$\begin{aligned}\overline{T}_3^{(30)} &= \mathrm{smm}\left(l_1\hat{C}^{(30,31)}\overline{u}_1^{(31)}\right)\hat{C}^{(30,32)}\overline{F}_{12}^{(32)} \\ &+ \mathrm{smm}\left(\overline{l}_{m1}^{(30)}\right)\hat{C}^{(30,w)}\overline{g}^{(w)}m_1 \\ &+ \mathrm{smm}\left(\overline{l}_{m3}^{(30)}\right)\hat{C}^{(30,w)}\overline{g}^{(w)}m_3 \\ &+ \mathrm{smm}\left(l_1\hat{C}^{(30,31)}\overline{u}_1^{(31)}\right)\hat{C}^{(30,w)}\overline{g}^{(w)}m_{platform}\end{aligned}$$

where $\vec{T_1}$, $\vec{T_2}$ and $\vec{T_3}$ are the torques on the related actuators; m_1 and m_3 are the masses of the link 1 and link 3; l_1 is the length of link 1; $\vec{l}_{m1}^{(i0)}$and $\vec{l}_{m3}^{(i0)}$ are the mass center position vectors that are defined with respect to the 0^{th} frame of the i^{th} limb that originate from their respective rotation centers. In this equation set, smm(·) operator is used to transform column matrices to skew-symmetric (cross-product) matrices.

It should be noted that only 3rd serial chain (limb) carries the weight of platform which is $\overline{g}^{(w)}m_{platform}$. Here, $m_{platform}$ is the mass of the mass of the mobile platform.

4. Experimental Verification

Initially, the analysis results are verified through simulations. Verification of these calculations are executed in MATLAB Simulink using first generation of SimMechanics module. The CAD model of HIPHAD is translated to the Simulink environment. Calculations of the quasi-static equilibrium equations and SimMechanics model simulation are executed simultaneously and resulting forces obtained from the simulation of HIPHAD and mathematical model is compared. In simulation tests, HIPHAD is positioned in several points step by step and through the workspace of the device. The difference between the torques that are calculated by using the equations and SimMechanics model came out to be in the range of 10^{-8} Nm for static tests in which the maximum torque calculated was around 0.3 N·m. The difference can be considered in an acceptable range for numerical errors. In order to verify the analysis results by experimentation, the first work is carried out to match the real system working conditions to the ideal model as much as possible. The first consideration is about the assumption that the gravitational acceleration acts along the $-\vec{u}_3^{(w)}$ axis; however, due to the deformation in the base of HIPHAD this assumption is not valid. Therefore, basement of HIPHAD has to be corrected by orienting it on the ground so that its $\vec{u}_1^{(w)}$, $\vec{u}_2^{(w)}$ and $\vec{u}_3^{(w)}$ axes are aligned with the world frame coordinates.

The second and final work before running the calibration routines for the motion and force exertion of the device is carried out for matching the inertial properties of the device with the model. Although the mathematical and SimMechanics models match, the resultant dynamic forces of these two cannot be compared to the results of the experiments since the inertia of components of the real device might differ due to some non-idealities such as manufacturing faults, bearing and fasteners that are not considered in the model. The source of this possible error is compensated by weighing every component of the links, which are screws and links, within 0.02 g tolerance scales and the obtained values are added to mathematical model and also the mass center positions are recalculated.

Next, the experimental setup was established to conduct tests of the device, which is denoted with 1 in Fig. 6. In each limb, YUMO E6B2-CWZ3E incremental encoders, which are denoted with 3 in Fig. 6, are used on one of the legs of the parallelograms to measure the rotation of the first link and on the other leg the Maxon EC 45 brushless DC actuators, which are denoted with 2 in Fig. 6, are used provide moment to the respective limb. It should be noted that no reduction system is used and this characterizes the system as a direct-drive system. Maxon 4-Q-EC Amplifier 70/10 drivers, which are denoted with 4 in Fig. 6, are used to drive the actuators. The information exchange between the components and the control computer is established via Humusoft MF624 data acquisition (DAQ) card, which is denoted with 5 in Fig. 6, by using MATLAB 2014a Simulink in external real-time windows target mode. Shielded cables are used to minimize the noise effects on analog signals between the DAQ and drivers. The sampling time is selected as 1 ms.

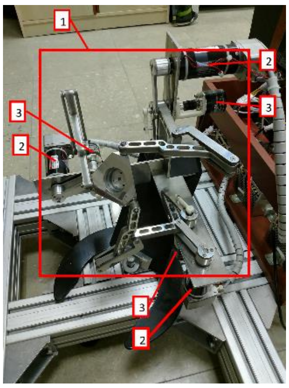

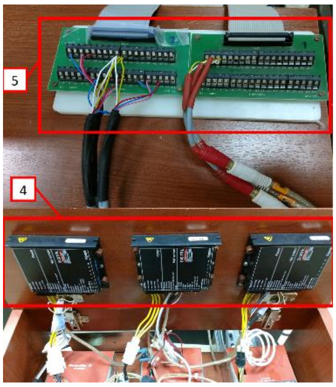

Fig. 6. Experimental setup components

After the necessary connections are made, the offset values for drivers are set to sustain the positioning of the actuator shafts when there are no loads attached to them. This offset value sets the amount of current supplied to actuator when the controller signal is zero. Torques comments to be supplied to the actuators in experiments are received in VDC. Therefore, they are multiplied by the torque constant that is given in datasheet as 45.5 mN·m/A. However, the driving signal send to the drivers is in VDC so a mapping is required to determine generated current per given VDC. Since the drivers can receive ±10VDC driving signals and Humusoft MF624 can send ±10VDC driving signal, this corresponds to 1 to 1 mapping and 45.5 mN·m/VDC torque constant can be used instead. This mapping is confirmed by monitoring the output current from the driver for a given VDC signal by using 'monitor' port on the driver. Also, a certain amount of torque is exerted to the actuator externally and the amount of current to withhold this external torque is measured, which matched with the datasheet value of 45.5 mN·m/A. The exchange of the information among the components of the experimental setup is represented in Fig.7.

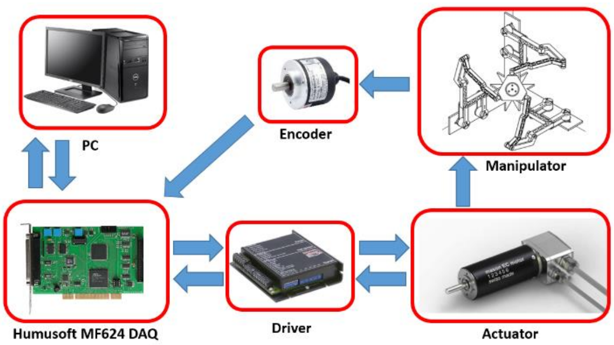

Fig. 7. Information exchange among the experimental setup components

Due to its mechanical limitations, parallelograms of each limb can move a total of 136° about their axis of motion and this full range is divided into half which are negative and positive partitions. This data is verified by tests in which the zero position of parallelograms is the middle points of the full range as it is illustrated in Fig. 2. A detailed motion calibration procedure of this device when potentiometers as position sensors was used is provided in [18].

The control algorithm of HIPHAD that was used in the tests has phases that are run one after another within a procedure. The first step of this procedure is homing and this phase of the algorithm works every time the device is initiated. This sub-controller provides enough amount of torque to settle the mechanism to its most extended and the most folded positions and record the angular positions of the actuators. After acquiring the positions of the actuator at the workspace limits, zero (initial) position of the mechanism is calculated. Then, HIPHAD's moving platform is moved to this zero position using a PID controller. This PID controller closes the feedback control loop by using the joint sensors (encoders). Once this sub-controller finishes its routine, HIPHAD is ready for the tests.

In the experiments, initially, torques generated by the actuators are measured for maintaining static conditions at every integer angular position which results in discontinuous measurements. Secondly, full range of mechanism is scanned by moving the device in each axis by a 0.25 °/s speed and actuator torques are measured. Dynamic motion effects generated in slow operation are calculated to be in the range of ± 6.10^{-9} N·m in the simulation tests and thus, they can be neglected. As a matter of fact, experiment results showed that there is a small difference between continuous and discontinuous motion experiments. Although the values of the outputs were not exactly the same for the recorded positions, the behavior of both errors resembled each other.

The amounts of torques supplied to each actuator during the motion along their respective axis by a 0.25 °/s speed are shown Fig. 8. It should be noted that during the motion along one axis the others are locked at their zero positions in order to identify the calculation errors of the torques generated by the specific axis motors. A PID controller is used to regulate the motion at the required speed to move from the folded positions to extended positions (in between the workspace boundaries). The actuator that provides motion along the $\vec{u}_3^{(w)}$ axis results in highest torque generation since it axis of action is aligned with the gravity axis. Nevertheless, the result for this axis reveals some anomalies. These are the sharp corners which normally should not exist and this can be seen when the devices reaches -34° and +22°

in $\vec{u}_3^{(w)}$ axis.

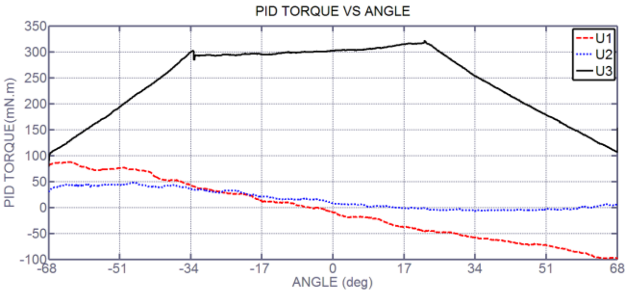

Fig. 8. The measured torques as applied by PID controller

The error between the measured and the calculated torques are calculated and plotted in Fig. 9. In this figure, it can be clearly observed that the peak errors for the calculations in the $\vec{u}_3^{(w)}$ axis actuator occur at -34° and +22° angular positions.

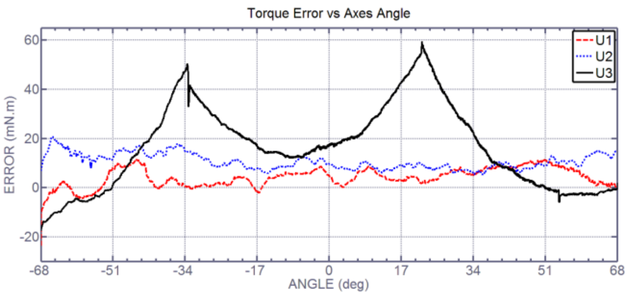

Fig. 9. Calculated error for torques supplied by each axis actuator. ($T_{error}=T_{calculated}-T_{PID}$)

When the calculations and measurements made for the $\vec{u}_1^{(w)}$ axis actuator is individually examined, measured torques and calculated ones almost perfectly overlap with each other as shown in Fig. 10. The maximum error is around 10mN·m. Throughout the whole scanned range, the maximum nominal error is around +5 mN·m. The error distribution for the scanned range varies as a result of the applied torque range.

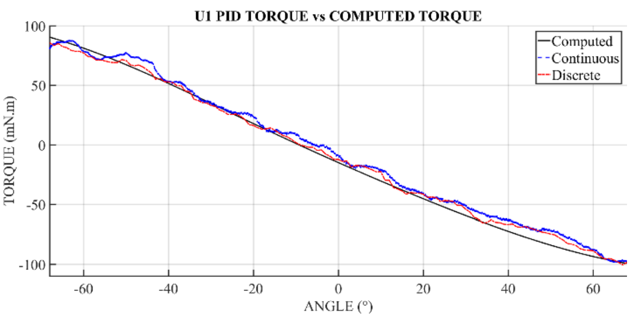

Fig. 10. Calculated Torque vs measured torque for $\vec{u}_1^{(w)}$ axis motion.

The measured torques in $\vec{u}_2^{(w)}$ axis shows a constant offset of +10mN·m from the calculated torques yet it can follow the calculated torque values as shown in Fig. 11.

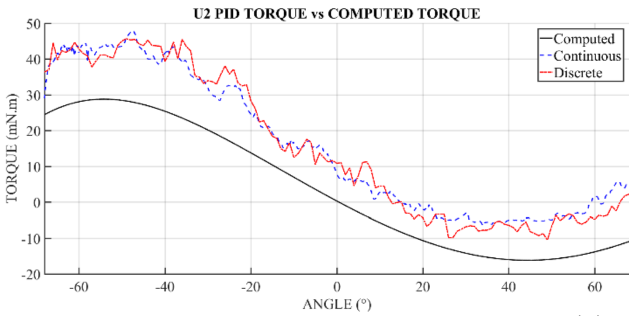

Fig. 11. Calculated Torque vs measured torque for $\vec{u}_2^{(w)}$ axis motion

Fig. 12 shows that the error in the measurements versus the calculated torques for the $\vec{u}_3^{(w)}$ axis actuator has a different characteristic compared to the errors calculated for the previous axis actuator torques. In the previous ones, the errors are almost constant however, the error revealed for axis $\vec{u}_3^{(w)}$ seems to heavily depend on the angular position of the actuator on $\vec{u}_3$.

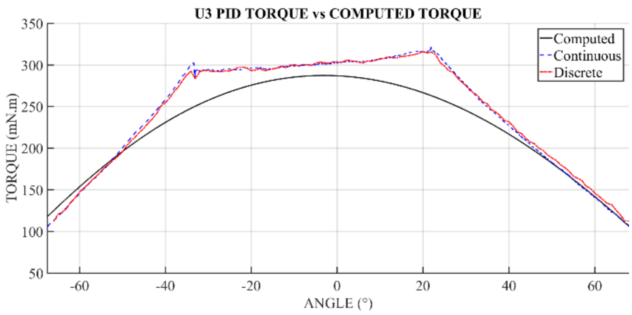

Fig. 12. Calculated Torque vs measured torque for $\vec{u}_3^{(w)}$ axis motion

The actuator providing the motion along the $\vec{u}_3^{(w)}$ axis carries most of the weight of the manipulator and thus, this actuator generates the highest overall torques. The experiments revealed that it has the highest errors at the angles -34° and +22° with 50 mN·m and 60 mN·m torque errors, respectively. A ‘tick’ sound is heard at these angles. Maxon EC 45 actuators are brushless three-phase actuators and the ‘tick’ sound is an indication of the phase transitions. The nonlinearity in generated torques during this mechanical phase transitions becomes more noticeable at higher torque values such as the torques generated by this actuator. This is the main reason that there are higher errors in the vicinity of these phase transitions.

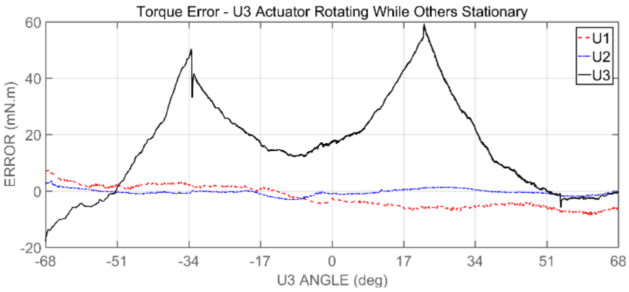

Fig. 13. Computed error data while there is a motion along $\vec{u}_3^{(w)}$ with 0.25 °/s and there is no motion along the other axes

A final test is carried out to understand the errors calculated for the $\vec{u}_1^{(w)}$ and $\vec{u}_2^{(w)}$ axes actuators. A 0.25 °/s speed slow motion provided along the $\vec{u}_3^{(w)}$ axis while keeping the positions along the other axes are maintained at their zero position by control. During this motion, the torques supplied to the $\vec{u}_1^{(w)}$ and $\vec{u}_2^{(w)}$ axes actuators are acquired. Then, the torque errors of these two axes actuators are calculated. In the full range of motion along $\vec{u}_3^{(w)}$ axis, the torque errors of the other two axes range between ±10mN·m as provided in Fig. 13. The cause of the errors of $\vec{u}_1^{(w)}$ and $\vec{u}_2^{(w)}$ is that the mechanism's frame is not exactly orthogonal and matched with the world frame.

6. Conclusions

In this work quasi-static equilibrium analysis of a haptic device is presented. The analysis results are first verified through a simulation model which is generated by using Matlab SimMechanics model. Then, the analysis results are experimentally tested.

The experiments revealed that the equations derived as a result of the analysis matches the experimental results in a larger extend for the actuators that provide motion along $\vec{u}_1^{(w)}$ and $\vec{u}_2^{(w)}$ axes. The errors that are calculated between the computed torques and measured torques can be considered as related with the imperfections of the mechanism frame's orthogonality and alignment with the world frame. These errors can be minimized by calculating the deviation of the mechanism frame from the ideal model.

The phase transition locations of the actuator that provides motion along the $\vec{u}_3^{(w)}$ are much more noticeable than the other two actuators due to the increased torque demands. The errors in torque calculations become larger in the vicinity of these phase transitions.

During the experimentation, it was also observed that actuators heat up in time causing a reduction of performance over time. The main reason of the heating of the actuators is due to the gravitational load.

The characterization of the device's static operation is completed by the experimental tests. One of the main observations is that for a better matching between the calculations and the actual system performance, passive balancing with respect to gravity can be implemented. This will reduce the work load of the actuators and thus, decrease the heating problem and amplification of the phase transition effects.

As future work, the analysis presented in this paper can be extended to account for the imperfections of the device such as the frame deviations and actuator's phase transitions. Also, a work on the dynamic analysis and verification of this dynamic analysis will be carried out.

Acknowledgements

This work is partially supported by The Scientific and Technological Research Council of Turkey via grant number 115E726.

References

[1]. M.Takaiwa & T.Noritsugu, Application of Pneumatic Parallel Manipulator as Haptic Human Interface, IEEE/ASME International Conference on Advanced Intelligent Mechatronics, Atlanta, GA, USA, September 19-23, 1999.

[2]. E.L.Faulring, J.E.Colgate and M.A.Peshkin, A high performance 6-DOF haptic Cobot, Robotics and Automation, Proceedings. ICRA '04. 2004 IEEE International Conference on, pp. 1980-1985 Vol.2., 2004

[3]. Web, http://www.forcedimension.com/products/sigma-7/overview (2017)

[4]. M.Benali-Khoudja, M.Hafez & A.Kheddar, VITAL: An electromagnetic integrated tactile display, Displays, vol. 28, is. 3, pages 133–144, 2007.

[5]. Kang Wen, D. Necsulescu and G. Basic, Development system for a haptic interface based on impedance/admittance control, Proceedings. Second International Conference on Creating, Connecting and Collaborating through Computing, pp. 147-151, 2004.

[6]. C.R.Carignan, & K.R.Cleary, Closed-loop force control for haptic simulation of virtual environments, 2000.

[7]. A.Peer & M.Buss, A New Admittance-Type Haptic Interface for Bimanual Manipulations, IEEE/ASME Transactions On Mechatronics vol. 13, is. 4, pages 416–428, 2008.
[8]. Web, http://www.dextarobotics.com (2017)
[9]. C.Carignan, J. Tang & S. Roderick, Development of an Exoskeleton Haptic Interface for Virtual Task Training, The 2009 IEEE/RSJ International Conference on Intelligent Robots and Systems, St. Louis, USA, October 11-15, 2009.
[10]. Web, http://axonvr.com/#virtual-reality-you-can-feel (2017)
[11]. J.Sone, R.Inoue, K.Yamada, T.Nagae, K.Fujita & M. Sato, Development of a Wearable Exoskeleton Haptic Interface Device, Journal of Computing and Information Science in Engineering, vol. 8, is. 4, pages 041009-1:12, 2008.
[12]. Schiele, André, and Gerd Hirzinger. "A new generation of ergonomic exoskeletons-the high-performance x-arm-2 for space robotics telepresence." Intelligent Robots and Systems (IROS), 2011 IEEE/RSJ International Conference on. IEEE, 2011.
[13]. P.Gallina & G.Rosati, Manipulability of a planar wire driven haptic device, Mechanism and Machine Theory, vol. 37, is. 2, pages 215-228, 2002.
[14]. J.W.Kim, D.H.Park, H.S.Kim & S.H.Han, Design of a Novel 3- DOF Parallel-type Haptic Device with Redundant Actuation, International Conference on Control, Automation and Systems, Seoul, Korea, Oct. 17-20, 2007.
[15]. Yang, Guilin, et al. "A haptic device wearable on a human arm." Robotics, Automation and Mechatronics, 2004 IEEE Conference on. Vol. 1. IEEE, 2004.

[16]. T.Bilgincan, E.Gezgin, and M. I. C.Dede, "Integration of the Hybrid-Structure Haptic Interface HIPHAD v1.0,": Proceedings of the International Symposium of Mechanism and Machine Theory, Izmir, Turkey, pp. 267-284, October 5-8, 2010.
[17]. Li, W., Gao, F., and Zhang, J.: R-CUBE, a Decoupled Parallel Manipulator only with Revolute Joints, Mech. Mach. Theory, 40, 467-473, 2005.
[18]. M.İ.C. Dede, B.Taner, T.Bilgincan, and M. Ceccarelli "Kinematic Analysis Validation and Calibration of a Haptic Interface," Advances on Theory and Practice of Robots and Manipulators Mechanisms and Machine Science, Marco Ceccarelli and Victor A. Glazunov (Eds.), Volume 22, pp 375-381 Springer, Dordrecht, The Netherlands, 2014 (ISBN: 978-3-319-07057-5).

EasyLap-New Robotic System for Single and Multiple Access Laparoscopy Using almost only Traditional Laparoscopic Instrumentation

Gionata FRAGOMENI[1], Gianluca GATTI[2], Pasquale F. GRECO[2], Paola NUDO[3], Michele PERRELLI[2], Basilio SINOPOLI[3], Antonia RIZZUTO[1] and Guido DANIELI[3*]
[3*]Calabrian High tech S.r.l.
Via Ponte Bucci Cubo 45C – 87036 Rende (CS)-Italy
E-mail: guido.danieli@unical.it
[1] Magna Græcia University - 88100 Catanzaro (CZ)-Italy
[2] DIMEG – Calabria University – 87036 Rende (CS)-Italy

Abstract
A new robotic system for single and multiple access laparoscopy is presented, using almost only traditional laparoscopic instrumentation, including very small diameter instruments for babies, based on an evolution of previous research by this research group. Main idea behind this system is to make simple its use, for instance instructing the optics to point always the tip of the instrument on which the surgeon is acting in a totally automatic way; a second important feature is the ability to guide also the motion of the instrument on which the surgeon is acting so that it corresponds to the joystick motion as seen from the monitor. All instruments are traditional, but for a special edition of SAL Twin Forceps, and a second instrument similar to the wrist of da Vinci but reusable and sterilizable since it uses only rods and gears for its motion.
Keywords: Robotized System for Traditional

Instrumentation; Automation of Optics Motion.

1. Introduction

The paper presents a new robotic system for single and multiple access laparoscopy which uses almost only traditional laparoscopic instrumentation, including instruments of very small diameter for babies, which, at present day, is impossible with other systems. The research is based on an evolution of previous research by this research group, deriving from the experience of Navi-Robot [1-5], DARTAGNAN [6-9] and the study of special end effectors for laparoscopy [10-12]. One of the first robotized surgical systems applied to in the laparoscopic field was Aesop [13] which guided the optics on voice command while Zeus was moving the instruments, both absorbed by da Vinci [14-21] that is so far the winner. However while this system is diffused in the States and weirdly enough in Italy, in the rest of the world, and in Europe in particular, its sales are low mainly, but not only, for cost reasons, another problem being the need for a long instruction period. A number of other systems were proposed by different research groups, such ad MiroSurge by DLR Institute of Robotics and Mechatronics, Germany [22], similar in concept to Da Vinci being multi arm (as our proposal), with some advantage on an easier access for the surgeons to the operatory table, but also in this case, using proprietary instrumentation, or SOFIE [23] other robot made in Eindhoven, again a robot da Vinci type using again proprietary tools, or SPORT™ Surgical System briefly described in [24], new system by Titan Medical, that seem very near commercialization.

Socrates [25] instead is made to ease communications between doctors located in different places anywhere in the world, this may help, but is not a surgical robotic system.

A different concept is presented by Sprint [26], a two arm system for SILS, that is meant to be introduced through a bigger orifice directly inside the patient, thus again using only its own tools, in this being similar to SAIT (Samsung Advanced Institute of Technology, 138 Gyeonggi-do, Korea), that carries also the optics and a third operatory arm [27]. Complete recent reviews of the various robot are provided in [28-29].

2. The Robotic System

The actual system under development by our research group presents four to six arms fixed on a common base (usually five), each being a passively self balanced six degrees of freedom (DoF) fully actuated system but for the arm dedicated to the optics which presents only four hinges actuated, with the last two that are simply equipped with encoders. In all cases the axes of the last three DoF will cross forming a spherical hinge.

Each arm presents a first joint (1) having vertical axis, while, the second joint (2), horizontal, belongs to a parallel arm four bar link that allows changing the vertical position of the end effector while maintaining hinges (3) and (4) with vertical axes. Joint (5) again presents horizontal axis, while the last hinge axis is perpendicular to the previous. Moreover, the presence of counterweight (7) completely balances the entire structure. A force sensor (8) is mounted on the end effector, that ends with a male quick connector (9), bearing also the electronic connectors.

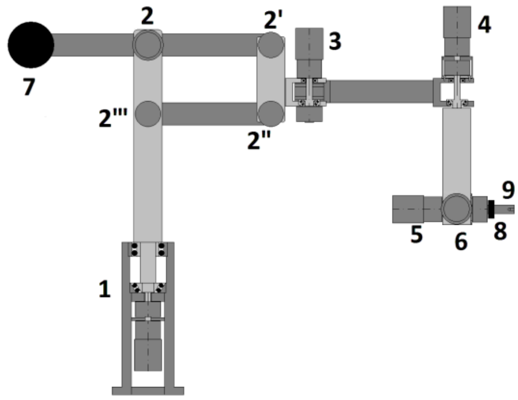

Figure 1. Scheme of an EasyLap arm

As can be seen in Figure 1, the first three degrees of freedom (1-3) allow positioning the fourth hinge in any position in space in a cylindrical space around the first vertical hinge, while the last three degrees instead allow positioning the final end effector with any direction within the workspace. Clearly special actuators are needed to mount each instrument on the end effector, also because their position may change depending on the surgery. They are obviously reusable, hold both motors and control electronics, present a female quick connector that allows determining the position of the instrument in a unique way. Each joint is moved by a Maxon motor-reducer-relative encoder group, whose angles are measured by a 16 bit digital encoder being each joint controlled by a Maxon Epos2 board connected in CAN®open. On all the sixth end effector are mounted the instruments actuators (two controlled motors for traditional instruments, four for SAL Twin Forceps and the wrist instrument).

Figure 2 shows the CAD model of a possible 5 arm version of EasyLap, being the five arms mounted on a single chart that can be moved over the surgical table to dominate the surgical theatre, with the central arm (23) hosting the optics.

At the beginning of the surgery, it is first necessary to select the sterile instruments to be used, mounting them on the appropriate motorized adapter. Then, having placed all trocars on the abdomen and moving over the chart of Figure 2, each instrument has to be introduced in its trocar, penetrating just till the level of the patient's skin, moving the relative arm that will follow the small forces applied to move it. After positioning all of them, simply pressing start surgery, the system will record the coordinates of all trocar entry points. From now on the system knows that it will always have to leave this point fixed, being able to vary depth and inclination of each instrument, under the doctor control. Clearly each instrument may be always rotated about its axis.

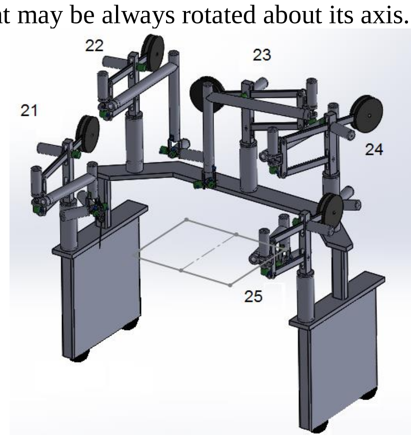

Figure 2. A possible 5 arm Easy Lap version

Note that being all instruments mounted around the abdomen of the patient, and being many of them, it is very important that they do not disturb each other and in particular that the adapters stay well separate. This causes the necessity to control separately the instrument's cannula rotation from the joint's position. Moreover, since not all the traditional instruments allow rotating the handle with respect to the surgical instrument, two different adapters will be needed. In every case it is possible to keep the body of the adaptor oriented always radially, while moving the instrument as requested.

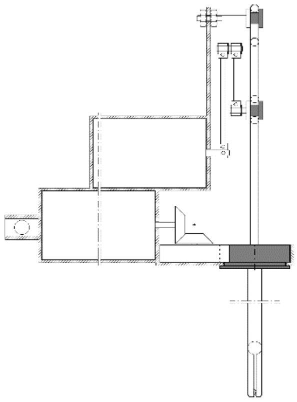

Fig. 3. Scheme of an adapter for traditional instruments able to rotate the handles with respect to the cannula

Next Figure 3 shows a possible adaptor for a traditional instrument, in which one motor is dedicated to opening and closing the forceps, while the second rotates the instrument's cannula. Naturally many are the possible configurations in this case, this is just an example, where the dark components must be sterilized each time.

As far as the adapter for instruments needing four controls (cannula rotation plus three actuators), such as SAL Twin Forceps [30-31] or wrist, or any other, this is presented in the Figure 4. On the left side we observe the position of the four motors, each of which has a spur gear (all identical) mounted on its exit shaft. On the side of each gear, a second gear meshes with it (the red circles, always on the left), so that their axes lay in a plane. Passing to the sketch on the right side, in which the motors are not aligned just put in evidence the fact that they not coplanar, note that each red spur gear, held in position by suitable bearings, gives origin to short shafts on which are mounted incremental encoder disks (green) and a bevel gear, which mesh with other spur gears, the first being fixed to the special instrument cannula. The following, free to rotate with respect to the instrument's cannula, transmit the rotation to a second set of bevel gears, mounted every 90° and fixed to internal mechanisms actuating the three instrument controls.

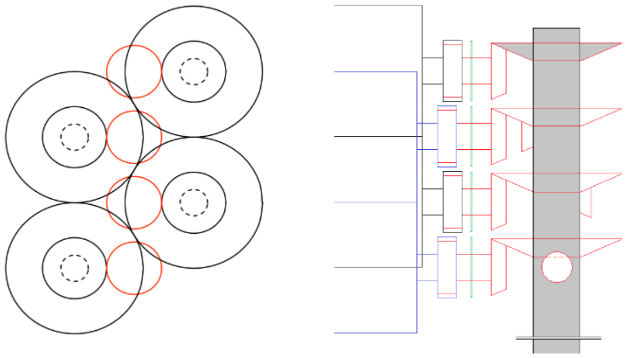

Figure 4. Adapter for instruments needing four controls

Notice that the motor dedicated to instrument's rotation moves the cannula, while all other can move a single control. However, if the cannula is rotated, all other three motors must rotate in the same direction and speed in order to preserve the configuration of each control. The robotic edition of SAL Twin Forceps differs only in the portion that substitute the handle, with the second and third bevel gear of figure 4 being connected on a small drum around which is wrapped around the cable that controls forceps opening, while the last bevel gear is coupled internally to a small spur gear acting on a rack, which commands opening and closing of the instrument's arms.

Fig. 5 shows the EasyLap NWrist, similar to the wrist of da Vinci [32] but reusable and sterilizable since it uses only rods and gears for its motion and whose initial portion is identical to the previous. Let's start to examine the instrument's tip. As can be seen, the two elements of the forceps/scissor open symmetrically thank to the use of five tiny spur gears, 1 and 3 fixed on the same axis. Furthermore the distance between gears 1-2 and 3-5 is identical, being gear 4 idle, used to invert the motion of gears 2 and 5, and the two elements of forceps/scissors fixed to gear 2 and 5. Motion to gear 1 is produced by gear 6, which is partly spur and partly bevel, actuated by 7, sector of bevel gear. In parallel, a second sector of bevel gear, 8, acts on the bevel part of gear 9, which, with its portion spur, moves gear 10, fixed to the small frame holding gears 1 to 5. Rotating then only gear 6 by 20°, we obtain the opening of forceps/scissors by 40°, rotating in the same direction and quantity gears 6 and 9, we obtain configuration d with closed forceps, rotating further gear 6 the forceps opens even if inclined by 90° and in the direction of the same curvature. Gear 6 is actuated by rods connected to a first external motor controlling rotation of wheel 11, while wheel 12 acts on 10. Finally to obtain configuration b is necessary to act in the same time on wheels from 11 to 13, last one being connected via tiny rods to frame 14, and, rotating further wheel 11 we obtain forceps opening, in the direction perpendicular to the curvature. Motion transmission between the initial wheels and the final gears is performed with tiny rods.

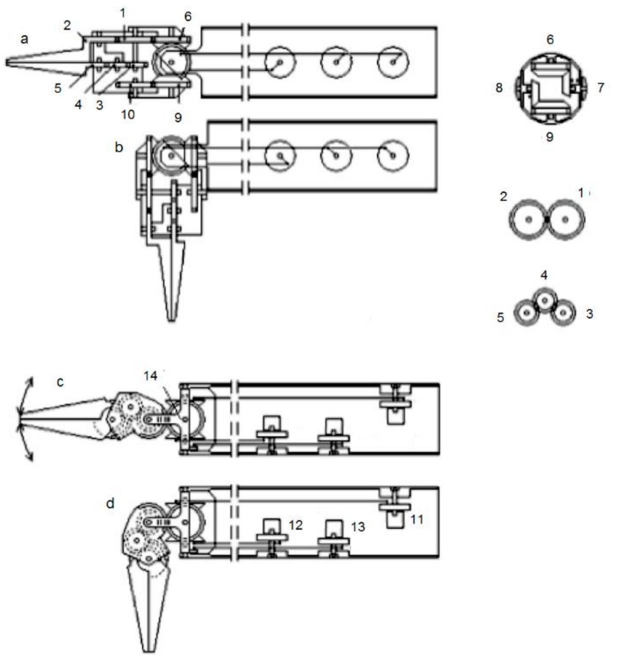

Figure 5. EasyLap version of Wrist instrument.

Naturally each adaptor will receive its commands via CAN®open so that there is only the need to add the DC power supply, since the controlling board will be present on the adaptor.

Passing to the console, only two joystick will be present, plus the start button, four buttons to select the instrument one wants to control, and a number of knobs to control the various options. This part is clearly not yet well defined, we will need the feedback from the users, to understand which is the simplest way to transmit the message.

3. EasyLap kinematic model and algorithms

Fig. 6 shows the kinematic model of an EasyLap arm, with relative Denavit Hartenberg [33] transformation table for the serial portion of this robot.

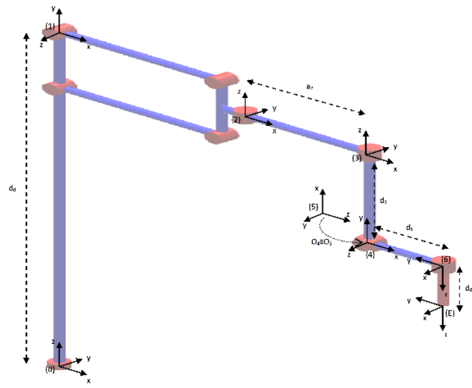

Transf	θ_i	d_i	α_i	a_i
0→1	q_0	d_0	$\pi/2$	0
1→2	D-H not applicable to closed loop kinematic chain			
2→3	q_2	0	0	a_2
3→4	q_3	$-d_3$	$\pi/2$	0
4→5	q_4	0	$\pi/2$	0
5→6	q_5	d_5	$-\pi/2$	0
6→E	q_6	d_6	0	0

Figure 6. EasyLap kinematic model and DH table for the serial part of this robot

For the closed loop kinematic chain, showed in Fig.7, it is not possible to apply the canonical Denavit-Hartemberg method. The transformation between frame 1 and 2, was so calculated by using the Denavit-Hartemberg method extended to closed loop kinematic chain obtaining the transformation matrix of Figure 7.

As we mentioned before, to make the system really easy to use, two problems are to be solved. First problem, the automatic pointing of the optic on the instrument in use, when the doctor passes to a different one. In fact the tip position of each instrument in terms of quaternion, as the result of the product of the sequence of quaternions representing in terms of the sequence of joints, is always known. However not all the optics have straight vision, some have vision inclined by 30, 60 or even 90 degrees. Thus, in the case of straight vision, it is enough to move the optic computing the directional cosines of the line that joins the tip of the instrument to be observed and the entry point of the optic into the patient abdomen, and move the arm accordingly. More complicate may be the case in which the optic presents an angular deviation, whose direction of observation is also known, as always in terms of last end effector quaternion. Now we have three points to take into account, the tip of the instrument to be observed, the tip of the optic and the entry point in the patient's abdomen. First we have to bring the observation direction to lie on the plane passing from these three points, rotating the optics, secondly we might have to change inclination of the optic to center the vision on the point of interest. Moreover, the global surgical field (previously recorded) will be shown in a second image, circling the region actually treated.

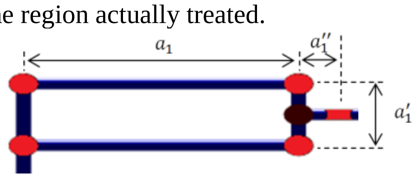

$$T_2^1 = \begin{bmatrix} 1 & 0 & 0 & a_1'' + a_1 \cdot \cos(q_1) \\ 0 & 0 & 1 & -a_1' + a_1 \cdot \sin(q_1) \\ 0 & -1 & 0 & 0 \\ 0 & 0 & 0 & 1 \end{bmatrix}$$

Fig. 7. Transformation for closed loop chain of an EasyLap arm

Similarly, since the position of the optic is always perfectly known in terms of directional cosines, which are associated with the camera position, then moving the joystick in a direction with respect to the monitor, means to be willing to move the instrument in the same direction, hence supplying the system the desired direction of motion. Thus it is easy to compute the new position of the tip of the instrument using line's parametric equations starting from the actual instrument's tip coordinates, then remembering that the entry point into the patient abdomen is a fixed point, we obtain the new instrument orientation, and from this, via inverse kinematic, the set of new joint parameters to be reached linearly. Of course it seems a very long process, but once programmed in C, it takes nothing. And this allows establish the instrument's direction of motion so as to correspond to the direction required as seen in the monitor frame of reference.

Finally this system, having five arms on which is possible to pre-mount a number of different tools, including for instance a stapler, can be used especially for SAL, allowing to extract the surgical instrument to replace it with the stapler in a quasi automatic way (it will extract the instrument, reposition the new tool on the trocar, and re-enter the abdominal cavity under surgeon control).

4. Conclusions

This is at the moment just a first description of this system, that will be built and tested during the next two years, after presenting it to our Regional Authority for funding. In fact it derives from our previous experience thus is just not a dream, even if the control electronics for the adaptors is still to be developed. Many components will be built using 3D printing both in stainless steel and plastic, while the arm's structure will be mainly in aluminum. A first Italian patent application has also been presented [34].

References

[1]. G. Danieli *Measuring open kinematic chain able to turn into a positioning Robot*, EP1843876, granted February 2009.

[2]. G. Danieli, G. Fragomeni, G. Gatti, A. Merola and D. Moschella *Actual Developments of Navi-Robot, a Navigator Able to Block itself in the Correct Position during Orthopedic Surgical Procedures*, paper 497-691, WSEAS Congress Athens, July 11-13 2005,

[3]. D. Moschella, G. Gatti, F.I Cosco, E. Aulicino, P. Nudo and G. Danieli, *Development of Navi-Robot, a New Assistant for the Orthopedic Surgical Room*, paper 713, 12th IFToMM World Congress, Besançon (France), June18-21, 2007

[4]. M. Donnici, S. Meduri, M. Perrelli, D. Battaglia, G. Gatti, C. Pace and G. Danieli, *Stochastic Deterministic Calibration of a Self Balanced Hybrid Parallel/Serial Robotic Structure*, No 2 (54), 2014, Problems of Mechanics, pp. 45-56

[5]. M. Donnici, G. Lupinacci, P. Nudo, M. Perrelli and G. Danieli, *Needle Insertion Test Using Navi-Robot and a CT Scanner*, 5° International Conference on Health Science and Biomedical System (HSBS'16), Ischia, June 17-19 2016

[6]. G. Danieli, *Robot riabilitativo auto-bilanciato in grado di lavorare sia in modo attivo che passivo sia su arti superiori che inferiori, sia destri che sinistri*, Italian Patent Application CS2015A000001, deposited January the 18th 2015

[7]. G. Danieli, G. Lupinacci, P. Nudo and V. Loiero V., *Design and simulation of a self – balanced rehabilitation Robot able to work in active and passive modes on both sides of upper and lower limbs* 6th International Conference on BIOSCIENCE and BIOINFORMATICS (ICBB '15) , February 22-24 2015 Dubai, paper 72209-124

[8]. G. Danieli G., *Self Balanced Rehabilitation Robot Able to Work in Active and Passive Modes on Upper and Lower Limbs, Left and Right*, PCT CS2015A000001, deposited January the 18th 2016

[9]. G. Danieli, P. Nudo, M. Perrelli and M. Iocco, *DARTAGNAN a self - balanced rehabilitation Robot able to work in active and passive modes on both sides of upper and lower limbs* 1st International Conference of IFToMM Italy, Vicenza, December 1-

2, IFIT 2016, paper_6
[10]. G. Danieli and G. Riccipetitoni, *Robotized System of control and micrometric actuation of an endoscope*, PCT/IT05/000486 del 08/08/2005, WO2006016390 A1 of February 16th 2006, EP05778903.4
[11]. D. Moschella and G. Danieli, *Controlling The Traditional Rigid Endoscopic Instrumentation Motion*, Proceedings of Eucomes 2008 Congress in Cassino 13-19 September 2008, Springer, ISBN 978-1-4020-8914-5, pp. 615-622
[12]. M. Perrelli, P. Nudo, D. Mundo and G. Danieli, *Robotic Control of the Traditional Endoscopic Instrumentation Motion*, 3rd Eucomes Conference, , 14-18 September 2010, Cluj-Napoca, Romania
[13]. H. Reichenspurner, R.J. Damiano, M. Mack, D.H. Boehm, H. Gulbins, C. Detter, B. Meiser, R. Ellgass, B. Reichart, *Use of the Voice-Controlled and Computer-Assisted Surgical System Zeus for Endoscopic Coronary Artery Bypass Grafting*, The Journal of Thoracic and Cardiovascular Surgery July 1999, 118, 11-6
[14]. G. Tak Sung and I.S. Gill, *Robotic Laparoscopic Surgery: a Comparison of the Da Vinci and Zeus Systems*, Urology 58: 893–898, 2001. © 2001, Elsevier Science Inc.
[15]. G.F. Dakin, M. Gagner, *Comparison of laparoscopic skills performance between standard instruments and two surgical robotic systems*, Surg Endosc (2003) 17: 574–579
[16]. A. Tewari, J. Peabody, R. Sarle, G. Balakrishnan, A. Hemal, A. Shrivastava and M. Menon, *Technique of da Vinci Robot-Assisted Anatomic Radical Prostatectomy*, Urology 60: 569–572, 2002. © 2002, Elsevier Science Inc
[17]. L. Su, *Role of robotics in modern urologic practice*, Curr. Opin. Urology, 2009, 19(1):63–64
[18]. D.I. Lee, *Robotic prostatectomy: what we have learned and where we are going*, Yonsei Med J, 2009, 50:177–181
[19]. J.H. Palep, *Robotic assisted minimally invasive surgery*. J Minim Access Surg 2009, 5(1):1–7
[20]. Sang-Wook Kang, Seung Chul Lee, So Hee Lee, Kang Young Lee, Jong Ju Jeong, Yong Sang Lee, Kee-Hyun Nam, Hang Seok Chang, Woong Youn Chung, and Cheong Soo Park, *Robotic thyroid surgery using a gasless, transaxillary approach and the da Vinci S system: The operative outcomes of 338 consecutive patients*, Surgery 2009;146:1048-55
[21]. P. Babbar, A.K. Hemal, *Robot-assisted urologic surgery in 2010 - Advancements and future outlook*, Urol Ann. 2011 Jan;3(1):1-7.
[22]. U. Hagn, R. Konietschke, A. Tobergte, M. Nickl, S. Jörg, B. Kübler, G. Passig, M. Gröger, F. Fröhlich, U. Seibold, L. Le-Tien, A. Albu-Schäffer, A. Nothhelfer, F. Hacker, M. Grebenstein, G. Hirzinger (2010) *DLR MiroSurge: a versatile system for research in endoscopic telesurgery*. Int J Comput Assist Radiol Surg 5(2):183–193
[23]. R. Bogue, *Robots in healthcare*, Industrial Robot: An International Journal, 2011, Vol. 38 Iss: 3, pp.218 – 223
[24]. J. Saurabh and G. Gagan, *Robotics in urologic oncology*, J Minim Access Surg. 2015 Jan-Mar; 11(1): 40–44
[25]. I. Mendez, R. Hill, D. Clarke, G. Kolyvas, S. Walling, *Robotic long-distance telementoring in neurosurgery*. Neurosurgery, 2005 - Volume 56 - Issue 3 - pp 434-440
[26]. G. Petroni, M. Niccolini, A. Menciassi, P. Dario, A. Cuschieri, *A novel intracorporeal assembling robotic system for single-port laparoscopic surgery*, Surgical Endoscopy, February 2013, Volume 27, Issue 2, pp 665–670
[27]. H. Choi, H.S. Kwak, Y.A. Lim, H.J. Kim. *Surgical robot for single-incision laparoscopic surgery*, IEEE Trans Biomed Eng. 2014; 61:2458–66.
[28]. A. Simorov, R.S. Otte, C.M. Kopietz and D. Oleynikov, *Review of surgical robotics user interface: what is the best way to control robotic surgery?*. Surgical Endoscopy, 2012, Volume 26, Issue 8, pp 2117-2125
[29]. Z. Jiangran, F. Bo, Z. Min-Hua & X. Kai, *Surgical robots for SPL and NOTES: A review*, Pages 8-17, Journal Minimally Invasive Therapy & Allied Technologies Volume 24, 2015 - Issue 1
[30]. A. Rizzuto, G. Danieli, M. Donnici, P. Nudo, P.F. Greco and R. Sacco, *Twin Forceps for Single Access Laparoscopy*, PCT/IT2013/00052, February the 19th 2013
[31]. A. Rizzuto, M. Donnici, P. Nudo, B. Sinopoli, R. Sacco and G. Danieli, *The Twin Forceps, a new instrument for SILS*, BioMed Research International, Volume 2015 (2015)
[32]. A.J. Madhani, J.K. Salisbury, *Articulated Surgical Instrument for Performing Minimally Invasive Surgery with Enhanced Dexterity and Sensitivity* US Application 857,776, May 16th 1997, granted August 11, 1998, US5792135
[33]. L. Denavit and R.S. Hartenberg, *A kinematic notation for lower-pair mechanism based on matrices*. ASME J. Appl. Mechanics 1955; 77: 215-221
[34]. G. Danieli, *Easy-Lap, a robotic system for single and multi access laparoscopy using mainly traditional instrumentation already present in the hospitals* Italian Patent Application 102017000004119, deposited January the 16th 2017.

Proceedings of the International Symposium of Mechanism and Machine Science, 2017
AzC IFToMM – Azerbaijan Technical University
11-14 September 2017, Baku, Azerbaijan

Forward and Inverse Kinematics Analysis of Denso Robot

Mehmet Erkan KÜTÜK [1]*, Memik Taylan DAŞ[2], Lale Canan DÜLGER[1]

[1*]Mechanical Engineering Department, University of Gaziantep
Gaziantep/ Turkey
E-mail: mekutuk@gantep.edu.tr
[2] Mechanical Engineering Department, University of Kırıkkale

Abstract
A forward and inverse kinematic analysis of 6 axis DENSO robot with closed form solution is performed in this paper. Robotics toolbox provides a great simplicity to us dealing with kinematics of robots with the ready functions on it. However, making calculations in traditional way is important to dominate the kinematics which is one of the main topics of robotics. Robotic toolbox in Matlab® is used to model Denso robot system. GUI studies including Robotic Toolbox are given with simulation examples.
Keywords: Robot Kinematics, Simulation, Denso Robot, Robotic Toolbox, GUI

1. Introduction

Robot kinematics specifies the analytical study of the motion of a robot manipulator. Formulating the reasonable kinematics models for a robot mechanism is very important in order to investigate the behaviour of industrial manipulators. There are two different spaces used in kinematics modelling of manipulators. They are called Cartesian space and Quaternion space. The transformation between two Cartesian coordinate systems can be decayed into a rotation and a translation. There are a lot of approaches to represent rotation like Euler angles, Gibbs vector, Cayley-Klein parameters, orthonormal matrices etc. Homogenous transformations based on 4x4 real matrices have been used dominantly in robotics [1].

Robotics Toolbox contains a lot of functions that are demanded in robotics and addresses fields such as kinematics, dynamics, and trajectory generation. The Toolbox is convenient for simulation besides analyzing results from experiments with real robots. It is also an effective tool for education. The Toolbox is organized on a very common method of representing the kinematics and dynamics of serial-link manipulators. It is described by the matrices. These include, in the basic case, the Denavit and Hartenberg parameters of the robot [2]. Any serial-link manipulator can be configured by the user. A number of examples are provided for well-known robots such as the Puma 560 and the Stanford arm [3]. Constantin et al. used Robotic Toolbox in forward kinematics analysis of an industrial robot [4].

This study includes kinematics of robot arm which is available Gaziantep University, Mechanical Engineering Department, Mechatronics Lab. Forward and Inverse kinematics analysis are performed. Robotics Toolbox is also applied to model Denso robot system. A GUI is built for practical use of robotic system.

2. Robot Arm Kinematics

The robot kinematics can be categorized into two main parts; forward and inverse kinematics. Forward kinematics problem is not difficult to perform and there is no complexity in deriving the equations in contrast to the inverse kinematics. Especially nonlinear equations make the inverse kinematics problem complex. They may also be coupled and have not got unique solutions. Thus solutions obtained mathematically may not solve the problem physically [5]. Liu et al. applied geometric approach for inverse kinematics analysis of a 6 dof robot [6]. Qiao et al. used double quaternions to get solution for inverse kinematics problem [7]. Nubiola and Bonev offered a simple and efficient way to solve inverse kinematics problem for 6R robots [8]. It is noticed that, Artificial Intelligence (AI) methods are frequently used in inverse kinematics problem [9, 10, 11] in recent years.

2.1 Forward Kinematics Analysis

The forward kinematics problem is related between the individual joints of the robot manipulator and the position and orientation of the tool or end-effector. The joint variables are the angles between the links for revolute or prismatic joints, and the link extension in the prismatic or sliding joints [12]. A systematic way of describing the geometry of a serial chain of links and joints was proposed by Denavit and Hartenberg and is known today as Denavit-Hartenberg (DH) notation [2]. The matrix A representing four movements is found by postmultiplying the four matrices giving four movements to reach frame {j-1} to frame {j} in Figure 1.

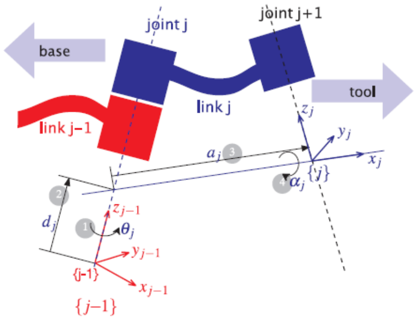

Fig. 1. DH representation of a general purpose joint-link combination

Transformation between two joints in a generic form [3] is given in Eq. (1).

$$ {}^{j-1}A_j = \begin{bmatrix} \cos\theta_j & -\sin\theta_j\cos\alpha_j & \sin\theta_j\sin\alpha_j & a_j\cos\theta_j \\ \sin\theta_j & \cos\theta_j\cos\alpha_j & -\cos\theta_j\sin\alpha_j & a_j\sin\theta_j \\ 0 & \sin\alpha_j & \cos\alpha_j & d_j \\ 0 & 0 & 0 & 1 \end{bmatrix} \tag{1} $$

Denso Robot is a 6 Degrees-of-Freedom (DOF) robotic manipulator. The link lengths are given in Figure 2(a). World frame and joint frames used in calculations and home position of Denso robot are shown in Figure 2b and Figure 2c, respectively.

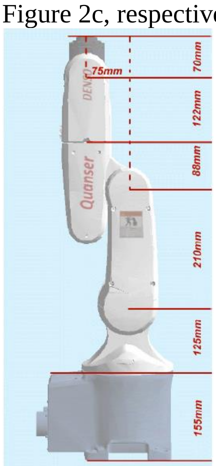

(a) Link lengths

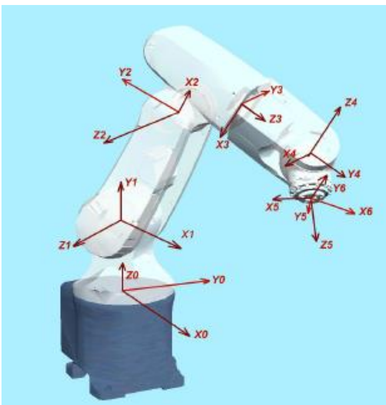

(b) World frame and joint frames

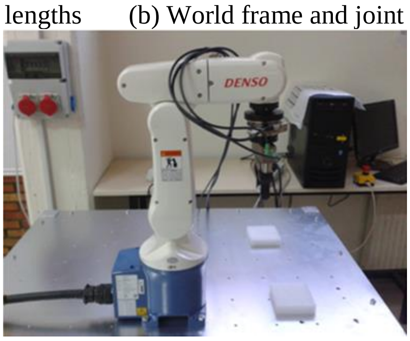

(c) Home position

Fig.2. General overview of DENSO

The following table shows DH parameters of the Denso robotic arm necessary to derive the kinematics of the robot. Gripper is not included in the analysis.

Table 1. DH Parameters of the Denso Robotic Arm

Joint i	θ_i	d_i	a_i	α_i	Joint Limits (degrees)
1	q_1	d_1	0	$\pi/2$	−160, 160
2	q_2	0	a_2	0	−120, 120
3	q_3	0	a_3	$-\pi/2$	20, 160
4	q_4	d_4	0	$\pi/2$	−160, 160
5	q_5	0	0	$-\pi/2$	−120, 120
6	q_6	d_6	0	0	−360, 360

where d_1 = 0.125m, a_2 =0.21m, a_3 =-0.075m, d_4 = 0.21m and d_6 = 0.07m.

Transformation matrix for each joint can be obtained by using Eq. (1). The parameters given in Table 1 are substituted into Eq. (1) to find each of them. Six transformation matrices are presented in Eq. (2).

$$ A_1 = \begin{bmatrix} C_1 & 0 & S_1 & 0 \\ S_1 & 0 & -C_1 & 0 \\ 0 & 1 & 0 & d_1 \\ 0 & 0 & 0 & 1 \end{bmatrix} \quad A_2 = \begin{bmatrix} C_2 & -S_2 & 0 & a_2C_2 \\ S_2 & C_2 & 0 & a_2S_2 \\ 0 & 0 & 1 & 0 \\ 0 & 0 & 0 & 1 \end{bmatrix} $$

$$ A_3 = \begin{bmatrix} C_3 & 0 & -S_3 & a_3C_3 \\ S_3 & 0 & C_3 & a_3S_3 \\ 0 & -1 & 0 & 0 \\ 0 & 0 & 0 & 1 \end{bmatrix} \quad A_4 = \begin{bmatrix} C_4 & 0 & S_4 & 0 \\ S_4 & 0 & -C_4 & 0 \\ 0 & 1 & 0 & d_4 \\ 0 & 0 & 0 & 1 \end{bmatrix} $$

$$ A_5 = \begin{bmatrix} C_5 & 0 & -S_5 & 0 \\ S_5 & 0 & C_5 & 0 \\ 0 & -1 & 0 & 0 \\ 0 & 0 & 0 & 1 \end{bmatrix} \quad A_6 = \begin{bmatrix} C_6 & -S_6 & 0 & 0 \\ S_6 & C_6 & 0 & 0 \\ 0 & 0 & 1 & d_6 \\ 0 & 0 & 0 & 1 \end{bmatrix} \tag{2} $$

where Cos and Sin are abbreviated to C and S, respectively. The total transformation between the base of the robot and the hand is;

$$ {}^{R}T_H = A_1A_2A_3A_4A_5A_6 \tag{3} $$

Transformation matrices for six axes given in Eq. (2) are postmultiplied in an order which is given in Eq. (3). This equality is shown in Eq. (4).

$$\begin{bmatrix} n_x & o_x & a_x & P_x \\ n_y & o_y & a_y & P_y \\ n_z & o_z & a_z & P_z \\ 0 & 0 & 0 & 1 \end{bmatrix} = A_1A_2A_3A_4A_5A_6 \tag{4}$$

where n (normal), o (orientation), a (approach) elements are for orientation and P (position) elements are position elements relative to the reference frame [12]. The elements of the matrix shown in left hand side of Eq. (4) are given in Eqs. (5, 6, 7 and 8).

$$\begin{aligned} n_x &= -S_6(C_4S_1 + S_4(C_1C_2C_3 - C_1S_2S_3)) - C_6(C_5(S_1S_4 - C_4(C_1C_2C_3 - \\ &\quad C_1S_2S_3)) + S_5(C_1C_2S_3 + C_1C_3S_2)) \\ n_y &= S_6(C_1C_4 + S_4(S_1S_2S_3 - C_2C_3S_1)) + C_6(C_5(C_1S_4 - C_4(S_1S_2S_3 - \\ &\quad C_2C_3S_1)) - S_5(C_2S_1S_3 + C_3S_1S_2)) \\ n_z &= C_6(S_5(C_2C_3 - S_2S_3) + C_4C_5(C_2S_3 + C_3S_2)) - S_4S_6(C_2S_3 + C_3S_2) \end{aligned} \tag{5}$$

$$\begin{aligned} o_x &= S_6(C_5(S_1S_4 - C_4(C_1C_2C_3 - C_1S_2S_3)) + S_5(C_1C_2S_3 + C_1C_3S_2)) - \\ &\quad C_6(C_4S_1 + S_4(C_1C_2C_3 - C_1S_2S_3)) \\ o_y &= C_6(C_1C_4 + S_4(S_1S_2S_3 - C_2C_3S_1)) - S_6(C_5(C_1S_4 - C_4(S_1S_2S_3 - \\ &\quad C_2C_3S_1)) - S_5(C_2S_1S_3 + C_3S_1S_2)) \\ o_z &= -S_6(S_5(C_2C_3 - S_2S_3) + C_4C_5(C_2S_3 + C_3S_2)) - C_6S_4(C_2S_3 + C_3S_2) \end{aligned} \tag{6}$$

$$\begin{aligned} a_x &= S_5(S_1S_4 - C_4(C_1C_2C_3 - C_1S_2S_3)) - C_5(C_1C_2S_3 + C_1C_3S_2) \\ a_y &= -S_5(C_1S_4 - C_4(S_1S_2S_3 - C_2C_3S_1)) - C_5(C_2S_1S_3 + C_3S_1S_2) \\ a_z &= C_5(C_2C_3 - S_2S_3) - C_4S_5(C_2S_3 + C_3S_2) \end{aligned} \tag{7}$$

$$\begin{aligned} P_x &= d_6(S_5(S_1S_4 - C_4(C_1C_2C_3 - C_1S_2S_3)) - C_5(C_1C_2S_3 + C_1C_3S_2)) - d_4(C_1C_2S_3 \\ &\quad + C_1C_3S_2) + a_2C_1C_2 + a_3C_1C_2C_3 - a_3C_1S_2S_3 \\ P_y &= a_2C_2S_1 - d_6(S_5(C_1S_4 - C_4(S_1S_2S_3 - C_2C_3S_1)) + C_5(C_2S_1S_3 + C_3S_1S_2)) - \\ &\quad d_4(C_2S_1S_3 + C_3S_1S_2) + a_3C_2C_3S_1 - a_3S_1S_2S_3 \\ P_z &= d_1 + d_4(C_2C_3 - S_2S_3) + d_6(C_5(C_2C_3 - S_2S_3) - C_4S_5(C_2S_3 + \\ &\quad C_3S_2)) + a_2S_2 + a_3C_2S_3 + a_3C_3S_2 \end{aligned} \tag{8}$$

2.2 Inverse Kinematics Analysis

The transformation process of the position and orientation of an end-effector from Cartesian space to joint space is defined as inverse kinematics problem. There are three solutions approaches; analytical, numerical and semi analytical [5]. Analytical approach is used herein.

To find the inverse kinematics solution for the 1st joint θ_1 as a function of the known elements, the 6th link transformation inverse is postmultiplied as follows in Eq. (9).

$$A_1A_2A_3A_4A_5A_6A_6^{-1} = \begin{bmatrix} n_x & o_x & a_x & P_x \\ n_y & o_y & a_y & P_x \\ n_z & o_z & a_z & P_x \\ 0 & 0 & 0 & 1 \end{bmatrix} xA_6^{-1} \tag{9}$$

where $A_6A_6^{-1} = I$. I is identity matrix. In this case, the above equation is resulted in Eq. (10).

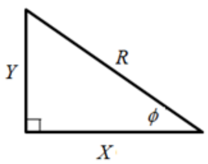

$$A_1A_2A_3A_4A_5 = \begin{bmatrix} n_x & o_x & a_x & P_x \\ n_y & o_y & a_y & P_x \\ n_z & o_z & a_z & P_x \\ 0 & 0 & 0 & 1 \end{bmatrix} xA_6^{-1} \tag{10}$$

The required multiplication in Eq. (10) is carried out and it yields as Eq. (11).

$$\begin{bmatrix} " & " & " & C_1 \\ " & " & " & S_1 \\ " & " & " & " \\ 0 & 0 & 0 & 1 \end{bmatrix} = \begin{bmatrix} n_xC_6 - o_xS_6 & o_xC_6 + n_xS_6 & a_x & P_x - a_xd_6 \\ n_yC_6 - o_yS_6 & o_yC_6 + n_yS_6 & a_y & P_y - a_yd_6 \\ n_zC_6 - o_zS_6 & o_zC_6 + n_zS_6 & a_z & P_z - a_zd_6 \\ 0 & 0 & 0 & 1 \end{bmatrix} \tag{11}$$

It is noticed that the elements located in 1st row & 4th column (abbreviated to (1, 4)) and 2nd row & 4th column (abbreviated to (2, 4)) can be used in defining θ_1 (these abbreviations are also used in the remaining part of the inverse kinematics analysis). All elements in the left-hand side of the Eq. (11) are known. However, all of them are not used in calculation of θ_1 because of limitations of space. Due to these reasons, they are not written. The symbol ‘ " ’ is used instead of them. From (1, 4) and (2, 4) elements, θ_1 is found in Eq. (12).

$$\theta_1 = \tan^{-1}\left(\frac{P_y - a_yd_6}{P_x - a_xd_6}\right) \pm pi \tag{12}$$

The 1st link inverse transformation matrix is premultiplied by Eq. (10) to find the inverse kinematics solution for the 3rd joint (θ_3) as a function of the known elements. It is given in Eq. (13).

$$A_1^{-1}A_1A_2A_3A_4A_5 = A_1^{-1}x\begin{bmatrix} n_x & o_x & a_x & P_x \\ n_y & o_y & a_y & P_x \\ n_z & o_z & a_z & P_x \\ 0 & 0 & 0 & 1 \end{bmatrix} xA_6^{-1} \tag{13}$$

where $A_1A_1^{-1} = I$. I is identity matrix. In this case the above equation is resulted in Eq. (14).

$$A_2A_3A_4A_5 = A_1^{-1}x\begin{bmatrix} n_x & o_x & a_x & P_x \\ n_y & o_y & a_y & P_x \\ n_z & o_z & a_z & P_x \\ 0 & 0 & 0 & 1 \end{bmatrix}xA_6^{-1} \qquad (14)$$

The required multiplication in Eq. (14) is carried out and it yields as Eq. (15).

$$\begin{bmatrix} " & " & " & a_3C_{23} - d_4S_{23} + a_2C_2 \\ " & " & " & d_4C_{23} + a_3S_{23} + a_2S_2 \\ " & " & " & " \\ 0 & 0 & 0 & 1 \end{bmatrix} = \begin{bmatrix} " & " & " & C_1(P_x - a_xd_6) + S_1(P_y - l_5a_y) \\ " & " & " & P_z - d_1 - l_5a_z \\ " & " & " & " \\ 0 & 0 & 0 & 1 \end{bmatrix} \qquad (15)$$

S_{23} and C_{23} refer to $\mathrm{Sin}(\theta_2 + \theta_3)$ and $\mathrm{Cos}(\theta_2 + \theta_3)$, respectively. From (1, 4) and (2, 4) elements of the equation,

$$\begin{aligned} a_3C_{23} - d_4S_{23} + a_2C_2 &= C_1(P_x - a_xd_6) + S_1(P_y - l_5a_y) \\ d_4C_{23} + a_3S_{23} + a_2S_2 &= P_z - d_1 - l_5a_z \end{aligned} \qquad (16)$$

Right hand side of the Eq. (16) is known. They are recalled as;

$$\begin{aligned} A &= C_1(P_x - a_xd_6) + S_1(P_y - l_5a_y) \\ B &= P_z - d_1 - l_5a_z \end{aligned} \qquad (17)$$

Eq. (16) can be rewritten as below.

$$\begin{aligned} a_3C_{23} - d_4S_{23} + a_2C_2 &= A \\ d_4C_{23} + a_3S_{23} + a_2S_2 &= B \end{aligned} \qquad (18)$$

Having taken the squares of these expressions, they are added to each other and it yields as;

$$a_2^2 + a_3^2 + d_4^2 + 2a_2a_3\underbrace{(C_2C_{23} + S_2S_{23})}_{\mathrm{Cos}(-\theta_3)} + 2a_2d_4\underbrace{(S_2C_{23} - C_2S_{23})}_{\mathrm{Sin}(-\theta_3)} = A^2 + B^2 \qquad (19)$$

The known parts are taken to the right hand side as shown in Eq. (20),

$$2a_2a_3\,\mathrm{Cos}(-\theta_3) + 2a_2d_4\,\mathrm{Sin}(-\theta_3) = A^2 + B^2 - a_2^2 - a_3^2 - d_4^2 \qquad (20)$$

Eq. (20) is then simplified and rewritten as Eq. (21),

$$X\,\mathrm{Cos}(-\theta_3) + Y\,\mathrm{Sin}(-\theta_3) = Z \qquad (21)$$

where

$$\begin{aligned} X &= 2a_2a_3 \\ Y &= 2a_2d_4 \\ Z &= A^2 + B^2 - a_2^2 - a_3^2 - d_4^2 \end{aligned} \qquad (22)$$

A triangle including X and Y can be formed to solve Eq. (21) as an auxiliary technique.

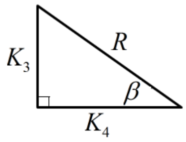

where $X = R\,\mathrm{Cos}\,\phi$ $\quad Y = R\,\mathrm{Sin}\,\phi$

$R = \sqrt{X^2 + Y^2}$ $\quad \phi = \mathrm{Tan}^{-1}\left(\frac{Y}{X}\right)$

X and Y expressions are substituted in Eq. (21), it yields,

$$R\,\mathrm{Cos}\,\phi\,\mathrm{Cos}(-\theta_3) + R\,\mathrm{Sin}\,\phi\,\mathrm{Sin}(-\theta_3) = Z \qquad (23)$$

Eq. (24) is obtained by using trigonometric addition formula in Eq. (23),

$$\mathrm{Cos}(\phi + \theta_3) = Z / R \qquad (24)$$

with the inverse cosine operation, $\phi + \theta_3 = \pm\mathrm{Cos}^{-1}(Z / R)$ equality is obtained. Then θ_3 is found as given in Eq. (25).

$$\theta_3 = \pm\mathrm{Cos}^{-1}(Z / R) - \phi \qquad (25)$$

The 2nd link inverse transformation matrix is premultiplied by Eq. (14) to find the inverse kinematics solution for the 2nd joint (θ_2) as a function of the known elements in Eq. (26).

$$A_2^{-1}A_2A_3A_4A_5 = A_2^{-1}A_1^{-1}x\begin{bmatrix} n_x & o_x & a_x & P_x \\ n_y & o_y & a_y & P_x \\ n_z & o_z & a_z & P_x \\ 0 & 0 & 0 & 1 \end{bmatrix}xA_6^{-1} \qquad (26)$$

where $A_2A_2^{-1} = I$. I is identity matrix. In this case the above equation is resulted in Eq. (27).

$$A_3A_4A_5 = A_2^{-1}A_1^{-1}x\begin{bmatrix} n_x & o_x & a_x & P_x \\ n_y & o_y & a_y & P_x \\ n_z & o_z & a_z & P_x \\ 0 & 0 & 0 & 1 \end{bmatrix}xA_6^{-1} \qquad (27)$$

The required multiplication in Eq. (27) is carried out, and then yields Eq. (28).

$$\begin{bmatrix} " & " & " & a_3C_3 - d_4S_3 \\ " & " & " & d_4C_3 + a_3S_3 \\ " & " & " & " \\ 0 & 0 & 0 & 1 \end{bmatrix} = \begin{bmatrix} " & " & " & C_2(C_1(P_x - a_xd_6) + S_1(P_y - a_y - d_6)) - a_2 - S_2(d_1 - P_z + a_zd_6) \\ " & " & " & -S_2(C_1(P_x - a_xd_6) + S_1(P_y - a_yd_6)) - C_2(d_1 - P_z + a_zd_6) \\ " & " & " & " \\ 0 & 0 & 0 & 1 \end{bmatrix} \qquad (28)$$

From (1, 4) element of the equation above,

$$a_3C_3 - d_4S_3 = C_2(C_1(P_x - a_xd_6) + S_1(P_y - a_y - d_6)) - a_2 - S_2(d_1 - P_z + a_zd_6) \qquad (29)$$

Eq. (29) can be rewritten as,

$$C_2K_1 + S_2(-K_2) = D \qquad (30)$$

where

$$K_1 = (C_1(P_x - a_x d_6) + S_1(P_y - a_y - d_6))$$
$$K_2 = (d_1 - P_z + a_z d_6)$$
$$D = a_3 C_3 - d_4 S_3 + a_2$$

A triangle including K_1 and K_2 can be formed to solve Eq. (30) as an auxiliary technique. The procedure applied in determination of θ_3 is carried out. So, all steps are not explained.

where $\quad S = \sqrt{K_1^2 + K_2^2} \quad \gamma = \mathrm{Tan}^{-1}\left(\dfrac{-K_2}{K_1}\right)$

Then, θ_2 is found as given in Eq. (31)

$$\theta_2 = \gamma \pm \mathrm{Cos}^{-1}(D/S) \tag{31}$$

θ_2 expression can also be obtained from (2,4) elements of Eq. (28),

$$d_4 C_3 + a_3 S_3 = -S_2(C_1(P_x - a_x d_6) + S_1(P_y - a_y d_6)) - C_2(d_1 - P_z + a_z d_6) \tag{32}$$

Eq. (32) can be rewritten as,

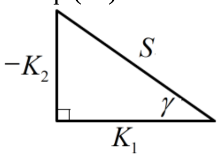

$$S_2 K_3 + C_2 K_4 = E \tag{33}$$

where

$$K_3 = (C_1(P_x - a_x d_6) + S_1(P_y - a_y d_6))$$
$$K_4 = (d_1 - P_z + a_z d_6)$$
$$E = -d_4 C_3 - a_3 S_3$$

A triangle including K_3 and K_4 can be formed to solve Eq. (33) as done in the previous steps.

where $\quad R = \sqrt{K_3^2 + K_4^2} \quad \beta = \mathrm{Tan}^{-1}\left(\dfrac{K_3}{K_4}\right)$

Then, θ_2 is found as given in Eq. (34).

$$\theta_2 = \beta \pm \mathrm{Cos}^{-1}(E/R) \tag{34}$$

The inverse transformation matrices of 1st, 2nd and 3rd joints are premultiplied by Eq. (4) to find the inverse kinematics solution for the 5th joint (θ_5). It is given in Eq. (35).

$$(A_1A_2A_3)^{-1}A_1A_2A_3A_4A_5A_6 = (A_1A_2A_3)^{-1}x\begin{bmatrix} n_x & o_x & a_x & P_x \\ n_y & o_y & a_y & P_x \\ n_z & o_z & a_z & P_x \\ 0 & 0 & 0 & 1 \end{bmatrix} \tag{35}$$

where $(A_1A_2A_3)^{-1}A_1A_2A_3 = I$. I is identity matrix. The above equation is resulted in Eq. (36).

$$A_4A_5A_6 = (A_1A_2A_3)^{-1}x\begin{bmatrix} n_x & o_x & a_x & P_x \\ n_y & o_y & a_y & P_x \\ n_z & o_z & a_z & P_x \\ 0 & 0 & 0 & 1 \end{bmatrix} \tag{36}$$

The required multiplication in Eq. (36) is carried out, and it is given in Eq. (37).

$$\begin{bmatrix} '' & '' & '' & '' \\ '' & '' & '' & '' \\ '' & '' & C_5 & '' \\ 0 & 0 & 0 & 1 \end{bmatrix} = \begin{bmatrix} '' & '' & '' & '' \\ '' & '' & '' & '' \\ '' & '' & '' & a_z C_{23} - a_x S_{23} C_1 - a_y S_{23} S_1 \\ 0 & 0 & 0 & 1 \end{bmatrix} \tag{37}$$

From (3, 3) elements of the equation above,

$$C_5 = a_z C_{23} - a_x S_{23} C_1 - a_y S_{23} S_1 \tag{38}$$

Then, θ_5 is found as given in Eq. (39).

$$\theta_5 = \pm \mathrm{Cos}^{-1}(a_z C_{23} - a_x S_{23} C_1 - a_y S_{23} S_1) \tag{39}$$

The inverse transformation matrices of 1st, 2nd and 3rd joints are premultiplied by Eq. (4) to find the inverse kinematics solution for the 4th joint (θ_4) as a function of the known elements. Multiplied matrix used in previous step is also used in determination of θ_4 angle. It is given in Eq. (40). The elements (1, 3) and (2, 3) of the equation are preferred in Eq. (42).

$$\begin{bmatrix} '' & '' & -C_4 S_5 & '' \\ '' & '' & -S_4 S_5 & '' \\ '' & '' & '' & '' \\ 0 & 0 & 0 & 1 \end{bmatrix} = \begin{bmatrix} '' & '' & a_z S_{23} + a_x C_{23} C_1 + a_y C_{23} S_1 & '' \\ '' & '' & a_y C_1 - a_x S_1 & '' \\ '' & '' & '' & '' \\ 0 & 0 & 0 & 1 \end{bmatrix} \tag{40}$$

Then, θ_4 is found as in Eq. (41).

$$\theta_4 = \tan^{-1}\left(\frac{a_y C_1 - a_x S_1}{a_z S_{23} + a_x C_{23} C_1 + a_y C_{23} S_1}\right) \tag{41}$$

The inverse transformation matrices of 1st, 2nd and 3rd joints are premultiplied by Eq. (4) to find the inverse kinematics solution for the 6th joint (θ_6) as a function of the known elements. Multiplied matrix used in previous two steps (θ_5 and θ_4) is also used in determination of θ_6 angle. It is given in Eq. (35). The elements (3, 1) and (3, 2) of the equation are given in Eq. (42),

$$\begin{bmatrix} '' & '' & '' & '' \\ '' & '' & '' & '' \\ C_6S_5 & -S_5S_6 & '' & '' \\ 0 & 0 & 0 & 1 \end{bmatrix} = \begin{bmatrix} '' & '' & '' & '' \\ '' & '' & '' & '' \\ n_zC_{23} - n_xS_{23}C_1 - n_yS_{23}S_1 & o_zC_{23} - o_xS_{23}C_1 - o_yS_{23}S_1 & '' & '' \\ 0 & 0 & 0 & 1 \end{bmatrix} \quad (42)$$

Then, θ_6 is found as given in Eq. (43).

$$\theta_6 = \tan^{-1}\left(\frac{-(o_zC_{23} - o_xS_{23}C_1 - o_yS_{23}S_1)}{n_zC_{23} - n_xS_{23}C_1 - n_yS_{23}S_1}\right) \quad (43)$$

Inverse problem solution does not always give one solution; the same end effector pose can be reached in many different configurations [13]. Previous positions of the motors are fed to the program in each step in order to offer a solution to this problem in Denso robot system. The difference between calculated position and previous position are obtained. The solution having the minimum difference is selected. So the robot will not try to jump to far positions; it will go to the reach the nearest solution. Each solution obtained by the inverse kinematics analysis should be tested in order to determine whether or not they bring the end-effector to the desired position.

3. Robotics Toolbox in Matlab®

The Toolbox performs many functions for analyzing and simulation of arm type robotics in fields of kinematics, dynamics, and trajectory generation. The Toolbox is based on a very general method of representing the kinematics and dynamics of serial-link manipulators. These parameters are included in MATLAB® objects [3]. Designed model by robotics toolbox is given in Figure 3.

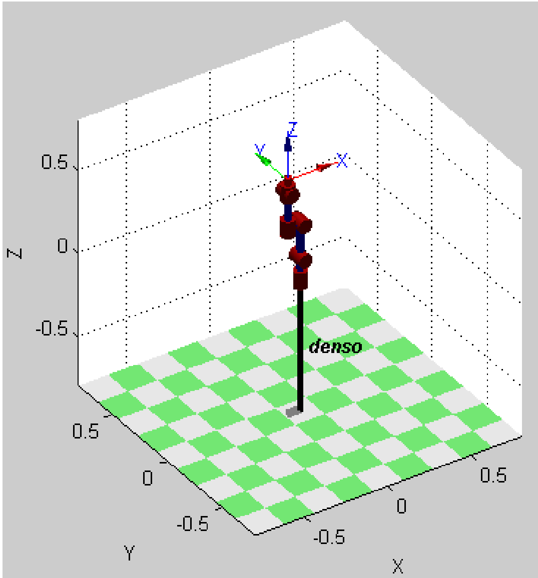

Fig. 3. Robotics toolbox with Denso

The joint space trajectories can be calculated by inverse kinematics and a simulation for robot can be done to move robot from initial position to final position in Cartesian space.

A straight line whose initial and final coordinates in X, Y, Z coordinates are [0.35 0 0.4] m. and [0.2 0.1 0.5] m. respectively is given in Figure 4. It is desired to plan the path composed of N number of points; N= 50 in this example.

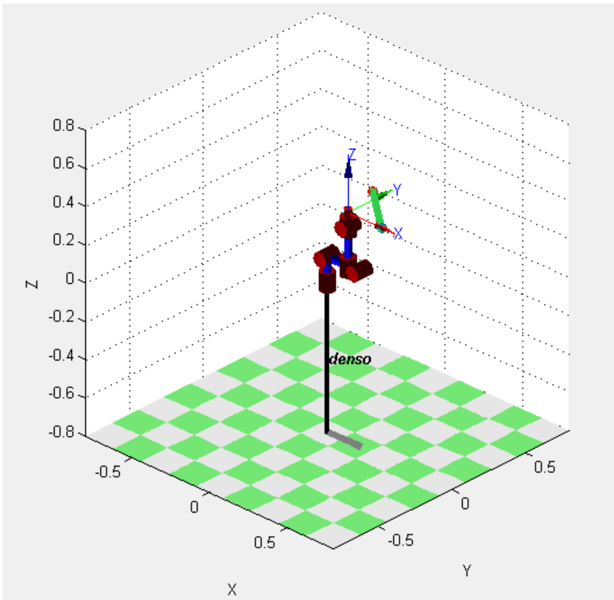

Fig. 4. Planned path

The Cartesian coordinates (X, Y and Z) of the path is given in Figure 5.

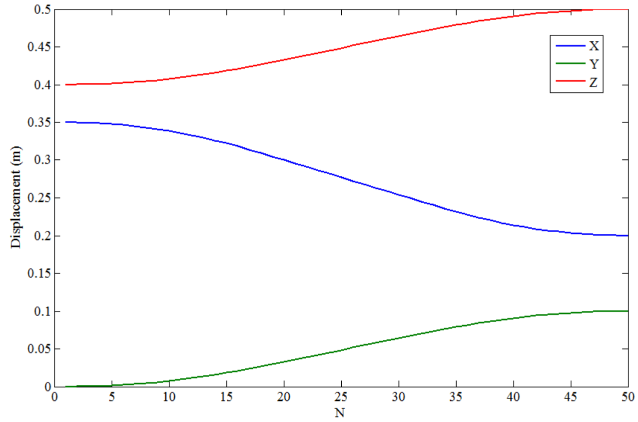

Fig. 5. Coordinates of the path

Transformation matrices are calculated by using the path data. Inverse kinematics analysis is applied. The angular displacements of the links of the robot are obtained as in Figure 6.

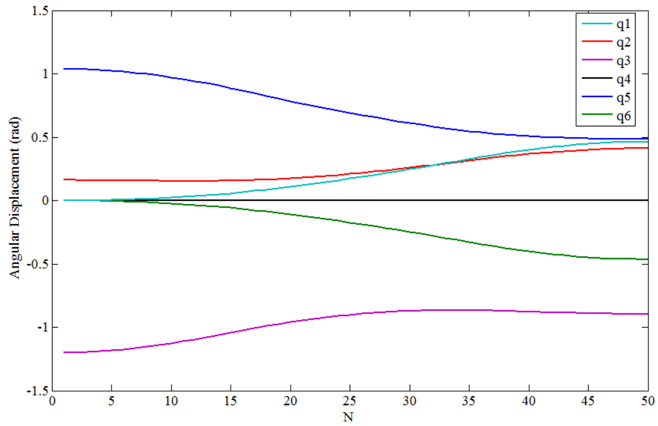

Fig. 6. Angular displacements of the robot links

Initial and final configurations of the robot are shown in Figure 7 (a, b), respectively.

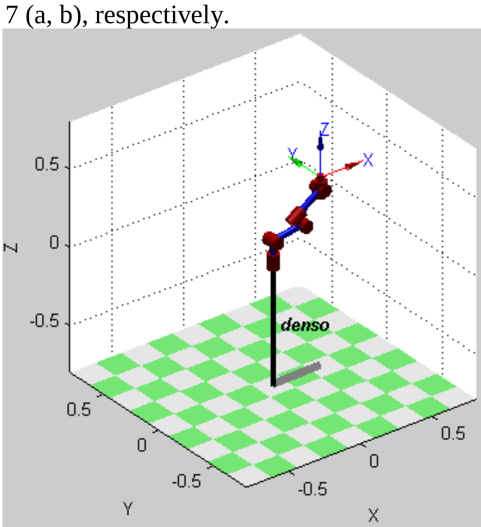

(a)

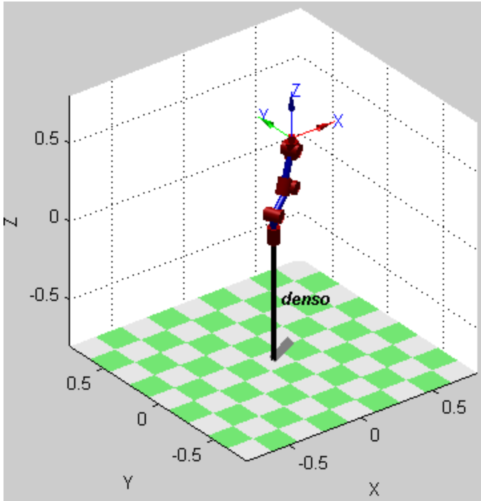

(b)

Fig. 7. Initial and final configurations of the robot

4. Guide User Interface (GUI)

Graphical User Interface development environment offers a set of tools in order to generate graphical user interfaces (GUIs) [14]. They greatly facilitate the operation of designing and building GUIs. A GUI example has been prepared for Denso robot including the forward kinematics. GUI is given in Figure 8. Push buttons, sliders, axes etc. can be added on it. Additions are being visible on the m. file simultaneously as a function. Robotics Toolbox is embedded to GUI. The results are compared with the expressions obtained in the analytical solution. It is proved that same results are obtained by the robotic toolbox and the analytical solution.

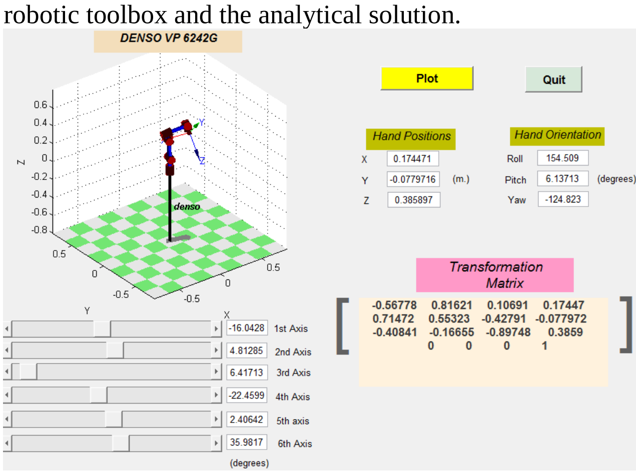

Fig. 8. Designed GUI example I

Figure 9 shows the designed simulation program by MATLAB/GUIDE to create serial link robot (Link 1-6) and control the joint angles (q_1, q_2, q_3, q_4, q_5 and q_6). DH parameters can directly be changed. Figure 9(a) and Figure 9(b) show the initial condition of the robot and the path generated with the given coordinates, respectively.

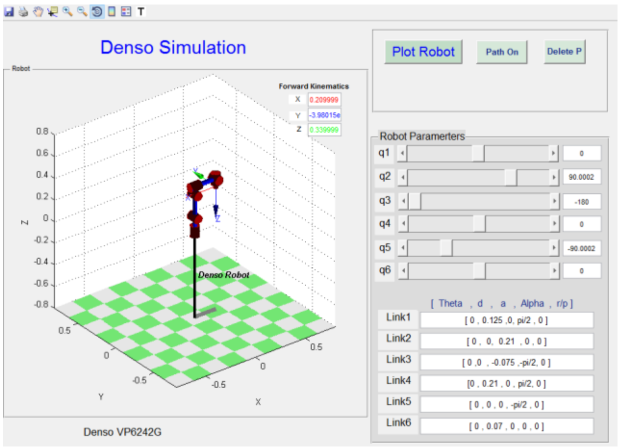

(a)

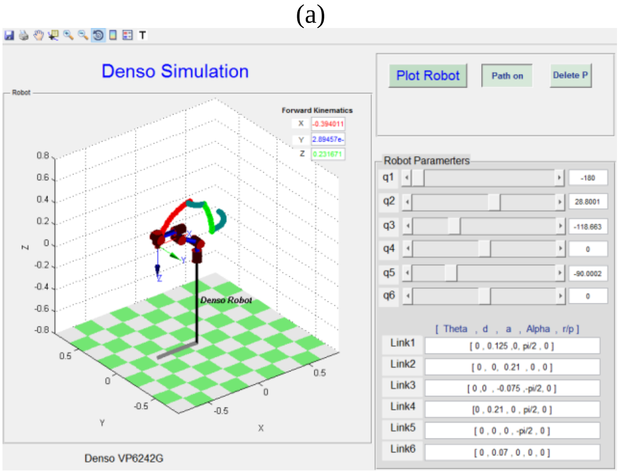

(b)

Fig. 9. Designed GUI example II

5. Conclusion

In this study, it is focused on determining the analytical solution of forward & inverse kinematics of the Denso 6 axis robot which is available in the laboratory. The equations obtained are reported.

Robotics toolbox is provided a great simplicity to us about kinematics of robots with the ready functions on it. However, making calculations in traditional way is important in order to control the robot and to form a background for further studies. Toolbox is then used to verify the results obtained by analytical way. The results are the same. User interfaces are the effective tools to show many works in a compact way. Due to this reason, Guide User Interface is performed. It is possible to reach simultaneous transformation matrix, position & orientation of robot hand when angular displacements of the motors are changed one by one.

This study is contained a part of theoretical and numerical kinematics analysis of Denso robot. It is performed to build a background study for rehabilitation robotics issues. Studies on adapting Denso robot for upper extremity rehabilitation are going on in Mechatronics Laboratory at Gaziantep University.

References

[1]. J. Funda, R. H. Taylor and Paul R.P, *On homogeneous transforms, quaternions, and computational efficiency*, IEEE Trans. Robot. Automation 6, pages 382–388. 1990.

[2]. J. Denavit& R. S. Hartenberg, *A kinematic notation for lower-pair mechanisms based on matrices*, Journal of Applied Mechanics 1. pages 215-221, 1955.

[3].P. Corke. *Robotics, Vision and Control, Fundamental Algorithms in Matlab®*. Springer, 2011.

[4].D. Constantin, M. Lupoae, C. Baciu, D.Buliga, *Forward kinematic analysis of an industrial robot*, Proceedings of the International Conference on Mechanical Engineering (ME 2015), 90-95, 2015.

[5]. S. Kucuk & Z. Bingul, *The Inverse kinematics solutions of industrial robot manipulators*, IEEE Conferance on Mechatronics, pages 274-279, (2004).

[6]. Y. Liu, D. Wang, J. Sun, L. Chang, C. Ma,Y. Ge and L. Gao, *Geometric approach for inverse kinematics analysis of 6-dof serial robot*, IEEE International Conference on Information and Automation, pages 852-855, 2015.

[7]. S. Qiao, Q. Liao, S. Wei, H.Su, *Inverse kinematic analysis of the general 6R serial manipulators based on double quaternions*, Mechanism and Machine Theory 45, 193-199, 2010.

[8]. A. Nubiola & I.A. Bonev, *Geometric approach to solving the inverse displacement problem of Calibrated decoupled 6R serial robots*, Transactions of the Canadian Society for Mechanical Engineering 38, 31-44, 2014.

[9]. A.R.J. Almusawi, L.C. Dülger, and S. Kapucu, *A new artificial neural network approach in solving inverse kinematics of robotic arm (denso vp6242)*, Computational Intelligence and Neuroscience, 2016.

[10]. R. Köker, *A genetic algorithm approach to a neural-network-based inverse kinematics solution of robotic manipulators based on error minimization*, Information Sciences 222, 528-543, 2013.

[11]. A. V. Duka, *Neural network based inverse kinematics solution for trajectory tracking of a robotic arm*, Procedia Technology 12, 20-27, 2014.

[12]. S. B. Niku . *Introduction to Robotics: Analysis, Systems, Applications*. Prentice Hall, 2001

[13]. D. Manocha & J. F. Canny, *Efficient inverse kinematics for general 6r manipulators*, IEEE Transactions on Robotics and Automation. 10, 648-657, 1994.

[14]. Creating Graphical User Interfaces, (2015). Mathwork.

Proceedings of the International Symposium of Mechanism and Machine Science, 2017
AzC IFToMM – Azerbaijan Technical University
11-14 September 2017, Baku, Azerbaijan

Kinematic analysis of the 3-R$\underline{\text{P}}$S manipulator using the geometry of plane curves

Sandipan BANDYOPADHYAY[1*], Teja Krishna MAMIDI[2], Aravind BASKAR[3]

[1*]Assistant Professor
Department of Engineering Design
Indian Institute of Technology Madras
Chennai 600 036
e-mail: sandipan@iitm.ac.in

[2]Research Scholar
e-mail: tejaiiit27@gmail.com

[3]Research Scholar
e-mail: krishna.arvind91@gmail.com

Abstract

This paper reports a number of interesting observations regarding the kinematics and singularities of a spatial parallel manipulator, namely, the 3-R$\underline{P}$S manipulator. It is well known in literature that the manipulator has two operation modes. Recently, it was shown that the forward kinematic problem of the manipulator is equivalent to the intersection of a circle with a pair of quad-circular octic curves, corresponding to the two operation modes, in the plane of the said circle. In this work, some special points of these octic curves are analysed and corroborated against the singularities of the manipulator. The transition between the modes are also examined from the perspective of the intersection of the octic curves. Finally, the conditions leading to finite self motions of the manipulator are derived and validated against those in the existing literature. The method of analysis is intuitive, simple, and at the same time, quite capable of retrieving existing results, as well as deriving fresh ones.

Keywords: 3-R$\underline{\text{P}}$S manipulator, Singularity, Finite self-motion, Double point, Quad-circular octic curve

1. Introduction

In the study of kinematics of manipulators one often encounters *circular* curves. One of the most famous examples of this is the coupler-curve of the planar four-bar mechanism, which is perhaps the most well-known *tri-circular* sextic in existence, and deserves a catalogue of its own [1]. The curve reappears in the problem of forward kinematics of planar parallel manipulators, where the problem reduces to the intersection of a circle with a tri-circular sextic curve [2]. Recently, a new circular curve has been associated with the forward kinematics of a spatial manipulator, namely, the 3-R$\underline{\text{P}}$S manipulator. It was shown in [3], that all the poses of the manipulator (for a given set of inputs) correspond to the points of intersection of a circle with a *quad-circular octic* curve in the plane of the said circle. Such a reduction of the forward kinematic problem affords a unique geometric understanding, from the perspective of the geometry of plane curves, which have been documented exhaustively in many classical works, e.g. [4].

Armed with these known results, this work tries to investigate the special geometric conditions that may occur, and the kinematic consequences thereof. In particular, this work looks at the special points of intersection, which covers the tangency of the octic curve with the circle, and the double points in the octic curve itself, which coincide with the point of intersection with the circle. It is interesting to note that while all of these cases lead to the merger of the roots of the *forward kinematic univariate* (FKU) (see [5] for a discussion on the FKU of this manipulator), not all of them are associated with the kinematic singularities of the manipulator. In other words, an interesting question emerges from these observations: "When does the (geometric) singularity of the constraint curves lead to a (kinematic) manipulator, and when does it not?" Only a rigorous analytical study can answer that question in a comprehensive manner. While that is out of scope of this paper, it does document a number of interesting situations, relating to the tangency condition, as well as the three possible types of double points, namely: the cusp, the crunode, and the acnode. At each of these situations, the following geometric/algebraic/kinematic conditions are studied, with an attempt towards correlating these conditions: the formal algebraic condition for the $\mathbf{\Sigma}^1$ singularity[1] of the manipulator, as given in [7] (henceforth referred to simply as the "singularity"); the geometric condition for the case 2 of the singularity reported in [8]; the coplanarity of one of the legs with the moving platform (as shown in an example in [5]); the condtion for obtaining a double root of the FKU, derived in terms of the Stüdy parameters in this work. The study and the results thereof are by no means complete, or conclusive. They are presented here to document a few possibilities, as hinted by the numerical examples, which need to be either proven or dismissed formally through rigorous analytical studies in the future.

The rest of the paper is oragnised as follow: the geometry and the forward kinematics problem of the 3-R$\underline{\text{P}}$S manipulator are presented in Section 2. The intersections of the octic curves with the circle at the special points, and the kinematic consequences thereof are studied via numerical examples in Section 3. A special case where the manipulator exhibits finite self-motion is discussed in Section 4, and the results are summarised in Section 5.

[1]According to Thom-Boardman classification of singularities of a differential map f, a point x belongs to the class $\mathbf{\Sigma}^n$ if the kernel of $Df(x)$, (i.e., the differential of f at x) is of dimension n [6].

2. Geometry and kinematics of the 3-R̲PS manipulator

The 3-R̲PS manipulator has three RPS-chains, each connected at a vertex of the fixed platform $\boldsymbol{b}_1\boldsymbol{b}_2\boldsymbol{b}_3$ by a rotary joint, and to the moving platform $\boldsymbol{p}_1\boldsymbol{p}_2\boldsymbol{p}_3$, by a spherical joint, as depicted in Fig. 1. The fixed and moving platforms are equilateral triangles of circumradius b and a, respectively. A fixed frame of ref-

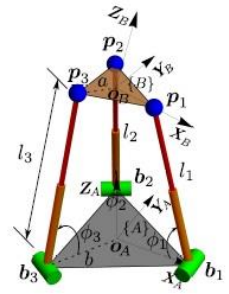

Fig. 1: Schematic of the 3-R̲PS manipulator

erence $\{A\}$, given by $\boldsymbol{o}_A$-$\boldsymbol{X}_A\boldsymbol{Y}_A\boldsymbol{Z}_A$, and a moving frame of reference $\{B\}$, given by $\boldsymbol{o}_B$-$\boldsymbol{X}_B\boldsymbol{Y}_B\boldsymbol{Z}_B$, are attached to the centroids of the fixed and the moving platforms, respectively. The actuated prismatic joint variables $\boldsymbol{l} = [l_1, l_2, l_3]^\top$ and the passive rotary joint variables $\boldsymbol{\phi} = [\phi_1, \phi_2, \phi_3]^\top$ constitute the *configuration space* of the manipulator. The forward kinematic (FK) problem of the 3-R̲PS manip-

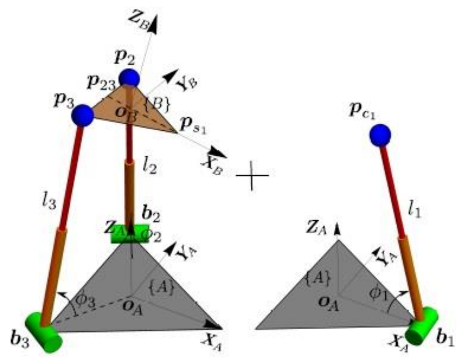

Fig. 2: Kinematic sub-chains of the 3-R̲PS manipulator

ulator is to determine the pose of the moving platform $\boldsymbol{p}_1\boldsymbol{p}_2\boldsymbol{p}_3$, for a given set of inputs $\boldsymbol{l}$. The problem can be addressed by hypothetically breaking the 3-R̲PS manipulator into two kinematic chains, and then finding the conditions for the two chains to close simultaneously. It can be done by removing one of the spherical joints, as shown in [3]. For instance, if the spherical joint at $\boldsymbol{p}_1$ is removed, a spatial RSSR closed chain is obtained, along with an open RP planar chain, as shown in Fig. 2. The point $\boldsymbol{p}_{s_1}$ of the RSSR-chain and the point $\boldsymbol{p}_{c_1}$ of the RP-chain coincide at the point $\boldsymbol{p}_1$ to form the 3-R̲PS manipulator shown in Fig. 1. By casting these geometric conditions in terms of equations and subsequently solving them, the unknown variable $\boldsymbol{\phi}$ can be obtained. The details of the process are given in [3]. The key points relevant to the present work are:

1. The surface traced by the point $\boldsymbol{p}_{s_1}$ of the RSSR-chain, when intersected by the plane of the RP chain forms the curve $\alpha(x,z) = 0$, where $\alpha(x,z)$ decomposes into the following factors:
$$\alpha(x,z) = \beta(x,z)O_1(x,z)O_2(x,z), \text{ where}$$
$$\beta = \left((2b+x)^2 + 4z^2\right)^2. \tag{1}$$
2. The perfect square factor $\beta = 0$ does not have any real intersection with the circle $C(x,z) = 0$ traced by $\boldsymbol{p}_{c_1}$, except when $z = 0$. This special case has been discussed in Section 4.
3. The factors $O_i(x,z)$ describe *quad-circular octic curves*. The FK problem, therefore, reduces largely to the computation of the intersection of the curves $O_i(x,z)$ with the circle $C(x,z) = 0$. It is also known that the *constraint ideal* $\langle O_i, C\rangle$ defines the ith *operation mode* of the manipulator [7].

The above geometric description of the FK problem of the 3-R̲PS manipulator is analysed further in this work, from the perspective of *special situations*, as explained in the following section.

3. Special points at the intersection of the octic curves with the circle

Ordinarily, the octic curves $O_i = 0$ are completely disjoint, i.e., in general, the modes are independent of each other. Furthermore, $O_i = 0$ intersect the circle $C = 0$ at *distinct* points, each such point leading to an *assembly mode* of the manipulator, inside the ith operation mode. However, there are special cases, where it is possible for $O_1 = 0$, $O_2 = 0$ and $C = 0$ to share common point(s), and so on. Some of these cases are discussed in the following. It may be noted that a complete, exhaustive geometric study of all the special cases, and their mathematical/physical consequence is beyond the scope of the current work, and is a subject matter of ongoing research.

In the following, three special cases of interest are described:

1. *Points of tangency*, S_1: The circle $C = 0$ is tangent to one of the octic curves $O_1 = 0$ or $O_2 = 0$.
2. *Transition points*, S_2: The octic curves $O_1 = 0$ and $O_2 = 0$ share a common point, and the circle $C = 0$ also passes through this point.
3. *Double points*, S_3: One (or both) of the octic curves has a double point, and the circle $C = 0$ passes through this point.

A detailed description of these three geometric cases, and their kinematic consequence are presented in the Sections 3.1, 3.2 and 3.3, respectively.

3.1. Points of tangency, S_1

The point $\boldsymbol{p}_t = [x_t, z_t]^\top$ is a *double root*, when the octic curve $O_i = 0$ of the operation mode i and the circle $C = 0$, share a common tangent at the said point. One pair of double roots indicate a merger of a pair of forward kinematic branches of the manipulator.

The algebraic conditions for the curves $C = 0$, $O_i = 0$ to have a common tangent at their intersection point $\boldsymbol{p}_t$ are:

1. The said curves should pass through the *simple* point $\boldsymbol{p}_t$, implying:
$$C(x_t, z_t) = 0, \tag{2}$$
$$O_i(x_t, z_t) = 0. \tag{3}$$
2. The tangents of the curves $C = 0$, $O_i = 0$ should have the same slopes at the intersection point $\boldsymbol{p}_t$:
$$\left.\frac{\partial C}{\partial x}\right|_{\boldsymbol{p}_t} \left.\frac{\partial O_i}{\partial z}\right|_{\boldsymbol{p}_t} - \left.\frac{\partial C}{\partial z}\right|_{\boldsymbol{p}_t} \left.\frac{\partial O_i}{\partial x}\right|_{\boldsymbol{p}_t} = 0, \tag{4}$$
$$\Rightarrow z_t h_i(x_t, z_t) = 0. \tag{5}$$

The algebraic condition for tangency in Eq. (4) reduces to Eq. (5), in which the polynomial $h(x_t, z_t)$ is of degree 6 in x_t, z_t. The condition $z_t = 0$ is a very special one, which aligns the tangent at the point $\boldsymbol{p}_t$ with the axis X_A itself. This special case is not discussed in detail due to want of space; however, one example of such a situation, where the manipulator can have finite self-motions, is discussed in Section 4.

The variety S_1 is expressed in the architecture parameters a, b, and the active joint variables l_1, l_2, l_3, after eliminating x_t, z_t from Eqs. (2, 3, 5). First, z_t is eliminated, as shown in the schematics (6) and (7):

$$\left.\begin{array}{r} O_i(x_t, z_t) = 0 \\ C(x_t, z_t) = 0 \end{array}\right) \xrightarrow{\times z_t} f_{1_i}(x_t) = 0, \tag{6}$$

$$\left.\begin{array}{r} h_i(x_t, z_t) = 0 \\ C(x_t, z_t) = 0 \end{array}\right) \xrightarrow{\times z_t} f_{2_i}(x_t) = 0. \tag{7}$$

These steps result in two polynomials $f_{1_i}(x_t)$, $f_{2_i}(x_t)$ of degree 4 and 3 in x_t, respectively. The symbol '$\xrightarrow{\times z_t}$' denotes the elimination of the variable z_t from the polynomial equations preceding it.

The eliminant E_1 is obtained on eliminating the variable x_t from the polynomial equations $f_{1_i} = 0, f_{2_i} = 0$, as shown in the schematic (8).

$$\left.\begin{array}{r} f_{1_i}(x_t) = 0 \\ f_{2_i}(x_t) = 0 \end{array}\right) \xrightarrow{\times x_t} E_{1_i} = 0, \tag{8}$$

The eliminant E_{1_i} splits into a number of factors:

$$\begin{aligned} E_{1_i} =& (l_1 - l_2)^2 (l_1 + l_2)^2 (l_1 - l_3)^2 (l_1 + l_3)^2 (l_2 - l_3)^2 \\ & \times (l_2 + l_3)^2 \, \zeta_i(a, b, l_2, l_3) \, \tau_i(a, b, l_1, l_2, l_3), \; i = 1, 2. \end{aligned} \tag{9}$$

The factors $(l_j - l_k)^2$ can be ignored, since by themselves, they *do not necessarily* imply tangency between curves intersecting at $\boldsymbol{p}_t$. The factor ζ_i in Eq. (9) being the leading co-efficient of the polynomial $f_{1_i}(x_t)$, its vanishing signifies the break-down of the elimination process depicted in the schematic (8), hence $\zeta_i = 0$ is also ignored in the following. The remaining factor, τ_i, is of degree 24 in l_1, l_2, l_3.

The polynomials τ_1, τ_2 describing the two operation modes exhibit a functional relation:

$$\tau_1(a) = \tau_2(-a). \tag{10}$$

This is analogous with the relation $g_1(a) = g_2(-a)$ between the two factors g_1, g_2 of the *forward kinematic univariate* (FKU) of the manipulator, reported in [5]. Together, these conditions signify that the π-screw motion mentioned in [7] is equivalent to the *inversion* of the top platform.

An example of such a case is obtained for the parameter values[2] $a = 9/5, b = 1, l_1 = -41/10, l_2 = 23/10, l_3 = 5.262$. The octic curves $O_1 = 0, O_2 = 0$ and the circle $C = 0$ are shown for these numbers in Fig. 3. As can be seen in the figure, the curve O_1 is tangential to the circle $C = 0$ at $\boldsymbol{p}_t$. The line $z = 0$ acts as a mirror plane of symmetry, as mentioned in [3].

Since the tangency implies the merger of two pairs (counting the mirror image) of FK solutions, this condition implies a *gain-type* or FK singularity of the manipulator. The corresponding pose of the manipulator along with the branches that are merging is presented in Fig. 4.

[2]All the length parameters/variables are dimensionless in this paper, as these have been scaled by the circumradius of the fixed platform, b, without any loss of generality. All angles are measured in radians, unless mentioned explicitly otherwise.

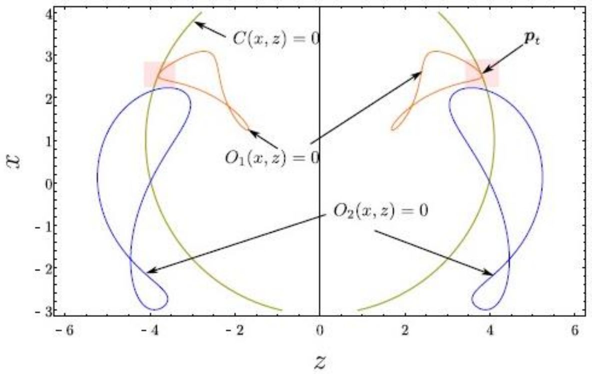

Fig. 3: Plot of the octic curves $O_1 = 0, O_2 = 0$ and the circle $C = 0$ for the tangency condition $\tau_1 = 0$.

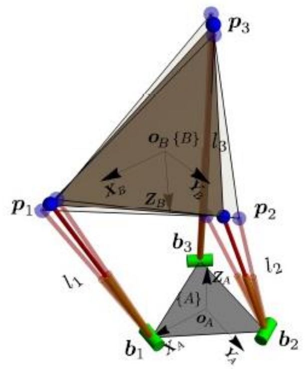

Fig. 4: Singular pose of the 3-R$\underline{P}$S manipulator where the FK branches merge.

3.2. Points of transition, S_2

A point $\boldsymbol{p}_m = [x_m, z_m]^\top$ denotes the *transition point* between the operation modes, when it is at the intersection of the octic curves $O_1(x,z) = 0$, $O_2(x,z) = 0$, as well as the circle $C(x,z) = 0$. Hence, the following conditions define such a point:

$$C(x_m, z_m) = 0, \; O_1(x_m, z_m) = 0, \; O_2(x_m, z_m) = 0. \tag{11}$$

As in the case of S_1, the variety S_2 is obtained in the variables l_i, and the parameters a, b, after the elimination of x_m, z_m from Eq. (11). The elimination process is briefly described in the following schematics:

$$\left.\begin{array}{r} O_1(x_m, z_m) = 0 \\ C(x_m, z_m) = 0 \end{array}\right) \xrightarrow{\times z_m} f_3(x_m) = 0, \tag{12}$$

$$\left.\begin{array}{r} O_2(x_m, z_m) = 0 \\ C(x_m, z_m) = 0 \end{array}\right) \xrightarrow{\times z_m} f_4(x_m) = 0. \tag{13}$$

The resultant of f_3 and f_4 w.r.t. x_m results in the eliminant E_2 as depicted in the schematic (14):

$$\left.\begin{array}{r} f_3(x_m) = 0 \\ f_4(x_m) = 0 \end{array}\right) \xrightarrow{\times x_t} E_2 = 0. \tag{14}$$

The eliminant E_2 splits into five factors:

$$E_2 = a^4 \xi_1 \xi_2 \xi_3 \xi_4 = 0. \tag{15}$$

The polynomials $\xi_1, \xi_2, \xi_3, \xi_4$ are of degree 8, 8, 8 and 24, respectively, in the variable l_1, l_2, l_3. It is verified that each of these factors admit real solutions. Some of these real solutions are analysed numerically and geometrically, from which the following observations emerge:

1. Only the vanishing of ξ_3 corresponds to the condition for the transition point between the operation modes. It is verified, numerically, that such transition points are singular as well, as mentioned in [7].
2. The conditions $\xi_1 = 0$, $\xi_2 = 0$ cause two *distinct non-singular* poses of the manipulator, belonging to distinct operation modes, to have one of the sides of the moving platform in common. Such a situation is depicted in Fig. 8, where the side $\boldsymbol{p}_1\boldsymbol{p}_3$ is common between the operation modes of the manipulator. In this work, the sides involved can only be $\boldsymbol{p}_1\boldsymbol{p}_2$ or $\boldsymbol{p}_1\boldsymbol{p}_3$, since the manipulator was broken at this point for the present analysis.
3. The equation $\xi_4 = 0$ describes the condition for two *distinct non-singular* poses of the manipulator belonging to distinct operation modes to have a point in common. For reasons explained above, the said point can only be $\boldsymbol{p}_1$ in this work.

From these observations, it appears that the factors 2 and 3 are artefacts of the resultant-based elimination process. For the above said reasons cases 2, 3 do not represent a transition.

The polynomial ξ_3 being symmetric in l_1, l_2, l_3, distinguishes itself from the others in Eq. (15). Similarly, the polynomials ξ_2, ξ_1 are symmetric in l_2, l_3 and the polynomial ξ_4 is not symmetric in any of the input joint parameters l_1, l_2 or l_3.

It is important to note here that the observations made above are based on numerical examples, and not exhaustive mathematical analysis. Hence, interesting as they are, they can only hoped to be indicative at this point.

An example for the case where $\zeta_3 = 0$ is obtained for the parameter values $a = 1/2$, $b = 1$, $l_1 = 22/10$, $l_2 = 23/10$, $l_3 = 2.936$. For these values, the curves $O_1 = 0$, $O_2 = 0$, $C = 0$ meet at a common point $\boldsymbol{p}_{m_1}$ as depicted in Fig. 5. This point $\boldsymbol{p}_{m_1}$ represents the transition point between the operation modes of the manipulator.

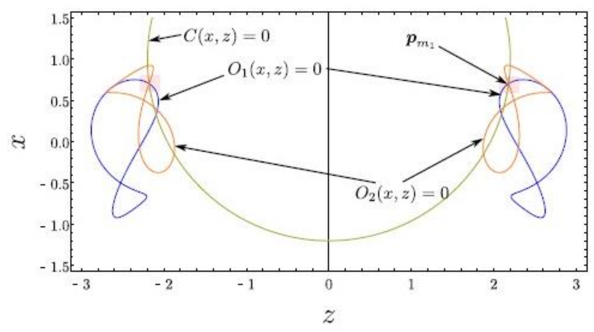

Fig. 5: Plot of the octic curves $O_1 = 0$, $O_2 = 0$, circle $C = 0$ for $\xi_3 = 0$.

The singular pose of the manipulator at this transition point $\boldsymbol{p}_{m_1}$ is shown in Fig. 6. The fixed and moving platforms of the manipulator are in parallel planes with the latter flipped by π w.r.t to the former. A similar configuration is reported as the constraint singularity of the 3-RPS manipulator in [9] and as the transition between the operation modes $x_0 = 0, x_1 = 0$ in [10].

An example for the case, where the octic curves $O_1 = 0, O_2 = 0$, and the circle $C = 0$ meet at a common point $\boldsymbol{p}_{m_2}$ for the values of the parameters $b = 1$, $l_1 = 22/10$, $l_2 = 23/10$, $l_3 = 1.930$ satisfying $\zeta_1 = 0$ is shown in Fig. 7. This point $\boldsymbol{p}_{m_2}$ does not represent a transition point for the above discussed reasons.

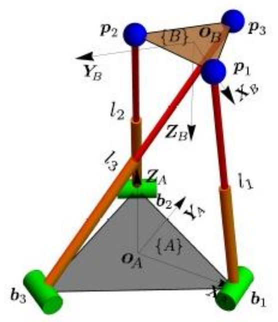

Fig. 6: Pose of the 3-RPS manipulator at the transition.

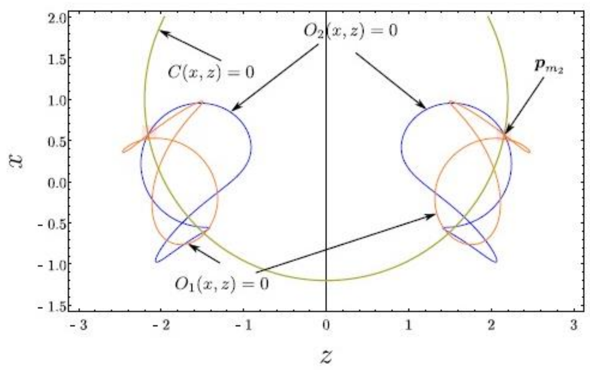

Fig. 7: Plot of the octic curves $O_1 = 0, O_2 = 0$ and the circle $C = 0$ for $\xi_1 = 0$.

The corresponding *non-singular* poses of the manipulator at the point $\boldsymbol{p}_{m_2}$ are as depicted in Fig. 8. Clearly, these are two different poses of the manipulator except for the common side $\boldsymbol{p}_3\boldsymbol{p}_1$.

3.3. Double points of the octic at the intersection with the circle, S_3

Another interesting class of special points are the *double points* on either $O_1 = 0$ or $O_2 = 0$, when the circle $C = 0$ also passes through it. Since the said curves are octic in nature, there can be up to four pairs of double points on each (e.g., the points at infinity in each). However, in this work, only one pair of double points is considered due to space constraints. According to [4], pp. 2, "A *double point* of a curve is a point P such that *every* line through P meets the curve *twice* at P". These are further classified as *infinite* and *finite* double points, depending upon whether they are at infinity, or not.

3.3.1. Finite double points

The conditions for obtaining a finite double point, denoted by $\boldsymbol{p}_d = [x_d, z_d]^\top$, on the octic curve $O_i = 0$ intersecting with the circle $C = 0$ are:

1. The gradient of the octic curve $O_i = 0$ along x, z at the point $\boldsymbol{p}_d$ should be zero. Therefore, $\boldsymbol{p}_d$ is a double point of the octic

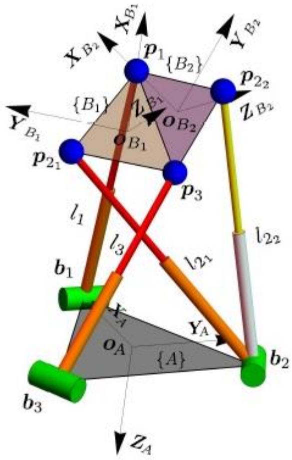

Fig. 8: Non-singular distinct poses of the 3-RPS manipulator.

curve $O_i = 0$, provided:

$$O_i(x_d, z_d) = 0, \left(\frac{\partial O_i}{\partial x}, \frac{\partial O_i}{\partial z}\right)^{\top}_{\boldsymbol{p}_d} = \mathbf{0}. \tag{16}$$

2. The double point $\boldsymbol{p}_d$ is required to lie on the circle $C = 0$ as well:

$$C(x_d, z_d) = 0. \tag{17}$$

As in the case of S_2, the variety S_3 is obtained by first eliminating the variables x_d, z_d from the Eqs. (16, 17), to obtain an equation in the parameters a, b, and the variables l_1, l_2, l_3. The elimination process is briefly described by the following schematics:

$$\left.\begin{array}{l} O_i(x_d, z_d) = 0 \\ C(x_d, z_d) = 0 \end{array}\right) \xrightarrow{\times z_d} f_{5_i}^2(x_d) = 0, \tag{18}$$

$$\left.\begin{array}{l} \frac{\partial O_i}{\partial x}\Big|_{\boldsymbol{p}_d} = 0 \\ C(x_d, z_d) = 0 \end{array}\right) \xrightarrow{\times z_d} f_{6_i}^2(x_d) = 0, \tag{19}$$

$$\left.\begin{array}{l} \frac{\partial O_i}{\partial z}\Big|_{\boldsymbol{p}_d} = 0 \\ C(x_d, z_d) = 0 \end{array}\right) \xrightarrow{\times z_d} (b - l_1 - x_d)(b + l_1 - x_d) f_{7_i}^2(x_d) = 0. \tag{20}$$

The polynomials $f_{5_i}, f_{6_i}, f_{7_i}$ are of degree 4, 4 and 3 in x_d, respectively. The factors preceding the equation $f_{7_i} = 0$ in Eq. (20) correspond to the case when $z_d = 0$, the details of which are discussed in Section 4. The resultant of the polynomial equations $f_{5_i} = 0$, $f_{6_i} = 0$ with the equation $f_{7_i} = 0$ in x_d, results in two polynomials r_{1_i}, r_{2_i} in the parameters a, b, l_1, l_2, l_3 as depicted in the schematics (21, 22).

$$\left.\begin{array}{l} f_5 = 0 \\ f_7 = 0 \end{array}\right) \xrightarrow{\times z_d} r_{1_i} = 0, \tag{21}$$

$$\left.\begin{array}{l} f_6 = 0 \\ f_7 = 0 \end{array}\right) \xrightarrow{\times z_d} r_{2_i} = 0. \tag{22}$$

Once again, it may be noted that the expressions for r_{1_i}, r_{2_i} for the two operation modes vary only by the sign of the parameter a, i.e.:

$$r_{1_i}(a) = r_{2_i}(-a). \tag{23}$$

Furthermore, r_{1_i}, r_{2_i} factorises as shown in Eqs. (24, 25), respectively:

$$\begin{aligned} r_{1_i} =& (l_1 - l_2)^2 (l_1 + l_2)^2 (l_1 - l_3)^2 (l_1 + l_3)^2 (l_2 - l_3)^2 \\ &\times (l_2 + l_3)^2\, \delta_i(a, b, l_1, l_2, l_3) = 0, \end{aligned} \tag{24}$$

$$\begin{aligned} r_{2_i} =& (a - 2b)(l_1 - l_2)^2 (l_1 + l_2)^2 (l_1 - l_3)^2 (l_1 + l_3)^2 \\ &\times (l_2 - l_3)^2 (l_2 + l_3)^2 (3a^2 - 6ab - 6b^2 - l_2{}^2 - l_3{}^2) \\ &\times \mu_i(a, b, l_1, l_2, l_3) = 0. \end{aligned} \tag{25}$$

The polynomials δ_i, μ_i in Eqs. (24, 25) are each of degree 24 in the variables l_1, l_2, l_3.

The factors $(l_j - l_k)^2$ represent the symmetry in the kinematic sub-chains of the manipulator. In particular, when $l_2 = l_3$ the octic curves split into a pair of coincident circles and a quartic curve (shown in Fig. 11). As mentioned in Section 3.1, these do *not necessarily* enforce the tangency between the circle and the octic curve, but the octic curve intersects the circle at the double point.

At a double point $\boldsymbol{p}_d$ of the octic curve $O_i = 0$, the equation of the *tangents* is given by:

$$\begin{aligned} t_{o_i} = & \frac{\partial^2 O_i}{\partial^2 x}\Big|_{\boldsymbol{p}_d} (x - x_d)^2 + 2\,\frac{\partial^2 O_i}{\partial x \partial z}\Big|_{\boldsymbol{p}_d} (x - x_d)(z - z_d) \\ & + \frac{\partial^2 O_i}{\partial^2 z}\Big|_{\boldsymbol{p}_d} (z - z_d)^2 = 0. \end{aligned} \tag{26}$$

The discriminant Δ of the quadratic equation given in Eq. (26) is:

$$\Delta = \frac{\partial^2 O_i}{\partial^2 x}\Big|_{\boldsymbol{p}_d} \frac{\partial^2 O_i}{\partial^2 z}\Big|_{\boldsymbol{p}_d} - \left(\frac{\partial^2 O_i}{\partial x \partial z}\Big|_{\boldsymbol{p}_d}\right)^2. \tag{27}$$

Based on the value of this discriminant Δ, the double point $\boldsymbol{p}_d$ is qualified to be any one of the following:

1. A *crunode* $\boldsymbol{p}_{n_1}$: There exists two distinct tangents at this point and the discriminant is less than zero ($\Delta < 0$).
2. An *acnode* $\boldsymbol{p}_{n_2}$: The equation of the tangents $t_{o_i} = 0$ does not admit any real solutions as the discriminant is greater than zero ($\Delta > 0$). Hence, there are no tangents at this point.
3. A *cusp* $\boldsymbol{p}_c$: The two tangents at this point coincide as the discriminant is zero ($\Delta = 0$).

An example for case 3, where a cusp $\boldsymbol{p}_c$ occurs at the intersection of $O_1 = 0$ with the circle $C = 0$ for the following numerical values: $a = 2$, $b = 1$, $l_1 = -29/10$, $l_2 = 29/10$, $l_3 = \frac{(-30-\sqrt{1141})}{10}$ is shown in the Fig. 9. The corresponding pose of the manipulator is shown in Fig. 10.

As can be seen from the Fig. 10, the pose of the manipulator is special from multiple perspectives:

1. The third leg lies in the plane of the moving platform.
2. The lines joining the spherical joints $\boldsymbol{p}_3$, $\boldsymbol{p}_2$ and $\boldsymbol{p}_3$, $\boldsymbol{p}_1$ intersect the axis of the rotary joint at $\boldsymbol{b}_3$. This pose exemplifies case 2 of the singularity conditions of the manipulator, as presented in [8]. The same configuration has been characterised under *constraint singularity* in [9].
3. The axes of all the three legs intersect the line $\boldsymbol{p}_1\boldsymbol{p}_2$.

The kinematic consequence of this condition is that the manipulator is singular. However, it is also possible to have a situation, where the circle $C = 0$ intersects one of the octic curves at a double point, but the manipulator is *not* singular. Such a configuration is obtained for the following set of values: $l_2 = l_3 = 1$, $l_1 = 3/2$, $a = 1/2\, b = 1$. In this case $O_1 = 0$ splits into two components, i.e., $O_1 = O_{1a} O_{1b} = 0$, which have the following nature:

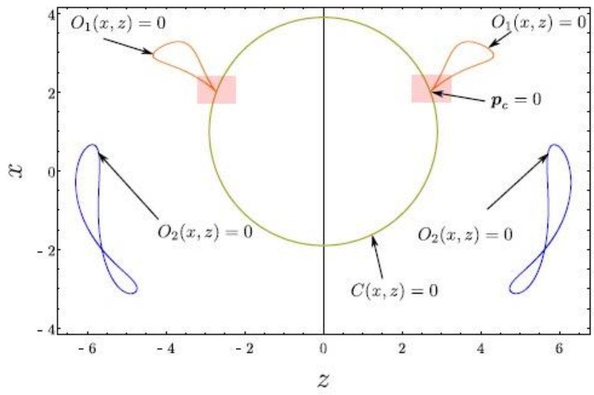

Fig. 9: Plot of the octic curves $O_1 = 0$, $O_2 = 0$ and the circle $C = 0$ at $a = 2b$, $l_1 = l_2$ and $\mu_1 = 0$.

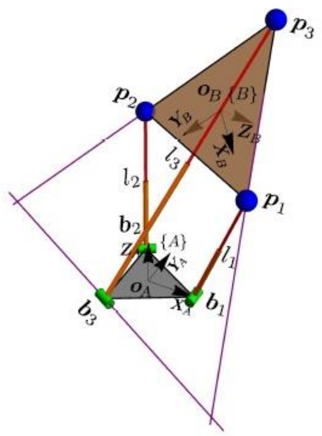

Fig. 10: Singular pose of the 3-RPS manipulator at the cusp $\boldsymbol{p}_c$.

1. The curve $O_{1a} = 0$ is a pair of *coincident* circles, shown in solid (blue) line-type in Fig. 11.
2. The curve $O_{1b} = 0$ decomposed into two components, each being a circle, shown in dashed (blue) line-type in Fig. 11.

Similarly, the curve $O_2 = 0$ splits into two quartic curves $O_{2a} = 0$, $O_{2b} = 0$, whose nature is:

1. The curve $O_{2a} = 0$ further decomposes to a pair of *coincident circles* shown in dotted (orange) line-type in Fig. 11.
2. The other quartic curve $O_{2b} = 0$ does not admit any real solution.

Clearly, any intersection of $O_{1a} = 0$ with $C = 0$ would be a double point of the former. However, it can be verified, that this double point does not signify a singularity. The poses of the manipulator corresponding to point $\boldsymbol{p}_{d_1}$ in Fig. 11 are shown in Fig. 12. It can be seen that only the vertex $\boldsymbol{p}_1$ is the same between the two poses, but that is not enough to cause a singularity in the manipulator.

3.3.2. Double points at infinity

In order to study the double points at infinity, one needs to resort to the use of projective/homogeneous coordinates. Let w be the *homogenising coordinate*, so that the projective versions of the octic

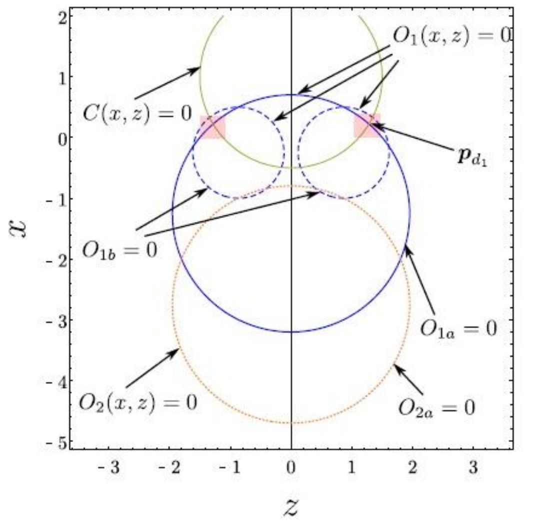

Fig. 11: Plot of the octic curves $O_1 = 0, O_2 = 0$ and the circle $C = 0$ at the double point satisfying $l_2 = l_3$.

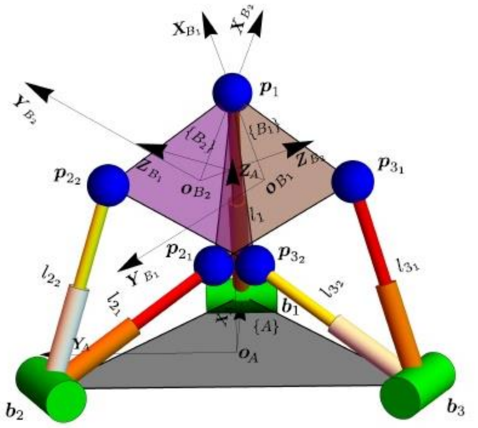

Fig. 12: Non-singular poses of the 3-RPS manipulator at the double point satisfying $l_2 = l_3$.

curves can be written as $O_{h_i}(X,Z,w) = 0$, where:

$$X = \frac{x}{w},\ Z = \frac{z}{w}. \tag{28}$$

In this framework, a double point $\boldsymbol{p}_h$ can be expressed as $\boldsymbol{p}_h = [x_h, z_h, w]^\top$. The point $\boldsymbol{p}_h$ becomes a double point at infinity, when the gradient of $O_{h_i} = 0$ w.r.t. $[X,Z,w]^\top$ vanishes at $\boldsymbol{p}_h$, and in addition, $w = 0$:

$$\begin{aligned}&\left.\frac{\partial O_{h_i}}{\partial X}\right|_{\boldsymbol{p}_h,w=0} = 0,\ \left.\frac{\partial O_{h_i}}{\partial w}\right|_{\boldsymbol{p}_h,w=0} = 0,\ \left.\frac{\partial O_{h_i}}{\partial Z}\right|_{\boldsymbol{p}_h,w=0} = 0,\\ &\Rightarrow 8x_h\left(x_h^2+z_h^2\right)^3 = 0,\ 4(a-2b)x_h\left(x_h^2+z_h^2\right)^3 = 0, \text{ and}\\ &\quad 8z_h\left(x_h^2+z_h^2\right)^3 = 0.\end{aligned} \tag{29}$$

The only real solution to Eq. (29) is $x_h = 0$, $z_h = 0$, $w = 0$, which is not included in the projective space. The result supports the fact that the quad-circular octic curve $O_i = 0$ do not have asymptotes.

4. Special case of $z = 0$

At several places in the previous sections, $z = 0$ came up as a special case, the discussions on which have been deferred to this section. As may be expected, the implication of this additional condition varies from one case to the other. Some of these are discussed in the following.

4.1. Implication of $z = 0$ in the FK problem

In Eq. (1) of Section 2 it was shown that the FK problem of the 3-RP̲S manipulator is equivalent to the intersection of a curve $\alpha(x,z) = 0$ with a circle in the same vertical plane, where one of the components of the said curve is given by:

$$\beta(x,z) = \left((2b+x)^2 + 4z^2\right)^2 = 0. \tag{30}$$

The only real solution to the problem is: $x = -2b$, $z = 0$. Since the circle $C = 0$ needs to pass through this point, given by, say, $\boldsymbol{p}_a = [-2b, 0]^\top$, one can write:

$$C(x,y)_{\boldsymbol{p}_a} = 0 \Rightarrow l_1{}^2 - 9b^2 = 0. \tag{31}$$

At point $\boldsymbol{p}_a$ the octic curve $O_i = 0$ admits a real solution when:

$$O_i(x,y)_{\boldsymbol{p}_a} = 0 \Rightarrow l_2^2 = 3a^2 - 3b^2,\ l_3^2 = 3a^2 - 3b^2. \tag{32}$$

Clearly, the solution is independent of the operation mode of the manipulator. The conditions in Eqs. (31, 32) lead to *finite self-motions* in the 3-RP̲S manipulator, as reported in [11]. Interestingly, the point $\boldsymbol{p}_a$ is an *acnode* of the curve $\beta = 0$. For the numeric values $a = 3/2$, $b = 1$, $l_1 = 3$, $l_2 = \sqrt{15}/2$, $l_3 = \sqrt{15}/2$ that satisfy Eqs. (31, 32), the plots of the curves are shown in Fig. 13.

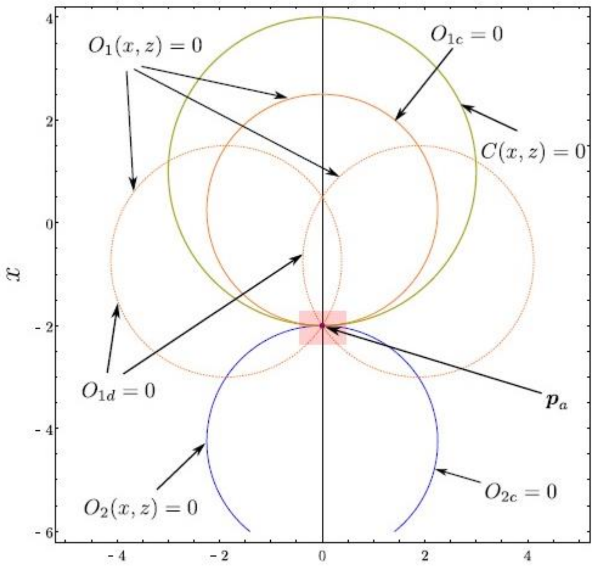

Fig. 13: Plot of the octic curves $O_1 = 0$, $O_2 = 0$, the circle $C = 0$ intersecting at the acnode of the curve $\beta = 0$.

The octic curve $O_1 = 0$ splits into $O_1 = O_{1c}O_{1d} = 0$ and the nature of these curves are:

1. The curve $O_{1c} = 0$ is a pair of coincident circles, as depicted in solid (orange) line-type in Fig. 13. This pair is tangent to the circle $C = 0$ at the *tacnode* $\boldsymbol{p}_a$.
2. The component $O_{1d} = 0$ further decomposes to two circles as shown in dotted (orange) line-type in Fig. 13. Each of these circles intersect the circle $C = 0$ at the point $\boldsymbol{p}_a$.

The curve $O_2 = 0$ splits into two factors $O_2 = O_{2c}O_{2d} = 0$, whose nature is:

1. Similar to the curve $O_{1c} = 0$, $O_{2c} = 0$ is also a pair of *concentric circles* represented in solid (blue) line-type in Fig. 13. This pair is tangent to the circle $C = 0$ at the point $\boldsymbol{p}_a$.
2. The curve $O_{2d} = 0$ admits two repeated real solutions at the point $\boldsymbol{p}_a$, hence the said point is an *acnode* of this curve.

The curve $\beta = 0$ has an *acnode* at $\boldsymbol{p}_a$ highlighted by a translucent rectangle, as shown in Fig. 13.

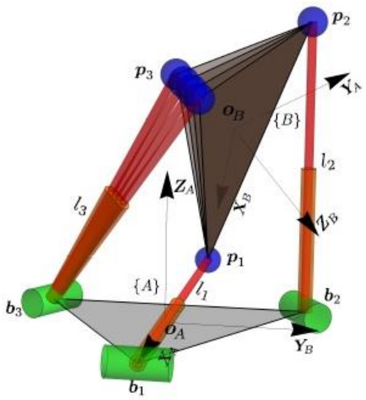

Fig. 14: Finite self-motion of the manipulator at the point $\boldsymbol{p}_a$.

The manipulator is known to exhibit finite self-motion in this case and this corresponds to the case 2(a) reported in [11]. For the given input parameters $\boldsymbol{l}$, maintaining the position of the point $\boldsymbol{p}_1$ the RSSR sub-chain exhibits the finite self-motion as shown in Fig 14.

5. Conclusion

In this paper, the special cases in the forward kinematics of the 3-RP̲S manipulator are analysed, using only the concepts of geometry of plane curves. It turns out that this technique is as powerful, as it is intuitive. It has been able to recover results in existing literature, which have been obtained using algebraic means. Moreover, it has been able to associate geometric implications to each of these cases, e.g., singularities, transitions between modes, finite self-motions, etc. These special cases have been studied via numerical examples, the results of which have been tabulated in Table 1. The table suggests that the geometric condition for singularity in Basu and Ghosal [8] may be geometrically equivalent to an octic curve intersecting a circle at a cusp. Similarly, the finite self-motion of the manipulator may be associated with the a quadratic curve having an acnode on the same circle. It needs to be noted, however, that these results are by no means exhaustive. While they hint at various possibilities, they need to be studied in depth, analytically, in order to establish the inter-relationships between various geometric conditions, their algebraic implications, and kinematic consequences. It is definitely worth undertaking such a study, as there are multiple spatial manipulators whose kinematics are fairly *similar* to that of the 3-RP̲S manipulator, namely, the 3-R̲RS, MaPaMan-I, 3-R̲P̲RS. A thorough understanding of the kinematics of the 3-RP̲S should help develop significant understanding of the kinematics of these manipulators as well.

Table 1: Relationships between various geometric conditions and their kinematic consequences.

$\mathbf{\Sigma}^1$: The algebraic conditions for the *gain-type* singularity of the 3-RPS manipulator discussed in [7],
B : Case 2 of the geometric condition of singularity of the 3-RPS manipulator reported in [8],
D : A double root of the FKU defined in Stüdy parameters,
P : The condition for any one of the legs of the 3-RPS manipulator co-planar with the moving platform.

Figure	Examples	$\mathbf{\Sigma}^1$	B	D	P
3	The octic curve $O_i = 0$ is tangent to the circle $C = 0$.	✓	×	✓	×
5	The curves $O_1 = 0, O_2 = 0$, $C = 0$ intersect at a point. Transition between the operation modes	✓	×	✓	×
7	The octic curves $O_1 = 0$, $O_2 = 0$ have a common point on the circle $C = 0$. Two distinct poses share a common side of the moving platform.	×	×	×	×
9	A cusp of the octic curve $O_i = 0$ appears on the circle $C = 0$.	✓	✓	✓	✓
11	A double pointof the octic curve $O_i = 0$ occurs on the circle $C = 0$ and the RSSR sub-chain is symmetric.	×	×	×	×
13	An acnode of the curve $\beta = 0$ appears on the circle $C = 0$. Manipulator exhibits finite self-motion.	✓	×	✓	×

References

[1] J. A. Hrones and G. L. Nelson, *Analysis of the Four-bar Linkage*. New York: The Technology Press of the Massachusetts Institute of Technology and John Wiley & Sons, Inc., 1951.

[2] K. Hunt, "Structural kinematics of in-parallel-actuated robot-arms," *Journal of Mechanisms, Transmissions, and Automation in Design*, vol. 105, no. 4, pp. 705–712, 1983.

[3] T. K. Mamidi, A. Baskar, and S. Bandyopadhyay, "A novel geometric analysis of the kinematics of the 3-RPS manipulator," *Accepted to be presented in 7th IFToMM International Workshop on Computational Kinematics*, (Futuroscope-Poitiers), 2017.

[4] E. J. F. Primrose, *Plane Algebraic Curves*. MacMillan & Co Ltd., 1955.

[5] R. A. Srivatsan and S. Bandyopadhyay, "Analysis of constraint equations and their singularities," in *Advances in Robot Kinematics*, pp. 429–436, Springer, 2014.

[6] V. I. Arnold, S. M. Gusein-Zade, and A. N. Varchenko, *Singularities of Differentiable Maps, Volume 1*. Boston: Birkhüser, 1985.

[7] J. Schadlbauer, D. Walter, and M. Husty, "The 3-RPS parallel manipulator from an algebraic viewpoint," *Mechanism and Machine Theory*, vol. 75, pp. 161–176, 2014.

[8] D. Basu and A. Ghosal, "Singularity analysis of platform-type multi-loop spatial mechanisms," *Mechanism and Machine Theory*, vol. 32, pp. 375–389, April 1997.

[9] D. Zlatanov, I. A. Bonev, and C. M. Gosselin, "Constraint singularities of parallel mechanisms," in *International Conference on Robotics and Automation*, (Washington D.C), pp. 496–502, May 2002.

[10] J. Schadlbauer, D. Walter, and M. Husty, "A complete kinematic analysis of the 3-RPS parallel manipulator," in *15th National Conference on Machines and Mechanisms*, (Indian Institute of Technology Madras, Chennai), pp. 1–10, 2011.

[11] J. Schadlbauer, M. L. Husty, S. Caro, and P. Wenger, "Self-motions of 3-RPS manipulators," *Frontiers of Mechanical Engineering*, vol. 8, no. 1, pp. 62–69, 2013.

Proceedings of the International Symposium of Mechanism and Machine Science, 2017
AzC IFToMM – Azerbaijan Technical University
11-14 September 2017, Baku, Azerbaijan

Particular drawing biquaternion closure equations of complex spatial mechanisms

Firuz Mammadov Gabibulla oglu,
"Theory of mechanisms and machines" Department, Ave. H.Javid 25, Azerbaijan
Azerbaijan Technical University, AZ 1073, Baku city,
E-mail: furuzhmemmedov@gmail.com

Abstract

This study focuses on one of the immensely important problems in the theory of mechanisms and machines - kinematic analysis of complex spatial mechanisms. The solution of this problem is related to the spatial transformations of coordinate systems. For this purpose we use quaternions, which are the most effective and versatile mathematical tools for spatial transformations. Using the principle of the transfer by Study-Kothelnikov the spatial transformation turning around point with respect to the quaternion expressions are compiled by biquaternions and these equations correspond to the transformation of coordinate system bypass circuit mechanisms. Using examined loop - closure equations for spatial 7R mechanism it were introduced the direct and inverse problem of 6R serial manipulator.

Keywords: quaternions, dual, numbers, mechanism, manipulator, transformations, analysis.

1. Introduction

The problem of analisis and sinthesis of spatial mechanisms by using quaternions algebra have been studied by several researchers. Mamedov[1] derived the formulas for relationship of quaternions with matrix mathematical apparatus for spatial transformation, and then using the principle of the transfer by Kothelnikov solved the problem of velocities and accelerations for different spatial mechanisms. F.M.Dimentberg [2] described the theory of screws, the algebra of dual numbers, performs a kinematic analysis of the spatial mechanisms on the basis of the screws algebra, describes the different groups of screws. In profound work V.N.Branets and I.P.Shmyglevskiy[3] describes in detail the shape of the quaternion algebra and their property as an operator of rotation spatial solid. The paper V.N.Branets and I.P.Shmyglevsky [3] describes in detail the shape of the algebra of quaternions and their property as an operator of the spatial turn of rigid body. It has been derived the equations of a rigid body kinematics in the quaternion presentation. The fundamental work of Kothelnikov [4] theory of screws are submitted in biquaternions presentation. It describes the essence of the important principle of mechanics - principle of "transference." The results are applied to some problems of mechanics and solid. Chevallier [5] discussed about dual quaternions in kinematics. Collins et.al. [6] studied the workspace and singular configurations of the 3- RPR parallel manipulator, where they also used quaternions. Larochelle [7] used planar quaternions to create synthesis equations for planar robots, and created a virtual reality environment that could promote the design of spherical manipulators. Martines et. al. [8] presented quaternion operators for describing the positions, angular velocity and acceletions for a spherical motion of a rigid body with respect to the reference frame. McCarthe et. al. [9] used Clifford algebra exponentials in the kinematics synthesis. Dai [10] reviewed theoretical development of rigid body displacement where he also mentions about quaternions and biquaternions. Roy et. al.[11] used quaternion interpolation in the finite element approximation of geometrically exact beam. Zupan [12] tried to implement rotational quaternions into the geometrically exact three dimensional beam theory and novel finite element formulation was proposed. Pennestri et.al. [13] used dual quaternions for the analysis of rigid body motions and tries to the kinematic modeling of the human joints. Cellodoni et.al. [14] investigated an elastic model of rod and carried out the group of rotations by using quaternions. Banavar et.al.[15] developed an analytical model of a novel spherical robot by using quaternion algebra. Liao et.al. [16] used biqutернions in the inverse kinematic analysis of general 6R manipulators.

2. A brief note about quaternions.

Quaternion is a complex number made up of the real unit *1* and three imaginary units $\bar{\boldsymbol{i}}_1, \bar{\boldsymbol{i}}_2, \bar{\boldsymbol{i}}_3$ with real elements:

$$\boldsymbol{\lambda} = 1\lambda_o + \lambda_1\bar{\boldsymbol{i}}_1 + \lambda_2\bar{\boldsymbol{i}}_2 + \lambda_3\bar{\boldsymbol{i}}_3 \tag{1}$$

Terms of multiplying the following units:

$$1\circ\bar{\boldsymbol{i}}_1 = \bar{\boldsymbol{i}}_1\circ 1 = \bar{\boldsymbol{i}}_1,\ 1\circ\bar{\boldsymbol{i}}_2 = \bar{\boldsymbol{i}}_2\circ 1 = \bar{\boldsymbol{i}}_2,\ 1\circ\bar{\boldsymbol{i}}_3 = \bar{\boldsymbol{i}}_3\circ 1 = \bar{\boldsymbol{i}}_3,$$
$$\bar{\boldsymbol{i}}_1\circ\bar{\boldsymbol{i}}_1 = -1,\ \bar{\boldsymbol{i}}_2\circ\bar{\boldsymbol{i}}_2 = -1,\ \bar{\boldsymbol{i}}_3\circ\bar{\boldsymbol{i}}_3 = -1,$$
$$\bar{\boldsymbol{i}}_1\circ\bar{\boldsymbol{i}}_2 = -\bar{\boldsymbol{i}}_2\circ\bar{\boldsymbol{i}}_1 = \bar{\boldsymbol{i}}_3,\ \bar{\boldsymbol{i}}_3\circ\bar{\boldsymbol{i}}_1 = -\bar{\boldsymbol{i}}_1\circ\bar{\boldsymbol{i}}_3 = \bar{\boldsymbol{i}}_2,$$
$$\bar{\boldsymbol{i}}_2\circ\bar{\boldsymbol{i}}_3 = -\bar{\boldsymbol{i}}_3\circ\bar{\boldsymbol{i}}_2 = \bar{\boldsymbol{i}}_1,\ 1\circ 1 = 1,$$

Rules multiplying the imaginary units stored using Fig.1 : the multiplication of two unit located on the clockwise, obtained the third unit with the sign "+", while in the reverse direction unit is obtained with the sign "-".

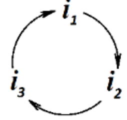

Figure 1. Rules multiplying the imaginary units

These rules indicate that the multiplication by *1* does not change the quaternion, so in the future in terms of the quaternion first term λ_o will be designated without unity.

Units $\bar{\boldsymbol{i}}_1, \bar{\boldsymbol{i}}_2, \bar{\boldsymbol{i}}_3$ can be identified by the three-dimensional vector space and consider the coefficients of these units as a component of the vector. Accordingly, the quaternion can be represented as the sum of the scalar and vector parts:

$$\boldsymbol{\lambda} = sqal\, \boldsymbol{\lambda} + vect\, \boldsymbol{\lambda}$$

The multiplication of quaternions has associative and distributive properties with respect to addition:

$$(\boldsymbol{\lambda_1\lambda_2})\boldsymbol{\lambda_3} = \boldsymbol{\lambda_1}(\boldsymbol{\lambda_2\lambda_3}),\ \boldsymbol{\lambda_1}(\boldsymbol{\lambda_2} + \boldsymbol{\lambda_3}) = \boldsymbol{\lambda_1\lambda_2} + \boldsymbol{\lambda_1\lambda_3},,$$

but multiplication of quaternions is not commutative. Indeed, by doing quaternion multiplication of two quaternions $\boldsymbol{\lambda}$ and $\boldsymbol{\mu}$ we obtain:

$$\boldsymbol{\lambda} \circ \boldsymbol{\mu} = \lambda_0\mu_0 - \lambda_1\mu_1 - \lambda_2\mu_2 - \lambda_3\mu_3 + \\ +\lambda_o\left(\mu_1\bar{\boldsymbol{i}}_1 + \mu_2\bar{\boldsymbol{i}}_2 + \mu_3\bar{\boldsymbol{i}}_3\right) + \\ +\mu_0\left(\lambda_1\bar{\boldsymbol{i}}_1 + \lambda_2\bar{\boldsymbol{i}}_2 + \lambda_3\bar{\boldsymbol{i}}_3\right) + \begin{vmatrix} \bar{\boldsymbol{i}}_1 & \bar{\boldsymbol{i}}_2 & \bar{\boldsymbol{i}}_3 \\ \lambda_1 & \lambda_2 & \lambda_3 \\ \mu_1 & \mu_2 & \mu_3 \end{vmatrix} \quad (2)$$

From this expression it is clear that $\boldsymbol{\lambda} \circ \boldsymbol{\mu} = \boldsymbol{\mu} \circ \boldsymbol{\lambda}$ only when disappear determinants. This is possible either when $\lambda_1 = \lambda_2 = \lambda_3 = 0$, or $\mu_1 = \mu_2 = \mu_3 = 0$, that is, when one of the factors is a scalar, or when $\boldsymbol{\lambda} = a\,\boldsymbol{\mu}$ (*a* real number). From the last expression as well we conclude that quaternion multiplication of two vectors containing the scalar and vector product of these vectors. Indeed, if in Eq.(2) to take
$\lambda_o = \mu_0 = 0$**,** we get:

$$\boldsymbol{\lambda} \circ \boldsymbol{\mu} = -\lambda_1\mu_1 - \lambda_2\mu_2 - \lambda_3\mu_3 + \begin{vmatrix} \bar{\boldsymbol{i}}_1 & \bar{\boldsymbol{i}}_2 & \bar{\boldsymbol{i}}_3 \\ \lambda_1 & \lambda_2 & \lambda_3 \\ \mu_1 & \mu_2 & \mu_3 \end{vmatrix}$$

The norm of a quaternion is the product $\boldsymbol{\lambda}$ on conjugate quaternion $\tilde{\boldsymbol{\lambda}}(\lambda_o - \lambda_1\bar{\boldsymbol{i}}_1 - \lambda_2\bar{\boldsymbol{i}}_2 - \lambda_3\bar{\boldsymbol{i}}_3)$**:**

$$\boldsymbol{\lambda} \circ \tilde{\boldsymbol{\lambda}} = \tilde{\boldsymbol{\lambda}} \circ \boldsymbol{\lambda} = \lambda_o^{\,2} + \lambda_1^{\,2} + \lambda_2^{\,2} + \lambda_3^{\,2}$$

This expression is obtained based on the expression (2). The norm of a quaternion is denoted by $|\boldsymbol{\lambda}|$ or λ**.** If $|\boldsymbol{\lambda}| = 1$**,** called the unity quaternion.

Any quaternion (1) may be represented by a trigonometric form:

$$\boldsymbol{\lambda} = \lambda(cos\varphi + \boldsymbol{e}\, sin\varphi)$$

where λ norm of a quaternion;

Accordingly, trigonometric unit quaternion expression will be the following:

$$\boldsymbol{\lambda} = cos\varphi + \boldsymbol{e}\, sin\varphi$$

***e* -** is unit vector of the vector part of the quaternion $\boldsymbol{\lambda}$**:**

$$\boldsymbol{e} = \frac{vect\,\lambda}{\sqrt{\lambda_1^{\,2}+\lambda_2^{\,2}+\lambda_3^{\,2}}} = \frac{\lambda_1\bar{i}_1+\lambda_2\bar{i}_2+\lambda_3\bar{i}_3}{\sqrt{\lambda_1^{\,2}+\lambda_2^{\,2}+\lambda_3^{\,2}}}, \quad (3)$$

$$cos\varphi = \frac{\lambda_o}{\lambda_o^{\,2}+\lambda_1^{\,2}+\lambda_2^{\,2}+\lambda_3^{\,2}}\ ;\ \sin\varphi = \frac{\sqrt{\lambda_1^{\,2}+\lambda_2^{\,2}+\lambda_3^{\,2}}}{\lambda_o^{\,2}+\lambda_1^{\,2}+\lambda_2^{\,2}+\lambda_3^{\,2}}$$

Turning operation.

Quaternion algebra allows us to represent a spatial transformation in a simple form. Let λ and $\boldsymbol{r}$ are non-scalar quaternions, then the value

$$r' = \lambda \circ r \circ \tilde{\lambda} \quad (4)$$

is also a quaternion scalar norm and part of which is equal to the norm and the scalar part of the quaternion $\boldsymbol{r}$ **.** Vector part $vect\ \boldsymbol{r'}$ obtained by rotating $vect\ \boldsymbol{r}$ around the cone axis by double angle $2\,\varphi$ **.** Operation (4) changes only the vector part of the quaternion, so that operation can be regarded as the transformation operation r of the vector into the vector $\boldsymbol{r'}$**.** Because the quaternion norm $\boldsymbol{r}$ does not change transformation (4), the module of the vector part $\boldsymbol{r}$ as remains unchanged. This implies that transformation (4) is orthogonal.

After completing quaternion multiplication (4) and equating the coefficients of the four units, we obtain the transformation (4) in the coordinates(for unit quaternions):

$$r_1' = (\lambda_0^2 + \lambda_1^2 - \lambda_2^2 - \lambda_3^2)r_1 + 2(\lambda_1\lambda_2 - \lambda_0\lambda_3)r_2 + \\ +2(\lambda_1\lambda_3 + \lambda_0\lambda_2)r_3$$

$$r_2' = 2(\lambda_1\lambda_2 + \lambda_0\lambda_3)r_1 + (\lambda_0^2 + \lambda_2^2 - \lambda_1^2 - \lambda_2^2)r_2 + \\ +2(\lambda_2\lambda_3 - \lambda_0\lambda_1)r_3 \quad (5)$$

$$r_3' = 2(\lambda_1\lambda_3 - \lambda_0\lambda_2)r_1 + 2(\lambda_2\lambda_3 + \lambda_0\lambda_1)r_2 + \\ +(\lambda_0^2 + \lambda_3^2 - \lambda_1^2 - \lambda_2^2)r_3$$

For example, let the vector $\boldsymbol{r}$ subjected to a sequence of transformations and rotations are defined by the quaternions $\boldsymbol{\lambda_1}, \boldsymbol{\lambda_2}, \dots, \boldsymbol{\lambda_n}$**.** The resulting quaternion for rotation is determined by $\boldsymbol{\lambda}$**:**

$$\lambda = \lambda_n \circ \lambda_{n\text{-}1}, \dots, \circ \lambda_1, \quad (6)$$

where quaternions $\boldsymbol{\lambda_1}, \boldsymbol{\lambda_2}, \dots, \boldsymbol{\lambda_n}$ expressed in the original coordinate system. Of course, encreesing the number of successive transformations the expression (6) becomes laborious.

But if, quaternions are given as sequence of turns, using Rodrigues-Hamilton parameters, the resulting quaternion is determined by [3]:

$$\boldsymbol{\lambda} = \boldsymbol{\lambda_1} \circ \boldsymbol{\lambda_2} \circ, \dots, \circ \boldsymbol{\lambda_n}$$

The components of the quaternion in the basis, convertible by the same quaternion, is called Rodrigues-Hamilton parameters. This quaternion components is equal in both coordinate systems because that quaternion determine the transformation from one coordinate system to another.

Dual numbers.

The dual number is as follows:

$$A = a + \delta a^0$$

where *a* - the main, a^0- moment part of the dual umber, δ - operator Clifford has property $\delta^2 = 0$. Dual numbers are denoted by basic letters. Operations on dual numbers are made according to the formulas:

$$A \pm B = (a \pm b) + \delta(a^o \pm b^o);$$

$$\mathrm{A} \cdot \mathrm{B} = \mathrm{a} \cdot \mathrm{b} + \delta(\mathrm{a^o b} + \mathrm{a b^o});$$

$$\frac{A}{B}=\frac{a}{b}+\delta\frac{a^o b+ab^o}{b^2};\quad A^n=a^n+\delta n a^o a^{n-1};\ A^{\frac{1}{n}}=a^{\frac{1}{n}}+\delta\frac{a^o}{na^{\frac{n-1}{n}}}$$

The function of the dual number is as follows:

$$F(X)=f(x+\delta x^o)=f(x)+\delta x^o f'(x);$$
$$F(X,A_1,A_2,\dots,A_n)=F(x,a_1,a_2,\dots,a_n)+$$
$$+\delta\left(x^o\frac{dF}{dx}+a_1^o\frac{dF}{da_1}+a_2^o\frac{dF}{da_2}+\dots+a_n^o\frac{dF}{da_n}\right)$$

The trigonometric functions of the dual number $X=x+\delta x^o$ can be expressed as follows:

$\sin X=\sin x+\ \delta x^o\cos x;\ \ cosX=cosx+\delta x^o\,sinx;\ \ tgX=tgx+\ \delta x^o\ \frac{1}{cos^2x}$

Dual quaternions, the transfer principle.

If in the expression (1) real numbers $\lambda_o,\lambda_1,\lambda_2,\lambda_3$ replaced by dual, we obtain an expression of the dual quaternion:

$$\Lambda=\Lambda_o+\Lambda_1\bar{i}_1+\Lambda_2\bar{i}_2+\Lambda_3\bar{i}_3 \tag{7}$$

where $\Lambda_\kappa=\lambda_\kappa+\ \delta\lambda_\kappa^0$ *(k=0,1,2,3)* the components of the dual quaternion. Transform the expression (7):

$$\boldsymbol{\Lambda}=(\lambda_o+\delta\lambda_0^0)+(\lambda_1+\delta\lambda_1^0)\bar{\boldsymbol{i}}_1+(\lambda_2+\delta\lambda_2^0)\bar{\boldsymbol{i}}_2+$$
$$+(\lambda_3+\delta\lambda_3^0)\bar{\boldsymbol{i}}_3=\lambda_o+\lambda_1\bar{\boldsymbol{i}}_1+\lambda_2\bar{\boldsymbol{i}}_2+\lambda_3\bar{\boldsymbol{i}}_3+ \tag{8}$$
$$+\delta\left(\lambda_0^0+\lambda_1^0\bar{\boldsymbol{i}}_1+\lambda_2^0\bar{\boldsymbol{i}}_2+\lambda_3^0\bar{\boldsymbol{i}}_3\right)=\boldsymbol{\lambda}+\delta\boldsymbol{\lambda}^0$$

Equation (8) is an expression of biquaternion. It should be noted that the expression "biquaternion" and "dual quaternion" very relative, so they are equivalent and means the same operator for most common spatial transformation. Like quaternions the biquaternion (unity) can be reduced to trigonometric form:

$$\Lambda=\cos\Phi+E\sin\Phi$$

where $\boldsymbol{E}$ - the unit screw of the biquaternion; Φ - dual argument (dual angle) biquaternion.

Like the formulas (3):

$$\boldsymbol{E}=\frac{\mathrm{vect}\,\Lambda}{\sqrt{\Lambda_1{}^2+\Lambda_2{}^2+\Lambda_3{}^2}}=\frac{\Lambda_1\bar{i}_1+\Lambda_2\bar{i}_2+\Lambda_3\bar{i}_3}{\sqrt{\Lambda_1{}^2+\Lambda_2{}^2+\Lambda_3{}^2}}$$

$$\cos\Phi=\frac{\Lambda_o}{\Lambda_o{}^2+\Lambda_1{}^2+\Lambda_2{}^2+\Lambda_3{}^2};$$

$$\sin\Phi=\frac{\sqrt{\Lambda_1{}^2+\Lambda_2{}^2+\Lambda_3{}^2}}{\Lambda_o{}^2+\Lambda_1{}^2+\Lambda_2{}^2+\Lambda_3{}^2}.$$

In the fundamental paper [4] it is proved that all the formulas written for the quaternion are non-deployed biquaternion formulas. This principle is called the principle of "transference." For example, applying this principle to the rotation operation (4), we can write

$$R'=\Lambda\circ R\circ\tilde{\Lambda},$$

where screw R' is obtained by moving the screw $\boldsymbol{R}$ along the unit screw $\boldsymbol{E}$ by the double dual angle $\boldsymbol{2\Phi}$.

3. Creation of closed-loop equations of the 7R spatial mechanisms.

As is known, that the composition of close-loop equations of spatial mechanisms is a time-consuming task and the output equations of the relationship between the parameters of the mechanisms by performing multiplication in the close-loop equations is almost an impossible task for the complex spatial mechanisms with traditional spatial transformation operators, in particular using matrix form. As was shown in [1] the condition of closed form, single-loop spatial seven-bar mechanism (Figure 2) had been expressed by biquaternions product as follow:

$$\Lambda_1{\circ}A_1{\circ}\Lambda_2{\circ}A_2{\circ}\dots{\circ}\Lambda_7{\circ}A_7=1 \tag{9}$$

where $\Lambda_i=cos\,\Phi_k+\bar{\boldsymbol{i}}_3 sin\,\Phi_k\ (k=1,2,\dots,7)$ are biquaternions characterize movement in kinematic pairs, these biquaternions can be called as "variable",$\Phi_k=\varphi_k+\delta\varphi_k^0$ (see Figure 2);

$A_i=\cos B_k+\bar{i}_2\sin B_k(k=1,2,\dots,7)$ are biquaternions, characterizing link parametrers of mechanism, these biquaternions can also be called "permanent",

$B_k=\beta_k+\delta\beta_k^0$ (shown in Figure *2* for the 1st. link). In reference [1] it is shown that the equation (9) is the common for all single-loop arrangements (including the plane four-link mechanism).

Using biquaternions as operators in spatial transformation it is ability to simplify a drawing and the deployment of the loop-closure equations.

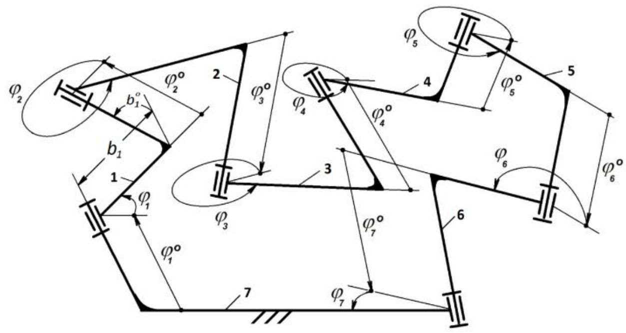

Fig. 2. The spatial 7R mechanism

Let us consider the possibility of simplifying the equations in more detail.So the equation (9) can be written as follows:

$$\left(cos\Phi_1+\bar{\boldsymbol{i}}_3 sin\,\Phi_1\right)\circ(cosB_1+\bar{\boldsymbol{i}}_2 sin\,B_1)\circ$$
$$\left(cos\Phi_2+\bar{\boldsymbol{i}}_3 sin\,\Phi_2\right)\circ(cosB_2+\bar{\boldsymbol{i}}_2 sin\,B_2)\circ\cdots$$
$$\cdots\circ\left(cos\Phi_7+\bar{\boldsymbol{i}}_3 sin\,\Phi_7\right)\circ(cosB_7+\bar{\boldsymbol{i}}_2 sin\,B_7)=1$$

Biquaternions multiplication in this equation it is possible to perform a variety of options. For example, if biquaternions distributed evenly on both sides of the equation, we get:

$$\Lambda_1{\circ}A_1{\circ}\Lambda_2{\circ}A_2{\circ}\Lambda_3{\circ}A_3{\circ}\Lambda_4=\tilde{A}_7{\circ}\tilde{\Lambda}_7{\circ}\tilde{A}_6{\circ}\tilde{\Lambda}_6{\circ}\tilde{A}_5{\circ}\tilde{\Lambda}_5{\circ}\tilde{A}_4 \tag{10}$$

where $\tilde{\Lambda}_7,\tilde{A}_7,\tilde{\Lambda}_6,\tilde{A}_6,\tilde{\Lambda}_5,\tilde{A}_5,\tilde{A}_4$ biquaternions conjugate.

Disclosed, for example the left side of the biquaternion product (10), we obtain the following expression:

$$a_1\,(C\beta_3 C\Phi_4 + i_3 C\beta_3 S\Phi_4 + i_2 S\beta_3 C\Phi_4 + i_1 S\beta_3 S\Phi_4) +$$
$$+a_2(-C\,\beta_3 C\Phi_4 - i_3 C\beta_3 S\Phi_4 - i_2 S\beta_3 C\Phi_4 - i_1 S\beta_3 S\Phi_4) +$$
$$+a_3(-C\,\beta_3 C\Phi_4 - \boldsymbol{i_3} C\,\beta_3 S\Phi_4 - \boldsymbol{i_2} S\,\beta_3 C\Phi_4 - \boldsymbol{i_1} S\,\beta_3 S\Phi_4) +$$
$$+a_4(-C\,\beta_3 C\Phi_4 - \boldsymbol{i_3} C\,\beta_3 S\Phi_4 - \boldsymbol{i_2} S\,\beta_3 C\Phi_4 - \boldsymbol{i_1} C\,\beta_3 S\Phi_4) +$$
$$+a_5(-\boldsymbol{i_1} C\,\beta_3 C\Phi_4 + \boldsymbol{i_2} C\,\beta_3 S\Phi_4 + \boldsymbol{i_3} S\,\beta_3 C\Phi_4 - S\,\beta_3 S\Phi_4) +$$
$$+a_6(\,i_1 C\,\beta_3 C\Phi_4 - i_2 C\,\beta_3 S\Phi_4 + i_3 S\,\beta_3 C\Phi_4 - S\,\beta_3 S\Phi_4) +$$
$$+a_7(-i_1 C\,\beta_3 C\Phi_4 + i_2 C\,\beta_3 S\Phi_4 - i_3 S\,\beta_3 C\Phi_4 + S\,\beta_3 S\Phi_4) +$$
$$+a_8(-\boldsymbol{i_1} C\,\beta_3 C\Phi_4 + \boldsymbol{i_2} C\,\beta_3 S\Phi_4 - \boldsymbol{i_3} S\,\beta_3 C\Phi_4 + S\,\beta_3 S\Phi_4) +$$
$$+a_9(\,\boldsymbol{i_2} C\,\beta_3 C\phi_4 + \boldsymbol{i_1} C\,\beta_3 S\phi_4 - S\,\beta_3 C\phi_4 - \boldsymbol{i_3} S\,\beta_3 S\phi_4) +$$
$$+a_{10}(\boldsymbol{i_2} C\,\beta_3 C\Phi_4 + \boldsymbol{i_1} C\,\beta_3 S\Phi_4 - S\,\beta_3 C\Phi_4 - \boldsymbol{i_3}\,S\,\beta_3 S\Phi_4) +$$
$$+a_{11}(-\boldsymbol{i_2} C\,\beta_3 C\Phi_4 - \boldsymbol{i_1} C\,\beta_3 S\Phi_4 + S\,\beta_3 C\Phi_4 + \boldsymbol{i_3} S\,\beta_3 S\Phi_4) +$$
$$+a_{12}(-\boldsymbol{i_2} C\,\beta_3 C\Phi_4 + \boldsymbol{i_1} C\,\beta_3 S\Phi_4 - S\,\beta_3 C\Phi_4 + \boldsymbol{i_3} S\,\beta_3 S\Phi_4) +$$
$$+a_{13}(i_3 C\,\beta_3 C\Phi_4 - C\,\beta_3 S\Phi - i_1 S\,\beta_3 C\Phi_4 + i_2 S\,\beta_3 S\Phi_4) +$$
$$+a_{14}(\boldsymbol{i_3} C\,\beta_3 C\Phi_4 - C\,\beta_3 S\Phi_4 - \boldsymbol{i_1} S\,\beta_3 C\Phi_4 + \boldsymbol{i_2} S\,\beta_3 S\Phi_4) +$$
$$+a_{15}(\boldsymbol{i_3} C\,\beta_3\, C\Phi_4 - C\,\beta_3 S\Phi_4 - \boldsymbol{i_1} S\,\beta_3 C\Phi_4 + \boldsymbol{i_2} S\,\beta_3 S\Phi_4) +$$
$$+a_{16}(-\boldsymbol{i_3} C\,\beta_3 C\Phi_4 + C\,\beta_3 S\Phi_4 - \boldsymbol{i_1} S\,\beta_3 C\Phi_4 - \boldsymbol{i_2} S\,\beta_3 S\Phi_4);$$

where:

$$a_1 = C\phi_1 C\beta_1 C\beta_2\, C(\Phi_2 + \Phi_3);$$
$$a_2 = C\phi_1 S\beta_1\, S\beta_2\, C(\Phi_2 - \Phi_3);$$
$$a_3 = S\phi_1 C\beta_1 C\beta_2\, S(\Phi_2 + \Phi_3);$$
$$a_4 = S\phi_1\, S\beta_1\, S\beta_2\, S(\Phi_2 - \Phi_3);$$
$$a_5 = C\phi_1 C\beta_1\, S\beta_2\, S(\Phi_2 - \Phi);$$
$$a_6 = C\phi_1 S\beta_1 C\beta_2\, S(\Phi_2 + \Phi);$$
$$a_7 = S\phi_1 C\beta_1\, S\beta_2\, C(\Phi_2 - \Phi);$$
$$a_8 = S\phi_1 S\beta_1\, C\beta_2\, C(\Phi_2 + \Phi_3);$$
$$a_9 = C\phi_1 C\beta_1\, S\,\beta_2\, C(\Phi_2 - \Phi_3);$$
$$a_{10} = C\phi_1\, S\,\beta_1 C\beta_2\, C(\Phi + \Phi_3);$$
$$a_{11} = S\phi_1\, C\,\beta_1\, S\beta_2\, S(\Phi_2 - \Phi);$$
$$a_{12} = S\phi_1\, S\,\beta_1 C\beta_2\, S(\Phi + \Phi_3);$$
$$a_{13} = C\phi_1 C\beta_1\, C\beta_2\, S(\Phi_2 + \Phi_3);$$
$$a_{14} = C\phi_1 S\beta_1\, S\beta_2\, S(\Phi_2 - \Phi_3);$$
$$a_{15} = S\phi_1 C\beta_1\, C\beta_2\, C(\Phi_2 + \Phi_3);$$
$$a_{16} = S\phi_1 S\beta_1\, S\beta_2\, C(\Phi - \Phi_3).$$

The trigonometric expressions *sıne* and *cosine* functions are represended by *S* and *C*,

After some transformations, and grouping the terms in *1*, $\boldsymbol{i_1}, \boldsymbol{i_2}, \boldsymbol{i_3}$, we will get:

$$C\phi_1 C\beta_1 C\beta_2 C\beta_3\, C(\Phi_2 + \Phi_3 + \Phi_4) -$$
$$-C\phi_1 C\beta_1 S\beta_2 S\beta_3\, C(\Phi_2 - \Phi_3 + \Phi_4) -$$
$$-C\phi_1 S\beta_1 S\beta_2 C\beta_3\, C(\phi_2 - \phi_3 - \phi_4) -$$
$$-C\phi_1 S\beta_1 C\beta_2 S\beta_3\, C(\phi_2 + \phi_3 - \phi_4) -$$
$$-S\phi_1 C\beta_1 C\beta_2 C\beta_3\, C(\phi_2 + \phi_3 + \phi_4) -$$
$$-S\phi_1 C\beta_1 S\beta_2 S\beta_3\, S(\phi_2 - \phi_3 + \phi_4) -$$
$$-S\phi_1 S\beta_1 S\beta_2 C\beta_3\, S(\phi_2 - \phi_3 - \phi_4) -$$
$$-S\phi_1 S\beta_1 C\beta_2 S\beta_3\, S(\phi_2 + \phi_3 - \phi_4) +$$
$$+\boldsymbol{i_1}[\,C\phi_1 C\beta_1 C\beta_2 S\beta_3\, C(\phi_2 + \phi_3 - \phi_4) -$$
$$-C\phi_1 C\beta_1 S\beta_2 C\beta_3\, S(\phi_2 - \phi_3 - \phi_4) -$$
$$-C\phi_1 S\beta_1 S\beta_2 S\beta_3\, S(\phi_2 - \phi_3 + \phi_4) -$$
$$-C\phi_1 S\beta_1 C\beta_2 C\beta_3\, S(\phi_2 + \phi_3 + \phi_4) -$$
$$-S\phi_1 C\beta_1 C\beta_2 C\beta_3\, C(\phi_2 + \phi_3 - \phi_4) -$$
$$-S\phi_1 C\beta_1 S\beta_2 C\beta_3\, C(\phi_2 - \phi_3 - \phi_4) -$$
$$-S\phi_1 S\beta_1 S\beta_2 S\beta_3\, C(\phi_2 - \phi_3 + \phi_4) -$$
$$-C\phi_1 S\beta_1 C\beta_2 C\beta_3\, C(\phi_2 + \phi_3 + \phi_4)] +$$
$$+\boldsymbol{i_2}[\,C\phi_1 C\beta_1 C\beta_2 S\beta_3\, C(\phi_2 + \phi_3 - \phi_4) - \qquad (11)$$
$$-C\phi_1 C\beta_1 S\beta_2 C\beta_3\, C(\phi_2 - \phi_3 - \phi_4) -$$
$$-C\phi_1 S\beta_1 S\beta_2 S\beta_3\, C(\phi_2 - \phi_3 + \phi_4) -$$
$$-C\phi_1 S\beta_1 C\beta_2 C\beta_3\, C(\phi_2 + \phi_3 + \phi_4) -$$
$$-S\phi_1 C\beta_1 C\beta_2 S\beta_3\, S(\phi_2 + \phi_3 - \phi_4) -$$
$$-S\phi_1 C\beta_1 S\beta_2 C\beta_3\, S(\phi_2 - \phi_3 - \phi_4) -$$
$$-S\phi_1\, S\beta_1 S\beta_2 S\beta_3\, S(\phi_2 - \phi_3 + \phi_4)$$
$$-S\phi_1 S\beta_1 C\beta_2 C\beta_3\, S(\phi_2 + \phi_3 + \phi_4)] +$$
$$+\boldsymbol{i_3}\,[\,C\phi_1 C\beta_1 C\beta_2 C\beta_3\, S(\phi_2 + \phi_3 + \phi_4) -$$
$$-C\phi_1 C\beta_1 S\beta_2 S\beta_3\, S(\phi_2 - \phi_3 + \phi_4) +$$
$$+C\phi_1 S\beta_1 S\beta_2 C\beta_3\, S(\phi_2 - \phi_3 - \phi_4) -$$
$$-C\phi_1 S\beta_1 C\beta_2 S\beta_3\, S(\phi_2 + \phi_3 - \phi_4) -$$
$$-S\phi_1 C\beta_1 C\beta_2 C\beta_3\, C(\phi_2 + \phi_3 + \phi_4) -$$
$$-S\phi_1 C\beta_1 S\beta_2 S\beta_3\, C(\phi_2 - \phi_3 + \phi_4) -$$
$$-S\phi_1 S\beta_1\, S\beta_2 C\beta_3\, C(\phi_2 - \phi_3 - \phi_4) -$$
$$-S\phi_1 S\beta_1 C\beta_2 S\beta_3\, cos(\phi_2 + \phi_3 - \phi_4)]$$

After deploying the right side of biquaternions expression (10) we obtain similar expression, which will be featured unknown angles Φ_5, Φ_6, Φ_7. Equating the terms in $\boldsymbol{i_1}, \boldsymbol{i_2}, \boldsymbol{i_3}, \boldsymbol{1}$ we get four dual equation. There is a dual dependence on the norm of biquaternion between these equations. Therefore, from the four dual equations only three are independent. Thus, taking any three equations of four and dividing them into the main and torque parts, we get six real equations for determining angles, $\varphi_2, \varphi_3, \varphi_4, \varphi_5, \varphi_6, \varphi_7$, which are the main parts of the dual angles $\Phi_2, \Phi_3, \Phi_4, \Phi_5, \Phi_6, \Phi_7$.

As it can be seen, that to make use of quaternions significantly simplify and get the ultimate expression for the loop-closure conditions of the spatial seven link mechanism, which is known as most complex single-loop mechanisms. These expressions are universal for all single-loop mechanisms.

But the most important advantage of expression (11) is that they are linear with respect to the sines and cosines angles $\Psi_1, \Psi_2, \dots, \Psi_8$:

$$\Psi_1 = \Phi_2 + \Phi_3 + \Phi_4; \quad \Psi_5 = \Phi_5 + \Phi_6 + \Phi_7$$
$$\Psi_2 = \Phi_2 - \Phi_3 + \Phi_4; \quad \Psi_6 = \Phi_5 - \Phi_6 + \Phi_7 \qquad (12)$$
$$\Psi_3 = \Phi_2 + \Phi_3 - \Phi_4; \quad \Psi_7 = \Phi_5 + \Phi_6 - \Phi_7$$
$$\Psi_4 = \Phi_2 - \Phi_3 - \Phi_4; \quad \Psi_8 = \Phi_5 - \Phi_6 - \Phi_7$$

There are two dependencies between the unknown angles $\Psi_1, \Psi_2, \dots, \Psi_8$:

$$\Psi_1 + \Psi_4 = \Psi_2 + \Psi_3; \quad \Psi_5 + \Psi_8 = \Psi_6 + \Psi_7 \qquad (13)$$

As a result, the mathematical model of single-loop spatial seven-bar mechanism is described by relatively simple equations, and therefore their numerical solution is not difficult.

If the terms of biquaternions leave to one side in equation (9) and perform the biquaternions multiplication, and then after equating the coefficients of the unit vectors ***1***, ***i₁***, ***i₂***, ***i₃***, we will get as unknowns the *sines* and *cosines* of the following angles:

$$\Psi_k = \Phi_2 \pm \Phi_3 \pm \Phi_4 \pm \Phi_5 \pm \Phi_6 \pm \Phi_7,$$
$$k = 1,2,\dots,32 \quad (14)$$

Between angles (14) there are 26 corners dependencies such expressions (13). The resulting equations are also linear relatively unknown parameters, but in this case the number is much higher. Therefore, in the preparation of the closure equations the biquaternions advisable to distribute on both sides of the loop-closure equation.

Of course, the above very effectively and simply necessary in the preparation of loop-closure equations for platform type multi-loop mechanisms.

4. Kinematic analysis of serial 6R manipulator.

Consider the direct problem of 6R open spatial kinematic chain(Figure 3). In the direct problem it is given the set movements of the kinematic pairs. The problem is to determine the position and orientation of the gripper. Biquaternions defining the position and orientation of the rigid body is denoted by **X**:

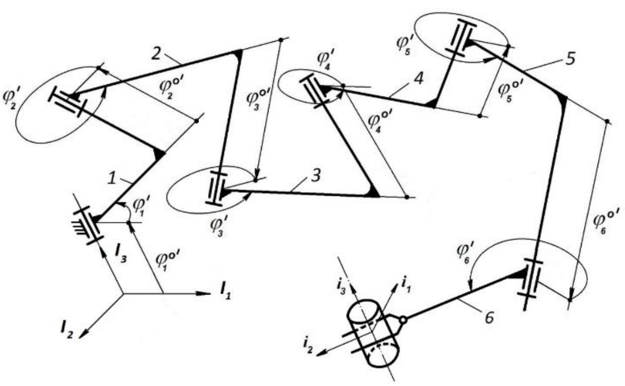

Fig. 3. Spatial 6R manipulator

$$\mathrm{X} = \mathrm{X}_o + \mathrm{X}_1\bar{\mathrm{i}}_1 + \mathrm{X}_2\bar{\mathrm{i}}_2 + \mathrm{X}_3\bar{\mathrm{i}}_3, \quad (15)$$

Equation (15) can be expressed as the product of a quaternion:

$$\mathrm{X} = \Lambda_1 \circ \mathrm{A}_1 \circ \Lambda_2 \circ \mathrm{A}_2 \circ, \dots, \circ \Lambda_6 \circ \mathrm{A}_6 \ , \quad (16)$$

or

$$\boldsymbol{X} = \left(cos\Phi_1 + \bar{\boldsymbol{\imath}}_3 sin\,\Phi_1\right) \circ \left(cosB_1 + \bar{\boldsymbol{\imath}}_2 \sin B_1\right) \circ$$
$$\circ\left(cos\Phi_2 + \bar{\boldsymbol{\imath}}_3 sin\,\Phi_2\right) \circ \left(cosB_2 + \bar{\boldsymbol{\imath}}_2 sin\,B_2\right) \circ$$
$$\circ\left(cos\Phi_6 + \bar{\boldsymbol{\imath}}_3 sin\,\Phi_6\right) \circ \left(cosB_6 + \bar{\boldsymbol{\imath}}_2 sin\,B_6\right)$$

where $\boldsymbol{\Phi_k}$ dual movement parameters in kinematic pairs, $\boldsymbol{B_k}$ dual number of links parameters $(k = 1,2,\dots,6)$, which are discussed above. Thus, the direct problem positions of the manipulator is to implement quaternion multiplication, that can be simplified as discussed above and are described by formulas (11).

Consider the inverse problem of *6R* spatial serial manipulator. This problem can be formulated as follows. The position and orientation of the solid body(gripper) are determined by biquaternions as follow

$$\boldsymbol{X} = X_o + X_1\bar{\boldsymbol{\imath}}_1 + X_2\bar{\boldsymbol{\imath}}_2 + X_3\bar{\boldsymbol{\imath}}_3 =$$
$$= (x_o + \delta x_0^0) + \bar{\boldsymbol{\imath}}_1(x_1 + \delta x_1^0) + \bar{\boldsymbol{\imath}}_2(x_2 + \delta x_2^0) + \bar{\boldsymbol{\imath}}_3(x_3 + \delta x_3^0)$$

which determines the location of the moving coordinate system $(\bar{\boldsymbol{\imath}}_1,\ \bar{\boldsymbol{\imath}}_2,\ \bar{\boldsymbol{\imath}}_3)$ relative to the reference coordinate system $(\bar{\boldsymbol{I}}_1, \bar{\boldsymbol{I}}_2, \bar{\boldsymbol{I}}_3)$. Required to determine the movement in kinematic pairs, providing a predetermined position of the solid. We transform the expression (16) to the following form:

$$\boldsymbol{\Lambda_1 \circ A_1 \circ \Lambda_2 \circ A_2 \circ \Lambda_3 \circ A_3 = X \circ \widetilde{A}_6 \circ \widetilde{\Lambda}_6 \circ \widetilde{A}_5 \circ \widetilde{\Lambda}_5 \circ \widetilde{A}_4 \circ \widetilde{\Lambda}_4} \quad (17)$$

We use equation (17) in the following notation:

$$\Lambda_1 \circ \mathrm{A}_1 \circ \Lambda_2 \circ \mathrm{A}_2 \circ \Lambda_3 \circ \mathrm{A}_3 = \mathrm{M} \quad (18)$$

$$\widetilde{\mathrm{A}}_6 \circ \widetilde{\Lambda}_6 \circ \widetilde{\mathrm{A}}_5 \circ \widetilde{\Lambda}_5 \circ \widetilde{\mathrm{A}}_4 \circ \widetilde{\Lambda}_4 = \mathrm{N} \quad (19)$$

where

$$\mathrm{M} = \mathrm{M}_o + \mathrm{M}_1\bar{\mathrm{i}}_1 + \mathrm{M}_2\bar{\mathrm{i}}_2 + \mathrm{M}_3\bar{\mathrm{i}}_3$$
$$\mathrm{N} = \mathrm{N} + \mathrm{N}_1\bar{\mathrm{i}}_1 + \mathrm{N}_2\bar{\mathrm{i}}_2 + \mathrm{N}_3\bar{\mathrm{i}}_3$$

After completing quaternion multiplication (18), we obtain components of biquaternion M:

$$M_o = cosB_1 cosB_2 cosB_3\, cos(\Phi_1 + \Phi_2 + \Phi_3) -$$
$$- sinB_1 sinB_2 cosB_3\, cos(\Phi_1 - \Phi_2 + \Phi_3) -$$
$$- cosB_1 sinB_2 sinB_3\, cos(\Phi_1 + \Phi_2 - \Phi_3) -$$
$$- sinB_1 cosB_2 sinB_3\, cos(\Phi_1 - \Phi_2 - \Phi_3)$$
$$M_1 = -cosB_1 sinB_2 cosB_3\, sin(\Phi_1 + \Phi_2 - \Phi_3) -$$
$$- sinB_1 cosB_2 cosB_3\, sin(\Phi_1 - \Phi_2 - \Phi_3) -$$
$$- cosB_1 cosB_2 sinB_3\, sin(\Phi_1 + \Phi_2 + \Phi_3) +$$
$$+ sinB_1 sinB_2 sinB_3\, sin(\Phi_1 - \Phi_2 + \Phi_3)$$
$$M_2 = cosB_1 cosB_2 sinB_3\, cos(\Phi_1 + \Phi_2 + \Phi_3) -$$
$$- sinB_1 sinB_2 sinB_3\, cos(\Phi_1 - \Phi_2 + \Phi_3) +$$
$$+ cosB_1 sinB_2 cosB_3\, cos(\Phi_1 + \Phi_2 - \Phi_3) +$$
$$+ sinB_1 cosB_2 cosB_3\, cos(\Phi_1 - \Phi_2 - \Phi_3)$$
$$M_3 = -cosB_1 sinB_2 sinB_3\, sin(\Phi_1 + \Phi_2 - \Phi_3) -$$
$$- sinB_1 cosB_2 sinB_3\, sin(\Phi_1 - \Phi_2 - \Phi_3) +$$
$$+ cosB_1 cosB_2 cosB_3\, sin(\Phi_1 + \Phi_2 + \Phi_3) -$$
$$- sinB_1 sinB_2 cosB_3\, sin(\Phi_1 - \Phi_2 + \Phi_3).$$

After completing quaternion multiplication (19), we obtain components of biquaternion *N*:

$$N_o = cosB_6 cosB_5 cosB_4\, cos(\Phi_4 + \Phi_5 + \Phi_6) -$$
$$- sinB_1 sinB_2 cosB_3\, cos(\Phi_4 - \Phi_5 + \Phi_6) -$$
$$- cosB_6 sinB_5 sinB_4\, cos(\Phi_4 + \Phi_5 - \Phi_6) -$$
$$- sinB_6 cosB_5 sinB_4\, cos(\Phi_4 - \Phi_5 - \Phi_6)$$

$$N_1 = \ cosB_6 sinB_5 cosB_4 \, sin(\Phi_4 - \Phi_5 + \Phi_6) - \\ -sinB_6 cosB_5 cosB_4 \, sin(\Phi_4 + \Phi_5 + \Phi_6) + \\ +cosB_6 cosB_5 sinB_4 \, sin(\Phi_4 - \Phi_5 - \Phi_6) + \\ +sinB_6 sinB_5 sinB_4 \, sin(\Phi_4 + \Phi_5 - \Phi_6)$$

$$N_2 = \ cosB_6 cosB_5 sinB_4 \, cos(\Phi_4 - \Phi_5 + \Phi_6) - \\ -sinB_6 sinB_5 sinB_4 \, cos(\Phi_4 + \Phi_5 - \Phi_6) + \\ +cosB_6 sinB_5 cosB_4 \, cos(\Phi_4 + \Phi_5 - \Phi_6) + \\ +sinB_6 cosB_5 cosB_4 \, cos(\Phi_4 + \Phi_5 + \Phi_6)$$

$$N_3 = -cosB_6 sinB_5 sinB_4 \, sin(\Phi_4 + \Phi_5 - \Phi_6) + \\ +sinB_6 cosB_5 sinB_4 \, sin(\Phi_4 - \Phi_5 - \Phi_6) + \\ +cosB_6 cosB_5 cosB_4 \, sin(\Phi_4 + \Phi_5 + \Phi_6) + \\ +sinB_6 sinB_5 cosB_4 \, sin(\Phi_4 - \Phi_5 + \Phi_6)$$

We write the expression (17) with (18) and (19):

$$\mathrm{M} = \mathrm{X} \circ \mathrm{N}$$

After completing quaternion multiplication and equating the terms in $\boldsymbol{1}, \boldsymbol{i_1}, \boldsymbol{i_2}, \boldsymbol{i_3}$ get four dual expression:

$$M_o = X_o N_o - X_1 N_1 - X_2 N_2 - X_3 N_3 \\ M_1 = X_o N_o - X_1 N_1 - X_2 N_2 - X_3 N_3 \\ M_2 = X_o N_o - X_1 N_1 - X_2 N_2 - X_3 N_3 \\ M_3 = X_o N_o - X_1 N_1 - X_2 N_2 - X_3 N_3 \tag{20}$$

Between equations (20), there is a dual relationship to the norm biquaternion. Discarding any of them get three independent dual equations that are equivalent to six real equations. From these six equations are determined unknown corners $\varphi_1, \varphi_2, \varphi_3, \varphi_4, \varphi_5, \varphi_6,$, that is a major part of dual angles $\Phi_1, \Phi_2, \Phi_3, \Phi_4, \Phi_5, \Phi_6$..

Conclusions

Preparation a new method for closed-loop equations of mechanisms that particularly effective and a must in the preparation of these equations for complex multi-loop spatial mechanisms. When using offered method greatly simplified outline of the closed-loop equations of spatial mechanisms, whereby it becomes possible to express these equations in explicitly form.

Reference

[1]. Мамедов Ф.Г.(1994).«Бикватернионная алгебра в задачах анализа и синтеза механиз-мов.Диссертационная работа на соискание ученой степени кандидата технических наук.
[2]. Ф.М.Диментберг. (1978). Теория винтов и ее приложения. М., Наука.
[3]. В.Н.Бранец, И.П.Шмыглевский. (1973). Применение кватернионов в задачах ориентации твердого тела. М., Наука.
[4]. А.П. Котельников. (1895) Винтовое счисление и некоторые приложения к геометрии и механике. Казань.
[5]. Chevallier, D.P. (1991). Lie algebras, modules, dual quaternions and algebraic methods in kinematics. Mech. Mach. Theory, 26(6), 613-627.
[6]. Collins, C. L., McCarthy, J. M. (1998). The quartic singularity surfaces of planar platforms in the Clifford algebra of the projective plane. Mech. Mach. Theory, 33(7), 931-944.
[7]. Larochelle, P., (2000) Approximate motion synthesis via parametric constrain manifold fitting. Advances in Robot Kinematics, Kluwer Acad. Publ., Dordrecht.
[8]. Martines, J. M., Gallardo-Alvarado, J. (2000). A simple method for the determination of angular velocity and acceleration of a spherical motion through quaternion. Nederlands, Meccanica, 35, 111-118.
[9]. McCarthy, J. M., Perez-Gracia, A. (2006). Kinematic synthesis of spatial serial chains using Clifford algebra exponential. Proc. ImechE,220, Part C: J. Mechanical Engineering Science, 953-968.
[10]. Dai, S. J. (2006). An historical review of the theoretical development of rigid body displacement from Rodrigues parameters to the finite twist. Mech. Mach. Theory, 41, 41-42.
[11]. Roy, D., Ghosh, S. (2008). Consistent quaternion interpolation for objective finite element approximation of geometrically exact beam.Comput. Methods Appl. Mech. Engrg, 198, 555-571.
[12]. Zupan, D., Saje, M., Zupan, E.(2009). The quaternion-based three-dimensional beam theory. Computer Methods in Applied Mechanics and Engineering, 198(49-52),3944-3956.
[13]. Pennestri., Valentini, P. P. (2009). Dual quaternions as a tool for rigid body motion analysis: a tutorial with an application to biomechanics. Multibody Dinamics 2009, Eccomas Thematic Conference K. Arczewski, J. Frajaczek, M. Wojtyra (eds.) Warsaw, Poland, 1-17.
[14]. Cellodoni, E., Saftsrömç N. (2010). A Hamiltonian and multi-symplectic formulation of a rod model using quaternions. Computer Methods in Applied Mechanics and Engineering, doi: 10.1016/ j.cma. 2010.04.017.
[15]. Banavar, N. R. et. al. (2010) Design and analisis of a spherical mobile robot. Mech. Mach. Theory, 45, 130-136.
[16]. Liao , Q. (2010). Inverse kinematic analysis of the general 6R serial manipulator based on double quaternions. Mech. Mach. Theory, 45, 193-199.

Proceedings of the International Symposium of Mechanism and Machine Science, 2017
AzC IFToMM – Azerbaijan Technical University
11-14 September 2017, Baku, Azerbaijan

Sliding Mode Based Self-Tuning PID Controller for Second Order Systems

Alper BAYRAK

Department of Electrical & Electronics Engineering
Abant Izzet Baysal University
Golkoy, Bolu 14280 TURKEY
E-mail: alperbayrak@ibu.edu.tr

Abstract
In this paper, a sliding mode based self-tuning PID controller is proposed for second order systems. While developing the controller, it is assumed that the system model has a part which contains nonlinear terms similar to PID structure. The controller and update rules for PID parameters are obtained from Lyapunov stability analysis. Numerical simulations are conducted on a Twin-Rotor Multi-Input Multi-Output System (TRMS) model to show the performance of the proposed controller.
Keywords: Sliding Mode Controller, Self-Tuning PID.

1. Introduction

PID control is the most preferred control technique in industrial applications due to its simple structure and convenience in implementation [1]. However, the effectiveness of the PID controller is based on the accurate selection of its parameters. Despite the good performance results in linear systems, the selection of the parameters might be very difficult and time wasting with the rise of nonlinearities of the system. To deal with this problem many approaches of self-tuning PID controllers have been presented till today. These approaches can be divided into two main categories: i) model based approaches and ii) rule-based approaches. In model based approaches, the tuning mechanism is based on the knowledge of the system model [2]. In rule based approaches, the tuning is based on some optimization or estimation rules without model knowledge, which basically mimics an experienced operator's behavior [2]. A good survey can be found in [2] on this topic.

In the literature, many studies can be found on self-tuning PID controller and its applications. In [3], An *et. al.* presented a self-tuning method for PID controllers based on the theory of adaptive interaction for the quadrotor system. In [4], a self-tuning PID control scheme based on support vector machine (SVM) and particle swarm optimization (PSO) were presented. Jiang and Jiang proposed a fuzzy based self-tuning PID controller for temperature control [5]. Zheng *et. al.* used fuzzy module to tune PID controller parameters according to the error and change in error [6]. In [7] and [8], genetic algorithm was utilized to tune the PID parameters. Na presented a study on water level control of a nuclear steam generator with PID controller of which parameters were tuned by model predictive control (MPC) [9]. In [1], least squares support vector machine identifier was utilized to tune parameters of PID controller. Fan *et. al.* used neural network to tune PID controller for position tracking of a pneumatic artificial muscle [10]. Gundogdu and Komurgaz presented a self-tuning algorithm for PID controller based on adaptive interaction approach [11]. In [12], Howell and Best used continuous action reinforcement learning automata (CARLA) method to tune the PID controller parameters while controlling engine idle-speed. In [13], Shih and Tseng designed a self-tuning PID controller by using integral of time-weighted absolute error (ITAE) optimal control principle and the pole-placement approach to control position of a servo-cylinder. Dong and Mo presented model reference adaptive PID controller for motor control system with backlash [14]. In [15], Chamsai *et. al.* presented an adaptive PID controller combined with sliding mode controller for uncertain nonlinear systems. Chang and Yan proposed an adaptive PID controller based on sliding mode controller for uncertain chaotic systems [16]. Kuo *et. al.* presented an adaptive sliding mode controller with PID tuning method for a class of uncertain systems [17].

In this paper, a sliding mode based self-tuning PID controller is proposed for uncertain second order systems. Different from the literature, it is assumed that the model contain nonlinear terms similar to PID structure. The controller and update rules for PID parameters are obtained from Lyapunov stability analysis. Numerical simulations are conducted on a Twin-Rotor Multi-Input Multi-Output System (TRMS) model to test the performance of controller and parameter update rule.

The rest of the paper is organized as follows; the system model is presented in Section 2. Control and parameter update rule design are presented in Section 3. Numerical simulation results are given in Section 4.

Finally concluding remarks are presented in Section 5.

2. System Model

The following second order system is considered in this paper,

$$\dot{x}_1(t) = x_2 \quad (1)$$
$$\dot{x}_2(t) = f(\mathrm{x}) + u(t) \quad (2)$$

where $x(t) = [x_1(t), x_2(t)]^T$ is state vector, $u(t) \in R$ is control signal. The function $f(\cdot):R^2 \rightarrow R$ is assumed in the form of

$$f(x) = g(x) + k_p x_1(t) + k_d x_2(t) + k_i \int x_1(t)\,. \quad (3)$$

where $g(\cdot):R^2 \rightarrow R$ is unknown function, k_p, k_d and k_i are unknown system parameters.

Assumption 1: It is assumed that the function $g(\cdot)$ is bounded as

$$|g(x)| \le \rho \quad (4)$$

where ρ is known.

Assumption 2: It is assumed that the system parameters, k_p, k_d and k_i are in known bounded regions.

Assumption 3: It is assumed that x(t) is available and continuous.

3. Control and Parameter Update Rule Design

The objective of the controller is to utilize that $x_1(t)$ track a desired trajectory while updating PID parameters. To achieve this objective, the error system is designed as follows,

$$\tilde{x}_1(t) = x_{d1} - x_1 \quad (5)$$
$$\tilde{x}_2(t) = x_{d2} - x_2 \quad (6)$$

where x_{d1} and x_{d2} are desired trajectories. To construct sliding mode controller, the filtered error signal is designed as

$$s = \tilde{x}_2 + 2\lambda\tilde{x}_1 + \lambda^2 \int \tilde{x}_1\,. \quad (7)$$

The derivative of (7), which will be utilized later, is

$$\begin{aligned}\dot{s} &= \dot{\tilde{x}}_2 + 2\lambda\dot{\tilde{x}}_1 + \lambda^2\tilde{x}_1 \\ &= \dot{x}_{d2} - g - k_p x_1 - k_d \dot{x}_1 - k_i \int x_1 - u \\ &\quad + 2\lambda\dot{x}_{d1} - 1\lambda^2\dot{x}_1 + \lambda^2\tilde{x}_1\,. \end{aligned} \quad (8)$$

The control input is designed as

$$u = u_{PID} + u_R \quad (9)$$

where u_R is sliding part of the controller and

$$u_{PID} = \hat{k}_p\tilde{x}_1 + \hat{k}_d\dot{\tilde{x}}_1 + \hat{k}_i\int\tilde{x}_1 \quad (10)$$

where $\hat{k}_p$, $\hat{k}_d$ and $\hat{k}_i$ are estimates of k_p, k_d ve k_i, respectively.

By substituting the (9) and (10) in (8), it is obtained as

$$\begin{aligned}\dot{s} &= \dot{x}_{d2} - g - \tilde{k}_p x_1 - \tilde{k}_d\dot{x}_1 - \tilde{k}_i\int x_1 \\ &\quad - \hat{k}_p x_{d1} - \hat{k}_d\dot{x}_{d1} - \hat{k}_i\int x_{d1} - u_R \\ &\quad + 2\lambda\dot{x}_{d1} - 2\lambda\dot{x}_1 + \lambda^2\tilde{x}_1 \end{aligned} \quad (11)$$

where

$$\tilde{k}_p = k_p - \hat{k}_p\,,\ \tilde{k}_d = k_d - \hat{k}_d\,,\ \tilde{k}_i = k_i - \hat{k}_i\,. \quad (12)$$

The Lyapunov function in (13) is utilized to construct update rules for PID gains and design u_R

$$V = \frac{1}{2}s^2 + \frac{1}{2}\tilde{k}_p^2 + \frac{1}{2}\tilde{k}_d^2 + \frac{1}{2}\tilde{k}_i^2\,. \quad (13)$$

The derivative of (13) is obtained as

$$\begin{aligned}\dot{V} &= s\dot{s} + \tilde{k}_p\dot{\tilde{k}}_p + \tilde{k}_d\dot{\tilde{k}}_d + \tilde{k}_i\dot{\tilde{k}}_i \\ &= s(\dot{x}_{d2} - g - \hat{k}_p x_{d1} - \hat{k}_d\dot{x}_{d1} - \hat{k}_i\int x_{d1} - u_R \\ &\quad + 2\lambda\dot{x}_{d1} - 2\lambda\dot{x}_1 + \lambda^2\tilde{x}_1) - \tilde{k}_p(sx_1 + \dot{\hat{k}}_p) \\ &\quad - \tilde{k}_p(s\dot{x}_1 + \dot{\hat{k}}_d) - \tilde{k}_i(s\int x_1 + \dot{\hat{k}}_i) \end{aligned} \quad (14)$$

From (14), the update rules of $\hat{k}_p$, $\hat{k}_d$ and $\hat{k}_i$ are selected as in (15) to eliminate the terms with gain errors.

$$\dot{\hat{k}}_p = -sx_1\,,\ \dot{\hat{k}}_d = -s\dot{x}_1\,,\ \dot{\hat{k}}_i = -s\int x_1 \quad (15)$$

After substitution of (15) in (14), $\dot{V}$ is obtained as

$$\begin{aligned}\dot{V} &= s(\dot{x}_{d2} + 2\lambda\dot{\tilde{x}}_1 + \lambda^2\tilde{x}_1) - sg \\ &\quad - s(\hat{k}_p x_{d1} + \hat{k}_d\dot{x}_{d1} + \hat{k}_i\int x_{d1}) - su_R \end{aligned} \quad (16)$$

The input signal u_R should be designed to make $\dot{V}$ negative. To achieve this purpose, u_R will be investigated by separating into three terms as

$$u_R = u_1 + u_2 + u_3\,. \quad (17)$$

u_1, is designed as to eliminate first two terms in (16) as

$$u_1 = \dot{x}_{d2} + 2\lambda\dot{\tilde{x}}_1 + \lambda^2\tilde{x}_1 + k\,\mathrm{sgn}(s)\,,\ k \in R^+ \quad (18)$$

To eliminate the term sg in (16), the condition in assumption 1 can be utilized. From (4) the following inequality can be obtained

$$-sg \le |s|\rho\,,\ \rho \in R^+ \quad (19)$$

By using (19), u_2 is designed as follows

$$u_2 = \frac{|s|}{s}\rho . \quad (20)$$

By substituting (18) and (20) in (16), $\dot{V}$ is obtained as,

$$\dot{V} \le -k|s| - sL - su_3 \quad (21)$$

where

$$L = \hat{k}_p x_{d1} + \hat{k}_d \dot{x}_{d1} + \hat{k}_i \int x_{d1} . \quad (22)$$

An upper bound for L can be defined as

$$L_m > |\bar{k}_p||x_{d1}| + |\bar{k}_d||\dot{x}_{d1}| + |\bar{k}_i|\left|\int |x_{d1}|\right| . \quad (23)$$

where $\bar{k}_p$, $\bar{k}_d$ and $\bar{k}_i$ are upper bounds of k_p, k_d and k_i, respectively.

Hence, the following inequality can be written

$$-sL < |s|L_m \quad (24)$$

Remark 1: In (23), L_m may go to infinity for $x_{d1} \neq 0$ since integral term. But it should be kept in mind that the main interested term is $|s|L_m$. So if it can be proven that s(t) converge to 0, fast enough, then, it can be assumed that the term $|s|L_m$ stays bounded. So L_m can be accepted as bounded.

In the rest of the paper, it will be proven that s(t) converge to 0 with a tunable rate.

From (24),

$$\dot{V} = -k|s| + |s|L_m - su_3 . \quad (25)$$

So, u_3 can be obtained as

$$u_3 = \frac{|s|}{s} L_m \quad (26)$$

This leads

$$\dot{V} < -k|s| . \quad (27)$$

From (27), it can be said that s, $\hat{k}_p$, $\hat{k}_d$ and $\hat{k}_i$ are bounded. To show that s(t) goes to zero with respect to time, s(t) should be investigated in deep by taking the time derivative of s^2 as

$$\frac{1}{2}\frac{d}{dt}s^2 = s\dot{s}$$
$$= (\dot{x}_{d2} - g - k_p x_1 - k_d x_1 - k_i \int x_1 - u)$$
$$+ 2\lambda\dot{x}_{d1} - 2\lambda x_1 + \lambda^2 x_1)s . \quad (28)$$

By substituting (9) and (15) in (28), it is obtained as,

$$\frac{1}{2}\frac{d}{dt}s^2 < -k|s| + (-\tilde{k}_p x_1 - \tilde{k}_p \dot{x}_1 - \tilde{k}_i \int x_1)s . \quad (29)$$

If k is selected as

$$k > \left|\breve{k}_p x_1 + \breve{k}_d \dot{x}_1 + \breve{k}_i \int x_1\right| + \eta \quad (30)$$

where

$$\breve{k}_p = \bar{k}_p - \underline{k}_p \quad (31)$$

$$\breve{k}_d = \bar{k}_d - \underline{k}_d \quad (32)$$

$$\breve{k}_i = \bar{k}_i - \underline{k}_i , \quad (33)$$

where $\underline{k}_p$, $\underline{k}_d$ and $\underline{k}_i$ are lower bounds of k_p, k_d and k_i, respectively, (29) is obtained as

$$\frac{1}{2}\frac{d}{dt}s^2 < -\eta|s| \quad (34)$$

which leads

$$\dot{s} < -\eta|s| . \quad (35)$$

From (35), it is seen that starting from any initial condition, the state trajectory reaches to the surface in a finite time smaller than $|s(t=0)|/\eta$ and then converges to $x_d(t)$ exponentially with a time constant equal to $1/\lambda$ [18].

4. Numerical Simulations

The performance of the control law in (9) and update rule in (15) were evaluated by conducting numerical simulation by using the dynamic model of a 2-DOF helicopter which is known as TRMS.

During the simulation, the parameter values of input signal were selected as λ=diag(30,30), k=diag(1,1), ρ=$[1\ 1]^T$, $L_m = [1\ 1]^T$. The initial values of gain estimates were set to $k_p=[5\ 5]^T$, $k_d=[5\ 5]^T$ and $k_i=[5\ 5]^T$. The initial positions of the axes were $x(0)=[0.5\ 0.5]^T$ in radian and the desired positions were selected as $x_d=[0.4\ 0.3]^T$ in radian.

In the numerical simulations, it was observed that the control law performed satisfactorily. The position errors and the control inputs of yaw and pitch axes are presented in Figures 1, 2, 3 and 4, respectively. The PID gain estimates are given in Figures 5, 6 and 7. As can be seen in the figures, both the yaw and the pitch errors are driven to the vicinity of zero.

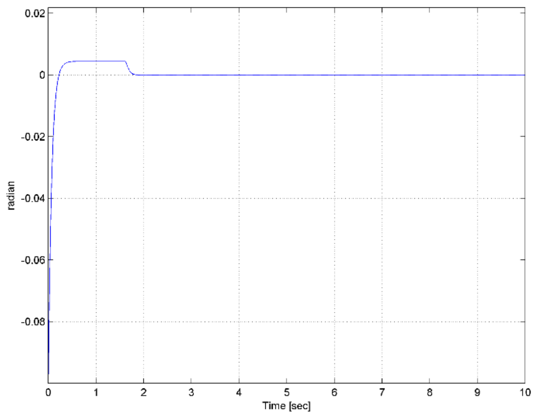

Fig. 1. Yaw axis position error

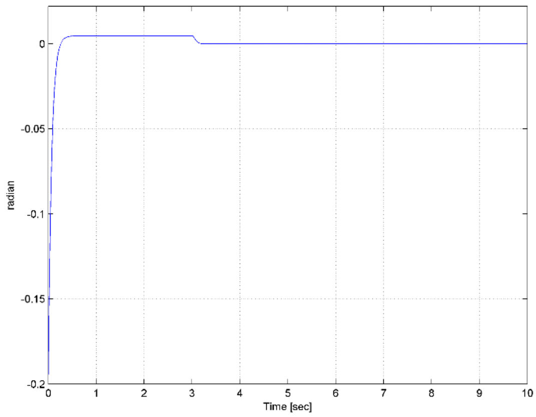

Fig. 2. Pitch axis position error

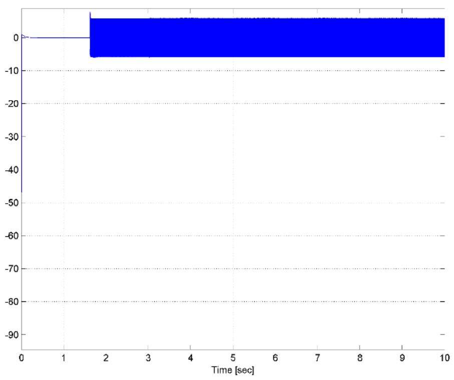

Fig. 3. Input signal for yaw axis

5. Conclusions

In this paper, a sliding mode based self-tuning PID controller was designed for second order systems. While designing the controller, it was assumed that the system model contain nonlinear terms similar to PID structure. The controller and update rule for PID parameters were obtained from Lyapunov stability analysis. The effectiveness of the controller and update rule were evaluated by conducting numerical simulation and achieved satisfactory results.

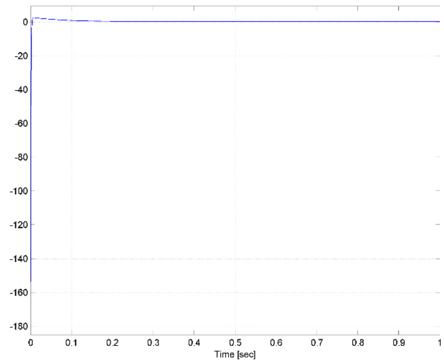

Fig. 4. Input signal for pitch axis

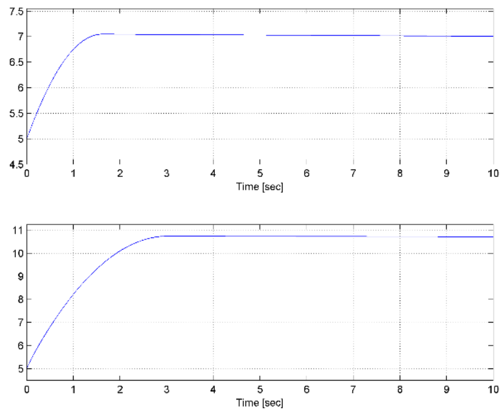

Fig. 5. K_p estimates for yaw axis (top) and pitch axis (bottom)

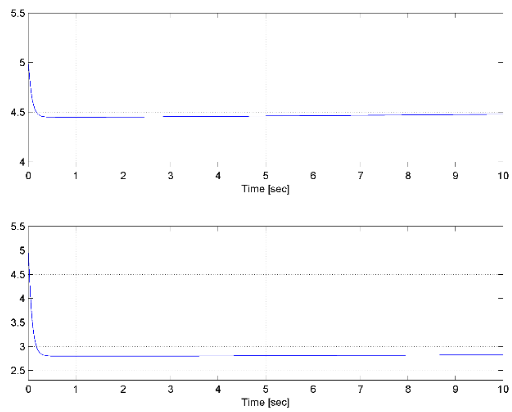

Fig. 6. K_d estimates for yaw axis (top) and pitch axis (bottom)

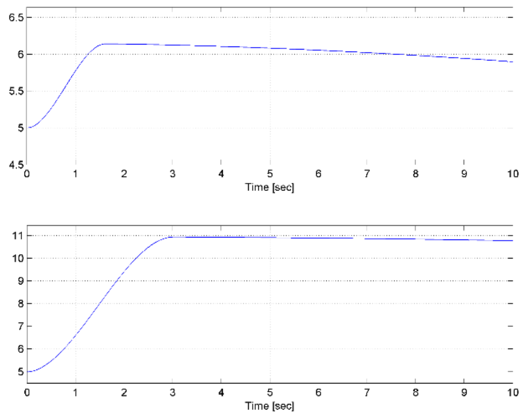

Fig. 7. K_i estimates for yaw axis (top) and pitch axis (bottom)

References

[1] S. Wanfeng, Z. Shengdun, and S. Yajing, “Adaptive PID controller based on online LSSVM identification,” in Int. Conf. on Advanced Intelligent Mechatronics, July 2008, pages 694–698.

[2] K. J. Astrom and T. Hagglund, “PID Controllers: Theory, Design and Tuning”, NC, USA: Instrument Society of America, 1995.

[3] An, S., Yuan, S., Li, H., “Self-tuning of PID controllers design by adaptive interaction for quadrotor UAV,” in Proc. Of IEEE Chinese Guidance, Navigation and Control Conference, Nanjing, China, August 2016, pages 1547-1552.

[4] J. Lu, C. Yang, B. Peng, R. Wan, X. Han, and Ma, “Self-tuning PID Control Scheme with Swarm Intelligence Based on Support Vector Machine,” in Proc. of IEEE Int. Conf. on Mechatronics and Automation, Tianjin, China, August 2014, pages 1554–1558.

[5] K. Jiang, W. Jiang, and X. Jiang, “Design of an intelligent temperature control system based on the fuzzy self-tuning PID,” Procedia Engineering, vol. 43, pages 307 – 311, 2012.

[6] J. ming Zheng, S. dun Zhao, and S. guo Wei, “Application of self-tuning fuzzy PID controller for a SRM direct drive volume control hydraulic press,” Control Engineering Practice, vol. 17, no. 12, pages 1398–1404, 2009.

[7] C. Li and J. Lian, “The application of immune genetic algorithm in PID parameter optimization for level control system,” in IEEE Int. Conf. on Automation and Logistics, Aug 2007, pages 782–786.

[8] Sreekanth, P., Hari, A., “Genetic Algorithm Based Self Tuning Regulator for ball and hoop system,” in Proc. Of Conference on Emerging Devices and Smart Systems, Tamilnadu, India, March 2016, pages 147-152.

[9] M. G. Na, “Auto-tuned PID controller using a model predictive control method for the steam generator water level,” IEEE Trans. on Nuclear Science, vol. 48, no. 5, pages 1664–1671, Oct 2001.

[10] J. Fan, J. Zhong, J. Zhao and Y. Zhu, “BP neural network tuned PID controller for position tracking of a pneumatic artificial muscle,” Technology and Health Care, vol. 23, no. 2, pages S231–S238, 2015.

[11] T. Gundog and G. Comoros, “Adaptive PID controller design by using adaptive interaction approach theory,” in Int. Conf. on Electric Power and Energy Conversion Systems, Oct 2013, pages 1–5.

[12] M. Howell and M. Best, “On-line PID tuning for engine idle-speed control using continuous action reinforcement learning automata,” Control Engineering Practice, vol. 8, no. 2, pages 147 – 154, 2000.

[13] M.-C. Shih and S.-I. Tseng, “Pneumatic servo-cylinder position control by PID-self-tuning controller,” JSME inter. journal. Ser. C, Dynamics, control, robotics, design and manufacturing, vol. 37, no. 3, pages 565–572, 1994.

[14] J. Dong and B. Mo, “The adaptive PID controller design for motor control system with backlash,” in Inter. Conf. on Intelligent Control and Information Processing, June 2013, pages 59–63.

[15] T. Chamsai, P. Jirawattana, and T. Radpukdee, “Robust adaptive PID controller for a class of uncertain nonlinear systems: An application for speed tracking control of an SI engine,” Mathematical Problems in Engineering, 2015.

[16] W.-D. Chang and J.-J. Yan, “Adaptive robust PID controller design based on a sliding mode for uncertain chaotic systems,” Chaos, Solitons & Fractals, vol. 26, pages 167 – 175, 2005.

[17] T. C. Kuo, Y. J. Huang, C. Y. Chen, and C. H. Chang, “Adaptive sliding mode control with PID tuning for uncertain systems,” Engineering Letters, vol. 16, no. 3, pages 311–315, 2008.

[18] J.-J. E. Slotine and W. Li, Applied Nonlinear Control. Englewood Cliffs: NJ:Prentice Hall, 1991.

Self-Calibrating Smart Mirror Design

Kaya MANOĞLU[1]*, Barış TANER[1], Onursal ÖNEN[1], Serhan OZDEMİR[1]

[1*]Izmir Institute of Technology
IzTech Robotics Laboratory, Gülbahçe Mah., Urla, İzmir, Turkey
E-mail: kayamanoglu@iyte.edu.tr

Abstract
Self-Calibrating Smart Mirror is a source tracking mirror that is designed in Izmir Instıtute of Technology. This device uses ARM Cortex M4 chip to calibrate itself using the sound in environment and execute tracking operations to direct the mirror to the user. In this paper, mathematical model, calibration, experiments for sensor capabilities and tracking operations are presented and the prototype is expressed.
Keywords: Robotics, human-machine interface, sound tracking, source localization.

1. Introduction

Smart devices became common with the development of processors and sensors which are used in devices surrounding us and make them smarter every day with the need of easier interaction of human and machine. Smarter machines are designed to have the same communication methods of human that are visual, tactile, kinesthetic and auditory sensors [1] to be more sociable in the use of a human.

These communication methods can be used for increasing human perception in the slave environment that is interfaced by a haptic device [2] or to increase level of perception of the human commands by the machine [3]. As pointed in a research [4], some arcade games are using visual, infra-red, inertial measurement units and ultrasonic sensors to locate the users for shaping game inputs. Tactile and kinesthetic information in action and sports games as a reaction to the user by haptic devices are widely used application examples of communication between human and machine.

Other than sensing the motion of the human user by haptic devices, the motion inputs of the user can be detected by other means such as visual sensors using cameras [5], IR sensors [6] and auditory sensors [7]. Visual and IR sensors are commonly used sensor types for tracking environmental changes. These sensors are powerful considering the achievable resolution of the tracked workspace with respect to the auditory sensors; However, they are limited with the field of view and cannot locate outside of this region [1]. The field of view depends on parameters such as focal length of the lens, image sensor dimensions and distance to the measured plane [8]. In some vision applications, field of view can be enlarged using stereo vision techniques which include rectification of multiple images and matching them to create a larger field of view but this method requires multiple cameras and greater computational costs [9].

One other way to locate user is using acoustic sensors. This method is used in real world by creatures to locate the sound source and give them a 360º field of view. It also allows them to locate sources that are obscured by any object that are not in the field of vision [1]. Researchers are using this method of localization in robots for tracking, socializing and navigating which has various application techniques.

In this paper, design of a smart mirror is described with its sensors, processor and mathematical model, which includes self-calibration, signal processing and source tracking in two-dimensional plane. The mirror is designed to be one Degree of Freedom (DoF) and uses an ARM Cortex M4 chip, which can locate the sound source using an array of microphones placed on the body.

2. Hardware used in Design

Device is composed of several electronics including processor, sensors and actuators. In this project an ARM based processor was selected and this chip was STM32F407VGT6. In the market, this chip is used by many third-party companies to build their own prototyping boards in which one of them is the STM32F4DISCOVERY Discovery board. This board allows users to easily develop applications with the STM32F407 high performance microcontrollers with ARM® Cortex®-M4 32-bit core. It includes an ST-LINK/V2 or ST-LINK/V2-A embedded debug tool, two ST MEM's digital accelerometers, a digital microphone, one audio DAC with integrated class D speaker driver, LEDs and push buttons and an USB OTG micro-AB connector [10].

A basic sound sensor card is used in this robotic application, which gives an analog output according to the sound level of the environment. The specifications of this sensor breakout are listed in Table 1.

Table 1. Sound sensor specifications

F1requency range	100 ~ 10,000 Hz
Sensitivity	- 46 ± 2.0, (0 dB = 1V/Pa) at 1K Hz
Power supply	5V maximum
Minimum Sensitivity to Noise Ratio	58dB for digital output

A light weight servo motor that can rotate approximately 180 degrees is placed beneath the mirror to rotate it around the azimuth axis. Body of the device is made out of a foam-board for minimizing the reverberation problems.

2. Deciding the Geometry

Sensor placement plays an important role in product design and cabling since the way sensors are placed changes both signal transfer and acquisition problems with the sound tracking performance of the mirror. To declare it clearly, sound acquisition performance of microphones is affected by direction of the microphones. This fact about the sensors is an outcome of the experiment executed in this work. The experiment aims to measure sound level using four identical sound sensors in two different formations. One of the formations was placing them as a linear array and the other one was placing them radially as provided in Figure 1.

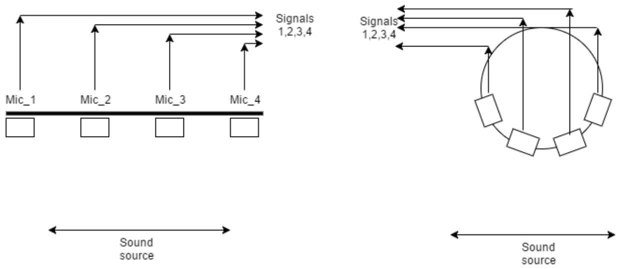

Fig.1. Test Formation for formation

The sensors in linear array set gives greater voltage values for the sounds sourced directly in front, however, other sensors in the same array set gives approximately close voltage levels that cannot be distinguished easily.
The sensors in radial array set gives higher voltages once the sound sourced from the normal angle like the previous array set, however, it is easier to transfer signals from the sensors to the microchip due to the tight packing of the sensors.

In order to decide the geometry of the device, an experiment is designed and executed, especially for defining the microphone sensitivities at varying facing angles and distances. In this experiment, source is placed at different azimuth angles with varying distances from the sensor and sound level is measured. The azimuth angle and distances are given in Table 2.

Table 2 The Trial Table

Angle (degrees)	Distance (cm)
0	10, 20, 40, 60, 80
30	10, 20, 40, 60, 80
45	10, 20, 40, 60, 80
60	10, 20, 40, 60, 80
90	10, 20, 40, 60, 80

Sound source is measured for an average duration of 6-7 seconds for every combination of Table 2. Sine wave of 500 Hz is used as a sound source. As additional information, it is known that the human sound is in a range of 85 to 1050 Hz, lowest frequency as a male bass sound and the highest as a female soprano. The results showed that the distance of the source has a significant effect in the sound level, as much as the microphone angle.

Measurements were mapped according to the distance and angle of the sound source with respect to the microphone. Five distinct measurements are executed for the angles of 0º, 30º, 45º, 60º and 90º, which include measurements of varying distances provided in Table 1. 0º is directly in front of the microphone and 90º is the perpendicular angle to the direct line of sight of the microphone. Tests are applied for every microphone and the measurements are illustrated only for one microphone.

Figures 2-6 provide the sound measurement of a microphone according to the different levels of distances for the same angle value, which are 0º, 30º, 45º, 60º and 90º respectively. Blue lines in these figures provide the information of the sound signal and the red lines give the measurement interval.

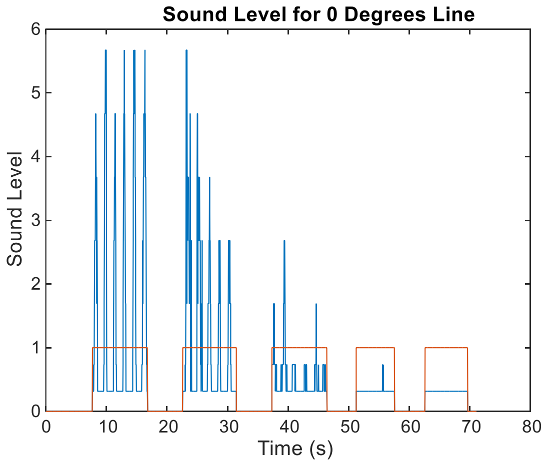

Fig.2. Sound level measurements for 0º azimuth angle

Fig. 2 illustrates the sound measurement of the microphone at 0º azimuth angle. At this angle, sound pressure is measured with the sensor and scaled to a 10-bit range. It is clear that sound level drops with increasing distance of the source, which is case for all other experiments executed for different azimuth angles, and maximum values are about 5.5 units.

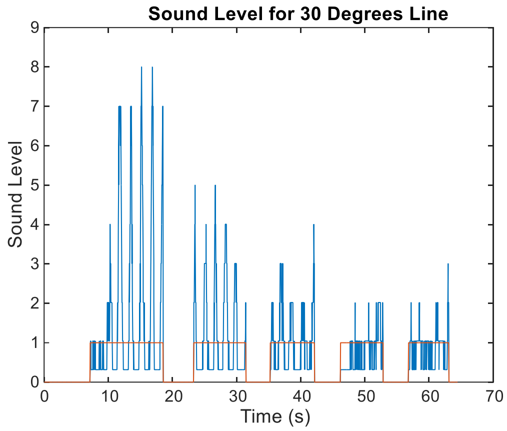

Fig.3. Sound level measurements for 30º azimuth angle

In Fig. 3, same sound measurement of the microphone at 30º azimuth angle is executed. In a 10-bit range, pressure levels are bounded between 0 and 9. It should be note that, maximum sound level increases from 5.5 to 9 units for this angle compared to the one obtained in 0º.

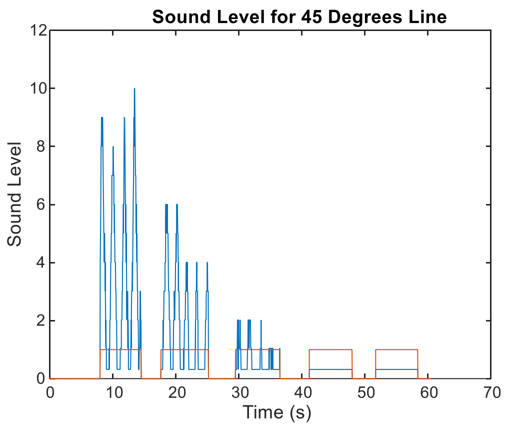

Fig.4. Sound level measurements for 45º azimuth angle

Fig. 4 provides the sound measurement of the microphone at 45º azimuth angle. In a 10-bit range, pressure values are bounded in a slightly greater region compared to the one acquired for 30º.

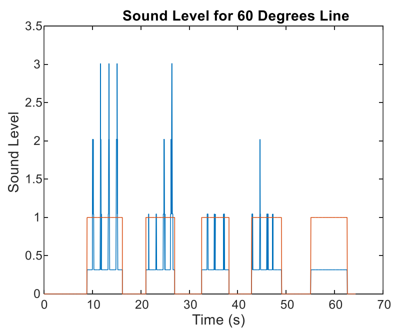

Fig.5. Sound level measurements for 60º azimuth angle

Fig. 5 designates the sound measurement of the microphone at 60º azimuth angle. In a 10-bit range, pressure values for different distances drop significantly to a range of 0.3 to 3 units.

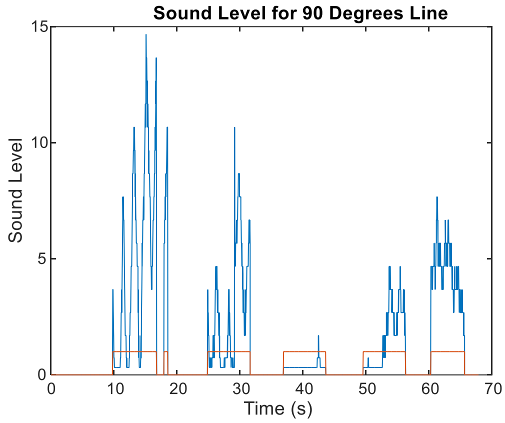

Fig.6. Sound level measurements for 90º azimuth angle

Fig. 6 marks the sound measurement of the microphone at 90º azimuth angle. It should be clarified that this is where the sound source is placed completely side of the microphone. At this angle device measures the source pressure level between the range of 0.3 and 15 units and measurements are not fitting in the expectations. To avoid any compromise due to the irregular behavior of the sensor at this azimuth angle, a foam body is designed to attenuate the signal coming from that angle.

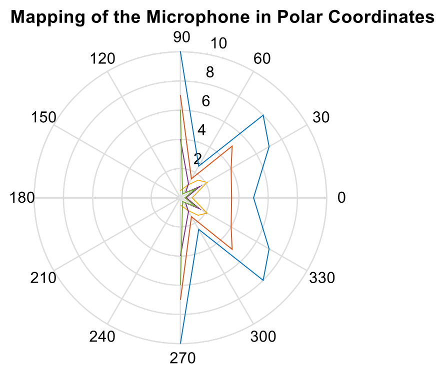

Fig.7. Sound level measurement in the sound sensor field of view

Fig. 7 connotes the overall 'field of view' of the sensor using polar coordinates. Blue, red, orange, green and purple lines show the sound pressure level of the source at 10, 20, 40, 60 and 80 cm distances respectively. As provided in this figure, microphone measures the sound pressure level of the source greater along 0º and smallest around 60º.

Using this knowledge, body is made of a foam material for minimizing the reverberation problem, which is shaped as a half circle with openings in four different locations on the arc. These openings are specially designed for not allowing the microphones getting signals from the sides Foam type materials are especially used for high frequency sound absorption above 2000 Hz, and it is possible to obtain better results by more proper material usage in the body. It is important to remark that this study is just a concept and in the process of development at the moment.

3. Localization Algorithm and Its Application

As expected, depending on the source location, different sound levels will be obtained by each microphone. Facing direction of each microphone is defined as a vector, which in the end will give the resultant vectors. It is said to be the logic of the system is based on the estimation of that resultant vector Fig. 8.

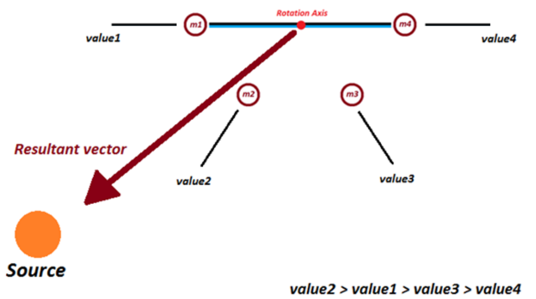

Fig.8. Sound levels from different source distances with varying microphone angles

A simple algorithm is developed for the system which is shown in Fig. 9.

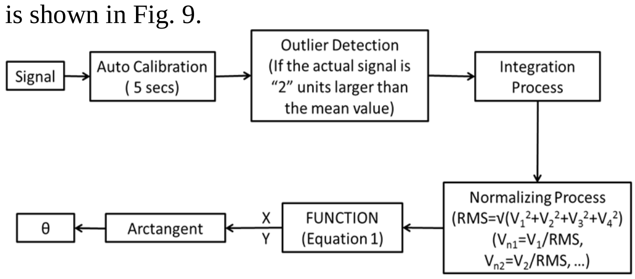

Fig.9. Diagram of the process

First step is the calibration process for the device. In order to do this, for 5 seconds, the device measures the average noise level of the room, which will be the mean value in the further calculations, to define the offset. This is illustrated in Fig. 10 with a block diagram.

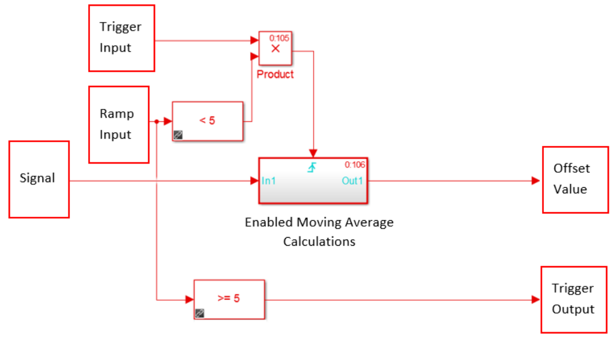

Fig.10. Block representation of auto-calibration function

Trigger and ramp input work together to enable the moving average calculations, which works for 5 seconds in this case, and at the end of this 5 second time interval, block releases the value as offset value. Trigger output in this sub-system is used as a switch to allow calibrated signal to be used in further calculations.

After 5 seconds, when the calibration is completed, the incoming signals are being started to be analyzed. Firstly, threshold value is used to allow calibrated signals that are powerful enough to be analyzed. This data is taken into the integration process in a specified time range which is between the rising and the dropping edges of the curve. This process is connoted in Figure 11.

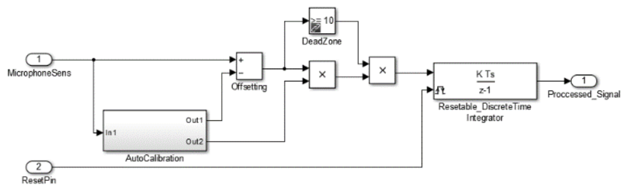

Fig.11. Block representation of signal processing phase

The normalizing step follows the integration procedure, which allows us to assign the value of "1" to the microphone signal that is the greatest and the other microphone values take values according to their value. This is provided in Fig. 12. To normalize signals their root mean square is calculated and every signal is then divided to this value. This is explained in Eq. 1.

$$N_j = \frac{s_j}{\sqrt{\sum_{i=1}^{4} s_i^2}}\ , \qquad j = 1,2,3,4 \qquad (1)$$

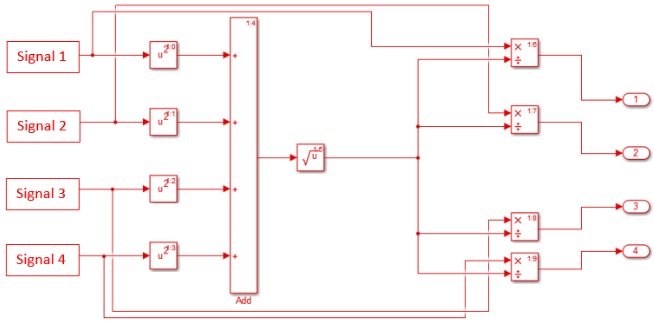

Fig.12. Block representation of normalization process

After this step, we are applying a function to the obtained microphone values to determine the direction of the sound source by distinguishing the x and y components of the required resultant normal vector using Eq 2. When x and y components are obtained, it becomes very simple to convert this to an angle of θ, by using the arctangent function.

$$\begin{bmatrix} X_{SS} \\ Y_{SS} \end{bmatrix} = \begin{bmatrix} \sum_{i=1}^{4}(Microphone\ Value)_i * cos\theta_i \\ \sum_{i=1}^{4}(Microphone\ Value)_i * sin\theta_i \end{bmatrix} \quad (2)$$

The code generation is executed using the Waijung module in Matlab Simulink. This module is third-party software that includes blocks for different operations such as mathematical operations, logic operations and etc. Using this software created model is downloaded in discovery board.

Microphones are placed on top of the mirror in a radial array and body of the mirror assembly is made out of foam due to previously designated experimental results. Servo motor is placed in the bottom part of the mirror assembly and the mirror is attached to the servo motor. The prototype is illustrated in Fig. 13.

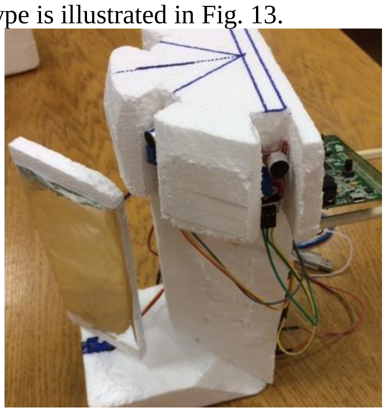

Fig.13. Experimental prototype of sound tracking mirror

4. Results

After manufacturing the smart mirror, simple tests are conducted to see if the algorithm is works as expected on the STM32F4 chip and prototype follows the sound source on 2-D plane. This is executed by clapping hand close to the smart mirror at angles ranges from 0º to 180^0. To visualize the working principle sound level measurements of the 3rd microphone is acquired from the raw signal stage to the processed signal stage. Fig. 14 gives the raw data that is acquired by the 3rd microphone. Before 5th second microphone receives only the surrounding sources that creates the noise. After 8th second microphone receives the clapping sound.

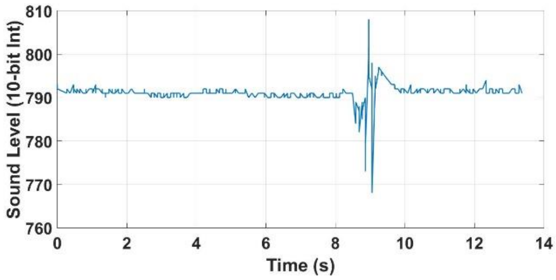

Fig. 14. Raw sound signal graph

This signal is then calibrated so that surrounding sound is eliminated. After calibration, the output signal of the calibration stage is integrated to store the value that will be used in calculation of angular position. Result of the integration of 3rd microphone signal is given in Fig.15.

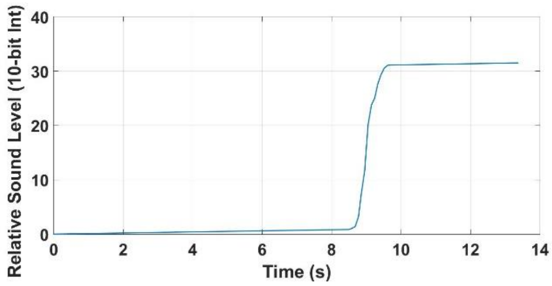

Fig. 15. Calibrated and processed signal

All four signals are run into the same algorithm, and the resultant signals of every one of them is sent to normalization stage but in results section and result of the normalization is given in Fig. 16. As given in Fig. 16 with the increasing value of the integration coming from the 3rd microphone, normalized signal of line of the 3rd microphone goes to one, while the others reduces in value. The yellow line in Fig 16. shows the value of the line of 3rd microphone.

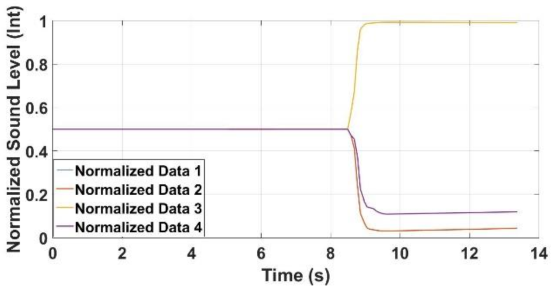

Fig. 16. Signals after normalization

After the normalization process, x and y components of the sound source vector is used to calculate the angular position of the sound source with respect to the mirror origin in 2-D plane. This is provided is Fig. 17.

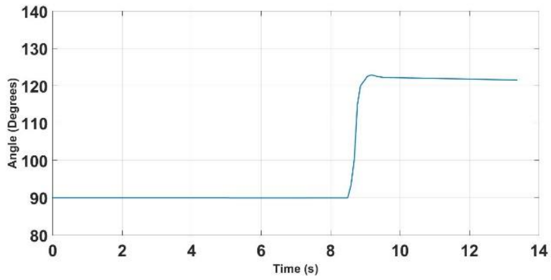

Fig. 17. Angle calculation graph

As given in Fig. 17 a series of clap that is close to the 3rd microphone, which is placed at 120º, results in a calculated angle of 124º, with an error of 4º.

5. Comments and Conclusion

In this paper, a 1 DoF smart mirror is designed using 4 radially placed sound sensors. The purpose of this mirror is to construct a system, which can be used in robotic systems that interacts with humans. The controller of the system is designed over the STM32F4 Discovery board and the system is deployed on the chip using Matlab.

In preliminary design, microphone field of view is revealed to be used in design of the mirror and sensors are placed using this information. Field of view experiments show that there is an unexpected rise in the sound level at 90º angle, where sound level is measured to be the largest. To eliminate this problem sensors are placed in a foam head that reduces the sound level coming from this angle. After this stage, control algorithm is deployed in the discovery board.

In this prototype, an integration is executed for every signal and the resultant signals are normalized. This is used to store the positional data, however, after several repetitions of localization, integrated values that are feed in the normalization get high values. This creates a problem of latency once another sound source transmits sound. In this particular case, device turns to the new source slowly, since integration of the acquired sound signal takes time to reach the previously integrated value. To overcome that problem, smart mirror has to be reset, which is done by a digital input given by the user.

Even though this system is designed as a smart mirror to interact with humans, it may very well be equipped with other device or objects along with a different line of sensors, oriented towards commercial or industrial purposes.

It should be mentioned that the curvilinear deployment of sound sensors may also be regarded as a distributed sensor network, whose detailed analysis is left for a later research. But it is seen that as the number of sensors is increased, localization resolution is also on the rise.

References

[1]. Murray, John C., Harry Erwin, and Stefan Wermter. "Robotics sound-source localization and tracking using interaural time difference and cross-correlation." AI Workshop on NeuroBotics. 2004.

[2]. Taner, B., and M. İ. C. Dede. "Image Processing Based Stiffness Mapping of a Haptic Device." New Advances in Mechanisms, Mechanical Transmissions and Robotics. Springer International Publishing, pages 447-454, 2017.

[3]. Web,http://web.media.mit.edu/~cynthiab/Papers/Breazeal-TICS02.pdf

[4]. Breazeal, Cynthia, et al. "Learning from and about others: Towards using imitation to bootstrap the social understanding of others by robots." Artificial life 11.1-2, pages 31-62, 2005.

[5]. Wermter, Stefan, et al. "Towards multimodal neural robot learning." *Robotics and Autonomous Systems* 47.2, pages 171-175 2004.

[6]. Zhang, Zhengyou. "Microsoft kinect sensor and its effect." *IEEE multimedia* 19.2 (2012): 4-10.

[7]. Nakadaij, Kazuhiro, et al. "Real-time tracking of multiple sound sources by integration of in-room and robot-embedded microphone arrays." *Intelligent Robots and Systems, 2006 IEEE/RSJ International Conference on*. IEEE, 2006.

[8]. Web,http://www.inf.u-szeged.hu/~kato/teaching/computervision/02-CameraGeometry.pdf

[9]. Web,http://vision.deis.unibo.it/~smatt/Seminars/StereoVision.pdf

[10]. Web,http://www.st.com/content/ccc/resource/technical/document/data_brief/09/71/8c/4e/e4/da/4b/fa/DM00037955.pdf/files/DM00037955.pdf/jcr:content/translations/en.DM00037955.pdf.

Proceedings of the International Symposium of Mechanism and Machine Science, 2017
AzC IFToMM – Azerbaijan Technical University
11-14 September 2017, Baku, Azerbaijan

Topological Structure Optimization and Kinematic Performance Improvement of 3-RRR Planar Parallel Manipulator*

Ke XU[1], Huiping SHEN*[2], Jiaming DENG[3], Yunyu SHEN[4]

[1] School of Mechanical Engineering, Changzhou University
Chang Zhou 213016 China
1375928645@qq.com
[2] * shp65@126.com
[3] czdydjm@126.com
[4] Business Administration Department, University of Northeastern
Shen Yang 110819 China
919304858@qq.com

Abstract

The typical 3-RRR planar parallel manipulator with two translations and one rotation has extensive applications such as plane location and motion transfer. But it suffers two disadvantages. One is its analytical direct kinematics is difficult to be got and another is not input-output motion decoupled. This paper focuses on its topological structure optimization and resulting kinematic performance improvementt. First, the coupling degree of this manipulator is calculated being k=1. Second, based on structure coupling--reducing principle, its coupling-reduced manipulator with zero coupling degree is designed, which not only leads to be easy to get its analytic direct kinematic solutions, but also makes input-output motion partially decoupled. Moreover, based on workspace and singularity of this coupling-reduced manipulator, comprehensive comparison of two manipulators before and after coupling--reducing showed that the main performances of structure coupling-reduced manipulator are superior than that of the typical mechanism. The work shows that structure coupling-reducing is effective method for optimization of topology structure.

Keywords: Parallel mechanism, Direct kinematics, Structure coupling-reducing, Performance analysis.

1. Introduction

3-RRR planar parallel manipulator has potential value in practical application. It not only can be used in guiding, location and transmission of rigid body, but also can obtain more accurate motion trajectory than general multi-bar linkages do [1].

At present, many scholars have had much more investigation for 3-RRR planar parallel manipulator. In the aspect of the direct kinematics, the number of the maximum direct kinematics of 3-RRR manipulator is 6, which is proved by [2]. Oetomo *et.al* [3] set up three constraint equations and then got one eighth degree polynomial to solution by using the elimination method.

In the way of mechanism's performance investigation, Gosselin[4] conducted the optimization parameter design of 3-RRR manipulator. Wu *et.al* [5] made comparisons on the peculiarities of statics and dynamics between 4-RRR, 3-RRR and 2-RRR. Taking prismatic pair as actuated one, Cha *et.al* [6] measured the range of 3-RRR manipulator's nonsingular paths. Wei *et.al* [7] analyzed 8 kinds topology structure of 3-RRR manipulator, and analyzed this manipulator dexterity by taking conditioning performance of Jacobian matrix as index. The reachable workspace of the symmetric 3-RRR parallel manipulator was analyzed by Li *et.al* [8]. The Dexterous workspace of 3-RRR manipulator was obtained in [9, 10]. Gao *et. al* [11] systematically analyzed the relationship between branched chains' length and the workspace shape of 3-RRR manipulator.

Obviously, current studies on 3-RRR manipulator s focus primarily on workspace, singularity, dexterity and stiffness performance. However, accuracy analysis and design of the manipulator are difficult and motion control is comparatively complex, the reasons of which are that the analytical solutions for this manipulator are not easy to get its direct kinematics, and further the manipulator does not possess input-output (*I-O*) motion decoupling.

Taking the two reasons stated above as target, this paper design firstly a novel kind of coupling-reduced mechanism(CRM) with low coupling degree, i.e., k=0, and motion-decoupling based on the structure coupling-reducing methodology. Not only are analytical solutions for direct kinematics obtained but also this manipulator has *I-O* decoupling, which accordingly leads to the precision design, motion planning and control of this manipulator be easy. Moreover, the workspace and singularity are analyzed. The work shows that the comprehensive performance of CRM is better than the typical manipulator 3-RRR. Therefore typical 3-RRR planar parallel manipulator could be replaced by the CRM.

2. 3-RRR PM and Its Topological Optimization Design

Typical 3-RRR planar manipulator is shown in Fig. 1. The digitals, from 1 to 7, are denoted as different rods. The moving platform 1, an equilateral triangle, connects with the static platform 0 through three RRR branch chains. The static coordinate system *o-xy* and the moving coordinate system *o'-x'y'* are established on the static platform 0, moving platform 1 respectively.

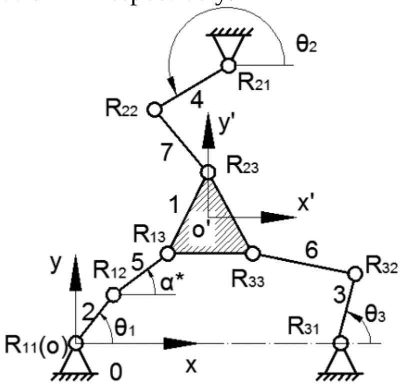

Fig. 1. 3-RRR planar parallel mechanism

Length for each link of three branch chains are given as follows, respectively.

$R_{11}R_{12}=l_1$, $R_{12}R_{13}=l_2$, $R_{21}R_{22}=l_7$,
$R_{22}R_{23}=l_6$, $R_{31}R_{32}=l_5$, $R_{32}R_{33}=l_4$.

The side length of moving platform 1 is l_3, its attitude angle γ is anticlockwise direction of x axis to x', The input angle of three actuated pairs, R_{11}, R_{21}, R_{31}, is θ_1, θ_2, θ_3 respectively, as shown in the Fig.1.

A. Coupling Degree (κ) of 3-RRR Manipulator

According to the structure composition theory of parallel mechanisms based on the ordered single-open-chain (*SOC*) [12], this mechanism can be decomposed into following two *SOC*s. The restraint degree (Δ) of each SOC is listed as follows, respectively.

$$SOC_1\{-R_{11}-R_{12}-R_{13}-R_{33}-R_{32}-R_{31}-\}$$

$$\Delta_1=\sum_{i=1}^{6} f_i - I_1 - \xi_{L_1} = 6-2-3=1$$

$$SOC_2\{-R_{21}-R_{22}-R_{23}-\}$$

$$\Delta_2=\sum_{i=1}^{3} f_i - I_2 - \xi_{L_2} = 3-1-3=-1$$

k of the manipulator is calculated by

$$k=\frac{1}{2}\sum_{j=1}^{2}\left|\Delta_j\right| = \frac{1}{2}(|1|+|-1|)=1$$

Here,

I_j - the number of inputs in the j^{th} SOC_j,
f_i - *DOF* of the i^{th} kinematic pairs,
ξ_{L_j} -the number of independent equations of j^{th},
Δ_j -constraint degree of j^{th} SOC_j.

Since the coupling degree of this manipulator is k=1, its numerical solutions of direct kinematics could be obtained by solving a one –variable polynomial equation. That is, one virtual variable is needed to be assigned to SOC_1 so that direct kinematic equation containing the variable can be established easily. Then one-dimensional search method is utilized easily to obtain its numerical direct solutions for this manipulator. The calculation is complicated and time-consuming, which is not benefit for real-time controlling. It does not good for the accuracy design of this manipulator as well.

At the same time, since every output parameter (x, y, γ) of moving platform 1 is related to all of three input angles θ_1, θ_2, and θ_3, the manipulator does not possess I-O motion decoupling, which is also undesirable for path planning and motion controlling.

B. Topological Optimization Design of the Structure

In order to improve the two disadvantages stated above, we implement an optimization design for topological structure of this manipulator. Based on the coupling-reducing principle of mechanism topology [13], we combine two arbitrary pairs on the movable platform, such as R_{13} and R_{33} in the Fig. 1, into one multiple joint, and other conditions are not changed, which lead to a modified manipulator shown in the Fig. 2.

For the modified manipulator, moving platform 1 has degenerated from three-joint rod to two-joint rod, i.e., R_3R_{23}. Its topological analysis can be decomposed into following:

$$SOC_1\{-R_{11}-R_{12}-R_3-R_{32}-R_{31}-\}$$

$$\Delta_1=\sum_{i=1}^{5} f_i - I_1 - \xi_{L_1} = 5-2-3=0$$

$$SOC_2\{-R_{21}-R_{22}-R_{23}-R_3-\}$$

$$\Delta_2=\sum_{i=1}^{3} f_i-I_2-\xi_{L_2}=4-1-3=0$$

Therefore, $k=\frac{1}{2}\sum_{j=1}^{2}\left|\Delta_j\right|=\frac{1}{2}(|0|+|0|)=0$

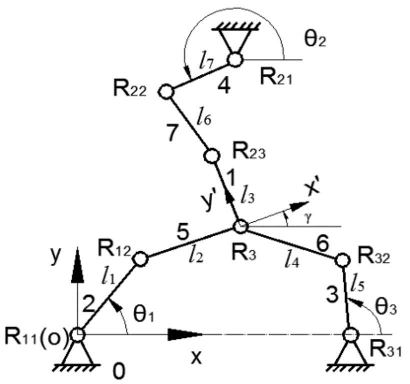

Fig 2. 3-dof coupling-reducing mechanism (CRM)

It means that the coupling degree of this modified manipulator is reduced form one to zero, and its analytic expression of direct kinematics can be directly and conveniently obtained. Meanwhile, the modified manipulator is now already I-O motion decoupled. The concrete analysis is as follows. We called the modified manipulator as coupling-reducing mechanism (CRM).

3. Kinematic Analysis of CRM

A. Direct Kinematics

The problem of the direct kinematics can be described as: with three known input angles θ_1, θ_2, and θ_3, it is required to solve the attitude angle γ and position (x, y) of revolute joint R_3 of the moving platform 1.

The static coordinate system *o-xy* is shown in Fig. 2, which is the same with it in Fig. 1. The moving coordinate system R_3-$x'y'$ are established on R_3, y' axis that coincides with the line R_3R_{23}. x' axis is perpendicular to this line. The attitude angle γ of the moving platform 1 is taken from forward direction of x' axis to x as well. The coordinates R_{11}, R_{21}, R_{31} are not changed such that (0,0), (l_9,l_{10}), (l_8,0) , respectively. When input angles θ_1, θ_2 and θ_3 are given, the coordinates of joints R_{12}, R_{22}, and R_{32} are easily got.

- Solve the coordinates of R_3 by using the positions of R_{12} ,R_{32}

  Based on $R_{12}R_3=l_2$, $R_{32}R_3=l_4$,

$$\begin{cases}(x_{R_3}-x_{R_{12}})^2+(y_{R_3}-y_{R_{12}})^2=l_2^2\\(x_{R_3}-x_{R_{32}})^2+(y_{R_3}-y_{R_{32}})^2=l_4^2\end{cases}$$

  It is obtained

$$\begin{cases}x_{R_3}=\dfrac{-E\pm\sqrt{E^2-4DF}}{2D}\\y_{R_3}=\dfrac{C}{B}-\dfrac{A}{B}x_{R_3}\end{cases}\qquad(1)$$

where

$$A=2(l_1\cos\theta_1-l_8-l_5\cos\theta_3),$$
$$B=2(l_1\sin\theta_1-l_5\sin\theta_3),$$
$$C=l_4^2-l_2^2+l_1^2-l_8^2-l_5^2-2l_5l_8\cos\theta_3,$$
$$D=A^2+B^2,$$
$$E=2l_1AB\sin\theta_1-2l_1B^2\cos\theta_1-2AC,$$
$$F=C^2+l_1^2B^2-2l_1BC\sin\theta_1-l_2^2B^2.$$

- Solve the coordinate of R_{23} by using the positions of R_{22}, R_3

  Based on $R_{23}R_3=l_3$, $R_{22}R_{23}=l_6$

$$\begin{cases}(x_{R_3}-x_{R_{23}})^2+(y_{R_3}-y_{R_{23}})^2=l_3^2\\(x_{R_{23}}-x_{R_{22}})^2+(y_{R_{23}}-y_{R_{22}})^2=l_6^2\end{cases}$$

  We have

$$\begin{cases}x_{R_{23}}=\dfrac{-e\pm\sqrt{e^2-4df}}{2d}\\y_{R_{23}}=\dfrac{c}{b}-\dfrac{a}{b}x_{R_{23}}\end{cases}\qquad(2)$$

Here,

$$a=2(x_{R_3}-l_9-l_7\cos\theta_2),$$
$$b=2(y_{R_3}-l_{10}-l_7\sin\theta_2),$$
$$c=l_6^2-l_3^2+x_{R_3}^2+y_{R_3}^2-l_9^2-l_7^2-l_{10}^2$$
$$-2l_{10}l_7\sin\theta_2-2l_9l_7\cos\theta_2,$$
$$d=a^2+b^2,$$
$$e=2y_{R_3}ab-2x_{R_3}b^2-2ac,$$
$$f=c^2+(x_{R_3}^2+y_{R_3}^2-l_3^2)b^2-2y_{R_3}bc.$$

Then, attitude angle γ is expressed as

$$\tan\gamma=(y_{R_{23}}-y_{R_3})/(x_{R_{23}}-x_{R_3})\qquad(3)$$

According to Eq.(1), the position of the moving platform 1, i.e., (xR3, yR3), is confirmed by two input angles θ1, θ3. It is also known from Eq. (3) that attitude angle γ is confirmed by three input angles θ1, θ2, and θ3. Therefore, the CRM possess *I-O* partial motion decoupling property. Consequently, it is easier to conduct path planning and motion control of the CRM compared with the typical manipulator.

B. *Inverse Kinematics*

The problem of the inverse kinematics analysis is described as for given attitude angle γ and position (x, y) of joint R_3 of moving platform 1, it is required to solve three input angles θ_1, θ_2, θ_3.

In the moving coordinate system R_3-$x'y'$, the coordinate of R'_{23} is (0, l_3). Through the coordinate system conversion between the static and moving coordinate one, the coordinate of R_3 is

$$\begin{bmatrix} x_{R_{23}} \\ y_{R_{23}} \end{bmatrix} = \begin{bmatrix} \cos\gamma & -\sin\gamma \\ \sin\gamma & \cos\gamma \end{bmatrix} \begin{bmatrix} 0 \\ l_3 \end{bmatrix} + \begin{bmatrix} x \\ y \end{bmatrix} = \begin{bmatrix} -l_3\sin\gamma + x \\ l_3\cos\gamma + y \end{bmatrix}$$

Based on $R_{12}R_3=l_2$, $R_{32}R_3=l_4$, $R_{22}R_{23}=l_6$, three constraint equations can be expressed as

$$(x_{R_{12}} - x_{R_3})^2 + (y_{R_{12}} - y_{R_3})^2 = l_2^2 \tag{4}$$

$$(x_{R_{22}} - x_{R_{23}})^2 + (y_{R_{22}} - y_{R_{23}})^2 = l_6^2 \tag{5}$$

$$(x_{R_{32}} - x_{R_3})^2 + (y_{R_{32}} - y_{R_3})^2 = l_4^2 \tag{6}$$

According to Eqs.(4)~(6), the inverse kinematic for the CRM can be expressed as

$$\theta_i = 2\arctan\frac{A_i \pm \sqrt{A_i^2 + B_i^2 - C_i^2}}{B_i - C_i}\text{, } i\text{=1, 2, 3} \tag{7}$$

Here,

$$A_1 = 2y_{R_3}l_1\text{ ; } B_1 = 2x_{R_3}l_1,$$

$$C_1 = l_2^2 - l_1^2 - x_{R_3}^2 - y_{R_3}^2,$$

$$A_2 = 2y_{R_{23}}l_7 - 2l_{10}l_7,$$

$$B_2 = 2x_{R_{23}}l_7 - 2l_9l_7,$$

$$C_2 = l_6^2 + 2x_{R_{23}}l_9 + 2y_{R_{23}}l_{10} - l_7^2 - l_9^2 - l_{10}^2 - x_{R_{23}}^2 - y_{R_{23}}^2,$$

$$A_3 = 2y_{R_3}l_5\text{ ; } B_3 = 2x_{R_3}l_5 - 2l_8l_5,$$

$$C_3 = l_4^2 + 2x_{R_3}l_8 - l_5^2 - l_8^2 - x_{R_3}^2 - y_{R_3}^2.$$

C. Numerical Examples

As shown in Fig. 2, the structural parameters, based on *Ref.*[4], of the CRM are shown as follows.

$l_1 = l_5 = l_7 = 400$, $l_8 = 600$, $l_2 = l_3 = l_4 = l_6 = 300$, $l_9 = 1054.1$, $l_{10} = 1045.4$ (units: *mm*).

Three input angles θ_1, θ_2, and θ_3 are 60°, 240°, 70°, respectively. The substitution of the known parameters into Eqs.(1)~(3) gives two sets direct kinematics solutions shown in Tab 1.

Tab 1. Direct kinematics of the CRM

	x	y	γ
I	461.1	494.1	-104.8544°
II	461.1	494.1	-20.0847°

It is easy to verify the correctness of these direct kinematics solutions by using the inverse kinematic Eq. (7). It is omitted for the limited space.

D. Workspace Analysis

- Reachable workspace

Reachable workspace is reachable area of a moving platform. It is one of main performance indexes to evaluate the kinematic performances of manipulator [8].

The CRM is derived from 3-RRR manipulator by combining two revolute joints R_{13} and R_{33}, and length of other links does not change at all. According to the structural parameters of [10], lengths of the CRM are as follows.

$l_1 = l_5 = l_7 = 200$, $l_2 = l_4 = l_6 = 200$, $l_3 = 100\sqrt{3}$, $l_8 = 300$, $l_9 = 150$, $l_{10} = 150\sqrt{3}$ (units：*mm*).

Through programming computation on MATLAB, the reachable workspace acreage of 3-RRR typical manipulator is $3.5868\times10^7 mm^2$, and its shape is shown in Fig.3 (*a*).The reachable workspace area of the CRM is $2.6095\times10^7\ mm^2$, and its shape is shown in Fig.3 (*b*).

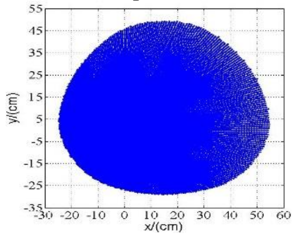

(*a*) Workspace of 3-RRR manipulator

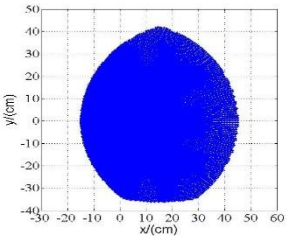

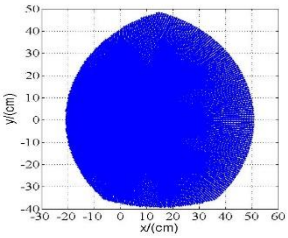

(*b*) Workspace of the CRM (*c*) Workspace of the CRM with modifying a link length

Fig 3. Reachable Workspace comparison between the CRM and typical mechanism

It is easy from the Fig.3 to find that the area of the CRM is 27.25% less than typical manipulator. However, reachable workspace of the CRM can be improved and became larger by means of increasing some link lengths. For instance, when length of the links 2,3,4,5,6, and 7 are increased to one-sixth of the length of link 1, i.e., l_3/6, the area of the CRM will be $3.7948\times10^7 mm^2$, for which the incremental of about 5.52% is made more than that of the typical manipulator. Moreover, the shape has symmetry and succession as well, as shown in Fig.3(*c*).

- Dexterous workspace

If the attitude angle can change arbitrarily in the range of 0° to 360° when the moving platform moves, the motion area of base point is called as dexterous workspace [9, 10].

For the 3-RRR typical manipulator shown in Fig.1, the center of the moving platform 1 is taken as the base point *O'*. If the base point *O'* in the range of dexterous workspace, the moving platform 1 can rotate completely around this base point.

We assume that the moving platform 1 is connected with the frame at the point *O'* using the revolute joint $R_{O'}$, and only one constraint chain *i*, *for example*, *i*=1, is considered, one fictitious and subsidiary four-bar linkage $R_{i1}R_{i2}R_{i3}R_{O'}$ is obtained. The length *L* of the frame will change along with the position change of the base point *O'*. But the crank $R_{i3}R_{O'}$ can move completely around the joint $R_{O'}$. The structural parameters of this subsidiary four-bar linkage are given as follows.

$R_{i1}R_{i2}=L_1$, $R_{i2}R_{i3}=L_2$, $R_{i3}R_{O'}=L_3$, $R_{i1}R_{O'}=L$.

Based on the crank existence conditions of the four-bar linkage, the range of length *L* can be taken as

$$L=(0,r_1]\cup[r_2,r_3]) \qquad (8)$$

where $r_1=L_3-(L_1-L_2)$, $r_2=(L_1-L_2)+L_3$, $r_3=(L_1+L_2)-L_3$.

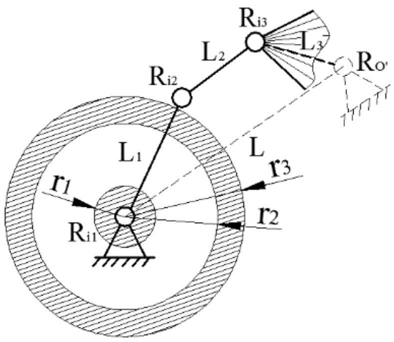

Fig. 4. Dexterous workspace in the constraint of branded chain *i*

If taking R_{i1} as center of a circle and r_1, r_2, r_3 as radius, three circles can be drawn respectively. Then, the base point *O'* locates inside the circle area of between radius r_2 and r_3 or the circle with a radius of r_1, i.e., the shadow area shown in Fig.4, which is denoted by I_i.

When we consider the combined action of three chains I_1 , I_2 *and* I_3, dexterous workspace *W* is the intersection workspace that chains I_1, I_2 and I_3 produce together.

For the CRM and its chain 1 and 3, we assign $r_1=r_2=0$, $r_3=400$, and we assign $r_1=r_2=0$, $r_3=300$ for the chain 2.

For 3-RRR manipulator and its three chains, we assign $r_1=r_2=0$, $r_3=300$. Therefore, the dexterous workspaces of the CRM and 3-RRR manipulator are calculated and shown in Fig.5(*a*) and Fig.5(*b*) respectively.

We find that the dexterous workspace area of the CRM and typical mechanism are 8.6567×10^6 mm^2, 6.3429×10^6 mm^2, respectively, and the former is 36.48% bigger than the later.

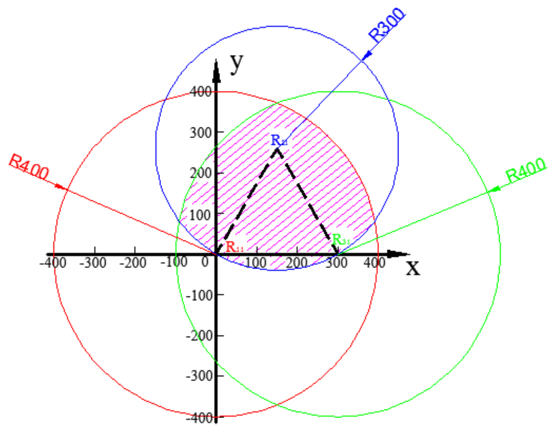

(*a*) Dexterous workspace of the CRM

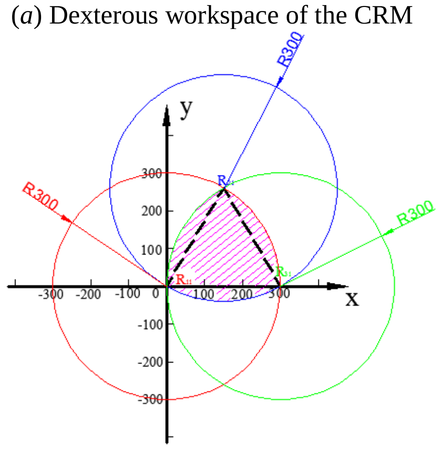

(*b*) Dexterous workspace of the 3-RRR typical manipulator

Fig. 5. Dexterous workspace comparison between the CRM and typical manipulator

E. Singularity Analysis

- Singularity analysis method

If vectors representing all input motions and output motions are denoted by $\boldsymbol{X}$ and $\boldsymbol{Y}$ respectively, the relationship between $\boldsymbol{X}$ and $\boldsymbol{Y}$ can be expressed as following [14].

$$F(\boldsymbol{X},\boldsymbol{Y})=0 \qquad (9)$$

By simplifying and rearranging equation (9), then taking the time derivative of the two sides of the resulting equation, the following equation is obtained.

$$\boldsymbol{J}_p\dot{\boldsymbol{Y}}-\boldsymbol{J}_q\dot{\boldsymbol{X}}=0 \qquad (10)$$

Based on whether $\boldsymbol{J}_P$ and $\boldsymbol{J}_q$ matrix are singular, the singular posture of the mechanism could be classified three types as follows

1. When $\det(\boldsymbol{J}_q)=0$, input singularity happens.
2. When $\det(\boldsymbol{J}_p)=0$, output singularity happens.
3. When $\det(\boldsymbol{J}_q)=\det(\boldsymbol{J}_p)=0$, hybrid singularity happens.

- Calculate of $\mathbf{J}_P$ and $\mathbf{J}_q$ matrix

By taking the time derivative of the two sides of Eqs. (4)~(6), the following equation is obtained.

$$u_{ii}\dot{\theta}_1 - f_{i1}\dot{x} - f_{i2}\dot{y} - f_{i3}\dot{\gamma} = 0,\ i=1,2,3. \quad (11)$$

Hence, $\boldsymbol{V} = [\dot{x} \quad \dot{y} \quad \dot{\gamma}]^T$ is the output speed of the end effector of the mechanism, while $\boldsymbol{\omega} = [\dot{\theta}_1 \quad \dot{\theta}_2 \quad \dot{\theta}_3]^T$ is actuated joint input angle velocity. The relationship between $\boldsymbol{V}$ and $\boldsymbol{\omega}$ is as:

$$\boldsymbol{J}_p\boldsymbol{V} = \boldsymbol{J}_q\boldsymbol{\omega} \quad (12)$$

Where,

$$\boldsymbol{J}_p = \begin{bmatrix} f_{11} & f_{12} & f_{13} \\ f_{21} & f_{22} & f_{23} \\ f_{31} & f_{32} & f_{33} \end{bmatrix};\ \boldsymbol{J}_q = \begin{bmatrix} u_{11} & & \\ & u_{22} & \\ & & u_{33} \end{bmatrix};$$

$$u_{11} = l_1(y_{R_{12}} - y_{R_3})\cos\theta_1 - l_1(x_{R_{12}} - x_{R_3})\sin\theta_1,$$

$$u_{22} = l_7(y_{R_{22}} - y_{R_{23}})\cos\theta_2 - l_1(x_{R_{22}} - x_{R_{23}})\sin\theta_2,$$

$$u_{33} = l_5(y_{R_{32}} - y_{R_3})\cos\theta_3 - l_5(x_{R_{32}} - x_{R_3})\sin\theta_3,$$

$$f_{11} = x_{R_{12}} - x_{R_3},\ f_{12} = y_{R_{12}} - y_{R_3},\ f_{13} = 0,$$

$$f_{21} = x_{R_{22}} - x_{R_{23}},\ f_{22} = y_{R_{22}} - y_{R_{23}},$$

$$f_{23} = l_3(x_{R_{23}} - x_{R_{22}})\cos\gamma + l_3(y_{R_{23}} - y_{R_{22}})\sin\gamma,$$

$$f_{31} = x_{R_{32}} - x_{R_3},\ f_{32} = y_{R_{32}} - y_{R_3},\ f_{33} = 0.$$

- Singularity comparison between the CRM and 3-RRR typical mechanism

(1) Input singularity

When the input singularity happens, the movable platform 1 of this mechanism will lose its motion ability along some directions. This moment, at least one motion chain reaches at the boundary of workspace, and we have

$$\det(\boldsymbol{J}_q) = 0$$

The solution set $\boldsymbol{A}$ of this equation is shown below

$$\boldsymbol{A} = \{\boldsymbol{A}_1 \cup \boldsymbol{A}_2 \cup \boldsymbol{A}_3\} \quad (13)$$

Here

$\boldsymbol{A}_1 = \{(y_{R_{12}} - y_{R_3})\cos\theta_1 - (x_{R_{12}} - x_{R_3})\sin\theta_1 = 0\}$, which means that three points R_{11}, R_{12} and R_3 are collinear.

$\boldsymbol{A}_2 = \{(y_{R_{22}} - y_{R_{23}})\cos\theta_2 - (x_{R_{22}} - x_{R_{23}})\sin\theta_2 = 0\}$, which means that three points R_{23}, R_{22} and R_{21} are collinear.

$\boldsymbol{A}_3 = \{(y_{R_{32}} - y_{R_3})\cos\theta_3 - (x_{R_{32}} - x_{R_3})\sin\theta_3 = 0\}$, which means that three points R_{31}, R_{32} and R_3 are collinear.

When three points R_{11}, R_{12} and R_3 are collinear, link 2 and link 5 have combined into one line 2-5. Then, an imaginary four-bar linkage is denoted by link 0, 2-5, 6 and 3, $\theta_3 = f(\theta_1)$, and θ_2 is also independent input angle. The path of joint R_3 on the moving platform 1 is the part arc with a radius of line 2-5. The length of this arc is determined by the two chains 2 and 3.

However, for the 3-RRR typical manipulator when three points R_{11}, R_{12} and R_{13} are collinear, three input angles are independent each other. Moreover, the motion of moving platform 1 is not restrictive when the joint R_{13} is fixed (Fig.1). The base point O' locates inside the circular ring that is determined by the circular radius $l_{2\text{-}5}+R_{13}O'$ and $l_{2\text{-}5}-R_{13}O'$, the upper and lower boundary of this part annulus are determined by the motion limitation of other two branded chains.

Because of the symmetry, singularity analysis for the case $\boldsymbol{A}_2$ and $\boldsymbol{A}_3$ is similar with that of the above stated.

(2) Output singularity

Under this circumstance, the movable platform 1 still has local motion when all actuated joints are locked. If the movable platform 1 is applied by a limited force, three input links need infinite actuated force to achieve force balance. By this time, we have $\det(\boldsymbol{J}_p) = 0$, the solution of the set $\boldsymbol{B}$ for this equation is shown below

$$\boldsymbol{B} = \{\boldsymbol{B}_1 \cup \boldsymbol{B}_2\} \quad (14)$$

Here,

$\boldsymbol{B}_1 = \{(x_{R_{23}} - x_{R_{22}})\cos\gamma + (y_{R_{23}} - y_{R_{22}})\sin\gamma = 0\}$, which means that three points R_{22}, R_{23} and R_3 are collinear.

$\boldsymbol{B}_2 = \{f_{12}f_{31} - f_{11}f_{32} = 0\}$, which means that three points R_{12}, R_{32} and R_3 are collinear.

Three kinds of the output singular configurations of the CRM are shown in Eq.(14). When the formula $\boldsymbol{B}_1$ is satisfied three points R_{22}, R_{23} and R_3 are collinear. When taking θ_1, θ_3 as the independent input angles, the angle θ_2, i.e., $\theta_2 = f(\theta_1, \theta_3)$, is a dependent input.

However, for 3-RRR typical mechanism, it exists four kinds of singular configurations as follows

1. Four joints R_{12}, R_{13}, R_{33} and R_{32} are collinear.
2. Four points R_{12}, R_{13}, R_{23} and R_{22} are collinear.
3. Four points R_{22}, R_{23}, R_{33} and R_{32} are collinear.
4. Links 5, 6 and 7 intersect at one point outside the moving platform.

For example, when the first kind of singularity of 3-RRR mechanism happens, i.e., case ①, input θ_1, θ_2 are taken as the independent ones, the angle θ_3 is dependent input such as $\theta_3 = f(\theta_1)$.

(3) Synthesis singularity

When $\det(\boldsymbol{J}_q) = \det(\boldsymbol{J}_p) = 0$ is satisfied, the input and output singularity will happen at the same time. For instance, if the equations $\boldsymbol{A}_1$ and $\boldsymbol{B}_1$ are satisfied, three points R_{11}, R_{12} and R_3, and another three points R_{22}, R_{23} and R_3 are collinear respectively.

It is clear that from the discussion above, the hybrid singularity analysis of the CRM is simpler than 3-RRR typical manipulator. This conclusion is obtained respectively by a comprehensive comparison of the input and output singularity of the two mechanisms.

4. Performance Comparison

In a word, the performance comparison of these two mechanisms is shown in Tab 2.

Table 2. Performance comparison of the CRM and 3-RRR typical manipulator

Performance	CRM	3-RRR
k	0	1
Direct kinematics	Analytic	Numerical
I-O decoupling	Yes	No
Reachable workspace	Slightly smaller*	Bigger
Dexterous workspace	Big	Small
Singularity	Simple	Complex

*Note: The size of reachable workspace of CRM could be improved or increased by magnified slightly the length of some links.

By comparing the six aspects such as direct kinematics, coupling degree, decoupling, reachable workspace, dexterous workspace and singularity, it is found that the comprehensive performance of the CRM is superior to that of 3-RRR typical manipulator.

5. Conclusions

Two disadvantages of the typical 3-RRR planar manipulator could be overcome by its topological structure optimization. It leads to the resulting kinematic performance are improved.

(1) The analytical solutions for the direct kinematics of the CRM can be obtained because of k=0. Its path planning, position control, and input-output motion decoupling properties are simpler.

(2) Based on the inverse kinematics, it can be obtained that the reachable workspace of the CRM is symmetric and continuous. Moreover, the dexterous workspace of it is bigger than typical mechanism's.

(3) Three kinds of singular configurations of this CRM are easier to be got. The singularity analysis of this mechanism is simpler than typical mechanism's.

In summary, the comprehensive kinematic performance of the coupling-reduced mechanism is superior. Structural decoupling-reducing is an effective approach for improving topological structure and its kinematic performances

Acknowledgements

This research is sponsored by the NSFC (Grant No. 51375062 and No.51475050), Jiangsu Key Development Project (No.BE2015043) and Jiangsu Scientific and Technology Transformation Fund Project (No. BA2015098).

References

[1] Z. Huang, L. F. Kong and Y. F. Fang, "Theory and control of parallel robot mechanism," BeiJing: China Machine Press, 1997:1-34.

[2] C. Gosselin and J. Merlet, "Direct kinematics of planar parallel manipulators: special architectures and number of solutions," Mechanism and Machine Theory, 1994: 1083-1097.

[3] D. Oetomo, H.C. Liaw, G. Alici and B. Shirinzadeh, "Direct kinematics and analytical solution to 3-RRR parallel planar mechanisms," International Conference on Control, 2006:1-6.

[4] C.M. Gosselin and J. Angeles, "The optimal kinematic design of a planar three-degree-of-freedom parallel manipulator, Journal of Mechanisms," Transmissions and Automation in Design, 1988, 110(3):35 -41.

[5] J. Wu, J.S. Wang and Z. You, "A comparision study on the dynamics of plannar 3-DOF 4-DOF,3-RRR and 2-RRR parallel manipulators," Robotics and Computer-Integrated Manufacturing, 2010, 2011, 27(1): 150-156.

[6] S.-H.Cha, T.A. Lasky and S.A. Velinsky, "Determination of the kinematically redundant active prismatic joint variable ranges of a planar parallel mechanism for singularity-free trajectories," Mechanism and Machine Theory, 44(2009) 1032-1044.

[7] X. Wei and J. Wu, " Dexterity of 3-RRR planar parallel manipulators," Machine tool and Hydraulics, 1001-3881 (2009) 10-051-3.

[8] D.H. Li and S.T. Song, 'Research of the reachable workspace of symmetrical planar 3-RRR parallel mechanism," Journal of Mechanical Transmission, 1004-2539(2015) 09-0029-03.

[9] J.K. Cui, "On the dexterous workspace of 3-RRR planar parallel manipulator," University of Shanghai for Science and Technology, 1007-6735(2005)04-0365-04.

[10] Z.H. Lan and M.W. Su, "Analysis of dextrous workspace and cavity of Planar Parallel Manipulator," Proceedings of the Twelfth National Institute of Institutional Studies, 2000.

[11] F. Gao, X.J. Liu and X. Chen, "The relationships between the shapes of the workspaces and the link lengths of 3-DOF symmetrical planer parallel manipulators," Mechanism and Machine Theory, 36 (2001)205-220.

[12] T. L Yang, A.X. Liu and Y.F Luo, "Theory and application of robot mechanism topology," Beijing: Science Press, 2012.

[13] H.P Shen, L.J. Yang, Q.M. Meng and H.B. Yin, "Topological structure coupling-reducing of parallel mechanisms," The14th IFToMM World Congress, Taipei, Taiwan, October 25-30, 2015.

[14] C. Gosselin and J. Angeles, "Singularity analysis of closed-loop kinematic chain," IEEE International Conference on Robotics and Automation, Cincinna tiohio: Computer Society Press, 1990, 6(3): 281-290.

Proceedings of the International Symposium of Mechanism and Machine Science, 2017
AzC IFToMM – Azerbaijan Technical University
11-14 September 2017, Baku, Azerbaijan

Механизмы параллельной структуры с пятью степенями свободы

В.А.Глазунов, д-р техн. наук, профессор;
А.М.Попов, д-р техн. наук, профессор;
А.Ю.Чунихин, А.В.Антонов, И.А.Орлов.
Институт машиноведения им. А.А.Благонравова
Российской академии наук,
Москва, Россия

Аннотация.

Рассмотрены задачи кинематического и силового анализа технологического робота параллельной структуры, соответствующей пяти степеням свободы. Данный механизм имеет три кинематические цепи, что обусловливает увеличение рабочей зоны за счёт уменьшения возможности взаимных помех между кинематическими цепями.

Работа выполнена в рамках гранта 16-29-04273 офи м. Авторы статьи приносят свою благодарность фонду РФФИ за оказанное содействие в проведении исследований.

Ключевые слова. Механизм параллельной структуры, платформа Гауфа, число степеней свободы.

Создание надежных многофункциональных механизмов и машин обуславливает объективную необходимость поиска эффективных технологических решений в области машиноведения [1, 2].

Как показывают комплексные исследования, проводимые в Институте машиноведения им. А.А. Благонравова Российской академии наук (Москва, Россия), одним из направлений для решения данной задачи является использование технологических механизмов параллельной структуры [3-11].

Такие механизмы имеют несколько кинематических цепей, связывающих основание с выходным звеном – рабочим органом и воспринимают нагрузку подобно пространственным фермам. Этим они отличаются от традиционных механизмов с последовательным расположением звеньев и приводов. Данное обстоятельство обусловливает повышенные показатели механизмов параллельной структуры по точности и грузоподъемности. Поэтому механизмы параллельной структуры нашли широкое применение в качестве технологических, манипулирующих, измерительных и медицинских систем.

Другим преимуществом механизмов параллельной структуры является возможность установить все приводы на основании механизма, что увеличивает их надежность. Кроме того, приводы могут быть установлены вне рабочей зоны, и это, в свою очередь, обусловливает возможность применения этих механизмов в агрессивных средах, а также в аэродинамических трубах.

Первые проекты механизмов параллельной структуры были связаны с использованием платформы Гауфа-Стюарта (гексапод). Как недостаток, эти устройства имели одну избыточную степень свободы, наличие особых положений (сингулярностей) и переменную жёсткость в рабочей зоне. Развитие механизмов рассматриваемого класса привело к увеличению числа степеней свободы, в частности, появлению в них линейных двигателей [12].

В данных устройствах, например, фирмы HERMES [13], имеются двигатели, установленные на основании, а также стержни, передающие движения на выходное звено механизма. Архитектура кинематических цепей, а также ферменная конструкция неподвижного и конечного звеньев, призваны повысить жёсткость при движениях элементов механизма по трём степеням свободы. Кроме того, выходное звено может быть снабжено механизмом, обеспечивающим движение по вертикали, а также вращение вокруг двух горизонтальных осей (трипод).

Одной из перспективных схем механизмов параллельной структуры является механизм технологического робота METROM [14], который представляет собой механизм параллельной структуры с пятью степенями свободы. Данный механизм имеет пять кинематических цепей, причём конечная кинематическая пара каждой цепи расположена по оси шпинделя.

Для эффективного управления механизмом необходимы знания размеров области рабочей зоны и поля скоростей его рабочих элементов.

Статья рассматривает алгоритм определения обобщенных координат и скоростей элементов механизма параллельной структуры с пятью степенями свободы и тремя кинематическими цепями типа METROM;

анализу обобщенных сил, действующих в его приводах.

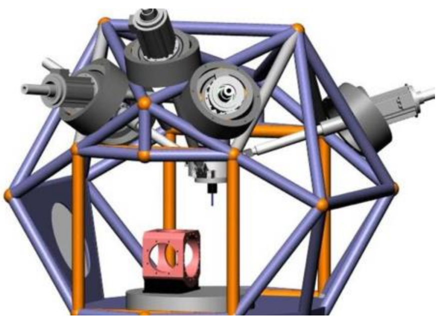

Рисунок 1

Пусть в рассматриваемой схеме механизма известно положение точек B_i, характеризующих основание механизма, точек C_i, расположенных на шпинделе, и длины звеньев C_iA_i. Каждое положение механизма можно задать через два угла поворота вокруг осей Y и Z, и линейное перемещение вдоль осей X,Y,Z.

Для определения обобщенных координат рассмотрим решение обратной задачи для первой кинематической цепи (рис. 2).При этом используем матрицу Денавита-Хартенберга

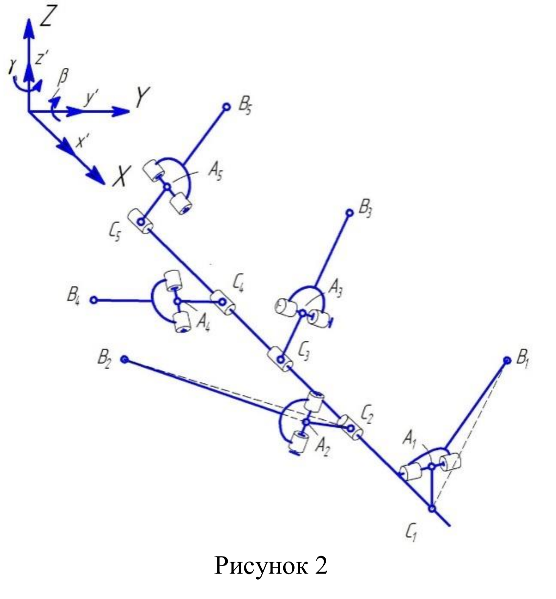

Рисунок 2

преобразования координат, описывающую поворот вокруг осей Y и Z, а также перемещение вдоль осей X, Y, Z [13]

$$\begin{pmatrix} \cos(\gamma)\cdot\cos(\beta) & -\sin(\gamma) & \cos(\gamma)\cdot\sin(\beta) & x \\ \sin(\gamma)\cdot\cos(\beta) & \cos(\gamma) & \sin(\gamma)\cdot\sin(\beta) & y \\ -\sin(\beta) & 0 & \cos(\beta) & z \\ 0 & 0 & 0 & 1 \end{pmatrix} \quad (1)$$

Здесь β и γ – углы поворота выходного звена; x, y, z– координаты центра выходного звена в неподвижной системе координат.

Рассмотрим положение точек A_1и C_1на платформе. Для этого определим координаты оси X' в подвижной системе координат. Имеем:

$$\begin{pmatrix} \cos(\gamma)\cdot\cos(\beta) \\ \sin(\gamma)\cdot\cos(\beta) \\ -\sin(\beta) \end{pmatrix}. \quad (2)$$

Используя матрицу (2), можно определить координаты вектора, соединяющего точки B_1 и C_1, а затем, векторно умножая указанный вектор на орт, направленный вдоль оси X' подвижной системы координат, можно получить координаты оси Y'подвижной координатной системы в неподвижной системе координат (рис.3).

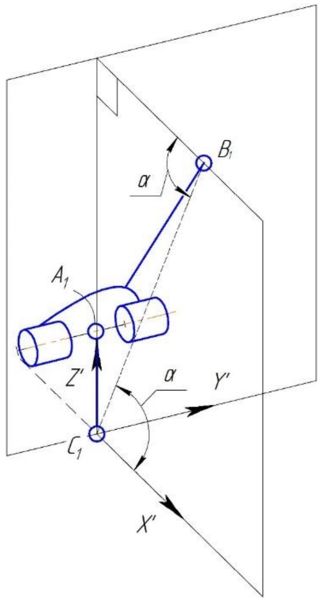

Рисунок 3

С другой стороны, единичный вектор, направленный вдоль оси Y' подвижной системы координат, может быть определен непосредственно из матрицы, описывающей повороты осей координат. В подвижной системе координаты этого единичного вектора равны (0, 1, 0), а в неподвижной системе:

$$\begin{pmatrix} \cos(\gamma)\cdot\sin(\beta)\cdot\sin(\alpha)-\sin(\gamma)\cdot\cos(\alpha) \\ \cos(\gamma)\cdot\cos(\alpha)+\sin(\gamma)\cdot\sin(\beta)\cdot\sin(\alpha) \\ \cos(\beta)\cdot\sin(\alpha) \end{pmatrix} \quad (3)$$

Сравнивая координаты (3), можно получить формулу для вычисления угла α, а затем выразить координаты точки A_1 в неподвижной системе координат. Отсюда, получаем решение обратной задачи о положениях для первой кинематической цепи как квадратный корень из суммы квадратов разностей координат точек A_1 и B_1.

Рассмотрим решение обратной задачи в общем виде для остальных кинематических цепей, которые отличаются от первой цепи. Очевидно, решение отыскивается аналогично решению задачи для первой кинематической цепи до момента определения модуля вектора, проведенного от точки C_1к точке B_1.

Опуская достаточно тривиальные, но громоздкие вычисления изложим алгоритм вычисления остальных координат точек звеньев. Запишем координаты точки B_2 в неподвижной системе координат, а координаты точки C_2 в подвижной системе координат. Далее находим скалярное произведение векторов C_2B_2 и оси X' (рис. 4). Из полученного произведения находим косинус угла φ_2''.

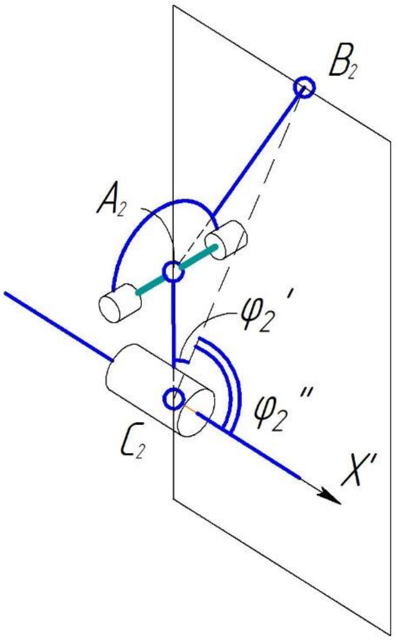

Рисунок 4

Заметим, что угол между A_2C_2 и осью X' равен $\pi/2$. Вычитая из заданного угла величину угла φ_2'', получаем угол φ_2' между линиями C_2B_2 и C_2A_2.

Рассмотрим треугольник $B_2C_2A_2$ (рис.4). Зная в данном треугольнике величины сторон B_2C_2 и C_2A_2, а также угол φ_2' между ними, находим длину B_2A_2 по теореме косинусов:

$$\left|A_2B_2\right| = \sqrt{\left|C_2B_2\right|^2 + \left|A_2C_2\right|^2 - \left|C_2B_2\right| \cdot \left|A_2C_2\right| \cdot \cos\varphi_2')}.$$

Это решение обратной задачи для координат точек второй цепи. Для остальных координат цепей решения совершенно аналогичны.

Рассмотрим плюккеровы координаты силовых винтов, определяемых кинематическими цепями данного механизма. Примем во внимание, что первая кинематическая цепь имеет пять кинематических пар пятого класса, она налагает одну связь на движение выходного звена. Эта кинематическая цепь при зафиксированном приводе соответствует двум силовым винтам, воздействующим на выходное звено.

Можно показать, что один силовой винт действует вдоль оси линейного двигателя, другой силовой винт должен проходить через точку B_1 и быть параллельным оси шарнира, соединяющего данную кинематическую цепь с выходным звеном.

Действительно, искомые силовые винты должны быть сонаправлены с ортами осей неприводных кинематических пар. Таковых кинематических пар четыре (считая все пары одноподвижными). Три кинематические пары – вращательные, пересекающиеся в точке B_1, ещё одна кинематическая пара – также вращательная пересекает точку A_1. Из изложенного следует, что два силовых винта $\boldsymbol{R}_1$,$\boldsymbol{R}_2$, уравновешиваемые реакциями в неприводных парах первой цепи, таковы: один из них проходит через точки B_1 и A_1, а другой параллелен оси шарнира A_1(рис. 2, 5).

В соответствии с изложенным, определим плюккеровы координаты для силовых винтов первой кинематической цепи.

Координаты векторной части первого силового винта $\boldsymbol{R}_1$ определяются как координаты вектора, проведенного из точки B_1 в точку A_1, поделенные на длину указанного вектора. Моментная часть указанного винта определяется как векторное произведение радиус-вектора точки B_1 на только что найденный вектор (векторная часть силового винта).

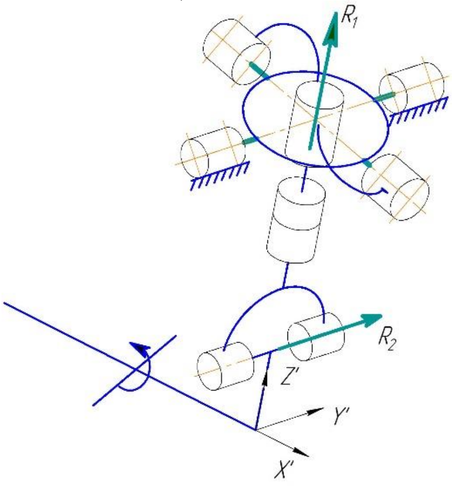

Рисунок 5

Для второго силового винта $\boldsymbol{R}_2$ первые три координаты определяются как координаты оси Y' подвижной системы координат в неподвижной системе координат. Вторые три координаты определяются как векторное произведение радиус-вектора точки B_1 на векторную часть силового винта.

Для второй цепи (рис. 2, 6) определяем вектор $\boldsymbol{R}_3$, являющийся третьим силовым винтом – реакцией. Очевидно, что этот вектор должен проходить через точки B_2 и A_2, так как в этом случае он пересекает оси всех неприводных кинематических пар.

Найдём координаты точки A_2. Для этого рассмотрим (рис. 3 и 5) скалярное произведение вектора, проведенного от точки C_2 до точки B_2, и единичного вектора, проведенного вдоль оси X'. Это произведение выражает проекцию указанного вектора на указанную ось. Соответственно сам указанный вектор может быть представлен как геометрическая сумма произведения данной проекции (скаляр) на единичный вектор оси X' плюс проекция вектора, проведенного от точки C_2 до точки B_2, на ось, перпендикулярную оси X', умноженную на единичный вектор этой оси.

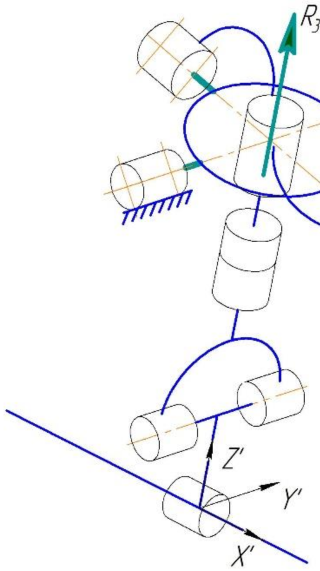

Рисунок 6

Упомянутая ось расположена вдоль вектора, проведенного от точки C_2 до точки A_2. Проекция рассматриваемого вектора на ось звена C_2A_2 равна геометрической разности вектора, проведенного от точки C_2 до точки B_2, и его проекции на ось X'. Зная длину звена C_2 A_2, находим координаты точки A_2.

Определим плюккеровы координаты для единичного силового винта второй цепи. Координаты векторной части определим как координаты вектора, проведенного от точки B_2 к точке A_2, деленные на модуль этого вектора. Моментную часть определим как векторное произведение только что найденного единичного вектора (векторная часть силового винта) и радиус-вектора точки B_2.

Плюккеровы координаты единичных силовых винтов для третьей, четвертой и пятой кинематических цепей найдем аналогичным образом.

На базе найденных плюккеровых координат проведем анализ скоростей механизма. Основываясь на зависимости между углами β, γ и углом α, можно вывести соотношение между производными от этих величин. Угол αвыражен через углы β и γ при решении задачи о положениях (см. рис. 3). Взаимосвязь между этими углами определена тем, что точки A_1, B_1, и C_1 лежат в плоскости, перпендикулярной оси Z' подвижной системы координат. Указанная зависимость может быть выражена в виде неявной функции

$$F(\alpha, \beta, \gamma) = 0,$$

которая зависит от параметров механизма и положения выходного звена.

Взяв частные производные от этой функции, можно выразить скорость изменения углаα через скорости изменения углов β и γ:

$$d\alpha/dt = -[(dF/d\beta)\,(d\beta/dt) + (dF/d\gamma)\,(d\gamma/dt)]/(dF/d\alpha).$$

Укажем на взаимосвязь между скоростями изменения углов α, β, γ и проекциями ω_x, ω_y, ω_z вектора угловой скорости на оси неподвижной системы координат. Последовательность поворотов от подвижной системы координат к неподвижной производится через уравнение [2]:

$$\begin{pmatrix} \dot{\alpha} \\ \dot{\beta} \\ \dot{\gamma} \end{pmatrix} = \begin{pmatrix} \cos(\beta)\cdot\cos(\gamma) & -\sin(\gamma) & 0 \\ \cos(\beta)\cdot\sin(\gamma) & \cos(\gamma) & 0 \\ -\sin(\beta) & 0 & 1 \end{pmatrix} \cdot \begin{pmatrix} \omega_X \\ \omega_Y \\ \omega_Z \end{pmatrix}.$$

Отсюда, по известным скоростям изменения углов α, β и γ найдем проекции угловой скорости на оси неподвижной системы координат:

$$\begin{pmatrix} \omega_X \\ \omega_Y \\ \omega_Z \end{pmatrix} = \begin{pmatrix} \dfrac{\cos\gamma}{\cos\beta} & \dfrac{\sin\gamma}{\cos\beta} & 0 \\ -\sin\gamma & \cos\gamma & 0 \\ \cos\gamma\cdot \mathrm{tg}\beta & \sin\gamma\cdot \mathrm{tg}\beta & 1 \end{pmatrix} \cdot \begin{pmatrix} \dot{\alpha} \\ \dot{\beta} \\ \dot{\gamma} \end{pmatrix}.$$

Зная скорости изменения углов α, β, γ, можно определить проекции вектора угловой скорости на координатные оси неподвижной системы.

Заметим, что эти проекции будут соответствовать трём плюккеровым координатам кинематического винта выходного звена. Другие три плюккеровы координаты (моментная часть кинематического винта) определятся как проекции линейной скорости центра подвижной системы координат выходного звена на координатные оси неподвижной системы. В результате будем иметь винтовое уравнение в матричном виде:

$$(E)(\Omega) = (\dot{q}),$$

здесь *(Ω)* – кинематический винт выходного звена, *(E)* – матрица плюккеровых координат силовых винтов, передаваемых кинематическими цепями, $(\dot{q})$ – вектор обобщённых скоростей в приводах.

Зададим вектор обобщённых скоростей. Будем иметь ввиду, что вторая обобщённая скорость равна 0. Это связано с тем, что в первой кинематической цепи имеют место два силовых винта. Один из них обусловлен связью, налагаемой этой цепью. Поэтому обобщённой скорости в данном случае нет.

Рассмотрим силовой анализ. Для этого нужно взять транспонированную матрицу плюккеровых координат, а затем разложить силовой винт, действующий на выходное звено, по этим плюккеровым координатам.

Для определения сил, действующих в приводах, нужно матрицу, обратную транспонированной матрице плюккеровых координат, умножить на вектор координат силового винта, действующего на выходное звено.

Таким образом, в данной статье решена задача о положениях для механизма параллельной структуры с пятью степенями свободы типа METROM. Определены плюккеровы координаты силовых винтов, действующих со стороны кинематических цепей на выходное звено, решена задача о скоростях и проведен силовой анализ.

Литература:

1. Ганиев Р.Ф. Проблемы механики машин и технологий. Перспективы развития Института машиноведения им. А.А. Благонравова РАН. // Проблемы машиностроения и надежности машин. 2010. № 1. С. 3-20.
2. Пространственные механизмы параллельной структуры. / В.А. Глазунов, А.Ш. Колискор, А.Ф. Крайнев – М.: Наука, 1991 – 95 с.
3. Глазунов В.А., Чунихин А.Ю. Развитие механизмов параллельной структуры. // Проблемы машиностроения и надежности машин. 2014. № 3. С. 37-43.
4. Хейло С.В., Глазунов В.А., Ширинкин М.А., Календарев А.В. Возможные применения механизмов параллельной структуры. // Проблемы машиностроения и надежности машин. 2013, № 5, с. 19-24.
5. Данилин П.О., Тывес Л.И., Глазунов В.А. Групповая кинематическая развязка двигателей в механизмах параллельной структуры. // Проблемы машиностроения и надежности машин. 2010, № 3, с. 27-35.
6. Глазунов В. А., Чунихин А. Ю. Определение числа степеней свободы пространственных механизмов для технологического оборудования. // Справочник. Инженерный журнал. 2014. № 12. С. 29-34.
7. Хейло С.В., Ширинкин М.А., Глазунов В.А. Определение собственных частот манипулятора параллельной структуры. // Известия ВУЗов. Технология текстильной промышленности. 2011. № 4. С. 120-123.
8. Рашоян Г.В., Ласточкин А.Б., Глазунов В.А. Кинематический анализ пространственного механизма параллельной структуры с круговой направляющей. // Проблемы машиностроения и автоматизации. 2014. № 2. С. 20-26.
9. Демидов С.М., Глазунов В.А., Ласточкин А.Б., Артеменко Ю.Н. Анализ углов давления и особых положений модулей параллельной структуры, предназначенных для механизмов относительного манипулирования. // Проблемы машиностроения и надежности машин. 2011, № 5, с. 11-20.
10. Патент № 2478464 Российская Федерация. B25J9/00. Модульная робототехническая технологическая установка. / Глазунов В.А., Ковалев В.Е., Левин С.В., Сухоруков Р.Ю., ШалюхинК.А.;, Оп. 10.04.2013. Бил. №10.
11. Патент № 115709 Российская Федерация. B25J 9/00. Робототехническая технологическая установка. / Глазунов В.А., Ковалев В.Е., Левин С.В., Сухоруков Р.Ю., Шалюхин К.А.; Оп. 10.05.2012. Бил. №13.
12. Металлорежущий станки: учебник. В 2-х т. / Т.М. Авраамова, В.В. Бушуев, Л. Я. Гиловой и др.; под ред. В.В. Бушуева. Т.2 – М.: Машиностроение, 2011.-586 с.; ил.
13. Lopez de Lacalle L. N., Lamikiz A. Machine Tools for High Performance Machining / Springer-Vergal London Limited, 2009-P. 435.
14. ПатентГермании № WO 03/037562 A1. Device for the displacement and/or positioning of an object in five axes / МПК B23Q 1/54, опубликован 08.05 2003.

Proceedings of the International Symposium of Mechanism and Machine Science, 2017
AzCIFToMM – Azerbaijan Technical University
11-14 September 2017, Baku, Azerbaijan

Исследование линейной скорости конусного дезинтегратора

[1]Яруллин Мунир Гумерович*, [2]Хабибуллин Фаниль Фаргатович

[1, 2] Казанский национальный исследовательский технический университет им. А.Н. Туполева-КАИ (КНИТУ-КАИ), г.Казань, ул.Карла Маркса, д.10,
[1]yarullinmg@yahoo.com*, [2]fanil_arsk@mail.ru

Abstract
Researched the parameters of the linear velocity of the characteristic points of the working body. Defined the values of the linear velocity on techniques: analytical calculations, CAD/CAE analysis, experimental measurements. Analyzing the values of extreme points obtained by all three methods.
Ключевые слова: механизм Беннетта, параллелограмм, антипараллелограмм, линейная скорость, точка экстремума.

Введение

Конусный дезинтегратор дробления, имеющий в приводе паралеллограмм и антипаралеллограмм Беннетта (см. рис. 1) [1], в отличии от дезинтегратора [2] за счет неравномерного вращения ведомых кривошипов [3-7] обеспечивает более качественное и эффективное дробление материала.

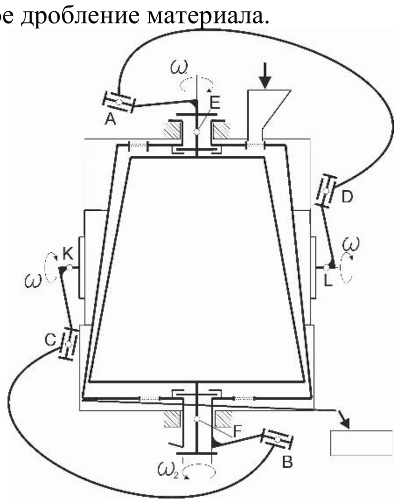

Рис. 1. Структурная схема дезинтегратора неравномерного дробления

Изучение параметров линейной скорости характерных точек конусов как одного из основных факторов, влияющих на процесс дробления [8], является весьма актуальной.

Линейные скорости и их свойства можно определить по следующим методам:

1. Аналитические расчеты;
2. CAD/CAE анализ;
3. Экспериментальные измерения.

С целью обеспечения точности и адекватности сравниваемых результатов указанными выше методами, введем понятие «характерные точки», расположенные на образующей линии конуса через фиксированнные расстояния. Для удобства технических измерений, в наших исследованиях характерные точки приняты согласно рисунку 2, причем l_1=15 мм, l_2=90 мм, l_3=115 мм и, соответственно, r_1=60 мм, r_2 =57,19 мм, r_3 =45,9 мм, а также частоту вращения ведомого звена принимаем n=120 об/мин. Угловая скорость определяется по формуле (1):

$$w = \frac{2\pi n}{60} = \frac{2\cdot 3{,}14159\cdot 120}{60} = 12{,}566 \text{ рад/с.} \quad (1)$$

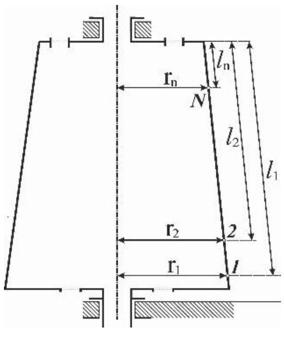

Рис. 2. Координаты расположения характерных точек на рабочем конусе

Метод аналитических расчетов

Значение средней линейной скорости на выбранных характерных точках определяется по формуле 2:

$$V_{n-mid}^{th} = w\cdot r_n \quad (2)$$

где w - углавая скорость конуса, рад/с;
r_n - радиус конуса на характерной точки, мм.

$V_{1-mid}^{th} = w \cdot r_1 = 12,56 \cdot 0,06 = 0,7536$ м/с =753,6 мм/с;
$V_{2-mid}^{th} = w \cdot r_2 = 12,56 \cdot 0,057 = 0,717$ м/с = 717,1 мм/с;
$V_{3-mid}^{th} = w \cdot r_3 = 12,56 \cdot 0,046 = 0,576$ м/с = 576,5 мм/с.

Метод CAD/CAE анализа

Рассмотрим компьютерную модель, в которой вращательное движение от ведущего звена к ведомому звену передается через механизм Беннетта. Ведущий кривошип вращается со скоростью 120 об/мин. Определяем поступательную скорость на поверхности конуса при r_1=60 мм, r_2 =57,19 мм, r_3 =45,9 мм. CAD/CAE анализ позволяет получить график изменений линейных скоростей в характерных точках (см. рис.3).

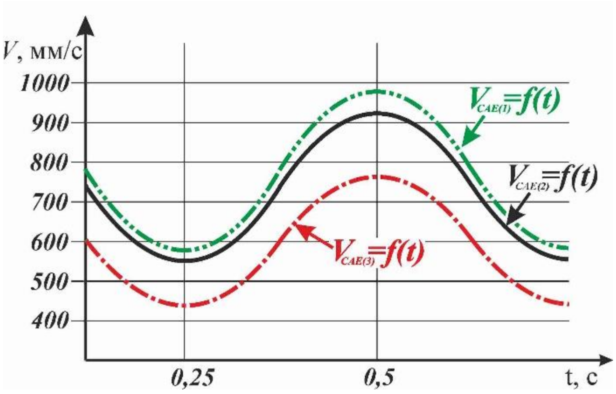

Рис. 3. График изменений линейных скоростей в характерных точках

Анализ графика изменений линейных скоростей показывает, что ведомый кривошип вращается с переменной скоростью. Максимальная линейная скорость харектерной точки при радиусе r=60 мм равна 984 мм/с, минимальная линейная скорость 580 мм/с. Среднее значение линейной скорости определяется по формуле (3):

$$V_{1-mid}^{CAE} = \frac{V_{1-max}^{CAE} + V_{1-min}^{CAE}}{2} \qquad (3)$$

Аналогичным способом определяются параметры линейной скорости при r_2 =57,19 мм, r_3 =45,9 мм (см. табл. 1).

Таблица 1. Значения линейных скоростей, полученных CAD/CAE анализом

l_n , мм	r_n , мм	V_n^{CAE} , мм/с		V_{n-mid}^{CAE} , мм/с
115	60	max	984	782
		min	580	
90	57,19	max	936	746
		min	556	
15	45,9	max	750	598
		min	446	

Таблица 2. Значения линейных скоростей, полученных экспериментальным путем

l_n , мм	V_n^{exp} , м/мин		V_n^{exp} , мм/с	V_{n-mid}^{exp} , мм/с
115	max	50,02	833,666	791,616
	min	44,974	749,566	
90	max	48,38	806,333	765,333
	min	43,46	724,333	
15	max	39,59	659,833	630,849
	min	36,112	601,866	

Таблица №3. Значения линейных скоростей, полученных аналитическим, CAD/CAE и экспериментальным методами

l_n , мм	V_{n-mid}^{th} ,мм/с	V_n^{CAE} , мм/с		V_n^{exp} /, мм/с	
		max/ min,	mid	max/ min,	mid
115	753,6	984	782	833,666	791,616
		580		749,566	
90	717,1	936	746	806,333	765,333
		556		724,333	
15	576,5	750	598	659,833	630,849
		446		601,866	

Метод экспериментальных измерений

Измерения линейной скорости поверхности внешнего конуса производились для тех же характерных точек, т.е. при l_1=15 мм, l_2=90 мм, l_3=115 мм, при соответствующих им радиусах r_1=60 мм, r_2 =57,19 мм, r_3 =45,9 мм. При измерениях цифровой тахометр АТТ-6001 показывал: максимальную V_{n-max}^{exp}, минимальную V_{n-min}^{exp} и среднюю линейную V_{n-mid}^{exp} скорости, м/мин.

С целью получения более точного среднего суммарного значения максимальных и минимальных параметров линейной скорости на каждой характерной точке, измерения проводились пятикратной повторяемостью. Полученные параметры представлены в таблице 2.

Анализ полученных данных

Для анализа и сравнения результатов исследуемых линейных скоростей, полученных выше указанными методами, приведена таблица №3 и рисунки 4,5.

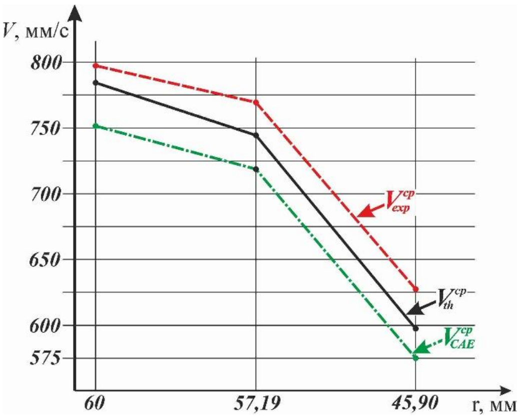

Рис. 4. График изменений средней линейной скорости в зависимости от радиуса характерных точек на поверхности конуса

На графике изменений средней линейной скорости по вертикальной оси представлены параметры линейной скорости (мм/с), по горизонтальной оси представлены параметры радиуса внешнего конуса (мм). Небольшая разница между средними значениями характерных точек теоретических, компьютерных и экспериментальных данных подтверждает достоверность полученных результатов.

Максимальные и минимальные параметры (экстремумы) линейной скорости неравномерного вращения компьютерной модели должны совпадать с соответствующими максимальными и минимальными параметрами, полученными экспериментальным путем.

$$\Delta w_{n-max} = w^{CAE}_{n-max} - w^{exp}_{n-max} \Rightarrow 0$$

$$\Delta w_{n-min} = w^{CAE}_{n-min} - w^{exp}_{n-min} \Rightarrow 0$$

На основе параметров, полученных при r_1=60 мм, построен график точек экстремумов, приведенный на рисунке 5.

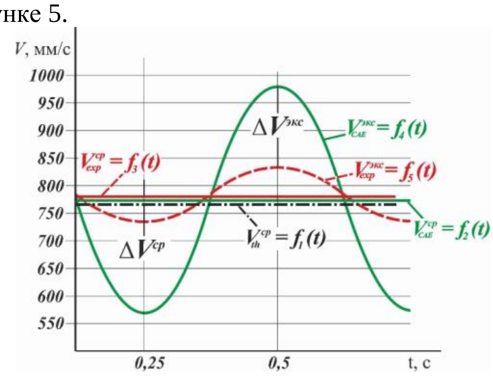

Рис. 5. График, построенный на значениях экстремума для характерной точки r_1=60

На графике по вертикальной оси представлена поступательная скорость в мм/с, а по горизонтальной оси представлено время в секундах с учетом, что ведомое звено за 0,5 секунду совершает один полный оборот.

Анализ графиков скоростей представленных на рисунке 4 показывает, что максимальная разница между средними значениями скоростей равна 38 мм/с, что составляет не более 4,92% относительной погрешности. Разница между значениями экстремума (максимальные, минимальные) составляет 16,53 % относительной погрешности. Что объяснятся силой инерции конуса, силой инерции звеньев и влиянием неравномерного вращения ведомого звена на ведущее звено.

Уменьшение неравномерности конуса для реальной установки по указанным выше причинам положительно влияет на динамику работы дезинтегратора, тем не менее, неравномерность вращения конуса положительно влияет на динамику процесса разрушения материала. Таким образом, результаты исследования кинематики характерных точек конуса дезинтегратора являются: во-первых, исходным материалом для исследования динамики дробления, режима работы и производительности устройства; во-вторых, подтверждает правильность полученных теоретических, компьютерных и экспериментальных исследований.

Список литературы

[1]. Пат. № 2581487 Российская Федерация МПК B02C 2/10. Дезинтегратор неравномерного дробления/ Яруллин М.Г., Мингазов М.Р., Исянов И.Р., Хабибуллин Ф.Ф. Казанский национальный исследовательский технический университет им. А.Н.Туполева (КНИТУ-КАИ), Регистрационный №2014153937/13 от 29 декабря 2014, опубл. 20.04.2016 Бюл. №11

[2]. Пат. 2538389 Российская Федерация, МПК B02C2/04, B02C13/20. Дезинтегратор /Ярullин М. Г., Хабибуллин Ф.Ф., Исянов И. Р.// заявитель Казанский государственный архитектурно-строительный университет (КГАСУ) Регистрационный № 2013125888/13 от 04 июня 2013 года, опубл. 10.12.2014. Бюл. №1

[3]. Ярullин М.Г., Хабибуллин Ф.Ф. Кинематика двухподвижного дезинтегратора с приводом на базе пространственных 4к-механизмов/ Вестник Казанского государственного технического университета им. А.Н. Туполева. 2015. Т. 71. С. 108-111.

[4]. Yarullin M.G., Khabibullin F.F., Isyanov I.R., Nonlinear crushing dynamics in two-degree of

freedom disintegrator based on the Bennett's linkage. Vibroengineering PROCEDIA, Vol. 8, 2016, p. 477-482.
[5]. Евграфов А.Н. Расчет геометрических и кинематических параметров пространственного рычажного механизма с избыточной связью /А.Н.Евграфов, Г.Н. Петров // Проблемы машиностроения и надежности машин. 2013. No3. с.3-8.
[6]. J. McCarthy, Geometric Design of Linkages, Springer, New York, 2000.
[7]. Rasim İ.Alizade et. al., 2014, Function Systhems of Bennet 6R Mechanisms Using Chebyshev Approximation.Elsevier, Mechanism and Machine Theory, Volume 81, pp.62-78
[8]. Яруллин М.Г., Хабибуллин Ф.Ф. Теоретические и практические условия проворачиваемости механизма Беннетта, Материалы 5-й Международной научно-практической конференции «Машиностроение. Наука и образование MMESE-2016». 30.06-01.07.2016, С 306-316.

Кинематика двухподвижного плоского пятизвенного механизма манипулятора

[1]Яруллин Мунир Гумерович*, [2]Исянов Илнур Рафаилевич*

[1, 2] Казанский национальный исследовательский технический университет им. А.Н. Туполева-КАИ (КНИТУ-КАИ), г.Казань, ул.Карла Маркса, д.10,
[1]yarullinmg@yahoo.com*, [2]isyanov1993@mail.ru

Abstract
The mathematical model of the kinematics of a planar five-link mechanism with two degrees of freedom. Shown the equations describing the velocity and acceleration of the characteristic points of the mechanism. Determined velocity and acceleration characteristic points E and K by using the system of symbolic calculations and CAD/CAE analysis. The results obtained kinematics in the form of graphs.

Ключевые слова: пятизвенные рычажные механизмы, двухподвижность, кинематика, манипуляторы.

Введение

Одним из путей совершенствования современных машин является применение в них механизмов, имеющих улучшенные кинематические параметры (характеристики). Широкое использование в технике получили плоские одноподвижные рычажные механизмы. Использование же плоских двухподвижных рычажных механизмов в качестве базового механизма различных мехатронных устройств и манипуляторов является весьма перспективным.

Структура и подвижность

Рассмотрим структурную схему двухподвижного плоского рычажного пятизвенного механизма (рис.1). Он образован на основе известного шарнирного четырехзвенника путем образования в шарнире ***A*** соосных двух вращательных пар вместо одной и превращения в стойку вал этих кинематических пар [1]. Таким образом, в новом механизме по сравнению одноподвижным четырёхзвенником имеем: первое звено остается ведущим кривошипом, шатун 2 остается шатуном, звено 3 – балансир становится шатуном, звено 4 со стойки превращается во второй ведущий кривошип, а вал соосных вращательных кинематических пар в шарнире ***A*** образуется в стойку.

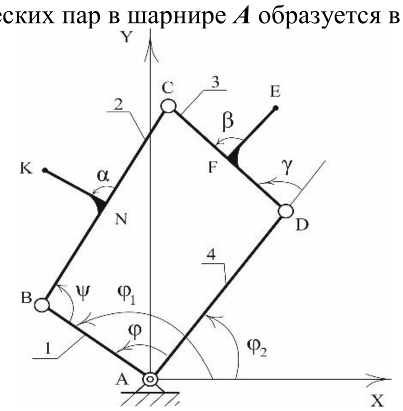

Рис. 1. Плоский двухподвижный пятизвенный рычажный механизм

Степень свободы, полученного механизма определяется по формуле Чебышева и будет равна

$$W = 3(m-1) - 2p_1 - p_2, \qquad (1)$$

где m – число звеньев; p_1-число высших (одноподвижных) кинематических пар; p_2-число низших пар.

Тогда имеем:

$$W = 3(5-1) - 2\times 5 = 2.$$

Поскольку механизм имеет два ведущих звена, его кинематика весьма сложна и интересна, поэтому использование его свойств в манипуляторах и в различных устройствах [2-5] является перспективным. Для практического использования этого механизма наиболее интересными являются наиболее отдаленные характерные точки – $\boldsymbol{E}$ и $\boldsymbol{K}$, на которых могут быть установлены рабочие органы. Поскольку двухподвижный пятизвенный рычажный механизм образован замкнутой кинематической цепью и имеет два входных звена: входными звеньями его являются ведущий кривошип 1 и ведущий стержень 4. Функции положения звеньев и характерных точек механизма определяются от входных координат φ_1 и φ_2(рис.2), которые представлены как функции от времени $\varphi_1(t)$ и $\varphi_2(t)$ [6].

Кинематика манипулятора

Для нахождения скоростей и ускорений необходимо решить задачу определения положений характерных точек механизма. Поскольку эти кинематические параметры являются справочным материалом для дальнейших исследований, прежде всего динамики, как механизма, так и технологических процессов устройства на базе этого двухподвижного пятизвенного рычажного механизма. Задача решается, если звенья стержневых механизмов заменить соответствующими векторами и на их основе построить векторный контур. Векторная интерпретация звеньев механизма изображена на рис. 2.

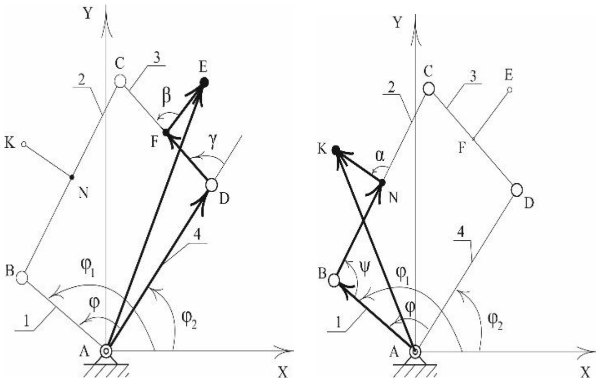

а) б)

Рис. 2. Векторные контуры: а) A-D-F-E-A
б) A-B-N-K-A

Рассмотрим замкнутый векторный контур A-D-F-E-A (рис.2а) и спроецируем его на координатные оси OX и OY. Положение характерной точки $\boldsymbol{E}$ будет определяться координатами X_E и Y_E. Тогда векторный контур рассматривается как сумма векторов:

$$\overrightarrow{AD} + \overrightarrow{DF} + \overrightarrow{FE} = \overrightarrow{AE}. \qquad (2)$$

Составим тригонометрические уравнения для кинематического анализа характерной точки E. Спроецируем выражение (2) на оси неподвижной системы координат OXY, учитывая, что $AE_X = X_E$ и $AE_Y = Y_E$:

$$\begin{cases} X_E = AD\cos\varphi_2 + DF\cos(\gamma+\varphi_2) + \\ \quad +FE\cos(\beta+\gamma+\varphi_2)\,; \\ Y_E = AD\sin\varphi_2 + DF\sin(\gamma+\varphi_2) + \\ \quad +FE\sin(\beta+\gamma+\varphi_2)\,. \end{cases} \qquad (3)$$

Для этой системы уравнений (3) примем, что $\varphi_2 = \omega_2 \cdot t$, причем $\omega_2 = const$; а $\beta = 90°$- принято конструктивно для удобства, поскольку отросток FE жестко связан со звеном CD. Угол γ имеет зависимость от входных координат φ_1 и φ_2, где $\varphi = \varphi_1 - \varphi_2$ и вычисляется выражением [4]:

$$\gamma = 2\tan^{-1}\cdot \left(\frac{AB\sin\varphi - \frac{1}{2}BC\sqrt{4 - \frac{(-AB^2 - AD^2 + BC^2 + 2AD\cdot AB\cos\varphi + CD^2)^2}{BC^2\cdot CD^2}}}{AB\cos\varphi + CD - AD - \frac{1}{2}\frac{-AB^2 - AD^2 + BC^2 + 2\cdot AD\cdot AB\cos\varphi + CD^2}{CD}} \right) \qquad (4)$$

Здесь также принято, что $\varphi_1 = \omega_1 \cdot t$ и $\omega_1 = const.$ Значения ω_1 и ω_2 – в расчетах обоснованно берется в зависимости от необходимого технологического режима работы механизма устройства.

Продифференцировав систему уравнений (3) по времени и учитывая, что $\cos\beta = 0$, $\sin\beta = 1$ получим проекции скорости характерной точки $\boldsymbol{E}$ на координатные оси OXY:

$$\begin{cases} V_E^X = AD\,(-\sin\varphi_2)\varphi_2{}' + DF(-\sin\gamma\cos\varphi_2\gamma' + \\ +\cos\gamma\,(-\sin\varphi_2)\varphi_2{}') - DF(\cos\gamma\sin\varphi_2\,\gamma' - \\ -\sin\gamma\cos\varphi_2\,\varphi_2{}') + FE(-\sin\gamma\sin\varphi_2\,\gamma' + \\ +\cos\gamma\cos\varphi_2\varphi_2{}') + FE(\cos\gamma\cos\varphi_2\,\gamma' - \\ -\sin\gamma\sin\varphi_2\varphi_2{}'); \\ V_E^Y = AD\cos\varphi_2\,\varphi_2{}' + DF(-\sin\gamma\sin\varphi_2\,\gamma' + \\ +\cos\gamma\,\cos\varphi_2\varphi_2{}') + DF(\cos\gamma\cos\varphi_2\,\gamma' - \\ -\sin\gamma\sin\varphi_2\varphi_2{}') - FE(-\sin\gamma\cos\varphi_2\gamma' - \\ -\cos\gamma\,\sin\varphi_2\varphi_2{}') + FE(\cos\gamma\sin\varphi_2\,\gamma' + \\ +\sin\gamma\cos\varphi_2\,\varphi_2{}'). \end{cases} \qquad (5)$$

Аналогичным образом получим уравнение проекции ускорения точки $\boldsymbol{E}$:

$$\left\{\begin{array}{l} a_E^X = (V_E^X)' = AD(-cos\varphi_2)({\varphi_2}')^2 + DF(-\cos\gamma \\ \cos\varphi_2(\gamma')^2 + 2\sin\gamma\sin\varphi_2\gamma'{\varphi_2}' - \sin\gamma\cos\varphi_2\gamma'' - \\ \cos\gamma\cos\varphi_2({\varphi_2}')^2 + DF(\sin\gamma\sin\varphi_2\,(\gamma')^2 - 2\cos\gamma \\ \cos\varphi_2\,\gamma'{\varphi_2}' - \cos\gamma\sin\varphi_2\,\gamma'' - \sin\gamma\sin\varphi_2({\varphi_2}')^2) \\ +FE((-\cos\gamma\sin\varphi_2(\gamma')^2 - 2\sin\gamma\cos\varphi_2{\varphi_2}'\gamma' - \\ -\sin\gamma\sin\varphi_2\,\gamma'' - \cos\gamma\sin\varphi_2\,({\varphi_2}')^2) + FE(- \\ -\sin\gamma\cos\varphi_2(\gamma')^2 - 2\cos\gamma\sin\varphi_2\,{\varphi_2}'\gamma' + \\ +\cos\gamma\cos\varphi_2\,\gamma'' - \sin\gamma\cos\varphi_2({\varphi_2}')^2); \\ a_E^Y = (V_E^Y)' - AD\sin\varphi_2({\varphi_2}')^2 + DF(-\cos\gamma\sin\varphi_2 \\ (\gamma')^2 - 2\sin\gamma\cos\varphi_2\,{\varphi_2}'\gamma' - \sin\gamma\sin\varphi_2\,\gamma'' - \\ -\cos\gamma\sin\varphi_2\,({\varphi_2}')^2) - DF(+\sin\gamma\cos\varphi_2(\gamma')^2 + \\ +2\cos\gamma\sin\varphi_2\,{\varphi_2}'\gamma' - \cos\gamma\cos\varphi_2\,\gamma'' + \sin\gamma \\ \cos\varphi_2({\varphi_2}')^2) - FE(-\cos\gamma\cos\varphi_2(\gamma')^2 + 2\sin\gamma \\ \sin\varphi_2\gamma'{\varphi_2}' - \sin\gamma\cos\varphi_2\gamma'' - \cos\gamma\cos\varphi_2({\varphi_2}')^2 \\ +FE(\sin\gamma\sin\varphi_2\,(\gamma')^2 - 2\cos\gamma\cos\varphi_2\,\gamma'{\varphi_2}' - \\ -\cos\gamma\sin\varphi_2\gamma'' - \sin\gamma\sin\varphi_2({\varphi_2}')^2). \end{array}\right. \qquad (6)$$

Поскольку дифференцирование выше указанных тригонометрических уравнений (4-7) является достаточно трудоемким, для решения этих уравнений была использована система символьных вычислений Maple 17 и CAD/CAE анализа в системе SolidWorks [11]. Результаты решений уравнений представлены на графиках, а именно в виде сравнения графиков полученных в двух разных системах вычислений (рис 3).

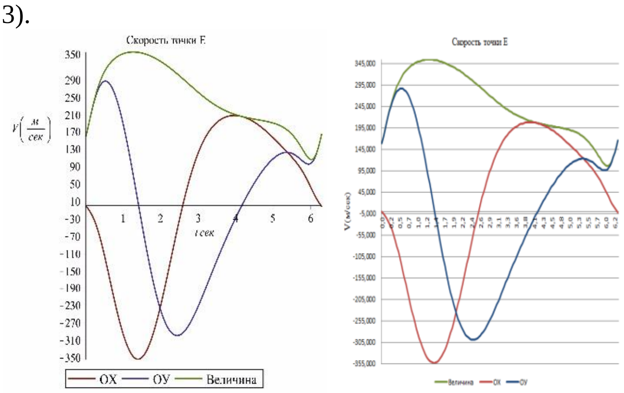

а) б)

Рис.3. Графики скорости характерной точки Е: а) – получены в системе символьных вычислений Maple 17, б) – получены в системе SolidWorks

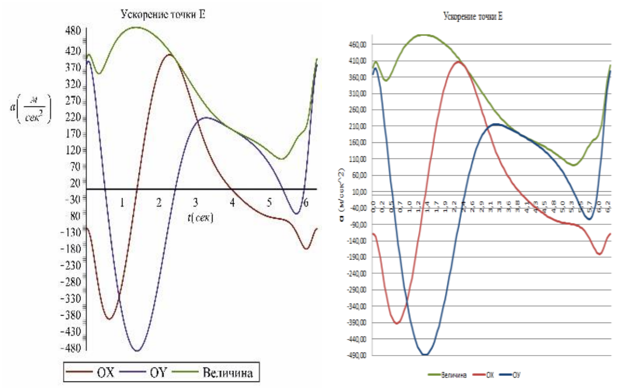

а) б)

Рис.4. Графики ускорения характерной точки Е: а) – получены в системе символьных вычислений Maple 17, б) – получены в системе SolidWorks

Представленные графики на рисунках (3 и 4) отображают результаты расчетов свойств кинематических параметров на промежутке $0 \le t \le 6.3$ (сек). Здесь принято $\omega_1 = 2\ c^{-1}$, $\omega_2 = 1\ c^{-1}$ (для простоты и удобства расчетов) и t=6,3 сек., как время, за которое характерная точка ***E*** механизма совершает полный цикл движения в неподвижной системе координат.

Для определения закона движения другой характерной точки ***K*** рассмотрим векторный контур A-B -N-K-A, имеющий уравнение:

$$\overrightarrow{AB} + \overrightarrow{BN} + \overrightarrow{NK} = \overrightarrow{AK}. \qquad (7)$$

Это уравнение в проекциях на оси системы координат OX и OY имеет вид:

$$\left\{\begin{array}{l} X_K = AB\cos\varphi_1 + BN\cos(\psi + \varphi_1) + \\ \quad +NK\cos(\alpha + \psi + \varphi_1)\,; \\ Y_K = AB\sin\varphi_1 + BN\sin(\psi + \varphi_1) + \\ \quad +NK\sin(\alpha + \psi + \varphi_1)\,. \end{array}\right. \qquad (8)$$

В уравнении (8) принят угол $\varphi_1 = \omega_1 \cdot t$, который является входной координатой ведущего звена AB, где $\omega_1 = const$. Угол $\alpha = 90°$ принят конструктивно, а угол ψ имеет зависимость от входных координат φ_1 и φ_2 ведущих звеньев AB и AD соответственно, также от противолежащих углов < ADC и <DCB и выражается уравнением:

$$\psi = 2\pi - \varphi - \cos^{-1}\left(\frac{BC^2 - AD^2 - AB^2 + k + CD^2}{2 \cdot BC \cdot CD}\right) - \tan^{-1}\left(\frac{AB\sin\varphi}{AD - AB\cos\varphi}\right) - \cos^{-1}\left(\frac{CD^2 - BC^2 + AD^2 + AB^2 - k}{2CD\sqrt{AD^2 + AB^2 - k}}\right). \qquad (9)$$

где применены следующие сокращения:

$\varphi = \varphi_1 - \varphi_2;\ k = 2 \cdot AD \cdot AB \cos \varphi.$

Дифференцируя уравнение (8) по времени получим проекции скорости характерной точки ***K*** на координатные оси OX и OY:

$$\begin{cases} V_K^X = AB\,(-\sin\varphi_1)\varphi_1{}' - BN(-\sin\psi\cos\varphi_1\psi' + \\ +\cos\psi\,(-\sin\varphi_1)\varphi_1{}') + BN(\cos\psi\sin\varphi_1\,\psi' + \\ +\sin\psi\cos\varphi_1\,\varphi_1{}') + NK(-\sin\psi\sin\varphi_1\,\psi' + \\ +\cos\psi\ \cos\varphi_1\varphi_1{}') + NK(\cos\psi\cos\varphi_1\,\psi' - \\ -\sin\psi\sin\varphi_1\varphi_2{}'); \\ V_E^Y = AB\cos\varphi_1\,\varphi_1{}' - BN(-\sin\psi\sin\varphi_1\,\psi' + \\ +\cos\psi\ \cos\varphi_1\varphi_1{}') - BN(\cos\psi\cos\varphi_2\,\gamma' - \\ -\sin\psi\sin\varphi_1\varphi_1{}') - NK\,(-\sin\psi\cos\varphi_1\psi' - \\ -\cos\psi\ \sin\varphi_1\varphi_1{}') + NK(\cos\psi\sin\varphi_1\,\psi' + \\ +\sin\psi\cos\varphi_1\,\varphi_1{}'). \end{cases} \qquad (10)$$

Продифференцируем полученное выражение (10) и определим ускорение точки ***K*** в проекциях на оси координатной системы OX и OY:

$$\begin{cases} a_K^X = (V_K^X)' = AB\,(-\cos\varphi_1)(\varphi_1{}')^2 + BN(\cos\psi \\ \cos\varphi_1(\psi')^2 - 2\sin\psi\sin\varphi_1\psi'\varphi_1{}' + \sin\psi\cos\varphi_1\psi'' \\ +\cos\psi\cos\varphi_1(\varphi_1{}')^2 + \cos\psi\sin\varphi_1\,\varphi_1{}'') + BN \\ (-\sin\psi\sin\varphi_1(\psi')^2 + 2\cos\psi\ \cos\varphi_1\psi'\varphi_1{}' + \\ +\cos\psi\sin\varphi_1\,\psi'' - \sin\psi\sin\varphi_1(\varphi_1{}')^2 + \sin\psi \\ \cos\varphi_1\,\varphi_1{}'') - NK(\cos\psi\sin\varphi_1(\psi')^2 + 2\sin\psi \\ \cos\varphi_1\psi'\varphi_1{}' + \sin\psi\sin\varphi_1\psi'' + \cos\psi\sin\varphi_1(\varphi_1{}')^2 \\ +\cos\psi\cos\varphi_1\,\varphi_1{}'') - NK\,(\sin\psi\cos\varphi_1(\psi')^2 + \\ +2\cos\psi\ \sin\varphi_1\psi'\varphi_1{}' - \cos\psi\cos\varphi_1\,\psi'' + \\ +\sin\psi\cos\varphi_1(\varphi_1{}')^2 + \sin\psi\sin\varphi_1\varphi_1{}''); \\ a_K^Y = (V_K^Y)' = -AB\sin\varphi_1(\varphi_1{}')^2 + BN(\cos\psi \\ \sin\varphi_1(\psi')^2 + 2\sin\psi\cos\varphi_1\psi'\varphi_1{}' + \sin\psi\sin\varphi_1\psi'' \\ +\cos\psi\sin\varphi_1(\varphi_1{}')^2 - \cos\psi\cos\varphi_1\,\varphi_1{}'') + \\ +BN(\sin\psi\cos\varphi_1(\psi')^2 + 2\cos\psi\ \sin\varphi_1\psi'\varphi_1{}' - \\ -\cos\psi\cos\varphi_1\,\psi'' + \sin\psi\cos\varphi_1(\varphi_1{}')^2 + \sin\psi \\ \sin\varphi_1\varphi_1{}'') + NK(\cos\psi\cos\varphi_1(\psi')^2 - 2\sin\psi\sin\varphi_1 \\ \psi'\varphi_1{}' + \sin\psi\cos\varphi_1\psi'' + \cos\psi\cos\varphi_1(\varphi_1{}')^2 + \\ +\cos\psi\sin\varphi_1\,\varphi_1{}'') + NK(-\sin\psi\sin\varphi_1(\psi')^2 + \\ +2\cos\psi\ \cos\varphi_1\psi'\varphi_1{}' + \cos\psi\sin\varphi_1\,\psi'' - \\ -\sin\psi\sin\varphi_1(\varphi_1{}')^2 + \sin\psi\cos\varphi_1\,\varphi_1{}''). \end{cases} \qquad (11)$$

На основании выведенных систем уравнений были получены графики скоростей и ускорений в системе символьных вычислений Maple 17 и в системе SolidWorks:

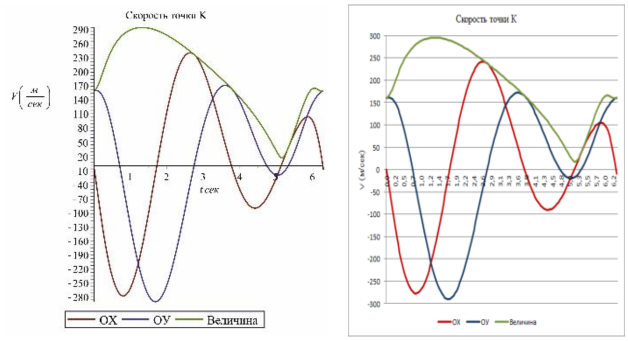

а) б)

Рис.5. Графики скорости характерной точки K:
а) – получены в системе символьных вычислений Maple 17,
б) – получены в системе SolidWorks

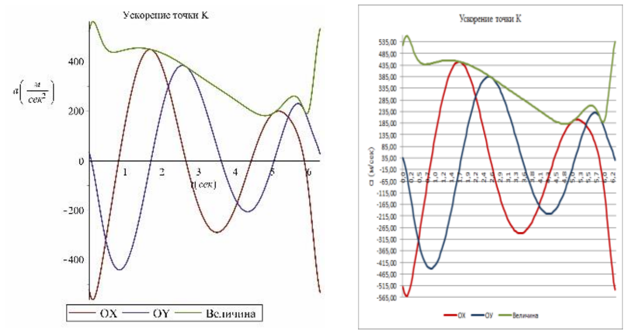

а) б)

Рис.6. Графики ускорения характерной точки K:
а) – получены в системе символьных вычислений Maple 17,
б) – получены в системе SolidWorks

Дифференцируя уравнения (4) и (9) по времени t можно найти уравнения для определения угловых скоростей и ускорений звеньев BC и CD. Ниже представлены эти уравнения:

$$\omega_{BC} = \frac{d\psi}{dt};\ \omega_{CD} = \frac{d\gamma}{dt};\ \varepsilon_{BC} = \frac{d^2\psi}{dt^2};\ \varepsilon_{CD} = \frac{d^2\gamma}{dt^2}. \qquad (12)$$

На рисунках (7) и (8) представлены результаты расчетов угловых скоростей и ускорений на промежутке времени $0 \le t \le 6.3$ (сек), решенных с помощью двух разных систем вычислений:

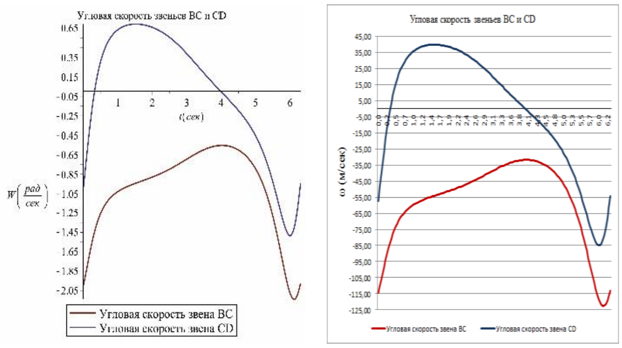

а) б)

Рис.7. Графики угловых скоростей звеньев BC и CD:
а) – получены в системе символьных вычислений Maple 17,
б) – получены в системе SolidWorks

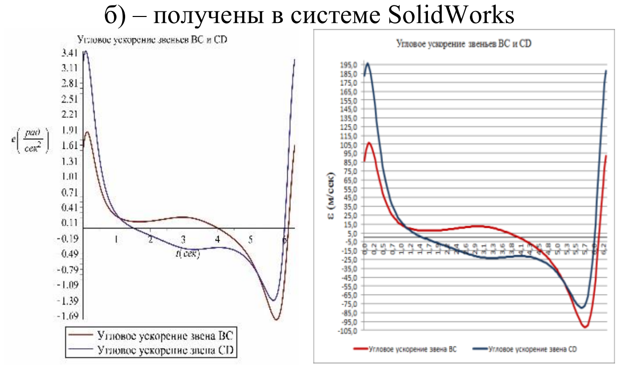

а) б)

Рис.8. Графики угловых ускорений звеньев BC и CD:
а) – получены в системе символьных вычислений Maple 17,
б) – получены в системе SolidWorks

Выводы

На основании анализа графиков (рис. 3-8) установлено, что расчеты кинематических параметров линейных и угловых скоростей и ускорений, вычисленных двумя различными способами, полностью совпадают между собой. Это показывает корректность полученных аналитических уравнений.

На основании анализа графиков получены следующие выводы:

1. Характерные точки E и K движутся с переменными скоростями и ускорениями.

2. Равномерное вращательное движение ведущих звеньев AB и AD преобразуется в неравномерное вращательное движение звеньев BC и CD с переменными угловыми скоростями и ускорениями относительно неподвижной системы координат.

3. Полученные формулы (2-12) и их результаты в виде графиков показывают, что характерные точки E и K двухподвижного плоского рычажного пятизвенного механизма совершают сложное планетарное движение.

4.Результаты расчетов полученных на основании решения уравнений кинематики показывают сложный характер движения, как характерных точек, так и шатунов, что является основой предполагать перспективность использования двухподвижного плоского пятизвенного рычажного механизма в качестве базовых механизмов при создании различных мехатронных устройств, инновационных технологий в машиностроении, сельском хозяйстве, в строительстве, в медицине и других отраслях промышленности.

Полученные нами уравнения кинематики являются универсальными и пригодны для определения положений, скоростей и ускорений характерных точек для двухподвижных плоских пятизвенных механизмов. Эти уравнения могут применяться для разных структурных параметров звеньев, для различных входных координат, и они представлены в удобном для инженерных расчетов виде.

Список литературы

[1]. Яруллин М.Г., Мингазов М.Р., *Способ образования двух подвижных 5R-Механизмов*, Научные труды III-й Международной научной конференции «Фундаментальные исследования и инновационные технологии в машиностроении». – М. Издательский дом «Спектр»,– с.380-382,2014

[2]. R.Alizade, *Structural Design of Parallel Manipulators with General Constraint One*. Mechanism and Machine Theory, Volume 45, Issue 1, pp. 1-14, et. al., 2010

[3]. Пат. 154612 на полезную модель МПК F16H 21/10, F16H 21/26. *Плоский дифференциальный шарнирно-рычажный механизм*, Яруллин М.Г., Мингазов М.Р., Исянов И.Р., опубл. 27.08.2015 Бюл. № 24.

[4]. Яруллин М.Г., Исянов И.Р. *Двухподвижный пятизвенный рычажный механизм*, Вестник КГТУ им. А.Н. Туполева. – 2015. – №2. – С. 97-102.

Proceedings of the International Symposium of Mechanism and Machine Science, 2017
AzCIFToMM – Azerbaijan Technical University
11-14 September 2017, Baku, Azerbaijan

Несимметричный адаптивный планетарный механизм

ИВАНОВ КОНСТАНТИН
Алматинский университет энергетики и связи, Институт Механики и машиноведения РК
Казахстан, Алматы, ул. Байтурсынова, 126
E-mail: ivanovgreek@mail.ru

Аннотация.
Объект исследования – это принципиально новый несимметричный планетарный механизм. Новый планетарный механизм создан на свойстве двух независимо вращающихся звеньев иметь некий центр совпадения линейных скоростей. Этот центр в виде полюса зацепления двух зубчатых колес, жестко связанных с независимо вращающимися телами, создает дополнительную связь между ними, не изменяя движения звеньев исходной кинематической цепи. Доклад посвящен анализу феномена дополнительной связи в планетарном механизме и созданию новых планетарных адаптивных механизмов.
Ключевые слова: несимметричный планетарный механизм, дополнительная связь, силовая. адаптация.

1. Введение

Планетарный механизм, как известно [1], содержит водило, сателлит и два центральных колеса. Планетарный механизм с несколькими сателлитами имеет симметричное расположение звеньев относительно центральной оси.

В последнее время планетарные механизмы были использованы для создания передач с непрерывным изменением передаточного отношения. Изобретатели создали ряд патентов, в которых двух подвижная планетарная кинематическая цепь обеспечивает бесступенчатое изменение передаточного отношения в зависимости от нагрузки [2-7].

Известно, что для определимости движения число степеней свободы кинематической цепи должно быть равно числу входных звеньев [1]. Поэтому надежность и определимость запатентованных схем с одним входным звеном вызывала сомнения. В этих патентах изобретателей теоретическое описание двух подвижной кинематической цепи было основано на закономерностях кинематической цепи с одной степенью свободы, что не могло соответствовать принципиально новым явлениям.

Автор доклада доказал на основе принципа возможных перемещений, что определимость движения двух подвижной цепи с одним входом создает подвижный замкнутый контур, составленный из зубчатых колес и накладывающий дополнительную связь. Иванов К.С. получил принципиально новые теоретические результаты, описывающие явление механической адаптации к силовой нагрузке в равномерном режиме движения [8-11].

На основе полученных закономерностей был разработан и запатентован адаптивный зубчатый вариатор [12, 13].

Выполненные исследования были представлены в виде теории силовой адаптации, основанной на научном открытии [14-18]. Сущность открытия: зубчатый планетарный механизм с двумя степенями свободы, имеющий один вход (входное водило), замкнутый контур, содержащий промежуточные зубчатые колеса, и выходное водило, обладает свойством определимости движения, которое обеспечивает адаптацию механизма к переменной нагрузке.

Однако наличие замкнутого контура определяет дополнительную связь только теоретически и отражает лишь необходимое условие определимости. В процессе исследования двух подвижной планетарной передачи был обнаружен неожиданный феномен – найден некий центр совпадения скоростей двух независимо вращающихся звеньев [19]. Этот центр в виде полюса зацепления двух зубчатых колес, жестко связанных с независимо вращающимися телами, создает дополнительную структурную связь между ними, не изменяя относительного движения исходной кинематической цепи. Дополнительная конструктивная связь обеспечивает достаточное условие определимости движения исходной кинематической цепи.

Найденный феномен позволяет значительно упростить исходную двух подвижную планетарную кинематическую цепь путем отказа от симметрии и создать упрощенный адаптивный механизм [20].

Статья посвящена расширенному анализу феномена дополнительной связи в планетарном механизме и его практической реализации.

2. Центр совпадения скоростей

Центр совпадения скоростей – это точка двух независимо вращающихся тел, в которой векторы линейных скоростей тел совпадают. Понятие центра совпадения скоростей определяется следующей теоремой.

Теорема 1 о центре совпадении скоростей.

Два независимо вращающихся тела имеют центр совпадения векторов линейных скоростей на линии, соединяющей центры вращения.

На рис. 1 тела 1 и 2 вращаются с заданными независимыми скоростями ω_1 и ω_2 вокруг центров вращения O_1 и O_2.

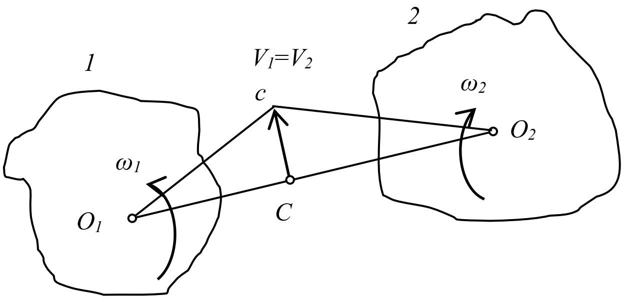

Рис. 1. К теореме о центре совпадении скоростей

Построим планы линейных скоростей тел относительно линии O_1O_2, соединяющей центры вращения. Линии, ограничивающие концы векторов линейных скоростей, пересекаются в некоторой точке c. Перпендикуляр cC, проведенный из точки c на линию O_1O_2, определяет вектор скорости точки C. Точка C принадлежит одновременно телу 1 и телу 2. Векторы линейных скоростей точек тел 1 и 2, в точке C совпадают $V_1 = V_2$. Следовательно, два независимо вращающихся тела имеют общую точку C совпадения векторов линейных скоростей на линии O_1O_2, соединяющей центры вращения O_1 и O_2, что и требовалось доказать. Точку C будем называть центром совпадения скоростей (ЦСС).

Положение точки с ЦСС определяется по формуле

$$O_1C = O_1O_2 \frac{\omega_2}{\omega_1 + \omega_2}. \qquad (1)$$

3. Практическая реализация ЦСС

Центр совпадения скоростей имеет некоторые свойства, которые могут быть использованы для практических целей. Эти свойства определяются следующими теоремами.

Теорема 2. Система двух вращающихся тел с двумя степенями свободы может быть преобразована в систему с одной степенью свободы без изменения состояния движения, если в центре совпадения скоростей разместить высшую кинематическую пару, обеспечивающую существующее кинематическое взаимодействие тел.

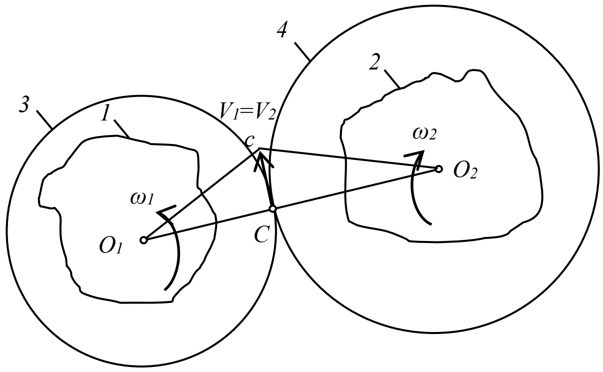

Рис. 2. Практическая реализация ЦСС

Для доказательства разместим в точке C полюс зацепления двух зубчатых колес. Колесо 3 жестко связано с телом 1 , колесо 4 жестко связано с телом 2. Колеса 3 и 4 имеют угловые скорости тел 1 и 2. Линейные скорости тел 1 и 2 в точке C равны между собой: $V_1 = \omega_1 \cdot O_1C, V_2 = O_2C$. Отсюда получим передаточное отношение тел 1 и 2 $u_{12} = O_2C / O_1C$. Передаточное отношение зубчатых колес 3 и 4 окажется равным передаточному отношению тел 1 и 2 $u_{34} = u_{12}$. Следовательно, колеса 3 и 4 обеспечивают реально существующее кинематическое взаимодействие тел 1 и 2. Вместе с тем введение контактной точки зубчатых колес 1 и 2 добавляет одну связь, что приводит к уменьшению числа степеней свободы исходной системы на единицу. Таким образом, введение высшей кинематической пары, обеспечивающей существующую кинематику, приводит к получению системы с одной степенью свободы, что и требовалось доказать.

Теорема 3. Введение высшей пары в виде зубчатого зацепления в ЦСС обеспечивает силовое взаимодействие независимо вращающихся тел.

Доказательство теоремы основано на природе зубчатого зацепления. Зубчатое зацепление обладает способностью произвольного расположения контактной точки зубьев на линии зацепления. Это свойство обеспечивает адаптацию положений контактных точек нескольких взаимодействующих зубчатых пар и возможность одновременного точного силового взаимодействия нескольких пар зубьев зубчатых колес с одинаковым передаточным отношением.

Положение контактной точки зубьев на линии зацепления может быть произвольным в определенных пределах, которые всегда обеспечены параметрами зацепления. Передача усилия в зубчатом зацеплении не зависит от положения контактной точки на линии зацепления. Поэтому введение высшей пары в виде зубчатого зацепления в ЦСС всегда обеспечивает силовое взаимодействие независимо вращающихся тел, что и требовалось доказать.

Примером реального силового взаимодействия звеньев с использованием нескольких одновременно реально контактирующих звеньев является планетарный механизм с несколькими сателлитами. В этом случае появление дополнительных высших кинематических пар приводит к разделению усилия взаимодействия центральных колес на число взаимодействующих пар.

Таким образом, ЦСС может быть использован в качестве реальной дополнительной связи, сохраняющей независимые движения звеньев исходной кинематической цепи. Если в точке C разместить полюс зацепления зубчатых колес, жестко связанных с телами 1 и 2, то рассматриваемая система с двумя степенями свободы приобретет дополнительную связь и превратится в определимую кигнематическую и силовую систему с одной степенью свободы.

Построим новый несимметричный планетарный механизм на основе найденных закономерностей.

4. Несимметричный планетарный механизм

Центр совпадения скоростей позволяет создать новый планетарный механизм. На рис. 3 представлен обычный планетарный механизм с двумя степенями свободы, содержащий водило H , сателлит 2 , солнечное колесо 1 и эпициклическое колесо 3. Справа от механизма представлен план линейных скоростей. Точки $A, E, B, D...$ на вертикальной линии соответствуют точкам, скорости которых равны нулю. Малые буквы $e, b, d...$ определяют концы векторов линейных скоростей точек, обозначенных большими буквами на вертикальной линии. Наклонные линии H, *1, 2, 3* на плане линейных скоростей определяют линии угловых скоростей звеньев.

Разместим на водиле H еще один несимметрично расположенный сателлит 4. На пересечении линий 3 и 4 построим точку c_{34} – конец вектора центра совпадения скоростей C_{34} звеньев 3 и 4.

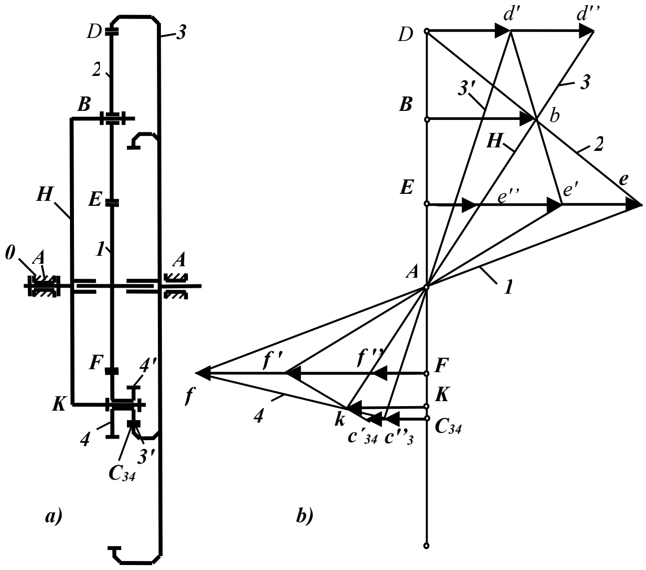

Рис. 3. Несимметричный планетарный механизм

Скорости звеньев 3 и 4 в точке C_{34} совпадают. Разместим в точке C_{34} высшую кинематическую пару в виде зубчатого зацепления колеса 3’ , жестко связанного с колесом 3 и колеса 4’. Получим некоторую дополнительную параллельно существующую кинематическую цепь, которая не изменяет кинематических параметров звеньев. Однако эта цепь, несомненно, будет вызывать силовое взаимодействие звеньев 4, 3 и H аналогично взаимодействию дополнительного сателлита (аналогичного сателлиту 2) с колесом 3 и водилом H в симметричном планетарном механизме. Полученный планетарный механизм содержит две независимые параллельные кинематические цепи, передающие движение от входного водила к выходному звену. Он отличается от обычного планетарного механизма с несколькими сателлитами тем, что параллельные кинематические цепи асимметричны и имеют разные геометрические параметры.

На рис. 3*b* фигура $DbeAfkc_{34}$ определяет план линейных скоростей механизма в состоянии с одной степенью свободы при неподвижном колесе 3 ($\omega_3 = 0$).

Фигура $d''be''Af''kc''_{34}$ определяет план линейных скоростей механизма в состоянии с одной степенью свободы при совместном вращении водила H и колес 3 и 1 ($\omega_3 = \omega_1 = \omega_H$). Силовое взаимодействие звеньев при совместном вращении водила H и колес 3 и 1 определяется условием $\omega_3 = \omega_1 = \omega_H$.

Фигура $d'be'Af'kc'_{34}$ определяет план линейных скоростей механизма в промежуточном состоянии с двумя степенями свободы при разобщенном вращении водила H и колес 3 и 1 ($\omega_3 \neq \omega_1 \neq \omega_H$).

Рассмотрим взаимодействие звеньев механизма. Будем считать водило H входным звеном, а колеса 1 и 3 выходными звеньями. Дополнительная силовая связь в точке C_{34} приводит к статической определимости системы.

Взаимодействие выходных звеньев 3 и 4 можно определить следующим образом.

Будем считать, что рассматриваемый механизм составлен из двух механизмов: верхнего и нижнего.

Верхний механизм расположен выше центральной оси $A-A$. Нижний механизм расположен ниже центральной оси $A-A$.

Взаимодействие звеньев в состоянии с двумя степенями свободы определяется условием распределения энергии по закону сохранения энергии.

Для верхнего механизма *(upper)*

$$M_{HU}\omega_H = M_{3U}\omega_3 + M_{1U}\omega_1 + M_{2U}\omega_{2U}. \quad (2)$$

Для нижнего механизма *(lower)*

$$M_{HL}\omega_H = M_{3L}\omega_3 + M_{1L}\omega_1 + M_{2L}\omega_{2L}. \quad (3)$$

Здесь для верхнего (индекс U) и для нижнего (индекс L) механизмов M_H - движущий момент, M_1, M_2, M_3 - моменты сопротивления.

Для всего механизма после сложения уравнений (2) и (3) получим

$$M_H\omega_H + M_3\omega_3 = M_1\omega_1 + M_{2U}\omega_{2U} + M_{2L}\omega_{2L}. \quad (4)$$

Здесь

$$M_H = M_{HU} + M_{HL},\ M_3 = M_{3U} + M_{3L},\ M_1 = M_{1U} + M_{1L}.$$

Правая часть уравнения (4) представляет собой сумму мощностей внутренних сил. Как было показано в работе [5] сумма работ (мощностей) внутренних сил оказывается равной нулю.

$$M_1\omega_1 + M_{2U}\omega_{2U} + M_{2L}\omega_{2L} = 0. \quad (5)$$

Левая часть уравнения (4) представляет собой сумму мощностей внешних сил. С учетом (5)

$$M_H\omega_H + M_3\omega_3 = 0. \quad (6)$$

Дополнительная силовая связь обеспечивает распределение скоростей точек D и E в соответствии с силовым воздействием на звенья 1 и 3, которые с помощью дополнительной связи C_{34} объединены в замкнутый подвижный контур 1-2-3-4’-4. Полученный механизм имеет одну степень свободы и обладает статической и кинематической определимостью.

Из формулы (6) следует

$$\omega_3 = M_H\omega_H / M_3. \quad (7)$$

Формула (7) определяет эффект силовой адаптации: при постоянной входной мощности $M_H\omega_H$ выходная угловая скорость адаптируется к переменному выходному моменту сопротивления.

Формула (7) выражает аналитически дополнительную связь, которая имеет место в кинематической цепи с двумя степенями свободы.

Таким образом, ЦСС позволяет создать адаптивный планетарный механизм.

Существующие зубчатые вариаторы являются сложными планетарными механизмами с двумя водилами и с двумя блоками колес.

Новый несимметричный зубчатый вариатор является более простым (с одним водилом и с одним блоком колес).

Заключение

Найденные закономерности построения несимметричного планетарного механизма определяют наличие дополнительной кинематической связи в виде центра совпадения скоростей звеньев. Центр совпадения скоростей может быть представлен конструктивно в виде геометрической связи двух зубчатых колес. Эта геометрическая связь изменяет структуру механизма и число степеней свободы. Конструктивно выполненная дополнительная связь обеспечивает надежность функционального действия адаптивного механизма в состоянии с одной степенью свободы при пуске и в состоянии с двумя степенями свободы в эксплуатационном режиме.

Научная реализация найденного эффекта открывает принципиально новые перспективы создания саморегулирующихся механизмов и механических систем во всех отраслях техники (в автомобильной промышленности, в робототехнике, в ветроэнергетике, в металлургии, в горнодобывающей промышленности, в разведочном бурении, в станкостроении и др.).

Практическая реализация найденного эффекта открывает принципиально новые перспективы создания машиностроительных производств. Одним из наиболее перспективных видов новой саморегулирующейся техники является саморегулирующийся зубчатый вариатор, заменяющий тяжелую и громоздкую коробку передач автомобиля.

Простота и идеальная адекватность саморегулирующегося зубчатого вариатора к условиям работы создают неоспоримые преимущества перед управляемыми ступенчатыми коробками передач и фрикционными вариаторами.

Литература

[1]. I.I. Artobolevsky *Theory of Mechanisms.* 'Science'. Moskow. 720 p. 1967.

[2]. K.S. Ivanov, N.A.Dmitrieva. *Nonreactive engine*. Copyright certificate of the USSR №769157 from 7.09.1980.

[3]. K.S.Ivanov, N.A.Dmitrieva. *Electromechanical self-controlled installation.* Copyright certificate of the USSR №1216489 from 7.03.1986.

[4]. J. Harries, *Force transmission system comprising two assigned of epicyclic gears.* Patent of Great Britain GB2238090 (A). 11 p. 1991

[5]. S. J. Crockett. *Shiftless, continuously-aligning transmission.* Patent of USA 4,932,928, Cl. F16H 47/08, U.S. Cl. 475/51; 475/47. 9 p. 1990

[6]. I.V. Volkov. *Way of automatic and continuous change of a twisting moment and speed of twirl of the output shaft depending on a tractive resistance and the device for its realization.* Invention description to the patent of Russia RU 2,234,626. (2004) 12 p.

[7]. K.S. Ivanov, *Transmission with automatically adjustable speed*. Preliminary patent of republic Kazakhstan № 3208. (1996) 5 p.

[8]. K.S.Ivanov *Creation of gear adaptive mechanism with constant engagement of wheels*. Proceedings of XXI conference on theory of machines and mechanisms. - Bielsko-Biala. Poland. Sept. 22-25. 2008. V.2. - P. 89 – 95.

[9]. Ivanov K.S. *Dynamics of gear torque variator.* Proceedings of XXI conference on theory of machines and mechanisms. - Bielsko-Biala. Poland. Sept. 22-25. 2008. V.2. - P. 112 – 116.

[10]. K.S.Ivanov, E.K.Yaroslavceva. *Synthesis of Gear CVT for Set Diapason of Transfer Ratio.* Machine Design. Vol. 4. No 5. ISSN 1821-1259. Warsaw. Poland. 2012. P. 48 – 62.

[11]. K.S.Ivanov. 5th International Conference on Advanced Design and Manufacture (ADM 2013). Valencia. Spain. 2013. PP 63-70.

[12]. K.S. Ivanov, Almaty, KAZ - Owner of the registered sample. *The name - Device of automatic and continuous change of rotation moment and change of rotation speed of output shaft depending on resistance moment.* The deed on registration of the registered sample № 20 2012 101 273.1. Day of Registration 02.05.2012. The German patent and firm establishment. Federal Republic Germany. (2012) 12 p.

[13]. K.S.,Ivanov, E.K. Yaroslavtseva. *Way of automatic and continuous change of a twisting moment and speed of rotation of the output shaft depending on tractive resistance and the device for its realisation.* Patent of Russia № 2398989 from September, 10th, (2010).12 p.

[14]. 14. K.S.Ivanov T*heory of Continuously Variable Transmission (CVT) with Two Degrees of Freedom. Paradox of mechanics.* Proceedings of the American Society of Engineers Mechanics (ASME) International Mechanical Engineering Congress & Exposition (IMECE 2012). Houston, Texas, USA. 2012. PP 543 – 562.

[15]. K.S. Ivanov. *Continuously Variable Transmission: Adaptive Gear Stepless Mechanical CVT.* International Conference of Gears with Exibition. VDI Wissensforum GmbH. Technical University of Munich (TUM) Garching (near Munich). Germany. 984 - 987. 2013.

[16]. K.S.Ivanov *Theory of the gear variator – gear box.* Monograph. Palmarium. Saarbruken. Germany. 67 p. 2014.

[17]. K.S. Ivanov. *Toothed variators.* Monograph. Raritet. ISBN 978-601-250-266-4. Almaty. 90 p. 2015.

[18]. K. S. Ivanov. *Theory of Force Adaptation.* Proceedings of 2015 IFToMM World Congress. Taipei, Taiwan, 8 p. 2015.

[19]. K.S.Ivanov. *Paradox in the Mechanism Science.* 1-st International Symposium on the Education in Mechanism and Machine Science. Madrid. Spain. P. 132-138. 2013.

[20]. К.С.Иванов. *Планетарный механизм.* Заявка на инновационный патент РК. №2016/0934.1. От 09.07.2016. Астана. 2016.

Proceedings of the International Symposium of Mechanism and Machine Science, 2017
AzC IFToMM – Azerbaijan Technical University
11-14 September 2017, Baku, Azerbaijan

Математическая модель инновационного схвата манипулятора робота для высокорадиоактивных тепловыделяющих элементов

Талгат КАЙЫМ[1], Асылбек ДЖОМАРТОВ[2] , Ербол ТЕМИРБЕКОВ[2] , Петр ПАВЛЕНКО[3] ,
Виталий ГРИБАНОВ[1], Сулеймен КАИМОВ[2], Абылай КАИМОВ[2],
Дарига АБИЛДАБЕКОВА[1], Гулназия КАИМОВА[4]
[1]Казахский национальный исследовательский технический университет имени К.И.Сатпаева
Алматы, Республика Казахстан, ул.Сатпаева, 22 А
Email: kayim4444@mail.ru

[2]Институт механики и машиноведения им. У.А.Джолдасбекова, Алматы, Республика Казахстан
[3]Национальный университет авиации, Киев, Украина
[4]Казахский агро-технический университет имени С.Сейфуллина Астана, Республика Казахстан

Аннотация
В данной работе специалистами предлагаются инновационные способы перегрузки тепловыделяющего элемента и/или тепловыделяющих элементов и др. из промежуточного контейнера с твердыми высокорадиоактивными отходами в полость (полости) основного контейнера, изготовленного из блока крепкой горной породы, реализацию которого предусматривается осуществлять с применением мирового уровня инновационной конструкции трехфалангового захватного устройства схвата манипулятора промышленного робота
Ключевые слова: контейнер, фаланга, схват, удерживающий зуб, тепловыделяющий элемент.

1. Введение

По данным Всемирной атомной ассоциации в настоящий период времени во всех странах мира эксплуатируются 449 атомных реактора, еще 62 атомных реактора строятся и около 150 атомных реакторов запланированы для строительства. Мировым лидером в атомной энергетике являются США, где эксплуатируются более 100 атомных реакторов. Быстрее всех «мирный атом» развивает Китай. В Китае строятся 27 атомных реакторов, возведение еще 50 атомных реакторов запланировано в этой стране в будущий период времени.

При эксплуатации атомной электростанции (АЭС) образуются твердые высокорадиоактивные отходы (ТВРАО), являющиеся тепловыделяющими элементами (ТВЭЛ-ами) тепловыделяющих сборок атомных реакторов.

Радионуклиды, содержащиеся в ТВРАО, губительно действуют на биосферу Земли и резко ухудшают экологию окружающей среды. В настоящий период времени специалистами предусматривается осуществлять захоронение ТВРАО в подземных хранилищах (могильниках) ТВРАО. При осуществлении этой технологической операции ТВЭЛ-ы загружаются в промежуточный контейнер, который транспортируется от АЭС до сборочно-перегрузочного пункта (СПП), сооруженного возле подземного хранилища (могильника) ТВРАО. В СПП из промежуточного контейнера ТВРАО перегружаются в полость (полости), сформированную в теле основного контейнера (контейнеров), изготовленного из блока крепкой горной породы. Эту техническую операцию предусматривается осуществлять рабочим (рабочими) вручную с применением специальных приспособлений, когда он (они) находится непосредственно возле ТВРАО. Безусловно, при выполнении этой операции не обеспечивается требуемая безопасность труда рабочего (рабочих).

В настоящий период времени специалистами созданы инновационный способ перегрузки ТВЭЛ-а и/или ТВЭЛ-ов и др. из промежуточного контейнера с ТВРАО в полость (полости) основного контейнера, изготовленного из блока крепкой горной породы, реализацию которого предусматривается осуществлять с применением мирового уровня инновационного схвата манипулятора промышленного робота (ПР) и инновационная конструкция трехфалангового адаптивного схвата-захватного устройства манипулятора ПР.

Для научно-обоснованного выбора и обоснования геометрических, структурно-кинематических и динамических параметров конструктивных элементов инновационного схвата манипулятора ПР разработана математическая модель их расчета с учетом стохастических процессов их взаимодействия с объектом, т.е. с ТВЭЛ-ом. Точность оценки определения геометрических, структурно-кинематических и динамических параметров конструктивных элементов трехфалангового адаптивного схвата манипулятора ПР с учетом стохастических процессов взаимодействия его с верхним участком тела ТВЭЛ-а производится на основе определения оптимального весового коэффициента Калмана [1-4].

2. Основное содержание

В настоящий период времени специалистами создан инновационный способ перегрузки ТВЭЛ-а и/или ТВЭЛ-ов и др. из промежуточного контейнера с ТВРАО в полость (полости) основного контейнера, изготовленного из блока крепкой горной породы, реализацию которого предусматривается осуществлять с применением инновационного схвата манипулятора ПР.

Конструкция ТВЭЛ-а, например, реактора РБМК приведена на фигуре 1.

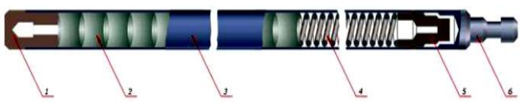

Фиг. 1. Конструкция ТВЭЛ-а реактора РБМК: 1- заглушка; 2- таблетки диоксида урана; 3-оболочка из циркония; 4-пружина; 5- втулка; 6-наконечник

В холодном состоянии общая длина столба таблеток в ТВЭЛ-е составляет 3530 мм. Длина трубки ТВЭЛ-а равна 3800 мм. Положение столба топливных таблеток фиксируется разрезными втулками из нержавеющей стали и пружиной, не препятствующими тепловым перемещениям [5-6].

Инновационный дистанционно управляемый мобильный ПР (фигура 2) с инновационным адаптивным исполнительным механизмом схвата состоит из опорных стоек 1, горизонтальной перекладины 2, средства передвижения 3 (колесное, гусеничное, шагающее и т.д.), к которому прикреплен манипулятор 4 ПР, имеющий несколько степеней свободы подвижности, подобно человеческой руке. К конечной части манипулятора 4 ПР прикрепляется инновационный схват 5 . Инновационным схватом 5 ТВЭЛ 6 извлекается из промежуточного контейнера 7 и перегружается в основной контейнер 8.

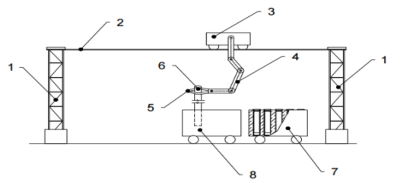

Фиг. 2. Схема перегрузки ТВЭЛ-а ТВРАО из промежуточного контейнера в основной контейнер с применением инновационного схвата манипулятора ПР: 1 – опорная стойка; 2 – горизонтальная перекладина; 3 – средство передвижения; 4 – манипулятор; 5 – инновационный схват; 6 – тепловыделяющий элемент (ТВЭЛ); 7 – промежуточный контейнер; 8 – основной контейнер

На основе анализа работ [7-26] специалистами создана мирового уровня инновационная конструкция трехфалангового адаптивного схвата - захватного устройства (ЗУ) манипулятора ПР.

Инновационная конструкция (фигура 3) трехфалангового адаптивного схвата манипулятора состоит из следующих конструктивных элементов: плитка-основание 1 для крепления фаланг – рычагов схвата, которая прикрепляется крепежным рычагом 2 к конечной части манипулятора.

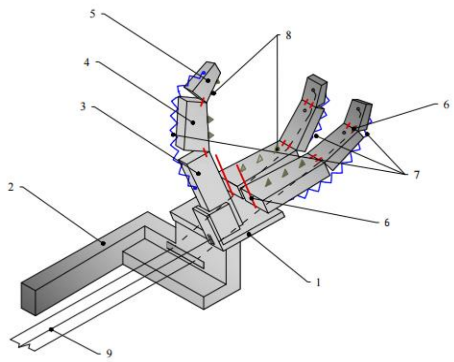

Фиг. 3. Трехфаланговый адаптивный схват манипулятора ПР для перегрузки ТВЭЛ-а и/или ТВЭЛ-ов из промежуточного контейнера в основной контейнер для ТВРАО при захоронении его в подземном хранилище (могильнике) ТВРАО: 1 – плитка-основание для крепления основной фаланги рычага схвата; 2 – крепежный рычаг манипулятора; 3- основная фаланга; 4 – средняя фаланга; 5 – конечная фаланга; 6- шарнир крепления смежных фаланг между собой; 7 – стягивающая пружина; 8 – удерживающий зуб; 9 – гибкий тяговый элемент.

ЗУ состоит из нескольких конструктивных элементов, так называемых схватывающих гибких рычагов схвата, кинематическая схема работы каждого из которых условно отождествляется с функционированием отдельного пальца руки человека. Каждый схватывающий гибкий рычаг схвата состоит, например, из 3-х фаланг: основной 3, средней 4 и конечной 5. Все фаланги 3–5 между собой соединяются шарнирами 6. Нижнее основание каждой основной фаланги 3 схватывающего гибкого рычага схвата крепится шарнирно к плитке – основанию 1. Между всеми смежнорасположенными фалангами 3–5 каждого рычага схвата устанавливаются стягивающие пружины 7. На участках внутренней поверхности каждой фаланги 3–5 каждого рычага схвата укрепляются удерживающие зубья 8.

Захватывание предмета, например, ТВЭЛ-а, предназначенного для перемещения его из промежуточного контейнера в основной контейнер для ТВРАО, осуществляется следующим образом. Схватывающие гибкие рычаги схвата, например, три схватывающих гибких рычага схвата позиционируются «рукой» манипулятора ПР над верхним участком тела ТВЭЛ-а, находящегося в промежуточном контейнере. Затем они перемещаются сверху вниз на тело верхнего участка ТВЭЛ-а и фиксируются напротив него таким образом, чтобы он был расположен между схватывающими гибкими рычагами схвата. В зависимости от конкретных условий, например, с одной стороны верхнего участка тела ТВЭЛ-а будут расположены два схватывающих гибких рычага схвата, а с противоположной стороны его–один схватывающий гибкий рычаг схвата. В теле каждой фаланги 3–5 каждого рычага схвата формируется отверстие, продольная ось которого совпадает с продольной осью фаланги. После соединения всех фаланг 3–5 между собой шарнирами 6 каждого рычага схвата, в каждой из них размещается гибкий тяговый элемент 9. Первый гибкий тяговый элемент 9 размещается в отверстиях фаланг 3-5 от верхнего основания конечной фаланги 5, проходя вдоль нее в отверстии, сформированном в средней фаланге 4, в отверстии, сформированном в основной фаланге 3, и противоположный его конец размещается за ее пределами. Конец второго гибкого тягового элемента 9 закрепляется в верхней части средней фаланги 4, размещается в отверстии, сформированном в теле основной фаланги 3, и противоположный конец его размещается за ее пределами. Конец третьего гибкого тягового элемента 9 закрепляется в верхней части основной фаланги 3, устанавливается в отверстии, сформированном в теле ее, и противоположный конец его размещается за ее пределами. Каждый противоположно расположенный конечный участок гибкого тягового элемента 9 закрепляется на специальном приводе, установленном в пункте управления манипулятором ПР. Аналогичным образом устанавливаются гибкие тяговые элементы 9 во всех фалангах 3-5 других схватывающих гибких рычагах схвата.

В зависимости от конкретных условий в полости, сформированной в основном контейнере, могут быть размещены один, два и более ТВЭЛ-ов и/или их части и др. Размещение ТВЭЛ-а и/или ТВЭЛ-ов и др. в других полостях, сформированных в основном контейнере, предусматривается осуществлять аналогичным образом.

При осуществлении технологической операции захватывания схватывающими гибкими рычагами схвата верхнего участка тела ТВЭЛ-а оператором на пункте управления специальным приводом осуществляется натяжение всех гибких тяговых элементов 9 схватывающих гибких рычагов схвата для осуществления прижатия внешних внутренних поверхностей всех фаланг 3-5, с прикрепленными к каждой из них удерживающими зубьями 8, схватывающих гибких рычагов схвата к поверхности верхнего участка тела ТВЭЛ-а и обеспечения требуемого усилия взаимодействия между соответствующими поверхностями всех фаланг 3-5, с прикрепленными к каждой из них удерживающими зубьями 8, схватывающих гибких рычагов схвата и боковой поверхностью верхнего участка ТВЭЛ-а для его надежного удержания и базирования.

Затем манипулятором ПР ТВЭЛ поднимается вверх из промежуточного контейнера и манипулятор ПР с ТВЭЛ-ом перемещается по транспортному пути до места установки основного контейнера, размещенного на СПП. Он устанавливается над соответствующей полостью, сформированной в основном контейнере, таким образом, чтобы нижнее основание ТВЭЛ-а совмещалось с участком верхнего основания полости, сформированной в основном контейнере.

В следующую очередь, оператор, находясь на пункте управления, дистанционно освобождает концы гибких тяговых элементов 9 от закрепления на специальном приводе в пункте управления. Схватывающие гибкие рычаги схвата под действием силы упругости специальных упругих элементов - пружин 7 отодвигаются от поверхности верхнего участка тела ТВЭЛ-а. При этом ТВЭЛ под действием собственного веса опускается в полость, сформированную в основном контейнере. Под действием силы упругости пружин 7 каждый схватывающий гибкий рычаг схвата выпрямляется и продольная ось каждого из них занимает горизонтальное и/или практически горизонтальное положение, возвращаясь в исходное нерабочее состояние.

Для повышения эффективности размещения ТВЭЛ-а и/или ТВЭЛ-ов и др. в полости, сформированной в основном контейнере, в ней предварительно устанавливается специальный направляющий элемент, например, воронка, изготовленная из металла и/или из пластика и др.

Применение данной технологической схемы перегрузки ТВЭЛ-а и/или ТВЭЛ-ов и др. из промежуточного контейнера в основной контейнер позволяет обеспечить высокую степень безопасности захоронения ТВРАО и безопасные условия работы персонала.

Для выбора и обоснования оптимальных структурно-кинематических параметров конструктивных элементов конструкции манипулятора ПР с схватывающими гибкими рычагами схвата разработаны научные основы имитационного моделирования функционирования многофункционального гибкого рычага схвата манипулятора ПР, адаптирующегося к размерам и формам ТВЭЛ-а, для его безопасной перегрузки в основной контейнер; математический метод построения оптимального варианта конструкции схватывающего гибкого рычага схвата манипулятора ПР для перегрузки ТВЭЛ-а и/или ТВЭЛ-ов и др. на основе решения минимаксной задачи определения его оптимальных параметров при составлении свертски систем ограничений в обобщенный их критерий для обеспечения надежного удерживания ТВЭЛ-а схватывающими гибкими рычагами схвата манипулятора ПР; математическая модель моделирования стохастических процессов работы высокоэффективного и надежного схватывания гибкими рычагами схвата манипулятора ПР для перегрузки ТВЭЛ-а и/или ТВЭЛ-ов и др. в основной контейнер; программное обеспечение дистанционного управления работой схватывающего гибкого рычага схвата манипулятора ПР для перегрузки ТВЭЛ-а и/или ТВЭЛ-ов и др. в основной контейнер с использованием сетевых протоколов и создание его имитационной модели [2-4].

Сила прижатия внешних внутренних поверхностей каждой фаланги 3–5, с прикрепленными к каждой из них удерживающими зубьями 8, каждого рычага схвата к внешней ограничивающей поверхности верхнего участка тела ТВЭЛ-а 10 (фигура 4) определяется по формуле:

$$P = K * G, \qquad (1)$$

где P – сжимающая сила, н; , K – коэффициент, учитывающий характеристики материалов конструктивных элементов рычага схвата, G – вес перегружаемого ТВЭЛ-а, кг.

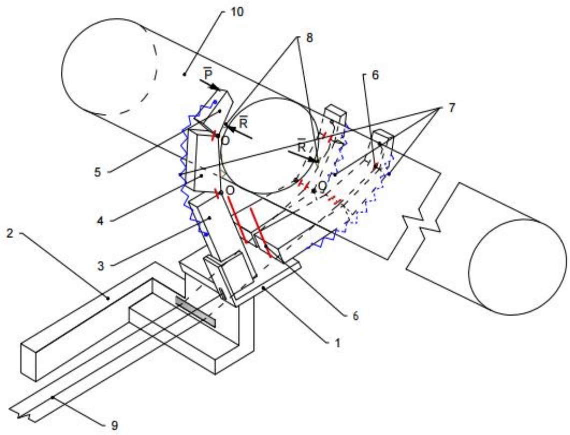

Фиг. 4. Трехфаланговый адаптивный схват манипулятора робота для перегрузки ТВЭЛ-а из промежуточного контейнера в основной контейнер для ТВРАО при захоронении его в хранилище (могильнике) ТВРАО: 1-плитка-основание для крепления основной фаланги рычага схвата; 2-крепежный рычаг манипулятора; 3-основная фаланга; 4-средняя фаланга; 5-конечная фаланга; 6-шарнир крепления смежных фаланг между собой; 7-стягивающая пружина; 8-удерживающий зуб; 9-гибкий тяговый элемент, 10 – ТВЭЛ.

Для освобождения верхнего участка тела ТВЭЛ-а 10 от каждой фаланги 3-5 каждого рычага схвата на пульте управления (на фигуре 4 не показано) механической рукой манипулятора ПР каждый конечный участок гибкого тягового элемента 9 освобождается от натяжения (фиксации) на приводе пункта управления. При этом сила прижатия каждой фаланги 3 – 5, с прикрепленными к каждой из них удерживающими зубьями 8, каждого рычага схвата к поверхности верхнего участка тела ТВЭЛ-а 10 становится равной нулю. Под действием силы упругости сжимающе-разжимающей пружины 7 внешние внутренние поверхности каждой фаланги 3-5, с прикрепленными к каждой из них удерживающими зубьями 8, каждого рычага схвата отодвигаются от внешней ограничивающей поверхности верхней части тела ТВЭЛ-а 10.

Из уравнения равновесия всех сил, действующих на схват механической руки ПР, определяется сила, необходимая для смыкания всех фаланг, с прикрепленными к каждой из них удерживающими зубьями 8, каждого рычага схвата вокруг поверхности верхнего участка тела ТВЭЛ-а.

Уравнение моментов сил, действующих на основную, среднюю и конечную фалангу каждого рычага схвата механической руки ПР относительно O (O_1, O_2, O_3), имеет вид:

$$\sum M_o(\varphi)=0, \qquad (2)$$

$$Pa(\varphi)=Rk_rb(\varphi)+fRc(\varphi)+mgl(\varphi), \qquad (3)$$

где P-сила, требуемая для надежного захвата всеми фалангами, с прикрепленным к каждой из них удерживающими зубьями, каждого рычага схвата верхнего участка тела ТВЭЛ-а, н; φ - обобщенная угловая координата, определяющая положения рычага схвата, рад.(на фигуре 4 не показана); R- сила реакции со стороны поверхности верхнего участка ТВЭЛа на внутреннюю поверхность каждой фаланги, с прикрепленными к каждой из них удерживающими зубьями каждого рычага схвата, н; a, b, c и l- плечи действия сил P и R относительно оси шарнира O каждой фаланги, с прикрепленными к каждой из них удерживающими зубьями, каждого рычага-схвата (на рисунке 4 не показано), мм; f – коэффициент трения между поверхностями верхнего участка ТВЭЛа и внутренними поверхностями каждой фаланги, с прикрепленными к каждой из них удерживающими зубьями, каждого рычага схвата (как правило, величина коэффициента трения скольжения между поверхностями конструктивных элементов, изготовленных из металлов , например, стали, равна 0,5).

Сила P прижатия каждой фаланги, с прикрепленными к каждой из них удерживающими зубьями, каждого рычага схвата к поверхности верхнего участка ТВЭЛ-а определяется по формуле:

$$P=(a(\varphi))^{-1}\{Rk_rb(\varphi)+fRc(\varphi)+mgl(\varphi)\}. \qquad (4)$$

По статистическим экспериментальным данным, полученными при исследовании операции прижатия каждой фаланги, с прикрепленными к каждой из них удерживающими зубьями, каждого рычага схвата к поверхности верхнего участка тела ТВЭЛ-а, проведенными в лабораторных условиях, получена следующая экспериментальная зависимость между силой P и величиной длины каждой фаланги, с прикрепленными к каждой из них удерживающими зубьями, каждого рычага схвата:

$$P(X)= 3{,}35X+ 0{,}05, \qquad (5)$$

где X – расстояние между точкой условной оси шарнира O, расположенного между каждыми двумя смежными фалангами, и точкой контакта внутренней поверхности каждой фаланги, с прикрепленными к каждой из них удерживающими зубьями, каждого рычага схвата с ограничивающей поверхностью верхнего участка тела ТВЭЛ-а, мм.

График зависимости для условного примера между силой P и расстоянием X между осью шарнира O и точкой контакта внутренней поверхности каждой фаланги, с прикрепленными к каждой из них удерживающими зубьями, каждого рычага-схвата с ограничивающей поверхностью верхнего участка тела ТВЭЛ-а приведен на фигуре 5.

Для повышения точности определения геометрических, структурно-кинематических и динамических параметров трехфалангового адаптивного схвата манипулятора ПР с учетом стохастических процессов взаимодействия его с поверхностью верхнего участка тела ТВЭЛ-а предлагается метод их оценки [2-4, 25-26].

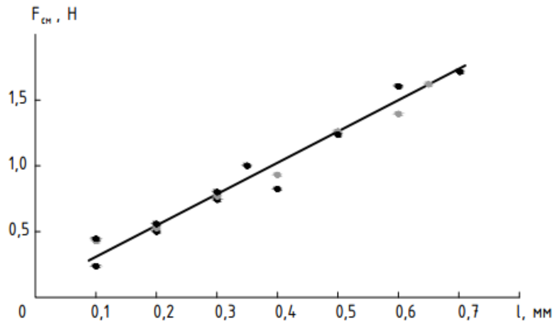

Фиг. 5. График зависимости для условного примера между силой P и расстоянием X между точкой условной оси шарнира O и точкой контакта внутренней поверхности каждой фаланги, с прикрепленными к каждой из них удерживающими зубьями, каждого рычага-схвата с ограничивающей поверхностью верхнего участка тела ТВЭЛ-а.

Величина силы P, т.е. P_k , с которой схват взаимодействует с верхним участком тела ТВЭЛ-а, определяется из следующей системы уравнений:

$$P_{k+1}=P_k+u_k+\gamma_k\,, \qquad (6)$$

$$z_k=P_k+\delta_k, \qquad (7)$$

где P_k - величина силы P, определяемая с учетом случайной ошибки ее отклонения в «идеальной модели»; P_{k+1}- величина силы P, определяемая с учетом случайной ошибки ее отклонения в «идеальной модели» в другом временном интервале; u_k - величина силы P, контролирующая эволюцию матрицы состояния изменения ее, с которой схват взаимодействует с поверхностью верхнего участка тела ТВЭЛ-а, которая определяется аналитически по формуле (4); z_k - величина силы P, определяемая экспериментально с учетом систематической ошибки, обуславливаемой точностью измерительных приборов; γ_k и δ_k – соответственно, ошибки математической модели аналитического расчета и экспериментального определения силы P, измеряемые техническими средствами измерения, и которые определяются по формулам (6) и (7).

При этом случайные ошибки, вызванные отклонением спроектированного трехфалангового адаптивного механизма схвата манипулятора ПР от его «идеальной» модели, и представляющие собой случайные ошибки, определяются статистическими моментами $M\gamma_i$, величины которых и их законы распределения не зависят от времени (номера итерации i); средние значения ошибок равны нулю: $M\gamma_i=M\delta_i=0$; сам закон распределения случайных величин может быть и не известен, но известны их дисперсии α_γ^2 и α_δ^2; предполагается, что все случайные ошибки независимы.

Предполагается, что на i-ом шаге найдено отфильтрованное значение с сенсора P_i^{opt}, которое приближает истинную координату системы P_i. Неизвестная величина P_{i+1} определяется по формуле:

$$P_{i+1}=P_i+u_i+\gamma_i, \tag{8}$$

где u_i – величина, контролирующая эволюцию матрицы состояния изменения силы P.

Идея состоит в том, чтобы получить наилучшее приближение к истинной координате P_{i+1} выбирается так называемая «золотая» середина между показанием z_{i+1} источника с сенсора и $P_i^{opt}+u_i$, являющимся его предсказанием. Показанию с сенсора дается весовой коэффициент Калмана K, а на предсказанное значение (1-K) величина P^{opt}_{i+1} определяется по формуле:

$$P^{opt}_{i+1}=K*z_{i+1}+(1-K)*(P^{opt}_i+u_i), \tag{9}$$

где K – весовой коэффициент Калмана, величина которого выбирается такой, чтобы получившееся оптимальное значение координаты P^{opt}_{i+1} было бы наиболее близко к величине истинной координаты P_{i+1}. Например, если известно, что показания с сенсора очень точные, то степень доверия к нему будет больше и значение z_{i+1} имеет больший вес (K близко единице). Если же с сенсор, наоборот, совсем неточный, тогда необходимо больше ориентироваться на теоретически предсказанное значение $P_i^{opt}+u_i$. В общем случае, чтобы найти точное значение коэффициента Калмана необходимо минимизировать величину случайных и систематических ошибок γ_i и δ_i.

В общем случае, чтобы найти точное значение коэффициента Калмана необходимо минимизировать величину e_{i+1} среднего значения математического ожидания от квадрата ошибки:

$$e_{i+1}=P_{i+1}- P_{i+1}^{opt} \tag{10}$$

После подстановки в уравнение (10) формулы (9) получается:

$$e_{i+1}=(1-K)*(e_i+\gamma_i)-K*\delta_{i+1}. \tag{11}$$

Минимизируется среднее значение математического ожидания от квадрата ошибки:

$$M(e_{i+1}{}^2) \to \min. \tag{12}$$

Математическое ожидание квадрата величины ошибки определения силы P взаимодействия трехфалангового адаптивного схвата манипулятора ПР с верхним участком тела ТВЭЛ-а при перегрузке его из промежуточного контейнера в основной контейнер определяется по формуле:

$$M(e^2_{i+1})=(1-K)(Me^2_i+\sigma^2_\gamma)+K^2\sigma_\delta^2. \tag{13}$$

Это выражение принимает минимальное значение при условии:

$$K_{i+1}=(Me_i^2+ e_\gamma^2)/ Me_i^2+ \sigma_\gamma^2+\sigma_\delta^2 . \tag{14}$$

Для определения весового коэффициента Калмана необходимо вычислить статистические моменты случайных ошибок математической модели и систематических ошибок измерений силы P трехфалангового адаптивного схвата манипулятора ПР при взаимодействии его с верхним участком тела ТВЭЛ-а. Таким образом, реализуется алгоритм решения разработанной математической модели, оценки стохастической системы динамического процесса взаимодействия трехфалангового адаптивного схвата манипулятора ПР с верхним участком тела ТВЭЛ-а с использованием итерационной формулы для вычисления весового коэффициента Калмана [2-4].

Результаты расчета зависимости значений функций случайного процесса изменения силы P от параметров трехфалангового схвата ПР при взаимодействии его с верхним участком тела ТВЭЛ-а при перегрузке его из одного контейнера в другой приведены в таблице.

График зависимости значений функций случайного процесса изменения силы Р от параметров трехфалангового схвата ПР при взаимодействии его с верхним участком тела ТВЭЛ-а при перегрузке его из одного контейнера в другой приведен на фигуре 6.

Таблица. Результаты расчета зависимости значений функций случайного процесса изменения силы Р от параметров трехфалангового схвата ПР при взаимодействии его с верхним участком тела ТВЭЛ-а при перегрузке его из одного контейнера в другой.

Показатели	Продолжительность периода времени измерения силы Р трехфалангового схвата манипулятора ПР при взаимодействии его с верхним участком тела ТВЭЛ-а, с				
	τ_1=0	τ_2=5	τ_2=10	τ_3=15	τ_5=20
Функция корреляции В(τ) в заданный период времени взаимодействия трехфалангового схвата при взаимодействии его с верхним участком тела ТВЭЛ-а, τ, с	2,82	2,2	0,04	03	0,05

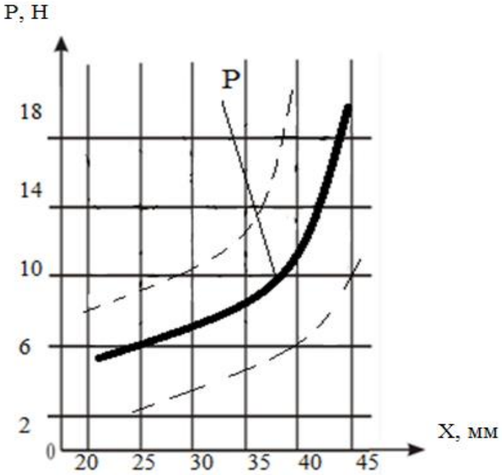

Фиг. 6. График зависимости силы Р от Х -расстояния от оси шарнира и точкой контакта внутренней поверхности каждой фаланги, с прикрепленными к каждой из них удерживающими зубьями, каждого рычага схвата с ограничивающей поверхностью верхнего участка тела ТВЭЛ-а.

3. Общие выводы

В данной работе представлена математическая модель расчета параметров трехфалангового адаптивного схвата манипулятора ПР для перегрузки ТВЭЛ-а из промежуточного контейнера в основной контейнер.

Разработаны математические методы расчета и выбора структурных, размерных и режимных параметров трехфалангового адаптивного схвата манипулятора ПР с учетом стохастических процессов его взаимодействия с ТВЭЛ-ом, перегружаемого из промежуточного контейнера в основной контейнер.

Создана мирового уровня инновационная конструкция трехфалангового адаптивного схвата манипулятора ПР с учетом его взаимодействия с ТВЭЛ-ом, применяемого при перегрузке его из промежуточного контейнера в основной контейнер.

Литература

[1] Kalman R.E. A new approach to linear filtering and prediction problems. //Journal of basic Engineering (82) (1). 1960. pp.35-454.

[2] Абылай Т.Каимов и др. Математическая модель стохастических процессов высокоэффективного разрушения грунта (россыпи, торф) инновационным отвалом бульдозера. Международный журнал //Поиск. Международный научный журнал-приложение Республики Казахстан. – Алматы. 2016. с. 253 – 259.

[3] Абылай Т.Каимов и др. Математическая модель повышения достоверности оценки эмпирических данных при разрушении грунта инновационным отвалом бульдозера со съемным режущим ножом. //Поиск. Международный научный журнал-приложение Республики Казахстан. – Алматы. 2016. с. 240 – 247.

[4] Kaiym T.T., Gribanov V.F., Kaimov A.T., Kaimov S.T., Abildabekova D.D. //Вестник Казахского национального исследовательского технического университета имени К.И.Сатпаева. №1(119). Алматы. 2017. с. 412 – 417.

[5] Самойлов А.Г. Тепловыделяющие элементы ядерных реакторов. /-М.: Энергоиздат. 1985. - 324 с.

[6] Доронин А.С., Духовянский А.С., Пунин Г.П., Медведев М.И., осадкий А.И., Пономарев-Степной Н.Н., Столярский А.Я. Тепловыделяющие элементы ядерного реактора. Описание изобретения к патенту №2095859 Российской Федерации. 10.11.1997 г. - 18 с.

[7] Ceccarelli M. Fundamentals of Mechanics of Robotic Manipulation. / Kluwer/Springer,Dordrecht, 2004.(ISBN 1-4020-1810-X).

[8] Bautista Paz E., Bernardos Rodriguez R., Ceccarelli M., et al Breve historia ilustrada de las maquinas. / ETSII, Madrid, 2007. (ISBN 978-84-7484-200-5).
[9] Lopez-Cajùn C.S., Ceccarelli M. Mecanismos: Fundamentos cinematicos para el diseno y la optimizacion de la maquinaria. / Trillas, Ciudad de Mexico, 2008 (ISBN 978-968-24-8181-9); 2nd Edition 2013.
[10] Bautista Paz E., Ceccarelli M.,Echavarri Otero J., Munoz Sanz, J.J. A brief illustrated history of machines and mechanisms, Science and Engineering, /Book series on History of Machines and Machine Science, Vol.10, Springer, Dordrecht, 2010. DOI 10.1007/978- 90-481-2512-8. ISBN: 978-90-481-2511-1.
[11] Трубин И.А. Анализ процессов захватывания и отпускания деталей схватом манипулятора. /Тр. ЛПИ. –Л.: 1982, № 382. с. 88-94.
[12] Колпашников С.Н., Челпанов И.Б. Задачи инженерного расчета схватов роботов. / Актуальные вопросы применения промышленных роботов для автоматизации производства. – Владимир. ВДНТИ. 1980. с.10 – 12.
[13] Захватные устройства промышленных роботов. Методические рекомендации. – М.: ВНИМС. 1982. – 55 с.
[14] Челпанов И.Б., Колпашников С.Н. Схваты промышленных роботов. –Л.: Машиностроение. 1989. – 287 с.
[15] Механика промышленных роботов: Учебное пособие для ВТУЗОВ: В 3 книгах. / Под ред. К.В.Фролова, Е.И.Воробьева. – М.: Высш.шк. 1988. – 304 с.
[16] Системы очувствления и адаптивные промышленные роботы. /Под ред. Е.П.Попова, В.В.Клюева. –М.: Машиностроение. – 1985. – 256 с.
[17] Динамика управления роботами. / В.В.Козлов, В.П.Макарычев, А.В.Тимофеев и др. –М.:Наука. 1984. – 336 с.
[18] Манипуляционные системы роботов. /Под ред.А.М.Корендясева. –М.:1989. – 472 с.
[19] Задачи и методы адаптивного управления при захватывании и удержании объектов схватами роботов. /Тр.6-й Всесоюзный конференции по управлению в механических системах. – Львов. 1988.
[20] Дворников Л.Ф., Спасенкова Ю.С. Двухуровневый манипулятор с замкнутой кинематической цепью. Описание изобретения к патенту № 2532751, RU. МПК B25J 9/02, F16H 21/14. 10.09.2014. Бюл. №25.- 5с.
[21] Кушманов Е.А., Кушманова Л.Е., Гонухов В.П., Сажко В.А., Итович Е.П. Манипулятор. Описание изобретения к авторскому свидетельству № 1355485. SU. МПК 4B25 J 18/00. 30.11.1987. Бюл.№44. – 5с.
[22] Смирнов А.Б., Крушинский И.А., Борисевич А.В. Пьезоэлектрический схват. Описание изобретения к патенту №2529126. RU. МПК B25J 15/08, B25J 7/00. 27.09.2014. Бюл.№27. -9с.
[23] Kashioka et al. An approach to the integrated intelligent robot with multiple sensory. Visual recognition techniques. 7th Symp on Ind. Robots. –Tokyo. 1977.
[24] Куафе Ф. Взаимодействие робота с внешней средой.: Пер. с франц. –М.: Мир. 1985. – 285 с.
[25] Т.Т. Қайым. Адаптирующиеся многоцелевые рабочие органы строительных и дорожных машин. /Монография. – Алматы. 1998. - 148 с.
[26] Т.Т.Қайым, С.М.Сейтбаталов, Е.И. Шокаев Механизация перегрузочных работе на транспорте. /Монография. – Алматы. 2002. - 323 с.

Topics 2. Kinematics and synthesis of mechanisms

Function Generation of a Watt II Type Planar Mechanism with Prismatic Output Using Decomposition and Correction Method

Gökhan KİPER

Izmir Institute of Technology
Mechanical Engineering Department
E-mail: gokhankiper@iyte.edu.tr

Abstract
The method of decomposition is a useful method for function generation with multi-loop mechanisms. Recently introduced correction methods applied together with the method of decomposition allows the designer to cancel out the errors in the first loop of a two-loop mechanism with the errors in the second loop. In this study, the decomposition and correction method is applied for a Watt II type planar six-link mechanism with prismatic output. Five design parameters are defined for each loop resulting in ten design parameters in total. The design parameters are determined analytically. The generation error is decreased by adjusting free parameters such as limits of some joint angles and parameters due to the decomposition of the function to be generated, while considering several constraints such as link lengths ratios and ranges of the joint variables. The success of the method is illustrated with a numerical example.
Keywords: Function generation, decomposition and correction method, planar Watt II mechanism with prismatic output.

1. Introduction

Recently Kiper et al. [1] introduced a new kinematic synthesis method for function generating multi-loop mechanisms based on the decomposition and correction method. For a two-loop mechanism, a function $y = f(x)$ is decomposed into two as $w = g(x)$ and $y = h(w) = h(g(x)) = f(x)$ [2]. The loops of a two-loop mechanism are used to generate the decomposed functions $w = g(x)$ and $y = h(w)$. In general for mechanisms with more than two successive loops, the function to be generated, may be decomposed into as many functions as the number of loops. The three different correction methods introduced in [1] aim neutralizing the generation error of the first loop by matching the errors due to the second loop. The correction method can be generalized for mechanisms with more than two loops as well. Kiper et al. [1] compare their methods with other function generation methods in the literature [3-5] and demonstrate the superiority of their methods for generation with less errors.

In [1], a Watt II type planar six-link mechanism with revolute joints only is used for an application of the decomposition and correction methods. Via numerical examples it is demonstrated that in general correction methods #2 and #3 provide superior results compared to correction method #1. Correction method #3 requires making use of the derivative of the loop closure equations and hence it is a relatively more complex method to apply. Therefore we choose to use correction method #2 in this study to formulize the function generation of a Watt II type planar six-link mechanism which comprises six revolute joints and a prismatic joint. The prismatic joint is the output of the mechanism. Such mechanisms are quite common in applications, where the first loop is a crank-rocker type four-bar loop and the second loop is a slider-crank loop. Some deep drawing, blanking and knuckle-joint presses comprise such mechanisms. It is not a straightforward task to formulize the design of such mechanisms as a function generation synthesis problem. Such formulizations are kept out of scope of this paper.

The paper is organized as follows: The description of the Watt II type six-link planar mechanism with prismatic output and the formulation for function generation is presented in Section 2. The correction method is explained in Section 3. A numerical example is given in Sections 4. Section 5 concludes the paper.

2. The Mechanism and Function Generation Problem Definition

The Watt II type planar six-link mechanism in this study comprises two ternary and four binary links connected to each other by six revolute joints and a prismatic joint (Fig. 1). The input/output (I/O) equation of a four-bar mechanism is not affected by the scale of the mechanism, and the four-bar loop A_0ABB_0 can be scaled independent from the slider-crank loop B_0CD, so without loss of generality we assume $|A_0B_0| = 1$. Once the synthesis task is done, the designer can scale the four-bar loop A_0ABB_0 with any desired scale ratio.

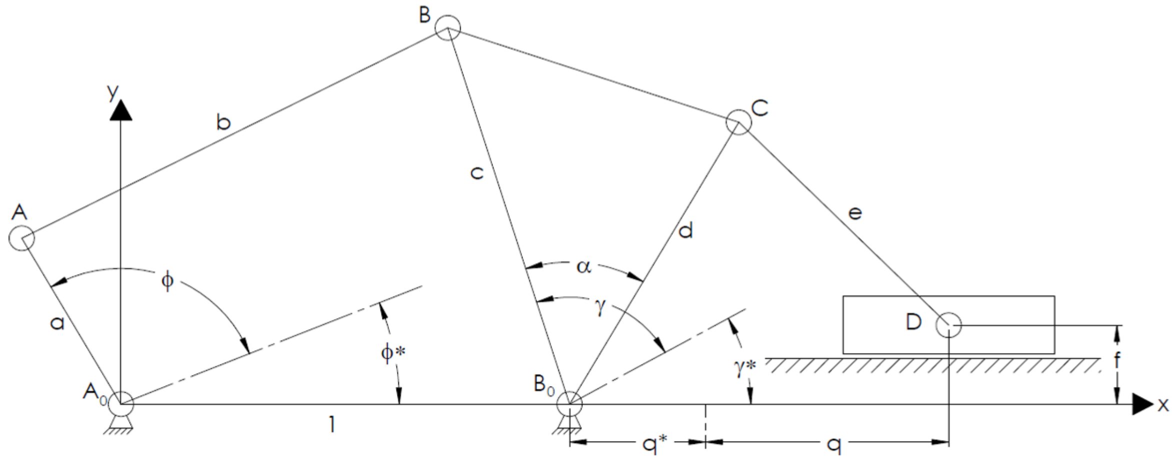

Fig. 1. Kinematic diagram of a Watt II mechanism

The origin of the coordinate frame is at A_0 and the x-axis is along A_0B_0. The link lengths of the mechanism for design are $|A_0A| = a$, $|AB| = b$, $|B_0B| = c$, $\measuredangle BB_0C = \alpha$, $|B_0C| = d$, $|CD| = e$ and the distance of point D to the x-axis is f. In Fig. 1, it is assumed that the slider displacement direction is along the x-axis, i.e. along A_0B_0. In general there might be a constant angle, say β, between the x-axis and the sliding direction of D. However, notice that the total effect of the constant angles α and β to the I/O equation of the slider-crank loop is cumulative, therefore without loss of generality one may assume $\beta = 0$ as in Fig. 1. If the designer wishes to have a nonzero β after the synthesis computations are performed, it is possible to select and arbitrary angle β and modify angle $\measuredangle BB_0C$ as $\alpha - \beta$ instead of α.

The input of the mechanism is angle ϕ and the output is the distance q. Angle γ is an intermediate variable to be used as the output of the four-bar loop and at the same time, the input of the slider-crank loop. In general the input angle can be measured from an inclined reference axis which makes an angle ϕ^* with the x-axis. ϕ^* can be used as a design parameters along with the link lengths. Similarly, angle γ may be measured from a reference axis which makes an angle γ^* with the x-axis. Also, the distance q may be measured from a constant distance q* measured from B_0.

$y = f(x)$ is to be generated for $x_0 \le x \le x_f$ using the six-link mechanism. The function $y = f(x)$ is decomposed into two as $w = g(x)$ and $y = h(w) = h(g(x)) = f(x)$. The intermediate function g() can be selected arbitrarily. Limits of w and y are computed as $w_0 = g(x_0)$, $w_f = g(x_f)$, $y_0 = f(x_0)$ and $y_f = f(x_f)$. Let $\Delta x = x_f - x_0$, $\Delta w = w_f - w_0$ and $\Delta y = y_f - y_0$. The function variables x, w, y are related with the mechanism variables ϕ, γ, q linearly as follows:

$$\frac{\phi-\phi_0}{\Delta\phi} = \frac{x-x_0}{\Delta x} \;,\; \frac{\gamma-\gamma_0}{\Delta\gamma} = \frac{w-w_0}{\Delta w} \;,\; \frac{q-q_0}{\Delta q} = \frac{y-y_0}{\Delta y} \qquad (1)$$

where $\phi_0 \le \phi \le \phi_f$, $\gamma_0 \le \gamma \le \gamma_f$, $q_0 \le q \le q_f$ and $\Delta\phi = \phi_f - \phi_0$, $\Delta\gamma = \gamma_f - \gamma_0$, $\Delta q = q_f - q_0$. The limits of the mechanism variables can be chosen arbitrarily. For given desired values of the function variables x, w, y, the corresponding mechanism variables ϕ, γ, q can be determined from Eq. (1) as:

$$\phi = \frac{\Delta\phi}{\Delta x}(x-x_0)+\phi_0 \;,\; \gamma = \frac{\Delta\gamma}{\Delta w}(w-w_0)+\gamma_0 \;, \qquad (2)$$
$$\psi = \frac{\Delta\psi}{\Delta y}(y-y_0)+\psi_0$$

Eq. (2) is used for determining the precision points of the I/O equations. Conversely, x, w, y can be determined in terms of ϕ, γ and q as

$$x = \frac{\Delta x}{\Delta\phi}(\phi-\phi_0)+x_0 \;,\; w = \frac{\Delta w}{\Delta\gamma}(\gamma-\gamma_0)+w_0 \;, \qquad (3)$$
$$y = \frac{\Delta y}{\Delta q}(q-q_0)+y_0$$

Eq. (3) is used after the synthesis procedure for checking the error between the desired y(x) and the generated y(q).

3. Formulation of the Design Equations and the Correction Method

In [1], three correction methods are presented for function generation with two-loop mechanisms. Correction method #1 assumes zero variable references ϕ^*, γ^*, q^*, etc., whereas correction method #2 assumes nonzero variable references. The precision points (points of zero error) for both loops are chosen to be common in these two correction methods. In correction method #3, the synthesis procedure for the first loop is the same as the other methods; however instead of equating the precision points of the two loops, the points which correspond to the extrema of the error in the first loop are used for the second loop. It is possible to use all three correction methods for the mechanism in Fig. 1, but for brevity only one correction method is used in this paper. As explained in Section 1, correction method #2 is used.

The I/O equation for the four-bar loop A_0ABB_0 reads

$$\left|\overrightarrow{AB}\right| = \left|\overrightarrow{A_oB} - \overrightarrow{A_oA}\right| \Rightarrow$$

$$\left\{\begin{matrix} -\dfrac{1+a^2-b^2+c^2}{2cc\gamma^*} + \dfrac{ac\phi^*}{cc\gamma^*}c\phi - \dfrac{as\phi^*}{cc\gamma^*}s\phi + \\ \dfrac{ac(\phi^*-\gamma^*)}{c\gamma^*}c(\gamma-\phi) + \dfrac{as(\phi^*-\gamma^*)}{c\gamma^*}s(\gamma-\phi) + t\gamma^* s\gamma \end{matrix}\right\} = c\gamma \tag{4}$$

where c, s and t are short for cosine, sine and tangent, respectively. Eq. (4) can be written in polynomial form for five precision points as

$$\sum_{j=1}^{6} P_j f_j(\mathbf{x}_i) - F(\mathbf{x}_i) = 0 \quad \text{for } i = 1, \dots, 5 \tag{5}$$

where $\mathbf{x}_i = \{\phi_i, \gamma_i\}$, $P_1 = -\dfrac{1+a^2-b^2+c^2}{2cc\gamma^*}$, $P_2 = \dfrac{ac\phi^*}{cc\gamma^*}$, $P_3 = \dfrac{as\phi^*}{cc\gamma^*}$, $P_4 = \dfrac{ac(\phi^*-\gamma^*)}{c\gamma^*}$, $P_5 = \dfrac{as(\phi^*-\gamma^*)}{c\gamma^*}$, $P_6 = t\gamma^*$, $f_1(\mathbf{x}_i) = 1$, $f_2(\mathbf{x}_i) = c\phi_i$, $f_3(\mathbf{x}_i) = -s\phi_i$, $f_4(\mathbf{x}_i) = c(\gamma_i - \phi_i)$, $f_5(\mathbf{x}_i) = s(\gamma_i - \phi_i)$, $f_6(\mathbf{x}_i) = s\gamma_i$ and $F(\mathbf{x}_i) = c\gamma_i$. There are five design parameters (a, b, c, ϕ^* and γ^*) in Eq. (5), so there should be five precision points: $\mathbf{x}_1$, $\mathbf{x}_2$, $\mathbf{x}_3$, $\mathbf{x}_4$ and $\mathbf{x}_5$. However there are six P_j's, hence they cannot be independent of each other. Indeed, $P_4(P_3 - P_2P_6) = P_5(P_2 + P_3P_6)$. The problem can be linearized by using a Lagrange's variable λ. Let $P_6 = \lambda$ and $P_j = m_j + n_j\lambda$ for j = 1, 2, 3, 4, 5. Substituting into Eq. (5):

$$\begin{aligned}
&\left\{\begin{matrix} m_1+n_1\lambda+(m_2+n_2\lambda)c\phi_1-(m_3+n_3\lambda)s\phi_1+ \\ (m_4+n_4\lambda)c(\gamma_1-\phi_1)+(m_5+n_5\lambda)s(\gamma_1-\phi_1) \end{matrix}\right\} = c\gamma_1 - \lambda s\gamma_1 \\
&\left\{\begin{matrix} m_1+n_1\lambda+(m_2+n_2\lambda)c\phi_2-(m_3+n_3\lambda)s\phi_2+ \\ (m_4+n_4\lambda)c(\gamma_2-\phi_2)+(m_5+n_5\lambda)s(\gamma_2-\phi_2) \end{matrix}\right\} = c\gamma_2 - \lambda s\gamma_2 \\
&\left\{\begin{matrix} m_1+n_1\lambda+(m_2+n_2\lambda)c\phi_3-(m_3+n_3\lambda)s\phi_3+ \\ (m_4+n_4\lambda)c(\gamma_3-\phi_3)+(m_5+n_5\lambda)s(\gamma_3-\phi_3) \end{matrix}\right\} = c\gamma_3 - \lambda s\gamma_3 \\
&\left\{\begin{matrix} m_1+n_1\lambda+(m_2+n_2\lambda)c\phi_4-(m_3+n_3\lambda)s\phi_4+ \\ (m_4+n_4\lambda)c(\gamma_4-\phi_4)+(m_5+n_5\lambda)s(\gamma_4-\phi_4) \end{matrix}\right\} = c\gamma_4 - \lambda s\gamma_4 \\
&\left\{\begin{matrix} m_1+n_1\lambda+(m_2+n_2\lambda)c\phi_5-(m_3+n_3\lambda)s\phi_5+ \\ (m_4+n_4\lambda)c(\gamma_5-\phi_5)+(m_5+n_5\lambda)s(\gamma_5-\phi_5) \end{matrix}\right\} = c\gamma_5 - \lambda s\gamma_5
\end{aligned} \tag{6}$$

In order for Eqs. (6) to be satisfied for an arbitrary λ, the coefficients of λ and the rest of each equation should be equal to zero. In matrix form:

$$\begin{bmatrix} 1 & c\phi_1 & -s\phi_1 & c(\gamma_1-\phi_1) & s(\gamma_1-\phi_1) \\ 1 & c\phi_2 & -s\phi_2 & c(\gamma_2-\phi_2) & s(\gamma_2-\phi_2) \\ 1 & c\phi_3 & -s\phi_3 & c(\gamma_3-\phi_3) & s(\gamma_3-\phi_3) \\ 1 & c\phi_4 & -s\phi_4 & c(\gamma_4-\phi_4) & s(\gamma_4-\phi_4) \\ 1 & c\phi_5 & -s\phi_5 & c(\gamma_5-\phi_5) & s(\gamma_5-\phi_5) \end{bmatrix} \begin{bmatrix} m_1 \\ m_2 \\ m_3 \\ m_4 \\ m_5 \end{bmatrix} = \begin{bmatrix} c\gamma_1 \\ c\gamma_2 \\ c\gamma_3 \\ c\gamma_4 \\ c\gamma_5 \end{bmatrix}$$

$$\text{and} \tag{7}$$

$$\begin{bmatrix} 1 & c\phi_1 & -s\phi_1 & c(\gamma_1-\phi_1) & s(\gamma_1-\phi_1) \\ 1 & c\phi_2 & -s\phi_2 & c(\gamma_2-\phi_2) & s(\gamma_2-\phi_2) \\ 1 & c\phi_3 & -s\phi_3 & c(\gamma_3-\phi_3) & s(\gamma_3-\phi_3) \\ 1 & c\phi_4 & -s\phi_4 & c(\gamma_4-\phi_4) & s(\gamma_4-\phi_4) \\ 1 & c\phi_5 & -s\phi_5 & c(\gamma_5-\phi_5) & s(\gamma_5-\phi_5) \end{bmatrix} \begin{bmatrix} n_1 \\ n_2 \\ n_3 \\ n_4 \\ n_5 \end{bmatrix} = \begin{bmatrix} -s\gamma_1 \\ -s\gamma_2 \\ -s\gamma_3 \\ -s\gamma_4 \\ -s\gamma_5 \end{bmatrix}$$

m_1, m_2, m_3, m_4, m_5, n_1, n_2, n_3, n_4 and n_5 are solved from Eqs. (7) by matrix inversion. λ is solved from $P_4(P_3 - P_2P_6) = P_5(P_2 + P_3P_6)$:

$$\left\{\begin{matrix} (n_3n_5+n_2n_4)\lambda^3 \\ +\left[m_5n_3+m_4n_2+n_5(m_3+n_2)+n_4(m_2-n_3)\right]\lambda^2 \\ +\left[m_5(m_3+n_2)+m_2n_5+m_4(m_2-n_3)-m_3n_4\right]\lambda \\ +m_2m_5-m_3m_4 \end{matrix}\right\} = 0 \tag{8}$$

Eq. (8) is a cubic equation in λ and can be solved analytically. Either there are one real and two imaginary solutions or three real solutions. In case of multiple solutions either solution can be used. Then, $P_j = m_j + n_j\lambda$ are determined for j = 1, …, 5. Finally, the design parameters are computed as $\gamma^* = \tan^{-1} P_6$, $\phi^*=\mathrm{atan2}(P_2, P_3)$, $a=\dfrac{P_4 c\gamma^*}{c(\phi^*-\gamma^*)}$, $c=\dfrac{ac\phi^*}{P_2 c\gamma^*}$ and $b=\sqrt{1+a^2+c^2+2cc\gamma^* P_1}$. $\gamma^* = \tan^{-1} P_6 + \pi$ is also possible. Once γ^* value is selected, ϕ^*, a, c and b are uniquely determined in terms of the P_j's, provided that b is real. a or c may be negative, in which case the limits of ϕ or γ should be increased by π. The resulting error variation is zero, that is $\delta_1 = w_{desired} - w_{generated1} = 0$, at least at five precision points (x_1, x_2, x_3, x_4 and x_5) if there is no branching problem, i.e. if $\delta_1 = 0$ at all precision points in the same assembly mode of the loop. The variation of δ_1 with respect to the function input x looks like the curve in Fig. 2.

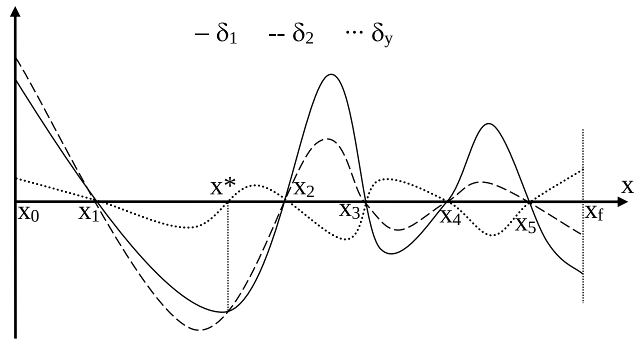

Fig. 2. Error curves for the loops (δ_1 and δ_2) and function output (δ_y)

In order to be able to compare the errors due to both loops, we assume that the outputs of both the four-bar and the slider-crank loops are link BB_0C and the output variable is γ. Hence we assume that slider displacement q is the input of the slider-crank loop and hence q is known as a linear function of the desired y values. The resulting γ as the output of the loop, and hence w values are obtained from the I/O equation of the slider-crank loop. Let $\delta_2 = w_{desired} - w_{generated2}$ as the error for given $y_{desired}(x)$ and the corresponding linearly related q values. For the dimensional synthesis of the slider-crank loop, the same precision points as the four-bar loop are used and δ_2 and δ_1 are forced to be approximately equal by changing the free variables such as the angle limits ϕ_0, ϕ_f, γ_0, γ_f. Changing linear variable limits q_0, q_f only affects the scale of the slider-crank loop, but has not effect on the amount of the generation error. The I/O equation for the slider-crank loop is given by

$$\left|\overrightarrow{CD}\right| = \left|\overrightarrow{B_oD} - \overrightarrow{B_oC}\right| \Rightarrow$$
$$\left\{\begin{aligned} &\frac{q^{*2}+d^2-e^2+f^2}{2dc(\gamma^*-\alpha)} + \frac{q^*}{dc(\gamma^*-\alpha)}q \\ &+\frac{1}{2dc(\gamma^*-\alpha)}q^2 + t(\gamma^*-\alpha)qs\gamma \\ &+\left[q^* t(\gamma^*-\alpha) - f\right]s\gamma - \left[q^* + ft(\gamma^*-\alpha)\right]c\gamma \end{aligned}\right\} = qc\gamma \tag{9}$$

Eq. (9) can be written in polynomial form Eq. (5) for five precision points where $\mathbf{x}_i = \{\gamma_i, q_i\}$, $P_1 = \dfrac{q^{*2}+d^2-e^2+f^2}{2dc(\gamma^*-\alpha)}$, $P_2 = \dfrac{q^*}{dc(\gamma^*-\alpha)}$, $P_3 = \dfrac{1}{2dc(\gamma^*-\alpha)}$, $P_4 = t(\gamma^*-\alpha)$, $P_5 = q^* t(\gamma^*-\alpha) - f$, $P_6 = q^* + ft(\gamma^*-\alpha)$, $f_1(\mathbf{x}_i) = 1$, $f_2(\mathbf{x}_i) = q_i$, $f_3(\mathbf{x}_i) = q_i^2$, $f_4(\mathbf{x}_i) = q_i s\gamma_i$, $f_5(\mathbf{x}_i) = s\gamma_i$, $f_6(\mathbf{x}_i) = -c\gamma_i$ and $F(\mathbf{x}_i) = q_i c\gamma_i$. The five precision points are selected as a function of y_i, hence as a function of x_i for i = 1, …, 5, where x_i are the precision points used for the four-bar loop. There are six P_j's in terms of five design parameters: α, d, e, f and q^*. P_j's are interrelated as $P_2\left(1+P_4^2\right) - 2P_3\left(P_4P_5 + P_6\right) = 0$. Let $P_4 = \lambda$ and $P_j = m_j + n_j\lambda$ for j = 1, 2, 3, 5, 6. Substituting into Eq. (9):

$$\begin{aligned}
&\left\{\begin{aligned} &m_1 + n_1\lambda + (m_2+n_2\lambda)q_1 + (m_3+n_3\lambda)q_1^2 \\ &\quad +(m_5+n_5\lambda)s\gamma_1 - (m_6+n_6\lambda)c\gamma_1 \end{aligned}\right\} = q_1c\gamma_1 - \lambda q_1 s\gamma_1 \\
&\left\{\begin{aligned} &m_1 + n_1\lambda + (m_2+n_2\lambda)q_2 + (m_3+n_3\lambda)q_2^2 \\ &\quad +(m_5+n_5\lambda)s\gamma_2 - (m_6+n_6\lambda)c\gamma_2 \end{aligned}\right\} = q_2c\gamma_2 - \lambda q_2 s\gamma_2 \\
&\left\{\begin{aligned} &m_1 + n_1\lambda + (m_2+n_2\lambda)q_3 + (m_3+n_3\lambda)q_3^2 \\ &\quad +(m_5+n_5\lambda)s\gamma_3 - (m_6+n_6\lambda)c\gamma_3 \end{aligned}\right\} = q_3c\gamma_3 - \lambda q_3 s\gamma_3 \\
&\left\{\begin{aligned} &m_1 + n_1\lambda + (m_2+n_2\lambda)q_4 + (m_3+n_3\lambda)q_4^2 \\ &\quad +(m_5+n_5\lambda)s\gamma_4 - (m_6+n_6\lambda)c\gamma_4 \end{aligned}\right\} = q_4c\gamma_4 - \lambda q_4 s\gamma_4 \\
&\left\{\begin{aligned} &m_1 + n_1\lambda + (m_2+n_2\lambda)q_5 + (m_3+n_3\lambda)q_5^2 \\ &\quad +(m_5+n_5\lambda)s\gamma_5 - (m_6+n_6\lambda)c\gamma_5 \end{aligned}\right\} = q_5c\gamma_5 - \lambda q_5 s\gamma_5
\end{aligned} \tag{10}$$

Separating the coefficients of λ and the rest of each equation in Eqs. (10) and writing in matrix form:

$$\begin{bmatrix} 1 & q_1 & q_1^2 & s\gamma_1 & -c\gamma_1 \\ 1 & q_2 & q_2^2 & s\gamma_2 & -c\gamma_2 \\ 1 & q_3 & q_3^2 & s\gamma_3 & -c\gamma_3 \\ 1 & q_4 & q_4^2 & s\gamma_4 & -c\gamma_4 \\ 1 & q_5 & q_5^2 & s\gamma_5 & -c\gamma_5 \end{bmatrix} \begin{bmatrix} m_1 \\ m_2 \\ m_3 \\ m_5 \\ m_6 \end{bmatrix} = \begin{bmatrix} q_1 c\gamma_1 \\ q_2 c\gamma_2 \\ q_3 c\gamma_3 \\ q_4 c\gamma_4 \\ q_5 c\gamma_5 \end{bmatrix}$$

and (11)

$$\begin{bmatrix} 1 & q_1 & q_1^2 & s\gamma_1 & -c\gamma_1 \\ 1 & q_2 & q_2^2 & s\gamma_2 & -c\gamma_2 \\ 1 & q_3 & q_3^2 & s\gamma_3 & -c\gamma_3 \\ 1 & q_4 & q_4^2 & s\gamma_4 & -c\gamma_4 \\ 1 & q_5 & q_5^2 & s\gamma_5 & -c\gamma_5 \end{bmatrix} \begin{bmatrix} n_1 \\ n_2 \\ n_3 \\ n_5 \\ n_6 \end{bmatrix} = \begin{bmatrix} -q_1 s\gamma_1 \\ -q_2 s\gamma_2 \\ -q_3 s\gamma_3 \\ -q_4 s\gamma_4 \\ -q_5 s\gamma_5 \end{bmatrix}$$

After m_1, m_2, m_4, m_5, m_6, n_1, n_2, n_4, n_5 and n_6 are solved from Eqs. (11) by matrix inversion, λ is determined using

$$P_2\left(1+P_4^2\right)-2P_3\left(P_4P_5+P_6\right)=0:$$

$$\left\{\begin{aligned} &\left(n_2-2n_3n_5\right)\lambda^3+\left[m_2-2\left(m_3n_5+n_3\left(m_5+n_6\right)\right)\right]\lambda^2 \\ &+\left[n_2-2\left(n_3m_6+m_3\left(m_5+n_6\right)\right)\right]\lambda+m_2-2m_3m_6 \end{aligned}\right\}=0 \quad (12)$$

Eq. can be solved analytically and results in either one or three real solutions for λ. Once λ is determined or selected, $P_3 = \lambda$ and $P_j = m_j + n_j\lambda$ are determined for j = 1, 2, 4, 5, 6. Finally the design parameters are solved as $\alpha = \gamma^* - \tan^{-1} P_4$ or $\alpha = \gamma^* - \tan^{-1} P_4 + \pi$, $d = 1/\left(2c\left(\gamma^*-\alpha\right)P_3\right)$, $q^* = P_2/(2P_3)$, $f = q^*P_4 - P_5$ and $e = \sqrt{q^{*2}+d^2+f^2-P_1/P_3}$. α is selected so that d is positive. e, f and q* are determined uniquely provided that e is real.

Representative δ_1 and δ_2 curves versus the function input x are illustrated in Fig. 2. As a result of the whole design process, the q output values of the 6-link mechanism result in corresponding $y_{generated}$ values as the output of the generated function. For given function input x, and hence corresponding mechanism input angle ϕ, the error variance $\delta_y = y_{desired} - y_{generated}$ is also depicted in Fig. 2. Definitely $\delta_y = 0$ at the precision points x_1, x_2 and x_3. There may be other points where $\delta_y = 0$ whenever δ_1 curve intersects δ_2, such as x* in Fig. 2.

The closer δ_1 and δ_2 curves, the lower are the δ_y values. In order to obtain lower δ_y error values the designer can adjust several freely selected parameters such as the limits ϕ_0, ϕ_f, γ_0, γ_f of the input joint variable ϕ and intermediate joint variable γ of the mechanism. Also, it is possible to adjust the intermediate function g(·) for most of the functions. When a software such as Microsoft Excel® is used for the computations, the designer can make use of spin buttons for varying the limits of the ϕ, γ and q and, if available, the intermediate function parameter(s) for g(·). By continuously changing the free parameters, the designer can immediately see the tendency of change in the error variations δ_1, δ_2 and δ_y. At the same time, it is possible to monitor a proper norm of the error, such as the maximum error $|\delta_y|_{max}$ or rms error of δ_y and minimize it. Meanwhile, certain design considerations such as maximum link length to minimum link length ratio, transmission angles, etc. can be monitored.

4. Numerical Example

The formulations in Section 3 are implemented in Excel and a design environment is constructed which can be used for any arbitrary function. For the example in Fig. 3, the function to be generated is $y = x^2$ for $1 \le x \le 5$. The intermediate function is $g(x) = x^k$, where k is an adjustment parameter for the designer. The synthesis computations described in Section 3 are implemented in the Loop1 and Loop2 sheets. In the sheet shown in Fig. 3 the designer can adjust the joint variable limits ϕ_0, ϕ_f, γ_0, γ_f, q_0, q_f with spin buttons; the configuration of the loops (config1 and config2); and select the Lagrange variable values λ_1 and λ_2 for the two loops – each out of three possible solutions from their respective cubic equations. By these adjustments, error variation curves δ_1, δ_2 and δ_y are monitored simultaneously. Also the maximum error $|\delta_y|_{max}$ and the ratio of the longest link (better less than 10) to the shortest link is monitored. Also the joint variable ranges $\Delta\phi$ and $\Delta\gamma$ should not be too small (better more than 20°). Also the mechanism is drawn and its motion can be simulated with a spin button. A good result is obtained usually in less than in hour – in less time than running any numerical optimization algorithm.

After several trials, a good result for the maximum error $|\delta_y|_{max} = 2.6 \times 10^{-4}$ is obtained for $|A_0B_0| = 1$, $|A_0A| = a = 0.379$, $|AB| = b = 2.090$, $|B_0B| = c = 2.702$, $\phi^* = 230.1°$, $\gamma^* = 78.6°$, $|B_0C| = d = 2.994$, $|CD| = e = 1.483$, $D_y = f = 1.251$, $\alpha = 10.6°$ and $q^* = -4.253$. The link lengths 1, a, b, c of the four-bar loop can be scaled arbitrarily. It is observed during the computations that the limits of the slider variable q has no effect on the error variations. The designer can adjust $\Delta q = q_f - q_0$ in order to scale the slider-crank loop link lengths d, e, f. The slider direction can also be adjusted by modifying the angle α as described in Section 2.

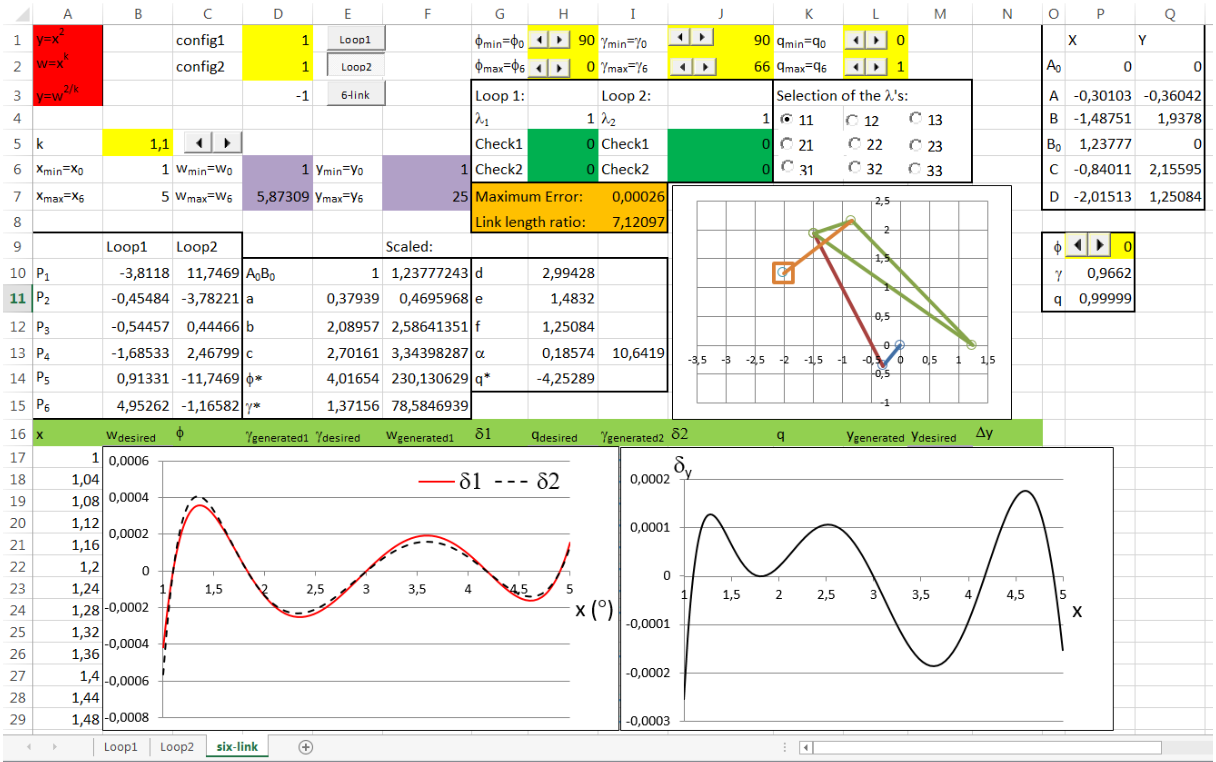

Fig. 3. Excel design sheet

5. Conclusions

In this paper, the method of decomposition and correction is applied for a Watt II type planar six-link mechanism with prismatic output. An analytical method for determining five design parameters for each loop, hence a total number of ten design parameters is presented. There are several free design parameters, such as the limits of the input and intermediate angles of the mechanism and the parameter or parameters that appear during the decomposition of the function to be generated. Also there may be multiple solutions due to the solution of the nonlinear equation in terms of Lagrange parameters. These free design parameters and options for the Lagrange parameters gives a great amount of flexibility to the designer in order to minimize the generation error while considering several constraints such as link lengths ratios and ranges of the joint variables. The method presented in the paper is illustrated with a numerical example. $y = x^2$ is generated for $1 \le x \le 5$ with a maximum error value of 2.6×10^{-4} for y. The generation precision is very good when compared to the other results in the literature.

Acknowledgments

The teachings of Prof. Dr. Tech. Sc. Rasim Alizade are gratefully acknowledged. Also, Dr. Can Dede, Mr. Omar Maaroof, Ms. Merve Özkahya and Mr. Cevahir Karagöz are acknowledged for the discussions on the subject of this paper.

References

[1]. G. Kiper, M.İ. C.Dede, O.W.Maaroof, & M. Özkahya, *Function generation with two loop mechanisms using decomposition and correction method*, Mechanism and Machine Theory 110, pages 16-26, 2017.

[2]. Alizade R.I., Aydazade K.P., Novruzbekov I.G.. *Analysis and synthesis of planar mechanisms by using decomposition method*, Journal of Mechanics of Machines, The Academy of Sciences of the USSR 57, pages 26-32, 1980.

[3]. E.C.Kinzel, J.P.Schmiedeler, & G.R.Pennock, *Function generation with finitely separated precision points using geometric constraint programming*, ASME Journal of Mechanical Design 129, pages 1185-1190, 2007.

[4]. W. M.Hwang, & Y.J.Chen, *Defect-free synthesis of Stephenson-II function generators*, ASME Journal of Mechanisms and Robotics 2(4), ID: 041012, 2010.

[5]. R. Sancibrian, *Improved GRG method for the optimal synthesis of linkages in function generation problems*, Mechanism and Machine Theory 46(10), pages 1350-1375, 2011.

Proceedings of the International Symposium of Mechanism and Machine Science, 2017
AzC IFToMM – Azerbaijan Technical University
11-14 September 2017, Baku, Azerbaijan

Hybrid Dimensional Synthesis of Planar Mechanisms for the Combination of Finite Positions and Path-Points

Mario MÜLLER[1]*, Esther HÖRTER[2], Mathias HÜSING[2], Burkhard CORVES[2]

[1*] Department of Mechanism Theory and Dynamics of Machines
RWTH Aachen University
mueller@igm.rwth-aachen.de

[2] Department of Mechanism Theory and Dynamics of Machines
RWTH Aachen University

Abstract
The combination of the established synthesis methods for finite positions and path-points leads to a hybrid dimensional synthesis method that is presented within this paper. This hybrid method combines the advantages of the established synthesis methods so that an adjustable definition of a synthesis task as well as a high performance of the algorithm can be ensured. To realize this combination, the established algorithms have to be modified as shown within this paper. Depending on the synthesis task and its degree of freedom, a solution can be found analytically or numerically. Both of these algorithms as well as the algorithm for the calculation of the synthesis degree of freedom is treated in this contribution. The shown approaches are validated by two examples.

Keywords: Dimensional Synthesis, Planar Mechanisms, Finite Position, Path-Point

1 Introduction

The process of mechanism synthesis can be divided into the two main tasks: structural synthesis and dimensional synthesis [1]. Based on several boundary conditions, the type synthesis process determines the most suitable structure of a mechanism. That includes the determination of the number and kinds of joints and links. The task of the dimensional synthesis is to identify the kinematic parameters of a chosen structure. So, based on a specific motion task or other specifications, the dimension of each link can be determined.

Both, the structural and the dimensional synthesis highly depend on the definition of the synthesis task. A synthesis task of a guidance mechanism can consist of finite positions or path-points [2]. For a linkage that is based only on revolute or prismatic joints the number of finite positions or path-points is limited. Such a four-bar-mechanism for instance can be synthesized with a maximum number of five finite positions. To determine the maximum number of synthesis task elements that can be realized by a specific mechanism, the value of the synthesis task (sDOF) can be calculated by [2]. Mechanisms can fulfill a synthesis task if their value is greater or equals to the value of this task. A four-bar mechanism with four revolute joints can theoretically fulfill up to five finite positions or nine path-points. This number of possible positions or points decreases if specific joint locations are prescribed.

Nowadays, dimensional synthesis methods mostly focus on either the specification of finite positions or the definition of path-points. Only few, such as [3], developed a method to combine both specifications. The main disadvantage of the developed algorithm in [3] is, that it does not allow the specification of joint locations. A hybrid dimensional synthesis, that allows the definition of finite positions, path-points as well as the location of joints combines the advantages of both established synthesis methods and allows a more adjustable but still robust way to design mechanisms. Some tasks in application, such as pick and place tasks, only require a limited number of finite positions [3–5]. For those tasks a hybrid dimensional synthesis gives the possibility to add additional specifications such as joint locations instead of arbitrary angles of a finite position.

2 Established Dimensional Synthesis Methods

The two most established dimensional synthesis methods are the finite position synthesis based on Burmester [6] and the definition of path-points.

2.1 Finite Position Synthesis

In 1888 Burmester published his approach to synthesize four-bar linkages for the maximum number of five precision positions [6]. Ever since, this approach has been modified and used for the dimensional synthesis of dyads and linkages [7–13].

The basic concept of this approach is the determination of the center-point curve and the corresponding circle-point curve based on the relative displacement poles [9]. Fig. 1 shows an example of these curves for four finite positions. Every point on the center-point curve k_M belongs to an RR chain that reaches all four positions and hence can be used as a stationary revolute joint of a four-bar mechanism. Every center-point has a corresponding circle-point on the circle-point curve k_{K1} which defines the location of the non-stationary revolute joint of the RR chain.

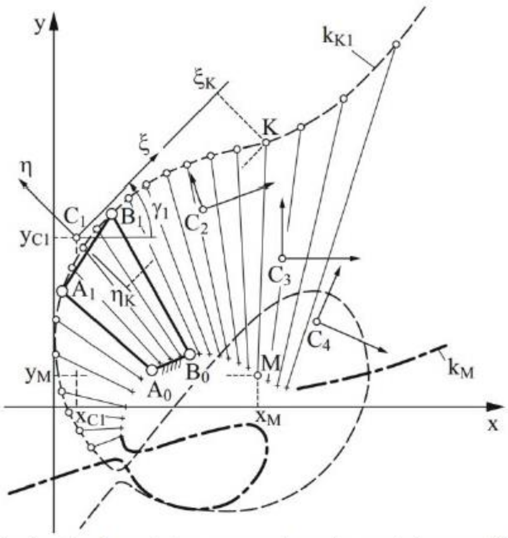

Fig. 1: Circle-point curve and center-point curve [2]

To solve the synthesis task for five finite positions algebraically Dittrich, Braune et al. developed in [7; 14] the nonlinear system of equations (1). This system of equation formulates the relation between the coordinates of the center-points (x_M, y_M) and the coordinates of the circle-point (ξ_K, η_K) in relation to the given finite positions. The coefficients A_j - G_j simply depend on these finite positions (2).

$$A_j + B_j\xi_K + C_j\eta_K + D_jx_M + E_jy_M + F_j(x_M\xi_K + y_M\eta_K) + G_j(y_M\xi_K - x_M\eta_K) = 0 \qquad j = 1,2,3 \tag{1}$$

$$A_j \dots G_j = f(x_{Ci}, x_{Ci+1}, y_{Ci}, y_{Ci+1}, \gamma_i, \gamma_{i+1}) \tag{2}$$

Since this approach leads to a cubic equation shown in [7], the solving algorithm is performant. The problem of this approach is that the synthesis task has to consist of finite positions. So even if a specific angle γ_i is not desired, it has to be defined to use the algorithm based on the Burmester theorem. That limits the solution space and reduces the number of additional boundary conditions.

2.2 Synthesis of Path-Points

The approach of the dimensional synthesis based on the definition of points of a coupler curve provides a relatively adjustable way of synthesis task definition. Here a four-bar linkage can be synthesized by specifying up to nine points of the coupler curve [11; 15; 16]. The unknown locations of the revolute joints can be calculated with the parameters shown in Fig. 2.

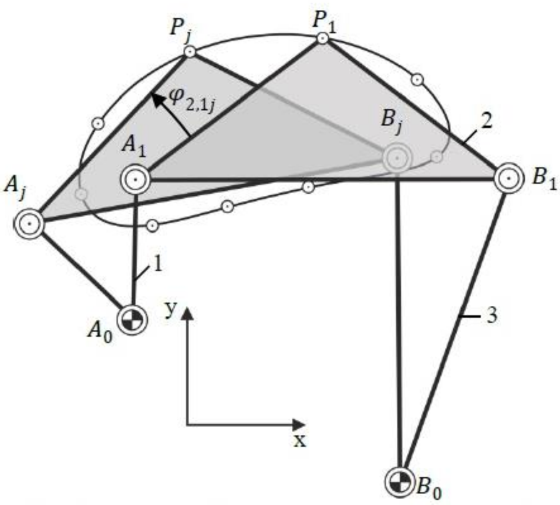

Fig. 2: Four-bar mechanism for the path-point synthesis

This approach is based on the motion of joint A respectively joint B in reference to the first path-point P_1 (3).

$$\begin{pmatrix} x_{P,j} - x_{A/B,j} \\ y_{P,j} - y_{A/B,j} \end{pmatrix} = \begin{pmatrix} \cos(\varphi_{2,1j}) & -\sin(\varphi_{2,1j}) \\ \sin(\varphi_{2,1j}) & \cos(\varphi_{2,1j}) \end{pmatrix} \begin{pmatrix} x_{P,1} - x_{A/B,1} \\ y_{P,1} - y_{A/B,1} \end{pmatrix} \tag{3}$$

The property that the length of each link does not change can be expressed by equation (4).

$$\left(x_{A/B,j} - x_{A0/B0}\right)^2 + \left(y_{A/B,j} - y_{A0/B0}\right)^2 = \left(x_{A/B,1} - x_{A0/B0}\right)^2 + \left(y_{A/B,1} - y_{A0/B0}\right)^2 \tag{4}$$

The specification of nine path-points leads to eight equations. These eight equations can be used to calculate the eight unknown locations of the revolute joint.

In comparison to the finite positions synthesis the performance and the chance to find a suitable solution is quite bad. The advantage is that the synthesis task and the boundary conditions can be specified adjustably.

3 Hybrid Dimensional Synthesis

The aim of the hybrid dimensional synthesis is the combination of the advantages of both mentioned approaches to create an adjustable as well as performant synthesis method. Unlike the approach described in [3], the following algorithm allows the specification of joint locations. Furthermore, an analytical synthesis algorithm is shown.

3.1 Value of the synthesis task

Since this hybrid approach will also have limitations concerning the maximum number of finite positions, points of a coupler curve and joint locations, it is necessary to consider the value of the synthesis task. The approach used here is distinguished from the approach mentioned in [2] to fit the special requirements of the hybrid dimensional synthesis. The used approach will be explained by the synthesis task in Fig. 3.

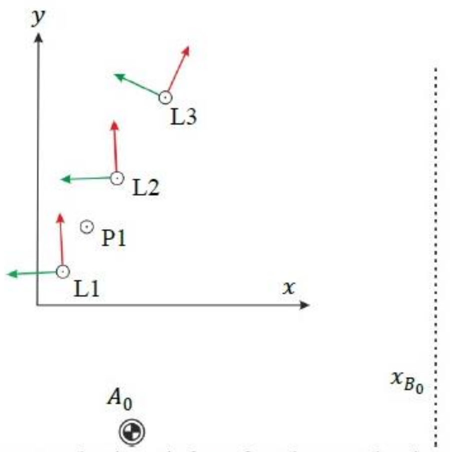

Fig. 3: Synthesis task for a four-bar mechanism

This synthesis task consists of three finite positions (L1 - L3), one point of a coupler curve (P1) and three specifications about the location of the joints (x_{Ao}, y_{Ao}, x_{Bo}). By the definition of at least one finite position or one point of the coupler curve, the remaining synthesis degree of freedom (sDOF) of a four-bar linkage is equal to the number of joints times two.

Since the finite position synthesis based on the Burmester theorem provides a synthesis method for dyads, the algorithm of identifying the sDOF has to check if the synthesis of one dyad is over-determined. The regulation for the sDOF calculation can be seen in Table 1.

A dyad based on two revolute joints ($n_1 = 2$) has the sDOF equals four. Each joint specification such as an x- or y-coordinate reduces the sDOF by one. The specification of the first finite position n_3 does not influence the sDOF since it defines the relative position of the coupler point. Each additional specification of a finite position n_3 reduces the sDOF by one as well.

Table 1: Calculation of the sDOF for a dyad

Dyad		*sDOF*
n_1	No. revolute joints	$+2 \cdot n_1$
n_2	No. Prismatic joints	$+1 \cdot n_2$
(n_3-1)	No. finite positions	$-1 \cdot (n_3-1)$
n_4	No. joint specifications	$-1 \cdot n_4$

The four-bar linkage of the synthesis task shown in Fig. 3 consists of the two dyads A_0AC and B_0BC where C represents the coupler point, that has to move through the three finite positions (L1 - L3) and point (P1). The sDOF specifications of each dyad based on Table 1 are listed in Table 2.

Table 2: sDOF specifications for A_0AC and B_0BC

A_0AC	*sDOF*
$n_1 = 2$	+4
$n_2 = 0$	0
$n_3 = 3$	-2
$n_4 = 2$	-2
Σ	**0**

B_0BC	*sDOF*
$n_1 = 2$	+4
$n_2 = 0$	0
$n_3 = 3$	-2
$n_4 = 1$	-1
Σ	**1**

It can be seen that the final sDOF of dyad A_0AC is equal to zero. There are no additional specifications possible for this dyad. The sDOF of dyad B_0BC is equal to one. The sDOF of the complete four-bar linkage is calculated by the sum of the dyads and so it is equal to one, too. Since the complete mechanism is underdetermined, there is the possibility of one additional specification concerning a desired path-point. So the overall sDOF of the synthesis task in Fig. 3 is equal to zero and can be solved exactly.

Table 3 shows the property of a synthesis task related to the sDOF. Overdetermined synthesis tasks cannot be solved exactly. They only can be approximated via an optimization. Underdetermined synthesis tasks have an infinitive number of possible solutions. They can be optimized concerning different criterions such as installation space, length of linkages, dynamical properties, transmission properties and so forth. This contribution deals with hybrid dimensional synthesis where the sDOF is equals to zero. If the synthesis task is solvable by linkages based on revolute and prismatic joints, there are always a limited number of solutions which exactly fulfill the synthesis task.

Table 3: Properties of the synthesis tasks

sDOF	*Property*
$sDOF < 0$	Overdetermined
$sDOF = 0$	Exact solution possible
$sDOF > 0$	Underdetermined

3.2 Algorithm for the synthesis

The algorithm explained within this chapter shows a new approach to synthesize these exact solutions for an sDOF equal to zero. It is necessary to distinguish between two different cases of synthesis tasks, the analytically solvable and the numerically solvable synthesis task.

3.2.1 Case 1: Analytically solvable synthesis task

The first case is the analytically solvable synthesis task. An algorithmic overview of such a task is given in Fig. 4. The specialty of this case is, that the sDOF of one dyad is equal to zero and hence can be synthesized via the finite position synthesis mentioned in chapter 2.1. The second dyad has to be underdetermined.

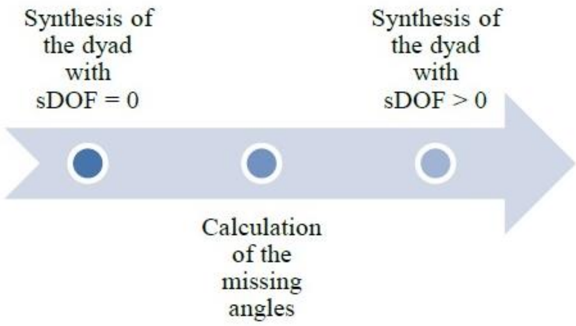

Fig. 4: Algorithm for analytically solvable synthesis tasks

To synthesize the second dyad the approach displayed in Fig. 5 based on [2] can be used. The coupler point of the synthesized dyad has to be moved in the desired path-points. Therefore it is necessary that the path-point can be reached by the dyad. Thus, the required angles of the coupler link in each point can be determined. These angles are the additional input for the synthesis of the second dyad.

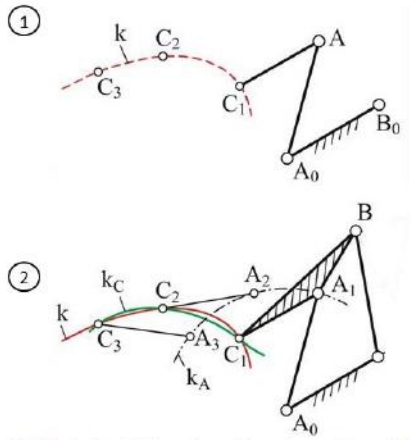

Fig. 5: Sketch of the algorithm based on [2]

To fulfill one point of the coupler curve C_i there are two possible angles γ_i of the coupler linkage (compare to Fig. 6 left).

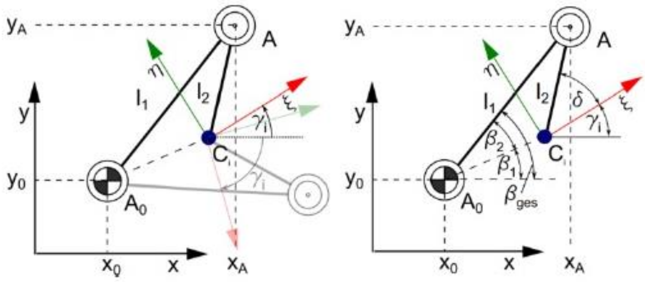

Fig. 6: Calculation of the missing angles

The angle γ_i can be calculated in subject to the already synthesized dyad A_0AC. Therefore, the angle δ can be calculated related to the position of the revolute joint A in the η,ξ-coordinate system of the coupler link:

$$\delta = \operatorname{atan2}\left(\frac{\xi_A}{\eta_A}\right) \tag{5}$$

The angles β_1 and β_2 can be calculated via equation (6) and (7) where l_C is the distance between the joint A_0 and the path-point C_i.

$$\beta_1 = \operatorname{atan2}\left(\frac{y_{Ci} - y_0}{x_{Ci} - x_0}\right) \tag{6}$$

$$\beta_2 = \operatorname{acos}\left(\frac{-l_2^2 + l_1^2 + l_C^2}{2 l_2 l_C}\right) \tag{7}$$

The angle β_{ges} now can have the two possible solutions (8) to calculate the global coordinates (9) of joint A.

$$\beta_{ges} = \beta_1 \pm \beta_2 \tag{8}$$

$$\begin{pmatrix} x_A \\ y_A \end{pmatrix} = \begin{pmatrix} l_1 \cos(\beta_{ges}) + x_0 \\ l_1 \sin(\beta_{ges}) + y_0 \end{pmatrix} \tag{9}$$

The resulting γ_i can be calculated via equation (10).

$$\gamma_i = \operatorname{atan2}\left(\frac{y_A - y_{Ci}}{x_A - x_{Ci}}\right) - \delta \tag{10}$$

Since now every path-point of the synthesis task has at least one angle γ_i, the sDOF of the second dyad is equal to zero and can be synthesized with the finite position synthesis. This approach uses the same algorithms as the finite position synthesis and so it is as performant as the established approach. Besides, it allows a more adjustable input for the synthesis task.

3.2.2 Case 1: Example of the analytical algorithm

The synthesis task shown in Fig. 3 is an example for a analytically solvable motion task. Here the synthesis of dyad A_0AC has the sDOF equal to zero so the finite position synthesis from section 2.1 can be used. Input for this synthesis is the location of joint A_0 and the three finite positions L1 - L3. With this information the grey dyad in Fig. 7 can be synthesized.

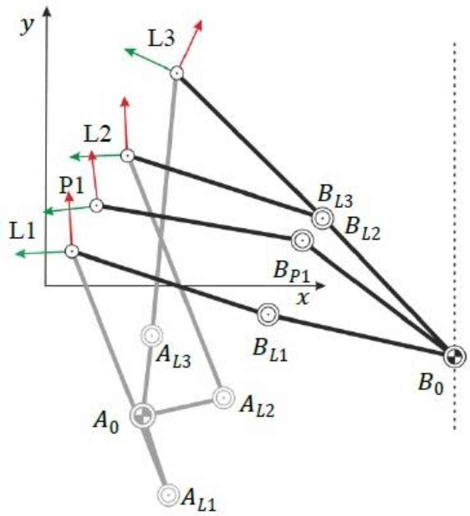

Fig. 7: Synthesis of case 1

In the next step the two possible angles γ_i of the coupler link in point P1 can be calculated via equation (5) - (10). Afterwards the next dyad can be synthesized via the input of x_{B0}, the finite positions L1 - L3 as well as the Postion P1 with the calculated angles γ_i. So this dyad is not underdetermined anymore. The black dyad in Fig. 7 shows one solution of the synthesis task for the underdetermined dyad.

Since there are two possible angles of the coupler linkage in each point, there is more than one solution for this task. Subsequently it is possible to choose from a set of solutions the best for the given synthesis task. This could be the property that all finite positions and path-points belong to the same coupler curve and thus can be reached without disassembling. This example shows the advantages of the new approach. Instead of the classical synthesis method the hybrid dimensional synthesis ensures that not only three finite positions can be specified for a given location of A_0.

3.2.3 Case 2: Numerically solvable synthesis task

If the sDOFs of both dyads are underdetermined the algorithm explained in chapter 3.2.1 is not applicable anymore. Here the recommended approach is still based on the finite position synthesis to fulfill the performance requirements. The difference is that the dyads of the linkage cannot be synthesized separately. So, the four-bar mechanism has to be considered in its entirety. For the specification of a finite position, equation (1) can be solved according to the finite position synthesis explained in section 2.1.

For the specification of a desired point of a coupler curve, the angle γ_{i+1} is not specified. Since each parameter A_j - G_j is a function of the finite positions (2) this equation system now changes if just a point of a coupler curve (x_{Cj+1}, y_{Cj+1}) is desired. The parameter A_j, D_j and E_j do not depend on the angle γ_{i+1}. All other parameters have to be itemized as shown in equation (11).

$$\begin{aligned} & A_j + D_j x_M + E_j y_M \\ & + [x_{Ci}\cos(\gamma_i) + y_{Ci}\sin(\gamma_i) - x_{Ci+1}\cos(\gamma_{i+1}) \\ & - y_{Ci+1}\sin(\gamma_{i+1})]\xi_K \\ & + [-x_{Ci}\sin(\gamma_i) + y_{Ci}\cos(\gamma_i) + x_{Ci+1}\sin(\gamma_{i+1}) \\ & - y_{Ci+1}\cos(\gamma_{i+1})]\eta_K \\ & + [-\cos(\gamma_i) + \cos(\gamma_{i+1})](x_M\xi_K + y_M\eta_K) \\ & + [-\sin(\gamma_i) + \sin(\gamma_{i+1})](y_M\xi_K - x_M\eta_K) = 0 \end{aligned} \tag{11}$$

This equation can be categorized by the terms $\cos(\gamma_{i+1})$ and $\sin(\gamma_{i+1})$ with the unknown angle γ_{i+1}. This leads to the equation (12) with the coefficients according to equation (13) - (15).

$$a_1 = a_2 \sin(\gamma_{i+1}) + a_3\cos(\gamma_{i+1}) \tag{12}$$

$$\begin{aligned} a_1 &= -A_j - D_j x_M - E_j y_M \\ &- [x_{Ci}\cos(\gamma_i) + y_{Ci}\sin(\gamma_i)]\xi_K \\ &- [-x_{Ci}\sin(\gamma_i) + y_{Ci}\cos(\gamma_i)]\eta_K \\ &+ \cos(\gamma_i)\,(x_M\xi_K + y_M\eta_K) \\ &+ \sin(\gamma_i)\,(y_M\xi_K - x_M\eta_K) \end{aligned} \tag{13}$$

$$a_2 = -y_{Ci+1}\xi_K + x_{Ci+1}\eta_K + \xi_K y_M - \eta_K x_M \tag{14}$$

$$a_3 = -x_{Ci+1}\xi_K - y_{Ci+1}\eta_K + \xi_K x_M + \eta_K y_M \tag{15}$$

Equation (12) has to be formulated for both dyads of the four-bar mechanism and thus leads to a linear equation system (16) with two equations and the two unknowns $\cos(\gamma_{i+1})$ and $\sin(\gamma_{i+1})$. This linear equation system can be solved with Cramer's rule.

$$\begin{pmatrix} a_{2,1} & a_{3,1} \\ a_{2,2} & a_{3,2} \end{pmatrix} \begin{pmatrix} \sin(\gamma_{i+1}) \\ \cos(\gamma_{i+1}) \end{pmatrix} = \begin{pmatrix} a_{1,1} \\ a_{1,2} \end{pmatrix} \tag{16}$$

The combination of the solution of (16) with (17) leads to the final equation (18).

$$\sin^2(\gamma_{i+1}) + \cos^2(\gamma_{i+1}) = 1 \tag{17}$$

$$\begin{aligned} &(a_{1,1}a_{3,2} - a_{3,1}a_{1,2})^2 + (a_{2,1}a_{1,2} - a_{1,1}a_{2,2})^2 \\ &- (a_{2,1}a_{3,2} - a_{3,1}a_{2,2})^2 = 0 \end{aligned} \tag{18}$$

Each specification of a finite position leads to a total of two equations of type (1) (one for each dyad). Each specification of a path-point leads to one equation of type (18). Since this system of equation is no longer analytically solvable, a numerical optimization method such as a particle swarm algorithm can be used. To increase the performance at this point, the optimization algorithm will use just as many joint locations as is necessary to solve all equations of type (1). The output of this equation system is the input for the objective function (18).

3.2.4 Case 2: Example of the numerical algorithm

To show an example of the numerical algorithm the task of Fig. 8 should be synthesized.

This synthesis task consists of the definition of both joint co-ordinates of A_0, two finite positions L1 and L2 as well as four desired points of the coupler curve P1 - P4. Analogously to section 3.1 the sDOF specifications for the two dyads of this synthesis are calculated in Table 4. Each dyad has an sDOF greater than zero, so no analytical approach is possible. The sum of the sDOF of both dyads is equal to four. That enables the definition of the four desired points of the coupler curve P1 – P4.

For the two finite positions L1 and L2 one equation of type (1) per dyad can be formulated. With the information of joint A_0 the mechanism now has the sDOF of 4. Thus four parameters have to be optimized via an optimization algorithm to fulfill the four equations of type (18). A solution of the synthesis task shown in Fig. 4 can be seen in Fig. 9.

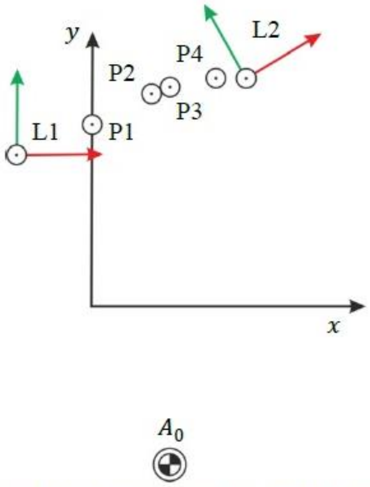

Fig. 8: Example for a numerically solvable synthesis task

Table 4: sDOF specifications for A_0AC and B_0BC

A_0AC	sDOF		B_0BC	sDOF
$n_1 = 2$	+4		$n_1 = 2$	+4
$n_2 = 0$	0		$n_2 = 0$	0
$n_3 = 2$	-1		$n_3 = 2$	-1
$n_4 = 2$	-2		$n_4 = 0$	0
Σ	**1**		**Σ**	**3**

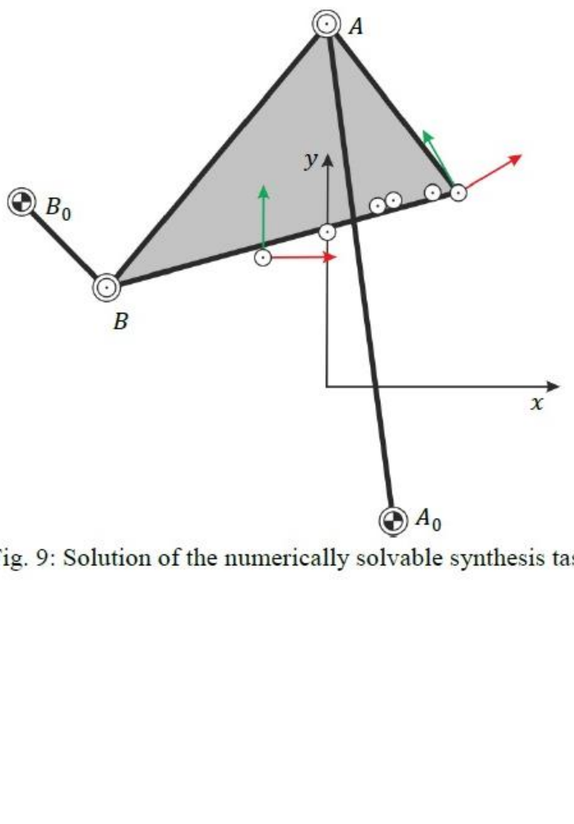

Fig. 9: Solution of the numerically solvable synthesis task

The used algorithm ensures that even if no mechanism can fulfill the synthesis task exactly, the algorithm finds an optimal solution that fulfills the finite positions exactly. The given points of the coupler curve then are just approximated as good as possible.

4 Conclusion

The shown hybrid dimensional synthesis method combines the advantages of the Burmester theorem for the synthesis of finite positions and the synthesis of path-points. This approach ensures an adjustable way of defining a synthesis task as well as a high performance of the algorithm.

By calculating the value of a synthesis task, the maximal number of finite positions, points of the coupler curve as well as joint locations can be determined. For a synthesis task that includes finite positions it is important to check the synthesis degree of freedom (sDOF) for each dyad so that no dyad is overdetermined and thus can be synthesized.

It is also shown that if one dyad of a four-bar-linkage has an sDOF equal to zero, it is possible to synthesize the mechanism analytically. Therefore the first step is the synthesis of the dyad with the sDOf equal to zero. The coupler point of this dyad now can be moved in the desired points of the coupler curve. By doing so, the possible coupler angles at these points can be calculated. They are the input for the calculation of the other dyads.

If no dyad has an sDOF equal to zero, no analytical synthesis is possible. Then the equation system based on the Burmester theorem can be modified. This modified equation system is the input for a numerical optimization algorithm. This algorithm ensures that an approximated solution can be found if no exact solution of the synthesis task is possible. The so synthesized mechanism fulfills the finite positions exactly.

References

[1] Zhao, P.; Ge, X.; Zi, B.; Ge, Q. J., *Planar Linkage Synthesis for Mixed Exact and Approximated Motion Realization Via Kinematic Mapping* Journal of Mechanisms and Robotics, 2016.

[2] Kerle, H.; Corves, B.; Hüsing, M., *Getriebetechnik,* Wiesbaden: Springer Fachmedien Wiesbaden, 5. Auflage, 2015.

[3] Tong, Y.; Myszka, D. H.; Murray, A. P., *Four-Bar Linkage Synthesis for a Combination of Motion and Path-Point Generation* Proceedings of the ASME International Design Engineering Technical Conferences and Computers and Information in Engineering Conference, 2014.

[4] Larochelle, P., *Synthesis of Planar Mechanisms for Pick and Place Tasks with Guiding Positions* Journal of Mechanisms and Robotics, 2015.

[5] Lin, S., *Getriebesynthese nach unscharfen Lagenvorgaben durch Positionierung eines vorbestimmten Getriebes.* Fortschr.-Ber. VDI Reihe 1, Düsseldorf: VDI-Verl., 1999.

[6] Burmester, L., *Lehrbuch der Kinematik,* Leipzig: Verlag von Arthur Felix, 1888.

[7] Braune, R., *Ein Beitrag zur Maßsynthese ebener viergliedriger Kurbelgetriebe,* Diss. RWTH Aachen, Inst. für Getriebetechnik und Maschinendynamik, 1980.

[8] Günzel, D., *Ein Beitrag zur rechnerunterstützten Typ- und Maßsynthese ungleichmässig übersetzender Mechanismen und Getriebe.* Fortschritt-Berichte VDI Reihe 1, Konstruktionstechnik, Maschinenelemente, Düsseldorf: VDI-Verlag, 1994.

[9] McCarthy, J. M.; Soh, G. S., *Geometric design of linkages.* Interdisciplinary applied mathematics, New York: Springer, 2nd ed., 2011.

[10] Pira, B.; Bajraktari, A.; Cunaku, I.; Ymeri, M., *Synthesis of Mechanisms with more than Four Bars using Burmester Theory* Proceedings of the 26th International DAAAM Symposium, 2011, pp. 1043–1044.

[11] Schreiber, H., *Maßsynthese ebener Kurbelgetriebe durch Kreispunktsuche und Homotopieverfahren, :* Lönnies & Schmitz, 1999.

[12] Stolle, G., *Verfahren zur Maßsynthese sechs- und achtgliedriger ebener Gliedführungs- und Übertragungsgetriebe,* Aachen: Shaker Verlag, 2005.

[13] Wohlenberg, P., *Auslegung von Koppelgetrieben mit wiederholtem Durchlauf interaktiv erstellter Bearbeitungsstrategien.* Fortschritt-Berichte / VDI Reihe 1, Konstruktionstechnik, Maschinenelemente, Düsseldorf: VDI-Verlag, 2001.

[14] Dittrich, G.; Braune, R.; Franzke, W., *Algebraische Masssynthese ebener viergliedriger Kurbelgetriebe,* Düsseldorf: VDI, 1983.

[15] Wampler, C. W.; Morgan, A. P.; Sommese, A. J., *Complete Solution of the Nine-Point Path Synthesis Problem for Four-Bar Linkages* Journal of Mechanical Design, pp. 153–159.

[16] Chase, T. R.; Mirth, J. A., *Circuits and Branches of Single-Degree-of-Freedom Planar Linkages* In: Journal of Mechanical Design, 115 (1993) 2, pp. 223–230.

Proceedings of the International Symposium of Mechanism and Machine Science, 2017
AzC IFToMM – Azerbaijan Technical University
11-14 September 2017, Baku, Azerbaijan

Radially Expandable Ring-Like Structure with Antiparallelogram Loops

Şebnem GÜR[1], Koray KORKMAZ[2]*, Gökhan KİPER[3]
[1, 2*]Izmir Institute of Technology
Department of Architecture
E-mail: sebnemgur@iyte.edu.tr, koraykorkmaz@iyte.edu.tr
[3] Izmir Institute of Technology
Department of Mechanical Engineering
E-mail: gokhankiper@iyte.edu.tr

Abstract
As they constitute a substantial percent of deployable structures, scissor mechanisms are widely studied. This being so, new approaches to the design of scissor mechanisms still emerge. Usually design methods consider the scissor elements as modules. Alternatively, it is possible to consider the loops as modules. In this paper, loop assembly method is used such that antiparallelogram loops are placed along a circle, to construct a deployable structure. The research shows that it is possible to construct radially deployable structures with identical antiparallelogram loops with this method. Then kinematic and geometrical properties of the construction are analyzed. It is found out that the links of such a structure turn out to be similar generalised angulated elements. Furthermore, similar loops are used for the construction and deployable rings are obtained.
Keywords: Deployable ring-like structure, antiparallelogram loop, loop assembly method, radial expansion, angulated scissor element.

1. Introduction

Deployable structures are mechanisms that can go under transformation in order to achieve a compact (stowed) and an open (deployed) configuration [1]. This change in size offers a great advantage in packing and also in mobility, therefore making them suitable for many applications varying from retractable roofs [2-4] to space antennas [5-7].

One of the most important units of deployable mechanisms are scissor-like elements (SLEs). SLE is composed of two straight bars connected with a revolute joint, which is perpendicular to the common plane of the bars, called pantographic elements [8]. In 1960's Pinero published the first academic studies on deployable structures made of SLEs [9]. Later on the foldability conditions of SLEs were defined by Felix Escrig [10, 11]. Kinematics of deployable structures continued to be a research area for many others [12-14].

Angulated elements were first introduced by Hoberman [15, 16]. This new type of SLEs were able to subtend a constant angle. We observe the same property in Servadio's foldable polyhedra [17]. Hoberman's latter work, the Iris Dome [16], is nothing but a circular application of the angulated unit subtending constant angle between the unit lines, therefore capable of radial deployment.

Angulated units were further explored by You and Pellegrino [18] after the invention of Hoberman. They derived the geometric conditions of radial deployment and came up with two types of generalized angulated elements (GAEs): equilateral (type I) and similar (type II) GAEs. After You and Pellegrino, further research was conducted on the kinematics and mobility analysis of angulated elements [19, 20]. Kiper et al. [21] showed that the motion of the angulated elements in a radially expanding structure is the Cardan Motion.

Instead of using the angulated elements as modules for deployable structure design, Hoberman uses rhombus loops as modules [22]. This loop assembly method first places identical rhombus loops along a curve and then the link lengths are determined. Liao and Li [23] and Kiper and Söylemez [24] have found similar results independently from Hoberman.

2. Loop Assembly Method

In the literature there are three types of scissor units: transitional, polar and angulated units. When the scissor hinge is in the middle of straight bars, the result is a translational scissor. Maden et al. [25] have examined the possible arrangements of different types of scissor units and provided formulations for their analysis and design. When several translational scissor units are assembled together in a row, the loops formed are rhombus loops (Fig. 1a). When the scissor hinge is not placed in the middle, polar units with kite loops are formed (Fig. 1b).

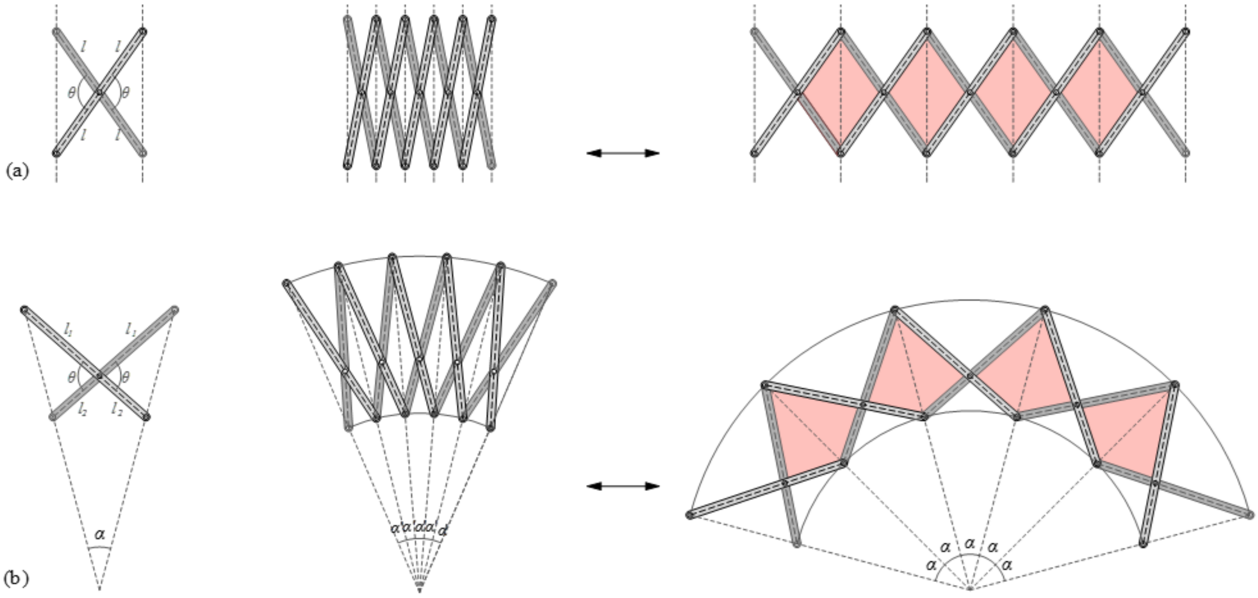

Fig. 1: a) Rhombus loops formed with translational scissor units
b) Kite loops formed with polar scissor units [26]

Hoberman devised a methodology using the loops to find the form of the links. By aligning rhombus loops on a curve, he derives angulated elements (Fig. 2). He also found out that it was possible to achieve deployable structures using different scales of the same rhombus along a given curve. In this study we use another type of loop, antiparallelogram loop, to compose single degree of freedom (DoF) radially expanding deployable structures.

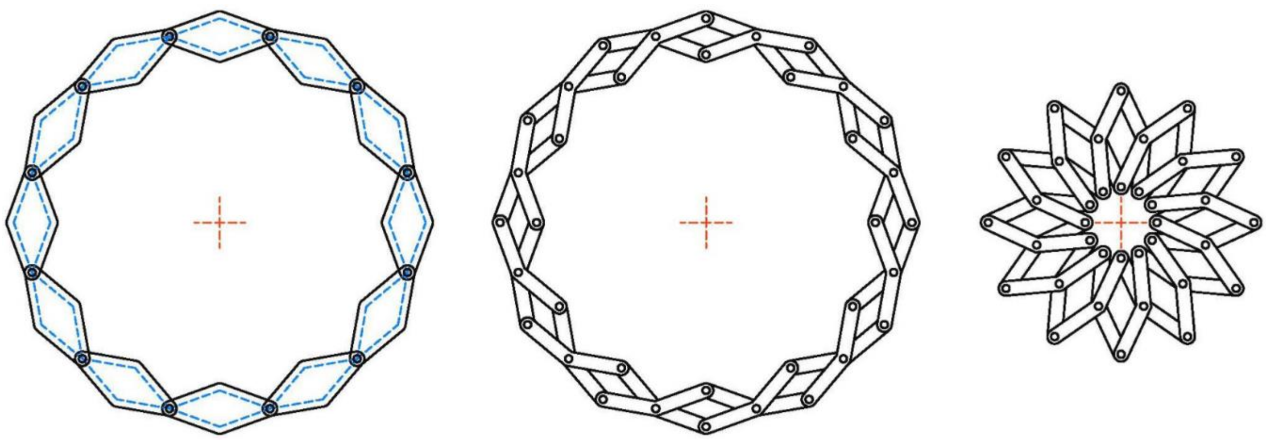

Fig. 2. Assembly of rhombi loops on a circle [22]

An antiparalellogram is also called a crossed parallelogram or a contraparallelogram. It is made up of two equal short and two equal long sides, in which long sides cross each other. During the motion the crossing point moves on the long edges and always stays on the mirror symmetry axis of the loop (Fig. 3).

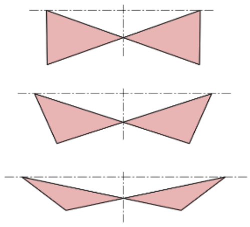

Fig. 3. Motion of antiparallelogram loop

In our study, we align antiparallelogram loops along a circle, similar to Hoberman's method. There are several variations of arrays in order to connect the loops at joints. Placing the loops in alternating order on the circle (sort of glide reflection along the circle) yielded a radially deployable structure (Fig. 4).

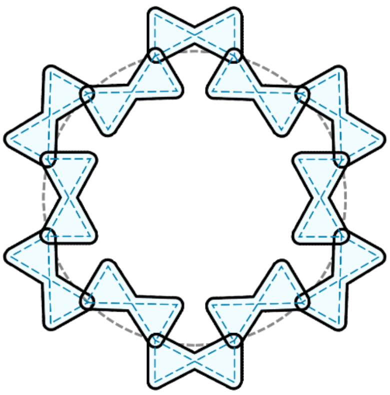

Fig. 4. Antiparallel loops along a circle

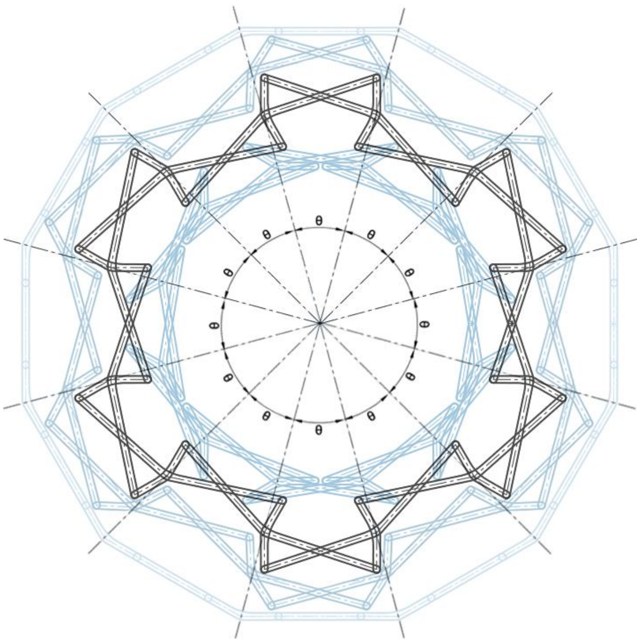

Fig. 5. Deployable antiparallelogram ring mechanism

In Fig. 5 it is seen that there is only one joint on each radial axis from the center, unlike the angulated scissor ring-like structures developed by Hoberman. Therefore it is not possible to locate the center with a single loop, but two loops are necessary so that the positions of three joints defines a circle. The relation between the subtended angle θ and kink angles α + β of the links can be observed with a geometrical analysis (Fig. 6). Also, due to alternating order of the loops, there are always even number of loops in the assembly.

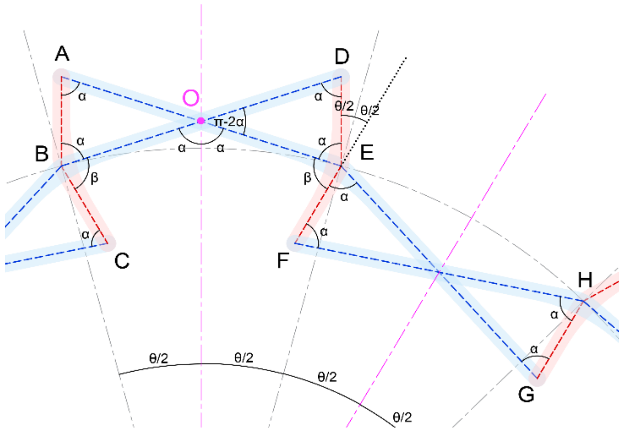

Fig. 6. Geometrical analysis of antiparallelogram ring mechanism

Initially AB arm of link ABC and DE arm of link DEF are parallel to each other. Let ∠EAB = α. Since |AB| = |DE| and |AE| = |BD|, all inner angles of ABDE antiparallelogram are equal to α. Let ∠AEF = β. It is seen from Fig. 6 that ∠DEF = ∠AEG = α + β, i.e. the kink angles of both types of angulated elements, DEF and AEG, are equal to each other. ∠BOE = 2α, being an outer angle of triangle OAB. A line through the intersection point O and parallel to AB and DE divides ∠BOE and also the subtended angle θ into two. The loop has mirror symmetry about this line. Such lines will be called unit lines. Since DE is parallel to the unit line through O, the angle between the radial axis through E and DE is equal to θ/2. Similarly one can conclude that the angle between EF and the radial axis through E is equal to θ/2. So, θ/2 + α + β + θ/2 = π, that is, the kink angles are α + β = π – θ.

Since identical loops are used to construct the mechanism, the two type of angulated links DEF and AEG have link lengths |DE| = |EF| and |AE| = |EG|. Also the kink angles of both type of angulated elements are equal. Therefore, the angulated elements are similar (type II) GAEs (Fig. 7). When the desired number of loops and the circle radius at the initial configuration is specified, one of the side lengths can be chosen freely and the other side length is dependent.

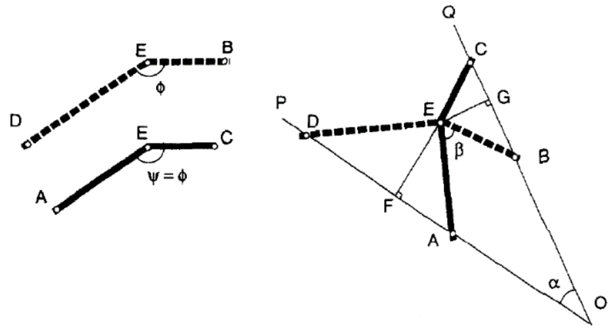

Fig. 7. Similar (type II) GAEs - |AE|/|DE| = |EC|/|EB| and $\psi = \phi$

Next, we construct a ring with similar loops, instead of identical loops. For this construction, a random sequence of three different angles, θ, ψ and δ, are used to divide the circle into sections. When the mechanism is drawn in Solidworks® it is seen that this construction also yields a deployable ring structure (Fig. 8).

Geometric principles of the mechanism can be found similar to the construction with identical loops (Fig. 9). The short edges of each loop are parallel to the unit lines passing through the center of the circle and crossing point of the loop. The unit lines bisect the corresponding subtended angles θ, ψ and δ. Again, similar GAEs are used with identical kink angles. This time, the kink angles are determined by two adjacent subtended angle values. For example, $\angle FED = \angle AEI = \alpha + \beta_2 = \pi - (\theta/2 + \psi/2)$. For the example in Fig. 8, there are 6 different pairs of angulated elements (Fig. 8b). Within each pair, two angulated links have the same kink angle and proportional arm lengths, i.e. they construct a similar GAE.

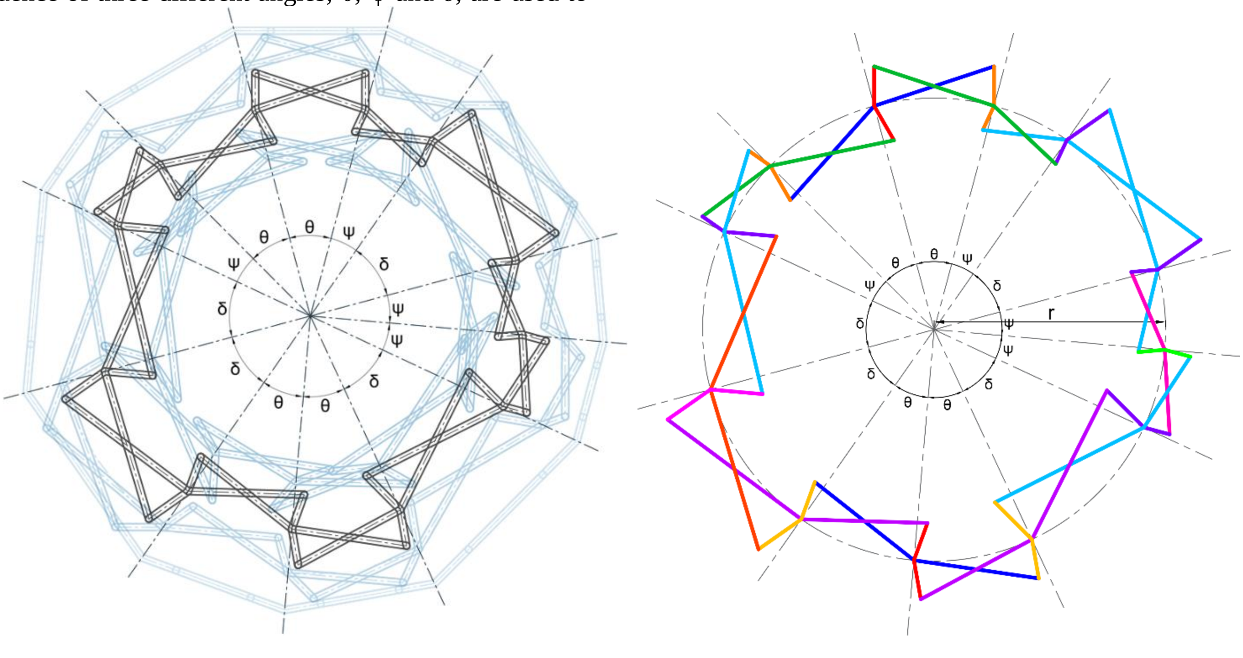

a) b)

Fig. 8: a) Deployable antiparallelogram ring mechanism with similar loops b) Link typology of the mechanism

3. Conclusions

Our study showed that it is possible to achieve deployable rings using antiparallelogram loops in alternating order on a circle using loop assembly method. The links resulted from the assembly are Type I GAE's with identical kink angles. Furthermore, the kink angles can be represented in terms of the subtended angles. It is seen that only one of the side lengths is independent when the number of loops and circle radius are given for the initial configuration. Unit lines of the loops do not pass through joints, but they are the symmetry axes of the loops.

In the second stage of the study, we used similar loops to construct and that also yielded a deployable mechanism, again resulting with Type I GAE's. In this construction the subtended angles varied. Once again, the kink angles can be represented in terms of the subtended angles.

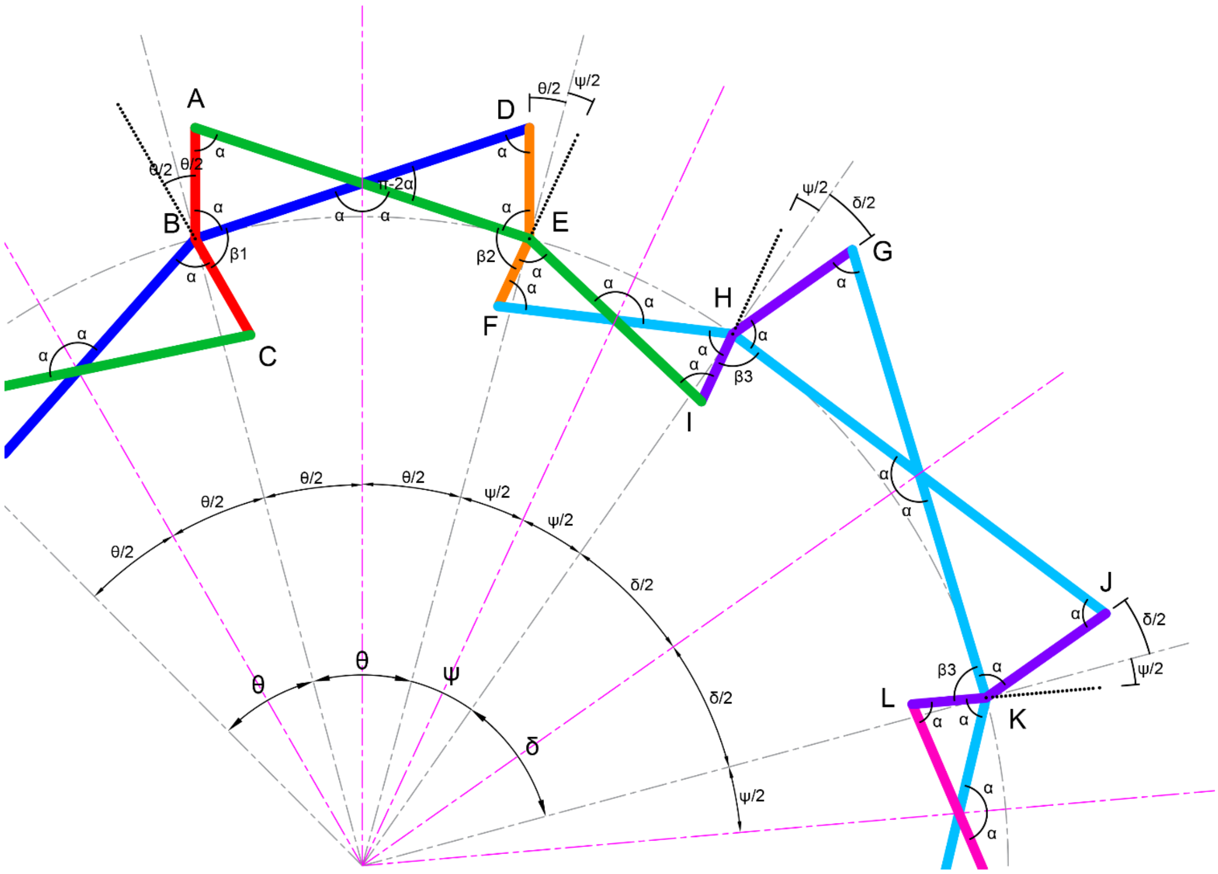

Fig. 9. Geometrical analysis of antiparallelogram ring mechanism with similar loops

Acknowledgment

This project has received funding from the European Union's Horizon 2020 research and innovation programme under the Marie Skłodowska-Curie grant agreement No 689983.

References

[1]. C.H. Hernandez Merchan, C.H., *Deployable Structures*. 1987, Massachusetts Institute of Technology.
[2]. Mao, D. and Y.Z. Luo, *Analysis and design of a type of retractable roof structure.* Advances in Structural Engineering, 2008. 11(4): p. 343-354.
[3]. Jiang, Y.B. and X.R. Wang, *Movable Roof Design and Analysis of Retractable Roof Structures.* Civil Engineering in China - Current Practice and Research Report, 2010: p. 357-361.
[4]. Cai, J.G., et al., *Geometry and Mechanical Behaviour of Radially Retractable Roof Structures During the Movement Process.* International Journal of Steel Structures, 2016. 16(3): p. 755-764.
[5]. G. Kiper & E. Soylemez, *Deployable Space Structures.* Rast 2009: Proceedings of the 4th International Conference on Recent Advances in Space Technologies, 2009: p. 131-138.
[6]. Wang, Y., et al., *Design and Deployment Analysis of Modular Deployable Structure for Large Antennas.* Journal of Spacecraft and Rockets, 2015. 52(4): p. 1101-1111.
[7]. Qi, X.Z., et al., *A large ring deployable mechanism for space satellite antenna.* Aerospace Science and Technology, 2016. 58: p. 498-510.
[8]. Gantes, C.J., *Deployable structures: analysis and design*. 2001: Wit Press.
[9]. Pinero, E., *Project for a mobile theatre.* Architectural Design, 1961. 12(1): p. 154-155.
[10]. Escrig, F. *Expandable space frame structures*. in *Proceedings of the 3rd International Conference on*

Space Structures, ed: Nooshin, H., University of Surrey, Guildford, UK, Elsevier Applied Science Publishers, London. 1984.

[11]. Escrig, F., *Expandable space structures.* International Journal of Space Structures, 1985. 1(2): p. 79-91.

[12]. Langbecker, T., *Kinematic Analysis of Deployable Scissor Structure s.* International Journal of Space Structures, 1999. 14(1): p. 1-15.

[13]. Nagaraj, B.P., R. Pandiyan, and A. Ghosal, *Kinematics of pantograph masts.* Mechanism and Machine Theory, 2009. 44(4): p. 822-834.

[14]. Zhao, J.S., F.L. Chu, and Z.J. Feng, *The mechanism theory and application of deployable structures based on SLE.* Mechanism and Machine Theory, 2009. 44(2): p. 324-335.

[15]. Hoberman, C., *Reversibly expandable doubly-curved truss structure*. 1990, Google Patents.

[16]. Hoberman, C., *Radial expansion/retraction truss structures*. 1991, Google Patents.

[17]. Servadio, I., *Deployable regular and semi-regular polyhedral structures using Hoberman's technique.* Bulletin of the International Association for Shell and Spatial Structures, 1995. 36(2): p. 91-97.

[18]. You, Z. and S. Pellegrino, *Foldable bar structures.* International Journal of Solids and Structures, 1997. 34(15): p. 1825-1847.

[19]. Patel, J. and G.K. Ananthasuresh, *A kinematic theory for radially foldable planar linkages.* International Journal of Solids and Structures, 2007. 44(18-19): p. 6279-6298.

[20]. Cai, J.G., X.W. Deng, and J. Feng, *Mobility analysis of planar radially foldable bar structures.* Proceedings of the Institution of Mechanical Engineers Part G-Journal of Aerospace Engineering, 2015. 229(4): p. 694-702.

[21]. G. Kiper, E. Söylemez & A.U.Ö. Kişisel, *A family of deployable polygons and polyhedra*, Mechanism and Machine Theory 43(5), 627-640, 2008

[22]. C. Hoberman, *Mechanical invention through computation - mechanism basics*, MIT Class 6.S080 online course material, http://courses.csail.mit.edu/6.S080/lectures/02_all.pdf , 2013.

[23]. Q. Liao & D. Li, *Mechanisms for scaling planar graph*, Chinese Journal of Mechanical Engineering 41, 140-143, 2005.

[24]. G. Kiper & E. Söylemez, *Irregular polygonal and polyhedral linkages comprising scissor and angulated elements*, In: Proc. 1st IFToMM Asian Conference on Mechanism and Machine Science (CD), Taipei, 455-459, 2010.

[25]. F. Maden, K. Korkmaz & Y. Akgün, *A review of planar scissor structural mechanisms: geometric principles and design methods*, Architectural Science Review 54, 246-257, 2011.

[26]. YAR, M., et al., *A Novel Planar Scissor Structure Transforming Between Concave And Convex Configurations.* International Journal of Computational Methods and Experimental Measurements, 2017. 5(4): p. 442-450.

Proceedings of the International Symposium of Mechanism and Machine Science, 2017
AzC IFToMM – Azerbaijan Technical University
11-14 September 2017, Baku, Azerbaijan

The Dynamic Synthesis of an Energy-Efficient Slider-Crank-Mechanism

Ferdinand SCHWARZFISCHER[1]*, Mathias HÜSING[2], Burkhard CORVES[2]
[1*]RWTH Aachen University, Department of Mechanism Theory and Dynamics of Machines
Kackertstraße 16-18, 52072 Aachen, Germany
E-mail: schwarzfischer@igm.rwth-aachen.de
[2] RWTH Aachen University, Department of Mechanism Theory and Dynamics of Machines

Abstract

When a mechanism is operated in its so-called Eigenmotion, the energy input to accelerate and decelerate the links of this mechanism is equal to zero. Therefore only the remaining forces like process forces, friction forces et cetera have to be overcome and the Eigenmotion results to be very energy-efficient. First this paper presents the underlying equations for the calculation of the Eigenmotion of a slider-crank-mechanism. Afterwards the derivation of an equivalent mechanical system of the mechanism is shown. Finally a method to synthesize an energy-efficient slider-crank-mechanism is presented. The dynamic synthesis is therefore formulated as a constrained optimization problem.

Keywords: Dynamic Synthesis, Eigenmotion, Mechanism Synthesis, Dynamic Balancing, Slider-Crank-Mechanism

1. Introduction

Mechanisms form part of many different production machines, e.g. weaving machines, printing machines or packaging machines. The energy-efficiency of their built-in mechanisms is crucial for the profitability of these machines. The following equations hold for plane mechanisms with a rotating input link (crank). The necessary power P_D to drive such a mechanism is the product of the drive torque T_D and the input velocity $\dot{\varphi}$:

$$P_D = T_D \cdot \dot{\varphi}$$

The drive torque can be written as follows [1]:

$$T_D = T_{kin} + T_{pot} + T_{diss} + T_{proc}$$

T_{kin} is the torque which is necessary to overcome the resistances from accelerating and decelerating the links of the mechanism. T_{pot} is the necessary torque to overcome the resistances which result from gravity or springs. T_{diss} and T_{proc} comprise the resistances following from dissipation effects and process forces. The torque T_{kin}, can be derived from the kinetic energy E_{kin} of the mechanism using the Lagrange Equations of 2nd kind [2]:

$$T_{kin} = \frac{d}{dt}\left(\frac{\partial E_{kin}}{\partial \dot{\varphi}}\right) - \frac{\partial E_{kin}}{\partial \varphi}$$

It is evident that the torque T_{kin} vanishes for a constant kinetic energy of the mechanism. The concept of driving a mechanism in its so-called Eigenmotion uses this fact. The Eigenmotion is the specific motion of the crank that results in a constant kinetic energy of the mechanism over the whole period of motion. [1; 3; 4]

The classical dimensional synthesis of mechanisms aims to finding the optimal kinematic parameters for a mechanism driven with a constant input motion [5; 6]. The goal of the methods of dynamic balancing is to find the optimal mass parameters for a mechanism with given kinematic parameters [1; 3]. The dynamic synthesis combines both concepts. It aims to finding the optimal mass and kinematic parameters of a mechanism [7].

The equations show that driving a mechanism in its Eigenmotion can decrease the necessary input torque and can result in lower energy consumption. Bench tests confirmed the effectiveness of driving a mechanism in its Eigenmotion with regard to energy consumption [8].

In this paper the synthesis of an energy-efficient slider-crank-mechanism is presented. First, the underlying equations of the slider-crank-mechanism are shown. The equation of the Eigenmotion of the slider-crank-mechanism is derived. Afterwards an equimomental system of the slider-crank-mechanism is presented. The Eigenmotion of the mechanism is rewritten for this equimomental system. The synthesis of a mechanism with a particular Eigenmotion is formulated as an optimization problem. The parameters of the equimomental system of the slider-crank-mechanism are taken as the design parameters of the optimization. The formulation of the objective function as well as the formulation of the optimization constraints is shown. The optimization results for an exemplarily synthesis are presented.

2. The Slider-Crank-Mechanism

The kinematic parameters and the mass parameters of the slider-crank-mechanism are shown in Fig. 1.

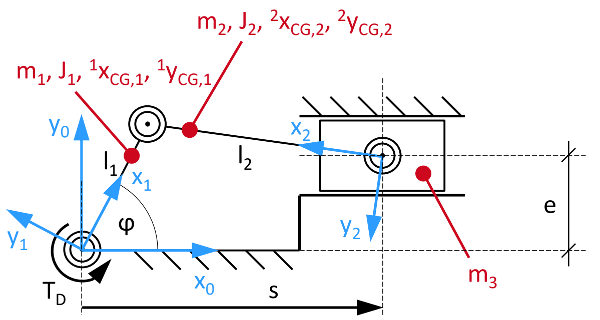

Fig. 1. The slider-crank-mechanism

The slider-crank-mechanism consists of three links. The crank (index '1') is driven by a motor with the drive torque T_D. The input angle is denoted by φ. The output of the mechanism is the stroke s of the slider (index '3'). Crank and slider are connected by the coupler (index '2'). The offset of the slider is denoted by e. The coordinate systems are highlighted in blue color. The coordinate system '0' is frame fixed. The other two Coordinate systems are body-fixed. The coordinate systems are right-handed, hence the z-axes point out of the image plane. The mass properties of the links are highlighted in red. The position of the center of gravity (CG) of the links is represented in the body-fixed systems. The superscript indicates the corresponding coordinate system. Positions of the center of gravity without superscript are formulated in the coordinate system '0'.
The coordinate system '2' is rotated about the angle ψ about the z-axis of the coordinate system '0'. The angle ψ can be calculated as follows:

$$\psi = \arcsin\left(\frac{l_1 \sin(\varphi) - e}{l_2}\right)$$

The stroke of the slider s reads:

$$s = l_1 \cos(\varphi) + l_2 \sqrt{1 - \frac{(l_1 \sin(\varphi) - e)^2}{l_2^2}}$$

The derivatives of the angle psi and the stroke s can be calculated as follows:

$$\frac{d\psi}{dt} = \frac{d\psi}{d\varphi}\dot{\varphi} = \frac{l_1 \cos(\varphi)}{l_2 \sqrt{1 - \frac{(l_1 \sin(\varphi) - e)^2}{l_2^2}}}\dot{\varphi}$$

$$\frac{ds}{dt} = \frac{ds}{d\varphi}\dot{\varphi} = -l_1 \sin(\varphi)\,\dot{\varphi} - \frac{(l_1 \sin(\varphi) - e) l_1 \cos(\varphi)}{l_2 \sqrt{1 - \frac{(l_1 \sin(\varphi) - e)^2}{l_2^2}}}\dot{\varphi}$$

In order to calculate the Eigenmotion of the mechanism, the kinetic energy has to be set up. The kinetic energy of the mechanism can be written as the sum of the kinetic energy of its three links:

$$E_{kin} = E_{kin,1} + E_{kin,2} + E_{kin,3}$$

The kinetic energy of a rigid body can be split into a translational (T) and a rotational (R) part:

$$E_{kin,i} = E_{kin,Ti} + E_{kin,Ri}$$

Hence the kinetic energy of the crank can be written as:

$$E_{kin,T1} = \frac{1}{2} m_1 \left({}^1x_{CG,1}^2 + {}^1y_{CG,1}^2 \right) \dot{\varphi}^2$$

$$E_{kin,R1} = \frac{1}{2} J_1 \dot{\varphi}^2$$

The kinetic energy of the coupler is:

$$E_{kin,T2} = \frac{1}{2} m_2 \left(\left(\frac{dx_{CG,2}}{d\varphi}\right)^2 + \left(\frac{dy_{CG,2}}{d\varphi}\right)^2 \right) \dot{\varphi}^2$$

$$E_{kin,R2} = \frac{1}{2} J_2 \left(\frac{d\psi}{d\varphi}\right)^2 \dot{\varphi}^2$$

The slider has only translational kinetic energy due to the translational guiding. Therefore its kinetic energy consists of only one term:

$$E_{kin,T3} = \frac{1}{2} m_3 \left(\frac{ds}{d\varphi}\right)^2 \dot{\varphi}^2$$

The reduced mass moment of inertia is defined as follows:

$$J_{red}(\varphi) = \frac{2 \cdot E_{kin}}{\dot{\varphi}^2}$$

It is the fictive mass moment of inertia of a rotating disk with the same kinetic energy as the mechanism [9]. The reduced mass moment of inertia is a function of the input angle φ. It depends on the kinematic parameters and the mass parameters. It can be written as the sum of the reduced mass moments of inertia of the links:

$$J_{red}(\varphi) = J_{red,1} + J_{red,2}(\varphi) + J_{red,3}(\varphi)$$

These reduced mass moments of inertia of the links are:

$$J_{red,1} = J_1 + m_1\left({}^1x_{CG,1}^2 + {}^1y_{CG,1}^2\right)$$

$$J_{red,2}(\varphi) = m_2\left(\left(\frac{dx_{CG,2}}{d\varphi}\right)^2 + \left(\frac{dy_{CG,2}}{d\varphi}\right)^2\right) + J_2\left(\frac{d\psi}{d\varphi}\right)^2$$

$$J_{red,3}(\varphi) = m_3\left(\frac{ds}{d\varphi}\right)^2$$

The Eigenmotion of a mechanism is defined as its intrinsic motion in the case of constant kinetic energy [1; 9]. It is denoted by the index 'e':

$$E_{kin} = \frac{1}{2}J_{red}(\varphi)\dot{\varphi}_e{}^2 = const. = \frac{1}{2}J_{red}(\varphi_0)\dot{\varphi}_0{}^2$$

It is [1; 9]:

$$\dot{\varphi}_e = \frac{\dot{\varphi}_0\sqrt{J_{red}(\varphi_0)}}{\sqrt{J_{red}(\varphi)}} = \frac{C}{\sqrt{J_{red}(\varphi)}}$$

The numerator of the equation is constant and denoted by C. The period time T of the Eigenmotion can be calculated by [9]:

$$T = \frac{1}{C}\int_{\varphi_0}^{\varphi_0+2\pi} \frac{1}{\sqrt{J_{red}(\tilde{\varphi})}}d\tilde{\varphi}$$

3. The Equimomental System

The reduced mass moment of inertia depends on the kinematic properties and the mass properties of a mechanism. Using dynamically equivalent systems for the particular links of the mechanism, the reduced mass moment of inertia can be reformulated. In the following, the equivalent systems of the crank and the coupler shall be presented. Afterwards the equimomental system of the complete slider-crank-mechanism is presented. The Eigenmotion of the mechanism is reformulated in terms of the parameters of the equimomental system. Information on equimomental systems can be found in [4; 10].

First, the equimomental system of the crank is defined. The reduced mass moment of inertia of the crank is constant. It depends on four parameters, which can be replaced by a mass m_{A1} as shown in Fig. 2.

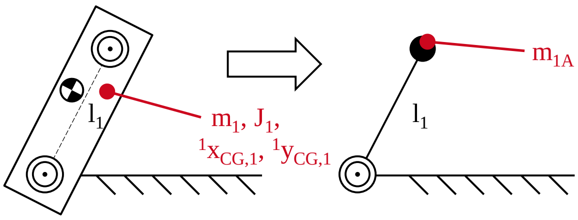

Fig. 2. The equimomental system of the crank

The mass m_{1A} is placed at the position of the connecting joint between the crank and the coupler. It holds:

$$m_{1A} = \frac{J_1 + m_1\left({}^1x_{CG,1}^2 + {}^1y_{CG,1}^2\right)}{l_1^2}$$

Second, the equimomental system of the coupler shall be defined. The assumption is made, that the center of gravity of the coupler lies upon the connecting line between the two joints of the coupler. Hence the equimomental system according to Fig. 3 can be used.

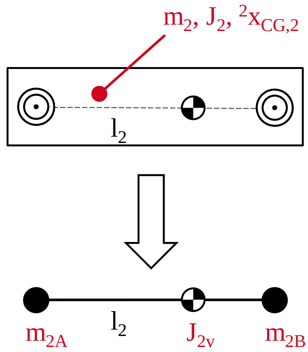

Fig. 3. The equimomental system of the coupler link

The mass parameters m_2, J_2 and ${}^2x_{CG,2}$ are replaced by the parameters m_{2A}, m_{2B} and J_{2v}. The original system and the equimomental system have to have the same mass and the same mass inertia about the center of gravity. Furthermore the position of the center of gravity has to be the same. Taking into account these conditions, the mass parameters of the equimomental system can be derived. It is:

$$m_{2A} = \frac{m_2\left(l_2 - {}^2x_{CG,2}\right)}{l_2}$$

$$m_{2B} = \frac{m_2\ {}^2x_{CG,2}}{l_2}$$

$$J_{2v} = J_2 + m_2\ {}^2x_{CG,2}\left({}^2x_{CG,2} - l_2\right)$$

The slider only possesses translational kinetic energy. Therefore only m_3 has to be taken into account. Fig. 4 finally shows the equimomental system of the complete slider-crank-mechanism.

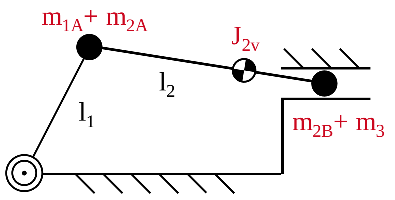

Fig. 4. The equimomental system of the mechanism

The point masses m_{2A} and m_{3A} are located on the same position. They can be replaced by a mass moment of inertia J_{1v}. It holds:

$$J_{1v} = (m_{1A} + m_{2A}) l_1^2$$

The point masses m_{2B} and m_3 also lie on the same position. The can be replaced by the mass m_{3v}:

$$m_{3v} = m_{2B} + m_3$$

Using the mass properties J_{1v}, J_{2v} and m_{3v} of the equimomental system, the Eigenmotion of the slider-crank-mechanism can be written as follows.

$$\dot{\varphi}_e = \frac{C}{\sqrt{J_{1v} + J_{2v}\left(\frac{d\psi}{d\varphi}\right)^2 + m_{3v}\left(\frac{ds}{d\varphi}\right)^2}}$$

In order to reduce the number of parameters the following dimensionless parameters are introduced:

$$\iota_{2v} = \frac{J_{2v}}{J_{1v}}, \quad \mu_{3v} = \frac{m_{3v} l_1^2}{J_{1v}}$$

Using these parameters the Eigenmotion can be rewritten as follows:

$$\dot{\varphi}_e = \frac{\tilde{C}}{\sqrt{1 + \iota_{2v}\left(\frac{d\psi}{d\varphi}\right)^2 + \frac{\mu_{3v}}{l_1^2}\left(\frac{ds}{d\varphi}\right)^2}}$$

The constant $\tilde{C}$ reads:

$$\tilde{C} = \frac{C}{J_{1v}^2}$$

By adjusting $\tilde{C}$, the Eigenmotion can be normalized with respect to a period time T of one second. Normalizing the Eigenmotion is helpful in order to compare the Eigenmotion to other motions. The normalized Eigenmotion is dependent on the following parameters listed within the parameter vector $\mathbf{p}_e$:

$$p_e = (l_1, l_2, e, \iota_{2v}, \mu_{3v})$$

4. The Dynamic Synthesis of the Slider-Crank-Mechanism as an Optimization Problem

The goal of the dynamic synthesis is to find a slider-crank-mechanism which is able to fulfill a desired motion when driven in its Eigenmotion.

In the following the task is formulated as an optimization problem. The goal of an optimization is to find the best set of design parameters **x** for a certain task. The task is formulated as an objective function **f**(x). The objective function is formulated in such way, that the best combination of parameters minimizes this function. Constraints, i.e. restrictions with respect to the combination of parameters, can also be taken into account. Constraints can be formulated as equality constraint equations h or as inequality constraint equations g and are also dependent on the design parameters. Acceptable combinations of the design parameters have to satisfy these constraint equations. The formal statement of the minimization formulation of an optimization problem is written as follows [11]:

$$\begin{gathered} \text{minimize } f(x) \\ \text{subject to } h(x) = 0, \\ g(x) \leq 0, \\ x \in X \subseteq R^n. \end{gathered}$$

The vector **h**(x) contains all equality constraints meanwhile **g**(x) contains all inequality constraints. A maximization formulation can be transformed into a minimization formulation by multiplying the objective function by minus one. Algorithms to find solutions of optimization problems are called optimization algorithms. A distinction is made between global and local optimization. Local optimization algorithms seek only local solutions, that is sets of parameters for which the objective function is smaller than at all feasible parameter combinations nearby. Local optimization algorithms do not always find the global minimum. In case of optimization problems, where local optimization algorithms are not suitable to find the global minimum, global optimization algorithms have to be applied. More information on local optimization can be found in [11–13]. Contrary to local optimization algorithms, global optimization algorithms are designed to find a good solution over all input values. A variety of algorithms exists for global optimization. Metaheuristics are procedures to find good (global) solutions for optimization problems. However, the discovery of the globally optimal solution is not guaranteed. This is due to the fact, that these methods do contain some kind of stochastic optimization. Examples for metaheuristics are the Particle Swarm Optimization or the Genetic Algorithm (GA). Information on these metaheuristics can be found in [14–16].

In order to conduct the dynamic synthesis of the slider-crank-mechanism the synthesis was formulated as an optimization problem. The set of design parameters contains the entries of the parameter vector $\mathbf{p}_e$ and is complemented by the initial angle φ_0. It reads:

$$x = (l_1, l_2, e, \iota_{2v}, \mu_{3v}, \varphi_0)$$

The necessary steps within the optimization process are shown in Fig. 5. The process of evaluating the optimization function is depicted within the doted rectangle. Inside of the evaluation of the optimization function the Eigenmotion $\dot{\varphi}_e$ is calculated for a set of design parameters. The Eigenmotion is calculated for the N points of the vector of normalized time **t**. The Eigenmotion is then integrated in order to achieve the crank angle of the Eigenmotion φ_e over the normalized time. The stroke of the slider-crank-mechanism in Eigenmotion s_e can then be calculated by inserting φ_e in the kinematic equations of the mechanism. In order to compare the stroke of the slider-crank-mechanism s_e in Eigenmotion to the desired ouput stroke s_d the sum of least squares of the difference between both motions is calculated:

$$f = \sum_{i=1}^{N} \left(s_e(i) - s_d(i)\right)^2$$

The vectors $\mathbf{s}_e$ and $\mathbf{s}_d$ contain the values of the Eigenmotion and the desired motion over the normalized time. The optimization process is repeated for different sets of design variables until a stop criterion is reached. A stop criterion could be for example the value of f being under a certain, predefined treshold.

In order to achieve feasible solutions, constraints have to be taken into account. First of all, upper and lower limits (boundaries) of the design parameters have to be determined. The upper and lower boundaries of the design variables are also called box-constraints. Second, the kinematic chain of the slider-crank-mechanism has to be closable for any input angle φ. Further constraints concerning can be implemented. These constraints can concern the dimensions of the mechanism, like for example a relationship between the lengths of different links. Furthermore requirements concerning the output motion could be implemented as constraints.

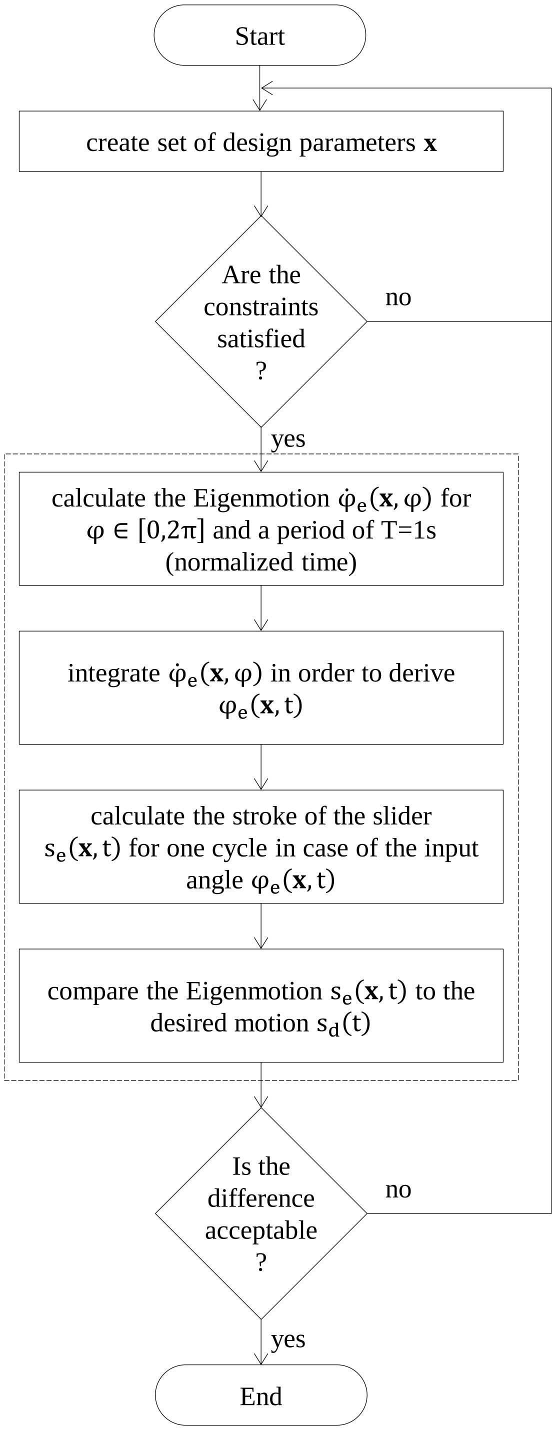

Fig. 5. Flow-chart of the optimization process

5. An Example of the Dynamic Synthesis of the Slider-Crank-Mechanism

In the following an example of the dynamic synthesis of the crank-slider-mechanism is presented. Fig. 6 shows the desired output motion of the crank-slider-mechanism. The output slider should fulfill a descending motion from 0.6 to 0.3 meters with approximately constant velocity between 0.6 and 0.9 seconds of normalized time.

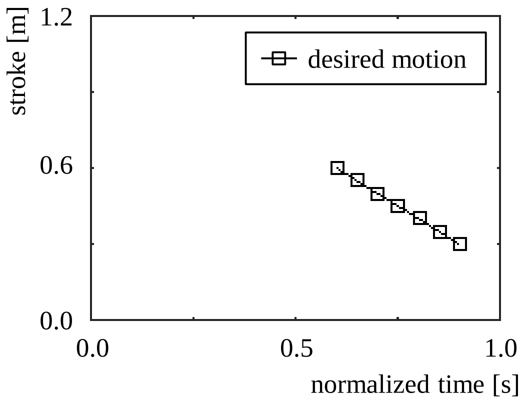

Fig. 6 : The desired output of the slider-crank-mechanism

The upper and lower values of the design parameters were set as listed in Table 1.

Table 1. The boundaries of the design parameters

parameter	*lower boundary*	*upper boundary*
l_1	0.10 m	1.00 m
l_2	0.10 m	1.00 m
e	-0.50 m	-0.50 m
ι_{2v}	-0.05	0.00
μ_{3v}	0.00	0.75
φ_0	0.00	2π

Apart of the box constraints and the closing condition of the linkage no more constraints were implemented.

6. The Results of the Dynamic Synthesis

In order to solve the optimization problem a genetic algorithm was used. The output parameters of this optimization were used as input parameters for a local optimization algorithm. The local optimization was carried out by using a barrier-method.

The result of the optimization is shown in Fig. 7. It can be seen that the output motion of the resulting slider-crank-mechanism in Eigenmotion is close to the desired output motion.

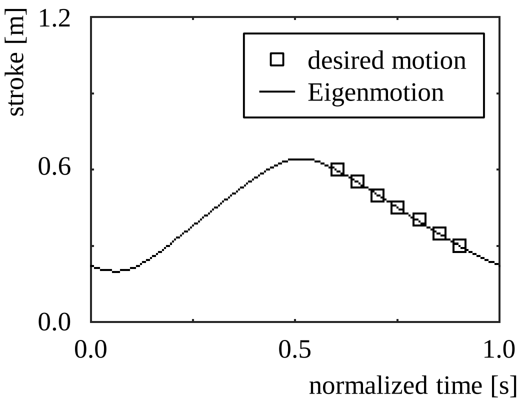

Fig. 7. The result of the dynamic synthesis

The resulting set of parameters of the optimization is listed in Table 2. The parameter φ_0 is the value of the crank angle at the beginning of a cycle. It has no influence on the design of the mechanism.

Table 2. The solution set of parameters

parameter	*value*
l_1	166.7 mm
l_2	557.0 mm
e	333.3 mm
ι_{2v}	-0.05
μ_{3v}	0.75
φ_0	3.6645

The parameters ι_{2v} and μ_{3v} can be used to derive the geometry of the coupler and the crank.

It can be thought of different ways to derive feasible links from these parameters. In the following one approach is shown in order to derive members of the mechanism. First of all, the mass property J_{1v} is set to a preliminary value (denoted by an asterisk):

$$J_{1v}^{*} = 1.0\,\mathrm{kg} \cdot l_1^2$$

Second, the geometry of the coupler link is set to be according to Fig. 8.

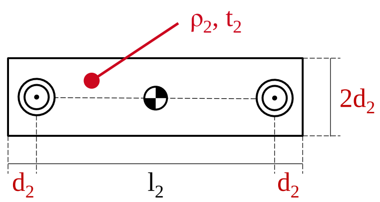

Fig. 8. The predefined geometry of the coupler link

The coupler link is set to be rectangular with its center of mass in the middle of the connecting line between the two joints. The density of the material is denoted ρ_2. Two geometric parameters d_2 and the width of the link t_2 are introduced. The value d_2 and ρ_2 are set to fixed values:

$$d_2 = 40 \text{ mm}, \quad \rho_2 = 2700 \frac{\text{kg}}{\text{m}^3}$$

Using the preliminary value for J_{1v} the mass of the coupler link can be calculated as follows:

$$m_2^* = \frac{\iota_{2v} \cdot J_{1v}^*}{\left(\frac{1}{12}((l_2 + 2d_2)^2 + 4d_2^2) - \frac{l_2^2}{4}\right)}$$

All values denoted by an asterisk are preliminary values which can be adjusted later. Now the preliminary mass of the slider can be calculated. It is:

$$m_3^* = \mu_{3v} \frac{J_{1v}^*}{l_1^2} - \frac{m_2^*}{2}$$

The mass of the output link is now set to a fixed value:

$$m_3 = 2.5 \text{ kg}$$

A correction factor for the mass parameters is calculated:

$$f^* = \frac{m_3}{m_3^*}$$

Hence:

$$J_{1v} = f^* \cdot J_{1v}^*$$

The mass of the coupler link can then be calculated as follows:

$$m_2 = f^* \cdot m_2^* = 1.5730 \text{ kg}$$

In order to define the coupler geometry the width of the link has to be calculated. It is:

$$t_2 = \frac{m_2}{\rho_2\big((l_2 + 2d_2) \cdot 2d_2\big)} = 11.4 \text{ mm}$$

After defining the coupler geometry, the crank geometry has to be derived. The point mass m_{1A} according to chapter 3 can be calculated as follows:

$$m_{1A} = \frac{J_{1v}}{l_1^2} - \frac{m_2}{2}$$

The crank has to have the same dynamic effect with respect to the reduced mass moment of inertia as the point mass m_{1A}. On the basis of geometry similar to the coupler geometry depicted in Fig. 8 the mass properties of the crank can be derived. The equation to calculate the mass reads:

$$m_1 = \rho_1\big((l_1 + 2d_1) \cdot 2d_1\big) \cdot t_1$$

The mass moment of inertia about the pivoting point in the frame can be set up as follows:

$$m_{1A} \cdot l_1^2 = \frac{m_1}{12}((l_1 + 2d_1)^2 + 4d_1^2) + m_1 \frac{l_1^2}{4}$$

In order to derive the mass m_1 from this equation, the value d_1 is set to a certain value:

$$d_1 = 50 \text{ mm}$$

The density of the material of the crank is then set to:

$$\rho_1 = 7870 \frac{\text{kg}}{\text{m}^3}$$

The width of the crank can then be calculated. It is:

$$t_1 = \frac{m_1}{\rho_1\big((l_1 + 2d_1) \cdot 2d_1\big)} = 27.1 \text{ mm}$$

The presented procedure of using the output values of the optimization in order to build feasible links is based on primitive geometries. Future work can be on the field of contemplating more complex geometries.

7. Conclusion

In this paper the Eigenmotion of the slider-crank-mechanism was presented. Therefore the underlying kinematic and dynamic equations were derived. An equimomental system of the slider-crank-mechanism was introduced in order to simplify the equations.

Subsequently a method for the dynamic synthesis of the crank-slider-mechanism was presented. Therefore the task was formulated as an optimization problem. The optimization problem was solved by the use of a genetic algorithm.

An example of the use of the method was shown. The results showed the suitability of the method to derive feasible mechanisms which can fulfill a desired output motion when moved in the Eigenmotion. In order to conclude the example, an approach of designing the links of the mechanism was presented.

References

[1] VDI-Richtlinie 2149, Blatt 1 *Getriebedynamik: Starrkörper Mechanismen* Norm, VDI, : Beuth, 2008.

[2] Shabana, A. A. *Dynamics of multibody systems* Cambridge, New York: Cambridge University Press, 3rd ed., 2005, ISBN 9780521850117.
[3] Dresig, H.; Vul′fson, I. I. *Dynamik der Mechanismen* Wien, New York: Springer, 1989, ISBN 9783326003610.
[4] Dresig, H.; Holzweißig, F. *Dynamics of Machinery*, Theory and Applications Berlin, Heidelberg: Springer, Online-Ausg, 2010, ISBN 3540899391.
[5] Uicker, J. J.; Pennock, G. R.; Shigley, J. E. *Theory of machines and mechanisms* New York: Oxford University Press, 4th ed., 2011, ISBN 0195371232.
[6] Kerle, H.; Corves, B.; Hüsing, M. *Getriebetechnik*, Grundlagen, Entwicklung und Anwendung ungleichmäßig übersetzter Getriebe Wiesbaden: Vieweg + Teubner, 4. Aufl., 2011, ISBN 978-3-8348-0961-2.
[7] Ren-Chung Soong; Hong-Sen Yan *Simultaneous Minimization of Shaking Moment, Driving Torque, and Bearing Reactions of Complete Force Balanced Linkages* In: Journal of the Chinese Society of Mechanical Engineers, 2007 (2007) C 28(3), S. 243–254.
[8] Thümmel, T. *Experimentelle Mechanismendynamik*, Messung, Modellierung, Simulation, Verifikation, Interpretation und Beeinflussung typischer Schwingungsphänomene an einem Mechanismenprüfstand Düsseldorf: VDI-Verl., Als Ms. gedr, 2012, ISBN 3183345110.
[9] Dresig, H. *Schwingungen und mechanische Antriebssysteme: Modellbildung, Berechnung, Analyse, Synthese* Berlin: Springer, 2006, ISBN 9783540296638.
[10] Chaudhary, H.; Saha, S. K. *Dynamics and balancing of multibody systems* Berlin, Heidelberg: Springer, 2009, ISBN 354078179X.
[11] Papalambros, P. Y.; Wilde, D. J. *Principles of Optimal Design*, Modeling and Computation Cambridge: Cambridge University Press, 2nd ed., 2000, ISBN 051162641X.
[12] Boyd, S. P.; Vandenberghe, L. *Convex optimization* Cambridge [u.a.]: Cambridge University Press, 9. print, 2011, ISBN 0521833787.
[13] Nocedal, J.; Wright, S. J. *Numerical optimization* New York: Springer, 2nd ed., 2006, ISBN 9780387987934.
[14] Mitchell, M. *An introduction to genetic algorithms* Cambridge, Mass.: MIT Press, 7. print, 2001, ISBN 0262631857.
[15] Kennedy, J.; Eberhart, R. *Particle swarm optimization* In: ICNN'95 - International Conference on Neural Networks, Perth, WA, Australia, Nov. 1995, ISBN 0-7803-2768-3, S. 1942–1948.
[16] Eberhart, R.; Kennedy, J. *A new optimizer using particle swarm theory* In: MHS'95. Proceedings of the Sixth International Symposium on Micro Machine and Human Science, Nagoya, Japan, 1995, ISBN 0-7803-2676-8, S. 39–43.

Proceedings of the International Symposium of Mechanism and Machine Science, 2017
AzC IFToMM – Azerbaijan Technical University
11-14 September 2017, Baku, Azerbaijan

Stability Analysis of Orthotropic Conical Shells Resting On Winkler Elastic Foundation Based on the FOSDST

Abdullah SOFIYEV[1*], Ali NAJAFOV[2]
[1*]Department of Civil Engineering of Engineering Faculty of Suleyman Demirel University, 32600, Isparta, Turkey, E-mail: abdullahavey@sdu.edu.tr
[2*]Institute for Machine Elements of Azerbaijan Technical University,
E-mail: ali.najafov@rohe.az

Abstract
In this study, the stability of freely supported orthotropic conical shells (OCS) resting on Winkler elastic foundation (WEF) on the basis of the first order shear deformation shell theory (FOSDST) is analyzed by using Donnell-type shell theory and Galerkin method.
KEYWORDS: Stability, Orthotropic Material, Elastic foundation, FOSDST, Critical pressure.

1. INTRODUCTION

The anisotropic constructions are widely used in automotive, marine and aerospace industries, which require a strong, rigid and lightweight construction. The possibility of predicting the reaction of composite orthotropic shells subjected to lateral pressure is of particular interest to researchers in the field of continuous mechanics. Previously, numerous studies have been carried out on the loss of stability of orthotropic conical shells using the classical theory of shells (CST) [1-3]. The development of the theory of shells made it possible to know the important role of shear stresses (or deformations) in the behavior of structures consisting of composite materials. Due to the increasing importance of orthotropic materials in the design of composite structures and their characteristics, the loss of stability, taking into account the effect of transverse shear strains or using shear deformations shell theory (SDST), is vital. In this context, the researchers have published some publications, taking into account the influence of shear deformations on the bending of structural elements [4-6]. In the above studies, the effect of continuous environments on the stability of the orthotropic conical shells is not taken into consideration. In recent years, orthotropic conical shells have been used in various elastic media. The effects of such environments on the stability behavior of the anisotropic conical shells have not yet been investigated based on the SDST [7, 8]. The purpose of this study is to solve the problem of loss of stability of orthotropic conical shells resting on WEF by using FOSDST.

2. METHOD OF SOLUTION

Consider orthotropic truncated conical shell subjected to the uniform lateral pressure, P, resting on the WEF in which the notations are presented in Fig. 1. Let the coordinate system ($Oz\theta r$) be chosen such that, the origin O is at the vertex of the whole cone.

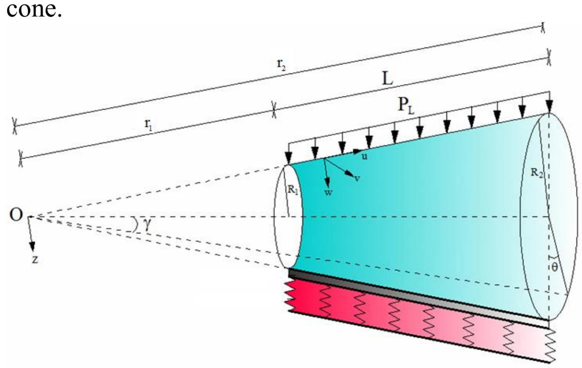

Figure 1. Orthotropic truncated conical shells on the WEF with the coordinate systems and notations

The effect of WEF is modeled as

$$R = K_w w \tag{1}$$

where R is the force per unit area, $K_w (N/m^3)$ is the Winkler foundation stiffness (spring stiffness) and w is the small deflection.

The stress-strain relationships of orthotropic conical shells within the first order shear deformations theory (FOSDST) are obtained as [9]:

$$\begin{bmatrix}\sigma_{11}\\ \sigma_{22}\\ \sigma_{12}\\ \sigma_{13}\\ \sigma_{23}\end{bmatrix}=\begin{bmatrix}\bar{E}_1 & \nu_{12}\bar{E}_2 & 0 & 0 & 0\\ \nu_{12}\bar{E}_1 & \bar{E}_2 & 0 & 0 & 0\\ 0 & 0 & G_{12} & 0 & 0\\ 0 & 0 & 0 & G_{13} & 0\\ 0 & 0 & 0 & 0 & G_{23}\end{bmatrix}\begin{bmatrix}\varepsilon_{11}\\ \varepsilon_{22}\\ \varepsilon_{12}\\ \varepsilon_{13}\\ \varepsilon_{23}\end{bmatrix} \qquad (2)$$

where $\sigma_{ij}(i,j=1,2,3)$ and $\varepsilon_{ij}(i,j=1,2,3)$ are the normal and shear components of strains and stresses of orthotropic conical shells, respectively; $\bar{E}_1=E_1/(1-\nu_{12}\nu_{21})$, $\bar{E}_2=E_2/(1-\nu_{12}\nu_{21})$, E_1 and E_2 are Young's moduli of the orthotropic material along r and θ directions, respectively; G_{ij} are shear moduli which characterize angular chances between principal directions r and θ, r and z, θ and z, respectively, ν_{12} and ν_{21} are the Poisson's ratios.

The shear stresses of conical shells resting on WEF within the FOSTSD expressed as [6, 8]:

$$\sigma_{13}=\frac{d\Gamma(z)}{dz}F_1,\ \sigma_{23}=\frac{d\Gamma(z)}{dz}F_2 \qquad (3)$$

where F_1 and F_2 are the rotations of normal's to the mid-surface with the respect to θ and r axes, respectively, $\Gamma(z)$ is shear stress or deformation function and z is the thickness coordinate of the conical shell.

The stability and compatibility equations of orthotropic truncated conical shells under lateral pressure and resting on the WEF within the FOSDST are obtained as [8]

$$\begin{bmatrix}L_{11} & L_{12} & L_{13} & L_{14}\\ L_{21} & L_{22} & L_{23} & L_{24}\\ L_{31} & L_{32} & L_{33} & L_{34}\\ L_{41} & L_{42} & L_{43} & L_{44}\end{bmatrix}\begin{bmatrix}\Phi\\ w\\ \varphi\\ \psi\end{bmatrix}=0$$
(4)

where $L_{ij}(i,j=1,2,6)$ are relevant differential operators, depending on the orthotropic conical shell characteristics within FOSDST , L_{42} contains lateral pressure and WEF, here Φ is the Airy stress function [8].

Due to the boundary conditions of the conical shell are freely-supported, the solution of Eq. (4) is sought as [8]:

$$\begin{aligned}\Phi&=\Phi_1 S_2\,\bar{r}^{(\eta+1)}\sin\left[\ln\bar{r}^{m_1}\right]\cos(m_2\phi)\\ w&=w_1\bar{r}^{\eta}\sin\left[\ln\bar{r}^{m_1}\right]\cos(m_2\phi)\\ \varphi&=\varphi_1\bar{r}^{\eta}\cos\left[\ln\bar{r}^{m_1}\right]\cos(m_2\phi)\\ \psi&=\psi_1\bar{r}^{\eta}\sin\left[\ln\bar{r}^{m_1}\right]\sin(m_2\phi)\end{aligned} \qquad (5)$$

where $\Phi_1, w_1, \varphi_1, \psi_1$ are unknown functions, η is a parameter that will be obtained from the minimum condition of the critical lateral pressure (CLP), $\bar{r}=r/s_2$, $m_1=\dfrac{m\pi}{\ln(s_2/s_1)}$, $m_2=\dfrac{n}{\sin\gamma}$, in which, *m* is the half wave number in meridional direction and *n* is the circumferential wave number.

Substituting (5) into Eq. (4) and employing Galerkin's method to the resulting equations, after some mathematical operations, the following expression is obtained for the CLP of orthotropic truncated conical shell resting on the WEF on the basis of the FOSDST:

$$P_{Lcrw}^{FOSDST}=\frac{U_3(U_2U_7-U_1U_5)-(U_2U_4-U_1U_5)U_6}{U_2U_3L_P}+\frac{L_wK_w}{L_P} \qquad (6)$$

where $U_j(i=1,2,...,7)$ are coefficients including the properties of orthotropic conical shell [6], the shear deformation functions and the following definitions apply:

$$\begin{aligned}L_P&=\frac{\left(2m_2^2+1\right)m_1^2(1-e^{2(\eta+1)r_0})\tan\gamma}{r_2\left[4m_1^2+(2\eta+1)^2\right](2\eta+1)},\\ L_w&=-\frac{1}{4}\frac{m_1^2(1-e^{2(\eta+1)r_0})}{\left[m_1^2+(\eta+1)^2\right](\eta+1)}\end{aligned} \qquad (7)$$

As the shear deformations are not considered, the expression for the CLP of orthotropic conical shell on the WEF on the basis of the CST is obtained in a special case.

3. CONCLUSIONS AND RESULTS

In this section, the effects of shear deformations and WEF on the CLPs of conical shells within CST and FOSDST are studied. The shear deformation function is $\Gamma(z)=z(1-4z^2/3h^2)$ and $z_1=z/h$ [9]. Table 1 shows the variation of the values of CLP of orthotropic conical shells on the WEF within CST and FOSDST versus the semi-vertex angle γ. The following orthotropic material properties and conical shell parameters are used [9]:

$E_1 = 53.7791\times10^9; E_2 = 17.9264\times10^9; \quad \nu_{12} = 0.25$ $G_{12} = G_{23} = 8.96325\times10^9$, $G_{13} = 3.4474\times10^9$, and $r_1 / h = 25$, $L/r_1 = 0.2$. The coefficient of WEF is $K_w = 2\times10^{10}\left(N/m^3\right)$. The values of the CLP for freely supported orthotropic conical shells are determined at $\eta = 2.4$. The values of CLPs for orthotropic conical shells with and without WEF in the framework of the CST and FOSDST decrease with the increasing the semi-vertex angle γ. As the semi-vertex angle γ increases, the difference between the CLPs within CST and FOSDST increases, moreover the shear deformations effect is more pronounced in orthotropic truncated conical shells. The maximum effects of shear deformations are 49.73% and 45.42% for unconstrained conical shell and conical shells resting on the WEF, respectively. As can be seen, considering the soil effect considerably reduces the effect of shear deformations on the CLP.

Table 1. Variation of CLP ($\times10^3$) of orthotropic conical shells on the WEF within CST and FOSDST versus the γ.

γ	P_{1Lcr}^{FOSDST}	P_{1Lcr}^{CST}	P_{1Lcrw}^{FOSDST}	P_{1Lcrw}^{CST}
0º	5.484	7.978	7.015	9.643
15º	4.723	7.506	6.135	9.077
30º	3.787	6.560	5.001	7.938
45º	2.799	5.237	3.755	6.347
60º	1.830	3.640	2.486	4.414

REFERENCES

[1] L. Tong, B. Tabarrok and T.K. Wang, 1992. Simple solution for buckling of orthotropic conical shells. *International Journal of Solids and Structures* 29, 933–46.

[2] H. Bellout and F. Bloom, 2001. Modeling the buckling of rectilinearly orthotropic truncated conical shells. *Math Comp Model* 34,195–227.

[3] A.H. Sofiyev, 2003. The buckling of an orthotropic composite truncated conical shell with continuously varying thickness subject to a time dependent external pressure. *Composites Part B-Engineering*, 34, 227–33.

[4] H.S. Shen, 2001. Postbuckling of shear deformable cross–ply laminated cylindrical shells under combined external pressure and axial compression. *International Journal of Mechanical Sciences* 43, 2493–523.

[5] M. Jabareen and I. Sheinman, 2009. Stability of imperfect stiffened conical shells. *International Journal of Solids and Structures* 46, 2111–25.

[6] A.H. Sofiyev, 2016. Buckling of heterogeneous orthotropic composite conical shells under external pressures within the shear deformation theory. *Composites Part B-Engineering*, 84, 175-187.

[7] D.V. Dung, L.K. Hoa, N.T. Nga, 2014. On the stability of functionally graded truncated conical shells reinforced by functionally graded stiffeners and surrounded by an elastic medium. *Composite Structures* 108;77–90.

[8] A.H. Sofiyev, F. Kadioglu, N. Kuruoglu, 2017. Influences of elastic foundations and shear deformations on the buckling behavior of functionally graded material truncated conical shells under axial compression. Mechanics Advances materials and Structures (in press)

[9] J.N. Reddy, Mechanics of laminated composite plates and shells, theory and analysis. CRC Press, New York, 2004.

Proceedings of the International Symposium of Mechanism and Machine Science, 2017
AzC IFToMM – Azerbaijan Technical University
11-14 September 2017, Baku, Azerbaijan

The effect of load on the tribological property of polyacetal and metallographic observation

Y.Şahin[1a], S.Yalçınkaya[2b], H.Mirzayev[3c]
[1]Department of Manufacturing Engineering, Gazi University, Besevler-06500, Ankara, Turkey,
E-mail: [a]ysahin@gazi.edu.tr
[2]Senai Yalcinkaya, [b]Department of Mechanical Engineering, Faculty of Technology, Marmara University, Kadikoy, 34722 Istanbul, Turkey,
E mail: [c]yalcinkaya2012@gmail.com
H. Mirzayev [3c]
[3]Department of Machine Elements, Azerbaijan Technical University, H.Javid av., 25, Baku, Azerbaijan
E mail: [b]mir_huseyn@aztu.edu.az

Abstract
The effects of applied loads on the dry sliding wear properties of polyacetals were investigated using on a conventional plate-disc-type reciprocating sliding wear of tribometer against a hardened 100Cr6 stainless steel as a counterface. The frictional behaviours were determined at a fixed speed. The wear surfaces and wear tracks for the polyacetal samples was observed with an optical microscope when tested at various conditions. The results showed that the specific wear rate decreased with increasing the loads. The static friction coefficient of polyacetals/steel tribo-pairs under 50N load was about 0.74, but decreased to 0.26 for 200N load. Furthermore, wear surfaces and wear tracks observation exhibited that ploughing and cutting were responsible for wear behaviour at lower load, but adhesion and plastic deformation seemed to be dominant for the higher load because increasing normal load also led to a rise in temperature at the frictional surface.

Keywords: Polymer, Polyacetal, Dry sliding, Load, Wear, Friction, Worn surface, Ploughing, Cutting.

1. Introduction

Polymers can be used for sliding friction systems such as ball joints, crane guidance and, roller and gears without lubrication. The most commonly used for polymers are PTFE, PA, POM, PEEK. Among the range of thermoplastics, POM are typical thermoplastic polymers, which is exhibited good sliding properties for different sliding applications because they exhibits low friction, wear and good fatique and creep resistance. Therefore, these polymers has been widely used as self lubricating materials in many fields like manufacturing and otomotive industry, electronic appliance and construction industry [1-3]. POM can replace not only non-ferrous metals but also iron casting, steel casting and stainless steels lighter. In most cases, however, it is of primary concern to develop polymeric materials that possess low friction and low wear properties under dry sliding conditions against smooth metallic counterparts [4, 5]. The transferred of polymer materials may deteriate or improve the service characteristics of a system due to adhesion between the contacting surfaces by directly taking part in a sliding operation. The transferred materials affect the friction coefficient and wear rate.

Numbers of friction and wear behaviour of POM have been performed on the hardened steel counterface in a pin-on-disc, pin-on-ring or reciprocating pin-on-flat. They provide fundamental information about friction and wear mechanisms, consequently used for development of new materials or surface treatments [6, 7]. Friedrich et al.(1995) studied the friction and wear properties of high temperature resistant polymers, particularly polyetheretherketone (PEEK) under various testing conditions against smooth steel counterpart. It is reported that the coefficient of friction increased with increase in load. Wang and Li [9] found that the sliding velocity influenced the sliding wear of UHMWPE polymer to a greater extent than the applied load [10, 11]. They distinguished the wear loss in three different periods during the operating time viz. the wear loss in running-in period, steady-state period and severe wear period. However, it is reported that the wear rates of POM and UHMWPE could decrease with increasing sliding speed when the roughness of the mating surface was low [5]. Bohm et al. [12] revealed that HDMWPE clearly outperformed all of other polymers tested while PEEK indicated the poor wear performance. Seabra and Baptisa [13] found that UHMWPE-green was found to be the lowest frictional coefficient and good wear resistance among the food grade polymers like PTFE, UHMWPE, HMW-PE, PA 6, POM-C and PETP under sugar interface dry sliding conditions**.** It is concluded that, this polymer was one of the best option to match stainless steel because of the presence of green pigments. The friction coefficients changed with counterface roughness, an optimal surface roughness of PETP/PTFE and POM-H which were lower than that of PA [14]. The wear rates were higher on rougher surfaces for PA. In case of PA 6G/oil, it strongly depended on the load and surface roughness. However, the wear resistance of PETP/PTFE and POM-H increased with increasing tensile strain at rupture. Samyn and De Baets [15] studied the friction of a commercial polyoxymethylene homopolymer (POM-H) on large-scale and small-scale reciprocating test rigs. No transfer was observed for small-scale tests, while a stable transfer film was developed under large-scale sliding with identical flash temperatures. Later work also showed that for a small scale tests, the calculated flash temperatures were between 60-180 ºC that not revealed melting. Samyn et al. [16] reported that PET/PTFE sliding against the stainless steel developing the transfer layer on to the steel surface, which led to reduction in friction coefficient. There was no wear debris found for UHMWPE/carbon against stainless steel [17]. SEM examination indicated that polymer transfer of POM-C was initiated by mechanical interlocking of metal asperities into the polymer. The resulting wear debris particles were smeared into the roughness valleys and, finally the most of the metal surface was covered by the polymer [18].

Liu et al. [19] made an attempt to model the wear behaviour of three polymers such as UHMWPE, PA-6/UHMWPE and PA-6 using a regression analysis. It is reported that the contact pressure was the main controlling parameter for the wear process compared to other influencing parameters such as the sliding distance and speed. Sahin [20] studied the abrasive wear behavior of polyamides through the combination effect of load, speed, distance and grit size. Optimal process parameters, which minimized the wear resistance was the factors combination of L1, S2, G2 and D1 for both polymeric materials [21]. Sagbas et al. [22] studied the abrasive wear of POM under various testing conditions using central composite design (CCD) and artificial neural network (ANN). Sahin et al. [23] investigated the dy sliding wear behaviour of POM using on a conventional flate plate-disc-type reciprocating sliding wear of tribometer. Cylindrical shape of the samples from POM tested against a hardened smooth steel counter face. Frictional behaviours were determined at fixed speed under two different loads. The experimental results showed that static and dynamic coefficients of friction under 100 N normal load varied between 0.432 and 0.266, respectively. In addition, the coefficient of friction and specific volumetric wear rate decreased with increasing the load.

The literature review demonstrated that the sliding wear behaviour of POM polymers were studied. However, there are limited numbers of studies on the sliding wear of the polymers using the effect of lower loads, and roughness [1, 4, 14, 15, 24, 25, 26]. Therefore, aim of this work was to study the dry sliding wear behaviour of POM by experimental base under different loads changing from 50N to 200N at dry sliding conditions. Furthermore, the worn surface observations were carried out to find responsible mechanisms during the dry sliding wear of the polyacetals.

2. Experimental

2.1. Materials and Apparatus

The POM used in this present study, which was commercially available from Ertacetal Company. The charactersitics of the POM-C (Ertacetal-C, white) thermoplastic wear samples. This POM keeps its favourable mechanical properties up to 92ºC. The experimental apparatus was a pin-on-flat wear-testing machine with a reciprocating motion. A pin specimen was fixed to a reciprocating stage or to a pin specimen holder by setting screws. The polymer bars were machined into small cylindrical shapes with lathe machine for the pin-on-disc wear testing. The diameter of the pin specimen was 8 mm with 15 mm in length. The pin was then mounted in a steel holder in the wear machine so that it was held firmly perpendicular to that of the flat surface of the rotating counter disc. The specimen of 8 mm in diameter for POMs tested under different loads against smooth hardened steels. Chemical, physical and mechanical properties of to be tested materials were given in Table 1. The normal load was applied through a spring and lever.

Table 1. Chemical, physical and mechanical properties of POM-C materials

Some properties	Metric units	POM-C
Density	gr/cm^3	1.41
Shore hardness	$N.mm^2$	85
Compressive strength at %5	MPa	72
Elastic modulus	MPa	2800

Friction force was measured with a strain-gauge detector installed on the wear-testing machine. POM was slid in a reciprocating motion against cold rolled steel AISI 42CrMo6 grinded to an average surface roughness, R = 0.20 - 0.40 µm perpendicular to the sliding direction. For the tests, a polymer cylinder was positioned into a moving head and was slid on its side (line contact) against a fixed steel counterface plate. The steel counterface was fixed to a base plate. The cylindrical samples had a diameter of 8 mm and a length of 15 mm, while the steel mating plate sizes 58 x 38 x 4mm, which was heat-treated to give a surface hardness of 59-62 RC. The tests were carried out at 50N, 100 N, 150N and 200 N normal load, corresponding to 0.99, 1.98, 2.99 and 3.98 MPa contact pressures. The sliding velocity was 0.3 m/s over a sliding stroke of 15 mm. The total sliding distance of 2160 and

4320 m ensures steady-state condition. The wear pin was cleaned in acetone prior to and after the wear tests, and then weighed on a microbalance with 0.1 mg sensitiveness. Each test was performed with new track of disc. The specific wear rate (Ks) was then expressed on volume loss basis:

$$Ks = \frac{\Delta M}{\rho L F n} \left(\frac{mm^3}{N.m}\right) \quad (1)$$

Where M is the mass loss in test duration (gm), ρ is the density of composite (gm/cm^3), F_n is the applied normal load (N) and L is the sliding distance (m). Three replicates were carried out for each material and results were averaged from the two test runs.

3.0 Results and discussion

3.1. Wear rate

The experimental results of the adhesive wear of polyacetals at diferent conditions are shown in Table 2. The tests relevant to this table were carried out at a fixed speed, but indicated loads. The temperature at the frictional surfaces increased with increasing the load and the frictional heat on polyacetal can not be distributed in time due to the poor ability of heat transfer. The asperity summits became blunt and the spaces between asperities were filled in the running-in period which resulted in lower wear in the steady-state phase. The duration of the running-in phase was dependent on the test condition. It is evident from the figure that the wear rate decreased with increasing applied load, which could be explained with the fact that the wear rate is determined by the pv–value, where p stands for the load and v for the velocity. For example, the wear rates of the samples at loads of 50 N and 200 N varied from 0.61x10^{-6} and 1.533x10^{-6} mm^3 / N.m. Samyn et al.[16] showed that the wear rates was ranged from 6x10^{-7} to 4x10^{-4} mm^3 / N.m. However, typical wear coefficients obtained from pin-on-disc tests with POM pins against rotating steel disc were found to be around 2x10^{-6} to 4x10^{-6} mm^3 / N.m in the available literature [4,10,31].

3.2. Effect of load

Fig.1 shows the influence of loads on the frictional and wear behaviour of polyacetal polymers at a constant speed of 0.3 m/s under different loads. It is observed that the weight loss increased more or less linearly due to increase the deformation of asperities at contacting points (Table 2). It is breaks off easily from the main body. However, the wear rate decreased with increasing the load because it is inversely proportional to the load and sliding distance. The temperature at the contacts rises decreased the shear strength of the polymer since the thermal softening of polymer occurred, which causes lower COF, and temperature also increased the real contact area by flowing across the counterpart surface. As a result of this, adhesion and transferring films became the dominant wear type instead of abrasion and micro-cutting (see Fig.3).

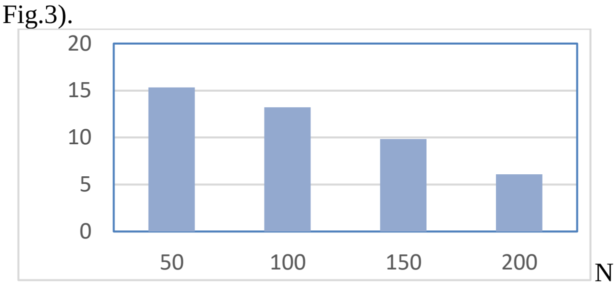

Fig.1. Specific wear rate of polyacetal at a constant speed under different loads

Table 2. The experimental results of the dry wear rate of POMs under different load conditions

Load	Weight loss,gr	Specific wear rate (mm^3/N.m) (10^{-6})	Average static COF	Average dynamic COF
50	0.02851	1.5330	0.74	0.33
100	0.04030	1.323241	0.42	0.30
150	0.0450	0.9850	0.36	0.28
200	0.03717	0.61023	0.26	0.25

3.3. Coefficient of friction

Table 2 shows the variations of coefficient friction with time for POM. The coefficient friction decreased with increasing the load, that is, it was varied from 0.74, 0.42, 0.33, and 0.26 for 50, 100 and 150 N, respectively. The high COF might be due to abrasive wear between the polymer and the surface of the counter face. The abrasive wear resulted in because of micro-ploughing action of the steel counter-face. The lowest static COF obtained was about 0.26 at 200 N load. The dynamic COF is 0.21-0.33 when the load is 50 N and decreased to 0.24 for higher load. The dynamic COF of POM-H at different conditions were about 0.78 and 0.60 at a fixed speed 0.3 m/s for 100 N and 200 N, respectively [16]. However, they measured the dynamic COF of about 0.33 under 200 N load at a speed of 1.2 m/s. The dynamic COF for POM-C, PEEK and PA6G (pv = 2 MPa.m/s) measured were about 0.20, 0.29 and 0.33, respectively [7].

Typical plots of the COF including static and dynamic as a function of the sliding times for POM under 100 N, 200 N contact loads at a fixed speed are envisaged in Fig.2 (a and b) respectively. The COF of the polymer/steel tribo-pairs was measured to be in the range 0.42 and 0.28 for static and dynamic component, respectively. Furthermore, the static and dynamic friction coefficients appeared to vary similarly as a function sliding distance or time, but the dynamic COF exhibited lower values than the static component, but indicated a stable behaviour with increasing the sliding distance (Fig.2). The static and dynamic friction coefficient plotted as a function of time in Fig.2 (b) under higher load, the static friction coefficient decreased at higher normal load. For example, the statistic and dynamic COF was about 0.28 and 0.21, respectively because the time to establish a steady-state friction shortened because of the frictional heat for the polymer, which increased the surface temperature. The literature indicated that transfer of the POM to the metal counterface led to an increase in the COF [25]. COF of POM-C sliding against AISI 100Cr6 steel was about 0.51, but decreased to 0.42 with the sliding speed of 0.05 m/s. The dynamic COF of POM at a reciprocating motion with polished steel slider was about 0.32 for POM. The materials were damaged rapidly when changed the sliding velocity from 0.42 to 0.84 m/s [30]. Therefore, the sliding velocity had a more obvious influence on the wear behaviour of POM-H than the nominal load.

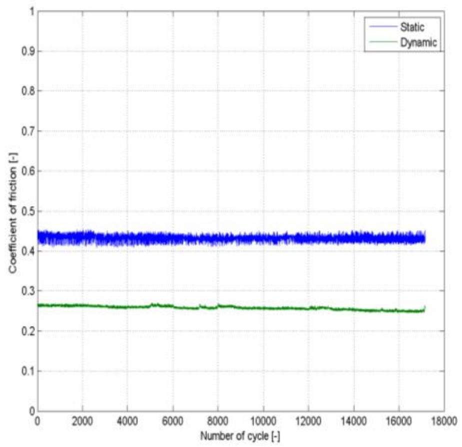

(a)

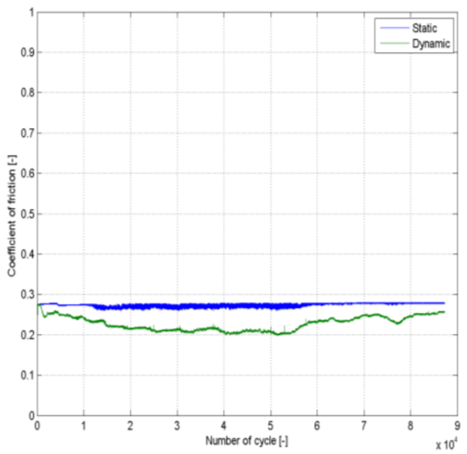

(b)

Fig.2. Static and dynamic coefficient of friction as a function of sliding time for POM sliding at 0.3 m/s against the smooth steel. (a) 100N load, 16.4x10^4 cycle, (b) under a 200 N load, 8.8x10^4 cycle

3.4. Wear surface observations

In order to understand the differences among the polymers, wear surfaces and wear tracks for each one is taken from an optical microscope at a similar condition. The unworn specimen, worn polymer specimens, and counter-faces are examined using an optical microscopy. Fig.3 (a,b and c) show the polymer pin track and worn surfaces at different conditions when sliding against steel counterpart. Fig.3 (a) exhibits a quite rough surface because its only showing a manufactured roughness, not testing one, which is about 3 µm while Fig.3 (b) indicates an abrasive grooves over the sliding surface because the asperities in the steel counter face easily removed the material from the soft polymer by cutting action, but depth ness of the grooves varies from local place to place. However, Fig.3 (c) shows a relatively smoother surface than that of the previous sample because the polymers are cut by counter face disc, transferred to the steel surface and its surface is covered with the transferred polymer. That is to say, the debris particles pressed into roughness of the valleys. Thus, the traces of ploughings are not visible on the pin surface in this micrograph. Namely, ploughing and cutting are responsible for wear of the first case, but adhesion and plastic deformation seem to be dominant for the last case because increasing normal load also lead to a rise in temperature at the frictional surface. The decrease in the depth of scratches may probably be attributed to the formation of stable, adhesive and intact transfer film on the counter-surface [31, 32].

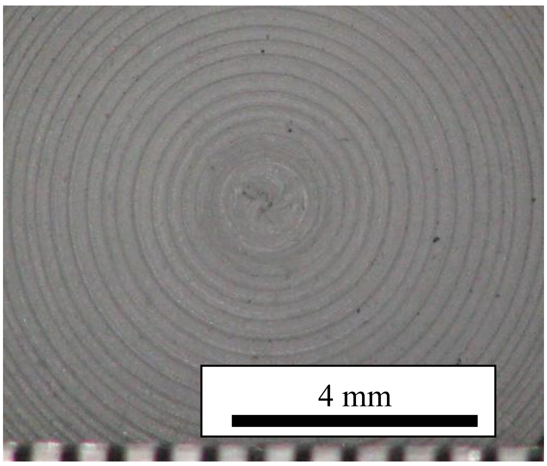

(a)

(b)

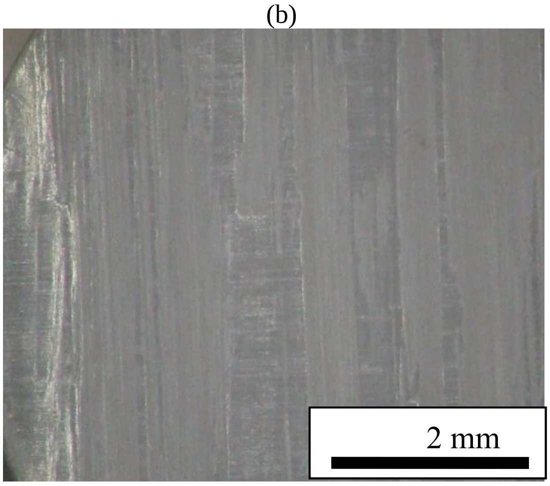

(c)

Fig. 3. Wear track and wear surface of polymer specimens under two different loads of 0.30 m/s. (a) The pin surface before testing, (b) The pin worn surface tested at 100 N load, indicating abrasive grooves parallel to the sliding direction, (c) The pin worn surface tested at 200 N load, showing adhesive wear of delamination

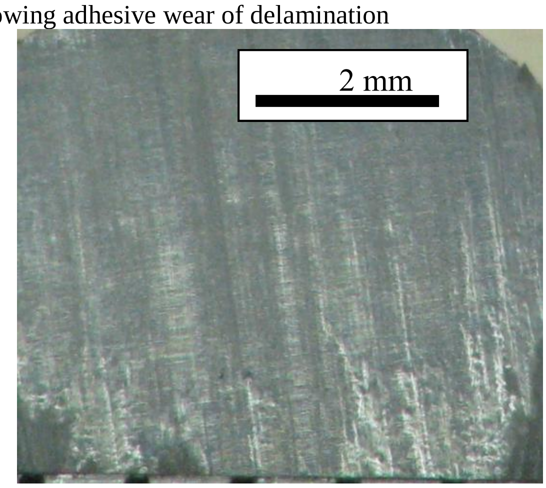

(a)

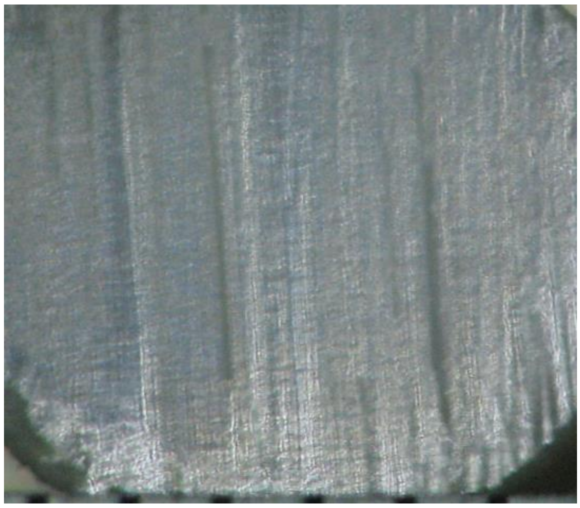

(b)

Fig. 4. Wear surface of the polymer sample tested at: (a) 150 N, (b) 200 N

Fig. 4 indicates the wear surface of the polymer samples tested under loads of 150 N, 200 N, respectively. A similar surface topography was observed for both loads. The average surface roughness of the POM samples was measured when tested at 100N load test without and after the test. The average surface rouhghness was about 0.470 and 0.40 µm, respectively. The surface roughness decreased about 15% due to machining the rough surface during the heavy loading. Fig. 5 shows the wear surface of counterpart, tested at 50 N load under low and higher magnification, respectively. This low magnification view indicates the thin films stretching across the abrasion grooves, and it is associated with ridge on sliding surface. The higher magnification also indicates polymeric materials are forced into the valleys between the ridges of the asperities and mechanically interlocks with the metal surface. Two dark lines also an indication of the transferred film is brown colour and adhered to the disc surface firmly. Mechanical anchoring and rolling effect is predominant for the lower load for POMs. This may be due to related to the debris formation, oxidation and surface roughness orientation during the rubbing process.

a)

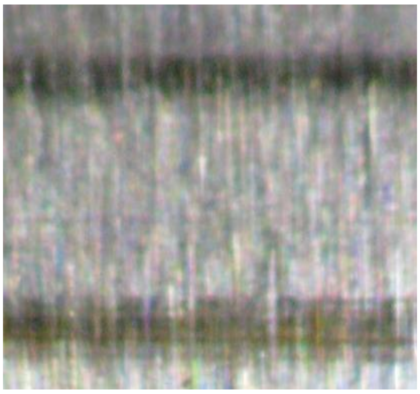

b)
(a) Lower magnification
(b) Higher magnification

Fig.5. Wear surface of counter-face plate under 50 N load at 0.30 m/s. (a) Lower magnification, indicating mechanical encoring, (b) Higher magnification, showing tribo film formation

Fig.6 shows the wear surface of counterpart, tested at 150 N load at low and higher magnification, respectively. This figure reveals in a more clearly that the transfer film, which formed on the steel plate surface, is built up of more or less continuous thin layer. These are adhered preferentially on the asperity ridges of the ground metal counter-face. The sliding surface was found to heat up which was likely result in increased adhesion. Therefore, there were a more smooth surface obtained at higher load condition

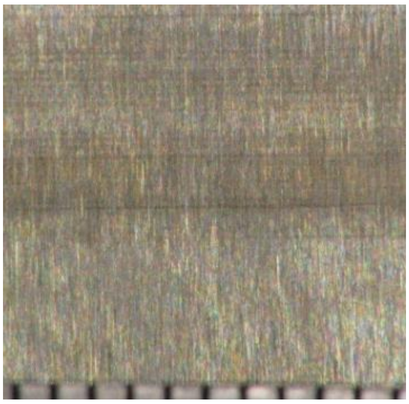

a)

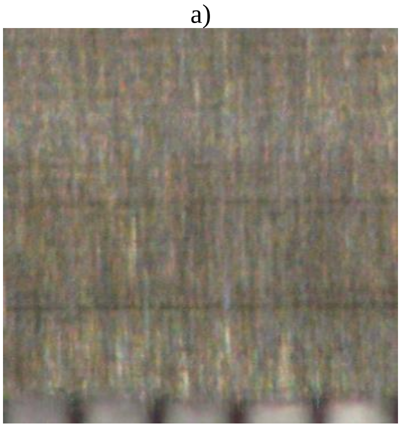

b)
(a) Lower magnification
(b) Higher magnification

Fig.6. Wear surface of counter-face plate under 150 N load at 0.30 m/s. (a) Lower magnification, exhibiting a formation of transfer film on the wearing surface of the pin, (b) Higher magnification, exhibiting a transfer film on the surface

A similar surface appearance was also observed from the tested conditions, but various loads were applied on both pin and disc surfaces, as shown in Fig.7 (a,b), respectively. This micrograph shows the increase of wear scar width with the load. For example, it was about 0.8 mm when tested at 50 N load, but increased up to more or less 2.2 mm. However, it couldnot observed the same trend for 200 N load. It might be the formation of wear transfer layers because a brown colour was evident for that case. The transfer film formed on the counterpart surface with increasing the load occurs more smooth, thin, uniform, and tenacious

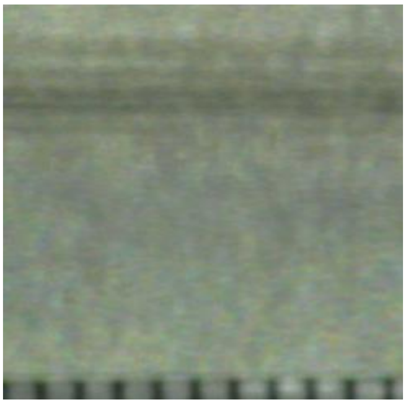

a)

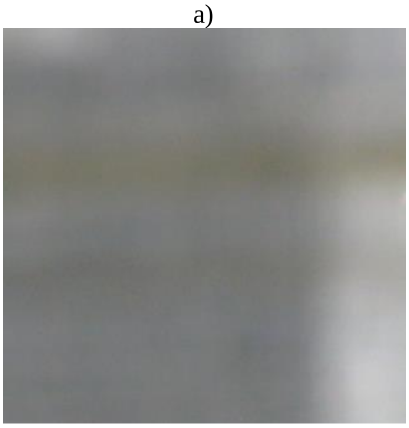

b)

Fig.7. Wear surface of counter-face plate tested at: (a) 150 N, (b) 200 N

4. Conclusions

The following conclusions were drawn based on the experimental results for the frictional and wear properties of polyacetal-steel combinations.

1. The experimental results showed that the wear rate of the polyacetals was influenced considerably by the load at increasing rate as approximately 2.5 times. The wear rates of the polymeric samples under the loads of 50N to 200N varied from $0.6102\text{x}10^{-6}$ to $1.533\text{x}10^{-6}$ mm^3/N.m.
2. The friction coefficient of POM/steel tribo-pairs when tested at 50N and 200N load was measured to be in the range 0.74 and 0.26 respectively, but there was no significant changes occurred with the loads for the dynamic COF of 0.24-0.33.
3. Moreover, the wear surface observations by optic microscopy exhibited that ploughing and cutting were responsible for the wear behaviour of lower loads, but adhesion and plastic deformation seemed to be dominant for the higher load applications because the increasing normal load also lead to a rise in temperature at the frictional surface of the tested polymeric samples.

References

[1] Huang T., Lu R., Wang H., Ma Y.& Tian J., Investigation on the tribological properties of POM modified by nano-PTFE, J.Macromolacular Sci.,Part B, Physics 50, 1235-1248 (2011).

[2] Chen J., Ca Y.& Li H., Investigation of the friction and wear behaviour of POM/linear low-density polyethylene/ethylene/acrylic/acid blends, Wear 260, 1342-1348 (2009).

[3] Sun LH., Yang ZG.& Li XH, Study on the friction and wear behaviour of POM/Al2O3 nancomposites, Wear 264, 693-700(2008).

[4] Franklin S.E., Wear experiments with selected engineering polymers and polymer composites under dry reciprocating sliding conditions, Wear 251, 1591–1598 (2001).

[5] Schwartz C.S.& Bahadur S., Studies on the tribological behaviour and transfer film counterface bond strength for polyphenlyene sulphide filled with nanoscale alumina particles, Wear 237, pp. 261-273 (2000).

[6] Ziemiankski K.& Capanidis D., The mechanism of dry friction of polyoxymethylene against steel, Wear 82, pp. 317 (1982).

[7] Kalácska G., An engineering approach to dry friction behaviour of numerous engineering plastics with respect to the mechanical properties, eXPRESS Polymer Letters, 7 (2),pp. 199–210(2013).

[8] Friedrich K., Lu Z.&Mager A.M., Recent advances in polymer composites Tribology, Wear 190, pp.139–144. (1995).

[9] Wang Y.Q.& Li J., Sliding wear behaviour and mechanism of ultra-high molecular weight polyethylene, Mater Science Engineering, A 266, pp. 155–160(1999).

[10] Unal H., Sen U.& Mimaroglu A., Dry sliding wear characteristics of some industrial polymers against steel counterface, Tribology International 37, pp.727–732 (2004).

[11] Watanabe M., The friction and wear properties of nylon, Wear 110, pp.379–188(1986).

[12] Bohm H., Betz Sntonio M. Baptista., Tribological behaviour of food grade polymers against stainless steel in dry sliding and with sugar, Wear 253, pp.394–402 (2002).

[14] Zsidai L., De Baets P., Samyn P., Kalacska G., Van Peteghem A.P.& Van Parys F., The tribological behaviour of engineering plastics during sliding

friction investigated with small-scale specimens, Wear 253, pp. 673–688 (2002).
[15] Samyn P. & De Baets P., Friction of polyoxymethylene homopolymer in highly loaded applications extrapolated from small-scale testing, Tribology Letters, Vol. 19 (3), pp. 177-189(2005).
[16] Samyn P. & De Baets P., Wear transition and stability of polyoxymethylene homopolymer in highly loaded applications compared to small-scale testing, Tribology International 40,pp. 819-833 (2005).
[17] Samyn P.& De Baets P., Friction and wear of acetal. A matter of scale, Wear 259, pp.697-702 (2005).
[18] Mergler Y.J., Schaake R.P.& Huis in't Veld A.J., Material transfer of POM in sliding contact, Wear 256, pp.294–301 (2004).
[19] Liu C.Z., Ren L.Q., Tong, J., Joyce T.J., Green S.M.% Arnell R.D., Statistical wear analysis of PA-6/UHMWPE alloy, UHMWPE and PA-6, Wear 249, pp.31–36 (2001).
[20] Şahin Y., 'Wear analysis of polyamide based on a statistical approach, Int. J. Mater. & Product. Technol. (IJMPT), 54 (1/2/3), pp.108-114 (2015).
[21] Şahin Y., 'Analysis of abrasive wear behavior of PTFE composite using Taguchi's technique', Cogent Engineering, 2, pp. 1-15 (2015).
[22] Sagbas A., Kahraman F.&Esme U., Modelling and predicting abrasive wear behaviour of POM using respondse surface methodology and neural networks, Metabk 48 (2), pp. 117-120(2009).
[23] Şahin Y., Pauw J.D., Sukumaran J.,&Patrick D.B., Sliding friction and wear of polyoxymethlyene polymer, Synergy International Conferences - Engineering, Agriculture and Green Industry Innovation, Godollő, Hungary, October 12-15, 2015.
[24] Marcus K.,&C., The sliding wear of ultrahigh molecular weight polyethylene in an aqueous environment, Wear 178, pp. 17-28 (1998).
[25] Sun L.H., Yang Z.G.& Li X.H., Study of the friction and wear behaviour of POM/Al2O3 nano composites, Wear 264, pp. 693-700 (2008).
[26] Cai H.C.& Yan F.Y., Investigation of tribological properties of Al2O3-polyimide nanocomposites', Polym. Test., 22, pp. 875-882 (2003).
[27] Kurukawa M., Uchiyama Y., Iwai T.& Nagai S., Tribological properties of Polyoxymethylene composites against aluminium, Journal of Tribology, 25, pp. 661-669 (2003).
[28] Hu X., Tribological behaviour of modified polyacetal against MC nylon without lubrication, Tribology Letters 5, pp. 313-317(1998).
[29]Mens J.W.M.& Gee A.W.J., Friction and wear behaviour of 18 polymers in contact with steel in environments of air and water, Wear 149, pp.255-268 (1991).
[31].Goyal, R.K.; Jagdale, P.A. & Mulik, U.P., Thermal, mechanical, and dielectric properties of polystyrene/expanded graphite nanocomposites, J. Appl. Polym. Sci. 111, pp. 2071-2077(2008).
[32] Goyal, R.K.& Yadav, M., Study on wear and friction behavior of graphite flake-filled PTFE composites, J. Appl. Polym. Sci. 127, pp.3186-3191

The tribological wear behavior of carbon fabric-reinforced epoxy composites

Yusuf Şahin[1*], Erdi Erdil [2] & Hakan Şahin [3]
[1]Department of Manufacturing Engineering, Gazi University, Besevler-06500, Ankara, Turkey, E-mail: ysahin@gazi.edu.tr, [2]Department of Mechanical Engineering, Gazi University, Besevler-06500, Ankara, Turkey, E-mail: erdiergul@gmail.com , [3]Institute of Natural Science and Technology of Gazi University, Beşevler-06500, Ankara, Türkiye, E-mail: hakansahin85@hotmail.com

Abstract
The tribological behavior of carbon fabric-reinforced epoxy composite (CFRC) and its nano-based composites including Al2O3 and PTFE powders produced by molding technique was investigated using a pin-on-disc configuration. Response surface methodology of Box-Behnken was utilized to model the effects of various variables such as applied load, rotational speed and material types on the weight loss under dry sliding conditions. The second order mathematical regression model was developed. Moreover, ANOVA indicated that the load was higher significant than the others at 95% confidence level. The percentage contributions of the linear were about 82 % (load (39.41%, speed 25.22%, and materials type 17.13%)), but square effect and two-way

interactions were about 11.5% and 1.43% on the weight loss, respectively. The error obtained was about 5% while the pure error was about 1.41.
Keywords: epoxy, carbon fabric, composite, load, speed, wear.

1. Introduction

Polymer based materials reinforced with various fibers or particles have gained considerable attentions in many industrial fields such as aircraft, space and automotive and marine applications because of their high specific/strength and easy of processing and thermal stability [1,2]. Among the reinforcements, carbon is the best choice for using such applications. The drawback of the carbon fibres in polymeric resins, however, is higher cost and their high brittleness. Thus, it is imperative to modify carbon fibers or to select the carbon fabrics. To improve the better mechanical and tribological properties and load carrying capacity, carbon fabrics were used owing to the orderly aligned structure. The mechanical properties of polymer based composites are greatly influenced by many factors such as the effect of fiber loading, fiber length, fibre type, fibre content, fiber/matrix property, fiber diameter, applied processing, fiber/matrix interface and orientation of fibers [3-11].

In recent years, much research has been devoted to exploring the potential advantage of polymeric matrix for composite applications using nano-scale inorganic compounds such as TiO2, ZnO, SiO2, Al2O3, Si3N4 etc. as the fillers of fabric composites to improve the tribological properties [12–17] due to their specific properties such as high surface activity and energy and small size effect of the nano-particulates. For instance, Deng et al. [12] studied the self-lubrication of Al2O3/TiC/CaF2 ceramic composites in sliding wear tests. The tribo-formation on the wearing surfaces resulted in lower wear because of acting as a lubricating additive between the sliding surfaces. Hyung et al. [13] investigated the effect of solid lubricants like graphite, Sb2S3, MoS2 for brake pad materials. The results indicated that amounts of solid lubricants in the friction materials affected the friction stability, fade resistance and wear of gray iron discs and pad friction materials. Tateoki et al. [14] demonstrated the tribological behavior of Mo5Si3 particle reinforced Si3N4 matrix composites. The friction and wear of an unoxidized Mo5Si3–Si3N4 composite, oxidized Mo5Si3–Si3N4 composites and Si3N4 were investigated under dry sliding. Basavarajappa et al. [15] revealed that the incorporation of graphite particles in the aluminum matrix as a secondary reinforcement increased the wear resistance of the hybrid metal matrix composites. The smearing of the graphite and formation of protecting layer between the pin and the counter face enabled in reducing the wear volume loss [16]. Chauhan et al. [17] concluded that the coefficient of friction and wear rate of carbon and glass fabric increased with increase in load/sliding velocity and depended on type of fabric reinforcement and temperature at the interphase. The excellent tribological characteristics were obtained with carbon fiber in vinyl ester.

Wang et al.[18] studied the friction and wear behaviour of basalt fabric composites filled with graphite and nano-SiO_2. The results showed that graphite was more beneficial than that of nano-SiO_2 due to formation of tranfer film. Suresha et al.[19] reported that coefficient friction and wear rate increased with increase in load/sliding speed for carbon and glass fabric reinforced vinyl ester composites. The best tribological properties were obtained with carbon fibre due to thin film formation on the counterface [20]. The influence of graphite fillers on two body abrasive wear behaviour of carbon fabric reinforced composites, and wear performance of carbon-epoxy (C-E) composites indicated that the graphite fillers resulted in enhancement of wear behaviour significantly [21]. Better abrasion wear resistance was observed in B-E composite compared to G–E composite because the more damage occurred to glass fiber compared to basalt fiber [22, 23]. Şahin investigated the wear behavior of PTFE and its composites including glass-filled composites and carbon-filled composites by Taguchi technique [24]. The wear rate decreased with increasing grit size, load, sliding distance, whereas, slightly with compressive strength. The dry wears of PTFE-based composites were investigated under different conditions. Taguchi L27 method was used to identify the effect of process parameters on the wear. ANOVA exhibited that the sliding distance was the most significant factor affecting the wear behavior of polymer composites [25]. Tribological behavior of unidirectional carbon fiber-reinforced epoxy composites containing 42wt.% (CU42) and 52wt.% (CU52) carbon fibers fabricated by molding technique was investigated on a pin-on-flat plate configuration [26]. The experimental results indicated the carbon fiber improved the tribological properties of thermoset epoxy by reducing wear rate, but increased the coefficient of friction (COF). The wear rate decreased with decreasing load while COF increased with decreasing load. Moreover, COF of composites of CU42 tested at 90 N load was measured to be in the range 0.35 and 0.13 for static and dynamic component, respectively. The last work by Sahin and Patrick [27] on the tribological behavior of carbon fabric-reinforced epoxy composites was shown that the wear rate considerably decreased by a factor of 8 when the reinforcing carbon fabrics were introduced into the epoxy matrix. The wear rate the composites increased with an increase in normal load. Moreover, COF for epoxy/steel and composites/steel tribo-pairs decreased with increasing load. Royal and Yadav [28] studied the wear rate and COF for graphite flake (GF)-filled polytetrafluoroethylene (PTFE) composites. The wear rates of 5 and 10 wt. % GF composites were reduced by more than 22 and 245 times, respectively. However, with increasing sliding distance up to 8 km, the wear rate of pure PTFE decreased by 1.4 times while it decreased up to three times for the composites.

The literature review above have indicated that number of studies are carried out on the effect of fillers on the wear behaviour of polymer based composites [12-21]. However, there are only few studies performed on the abrasive wear or statistical method on the fabric-reinforced composites [22-25]. The objectives of this work, thus, were to investigate the effects of load, speed and materials type on the tribological behavior of carbon fabric-reinforced epoxy composite (CFRC) and its nano-based composites using response surface methodology.

2. Experimental

2.1. Materials

Neat epoxy and carbon fabric reinforced epoxy composites were manufactured in laboratory by molding technique. The resin used in this work is commercial SR 8500 epoxy resin and hardener was SD 860x supplied by MCtechnic Ltd., Netherland. The filler materials used in this study was carbon fabrics supplied by MCtechnic Ltd. Carbon plain weave fabric with a fiber diameter of 7-10 µm and specific weight of 200 g/m^2 was used as a strengthener. The manufacturing process involved mixing of the epoxy resin with the hardener at a fixed ratio of 100:28.

For the manufacturing the nano-composites, the fillers material used are Al_2O_3 and PTFE, respectively. Al_2O_3-Alpha, 99.5% pure (grit size is about 40-60 nm) was provided from MKnano, Canada. The specific gravity is about 3.3 g/cm^3. PTFE (grit size is about 20 nm) was provided from Beijing Starget New Materials Limited in Zhejiang, China. PTFE powder-JX-16 type, 12-20 nm in size with 99.98% purity and white colour. Its specific gravity is about 2.16 g/cm^3. Three different types of specimens were prepared for this study. These three different types of specimens such as CF60 fabric-reinforced epoxy composite without nano particles, CF60+2.5wt.% nano Al_2O_3 epoxy composites and CF60+2.5wt.% nano PTFE reinforced epoxy composites were prepared, respectively. Nano particles/fillers were evenly dispersed in the epoxy resin by mechanical stirring for a period over 30 min.

The epoxy resin was mixed thoroughly with weight fractions of nano Al_2O_3 powders (2.5 wt.%) and nano PTFE particles (2.5 wt.%), respectively. The production process involved the mixing of the epoxy resin with a hardener at a fixed ratio to ensure complete mixing. Then the catalyzed resin mixtures were spatulated on a composite panel of a 100 x 100 mm^2 with a thickness of 4.0 mm. Alternate layers of the resin and reinforcement were finally put on the steel molding at 28 plies were stacked to achieve required final thicknesses and weight fractions (60 wt.%, referred to as C60) as a reference material. Particularly, they were performed using five prismatic samples for each composite type and its matrix.

Finally, post curing was done at 45 ºC for 24 hours. The specimens required for abrasive wear study (5x5x4 mm^3) were cut from the laminated composites by using a water jet machining.

2.2. Experimental design

The response surface methodology (RSM) design of experiment approach eliminates the need for repeated experiments and thus saves time, material, and cost. This approach identifies not only the significant control factors, but also their interactions influencing the wear rate predominantly. This experiment specifies three principle wear testing conditions including the applied load (L), rotational speed (S) and type of materials (M) of the tested materials as the process parameters. Codes and levels of control parameters and their levels were shown in Table 1. This table showed that the experimental plan had three levels. A standard RSM plan with notation L15 was chosen, as shown in Table 1.

An orthogonal array and ANOVA were applied to investigate the influence of process parameters on the wear behavior of composites.

Table 1. Control parameters and their levels.

Sym.	Controlling parameters	Level 1	Level 2	Level 3
L	Applied load, N	5 (-1)	10 (0)	15 (+1)
S	Speed, rpm	80 (-1)	140 (0)	200 (+1)
M	Material types, HRB	C60 (-1)	C60+ Al2O3 (0)	C60+PTFE (+1)

2.3. Wear tests

The experimental apparatus was a pin-on-disc type of wear-testing machine. A pin specimen was fixed to a rotational stage or to a pin specimen holder by setting screws. The pin was then mounted in a steel holder in the wear machine so that it was held firmly perpendicular to that of the flat surface. The normal load was applied through a spring and lever system. Carbon fiber-reinforced composite (CFRC) was slid in a circular rotational motion against cold rolled steel of AISI 4140 grinded to perpendicular to the sliding direction. The steel counter face was fixed to the base steel plate sizes of Ø120 x 14 mm with an average surface roughness of 0.30 - 0.50 µm perpendicular to the sliding direction. Silicon carbide (SiC) abrasive papers of grit 500 were fixed on the steel counter face for the abrasive wear testing process. The specimens were loaded under 5 N, 10 N and 15 N under three different sliding speeds of 80 rpm, 140 rpm and 200 rpm against the SiC emery papers. The total sliding distance was about 125 m. For each percentage of fiber volume fractions, three types of test specimens were prepared. The wear pin was cleaned in acetone prior to and after the wear tests, and then weighed on a microbalance with 0.1 mg sensitiveness. The weight loss was calculated from the mass loss method.

3. Results and discussion

3.1. Analysis of weight loss

The experimental data was analyzed using the software MINITAB 16. The experimental lay out and results of the abrasive wear of epoxy composites under different conditions were shown in Table 2. The tests relevant to this table were carried out at a fixed speed, but indicated parameters of loads. The weight loss of composites and its matrix experiments were plotted as a function of the control factors in Fig.3. The mean response referred to the average values of the performance characteristics at different levels. Among the control factors, the factor L (load) showed the highest effect on the weight loss because the penetration ability of SiC abrasives on the counter face disc increased with increasing the strength of laminate structure of the composites (Fig. 3a), followed by the factor S (speed) and the factor M (type of material), respectively (Fig. 3b,c).

It was revealed that the mean weight loss obtained was at the lower values for all cases. In other words, linear decreases were observed with load and sliding speed, but decreased remarkably for both nano-addition effect. However, it is noted that the sensitivity of the load was slightly higher than that of the sliding speed (Fig. 3b).They were clearly related to the Archard’s equation because it had proven very useful in describing the abrasive wear, which were in good agreement with this work [24].

However, it was contradictory to the some other tests carried out on the composites showed that the abrading distance was more effective on the wear of other parameters [16, 30]. Besides, the effect of load on the wear rate of Zinc based Al_2O_3 composite was more severe than that of abrasive sizes [29]. Recent work by Şahin [27] indicated that the sliding speed was not an effective on the wear of the polyamide samples due to the self-lubricated ability, but the abrasive size and sliding distance had great effects on the weight losses for Kestoil samples and Kestamid samples, respectively.

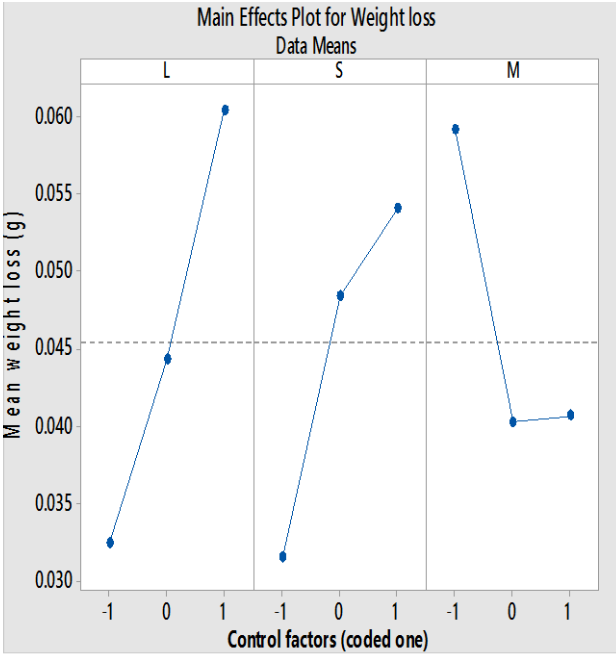

Fig. 3. Weight loss as a function of control factors for carbon fiber-reinforced epoxy composites, tested against the SiC abrasive emery paper

Fig.4 shows the surface plots of the combined effects of the independent variables on the weight loss of the carbon epoxy composites and including nano-additions to the carbon epoxy based composites. Fig.4 (a) indicates the WL vs. L&S Fig.4 (b) exhibits the WL vs. L&M, but Fig.4 (c) revealed the WL vs. M&S. These figure also indicated the load and speed were more effective on the wear behavior of the composites. There appeared a little variation with changing material from Al2O3 to PTFE in terms of the weight loss (Fig.4 (c)).

Moreover, contour plots of the combined effects of the independent variables on the abrasive wear of the tested samples are shown in Fig. 5 (a, b and c) respectively. Fig. 5 (d) shows the WL vs. L&S while Fig.5 (e) indicates the WL vs. M&L, and Fig.5 (f) exhibits the WL vs. S&M, respectively. These graphs also visualize the response surface of the tested samples, which are allowed to establish the response values and desirable wear testing conditions. Similar findings were observed for the UHMWPE composites using RSM and emprical models were also constructed to indicate the connection between the main control factors like filler loading, load and speed and wear rate and COF responses [31]. Their results revealed that the filler loading, applied load and sliding speed had a significant effect on the wear rate and COF.

Table 2. Abrasive wear results of FRPCs

Exp. Run	Applied load (N)	Rotational speed (rev/min)	Material types (HRB)	Weight loss (g)
1	-1	1	0	0.0351
2	1	-1	0	0.0380
3	-1	-1	0	0.0202
4	-1	0	-1	0.0524
5	0	0	0	0.0368
6	1	0	-1	0.0799
7	0	-1	-1	0.0393
8	0	1	-1	0.0648
9	-1	0	1	0.0220
10	0	1	1	0.0522
11	1	0	1	0.0597
12	0	-1	1	0.0288
13	1	1	0	0.0639
14	0	0	0	0.0473
15	0	0	0	0.0409

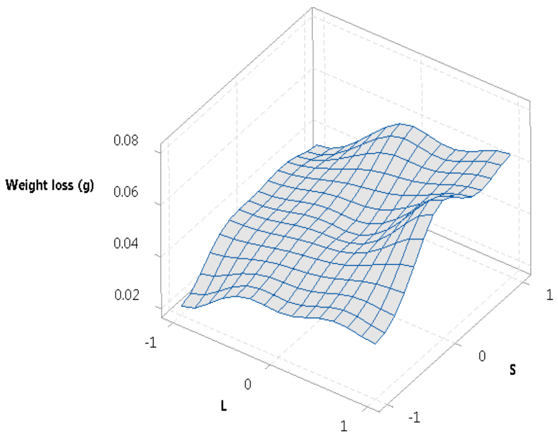

(a)

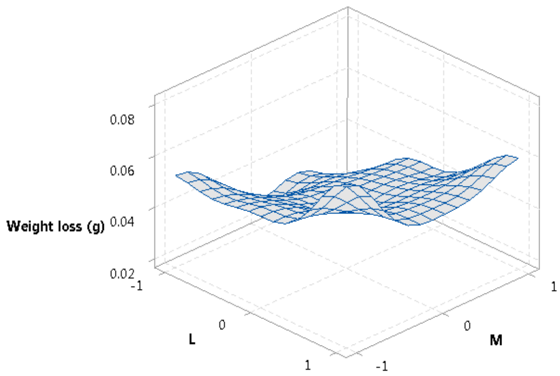

(b)

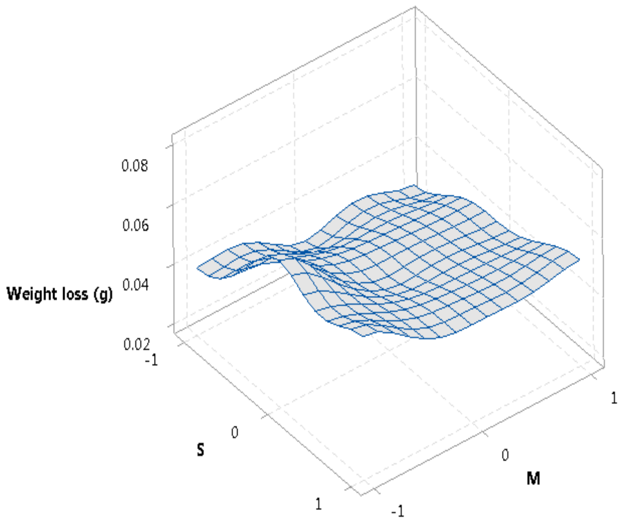

(c)

Fig. 4. Surface plots of the combined effects of the independent variables on the weight loss of the epoxy composites. (a) WL vs. L&S, (b) WL vs. L&M, (c) WL vs. M&S

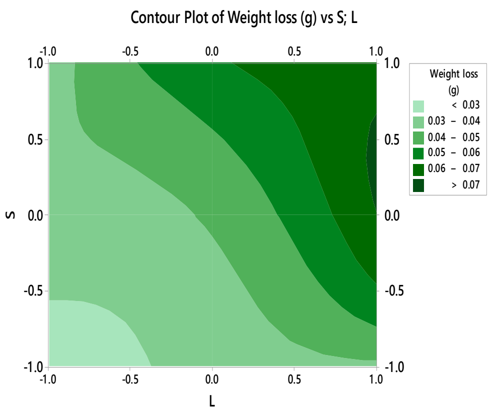

(a)

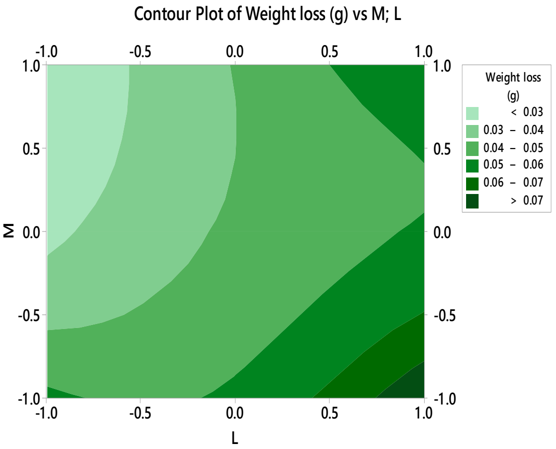

(b)

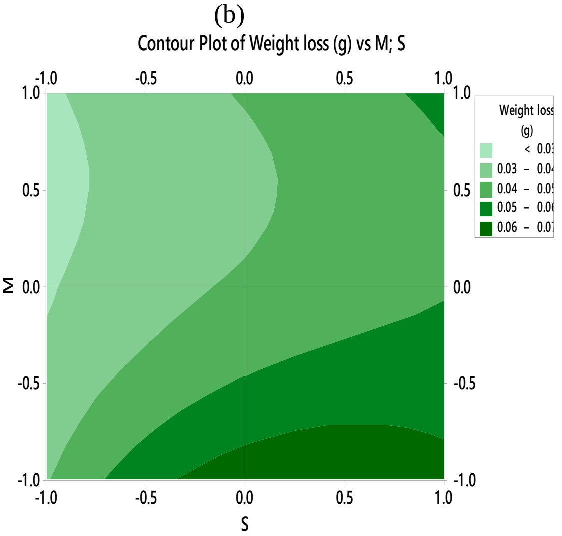

(c)

Fig. 5. Contour plots of the combined effects of the independent variables. (a) WL vs. L&S, (b) WL vs. M&L, (c) WL vs. S&

3.2. ANOVA

The ANOVA was used to investigate which design parameters significantly affect the quality characteristic for the weight loss of the composites. The ANOVA results for the abrasive dry sliding wear behavior of polymer composites under different conditions were listed in Table 3. This analysis was performed for the 5% significance level, that is, for the 95% confidence level.

This table showed the analysis of variance for the tested samples. It could be resulted that the probability value (P-value) for the weight loss was 0.002, 0.004 and 0.009 for L, S and M, respectively. The L parameter had a significant effect because the probability value of L parameter was lower than 0.05, but other two parameters had also significant influence on the response.

Table 3. Analysis of variance for the weight loss

Sour.	DF	Adj.SS	Adj.MS	F-value	Contr. P(%)	P-Value
Model	9	0.00376	0.00042	10.34	94.9	0.010
Linear	3	0.00324	0.00108	26.79	81.9	0.002
L	1	0.00156	0.00156	38.68	39.4	0.002
S	1	0.00100	0.0010	24.90	25.2	0.004
M	1	0.00067	0.00067	16.81	17.1	0.009
Square	3	0.00045	0.00015	3.76	11.5	0.094
L*L	1	0.00002	0.00002	0.54	0.55	0.496
S*S	1	0.00008	0.00008	2.10	2.14	0.207
M*M	1	0.00032	0.00032	8.08	8.25	0.036
2-Way Int.	3	0.00005	0.00002	0.47	1.43	0.714
L*S	1	0.00003	0.00003	0.75	0.75	0.426
L*M	1	0.00002	0.00002	0.64	0.65	0.459
S*M	1	0.000001	0.000001	0.03	0.25	0.875
Error	5	0.00020	0.00004	5.0		
Lack of Fit	3	0.00014	0.00004	1.74	3.68	0.386
Pure Error	2	0.000056	0.000028	1.41		
Total	14	0.003963				

DF = degrees of freedom, Seq SS = sequential sum of squares, Adj SS = adjusted sum of squares, Adj MS = adjusted mean squares.

Moreover, analysis of variance shown in this table that the linear effect (L,S,M) revealed the most significant (0.0032), followed by quadratic M*M (0.00045) and lastly two-way interactions of L*S (0.000057), respectively. Furthermore, the lack of fit values was about 0.00014, which was significant because it was lower than that of 0.05.

3.3. Multiple linear regression model

Regression technique was used to study the weight loss of the composites. The regression equation for the weight loss of epoxy and its composites when tested against the SiC paper can be expressed as follows.

To establish the correlation between the material properties and wear process parameters like load, speed and hardness, multiple linear regression model with uncoded units was obtained using statistical software"Minitab16". The second order model equation for the weight loss prediction is given by

$$\text{Weight loss}, WL\ (g) = 0.04167 + 0.01398\ L + 0.01121\ S - 0.00921\ M + 0.00243\ L*L - 0.00480\ S*S + 0.00940\ M*M + 0.00275\ L*S + 0.00255\ L*M - 0.00052\ S*M \quad (1)$$

where WL is the mean weight loss Eq. (1) indicated that the weight loss increased the load and speed, but decreased with changing material when testing against SiC abrasive papers. The model had an adjusted R^2 value of 94.9%. In other words, WL: weight loss of the samples (mg × m-1), L: load (N) and S: rotational speed (rpm) and M: Materials type of the tested samples. By substituting the recorded values of the variable for Eq. (1), WL of epoxy matrix composites was calculated (Fig.3). It could noted from this equation that the coefficients of load (L), speed (S) were positive, but material type (M) was negative. It was exhibited that load was the main factor on the weight loss, followed by speed while material type was less effective than the other factors. The higher value of regression coefficients would be directly translated into higher effect of the variables to the response.

4.0 Conclusions

The application of RSM modelling on the abrasive wear of the neat epoxy and carbon-fabric reinforced epoxy against the stainless steel was presented and second-order mathematical models were developed using three testing parameters. The following conclusions can be drawn from the present study.

The results showed that the load was found to be a dominant factor on the weight loss, followed by the speed factor, lastly the material's type. The optimum selected testing process parameters settings were at a load of 5N, spindle speed of 80 rpm, and running the composite of C60+2.5wt.% Al_2O_3-epoxy, which resulted in a minimum weight loss.

Moreover, ANOVA indicated that the load was higher significant but other factors were also significant effects on the weight loss at 95% confidence level. The percentage contributions of the linear ((load (39.41%), speed (25.22%) and material types (17.13%)) square, and two-way interactions were about 82%, 11.5%, and 1.43% on the weight loss, respectively. The error obtained was about 5% while the pure error was about 1.41.

References

[1]. B.R. Raju, B. Suresh and R.P. Swamy, Tribo-performance of silicon dioxide filled glass fabric reinforced epoxy composites, *ARPN Journal of Eng. Appl. Sci.*7 (4), pp.6604-6608 (2012).

[2]. F.H. Su, Z.Z. Zhang, K.Wang, W. Jiang, X.H. Men, and W.M. Liu, Friction and wear properties of carbon fabric composites filled with nano-Al2O3 and nano-Si3N4, *Composites: Part A* 37, pp. 1351–1357 (2006).

[3]. Y. Şahin, *Introduction to Composite Materials*, 3rd Press, Seckin Book Store & Distributions, Ankara, Turkey (2015).

[4]. H. Rahmani, S.H.M. Najafi, S. Saffarzadeh-Matin and A. Ashori, Mechanical properties of carbon fiber/epoxy composites: Effects of number of plies, fiber contents, *Poly. Eng.Sci*. 54 (11), pp. 2676-2681 (2014).

[5]. I.D.G.A.Subagia, Y. Kim, L.D. Tijing, C.S. Kim and H.K., Shon, Effect of stacking sequence on the flexural properties of hybrid composites reinforced with carbon and basalt fibers, *Compos. Part B* 58, pp.251-256 (2014).

[6]. Y.Zhou, F. Pervin, S.Jeelani and P.K.Mallick, Improvement in mechanical properties of carbon fabric–epoxy composite using carbon nanofibers, *J. Mater.Proces.Technol.*198 (1–3), pp.445–453 (2008).

[7]. S.H.Han, H.J. Oh, H.C. Lee and S.S. Su, The effect of post-processing of carbon fibres on the mechanical properties of epoxy composites, *Compos. Part B-Eng*. 45 (1), pp.172-177 (2012).

[8]. J.R.Tarpani, M.T. Milan, D. Spinelli and W.W.Bose, Mechanical performance of carbon-epoxy laminates Part I: quasi-static and impact bending properties, *Mat. Res. 9 (2)*, São Carlos, pp.115-120 (2006).

[9]. T. D.Jagannatha and G. Harish, Mechanical properties of carbon/glass fiber reinforced epoxy hybrid polymer composites, *Int. J. Mech. Eng. & Rob. Res*. 4 (2), pp.131-136 (2015).

[10]. U. Dwiedi and N.Chand, Influence of fibre orientation on friction and sliding wear behaviour of jute fibre reinforced polyester composite, *Appl. Comp. Mater.*16(2), pp.93-100 (2009).

[11]. M.P.Prasad,, B. Vinod and Dr.L.J. Sudev, Effect of fiber orientations on tribological behaviour of palf reinforced bisphenol-a composite, *Int. J. Eng. Res. &General Sci.* 2 (4), pp.809-814 (2014).

[12]. J.Deng, L.Liu, X.Yang, J. Liu, J.Sun and J.Zhao, Self lubrication of Al2O3/TiC/CaF2 ceramic composites in sliding wear tests and in machining processes, *Mater. Des*. 28, pp.757–64 (2007).

[13]. C.M.Hyung, J.Jeong, K.S.Jin and J.Ho, Tribological properties of solid lubricants (graphite, Sb2S3, MoS2) for automotive brake friction materials, *Wear 260*, pp.855–60 (2006).

[14]. I.Tateoki and K.Hideki, Tribological behavior of Mo5Si3 particle reinforced Si3N4 matrix composites, *Wear 258*, pp.877–89 (2005).

[15]. S. Basavarajappa, G. Chandramohan and J. Paulo Davim, Application of Taguchi techniques to study dry sliding wear behaviour of metal matrix composites, *Mater. Des.* 2006.

[16]. S.Basavarajappa, A.G.K. Joshi, V. Arun, A.P. Kumar and P.M. Kumar, Three-body abrasive wear behaviour of polymer matrix composites filled with SiC particles, *Polymer-Plastics Technology and Engineering*, Vol. 49 (1), pp.8–12 (2010).

[17]. S.Chauhan, A. Kumar, A. Patnaik, A. Satapathy and I. Singh, Mechanical and Wear Characterization of GF Reinforced Vinyl Ester Resin Matrix Composites With Different Co-Monomers, *J. Reinf. Plast. Comp.* 28, pp. 2675-2684 (2008).

[18]. Q.H.Wang, X.R.Zhang and X.Q. Pei, Study on the friction and wear behavior of basalt fabric composites filled with graphite and nano-SiO_2, *Mater.Des.* 31, pp.1403-1409 (2010).

[19]. B. Suresha, K.S. Kumar, S. Seetharamu and P.S. Kumaran, Friction and wear behaviour of carbon and glass fabric reinforced vinylester composites, *Tribol. Int.* 43, pp.602-609 (2010).

[20]. B.Suresha, G. Chandramohan, J.N. Prakash, V.Balusamy and K. Sankaranarayanasamy, The role of friction and slide wear characteristics in Glass-epoxy composite system, *J. Miner.Maters.Charact. Eng*. 5, pp.87-101 (2006).

[21]. B. Suresha, B.N. Ramesh, K.M. Subbaya, B.N.R. Kumar and G. Chandramohan, Influence of graphite filler on two body abrasive wear behaviour of carbon fabric reinforced epoxy composites, *Mater.Des.* **31**, pp.1833-1843 (2010).

[22]. C.A. Chairman and S.P. Kumaresh Babu, Three-body abrasive wear behavior of basalt and glass fabric reinforced epoxy composites, *Appl. Mech. Maters*. 121-126, pp.534-538 (2012).

[23]. N.Anjum, S.L.A. Prasad and B.Suresha, Role of SiO_2 filler on mechanical and dry sliding wear behaviour of Glass-Epoxy composites, *Adv. in Tribol*. ID 324952, pp.1-10 (2013).

[24]. Y. Şahin, Analysis of abrasive wear behavior of PTFE composite using Taguchi's technique, *Cogent Eng.* 2, 1000510 (2015).

[25]. Y. Şahin and H. Mirzayev, Wear characteristics of polymer-based composites, *Mech. Compos. Maters*. 51, pp.1-12 (2015).

[26]. Y. Şahin and D.B. Patrick, Tribological behaviour of unidirectional carbon fibre-reinforced epoxy composites, *The 13th International Conference on Tribology ROTRIB'16*, September 22-24, pp. (2016), Galati, ROMANIA.

[27]. Y. Şahin and D.B. Patrick, Friction and wear behaviour of carbon fabric-reinforced epoxy composites, *JOM*, pp.1-5 (2017).

[28]. R.K. Goyal and M. Yadav, Study on Wear and Friction Behavior of Graphite Flake-Filled PTFE Composites, *J. Appl. Polym. Sci*. pp.3186-191 (2013).

[29]. O.P.Modi, R.P.Yadav, D.P. Mondal, R.Dasgupta, S. Das and A.H. Yegneswaran, Abrasive wear of Zinc-Al alloy-10% Al2O3 composite through factorial design', *J.Mater.Sci.* 36, pp.1601–1607 (2001).

[30]. H.Unal, U.Sen and A. Mimaroglu, Abrasive wear behaviour of polymeric materials,*Mater. Des.* 26 (8), pp.705–710 (2005).

[31]. B.P.Chang, H.Md Akil, R.Bt Nasıırand A.Khan, Optimization on wear performance of UHMWPE composites using response surface methodolgy, *Tribol.Int.88*, pp.252-262 (2015).

Proceedings of the International Symposium of Mechanism and Machine Science, 2017
AzC IFToMM – Azerbaijan Technical University
11-14 September 2017, Baku, Azerbaijan

The Vibration of Non-Homogenous Nano-Micro Elements of The Euler-Bernulli Beam Theory According to The Nonlocal Theory

[1]Pirmammadov I.T., Latifov F.S., Radjabov V.G.
[1]Azerbaijan Technical University

Abstract
In this article, the vibration analysis of non-homogeneous nano and micro elements has been investigated with the applying of nonlocal elasticity theory. Beam has been chosen as the structural model type and also Euler-Bernoulli beam theories have been used for beam theories. The motion equations of Euler-Bernoulli beam theories were obtained by utilizing the nonlocal elasticity theory, which was proposed by Eringen. According to the different boundary conditions, the vibration equations of micro-nano beam has been generated. Analysis has been performed over the carbon nanotube and microtubules in order to observe the effect of nonlocal behavior and results have been compared with the classical theory.
Keywords: Nonlocal elasticity theory, nano-micro elements, non-homogeneous, Euler-Bernoulli beam theories, vibration, free vibration frequency.

1. Introduction

The vast majority of strength and stability of various beam layered structural theories are studied in detail in scientific literatues which is made different isotropic non-homogeneous elastic materials [1-3]. İn recent times, regarding the rapid advancement of artificial and composite material technologies, in most cases the structures are made with those materials. İn this case, isotropic properties are formed in various materials and it is necessary to take into consideration these factors to solve concrete problems. These factors are considerably important especially in the stability and vibration problems.

Nowadays, it is essential to utilize accurate hypotheses and theories while trying to solve numerous problems. One of these theories is the non-local elasticity theory which has proposed by Eringen. In number [4], bending problem of isotropic beams was investigated using these theories

In number [4-5] - The issue was isotropic nano – micro elements, stability and strength problems based on Eringen theory.

In numbers [6-7] - generally beams theory has established on the basis of this theory and on the basis of various speculation, stability and vibration that have been investigated.

The [8] - Regarding the non-local continuum theory the ortotrop nano plates model was realised as polymer plate then stability problems have been investigated.

The [9] - nano beams prepared from functional graded materials on the basis of non-local Timoshenko theory that vibration problem had been modeled and various problems had been solved.

The [10] - On the basis of thermo elastic non-local model called functional graded nano beams' vibration problem has been reviewed under sinusoidal pressure.

The [11] - symmetric stability problems of Nano beams on the vertical condition were investigated according to non-local discrete and continuum theories.

The [12] - generally main equations of beams' theories were obtained on the basis of non-local elasticity theory of Eringen and bending problems was investigated in detailed.

The [13] - on the basis of Timoshenko beam model of nano and microstructures, non-linear vibration problems were researched.

The [14] - non-linear equations of fluid flowing through the tubes were obtained and its stability condition was investigated.

The [15] - symmetric for layered beams due to tension theory the model was structured and deflection equation was obtained.

The [16] - the stability problems of non-linear beam were investigated on the basis of gradient theory.

The [17] - the vibration problems of micro plates were investigated with modified tensions theory.

The [18] - while solving the theory of displacement deformations of functional graded plates general condition and Karmans non-linear theory or finite elements method were analysed.

The [19] - the vibration problems was investigated in the elastic condition due to anisotrop layered beams theories.

Sizes effects have significantly importance on construction elements in nano and micro measured elements, nowadays, mostly elasticity theory (in scientific literature sometimes it is also called non-local elasticity theory) is used which has been proposed by Eringen. In classic elasticity theory which equilibrium equations are considered the same all parts of the object. This candition actually is true if dimensions of part would be large. However, if dimensions of part decreases, there would require to take into consideration inner structure of the body, so there should also take into account the interaction of the particles which close to point in the examined equations. Tensions at a point in calculating the amount which was proposed Eringen with the theory of elasticity, displacement and deformation at the point where you just know it is not enough and that is offered to them in the form of the dependence of all the points are a function of displacement.

For the reasons discussed article that bending and stability of heterogeneous beams' issues are studied based on the theory of Eringen.

MAIN PHYSICAL RELATIONS

Cauchy equations of motion in non-local theory of elasticity for the homogenous and isotropic body are:

$$\tau_{kl,l} + \rho\left(f_i - \frac{\partial^2 u_i}{\partial t^2}\right) = 0, \quad (1)$$

For general case, Eringen non-local elasticity theory, the physical equations of body are:

$$\tau_{kl}(x) = \int_v \ \varepsilon_{klmn}(x - x')\,\varepsilon_{klmn} dv(x'), \quad (2)$$

Here is τ_{kl} stress tensor, ρ density of body, f intensity of force for the body, u- displacement vector, v - the volume occupied by the body, t – time, ε_{kl} deformations and are defined below:

$$\varepsilon_{kl} = \frac{1}{2}\left(\frac{\partial u_k}{\partial x_l} + \frac{\partial u_l}{\partial x_k}\right). \quad (3)$$

ε_{klmn}, is the function of $x - x'$vector from where it can be seen that stresses in x point are dependent on the displacements and deformations in point x'. The stresses and deformations in point x' are:

$$\tau(x') = \lambda\varepsilon_{mn}(x')\delta_{ke} + 2\mu\varepsilon_{ke}(x'), \quad (4)$$

$$\varepsilon_{kl}(x') = \frac{1}{2}\left(\frac{\partial u_k(x')}{\partial x'_l} + \frac{\partial u_l(x')}{\partial x'_k}\right),$$

In those equations, $\tau(x')$ is the classic (Cauchy) or local stress tensor of the body in point x'. $\varepsilon_{kl}(x')$ is the linear deformation of particle in the x' point.

After some algebra, the equations of Eringen non-local elasticity theory are:

$$[1 - (l_0 a)^2 \nabla^2]\sigma_{kl} = \tau_{kl,} \quad (5)$$

$$[1 - (l_0 a)^2 \nabla^2]\tau_{kl} = \lambda\varepsilon_{kl}\delta_{kl} + 22\mu\varepsilon_{kl}.$$

a – inner characteristic length, l_0 is the constant coefficient for the material.

Hereby, the equalities can be written as follows;

$$\left[1 - (l_0 a)^2 \frac{\partial^2}{\partial x^2}\right]\sigma_{xx} = E\ \varepsilon_{xx,} \quad (6)$$

$$\left[1 - (l_0 a)^2 \frac{\partial^2}{\partial x^2}\right]\tau_{xx} = 2G\ \varepsilon_{xz,}$$

Assume that material is non-uniform like $E = E(z)$ (modulus of elasticity is the continuous function of thikness coordinate.

According to Euler Bernoulli beams theory

$$\varepsilon_{kl} = E\left(\frac{\partial u}{\partial x} - z\frac{\partial^2 w}{\partial x^2}\right) \quad (7)$$

expression is achieved. Here u is the displacement of the beam, w is the bending.

Force and moment are calculated as follows

$$P = \int_A \sigma_{xx} dA \quad N = \int_A \tau_{xz} dA, M = \int_A \sigma_{xx} z dA \quad (8)$$

After some algebra, the moment is calculated as:

$$M = -KI\frac{d^2 w}{dx^2}\ . \quad (9)$$

KI is the generalized hardness characteristic of the beam. If $E = E_0\left[1 + \gamma\frac{z^2}{h^2}\right]$, then in that case,

$$KI = E_0 I\left[1 + \gamma\frac{z^3}{20}\right], \quad (10)$$

where $E_0 I$ is the hardness of the homogenous beam.

The result from (6) is shown below:

$$M\left[1 - (e_0 a)^2\frac{\partial^2}{\partial x^2}\right] = -KI\frac{\partial^2}{\partial x^2}w. \quad (11)$$

FORMULATION OF THE VIBRATION PROBLEM

Now the vibration problem of the beam will be analysed. The equation of motion for the beam is as :

$$\frac{\partial P}{\partial x} + f = m_0\frac{\partial^2 U}{\partial t^2} \quad (12)$$

$$\frac{\partial^2 M}{\partial x} + q - \frac{\partial}{\partial x}\left(P\frac{\partial w}{\partial x}\right) = m_0\frac{\partial^2 w}{\partial t^2} - m_2\frac{\partial^2 w}{\partial x^2 \partial t^2} \quad (13)$$

$$m_0 = \int_s \ \rho ds = \rho s;\ m_2 = \int_s \ z^2 ds = \rho s\frac{h^2}{12} \quad (14)$$

The expressions for moment and force are:

$$P = Ks\frac{\partial U}{\partial x} + \mu\frac{\partial}{\partial x}\left(m_0\frac{\partial^2 U}{\partial t^2} - f\right) \quad (15)$$

$$M = -KI\frac{\partial^2 w}{\partial x^2} + \mu\left[\frac{\partial}{\partial x}\left(P\frac{\partial w}{\partial x}\right) - q - m_0\frac{\partial^2 w}{\partial t^2} - m_2\frac{\partial^2 w}{\partial t^2 \partial x^2}\right], \quad (16)$$

In here, $M = (e_0 a)^2$ and after substituting the formula of moment in the equation above, the result will be:

$$\frac{\partial^2}{\partial x^2}\left(-KI\frac{\partial^2 w}{\partial x^2}\right) + \mu\frac{\partial^2}{\partial x^2}\left[\frac{\partial}{\partial x}\left(P\frac{\partial w}{\partial x}\right) - q + m_0\frac{\partial^2 w}{\partial t^2} - m_2\frac{\partial^4 w}{\partial t^2 \partial x^2}\right] + q - \frac{\partial}{\partial x}\left(P\frac{\partial w}{\partial x}\right) = m_0\frac{\partial^2 w}{\partial t^2} - -m_2\frac{\partial^4 w}{\partial t^2 \partial x^2} \quad (17)$$

If boundry conditions is assumed to add into this equation, it could be obtained from the general statement of the problem.

SOLUTION OF THE PROBLEM

Generally the solution of the problem depends on various difficulties. In this case, it is examined in different certain conditions. Assume that, force is axially applied to the beam (in 17th equation, P=const, f=0, q=0 is accepted). After some calculations, specific vibration equations are obtained as below:

$$\frac{\partial^2}{\partial x^2}\left(-KI\frac{\partial^2 w}{\partial x^2}\right) + \mu\frac{\partial^2}{\partial x^2}\left[\frac{\partial}{\partial x}\left(P\frac{\partial w}{\partial x}\right) + m_0\frac{\partial^2 w}{\partial t^2} - m_2\frac{\partial^4 w}{\partial t^2 \partial x^2}\right] - \frac{\partial}{\partial x}\left(P\frac{\partial w}{\partial x}\right) = m_0\frac{\partial^2 w}{\partial t^2} - m_2\frac{\partial^4 w}{\partial t^2 \partial x^2} \quad (18)$$

We can accept 18th equations periodic solutions as below

$$w(x,t) = w_1(x)e^{i\omega t}. \quad (19)$$

We put (19) expression to (18) one in order to obtain following equation:

$$d_1\frac{d^4w_1}{dx^4}+d_2\frac{d^2w_1}{dx^2}-rw_1=0 \quad (20)$$

From here it can be write;

$$d_1=KI-\mu P-\mu m_2\omega^2$$
$$d_2=m_2\omega^2+P+\mu m_0\omega^2,\quad r=m_0\omega^2 \quad (21)$$

ω – is the vibration frequencey.

General solution of the (20) – equation is given below;

$$w_1=c_1\sin\alpha x+c_2\cos\alpha x+c_3\sin h\beta x+c_4\cos h\beta x \quad (22)$$

Here,

$$\alpha^2=\frac{1}{2d_1}\left(d_2+\sqrt{d_2^2+4d_1r}\right),\ \beta^2=\frac{1}{2d_1}\left(-d_2+\sqrt{d_2^2+4d_1r}\right) \quad (23)$$

c1, c2, c3, c4 are the integral constants with the accepted boundary conditions. In special condition, if a=b, P=0, m_2=0, μ=0 accepted, after classical elasticity theory the given problem coluld be solved.

Utilizing (22) expression with some calculations, it can be obtained as below:

$$\frac{dw_1}{dx}=\alpha(c_1\cos\alpha x-c_2\sin\alpha x)+\beta(c_3\cos h\,\beta x+c_4\cos h\beta x) \quad (24)$$

$$M=-d_1\frac{d^2w}{dx^2}-\mu rw_1=(d_1\alpha^2-\mu r)(c_1\sin\alpha x+c_2\cos\alpha x)-(d_1\beta^2+\mu r)(c_3\sin h\beta x+c_4\cos h\beta x) \quad (25)$$

$$N=-d_1\frac{d^3w_1}{dx^3}-d_2\frac{dw_1}{dx}=\alpha(d_1\alpha^2-d_2)(c_1\cos\alpha x-c_2\sin\alpha x)-\beta(d_1\beta^2+d_2)(c_3\cos h\beta x+c_4\sin h\beta x) \quad (26)$$

We obtained from (23) equation:

$$(2d_1\alpha-d_2)^2=d_2^2+4d_1r\quad or\quad d_1\alpha^4-d_2\alpha^2-r=0 \quad (27)$$

After some algebric operations:

$$(KI-\mu P-\mu m_2\omega^2)\alpha^4-(m_2\omega^2+P+\mu m_0\omega^2)\alpha^2-m_0\omega^2=0 \quad (28)$$

For general vibration equation:

$$\omega^2=\alpha^2\frac{KI\alpha^2-(1+\mu\alpha^2)P}{(m_0+m_2\alpha^2)(1+\mu\alpha^2)}. \quad (29)$$

If is looked at free vibration (P=0) it can be obtained for vibration frequency:

$$\omega=\alpha^2\sqrt{\frac{KI}{(m_0+m_2\alpha^2)(1+\mu\alpha^2)}} \quad (30)$$

While α is defined within various boundary conditions given edges of the beam which exclusive vibration frequencey (30) calculated.

Let's examine both edges of the beam on the slider fixed condition. In this case, if x=0 and x=a, following conditions should be accounted:

$$w_1=0\ and\ M=-d_1\frac{d^2w_1}{dx^2}-\mu m_0\omega^2w_1=0 \quad (31)$$

$$\text{or}\ \ w_1=0\ \text{and}\ \frac{d^2w_1}{dx^2}=0 \quad (32)$$

conditions must be to take into consideration.

$P\neq 0\ or\ \alpha^2\neq\beta^2$ we can get boundary condition such as

$$c_2=0\ and c_4=0,$$
$$c_1\sin\alpha a-c_3\sin h\beta a=0,$$
$$c_1\sin\alpha a(d_1\alpha^2-r\mu)-c_3\sin h\beta a(d_1\alpha^2+r\mu)=0. \quad (33)$$

Equations are obtained. Afterthat, in order to differentiate bending from 0, (33) systems expressions determinant would be 0;

$$\sin\alpha a=0\ or\ \alpha_n=\frac{n\pi}{a}. \quad (34)$$

In this case, it can be obtained exclusive vibration frequency from (29):

$$\omega_n=\left(\frac{n\pi}{a}\right)^2\sqrt{\frac{KI\left(\frac{n\pi}{a}\right)^2-\left[1-\mu\left(\frac{n\pi}{a}\right)^2\right]}{\left[m_0+m_2\left(\frac{n\pi}{a}\right)^2\right]\left[1+\mu\left(\frac{n\pi}{a}\right)^2\right]}}. \quad (35)$$

If loading is 0, we can obtain from (35) for vibration frequency:

$$\omega_n=\left(\frac{n\pi}{a}\right)^2\sqrt{\frac{KI}{\left[m_0+m_2\left(\frac{n\pi}{a}\right)^2\right]\left[1+\mu\left(\frac{n\pi}{a}\right)^2\right]}}. \quad (36)$$

Looking at the above candition (36), it can be get beams homogenious frequency of vibration:

$$\omega_n=\omega_n^R\sqrt{1+\frac{3}{20}\gamma}. \quad (37)$$

In here, ω_n^R is the vibration frequency which was obtained by J.Reddy [6] and calculated with following equation:

$$\omega_n=\left(\frac{n\pi}{a}\right)^2\sqrt{\frac{E_0I}{\left[m_0+m_2\left(\frac{n\pi}{a}\right)^2\right]\left[1+\mu\left(\frac{n\pi}{a}\right)^2\right]}}. \quad (38)$$

2. Now assume that both edges of the beam are clamped. In this case, the boundary canditions are as below:

$$x=0\ and\ x=a,\ W=0,\qquad \frac{dW}{dx}=0.$$

(22), (24) expressions while writing in this conditions and after some calculations, transendental equations are:

$$-2+2\cos\alpha a\cos h\beta a+\left(\frac{\alpha}{\beta}-\frac{\beta}{\alpha}\right)\sin\alpha a\sin h\beta a=0. \quad (39)$$

After solving (39) equation, the results of α together with (29) equation give the the natural frequency of the clamped Bernoulli beam.

For numerical calculations the following values of the parameters are utilized:

$$\rho=2300\,kg/m^3,$$
$$E=1000\,GPa,v=0.19,G=420\,GPa,$$
$$d=1.0\times10^{-9}m,I=\frac{\pi d^4}{64}=4.91\times10^{-38}m^4,$$
$$A=7.85\times10^{-19}m^2$$
$$K_s=0.877,\Omega_0=1.7\times10^{-3}m^2,$$
$$l_i=1.5\times10^{-9}m.$$

The results of calculations are presented in Table 1 and Figure 1. Here, dashed lines represent the solution of analogical homogeneous problem.

Table 1. Dimensionless frequency of vibration non-local e

e_0	γ	2	4	6	8	10
$e_0 = 0.33$	$\gamma = 0$	0.940	0.810	0.676	0.567	0.483
	$\gamma = 1$	1.008	0.868	0.725	0.608	0.518
	$\gamma = 2$	1.072	0.923	0.771	0.646	0.551
	$\gamma = -1$	0.865	0.745	0.622	0.522	0.444
	$\gamma = -2$	0.790	0.680	0.568	0.476	0.406
$e_0 = 0.67$	$\gamma = 0$	0.888	0.695	0.541	0.435	0.361
	$\gamma = 1$	0.952	0.745	0.580	0.466	0.387
	$\gamma = 2$	1.012	0.792	0.617	0.496	0.412
	$\gamma = -1$	0.817	0.639	0.498	0.400	0.332
	$\gamma = -2$	0.746	0.584	0.454	0.365	0.303
$e_0 = 1$	$\gamma = 0$	0.845	0.620	0.466	0.368	0.302
	$\gamma = 1$	0.906	0.665	0.499	0.394	0.324
	$\gamma = 2$	0.963	0.707	0.531	0.420	0.344
	$\gamma = -1$	0.777	0.570	0.429	0.339	0.278
	$\gamma = -2$	0.710	0.521	0.391	0.304	0.254

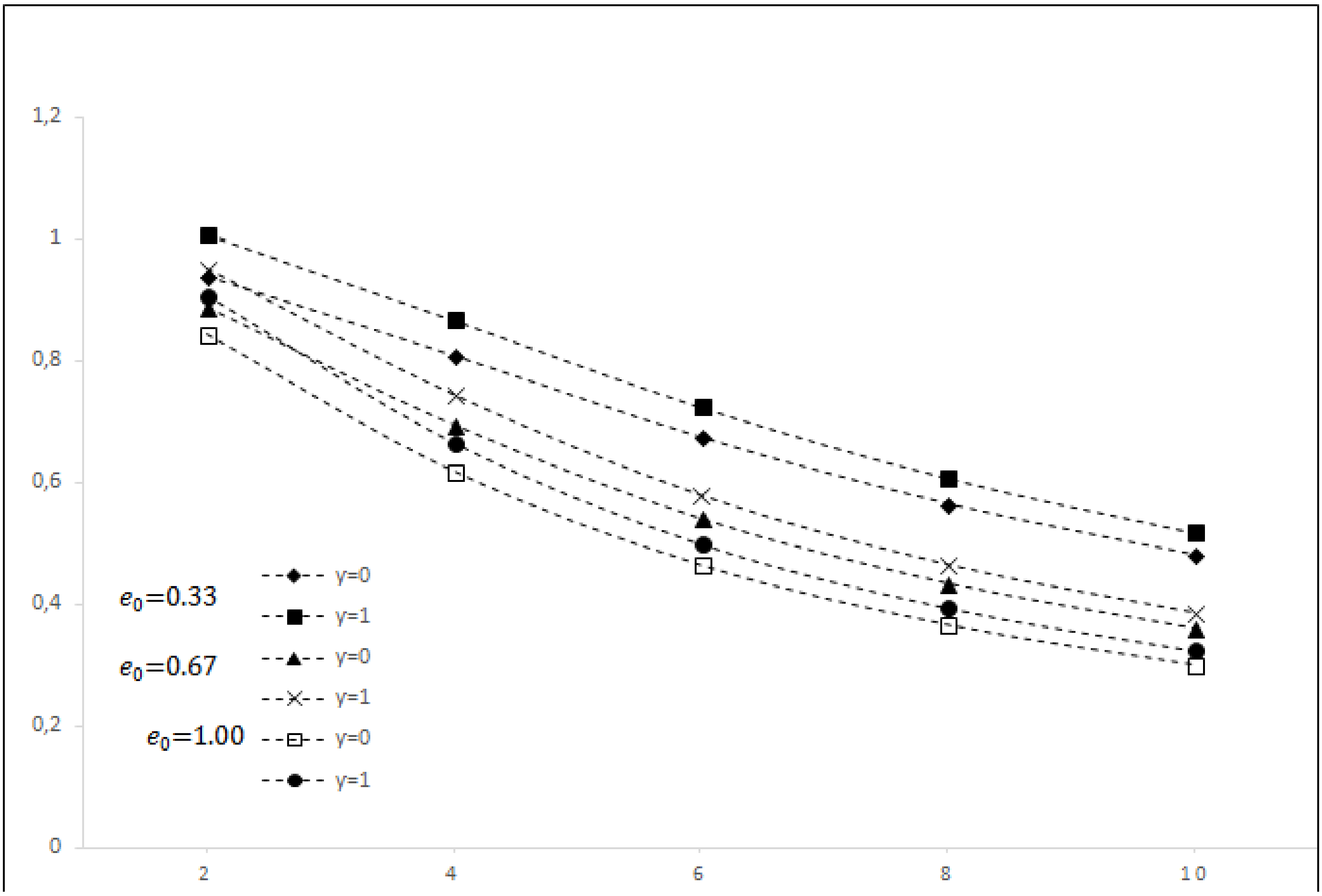

Fig 1. Dimensionless vibration equation from non-local theory (e_0) and homogeneous parameters (γ) dependence. Calculations analysis illustrate that consideration of homogeneousness could influence on the results

References:

1. Lomakin V.A. Teoriya upruqosti neodnorodnix tel. M., izd – vo MQU 1978, 245p.
2. Volmir A.S. Ustoychivost deformiruemix sistem. M., Nauka, 1967, 984 p.
3. Alfutov N.A., Einovev P.A., Papov B.G, Rascheti mnoqosloynix plastin I obolochek iz kompozichionnix materialov. M., Mashinostroenie, 1984, 264 p.
4. Isayev F.G., Radjabov V.G., The Stability of non-homogeneous nan0-micro elements based on nonlocal elasticity theory eringen Buletin of NTU “KhPI”. Series Mechanical-technological system and complexes. Kharkov NTU “KhPI”, 2015-N52 (1161) p.5-8
5. Reddy, J.N. Nonlocal theories for bending, buckling and vibration of beams. İnternational Journal of Engineering Science 2007,v.45: 288- 307
6. Reddy, J. N., Pang, S. D. Nonlocal continuum theories of beams for the analysis of carbon nanotubes. Journal of Applied Physics, *2008*,103(2): 023511.
7. Naderi A.,Saidi R.Nonlocal postbuckling analysis of graphene shects in a nonlinear polymer medium.İnternational Journal of Engineering Science.2014,v.81,pp.49-65.
8. Rahman O.,Pedram O.Analysis and modeling the size effect on vibration of functionally graded nanobeams based on nonlocal Timoshenko beam theory. İnternational Journal of Engineering Science.2014,v.77,pp.55-70.
9. AshrafiM.Zenkour, AhmedE.Abouelregal.Vibration of FG nanobeams induced by sinusoidal pulse-heating vian a nonlocal thermoelastic model. JournalActa Mechanica. 2014,v.225,N12,pp.3409-3421.
10. KeivanKiani.Axial buckling analysis of vertically aligned ensembles of single-walled carbon nanotubes using nonlocal discrete and continuous models. Journal Acta Mechanica.2014,v.225,N12,pp.3569-3589.
11. Reddy J.N.,Sami El-Borgi.Eringens nonlocal theories of beams accounting for moderate rotations. İnternational Journal of Engineering Science.2014,v.82,pp.159-177.
12. GhorbanpourArani A.,DashtiP.,Amir S.,YousefiM.Nonlinear vibration of conplednano and microstrusturesconvenying fluid based on Timoshenko beam model under two dimensional magnetic field. Journal Acta Mechanica.2015,v.226,N8,pp.1737-1756.
13. Dai H.I.,Wang L.,AbdelkefiA.,NiQ.On nonlinear behavior an buckling of fluid-transporting nanotubes. İnternational Journal of Engineering Science.2015,v.87,pp.13-22.
14. Amir Mehdi Dehrouyen-Semnami, MohammadDehrouyen, MostafaTorabi-Kafshgari, Mansour Nikkhah-Bahrami. Adamped sandwich beam model based on symmetric-deviatory couple stress theory. İnternational Journal of Engineering Science.2015,v.92,pp.83-94.
15. Li Li, Yu Jin Hu. Buckling analysis of size-dependent nonlinear beams based on a nonlocal strain gradient theory. International Journal of Engineering Science. 2015, v.97, pp.84-94.
16. M.Şimşek, M.Aydın, H.H.Yurtcu, J.N.Reddy. Size-dependent vibration of a microplate under the action of a moving load based on the modified couple stress theory. Acta Mechanica. 2015, v226, issue 11, pp.3807-3822.
17. Jinseok Kim, J.N.Reddy. A general third-order theory of functionally graded plates with modified couple stress effect and the von Karman nonlinearity: theory and finite element analysis. Acta Mechanica. 2015, v.226, issue 9, pp.2973-2998.
18. Paul R.Heyliger. Elasticity-based free vibration of anisotropic thin-walled beams. Journal of Thin-Walled Structures. 2015, v.95, pp.73-87.
19. Younghoon Song, Seungwan Kim, Ilwook Park, Usik Lee. Dynamics of two-layer smart composite Timoshenko beams: Frequency domain spectral element analysis. Journal of Thin-Walled Structures. 2015, v.89, pp.84-92.

Proceedings of the International Symposium of Mechanism and Machine Science, 2017
AzC IFToMM – Azerbaijan Technical University
11-14 September 2017, Baku, Azerbaijan

Experimental study of characteristics of microwave devices transition from rectangular waveguide to the megaphone

Islamov Islam Jamal oglu
Azerbaijan Technical University
E-mail: icislamov@mail.ru

Abstract
Reflection coefficient, transmission coefficient and orientation diagram of E -sector transition antenna from rectangular waveguide to the megaphone are defined as experimental. H_{10} type is determined as the main type in rectangular waveguide transmitting electromagnetic waves. The main parameters of the rectangular waveguide measuring $40\times 20mm$ are calculated by methods of Galerkin and Rits. Theoretical and experimental results have been compared and the error between them have been determined as satisfactory.
Keywords: reflection coefficient, transmission coefficient, orientation diagram, rectangular waveguide, electromagnetic waves, megaphone.

1. INTRODUCTION

Characteristics of the antenna system, also from rectangular waveguide to the megaphone need to improve for increasing information density transmitting radio channels. We can add reflection coefficient Q, transmission coefficient P and orientation diagram to the characteristics from rectangular waveguide to the megaphone. Thus, the transmission rate P determines orientation diagram and the form of side petals and its width. The reflection coefficient Q, determines the characteristic of the propagation regime of electromagnetic wave transmitting to antenna device from transceiver device [1-8].

We have to ensure escaping wave in the antenna-feeder tract to achieve antenna in maximum power transmitting transceiver device in the real practice. Therefore the obligation of issue of reducing of reflection coefficient Q, along tract appears. At the same time, number of side petals of orientation diagram must be minimum to create microwave communication in transmitter-receiver system for equal propagation of parabolic antenna. This, in turn, is achieved at the expense of reducing of the transmission coefficient P and alignment of front phase of electromagnetic wave [9-16].

As we see, at the same time the fulfillment of these conditions are complicated issue [17-20]. Therefore, the minimizing of reflection coefficient Q and transmission coefficient P can be carried out by methods of Galerkin and Rits. Transition from rectangular waveguide to the megaphone is investigated emitting microwave electromagnetic waves in this publication in order to minimize reflection coefficient Q and transmission coefficient P.

2. EXPERIMENTAL STUDY

In figure 1 space model of rectangular waveguide working in wave H_{10}, but in figure 2 the consolidation scheme to megaphone is shown. This rectangular waveguide works in frequency range $4,9\div 7,05GHz$. Its cross-sectional dimensions are $40\times 20mm$ and made of brass. Geometric length of microwave rectangular waveguide is $L=105$ mm.

Figure 1. Space model of rectangular waveguide working in wave H_{10}

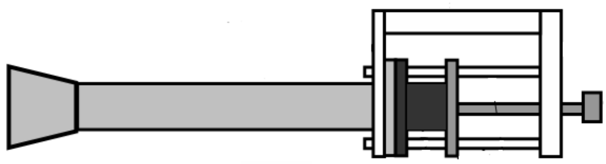

Figure 2. Consolidation scheme to megaphone of rectangular waveguide working in wave H_{10}

Experimental study of characteristics of microwave devices transition from rectangular waveguide to the megaphone is associated with determination of the orientation diagram and stagnant wave coefficient Q_{dd}.

The study has been carried out the price $\lambda = 3cm$ of wavelength and measurements have been fulfilled with waveguide measure line. The measurement of orientation diagram has been carried out with the help of laboratory complex. Block-diagram of device determining stagnant wave coefficient Q_{dd} has been shown in figure 3.

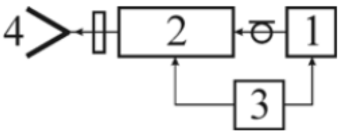

Figure 3. Block-diagram of device determining stagnant wave coefficient Q_{dd}:

1-ГС-11-type microwave signal generator; 2- $P1-28$ type waveguide measuring line; 3-power supply; 4-megaphone radiation

The measurement of following parameters has been carried out:
- stagnant wave coefficient Q_{dd} in microwave rectangular waveguide working in H_{10} type wave;
- orientation diagram.

Reflection coefficient Q is determined with the following formula:

$$Q = \frac{Q_{dd} - 1}{Q_{dd} + 1}. \tag{1}$$

Measurements have been carried out with the following methods. Megaphone radiation has been fixed to the output of measuring line of $P1-28$ type waveguide. Input of $P1-28$ type measuring line from generator is provided with $\lambda = 3cm$ length microwave signal. Millivoltmeter is connected to a measuring line via Hann diode. $\alpha_{\max}$ – maximum and $\alpha_{\min}$ – minimum prices are determined with the help of this millivoltmeter. Then, according to the following formula stagnant wave coefficient Q_{dd} is set for the voltage:

$$Q_{dd} = \sqrt{\frac{\alpha_{\max}}{\alpha_{\min}}}. \tag{2}$$

Then, according to formula (1), reflection coefficient Q is set. The experimental determination of orientation diagram has been carried out with the help of specially designed laboratory facility which the sizes are $4x6m$ in a closed room condition. Structural scheme of the measurement device in figure 4, a space model is shown in figure 5.

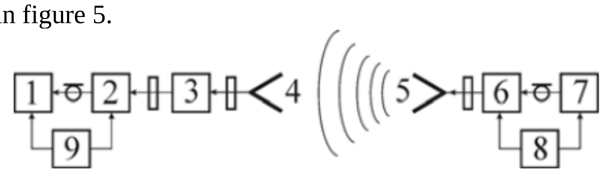

Figure 4. Block diagram of the experimental determination of orientation diagram:
1-indicator device; 2-receiver block; 3-adjustable attenuator; 4- receiver megaphone; 5- transmitter megaphone; 6-generator block; 7-modulated block; 8, 9-power supply

Figure 5. Space model of the experimental determination of orientation diagram

Measurement was carried out with the following methods. Microwave klystron generator 6 has been connected to the body together megaphone radiation 5. Receiver megaphone has been built at least 3 meters away (remote zone) from the transmitter. The transmitter and receiver megaphones have been built along an axis. Signal is given to millivoltmeter device of indicator block from the outlet of receiver megaphone. $U(mV)$ voltage is measured in output of the receiver device by changing the angle θ 1^0 discrete at the vertical plane. Then according to the intensity and strength of the field, normalized orientation diagrams are. The width of orientation diagram are determined with levels 0,707 and 0,5 of intensity and power by graphical method. According to the intensity of electromagnetic field, normalized orientation diagrams have been shown via curve 1 in figure 6.

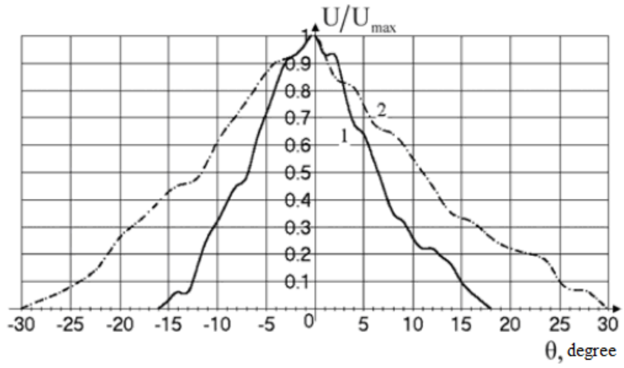

Figure 6. According to the intensity of field, orientation diagram of megaphone radiation:
1-orientation diagram at the vertical plane; 2-orientation diagram at the horizontal plane

Measurements have been carried out in relation to the axis of megaphone device at interval from -90^0 to $+90^0$ of θ.

The schemes for the measurement of transmission and reflection coefficients modules in figure 7 and figure 8, the curves obtained from the computer these parameters are shown in figure 9.

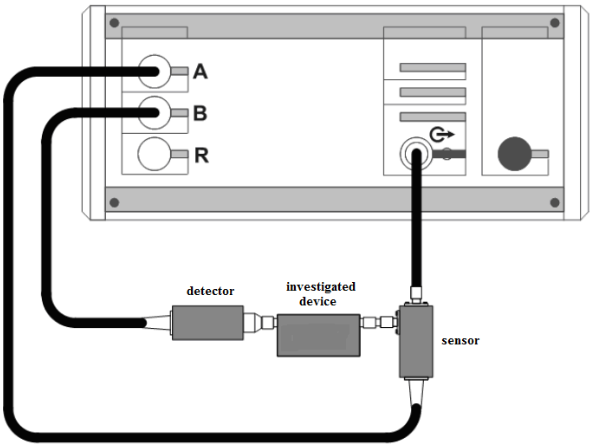

Figure 7. Scheme of measurement of transmission and reflection coefficients modules

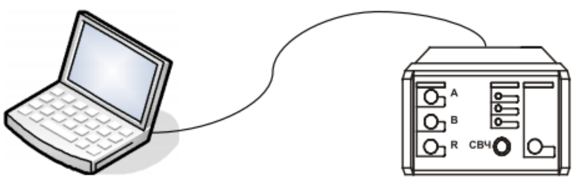

Figure 8. Connection of scheme of measurement of transmission and reflection coefficients modules to the computer

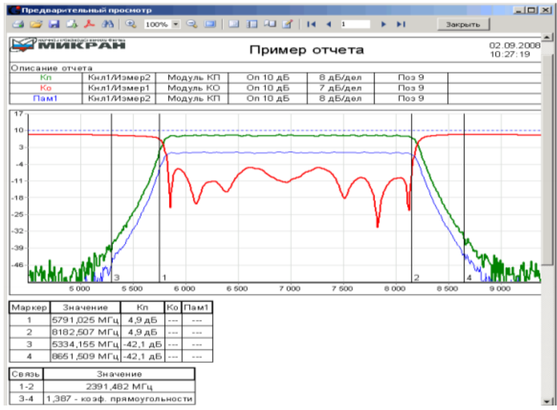

Figure 9. Results of modules of transmission and reflection coefficients obtained from computer

3. RESULTS AND DISCUSSION

According to the wavelength of $\lambda = 3cm$, standing wave ratio is $Q_{dd} = 1,42$, reflection coefficient is $Q = 0,17$. Standing wave ratio of investigated megaphone radiation is Q_{dd} =1,96, but the reflection coefficient is $Q = 0,32$. The price of standing wave ratio Q_{dd} of megaphone radiation is so great that his performance is due to the geometric dimensions. For this reason, smoothing of this part of megaphone has been fulfilled and following results have been obtained for standing wave ratio $Q_{dd} = 1,32$, $Q = 0,14$. According to the intensity of electromagnetic field, width of orientation diagram of megaphone radiation is $2\theta = 8,8^0$ at the level of 0,707.

4. CONCLUSION

As a result of study of the megaphone radiation, reflection coefficient Q and transmission coefficient P have been significantly improved. It also reduced the size of investigated rectangular waveguide and geometrical dimensions of megaphone devices. İnvestigated megaphone radiations can be used in ship's antenna complexes, as well as aviation and astronautics, radiolocation, radionavigation, television systems. Minimizing of reflection coefficient Q and transmission coefficient P is a new scientific result. The practical importance of the article is correlated with being created of broadband mirror parabolic antenna which manage orientation diagram and performance coefficient.

References

[1]. I.J.Islamov. Transaction of Azerbaijan Academy of Sciences, Series of Physical-mathematical and Technical sciences, Physics and Astronomy, XXIV №2 (2004) 48-57.

[2]. I.J.Islamov. Transaction of Azerbaijan Academy of Sciences, Series of Physical-mathematical and Technical sciences, Physics and Astronomy, XXIII №2 (2003) 205-214.

[3].E.G.Ismibayli, I.J.Islamov, Y.G.Gaziyev. Calculation Of The Electromagnetic Field Of The Microwave Of Devices With Use Of Method FDTD And Integral Kirchhoff. International Journal of Engineering Innovation and Research (IJEIR), Volume 5, Issue 1, (2016) 103-106.

[4]. E.G.Ismibayli, I.J.Islamov, Y.G.Gaziyev. Modeling Of Electromagnetic Fields Of Microwave Devices On The Basis Of Matlab Program. International Journal of Innovative Science, Engineering and Technology (IJISET), Volume 3, Issue 2, (2016) 61-63.

[5]. E.G.Ismibayli, I.J.Islamov, Y.G.Gaziyev. An Optimal Control Of An Electromagnetic Field In High-Powered Microwave Devices. International Journal of Trend in Research and Development (IJTRD), Volume 3(1), (2016) 246-249.

[6]. E.G.Ismibayli, I.J.Islamov, Y.G.Gaziyev. Modeling of Anisotropic Rectangular Waveguide Partially Embedded in an Anisotropic Substrate. Journal of Multidisciplinary Engineering Science and Technology (JMEST). Volume 2, Issue 2, (2015) 153-157.

[7]. Islam J. Islamov. Application of finite elements method by calculating electric field of hollow rectangular waveguide. *IASTED-2005*, Canada, Calgary, (2005) 26-32.

[8]. Islam J. Islamov. Numerical method for analysis of electromagnetic field of microwave waveguide. *International Conference on Antenna Theory and Techniques.* September 9-12, Sevastopol, Ukraine, (2003) 45-50.

[9]. E.G.Ismibeyli, I.D.Islamov. The Analysis of Magnetic Devices In Frequency Directors of Teledynamometring Systems. *The Third International Scientific Practical Conference "Khazarneftgasyatag-98"*, November, Baku, (1998) 10-13.

[10]. De Moerloose Jan, Dawson Trevor W., Stuchly Maria A. Application of the finite difference time domain algorithm to quasi-static field analysis. Radio Sci.-32, №2 (1997) 329-341.

[11]. M.Koshiba, M.Okada, M.Suzuki. Numerical analysis of two-dimensional piezoelectric waveguides for surface acoustic waves by finite-element method. “Electron. Lett.”, №17 (1981) 609-611.

[12]. Y.E.Elmoazzen, Shafai Lotfollah. Numerical solution of coupling between two collinear parallel-plate waveguides. *IEEE Trans. Microwave Theory and Techn.*, 23(11), (1975) 871-876.

[13]. T.P.Barton. Electromagnetic field calculations for irregularly shaped, layered cylindrical particles with focused illumination. *Appl. Opt.*, 36, (1997) 1312-1319.

[14] V.Iomota, P.Alotto. Magnetic field computation in media with hysteresis. *Rev. roum. sci. techn. Ser. Electrotechn. et energ*. 41(3), (1996) 291-296.

[15]. K.Dikshitulu Kalluri. Elektromaqnetic Waves. Materials and computation with Matlab. *CRS Press London-New York*, (2012) 835.

[16]. N.O.Matthew Sadiku. Numerical Techniques in Electromagnetic with Matlab. *CRS Press London-New York*, (2012) 707.

[17]. Munteanu Irina. A method for numerically solving Maxwell's equations in three dimension. *Politehn. Univ. Bucharest.* 56(1-4), (1994) 221- 238.

[18]. Miller Edmund K., Burke Gerald J. Low frequency computational electromagnetics for antenna analysis. *Proc. IEEE.* 80(1), (1992) 24-43.

[19]. Chen Bao Xue, Hamanaka Hiromi, Iwamura Kokya. *J. Opt. Soc. Amer.* 9(8), (1992) 1301-1305.

[20]. H.Cory, A.Novick-Cohen, D.Levy. Variational expression for propagation along a closed rectangular chiro waveguide. *Antennas and Propag.*, 143(2), (1996) 174-178.

Proceedings of the International Symposium of Mechanism and Machine Science, 2017
AzCIFToMM – Azerbaijan Technical University
11-14 September 2017, Baku, Azerbaijan

Способ уплотнения зазора штангового скважинного насоса продукцией скважины

[1]Рамиз Сейфулла оглы Гурбанов, [2]Тюркан Гейдар гызы Гурбанова
[1]Научно-исследовательский Институт «Геотехнологические проблемы нефти, газа и химии»
AZ 1010, г. Баку, ул. Д.Алиева 227; E-mail: ramiz.qurbanov@yahoo.com
[2]Азербайджанский Государственный Университет Нефти и Промышленности, AZ 1010, г.Баку, пр.Азадлыг, 20; E-mail: turkanqurbanzade@mail.ru

Аннотация

В данной работе рассматриваются вопросы по созданию уплотнительных систем в технологических оборудованиях. Также рассматривается вопрос утечки через зазор пары плунжер-цилиндр штангового скважинного насоса, в качестве уплотнительной среды используется продукция скважины. Для реализации указанной уплотнительной системы используется эффект микротрещина-жидкость. Это при определенных критических значениях раскрытости трещины приводит к изменениям реологических свойств продукции скважины и коэффициента подачи насоса.

Ключевые слова: продукция скважины, эффект микротрещина-жидкость, коэффициент подачи насоса, утечка, зазор, гидрозатвор.

Введение

Как известно одним из основных факторов, влияющих на коэффициент подачи насоса, является утечка жидкости из зазора пары плунжер–цилиндр штангового насоса [1]. С целью уменьшения утечки жидкости через зазор пары плунжер-цилиндр разработаны различные методы [2–4].

Анализ литературных данных и постановка проблемы

В литературе имеется большое количество работ, которые следует особо отметить, например, научные работы по применению уплотнительных элементов. На основе анализа литературных данных поставлена проблема возможности использования продукции скважины в качестве уплотнительной системы.

Штанговые скважинные насосы по размерам зазора пары плунжер–цилиндр, изготавливаются в трех группах:

– 20-70-микронный размер - первая группа;

–70-120-микронный размер - вторая группа;

–120-170-микронный размер относится к третьей группе.

Ограничениями, при применении указанных групп насосов в конкретных скважинах, являются следующие факторы: глубина спуска насоса, реологические параметры продукции скважины, процент обводненности, а также могут быть другие причины.

Проведенные в последние годы экспериментальные исследования воды, вязкой и аномальной нефти в трещинах с микронными размерами, показали, что механические свойства жидкостей в микротрещине существенно меняются [5–8].

В [1] указаны известные пути уменьшения утечки, а в работах [2,3,4] предложены различные неэффективные уплотнительные системы, которые не нашли широкого применения, в работах [5,6,7,8] приведены экспериментальные результаты по определению критических величин раскрытости трещины для воды, вязкой и аномальной нефти, результаты которых сравнены с данными приведенными в [9].

Изменение механических свойств жидкостей зависит от величины раскрытости трещины. Для каждой жидкости установлены определенные размеры трещин и при малых значениях раскрытости от определенного размера жидкость меняет свои механические свойства, а при больших - сохраняет их. Эти определенные размеры раскрытости трещины является критической раскрытостью для исследуемой жидкости.

В работах [6-8] получены экспериментальные результаты о движении вязкой жидкости в плоскорадиальной микротрещине [6], реологические свойства воды в каналах микротрещины [7], а также неньютоновской жидкости в микротрещине [8].

Цель и задачи исследования

Целью исследования является решение вопроса по использованию жидкостей в нефтепромысловых оборудованиях в качестве уплотнителей.

Основная часть – Результаты экспериментальных исследований и обоснование использования продукции скважины как уплотнитель

Влияние давления и растворенного в воде газа на вязкость пластовых вод очень мало. При температуре пласта в пределах 293-303 К и давлениях 0-300 МПа вязкость воды меняется в пределах 1,01-0,66 спз.

При движении воды и керосина в плоскопараллельных трещинах критические значения раскрытости $h_{кр}$ трещины для указанных жидкостей при температурах 306 и 313 К получены, соответственно, 25 и 65, 55 мкм; а для вязкой и аномальной нефти, при температурах 306, 313, 323, 333 К, соответственно, 130, 115, 100, 90 и 160, 130, 115, 105 мкм; для 0,3%-него раствора ПАА при температурах 303, 313, 323, 333 К при 90, 72, 60, 48 мкм; а для 0,15, 0,06 и 0,03%-них растворов ПАА при температуре 306 К, соответственно, 60, 50 и 42 мкм [5].

Критическое значение раскрытости трещины для воды в плоскорадиальной трещине при температурах 303 и 313 К получены, соответственно, 35 и 30 мкм, а для аномальной нефти при температуре 303К - 180 мкм [6, 7].

Критические значения раскрытости трещины для вязкой нефти получаются больше чем для воды. Причем, критические раскрытости трещины для вязкой нефти при температуре 303К составляют 110мкм, а для аномальной нефти – 180мкм. Таким образом, при величине зазора 20 мкм для насоса первой группы вода ведет себя как аномальная жидкость и утечка воды через зазор будет уменьшается. Как известно, для вязкой жидкости утечка определяется ниже следующей формулой.

$$Q = \frac{\pi D \Delta P \delta^3}{12\mu l}, \qquad (1)$$

где: D – диаметр плунжера; δ – размер зазора пары плунжер–цилиндр; ΔP – перепад давления; l – длина плунжера; μ – вязкость жидкости. На основе указанной формуле отношение δ^3/μ следует рассматривать как решающий фактор. Например, при зазоре с размером 20 мкм и температуре 293К вязкость воды получена 1,1 спз. При обычной температуре вязкость воды составляет 1сантипуаз. Значит, с учетом влияния раскрытости трещины, согласно формуле (1), потеря утечки будет меньше в 1,1 раз. С учетом начального предельного напряжения эти потери будут ещё больше.

Например, предположим, что по установленным правилам в настоящее время в скважину необходимо спускать насос первого класса с зазором 60 мкм, тогда утечка будет:

$$Q_1 = \frac{\pi D \Delta P \delta_1^3}{12\mu_1 l}$$

По предложенной методике для того чтобы, эффект «жидкость–трещина» в насосе имело место, в скважину необходимо спускать насос первого класса с зазором 20 мкм, тогда утечка будет

$$Q_2 = \frac{\pi D \Delta P \delta_2^3}{12\mu_2 l}$$

Сравним утечки при откачке воды $Q_1/Q_2 = \left(\frac{\delta_1}{\delta_2}\right)^3 \frac{\mu_2}{\mu_1} \approx 30$ т.е по предложенной методике утечка уменьшится в 30 раз.

Таким образом, когда значение зазора пары плунжер–цилиндр будет для жидкости ниже критических значений раскрытости, то продукция скважины станет уплотнительной системой. Таким образом, использование эффекта «жидкость-трещина», с целью предотвращения утечки жидкости при насосном способе эксплуатации, продукцию скважины можно использовать в качестве уплотнительной системы.

Целью данной работы является решение вопроса по обеспечению использования в оборудованиях движущейся жидкости в качестве уплотнительной системы.

До сих пор глубина спуска насоса определялась с учетом величины зазора пары плунжер-цилиндр, а с учетом эффекта «жидкость-трещина» в настоящее время ограничения, связанные с глубиной спуска насоса, могут не учитываться. В высоко обводненных скважинах не зависимо от глубины спуска будет более эффективным использование первой группы насосов (δ=20-70 мкм). В скважинах, добывающих вязкую нефть можно использовать насосы, имеющие зазор δ=70 мкм, а для скважины с аномальной нефтью – менее δ=180 мкм, что обеспечит существование эффекта «жидкость-трещина».

В настоящее время эффект «жидкость-трещина» дает возможность значительно увеличить глубину спуска насосов, производимых в республике. Такой подход дает возможность увеличения отбора нефти из скважин, а также уменьшения количества насосов в каждой скважине, используемых в течении одного года.

Первоначальным подходом для обеспечения производства и использования насосов должно являться исследование насосов с водой. Значит, в высоко обводнённых скважинах при наличии зазора пары плунжер-цилиндр в 25-35 мкм, в скважинах с вязкой нефтью в 35-100 мкм, а в скважинах с аномальной нефтью в 100-180 мкм, в процессе эксплуатации добываемая жидкость будет уплотнением для зазора пары плунжер-цилиндр.

Достижения такого подхода для увеличения объёма производства насосов первой группы должны считаться более эффективными. В процессе эксплуатации, если на внутренней поверхности цилиндра насоса имеется защитный слой азота толщиной в 550 мкм, а износ в произвольном сечении цилиндра будет более 50 мкм, то отработанные насосы могут подлежать капитальному ремонту 3-4 раза [9,10].

Капитально–отремонтированные насосы с уплотнением системы «зазор пары плунжер-цилиндр-продукция скважины» для конкретных скважин должны обеспечивать самоуплотнение.

Указанные критические значения раскрытости трещин должны создавать эффект «жидкость-трещина», т.е. продукция скважины может быть в насосе уплотнительной системой. Глубина спуска насоса и возможность образования эффекта «жидкость-трещина» в насосах будут факторами выбора насосов для скважин и проведения ниже следующих мероприятий:

– В чисто нефтедобывающих и мало обводненных скважинах независимо от глубины спуска использовать первые и вторые группы насосов.

– Для конкретной скважины при капитальном ремонте необходимо заказать размеры зазора, обеспечивающие эффект «жидкость-микротрещина».

– В целях обеспечения эффекта «жидкость-трещина» в затрубное пространство скважины регулярно подливать водно-полимерный раствор. В высоко обводненных скважинах независимо от глубины спуска использовать насосы первой группы.

– В относительно мало обводненных скважинах использовать третью группу насосов, подлежащих капитальному ремонту и имеющие соответственные зазоры.

– При добыче аномальной нефти использовать третью группу насосов.

Выводы

1. Обоснование в качестве уплотнительной системы в насосах использовать дебиты скважины.
2. С помощью микротрещины на основе изменения реологических свойств «зазор пары плунжер-цилиндр-продукция скважины» определены рациональные пределы уплотнения.

Литература

[1]. Амелин И.Д., Андчиасов Р.С., Гиматудинов Ш.К., Каратеев Ю.П, Левыкин Е.В., Лутошкин Г.С. Эксплуатация и технология разработки нефтяных и газовых месторождении. Москва, «Недра», 1978, 353 с.
[2]. Мирзаджанзаде А.Х., Гурбанов Р.С. и др. «Теория и практика применения глубинных насосов с гидравлическим затвором». Москва, «Недра» 1986, 210с.
[3]. Амиров А.Д., Хасанов А.М., Гурбанов Р.С. Рабочая жидкость гидрозатвора. Авторское свидетельство №32566,1971.
[4]. Костыченко Е.В., Сулейманов Т.С., Гурбанов Р.С. Скважинный штанговый насос.а. с.№1701981, 1991.
[5]. Гурбанов Р.С., Мамедова М.А., Мириев Г.М. Методическое руководство по определению параметров пластовых систем и эффективности применения полимерного воздействия в трещинных коллекторах. ─ Баку: АзНИПИнефть, 1986. ─35с.
[6]. Мамедова М.А. Исследование движения несжимаемой вязкой жидкости в плоскорадиальной микротрещине. Азербайджанское нефтяное хозяйство. 2007, №11, 1 2, стр.25 ─28.
[7]. Гурбанов Р.С., Мамедова М.А. Реологические исследование воды в каналах микронной толщины. АНХ, 03, 2015, стр.23-28.
[8]. Мамедова М.А. Экспериментальное исследование движения неньютоновских жидкостей в плоскорадиальной микротрещине. Научное обозрение. 2010, №5, стр.51─57.
[9]. Оркин К.Г., Кучинский П.К. Физика нефтяного пласте. Гостоптехиздат. 1955, 299 с.
[10]. Набиев Н.А. Разработка и исследования технических и технологических факторов, обеспечивающих повышение эксплуатационных показателей скважинных штанговых насосов, Диссертационная работа, 2010, 189 с.

Proceedings of the International Symposium of Mechanism and Machine Science, 2017
AzCIFToMM – Azerbaijan Technical University
11-14 September 2017, Baku, Azerbaijan

Гидродинамика жидкостей в микротрещинных каналах

Рамиз Сейфулла оглы Гурбанов[1], Малейка Агамоглан кызы Мамедова[2], Алиабас Алипаша оглы Гаджиев[3]
[1] НИИ «Геотехнологические Проблемы Нефти, Газа и Химии». г. Баку, AZ 1010 пр. Азадлыг. 20, E-mail: ramiz.qurbanov@yahoo.com
[2] Азербайджанский Государственный Университет Нефти и Промышленности, г.Баку, AZ 1010, пр. Азадлыг, 20. E-mail: mamedova-1944@mail.ru
[3] SOCAR, НИПИ «Нефтгаз» Азербайджан, AZ1012, г. Баку, проспект Зардаби, 88А. E-mail:aliabas.haciyev@socar.az

Abstract

There are numerous investigations of the fluids flow in the small-sized channels in the reference. It is shown that the experimental results of hydraulic resistances in these channels are more than the estimated ones according to theoretical formulas. There are given supposed different explanations without quantitative estimation. The numerous experimental results in the reliable setting are given in this work.

Firstly, the experimental-estimated methodology for “microcrack-fluid” system has been proposed and realized for the quantitative estimation of the hydraulic resistances. This approach allows to conduct hydrodynamic engineering evaluations for fluid flow in the cracked-porous medium, for lubrication in the systems of mechanical engineering, instrument engineering and also for solutions of the sealing problems in different branches of industry and medicine.

Ключевые слова: раскрытость, гидравлическое сопротивление, аномальная нефть, эффект «микротрещина – жидкость».

Введение

В настоящее время механические свойства жидкостей исследуется в трубах различного размера. Имеются исследования, в которых утверждается, что в трубах малых размеров сопротивление движению жидкости увеличивается по сравнению с расчетными формулами, и это явление объясняется с различными качественными факторами.

В настоящее время накоплен значительный фактический материал по изучению движения ньютоновких жидкостей в щелях, проведены многочисленные экспериментальные и теоретические исследования [1–4]. Но нет единого мнения о проявлении аномального поведения ньютоновских жидкостей и усиления реологических свойств неньютоновских систем в микротрещинах. Учитывая эти положения в области механики жидкости нами были проведены эксперименты в специально разработанной установке с различными жидкостями: водой, вязкой и аномальной нефтью [5, 6].

2. Экспериментальная установка и результаты исследования

В работе представлена методика определения параметров канальных пористых систем, а именно: величины раскрытости трещины, коэффициента пропускной способности среды и реологии жидкости в осложненных условиях. Экспериментальные исследования проведены на установках, позволяющих создать плоскопараллельные и плоскорадиальные трещины различной раскрытости h. Упуская, из-за простоты, описание плоскопараллельной установки, подробно остановимся на описании особенностей плоскорадиальной установки. Конструкция трещинной модели, имитирующая плоскорадиальное движение жидкости в недеформируемой среде, представлена на рис. 1. Кровлей 6 и подошвой 2 трещины являются плиты диаметром 168 мм, зажатые между фланцами 1 и 7. Под действием перепада давления исследуемая жидкость через штуцер 4 поступает во втулку 5, герметизирующую резиновыми уплотнителями 3 кольцевую полость, затем в трещину между плитами и далее в систему для замера протекающей жидкости в штуцер 8. С целью обеспечения недеформируемости трещины плиты изготовлены из стали 40Х, которые после термообработки токами высокой частоты имеют поверхностную твердость 40–50 единиц по Роквеллу.

Внутренняя поверхность плит обработана и отшлифована с точностью, соответствующей 10-ому классу. С целью получения трещины, заданной раскрытости были использованы несмачиваемые прокладки размерами 5 × 7 мм, расположенные под углом 120° относительно друг друга. Толщина прокладок выбиралась в зависимости от величины, требуемой раскрытости трещины.

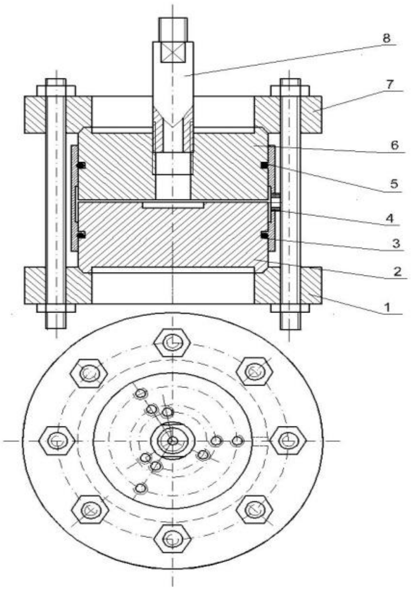

Рис.1. Модель плоскорадиальной трещины

Для контроля деформации трещины использовался индикатор часового типа, установленный на верхней плите модели. С целью контроля распределения давления по длине, т. е. по радиусу верхней плиты, кроме отверстий в центре и в контуре, были просверлены еще два отверстия. Отметим, что длина трещины L равна 84 мм. Радиусы окружностей, на которых под углом 120° относительно друг друга расположены отверстия, равняются 34 и 57 мм. Кроме того, вблизи этих отверстий на расстояниях 43 мм от центра трещины было расположено еще по одному отверстию.

Установка была проверена на герметичность при давлении 50 МПа для всех размеров трещины и проверены сохранность трещины во всех точках верхней плиты, где установлены индикаторы часового типа. В экспериментальных исследованиях максимальные давление было меньше 2 МПа.

Экспериментальные исследования в плоскорадиальных щелях проводились в двух сериях: моделировалось движение жидкости – первая серия от центра плоскорадиальной щели её контуру, а вторая серия от контура щели к центру. В обеих сериях эксперименты проводились на установившем режиме движения жидкости.

Опыты проводились при изотермических условиях. Все пути движения исследуемой жидкости в модели находилась в термованне. Постоянство температуры поддерживалось ультратермостатом, снабженным контактным термометром, установленным непосредственно в термованне.

В процессе опытов изменение толщины щели не наблюдалось, т.е. было устранено мнение об образовании жидкостных слоев на стенках канала.

Для исключения различных эффектов насыщение щели производились исследуемой жидкостью под небольшим давлением и одновременно вакуумированием.

В процессе опытов создавались различные перепады давления на трещинной модели, после достижения установившегося режима фильтрации, замерялись соответствующие объемные расходы воды Q. По полученным данным исследовались гидродинамические особенности различных жидкостей. В экспериментальных исследованиях для создания различных перепадов давления использовались образцовые манометры, с погрешностью δ= (0,2÷0,35) %. Массовый расход жидкости при различных перепадах давления взвешен на электронных весах с точностью 0,001мг. При определении полной абсолютной погрешности для градиента скорости и предельного напряжения сдвига с толщиной трещины 10 ÷ 240 мкм составляют соответственно (2÷3) % и (0,2÷1,2) %.

3. Результаты экспериментальных исследований, их обработка и обобщение.

Результаты опытов обрабатывались в координатах $\gamma - \tau$, где $\gamma = \dfrac{Q}{4\pi r h^2}$ – средний градиент скорости и $\tau = \dfrac{\Delta P h}{L}$ - касательное напряжение сдвига.

При экспериментальных исследованиях воды, вязкой и неньютоновской нефти в микротрещинах выявлен новый определяющий параметр – впервые выявленный эффект,— «микротрещина – жидкость», без учета которого невозможно осуществление различных технологических процессов нефтяной промышленности, машиностроения, приборостроения, медицины и. т. д..

При движении вязкой–однопараметрической жидкости в каналах с раскрытостью меньше критической $h<h_{кр}$, вязкая жидкость становится аномальной, т.е. двухпараметрической, а при движении в каналах $h>h_{кр}$, то однопараметрическая жидкость остается однопараметрической. Для аномальных жидкостей в каналах $h<h_{кр}$, реологические свойства жидкости усиливается, а в каналах $h>h_{кр}$ остаются без изменения.

В результате экспериментального исследования движения жидкости в микротрещине установлено что, при величинах раскрытости трещины ниже 30 и 35 мкм соответственно при температурах 293 и 303 *К*, вода ведет себя как неньютоновская жидкость. Такие свойства установлены для воды и ньютоновских жидкостей. Такая раскрытость названа критической раскрытостью. Для различных жидкостей установлены критические размеры трещины.

В случае движения неньютоновской нефти в плоских и плоскорадиальных трещинах с увеличением раскрытости предельное напряжение сдвига и структурная вязкость нефти уменьшаются до определенного значения раскрытости трещины. При значениях раскрытости 180мкм при температуре 303 К предельное напряжение сдвига и структурная вязкость не зависят от h и остаются постоянными.

На рис.2 и 3 представлены зависимости среднего градиента скорости – γ от касательного напряжения сдвига – τ в различных значениях величины раскрытости трещины при движении воды и аномальной нефти в плоскорадиальных микротрещинах при температуре 303 К.

Как видно из рис.2 и рис. 3 при $h \geq h_{кр}$ для различных величин раскрытости трещины все точки зависимостей $\gamma=\gamma(\tau)$ соответственно для воды (прямые 4 и 5) и аномальной нефти (прямые 4-6) укладываются на одной прямой как для вязкой, так и аномальной жидкости. $\gamma=\gamma(\tau)$. Это доказывает достоверность установленных критических значении раскрытости трещины.

Таким образом, впервые, на основе экспериментальных исследований, нами была установлена критическая величина раскрытости – $h_{кр}$, т.е., найдено, что при $h \geq h_{кр}$ изменения в реологических свойствах жидкости практически отсутствуют. При движении вязких жидкостей в трещине при $h<h_{кр}$ проявляются аномальные свойства, а при движении аномальных жидкостей усиливаются реологические параметры, а при $h>h_{кр}$ указанные эффекты исчезают.

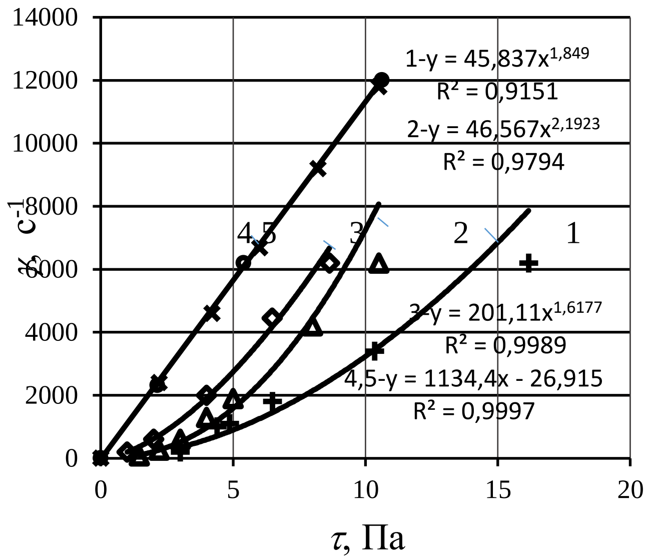

Рис. 2. Зависимость γ от τ при движении воды в плоскорадиальных микротрещинах, при значениях раскрытости, мкм:10 (кривая 1), 15 (кривая 2), 20 (кривая 3), 30 (прямая 4) и 35(прямая 5), T=303 *K*

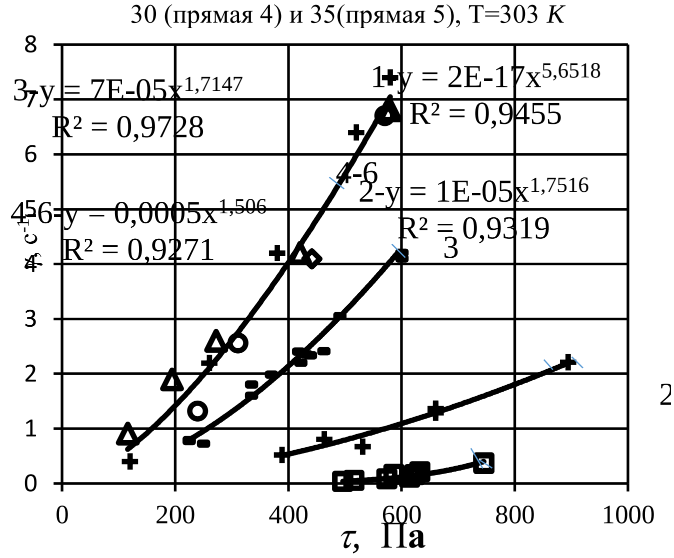

Рис. 3. Зависимость γ от τ при движении неньютоновской нефти в плоскорадиальных трещинах при значениях раскрытости, мкм: 90 (кривая 1), 120 (кривая 2), 160 (кривая 3), 180 (кривая 4), 220 (кривая 5) и 240 (кривая 6), T=303 *K*

Разработанный нами подход позволяет вести гидродинамические инженерные расчеты по движению жидкости в трещинно-пористой среде, по смазке в системах машиностроения, приборостроения, а также для решения проблем герметизации в различных отраслях промышленности и медицины.

4. Выводы

На основе экспериментальных исследований и теоретических обобщений результатов о движении различных жидкостей в трещинных каналах «разработаны основы механики жидкостей в сверхмало проницаемых средах и микротрещинных каналах»:

1. При движении жидкости в щели с раскрытостью $h \leq h_{kp}$ в системе «трещина-жидкость» проявляются неньютоновские свойства, для вязкой жидкости, и для аномальной жидкости усиливаются реологические свойства, а при $h > h_{kp}$ указанные микротрещинные эффекты отсутствуют.

2. Полученный микротрещинный эффект для однородной жидкости, очищенной от воздуха или газа, является как дополнительное сопротивление подобно эффекту Жамена и может при течения двух и трехфазных жидкостей в системах микротрещин более усилить влияния Жамена.

3. Установленные критические значения раскрытости трещины составляют для воды 35 и 30 мкм при температурах 293 и 303 K и вязкой и аномальной нефти при температуре 303 K соответственно 130 и 180мкм.

В гидродинамике жидкостей для устранения влияния степени раскрытости трещин, т.е. эффекта «трещина – жидкость» целесообразно оказывать воздействие на систему «микротрещина –жидкость» мощными ультразвуковыми, гидродинамическими, акустическими и другими волнами, что требует изготовить специальные установки.

Литература

[1]. Мархасин И.Л. Физико-химическая механика нефтяного пласта. Москва: Недра, 1977.
[2]. Ромм Е.С. Фильтрационные свойства трещиноватых горных пород. Москва: Недра, 1966.
[3]. Куштанова Г.Г. Нестационарная фильтрация жидкости в трещиновато-пористом пласте по неравновесному закону фильтрации //Изв. ВУЗов Нефть и газ.-2008.- № 5.-С.25-30.
[4]. Свалов А.М. Капиллярные эффекты в трещиноватых породах // Нефтяное хозяйство. - 2011. -N 1. - С. 59-63.
[5]. Мамедова М.А., Гурбанов Р.С. Исследование реологии жидкостей в трещинных и поровых каналах и определение их раскрытости // Инженерно-физический журнал, 2015, том 88, № 4, с. 790-799. Mamedova M.A., Gurbanov R.S. Investigation of the Rheology of Fluids in Fracture and Pore Channels and Determination of Their Opening. Journal of Engineering Physics and Thermophysics: Volume 88, Issue 4 (2015), Page 815-824.
[6]. Gurbanov R.S., Mammadova M.A. Rheological peculiarities of fluids flow in microcracked channels // Mechanika 2015,Vol 21, No 1, pp.34-39.

Modernization actuator zephyr finisher machine

Azizaga AZIZOV
Azerbaijan Technical University,
Baku - 1074, ave. Javid 25, Azerbaijan
E- mail: azizagaazizov@rambler.ru

Abstract
Forming casting marshmallow (marshmallow) in contemporary machines of the brand K-33 is carried out by the actuators comprising a cam-lever mechanism. The paper attempts to modernize these mechanisms, ie replacing them (the plunger mechanism and spool) on purely linkages, which improves machine performance.

Keywords: Executive mechanisms, zephyr, purely linkages.

1. Introduction

Zephyr is a type of casting pastes and different shape and lush texture. The technological process of preparation of marshmallow includes the use of apple puree with a solids content of about 15% with the addition of up to 8% apple-sugar mixture. Due to the large number of protein and prolonged knocking (22 ÷ 25 min), the mixture is a more lush. The adhesive syrup for zephyr mass is boiled to a large density than Pastila weight - up to a solids content of 84 ÷ 85%. Ready-agar syrup with a temperature of 90 ÷ 95 OC introduced into hit by an apple-sugar mixture in the ratio 1: 1 after which are added flavoring and aromatic substances.

Ready marshmallow mass has a density of 400 kg / m3, 28 ÷ 30% moisture., It has a high viscosity, these properties are explained by a high content of agar and allows mold casting weight.

The casting to produce marshmallow marshmallows jigs SA system Rabinovich and VN Sokolova.

2. The principle of operation of the drilling machine.

The machine (Figure 1) has a hopper (1) Dosing-depositor mechanism (2), the conveyor (3) for the trays. The hopper is provided with a water jacket for maintaining the temperature zefirnoy mass at a certain level.

Mass loaded into the hopper (1) by gravity or by means of a special boot device. In operation of the machine (Figure 1b), pistons (11) is sucked into the cylinders from the weight of the hopper and then spools (2) direct it, i.e. during the return stroke of the cylinder mass is deposited through flexible tubes (3) with serrated tips (5) to move along the conveyor trays.

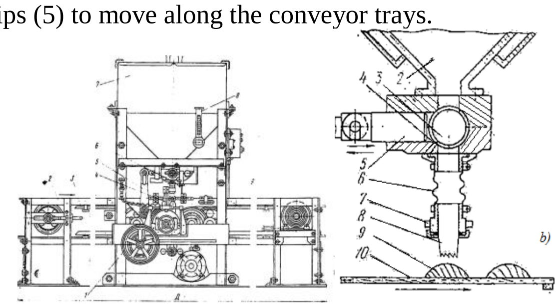

Fig. 1. Marshmallow Finish Machine

By means of a screw pair (10) can be adjusted stroke of plungers (11) and thereby providing a predetermined dosage weight portion, is deposited on the tray. Six coiled pipes (3) connecting the slide valve nozzle box with toothed lugs (5).

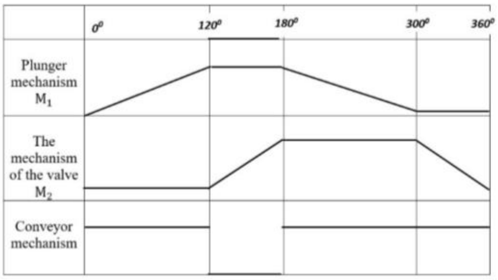

Fig. 2. The cycle chart and marshmallows sinhrogramma the casting machine.

A movable carriage (4), bearing the frame with toothed lugs fixed thereon, makes reciprocating movement along the conveyor and across it under the influence of the end (6) and the cylindrical cam (7) via a linkage system with a return spring.

As a result, a movable carriage makes complex longitudinal cross-forth motion, so that each portion is deposited zephyr mass acquires a circular shape with a corrugated surface ("shell"). Once the marshmallow is formed in an elongated shape such as "cakes".

3. Modernization of machine.

The aim of modernization is to replace cam mechanisms having a purely lever without changing the dimensions of the machine and accessories brand K-33 for the outflow of marshmallow. Such upgrading the one hand simplifies the structure of the actuators, on the other hand allows to increase the operating speed of the machine.

Dosage-dispensing head of the machine consists mainly of two mechanisms: the plunger and the valve mechanism. The cycle chart and sinhrogramma both mechanisms with the conveyor shown in Figure 2. The diagram shows that the plunger mechanism is in the final position of rotation of the main shaft Venue 60^0 machine. During this period, the valve mechanism itself turns the spool 90^0 and opens the way to the Gulf of mass. On the contrary, during this period the conveyor is at rest and ensures the implementation of the Gulf. actuators is shown in Fig. 3 (a, b).

Fig. 4 shows the proposed mechanisms to replace these mechanisms on a purely lever. However, resistance to prevent movement mechanism traverses plunger eccentric apply forklift mechanism shown in the first line of Fig. 4. This mechanism implements stop the driven member (in particular the plunger unit) to the desired angle (up to 60^0 reversal of the main shaft). If the plunger stroke reaches 92mm, the large radius of the eccentric takes R = 46mm, then φ_0 = (60) o-tion stop can be implemented with a maximum gap (Fig. 5):

$$\delta = R - R \cdot cos\frac{\varphi_o}{2} = 46 - 46cos\frac{60^o}{2}$$
$$= 46 - 46 \cdot 0{,}866 = 6{,}164mm$$

In view of the eccentric circle of radius R_e= 60mm and the minimum radius

r = 15mm, the distance between the forks of the mechanism is:

$$l = R_e + \delta = 60 + 6{,}164 = 66{,}164mm$$

In this case

$$h = R_e + (25 \div 30)mm = 46 + 26 = 72mm$$

In view of the pusher-plunger stroke distance is between the uprights of the mechanism:

$$A = 2R_e + (10 \div 15)mm = 2 \cdot 60 + 10 = 130mm$$

To ensure symmetry traverse plungers is provided on the main shaft of the machine are two eccentric arrangements with the respective pusher (Fig. 6).

The number of revolutions of the main shaft of the machine:

$$n = \frac{\Pi}{60 \cdot mq \cdot C} = \frac{312{,}5}{60 \cdot 6 \cdot 0{,}06 \cdot 0{,}8} = 18\,Rpm$$

where, $m=6$ - the number of dispensing plungers, q = 0,06kq - mass products, C = 0,8 - coefficient of r continuity process.

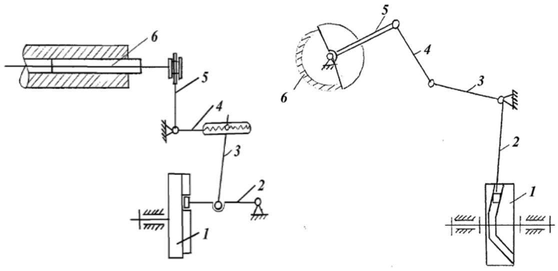

Fig. 3. Shema plunger mechanism and the spool

Thus, the shallow n = 24Rpm, define the necessary settings on the process, i.e. increasing the operating speed of the machine. Note that in addition to the eccentric mechanism, this mechanism may apply the slider-crank mechanism to hold out to the end positions (see.Figure 4).

As the valve mechanism is a mechanism shown in the third line of Figure 4. As follows from the chart move the slide lever is 120 ÷ 125^0 Venue cent in extreme positions, and its rotation is only 60^0 during the rotation of the main shaft. To implement this project the movement of the crank-rocker mechanism from 120^0 a dwell. Mechanisms must ensure the rotation of the lever l_3 = 60mm, ψ = (90) 0, and the distance between the axis of the spool and the main shaft is equal to a = 190mm.

Any equations or formulae should be centered; and there should be one blank between the texts and the formulas. The maximum magnitude of the spool lever in dwell time is: $l_{3-3} = l_3 \cdot 2\sin\frac{90^0}{2} = 84{,}6mm$

Dimensions and units r, l_2 determined from the cosine theorem. With the system of equations:

$$(l_3 + r)^2 = a^2 + l_3^2 - 2al_3 \cdot \cos(\psi_o + 90^0)$$

$$(l_3 - r)^2 = a^2 + l_3^2 - 2al_3 \cdot \cos\psi_o$$

From the layout of the machine $\psi_o = 34^0, r = 75{,}5mm\ l_2 = 329{,}5mm$

4. Conclusion.

Defined estimated size allows to make basic drawings zefirootlivochnoy machines and increase the operating speed of the machine is 1.5 times.

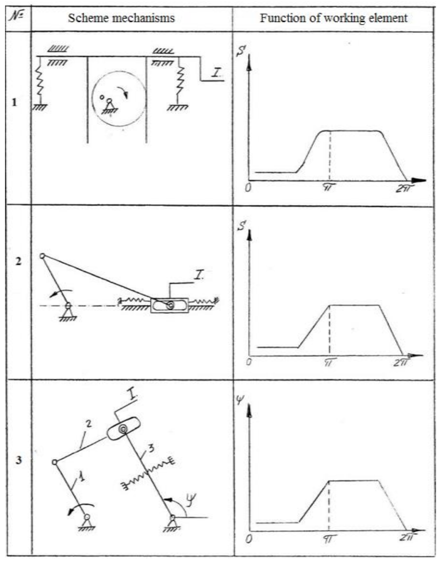

Fig. 4. Scheme of the proposed mechanisms

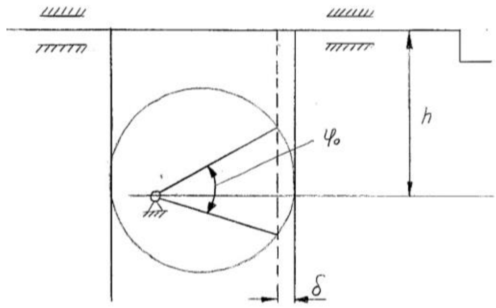

Fig. 5. Driving the eccentric mechanism.

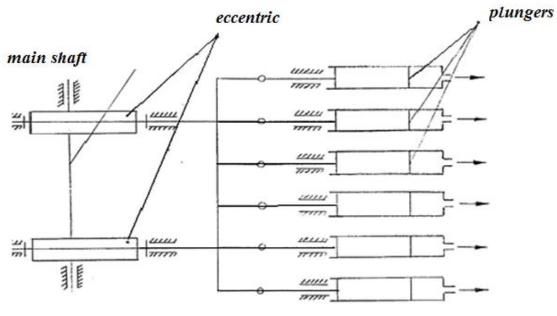

Fig. 6. Layout plunger mechanisms

References

[1]. О.Г.Лунин, А.И. Драгилев, А.Я. Черноиванник. Технологическое оборудование предприятий кондитерской промышленности. М., 1984, ЛПП, 382с.

[2]. Е.И.Журавлева и др. Технология кондитерского производства М., 1968.

[3]. А.А.Азизов, В.И.Гасанов, В.А.Мамедов. Проектирование исполнительных механизмов зефиротливочной машины. Ученые записки АзТУ, 2005, №4, Баку.

Proceedings of the International Symposium of Mechanism and Machine Science, 2017
AzC IFToMM – Azerbaijan Technical University
11-14 September 2017, Baku, Azerbaijan

Influence microgeometry offset printing plates for transfer ink from the printing form on dekel

Eldar Abbas oglu Aliyev
Mechanism and Machine Theory Department,
Azerbaijan Technical University, Azerbaijan
E-mail: elab57@mail.ru

Abstract:
This article is devoted to the study of the influence of the roughness of the surface shape in the paint transfer in the area of contact-form blanket. Given the impact of the space layer forms a rough surface on the amount of paint on the surface shape investigated form paint transfer blanket on the contact zone. The obtained formulas it can be concluded that the surface roughness of the printing plate has a significant impact on the amount of ink to print, the separation factor of the ink layer and transfer ink from the printing plate on the blanket in the contact zone.
Keywords: offset printing, contact area, roughness, blanket, the amount of ink, paint transfer.

1. Introduction

For any number of copies printed during the printing ink transfer from the inking unit on the printing plate and printing material to form. A recording apparatus, one of the main components of the printing machine, consists of a feed device, and dispensing and applying the ink on the printing plate, and also working elements performing a printing process [1-3]. The printing apparatus also consists of a carrier of the printing form and apparatus for producing pressure.

Rotary printing machines have a cylindrical printing plates and cylindrical pressure device. A recording apparatus for transferring ink from a certain number of printing elements to form the printed material with sufficient surface pressure and wiring of the printed material through a printing zone. Actions associated with the printing units of the printing plate and a view type of printed material is shown in [1, 2].

Transmission of information from the printing plate to the material can occur directly or indirectly. In indirect method, the ink is transferred onto the elastic intermediate surface and from it - to a printing material [1-4].

Indirect transfer with ink in offset printing is carried out in two stages. As indicated in [2], located on the print ink layer comes into contact with the rubber-plate (with deckle) of the blanket cylinder. In this part the layer remains on the wafer surface and the paint in contact with it deckle o

Rotary printing machines have a cylindrical printing plates and cylindrical pressure device. A recording apparatus for transferring ink from a certain number of printing elements to form the printed material with sufficient surface pressure and wiring of the printed material through a printing zone. Actions associated with the printing units of the printing plate and a view type of printed material is shown in [1, 2].

Transmission of information from the printing plate to the material can occur directly or indirectly. In indirect method, the ink is transferred onto the elastic intermediate surface and from it - to a printing material [1-4].

Indirect transfer with ink in offset printing is carried out in two stages. As indicated in [2], located on the print ink layer comes into contact with the rubber-plate (with deckle) of the blanket cylinder. In this part the layer remains on the wafer surface and the paint in contact with it deckle on the blanket cylinder.

However, as noted by the authors of [2-4], the adhesive forces that act between the ink and the printing form, deckle blanket cylinder and the impression material are always less than the cohesive forces acting in the printing ink. The above makes it possible to paint the required separation into layers.

2. Calculation scheme for transfer ink.

It is known that the printing elements and looseness on offset printing plate lie substantially in one plane. There are two contact zones in offset printing, so the two factors separating the ink layer (Fig. 1) is defined for them.

The first zone: printing form - offset plate (deckle)

$$v = \frac{m_i}{m - m_i}, \tag{1}$$

second zone : offset plate - printed material

$$v_i = \frac{p}{m_i - p}. \tag{2}$$

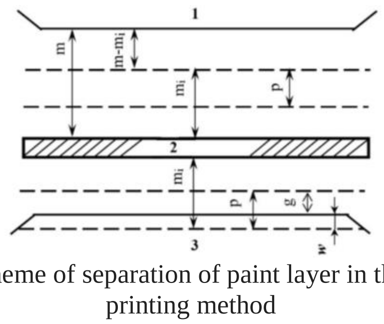

Fig. 1. Scheme of separation of paint layer in the indirect printing method

1 - printed form; 2 - offset rubber plate; 3 - paper; m - number of colors on the printed form before printing ; p - the amount of ink which has passed to the printed material; m_i - the amount of paint on the lid of the blanket cylinder before moving on to the printing material ; g - the number of colors, freely lying on the material ; w - quantity paint , absorbent printing material during the printing process.

An ink transfer from plate to rubber- plate (on deckle) basically corresponds to printing on non-absorbent material. The study results [2] show that the coat of paint which remains on the plate blanket cylinder (by deckle), is not directly involved in the division of the working layers of paint, so it can be ignored.

According to [2] transfer the ink from the printing plate to the plate of the blanket cylinder (deckle on) is

$$m_i = \alpha m\left(1 - e^{-\alpha^2 m^2}\right). \tag{3}$$

Transfer the paint from offset plate (with dressing) onto the printing material is

$$p = \left(1 - e^{-\alpha_i^2 m_i^2}\right)\left[(1-\alpha_i) w_{max}\left(1 - e^{-\frac{m_2}{w_{max}}}\right) + \alpha_i \cdot m_i\right] \tag{4}$$

where w_{max} -the maximum possible amount of paint , q/m^2;

α, α_i - coefficients of the partition paint layer

$$\alpha = \frac{g}{m - w}; \quad \alpha_i = \frac{g}{m_i - w}. \tag{5}$$

3. Influence microgeometry of printing form for transfer ink.

As seen from the calculation scheme when determining the amount of ink on the printing form before printing, as well as calculating the amount of ink on the lid of the blanket cylinder (to the deckle) is not considered microgeometry printing plate surface. To determine the amount of the paint layer based microgeometry printing plate surface, the ink layer separation circuit indirect printing process can be represented as follows (Fig. 2).

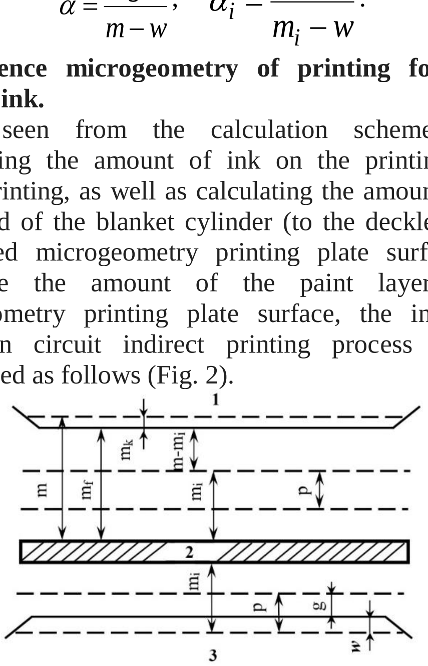

Fig.2 . Driving separation layer of paint indirect printing method taking into account the printing plate surface microgeometry

The new scheme of separation of the paint layer in the indirect method of printing is different from the existing schemes m_f parameters - amount of paint freely lying on the surface of the printing plate and m_k - the amount of ink on the rough area of the printing plate surface. Given these parameters, the amount of ink on the printing plate before printing define as follows

$$m = m_f + m_k. \tag{6}$$

Considering the formula (6), the formula (1) and (3) can be written as

$$v = \frac{m_i}{(m_f + m_k) - m_i}. \tag{7}$$

$$m_i = \alpha(m_f + m_k)\left(1 - e^{-\alpha^2 (m_f + m_k)^2}\right) \tag{8}$$

Partition coefficient layer of paint is:

$$\alpha = \frac{g}{(m_f + m_k) - w}. \tag{9}$$

As the authors note 2, the transfer of ink by dividing the paint layer is influenced by:

- Thickness of the paint layer on a printed form,
- The duration of the contact printing, which is determined by the printing speed and the construction of the printing apparatus,
- Specific pressure in printing,
- The rheological properties of the ink,
- Temperature and humidity conditions in the pressroom, which influences the rheological properties of the ink,
- The nature of the surface of the printed material.

Given that the offset printing ink layer separation occurs in the contact zone, the amount of ink to form useful to define a zone of contact with the printing plate blanket. Number of colors in print form the rough surface area can be calculated by the formula

$$m_k = \rho V_k, \tag{10}$$

where ρ – specific ink weight, v_k – ink amount space in the rough surface of the printing plate .

To determine the amount of ink on the print subject microgeometry printing plate surface using the calculation scheme proposed by the authors [5] .

Under this scheme, the amount of space of rough surface occupied paint, based on the formula I.V. Kragelskii [6], is defined by :

$$V_k = \frac{\pi R_1 \cdot L}{360^0}\gamma\left[R_{max}\left(1 - \frac{R_{max}}{R_1}\right) - 2R_a\right], \tag{11}$$

where R_1 – the radius of the cylinder shaped to fit the shape thickness, L–the length of the contact zone, γ – angle arc of wrap contact, R_{max} – the maximum height of unevenness of the printing plate surface, R_a – the arithmetic average height of the unevenness of the printing plate surface.

In view of formula (11), the formula (10) can be written as:

$$m_k = \frac{\rho\pi R_1 \cdot L}{360^0}\gamma\left[R_{max}\left(1-\frac{R_{max}}{R_1}\right)-2R_a\right], \quad (12)$$

Given (12), formulas (6÷9), can be written in the following forms:

$$m = m_f + \frac{\rho\pi R_1 \cdot L}{360^0}\gamma\left[R_{max}\left(1-\frac{R_{max}}{R_1}\right)-2R_a\right] \quad \mathbf{(13)}$$

$$v = \frac{m_i}{\left(m_f - m_i\right) + \frac{\rho\pi R_1 \cdot L}{360^0}\gamma\left[R_{max}\left(1-\frac{R_{max}}{R_1}\right)-2R_a\right]} \quad \mathbf{(14)}$$

$$m_i = \alpha\left\{m_f + \frac{\rho\pi R_1 \cdot L}{360^0}\gamma\left[R_{max}\left(1-\frac{R_{max}}{R_1}\right)-2R_a\right]\right\}\times$$
$$\times\left(1-e^{-\alpha^2\left\{m_f+\frac{\rho\pi R_1 \cdot L}{360^0}\gamma\left[R_{max}\left(1-\frac{R_{max}}{R_1}\right)-2R_a\right]\right\}}\right) \quad \mathbf{(15)}$$

$$\alpha = \frac{g}{\left(m_f - w\right) + \frac{\rho\pi R_1 \cdot L}{360^0}\gamma\left[R_{max}\left(1-\frac{R_{max}}{R_1}\right)-2R_a\right]} \quad \mathbf{(16)}$$

To determine the effect of surface roughness on printed form ink amount on the mold surface must carry out experimental studies.

4. Methods of research.

To determine the amount of print on ink gravimetric method was used [2,7]. This calculated difference between the masses of the printing plate with thumb paint and printing plate without ink. For this used proofing apparatus and analytical balances, whom error is ± 0.00001 g

For preparing the samples used in the printed form of the brand PRO-V company Fujifilm, which composes the dimensions 530×700 mm. The radius of the cylinder shaped 107 mm; the proportion of offset inks ρ=1,5 g/sm^3.

Using formula (13) theoretically calculated quantity paint on the printing plate surface.

The results of theoretical and experimental data are shown in Table 1.

Table 1. The dependence of the quantity of paint on the surface roughness of printing shape of the mold surface

Roughness parameters surface printing plate microns, mkm		**The amount of paint on surface shapes, m, g**	
R_{max}	R_a	theoretical	experimental
2,25	0,45	26,2945	27,6092
3,2	0,64	26,3133	27,6290
4,36	0,83	26,3390	27,6560
4,36	1,02	26,3595	27,6775
6,3	1,2	26,3687	27,6871

Number of colors on the printed form surface certain by calculated without taking into account the roughness of the surface shape is mp = 26.2511 g Comparison of the results obtained experimentally and theoretical ways showed the influence of roughness surface forms on the amount of ink on the form.

5. Conclusion.

As seen from the above formulas the amount of ink on the printing form before printing, the separation factor of the paint layer as, ink transfer the from the printing plate on the blanket depends on the radius of shaped cylinder and the contact area length, also, as was investigated and inserted the wrap angle arc of contact, and the parameters of microgeometry printing plate surface.

References

[1]. Tyurin A.A. Printing - Machines. Moscow, "Book", 1980. - p. 416

[2]. Germanies E. Handbook of technologist-printers. Moscow, "Book", 1982. - p. 336

[3]. Chehman Frenkel, Senka V.T., Birbraer E.G. Printing machine. Moscow, "Book", 1987. - p. 302

[4]. L.G. Varepo. The methodology of forecasting the quality of offset printing given microgeometry surface substrates. The thesis for the degree of Doctor of Technical Sciences. Moscow 2014.

[5]. Khalilov I.A., Aliyev E.A., Huseynzade E.M. Impact printing form surface roughness on the friction force in the contact zone. AzTU Scientists notes, Volume 1, №4, 2015, p. 33-36.

[6]. Kragelsky I.V., Mihin N.M., Units machines of friction: A. Handbook - M: Mechanical Engineering, 1984, p. 284

[7]. The division number of paint. [Electronic resource]: Access:hubergroup.ru/upload/Test-methods_RUS.pdf.

Proceedings of the International Symposium of Mechanism and Machine Science, 2017
AzC IFToMM – Azerbaijan Technical University
11-14 September 2017, Baku, Azerbaijan

Структурный синтез нового пространственного механизма RS_fSR шасси самолётов

Джавад Самедзаде
Магистр по специальности инженер-пилот,
E-mail: jsamadzade@azal.az

Аннотация
Система опор, именуемых шасси, служит для обеспечения передвижения самолёта по аэродрому на этапах руления, взлёта, посадки, стоянки, а так же для смягчения, поглощения и рассеивания энергии ударов и нагрузок, возникающих на данных этапах. Сегодня подавляющее большинство воздушных судов гражданской и военной авиации снабжено убирающимися шасси. Данный элемент конструкции занимает от трех до шести, а иногда и до десяти процентов всего веса самолёта. Это обусловлено тем, что шасси является одним из немногих недублированных и высоконагруженных элементов самолета. Целью данной работы является разработка схемы шасси с меньшим числом звеньев в кинематических цепях при использовании многоподвижных кинематических пар, которое послужит уменьшению веса шасси. В статье представлен структурный синтез нового пространственного механизма RS_fSR с использованием новых структурных формул, основанных на теории винтов.
Ключевые слова: Самолёт, шасси, механизм, синтез, формулы Р.И.Ализаде.

1. Введение

Разработка и внедрение механизмов шасси самолётов в эксплуатацию является трудоёмким процессом, включающим работу по нескольким дисциплинам, в том числе и по теории механизмов и машин. Процесс разработки хорошо описан в книге Конвея [1], Кёррея [2] и Ниу [3].
Ниже представлены основные понятия, связанные с данным объектом исследования.
Опорой самолёта называется устройство, воспринимающее нагрузки и удары при посадке, передвижении и стоянке на земле, палубе корабля или воде. Шасси самолёта - совокупность опор, необходимая для выполнения данных манёвров на предназначенной поверхности. Данная система бывает разных видов и в зависимости от этого включает в себя следующие составляющие:
Основные опоры - стойки с колёсами, лыжами, поплавками и другими видами шасси, размещённые вблизи центра тяжести самолёта и принимающие большую часть нагрузок;
Передняя опора – стойка с колёсами, лыжами и другими видами шасси, размещённая в носовой части фюзеляжа;
Подкрыльные опоры - стойки с колёсами, лыжами, поплавками и другими видами шасси, размещённые на консоли крыла самолёта;
Хвостовая опора - колесо, «костыль» или лыжа, размещённая в хвостовой части фюзеляжа.
Шасси бывают трёхопорного, многоопорного и велосипедного расположения. Трёхопорные, в свою очередь бывают с передней и хвостовой опорой. Большинство самолётов сегодня оснащены трёхопорным видом шасси в основном с передней направляющей опорой.
Так же различаются лыжные, гусеничные, поплавковые, колёсные виды шасси $[4-6]$.
Система может быть убирающейся или неубирающейся. Большинство шасси сегодня являются убирающимися из-за высоких скоростей полётов.
Основными частями шасси самолёта являются:
Стойка – часть опоры самолёта, являющаяся основным силовым элементом опоры;
Подкос стойки – часть опоры, предназначенная для принятия большей части продольных и поперечных нагрузок на себя. В основном является складывающимся элементом при уборке шасси;
Механизм ориентации стойки – часть шасси, предназначенная для ориентации или разворота стойки при её уборке и выпуске;
Раскос стойки – стержень, расположенный по диагонали шарнирного многоугольника, образованного стойкой и подкосом стойки шасси и обеспечивающий геометрическую неизменяемость этого многоугольника;
Замок выпушенного положения – замок подкоса стойки шасси самолёта, обеспечивающий фиксацию стойки шасси в выпущенном положении;
Замок убранного положения – замок подкоса стойки,

обеспечивающий фиксацию стойки шасси в убранном положении;
Тележка стойки – часть шасси самолета, состоящая из рамы и колёс.

2. Структурный анализ пространственного механизма шасси самолёта Boeing 757-200 с использованием новых формул Р.И.Ализаде

Современные самолёты используют пространственные механизмы для выпуска уборки шасси. Преимущество этих механизмов заключается в обеспечении минимального числа контуров.
Рассмотрим задачу структурного анализа механизма выпуска-уборки самолёта Boeing 757-200 (Рис. 2.1)

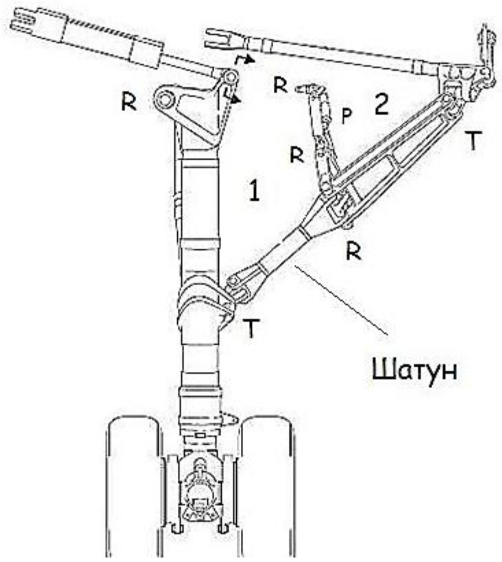

Рисунок 2.1. Шасси самолёта Boeing 757

Пространственный механизм данного шасси имеет следующую структуру: R-T-R (-R-P-R)-T. Шатун первого контура представляет собой платформу, который имеет три опорные кинематические цепи. Первая опорная цепь состоит из кинематической цепи TR, вторая стоит из RT, третья – RRPR. Необходимо просчитать число моторов рассматриваемого механизма [7], а также положение и ориентацию платформы. Используя новую структурную формулу Р.И. Ализаде [8, 9] для рассматриваемого механизма можем записать, при условии $j_h = 0$ и $L_b = 0$:

$$M = \lambda + \sum_{l=1}^{c_l}\left(\sum_{f=1}^{\lambda-1} f p_f - \lambda_l\right) =$$

$$=(P_1 + 2P_2 - 6) + (P_1 + 2P_2 - 6) + (P_1 - 3) =$$
$$=6 + (1 + 2 * 1 - 6) + (1 + 2 * 1 - 6) + (4 - 3) =$$
$$=6 + (-3) + (-3) + 1 = 1,$$

где
M – степень свободы механизма (число моторов)
j_h – связующие шарниры платформ;
L_b – контуры ветвей;
l – опорные кинематические цепи ;
λ_l – число независимых скалярных уравнений опорных кинематических цепей;
p_f – число шарниров с подвижностью f;
f – степень свободы шарниров относительного движения звеньев ;
Таким образом, число входных параметров для этой системы M=1.
Далее определим положение и ориентацию платформы данного механизма с теми же условиями: $j_h = 0$ и $L_b = 0$. Движение платформы определится следующим образом:

$$m = \lambda + c_l + \sum_{l=1}^{c_l}(d_l - D) =$$
$$= 6 + 3 + (2 - 3) + (2 - 3) + (2 - 3) = 6$$

где c_l – число опорных кинематических цепей;
d_l – количество размерности векторов опорных кинематических цепей в Евклидовых плоскостях;
D – количество размерности векторов в системе отсчёта.
Таким образом, мы можем утверждать, что платформа (шатун) шасси совершает в пространстве следующие движения: RRRPPP [10].

3. Структурный синтез пространственного механизма RS_fSR

Рассмотрим вторую задачу структурного синтеза нового предложенного механизма шасси. С этой целью рассмотрим пространственный механизм вида RS_fSR. Кинематическая схема показана на рисунке 2.2

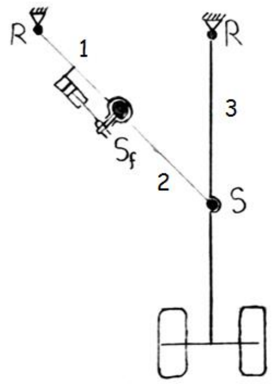

Рисунок 2.2. Кинематическая схема нового механизма шасси

Системы шасси определены на опорной

кинематической цепи (RS). Шатун 2 считается платформой, которая имеет 2 опорные кинематические цепи. Первая цепь – RS_f, вторая – RS. Входным звеном является опорная кинематическая цепь RS_f. Здесь S_f – шаровая кинематическая пара с пальцем, которая имеет два вращательных движения одного звена относительно другого. Первое вращение происходит вокруг оси пальца шарнира, второе вращение происходит вокруг перпендикуляра к плоскости прорези шаровой пары. По формуле Р.И. Ализаде [8, 9] определим число моторов рассматриваемого механизма (j_h=0,L_b=0)

$$M = \lambda + \sum_{l=1}^{c_l}\left(\sum_{f=1}^{\lambda-1} f p_f - \lambda_l\right) =$$
$$= 6 + (1 + 2 * 1 - 6) + (1 + 3 * 1 - 6) =$$
$$= 6 + (-3) + (-2) = 1$$

Положение и ориентация платформы определяется согласно второй формуле с теми же условиями (j_h=0,L_b=0):

$$m = \lambda + c_l + \sum_{l=1}^{c_l}(d_l - D) = 6+2+(2-3)+(2-3)=6$$

Таким образом, платформа механизма имеет три вращательных и три поступательных движения $RRRP_xP_yP_z$.

Во многих современных самолётах после выпуска шасси приходит в действие замок выпущенного положения, которое выводит из мёртвого положения замкнутый контур механизма, придавая угол давления в ведомой кинематической паре меньше 70 градусов. Известно, что если в замкнутом контуре подвижность M=0, то мы получаем неподвижную систему. В этом механизме предлагается новый метод для получения контура неподвижной системы. Для этой цели, на ведущем звене 1 (рис 2.2) жёстко насаживается привод, шток которого фиксирует палец двухподвижного звена S_f, превращая её в одноподвижную вращательную пару. Таким образом, мы получаем неподвижный замкнутый контур RRSR.Такой метод играет роль функции замка выпущенного положения. Рассмотрим степень свободы контура RRSR по другой формуле Р.И.Ализаде [8, 9]:

$$\mathrm{M} = \sum_{i=1}^{j} f_i - \sum_{k=1}^{L} \lambda_k = 6 - 6 = 0.$$

Получается структурная группа, степень свободы которой равна нулю.

Заключение

В ходе исследования было выявлено, что структурные схемы современных самолётов остаются почти неизменными в течении долгих лет и прогресса именно в этой сфере разработки шасси наблюдается мало. Так же, были встречены трудности в структурном анализе механизмов с различными подвижностями контуров.

Как следствие выше изложенного была предложена новая структурная схема механизма уборки-выпуска шасси вида RS_fSR с меньшим числом звеньев, а в перспективе весом, что внесёт свой вклад в улучшение таких лётно-технических характеристик как грузоподъёмность, пассажировместимость или дальность полёта. Так же были предложены новые формулы для структурного анализа механизмов с различными избыточными связями на основе теории винтов.

Литература

1. Conway, H.G., Landing Gear Design, Chapman and Hall, London, (1958).
2.Currey N.S., Aircraft Landing Gear Design: Principles and Practices, Washington D.C, (1988)
3.Niu, M. C. Y., Airframe Structural Design, Conmilit Press, Hong Kong, (1988)
4.В.Н.Зайцев, Г.Н.Ночевкин, В.Л.Рудаков, Ж.С.Черненко. Конструкция и прочность самолётов, Киев, (1974), с 295 – 300; 364 – 368.
5.О.А.Гребеньков. Конструкция самолётов, Москва, (1985),с 187 – 200; 227- 230.
6.ГОСТ. Шасси самолётов и вертолётов. Термины и определения, Москва, (1976)
7.О.Н.Левитский, Н.И.Левитская. Курс теории механизмов и машин, Москва, (1985), с 5 – 56
8.R.I.Alizade, F. C. Can, E. Gezgin, Structural synthesis of Euclidean platform robot manipulators with variable general constraints, IFToMM J. Mech. Mach. Theory 43 (2008) 1431-1449.
9.Rasim Alizade, Cagdas Bayram, Erkin Gezgin, Structural Synthesis of serial platform manipulators, IFToMM J., Mechanism and Machine Theory 42 (2007) 580-599.
10.Boeing. Company Maintenance Manual, Boeing 757 Main Gear Buildup 32-11-23,32-11-26, Seattle, Washington, USA, (2016).

Proceedings of the International Symposium of Mechanism and Machine Science, 2017
AzC IFToMM – Azerbaijan Technical University
11-14 September 2017, Baku, Azerbaijan

Burulmayan və burulan lifli materialların dartılması zamanı sürtünmə qüvvəsi sahəsinin təyini

Xəlilov Esmin Camal, Nuriyev Məhəmmədəli Nürəddin
Azərbaycan Texniki Universiteti, “Maşınların Konstruksiya Edilməsi” kafedrası
E-mail: esminkhalilov@yahoo.com
Azərbaycan Dövlət İqtisad Universiteti (UNEC)
E-mail: mehman62@mail.ru

Xülasə: Məqalədə əyricilik fabriklərində burulmayan və burulan lifli materialların dartılması zamanı sürtünmə qüvvəsi sahəsinin təyini kimi məsələlərə baxılmışdır.

Müəyyən edilmişdir ki, burulmayan məhsulda sürtünmə qüvvəsi sahəsi lifin ilişmə qabiliyyəti və deformasiyasından asılı olaraq yaranır. Sürtünmə qüvvəsi dartılma sahəsinin özündə məhsulun valiklə qidalandırıcı və buraxılış cütlərin silindrləri ilə qarşlıqlı təsiri hesabına əmələ gəlir. Lakin sürtünmə qüvvəsi sahəsinin gərginliyinin də çox az uzunluğu olduğu üçün cütlər arasında sürtünmə sahəsinin gərginliyi azdır. Bununla əlaqədar liflərin vaxtından əvvəl buraxılış cütlərinin sürətinə keçməsini dayandıra bilmir.

Açar sözlər: burulmayan lif, burulan lif, sürtünmə qüvvəsi, dartılma sahəsi, gərginlik, buraxılış cütləri.

Məsələnin qoyuluşu. Burulmayan məhsulda sürtünmə qüvvəsi sahəsi lif kütləsinin (lentin) sıxılması nəticəsində əmələ gələn deformasiya qüvvəsi və liflərin ilişməsi nəticəsində yaranır. Həmçinin, dartılma sahəsində sürtünmə qüvvəsi məhsulun valik və qidalandırıcı və buraxılış cütlərinin silindrləri ilə qarşılıqlı əlaqəsi hesabına əmələ gəlir. Lakin, onların yaratdığı sürtünmə qüvvəsi sahəsinin gərginliyi çox qısa uzunluqdadır, cütlər arasındakı sürtünmə qüvvəsi sahəsinin gərginliyi çox azdır və lifin vaxtından əvvəl buraxılış cütünün sürətinə keçməsini saxlamaq imkanına malik deyildir.

Dartıcı cihazın işinin vacib xarakteristikası cütlərin sıxıcılar arasındakı sürtünmə qüvvəsi sahəsidir [1, 2]. Bunun üçün heç olmasa dartıcı cihazın müxtəlif şəraitlərdə işini müqayisə etməyə imkan verən sürtünmə qüvvəsi sahəsinin nisbi xarakteristikasını müəyyən etmək lazımdır.

Tədqiqatlar göstərir ki, dartıcı cütlər arasındakı sürtünmə qüvvəsi sahəsinin gərginliyi lifin-lifə (bir–birinə) təzyiqi ilə müəyyən olunur və tədqiq olunan lifin digər liflərlə sürtünmə əmsalı və əlaqələrinin paylanma ehtimalı ilə ifadə oluna bilər.

Sürtünmə qüvvəsi sahəsinin gərginliyinin qiyməti liflər arasında yaranan sürtünmə qüvvələrinin diferensiallaşdırılması ilə təyin olunur. Sürtünmə qüvvəsi sahəsinin gərginliyinin qiymətinin təyini üçün düstur aşağıdakı kimidir:

$$q = \frac{dF_{sür}}{ndl} , \qquad (1)$$

burada n–tədqiq olunan kəsikdə liflərin sayı; l–lifin uzunluğudur.

İşin bu hissəsində arxa zonanın dartılma sahəsinin müxtəlif kəsiklərində sürtünmə qüvvəsi sahəsinin xarakteris-tikasını buraxılan məhsulun sıxlığı kimi qəbul edirik.

Dartılma prosesində hərəkətin xətti trayektoriyası üzrə
dartılma sahəsində məhsul tarımlanmaya məruz qalır. Bu zaman en kəsiyində sıxılma müqaviməti yaranır ki, bu da liflər arasında
sürtünmə qüvvəsi sahəsinin gərginliyini əmələ gətirir.

Bir millimetr uzunluğunda kəsikdə en kəsiyin gərginliyinin təyini üçün tənlik belə yazılır:

$$\sigma = a \cdot \gamma^{b} \cdot l_1 , \qquad (2)$$

burada *a və b*–lifin təbiətindən asılı olan empirik əmsalı; γ -məhsulun sıxlığı; l_1-bir millimetrə bərabər lifin uzunluğudur.

Lifin sıxlığı belə ifadə olunur:

$$\gamma = \frac{m}{V} , \qquad (3)$$

burada m–kəsilmiş nümunənin kütləsi; $V=S_l H_c$-tədqiq olunan kəsiyin həcmi; H_c -kəsiyin hündürlüyüdür.

Tədqiq olunan kəsiyin kütləsinin qiymətini nazilmə əyrisində alınan nəticələrə görə qəbul edək.

En kəsiyində gərginliyin əmələ gəlməsi dartılan məhsulda sürtunmə qüvvəsi sahəsinin gərginliyini müəyyən edir. Bu gərginlik liflərin ön cütlərin sürətinə keçməsini saxlayır. Onda yazmaq olar ki,

$$q = \frac{(\sigma \cdot \mu + h) \cdot l_B}{n} , \qquad (4)$$

burada μ -liflər arasında sürtünmə əmsalı; $l_B = 2\pi r$ -lifin səthinin uzunluğu; r - lifin radiusu; n - tədqiq olunan kəsikdə liflərin sayı; h - lifin ilişməsidir.

Yuxarıdakı düsturdan görünür ki, sürtünmə qüvvəsi sahəsinin gərginliyi buraxılan məhsulun sıxlığı və liflərin sayından asılıdır. Bir sıra tədqiqatçılar da [3, 4] belə bir fikrə gəlmişlər ki, dartıcı cihazda məhsulun sıxlığı sürtünmə qüvvəsi sahəsinin xarakterini aça bilər.

Dartılma sahəsinin kəsiyində sürtünmə qüvvəsi sahəsinin gərginliyinin dəyişməsinin dartılan məhsulun sıxlığından asılılığının öyrənilməsi liflər arasında sürtünmə qüvvəsinin tədqiqi zamanı vacib məsələlərdən biridir. Bu məsələnin həlli dartılma prosesində lentin sürtünmə qüvvəsi sahəsinin dəyişməsi tendensiyasını müəyyən etməyə imkan verər.

Məlumdur ki, liflərin ilişkənliyi onların faktiki toxunma sahəsindən, yəni əlaqələrin sayından, faktiki toxunma sahəsi isə məhsulun sıxlığından asılıdır.

Çoxlu sayda liflər real dartılma şəraitində məhsulun buraxılış nöqtəsində dartılmış olur və həmişə özünü radial təzyiq kimi göstərir. Dartılma sahəsində bu təzyiqlərin eksperimental
yolla təyini praktiki olaraq mümkün deyildir.

Xüsusi təzyiqin tədqiqi məhsulun buraxılış nöqtəsində
sıxlığı vasitəsilə öyrənilmişdir [5]:

$$\sigma = \frac{1750 \cdot K_3^3}{1 - K_3} \qquad (5)$$

Dartılma sahəsi kəsiyində sürtünmə qüvvəsi sahəsinin xarakteristikası məhsulun buraxılış nöqtəsindəki sıxlığı kimi qəbul olunur və məhsulun liftlərlə doldurulma əmsalı kimi ifadə edilir

$$K^3 = \frac{n_x S_b}{S_{meh}}\ , \qquad (6)$$

burada n_x- x dartılma sahəsinin kəsiyində liflərin sayı; S_b–lifin en kəsiyinin sahəsi; $S_{məh}$–məhsulun en kəsiyinin sahəsidir.

n_x həddi nazilmə əyrisindən götürülür. Məhsulun en kəsik sahəsi hər dartılma zonasında bərabər addımla qalınlığı və eni üzrə təyin olunur. Məhsulun diametri МБП-2 mikroskopunda baxılmaqla ölçülür. Mikroskopun 0,05 mm bölgülü ölçü xətkeşi vardır.

Məhsulun buraxılış nöqtəsində sıxlığı haqqında daha dəqiq məlumat almaq üçün ölçmələr üç kəsikdə aparılmışdır. Dartıcı cihazın xətaların ləğvi üçün isə kələf 10 maşında istehsal olunmuşdur. Tədqiqat statik şəraitdə və məhsulun kəsiyində liflərin sayılması ilə aparılmışdır. Dartıcı cihazın hər bir zonasında 50 ölçmə aparılmışdır. Alınmış ölçmələrdən orta qiymət hesablanmışdır.

Buraxılış nöqtəsində məhsulun en kəsiyi ellips formasında qəbul olunmuşdur, en kəsik belə hesablanmışdır:

$$S_{np} = \pi \frac{ab}{4}, \qquad (7)$$

burada a-ellipsin kiçik oxu; b-ellipsin böyük oxudur.

Əgər rulonun dartıcı cütlər arasında sürtünmə qüvvəsi sahəsinin təyini üçün ümumi düsturu qəbul etsək, onda

$$q = (\sigma\mu_1 + hK_3)2d\ , \qquad (8)$$

burada h- lifin ilişkənliyi, μ_1- liflər arasında sürtünmə əmsalı; σ-lifin digər lifə göstərdiyi udel təzyiq; d-lifin diametridir.

(5) və (8) ifadələrini qarşılıqlı həll etməklə sürtünmə qüvvəsi sahəsinin gərginliyinin təyini üçün aşağıdakı düsturu alırıq:

$$q = 2d\left(\frac{1750K_3^3}{1-K_3}\right), \mu_1 + hK_3 \qquad (9)$$

Burada dartıcı cihazda nəzarətedici orqanları nəzərə almadan dartılma prosesinin gedişinə baxılır. Yun əyriciliyi istehsalatında sürtünmə qüvvəsi sahəsinin gərginliyinin dəyişməsinin təyini üçün (2) və pambıq əyiriciliyində isə (9) analitik ifadələri alınmışdır. Alınmış asılılıqlar dartılma sahəsində liflərin hərəkətini proqnozlaşdırmağa imkan verir.

Burulmuş lifli məhsul dartılmaya məruz qaldıqda onun lifləri arasında eninə istiqamətlənmiş gərginlik yaranır. Bu zaman liflərin ayrı-ayrı xassələri öz aralarında cəmlənir və məhsulun deformasıyası zamanı verilmiş qüvvənin qiymətinə kompleks təsir edir.

Liflər arasında sürtünmə qüvvələri məhsulda liflərin
möhkəmliyinin istifadə dərəcəsini şərtləndirir. Sürtünmə qüvvəsinin qiyməti məhsulun burulması zamanı liflərin tarazlığının yaratdığı eninə gərginliyin qiymətindən asılıdır. Məhsulun burulması artdıqca yaranan eninə sıxılma (gərginlik) artır. Bu da öz növbəsində dartılma prosesində sürtünmə qüvvəsi sahəsinin yaranmasına bir tipik misal ola bilər.

Məsələnin həlli. Qoyulmuş məsələnin həlli üçün dartılması və burulması zamanı məhsulda yaranan qüvvələr arasında qarşılıqlı əlaqələri nəzərə almaq lazımdır. Tədqiqatların məqsədi məhsulun tarazlığı, dartılma zamanı gərginlik, eninə gərginlik, məhsulda lifin burulma bucağı kimi amillər arasında qarşılıqlı əlaqələri nəzərə almaqla burulmanın buraxılan həddi və maksimal burulma bucağının təyinidir. Maksimal burulma bucağı böyüdükcə məhsulun dağılması prosesi sürətlənir.

Tekstil maşının dartıcı cihazında burulmuş lifli məhsulun dartılması həndəsi modeli şəkil 1-də göstərilmişdir.

Burulmuş məhsulun həndəsi modeli göstərir ki, liflər yiv xətti üzrə düzülmüşlər. Yiv xəttinin addımı sapın cari radiusundan asılı deyil, yiv xəttinin qalxma bucağına bərabər olan ayrı-ayrı liflərin yerləşmə bucağı Θ isə β həddinə çatanda radius boyu dəyişir. Kələfin elastik deformasiyası bu yarımfabrikatı təşkil edən bütün liflərin burulma deformasiyasından toplanır.

İpliyin alınması zamanı burulma prosesində liflər tangensial, həm də radial gərginliyə məruz qalır. Tədqiq etdiyimiz məhsul kələfdir, burada burulma həddi kiçik olduğundan radial gərginliklə müqayisədə tangensial gərginlik azlıq təşkil edir. İşlətdiyimiz burulmuş məhsulun dartınması zamanı sürtünmə qüvvəsi sahəsinin təyini metodu universaldır və bütün növ liflərə tətbiq oluna bilər. Əyrilmənin planı liflərin qarışdırılmaya hazırlanması mərhələsində, həm də əyricilik istehsalatının proseslərində səmərəli qarışdırmanı təmin edir. Bununla əlaqədar hesab edirik ki, kələfdə liflər bərabər paylanmışdır.

Burulmuş məhsulun dartılması zamanı onun en kəsiyi kiçilir, liflər arasında ümumi daxili (radial və tangensial gərginliklərin cəmlənmiş həndəsi gərginlik) gərginlik ortaya çıxır. Məhsulun liflərinin məruz qaldığı daxili gərginliyin təyini üçün ifadə aşağıdakı kimi ola bilər:

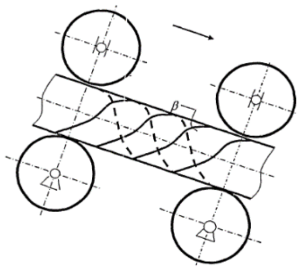

Şəkil 1. Burulmuş məhsulun dartılmasısının həndəsi modeli

$$\sigma_r = \sigma_f \cdot \cos^2\beta \frac{\left(1 - \frac{P^2}{R^2} \cdot \sin^2\beta - \cos^2\beta\right)}{2 \cdot \left(\left(\frac{P}{R}\right)^2 \cdot \sin^2\beta + \cos^2\beta\right)}, \quad (10)$$

burada σ_f - dartılma zamanı liflərin məruz qaldığı gərginlik; *P*- kəsikdə məhsulun oxundan tədqiq olunan lifə qədər olan məsafə; *R*- məhsulun radiusu; β-burulma bucağıdır.

Dartılma zamanı lifin gərginliyi belə təyin olunur:

$$\sigma_f = E_f \varepsilon_f, \quad (11)$$

burada E_f -lifin elastiklik modulu; ε_f -lifin nisbi uzanmasıdır.

Beləliklə, lifin OX xəttinə gətirilən radial gərginliyinin qiyməti belə təyin oluna bilər:

$$\sigma_r = E_f \cdot \varepsilon_f \cos^2\beta \frac{(1 - \frac{P^2}{R^2} \cdot \sin^2\beta - \cos^2\beta)}{2 \cdot \left[\left(\frac{P}{R}\right)^2 \sin^2\beta + \cos^2\beta\right]}. \quad (12)$$

İndi isə burulmuş məhsulda qonşu liflər arasında təsir edən tangensial gərginliyi təyin etmək üçün araşdırma aparaq.

Dartıcı cütlər arasında sıxılan məhsulun ixtiyari sahəsinə dartıcı qüvvənin təsiri zamanı əmələ gələn gərginliyin qiyməti dartıcı cihazın optimal yükləmə parametrlərinin təyini üçün lazımdır. Bizim tədqiqatlar hesablama metodunun elmi əsaslandırılmasına və tekstil müəssisələrində dartılma prosesinin texnoloji layihələndirilməsinə yönəlmişdir.

Aydındır ki, burulmuş lifli məhsul ayrı-ayrı liflərdən ibarətdir. Məhsuldakı liflər arasında labüd olan nisbi hərəkət zamanı yaranan sürtünmə qüvvəsinin gərginliyi liflərə təsir edir (şəkil 2). Lifin tarazılığı və məhsulun burulması çox olduqca, liflərdə eninə sıxlaşma daha güclü gedir və dolayısı ilə sürtünmə qüvvəsi artır. Onda yazmaq olar:

$$F_{sur} = \sigma_n \mu + h, \quad (13)$$

burada σ_n -liflər arasında normal təzyiq; μ -liflər arasında sürtünmə əmsalı; *h*- liflər arasında ilişkənlikdir.

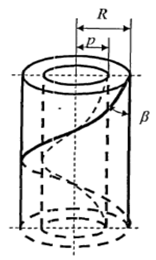

Şəkil 2. İpliyin burulması sxemi

Məhsul liflərinin burulması nəticəsində liflər sürüşməyə məruz qalır və toxunan gərginlik σ_τ ortaya çıxır (şəkil 3).

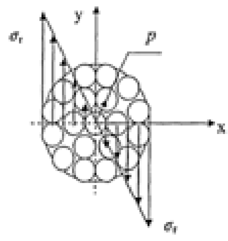

Şəkil 3. Məhsulun layları üzrə tangensial gərginliyin paylanma sxemi

Dartılma prosesində məhsulun lifləri arasında yaranan sürtünmə qüvvəsinin elementar qiyməti aşağıdakı kimi təyin olunur:

$$df = \mu\sigma_p(2\pi r dl_i),$$

burada *r*-lifin radius; dl_i -lifin toxunan gərginlik yaranan elementar uzunluğudur.

$$dl_i - \frac{Q}{2}\left[\frac{2U_i}{1-\cos^2\beta}\right] du_i,$$

burada *Q* –lifin hərəkət dövrü; *u* –məhsulda lifn radial vəziyyətin nöqtəsini xarakterizə edən amildir.

Lifə təsir edən sürtünmə qüvvələrinin əmələ gətirdiyi və onların sürüşməsinin qarşısını alan tangensial gərginlik aşağıdakı kimi təyin olunur:

$$\sigma_\tau = \frac{df}{2\pi rl}, \qquad (14)$$

burada *l*- lifin ştapel uzunluğudur.

Alınmış düstur məhsulun ixtiyari kəsiyində liflər arasında yaranan tangensial gərginliyi təyin etməyə imkan verir.

Beləliklə, məhsulun burulmasının dəyişməsi liflər arasında əmələ gələn gərginliyə təsir edir. Özü də bir laydan digərinə keçdikdə gərginlik dəyişmir. Burulmuş məhsulun müxtəlif laylarında deformasiyadan yaranan gərginlik fərqli olduğundan sürtünmə qüvvəsi sahəsinin gərginliyi də fərqli olur. Bu da dartıcı cihazın istənilən sahəsində liflərin hərəkətinə ciddi təsir edir [6].

Misal. Burulmuş lifli məhsulun layları arasında sürtünmə qüvvəsi sahəsinin gərginliyinin tangensial dəyişməsini təyin edək. Gərginliyin təyini zamanı qəbul olunmuşdur ki, məhsulda lifin yerləşmə bucağı sabit olmadığından burulmanın 30 bur/m qiymətində yerləşmə bucağının orta qiyməti 14°- dir. Hesablamalar kələfin xətti sıxlığı T=333teks, 64^k tərkibli yun qarışığı, I və II uzunluğu 100 %, lifin ştapel uzunluğu 72 mm-ə bərabər olan tədqiqat obyekti üçün aparılmışdır. Cədvəl 1-də dartıcı cihazın arxa zonasında formalaşan yarımfabrikatın müxtəlif laylarında radial və tangensial gərginliyin qiymətləri verilmişdir.

Cədvəl 1. Müxtəlif laylarda formalaşan radial və tangensial gərginliyin qiymətləri

№	P, mm	σ_P, q/mm^2	σ_τ, q/mm^2
1	0	0.0662	0.0014
2	0.15	0.0639	0.0037
3	0.30	0.0626	0.0050
4	0.45	0.0595	0.0081
5	0.60	0.0549	0.0125
6	0.75	0.0502	0.0167
7	0.90	0.0446	0.0224
8	1.05	0.0370	0.0291
9	1.20	0.0287	0.0361
10	1.35	0.0209	0.0410
11	1.50	0.0087	0.0524

Cədvəldə verilmiş məlumatlara görə belə nəticəyə gəlmək olar ki, mərkəzdəki lif daha çox radial gərginliyə məruz qalır və bu gərginlik liflərin səthinə doğru istiqamətdə tədricən azalır. Ən çox tangensial gərginliyə kənardakı liflər, mərkəzdə yerləşən liflər isə ümumi normal gərginliyin maksimum həddinə məruz qalır. Bu vəziyyət şəkil 4-də verilmiş burulmuş məhsulda gərginliyin dəyişmə qrafiki təsvir olunmuşdur.

Qeyd edək ki, liflərə təsir edən qüvvələrə dair məlumatlar burulmuş məhsulun dartılması zamanı əmələ gələn qüvvələrin təyini üçün çox vacibdir. Çünki dartıcı cihazın sıxıcı valiklərinə verilən yükün qiyməti dartılma prosesində əmələ gələn qüvvələrin təsirinin xarakterindən asılıdır.

Ümumi halda burulmuş məhsulda əmələ gələn gərginlik aşağıdakı kimi təyin olunur:

$$\sigma = \sqrt{\sigma_2^2 + \sigma_\tau^2}. \qquad (15)$$

Burulmuş məhsulda yerləşən lifin sürtünmə qüvvəsi isə belə təyin oluna bilər:

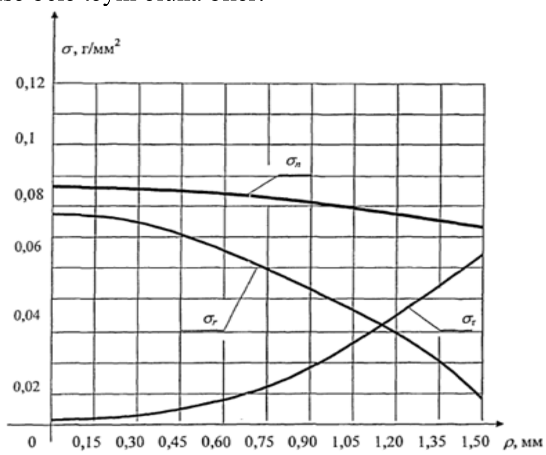

Şəkil 4. Burulmuş məhsulda yaranan gərginliyin lifin en kəsiyi boyunca dəyişmə qrafiki

$$F_{sur} = \int_0^1 (\sigma\mu + h)\cdot(2\pi r)dl, \qquad (16)$$

burada σ- lifin eninə gərginliyi; μ - liflər arasındakı sürtünmə əmsalı; *h*- lifin ilişkınliyi; *l*- lifin uzunluğudur.

Burulmanın maksimum qiymətini təyin edək. Aydındır ki, onun artması ilə liflər arasında sürtünmə qüvvəsi də əhəmiyyətli dərəcədə artacaqdır. Bir lifin buraxılan dartılma qüvvəsi belə təyin oluna bilər:

$$F_{dar} = E_f \cdot \varepsilon_f \cdot S_{np}. \qquad (17)$$

Sonuncu ifadə buraxılan dartılma qüvvəsini F_{dar} təyin edir. Bu qüvvənin artırılması ilə lifdə deformasiya başlayır və sonra onun qırılması baş verə bilər. Lifin ilişkənliyi nəzərə alınmadan sürtünmə qüvvəsini təyin edən tənliyi belə yazmaq olar

$$F_{dar} = \mu\sigma l L_B, \qquad (18)$$

burada *l*- lifin uzunluğu; $L_B = 2\pi r$ -lifin kəsiyinin uzunluğudur.

Dartılma prosesi aşağıdakı şərtlər daxilində mümkündür. Dartılma qüvvəsi lifin sürtünmə qüvvəsindən böyük yaxud ona bərabərdir, bu halda

$$F_{dar} \geq F_{sür}. \qquad (19)$$

(19) ifadəsi nəzərə alınmaqla (17) düsturundakı hədləri (18) ifadəsindəki hədlərlə bərabərləşdirməklə maksimal eninə gərginlik həddini müəyyən edirik:

$$\sigma = \frac{E_f \cdot \varepsilon_f \cdot S_{np}}{\mu \cdot l \cdot L_B}. \qquad (20)$$

Sonra alınmış (20) ifadəsini (10) ifadəsi ilə həll etməklə alarıq ki,

$$\frac{S_{np}}{\mu \cdot l \cdot L_B} = \cos^2\beta \cdot \frac{\left(1-\frac{P^2}{R^2}\sin^2\beta - \cos^2\beta\right)}{2\left[\left(\frac{P}{R}\right)^2 \sin^2\beta + \cos^2\beta\right]}.$$

Bu halda lifin burulma bucağı β- maksimal qiymətə
malik olur və bu, maksimal eninə gərginliyə uyğun gəlir.

Dəyişməni yerinə yetirsək,

$$a = \frac{1}{\mu \cdot l \cdot L_B},$$

$$g^2 = \left(\frac{P}{R_{np}}\right)^2; \quad z = \sin^2\beta$$

alırıq:

$$a = \cos^2 \frac{\left(1-g^2 z - \cos^2\beta\right)}{2\left(g^2 z + \cos^2\right)},$$

$$\cos^2\beta = 1-\sin^2\beta = 1-z,$$

$$a = (1-z)\frac{\left(1-g^2 z - 1 + z\right)}{2\left(g^2 z + 1 - z\right)} = \frac{(1-z)z\left(1-g^2\right)}{2\left(1-z\left(1-g^2\right)\right)},$$

$$1-g^2 = c,$$

$$a = \frac{(1-z)zc}{2(1-zc)},$$

$$-cz^2 + z(2ac+c) - 2a = 0.$$

Kvadrat tənliyi z-ə nəzərən həll edib və dəyişməni də nəzərə alsaq, yazmaq olar:

$$z = \frac{2\frac{S_{np}}{\mu l L_B}+1}{2} + \sqrt{\left(\frac{2\frac{S_{np}}{\mu l L_B}+1}{2}\right)^2 - \frac{2\frac{S_{np}}{\mu l L_B}}{2-\left(\frac{P}{R_{np}}\right)^2}}.$$

$$\beta_{\max} = \frac{1}{2}\arccos(1-2z),\ 0 \le z \le 1/2 \qquad (21)$$

$$\beta_{\max} = \frac{\pi}{2} - \frac{1}{2}\arccos(1-2z),\ 1/2 \le z \le 1 \qquad (22)$$

(21) yaxud (22) ifadələrində təyin olunan β bucağının qiyməti eninə gərginliyin maksimal həddinə uyğun olan buraxıla bilən həddir.

Burulmanın buraxıla bilən həddinin təyini üçün ifadə aşağıdakı ifadə tətbiq olunur:

$$K = 282 tg\beta_{\max}\sqrt{\gamma}\sqrt{\frac{l}{g}},$$

burada l- məhsulun ixtiyari kəsiyinin uzunluğu; g- məhsulun tədqiq olunan kəsiyinin kütləsi; γ- məhsulun həcmi kütləsidir.

Beləliklə, (12) ifadəsinin təhlili göstərir ki, eninə gərginlik bir çox amillərdən mürəkkəb funksional asılılığa malikdir:

$$\sigma = f\left(\varepsilon_f, E_f, \beta, P, R, l\right). \qquad (23)$$

Nəticə. Məhsulda əmələ gələn eninə gərginlik sürtünmə qüvvəsi sahəsinin gərginliyini müəyyən edir. Tədqiqatlar əsasında müəyyənləşdirilmişdir ki, məhsulda qeyri-bərabərlik lifin aralıq cütlərin sürətinə vaxtından əvvəl keçməsi hesabına əmələ gəlir. Məhsulun dartılması hələ dartıcı cihaza qədər başlayır ki, bu da lifin hərəkət qanununa əngəllik törədir. Dartıcı cihazların konstruksiyasında sıxıcılardan istifadə olunması dartılma prosesində liflərin hərəkətinə səmərəli nəzarəti təmin etmir.

Ədəbiyyat

1. Xəlilov E.C., Nuriyev M.N. Məhsulun dartılması zamanı onun keyfiyyətinə təsir edən parametrlər // Maşınşünaslıq, 2016, №1.
2. Капитанов А.Ф. Метод расчета нормального давления в ремешковом зажиме вытяжного прибора // Изв. вузов. Технология Текстильной промышленности. 1995, №2.
3. Зотиков В.Е. Основы прядения волокнистых материалов / Зотиков В.Е., Будников И.В. М., Гизлегпром, 1989, 345 с.
4. Чистобродов Г.И. Определение максимального угла кручения продукта // Изв. вузов. Технология текстильной промышленности, 2002, №2.
5. Аврелькин В.А. Исследование ноля сил трения. Молодые ученые-развитию текстильной и легкой промышленности. Тез. докл. межвузовской научно-технической конференции аспирантов и студентов / Иваново, ИГТА, 2002.
6. Дадыханов Н.К. Исследование контактной полоски вытяжных пар с учетом перекоса осей нажимного валика и цилиндра // Изд. Вузов. Технология текстильной промышленности, 2001, №2.

Proceedings of the International Symposium of Mechanism and Machine Science, 2017
AzC IFToMM – Azerbaijan Technical University
11-14 September 2017, Baku, Azerbaijan

Синтез кулачкового механизма с учетом условий передачи сил и контактной прочности

[1]И.А.Халилов, [2]С.Х.Керимов, [3]С.А.Багирова, [4]Ф.Ш.Гаджиева
[1,2,3,4] Азербайджанский Технический Университет
Азербайджан, Баку, прос. Г. Джавида, 25
E-mail: khalilov-isa@rambler.ru

Аннотация. Объект исследования – кулачковый механизм с роликовым толкателем. Разработан метод для определения минимального радиуса практического профиля кулачка r_0 и других конструктивных размеров кулачкового механизма, обеспечивающий условия передачи силы и контактной прочности для целого цикла движения кулачка.

Ключевые слова: кулачковый механизм, угол давления, контактное напряжение, минимальный радиус кулачка, радиус ролика, ширина ролика, радиус кривизны.

1. Введение

Кулачковые механизмы широко используются во многих современных технологических, транспортных и др. машин-автоматах. Эти механизмы наряду с простотой и компактностью обладают многими преимуществами.

В настоящее время достаточно широко и всесторонне исследован структурный, кинематический и динамический анализ, а также синтез различных широко распространённых в технике кулачковых механизмов [1, 2]. В существующих методах проектирования кулачковых механизмов обычно задаются следующие данные: кинематическая схема; закон движения кулачка; закон движения толкателя (обычно, аналог ускорения); ход толкателя; силы, действующие на механизм; максимальный угол давления толкателя и материалы. Определяется минимальный радиус кулачка и проводится профилирование кулачка. При таком подходе не прогнозируется контактная прочность и долговечность механизма. В этом случае может получиться так, что условие надежности не будет выполняться должным образом. Поэтому при проектировании кулачковых механизмов максимальный угол давления толкателя также должен обеспечить контактную прочность высшей кинематической пары «кулачок-толкатель». Надежность и долговечность кулачкового механизма в первую очередь зависит от контактной прочности между кулачком и толкателем. В свою очередь контактная прочность напрямую завистť от радиуса кривизны профиля кулачка. Радиус кривизны профиля кулачка, минимальный радиус кулачка и угол давления механизма взаимосвязаны. С учетом изменения рабочих нагрузок на толкатель решение контактной задачи еще больше усложняется. Определение радиуса ролика толкателя тоже тесно связано с радиусом кривизны кулачка. Поэтому определение оптимального значения минимального радиуса кулачка, обеспечивающее условия передачи сил и контактной прочности, является актуальной задачей.

2. Математическая модель

Рассмотрим центральный кулачковый механизм с роликовым толкателем, как наиболее распространенный. Расчетная схема динамического синтеза этого механизма представлена на рис.1 [3]. Здесь r_0 - минимальный радиус практического профиля кулачка, R - текущий радиус-вектор кулачка, φ_1 - угол поворота кулачка, S - текущий ход толкателя.

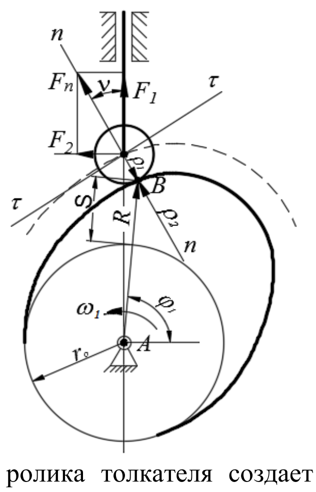

Рис. 1. Расчетная схема динамического синтеза центрального кулачкового механизма с роликовым толкателем

Контакт кулачка и ролика толкателя создает высшую кинематическою пару в виде контакта двух цилиндров и контакт происходит по линии. Тогда условие по контактной прочности между кулачком и роликом толкателя можно выразить, согласно уравнению Герца, следующим образом:

$$\sigma_H = 0{,}418\sqrt{\frac{F_n \cdot E_{np}}{b \cdot \rho_{np}}} \le [\sigma_H], \qquad (1)$$

где b - длина контактной линии или ширина ролика, мм; $[\sigma_H]$- допускаемое контактное напряжение, которое выбирается из справочной литературы согласно выбранного материала, МПа; $E_{np} = \frac{2E_1E_2}{E_1 + E_2}$ - приведенный модуль упругости материалов (E_1- модуль упругости ролика, E_2- модуль упругости кулачка) выбирается из справочной литературы согласно выбранного материала, МПа; ρ_{np}- приведенный радиус кривизны, который определяется следующим образом:

$$\frac{1}{\rho_{np}} = \frac{1}{\rho_1} \pm \frac{1}{\rho_2}, \qquad (2)$$

где ρ_1- радиус кривизны ролика толкателя, мм; ρ_2- радиус кривизны кулачка, мм.

Радиус кривизны ролика подбирается так, чтобы кривая профиля кулачка носил непрерывный характер. Конструктивный профиль кулачка не должен быть заостренным или срезанным. Для этого должно выполняться следующее условие:

$$\rho_1 \le 0{,}4r_0 \quad \text{или} \quad \rho_1 \le 0{,}7\rho_{2\min}, \qquad (3)$$

где, $\rho_{2\min}$- минимальный радиус кривизны центрового профиля кулачка.

Выполнение этих соотношений обеспечивает примерно равную контактную прочность как для кулачка, так и для ролика. Ролик обладает большей контактной прочностью, но так как его радиус меньше, то он вращается с большей скоростью и рабочие точки его поверхности участвуют в большем числе контактов. Рекомендуется выбирать радиус ролика из стандартного ряда диаметров в диапазоне

$$\rho_1 = (0{,}2 \div 0{,}35)r_0 \cdot \qquad (4)$$

Радиус кривизны кулачка можно определить следующим образом [3, 4]:

$$\rho_2 = \frac{\left(R^2 + (R')^2\right)^{\frac{3}{2}}}{R^2 + 2\cdot(R')^2 - R \cdot R''}, \qquad (5)$$

где, R'', R' и R- соответственно, аналог ускорения, аналог скорости и перемещение толкателя.

При синусоидальном законе движения толкателя [3]

$$S'' = \frac{2\pi h}{\varphi_y^2} \cdot \sin\frac{2\pi}{\varphi_y} \cdot \varphi_1, \qquad (6)$$

$$S' = \frac{h}{\varphi_y}\left(1 - \cos\left(\frac{2\pi}{\varphi_y} \cdot \varphi_1\right)\right), \qquad (7)$$

$$R = r_0 + S; \quad S = h \cdot \left(\frac{\varphi_1}{\varphi_y} - \frac{1}{2\pi}\sin\left(\frac{2\pi}{\varphi_y} \cdot \varphi_1\right)\right). \qquad (8)$$

Здесь $h = S_{\max}$ -полный ход толкателя, мм.

Так как r_0 постоянное число, то получим:

$$R = r_0 + S, \quad R' = S', \quad R'' = S''. \qquad (9)$$

Требуемая нормальная сила F_n толкателя на кулачок определяется следующим образом:

$$F_n = \frac{(F_{nc} + F_u + F_{mp} + F_G + F_{np})}{\cos\nu} = \frac{F_1}{\cos\nu}, \qquad 10)$$

где, F_{nc}- полезная сила сопротивления, Н; F_u - сила инерции толкателя, Н; F_{mp}- сила трения между толкателем и направляющей опорой, Н; F_G- сила тяжести толкателя, Н; F_{np}- упругая сила сопротивления пружины, сжимающей толкатель к кулачку, Н; F_1- составляющая нормальной силы вдоль направления толкателя, Н; ν - угол давления кулачкового механизма, град.

Угол давления кулачкового механизма можно определить из условия передачи силы:

$$\nu = arctg\frac{S'}{r_0 + S} \cdot \qquad (11)$$

Ширину ролика обычно определяют из условия контактной прочности. Из конструктивных соображений примем

$$b = (0{,}4 \div 1{,}2)\rho_1. \qquad (12)$$

Учитывая выражения (2)÷(12) в условии контактной прочности (1), можно определить минимальный радиус практического профиля кулачка r_0, обеспечивающий условия передачи силы и контактной прочности при минимальных габаритных размерах кулачкового механизма.

Таким образом, решение задачи зависит не только от выбора оптимального значения отношения $\frac{F_n}{\rho_{np}}$, но и от множества других параметров. Контактное напряжение является функцией многочисленных переменных:

$$\sigma_H = f(r_0, \nu, \rho_1, b, E_{np}, F_1, [\sigma_H]). \qquad (13)$$

С учетом деформаций, перемещений и трений в опорах ролика и податливости элементов конструкции задача еще более усложняется. Поэтому решение задачи можно осуществить методом многопараметрической оптимизации.

3. Результаты исследования

Согласно (1), проводим численный эксперимент и определим контактное напряжение и угол давления ν при следующих входных данных: фаза удаления - $\varphi_у = 60^0$, фаза верхнего выстоя - $\varphi_{вв} = 40^0$, фаза приближения - $\varphi_п = 60^0$, полный ход толкателя - $h = 20$ мм, составляющая нормальной силы вдоль направления толкателя - $F_1 = 1200$ Н, приведенный модуль упругости $E_{пр} = 2{,}1 \cdot 10^5 \frac{\text{Н}}{\text{мм}^2}$ (для сталей), ширина ролика $b = (0{,}4 \div 1{,}2)\rho_1$, допускаемое контактное напряжение - $[\sigma_H] = 594 \frac{\text{Н}}{\text{мм}^2}$.

В результате проведенного численного эксперимента построим графики зависимостей угла давления от угла поворота кулачка только для фазы удаления толкателя (рис 2). В фазах верхнего и нижнего выстоя угол давления не меняется. А фаза приближения идентична фазе удаления. Как видно из рисунка, угол давления уменьшается с увеличением минимального радиуса кулачка. Свое максимальное значение получает в районе 28^0 угла поворота кулачка. Значения минимального радиуса кулачка $r_0 = 50$ мм и $r_0 = 55$ мм не удовлетворяют заданному условию угла давления $\nu_{\max} \le 30^0$. А значения $r_0 = 65$ мм и $r_0 = 70$ мм будут необоснованно завышенными. Поэтому при приведенных начальных данных согласно рисунку, можно принять $r_0 = 60$ мм .

На рис. 3 приведены зависимости контактного напряжения от угла поворота кулачка для различных значений минимального радиуса кулачка. При $r_0 = 50$ мм и $r_0 = 55$ мм контактное напряжение превышает допускаемое значение $[\sigma_H] = 594$ МПа. А при $r_0 = 65$ мм и $r_0 = 70$ мм максимальное значение контактного напряжения не достигает и 500 МПа, что говорит о завышенных габаритах.

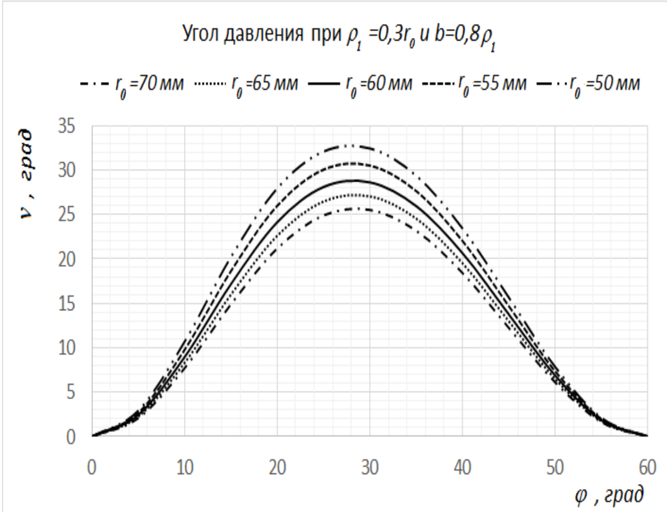

Рис. 2. Зависимость угла давления от угла поворота кулачка

На рис. 4 и 5 представлены изменения контактных напряжений в зависимости от радиуса и ширины ролика, соответственно. При перечисленных выше входных данных здесь тоже можно, согласно условия (1), определить оптимальные значения радиуса ролика $\rho_1 = 0{,}3r_0$ (рис.4) и $b = 0{,}7\rho_1$ (рис.5). Методом последовательных приближений эти значения также можно еще более уточнить.

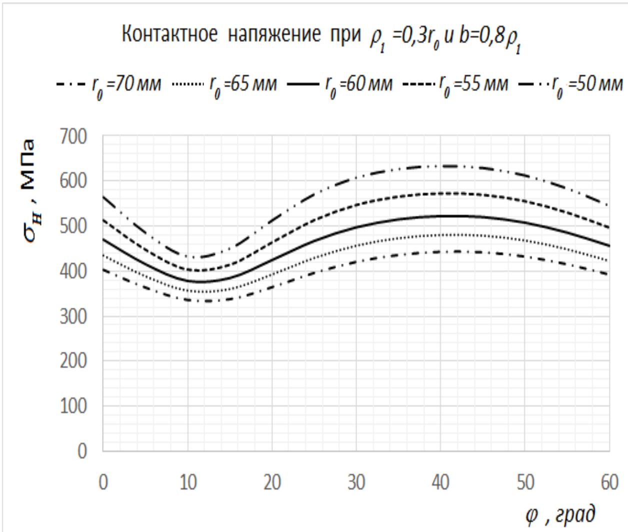

Рис. 3. Зависимость контактного напряжения от угла поворота кулачка

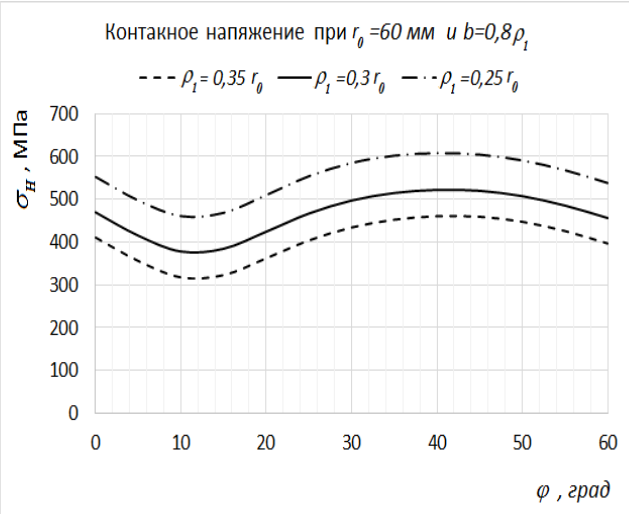

Рис. 4. Зависимость контактного напряжения от угла поворота кулачка для различных значений радиуса ролика

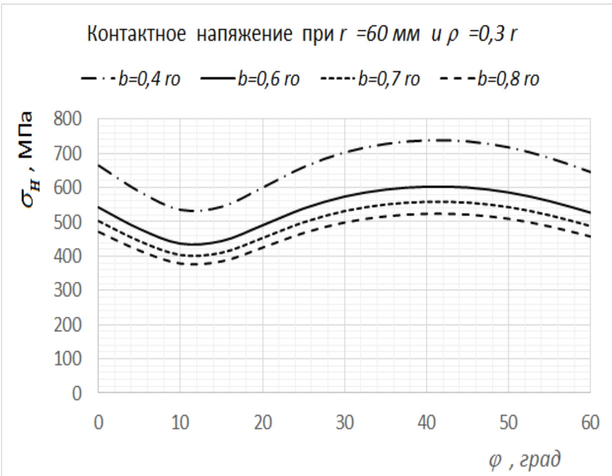

Рис. 5. Зависимость контактного напряжения от угла поворота кулачка для различных значений ширины ролика

Анализ рис. 2÷5 показывает, что угол давления и контактные напряжения свои максимальные значения достигают при различных углах поворота кулачка. Если угол давления получает свой максимум в районе 28^0, то контактные напряжения свои максимальные значения достигают при 41^0 угла поворота кулачка.

4. Выводы

Разработан метод для определения минимального радиуса практического профиля кулачка r_0 и других конструктивных размеров кулачкового механизма, обеспечивающий условия передачи силы и контактной прочности. Предложенный метод позволяет аналитически определить перемещения, скорости, ускорения, углы давления, радиусы кривизны кулачка и контактные напряжения между роликом и кулачком для целого цикла движения кулачка.

Литература

[1]. A.M. Kəngərli. Maşın və mexanizmlər nəzəriyyəsi. – Bakı: “Müəllim”, 2004. - 674s.
[2]. В.А. Юдин, Л.В. Петрокас. Теория машин и механизмов. –М.: «Высшая школа», 1977.
[3]. И.А. Халилов, С.Х. Керимов, А.С. Иманов. Аналитическое определение радиуса кривизны профиля кулачка кулачкового механизма с роликовым толкателем//Вестник Азербайджанской Инженерной Академии/ Баку-2017
[4]. В.А. Ильин, Э.Г. Позняк. Основы математического анализа. Часть II. – М.: «Физматлит», Ч.1 - 2005, 7-е изд., 648с.

Dekelin bərkliyinin ofset çapının kontrastlığına təsiri

Hüseynzadə Elnur Məqsəd oğlu
Azərbaycan Texniki Universiteti,
Maşın və mexanizmlər nəzəriyyəsi kafedrası
E-mail: elnur.huseynzade@hotmail.com

Xülasə
Məqalədə dekelin bərkliyinin ofset çap kontrastına təsiri eksperimental tədqiq edilmişdir. Müəyyən olunmuşdur ki, çap prosesində dekelin bərkliyi artdıqca ofset çap kontrastı azalmışdır. Kontrastın azalması ottisklərin keyfiyyətinin azalmasına səbəb olmuşdur.
Açar sözlər: ofset çapı.dekel, bərklik, çap kontrastı, ottiskin keyfiyyəti.

Çap prosesində mövcud olan əsas qüsurlardan biri rastrlı təsvirlərin kölgələrində qradasiyanın itməsidir. Aparılmış tədqiqat işlərində [1, 2-5] tədqiqatçılar bu qüsurun yaranma səbəblərini aydınlaşdırılmış və onun aradan qaldırılmasının müəyyən yollarını təklif etmişlər. Rastr təsvirlərinin kölgələrinin əks olunmasına nəzarət etmək üçün Şirmer əmsalı kimi məlum olan çap kontrast göstəricisindən istifadə edilir. Təcrübədə çap kontrastı spektrodensitometrlər vasitəsi ilə ölçülür [6]. Bu cihazlar çap kontrastının mütləq qiymətini ölçməyə imkan verir. Kontrastın ayrı-ayri rənglər üzrə təyin edilməsi çap keyfiyyətinin təmin olunmasında əsas amillərdən biri hesab edilir. Bu səbəbdən çap kontrastına texnoloji və konstruktiv parametrlərin təsirinin eksperimental tədqiq edilməsi olduqca vacibdir. Lakin bunlara baxmayaraq, texnoloji və konstruktiv parametrlərin çap kontrastına təsirinin tədqiq olunmasına aid işlər kifayət qədər deyil.

İşin məqsədi:

Bununla əlaqədar olaraq vərəqli ofset çap ottisklərinin kontrastının texnoloji və konsrtuktiv parametrlərdən asılı olaraq tədqiq edilməsinin zərurəti yaranmışdır. Bu məqsədlə dekel materialmm bərkliyinin çap kontrastına təsiri eksperimental olaraq tədqiq edilmişdir. Ottiskərin çap olunmasında “Hubergroup” şirkətinin istehsal etdiyi SURPRİZE tipli triada boyalarından istifadə edilmişdir.

Tədqiqatın metodikası:

Nümunələrin hazırlanması üçün Fujifilm şirkətinin istehsal etdiyi PRO-V markalı çap formalarmdan istifadə edilmişdir. PREPRESS proqramı vasitəsi ilə alınmış nəşrin rəqəmsal montajı rastr prosessorunda (RİP) rastrlanmışdır. Çap formaları kompüter-çap forması texnologiyası ilə Fujifilm şirkətinin istehsalı olan Luxel VX-9600 CTP modelli formaçıxarış qurğusunda eksponlaşdırılm işdir. Eksponlaşdınlmış çap forması Plate Prosessor FLP1260 modelli aşkarlayıcı prosessorda aşkarlanmışdır.

Tədqiqat üçün ottisklər “Komori” şirkətinin istehsalı olan Lithrone-28 modelli vərəqli ofset çap maşmmda çap edilmişdir. Çap sexində rütubət (64,7%) və tempratur (21° C) sabit saxlanmışdır.

Ottisklərin çap olunması üçün 50x70 sm formatlı 135 q/m^2 çəkili Galeri Art tipli parlaq təbaşirli və 80 q/m^2 çəkili “Maestro” tipli ofset kağızından istifadə olunmuşdur.

Nəmləndirici məhlul mövcud təlimata əsasən hazırlanmışdır. Çap zamanı kompressiyaedici CONTİ-AİR markalı dekellərdən istifadə olunmuşdur. Bu dekellərin bərkliyi Şorun A şkalası üzrə HSA 48-63 vahid, qalınlığı isə 1,95mm +_0,01 mm olmuşdur.

İlkin nizamlanmada bərkliyi HSA 55 vahid olan dekeldən istifadə edilmişdir. Bu halda texnoloji təzyiq p=0,65 MPa verilmişdir. Çap formasının səthinin kələ-kötürlüyü R_{max}=21 mkm olmuşdur.

Çap prosesi aşağıdakı qaydada aparılmışdır:

Çap formaları forma silindrlərində bərkidildikdən və çap zonasından ofset kağızı keçirildikdən sonra çap sürəti V=3,0 m/s həddinə qədər yüksəldilmiş, Cyan, Magenta Yellov rəngləri üçün ottisklərin optik sıxlığı 0,95D, Black rəngi üçün isə ottiskin optik sıxlığı 1,25 D -yə çatdırılmışdır.

Proses zamanı hər 3 dəqiqədən bir 5 nümunə götürülmüşdür.

Densitometrik ölçmələr ICplateII densitometrinin köməyi ilə aparılmışdır.

Eyni əməliyyatlar təbaşirli parlaq kağızda çap aparılarkən yerinə yetirilmişdir. Bu zaman ottisklərin optik sıxlığı Cyan, Magenta və Yellov rəngləri üçün 1,5D, Black rəngi üçün isə 1,85D -yə çatdırılmışdır.

Eksperimentlər bərkliyi HSA 48,52,59,63 vahid olan dekellərlə davam etdirilmişdir. Dekellər dəyişdirildikdə təzyiqin ilkin nizamına toxunulmamışdır.

Çapın kontrast göstəricisi olan Şirmer əmsalı K aşağıdakı düsturla hesablanmışdır[2,3].

$$K = \frac{D_s - D_t}{D_s}$$

burada - D_s- tam dolu ottiskin optik sıxlığı; D, - optik tonal sıxlıqdır.

Şəkil 1 və cədvəl 1-də ottisklərin kontrastının (75%-li rastrlı sahələr üçün) ölçülməsinin və hesablanmasının nəticələri verilmişdir.

Cədvəl 1. Şirmer əmsalının K dekelin bərkliyindən - HSA asılılığı

Dekel malerialınm bərkliyi HSA	Boyalar							
	C		M		Y		K	
	Kağızın növü (T- təbaşirli; O - ofset)							
	T	O	T	O	T	O	T	O
48	0,43	0,33	0,41	0,29	0,41	0,27	0,49	0,38
52	0,42	0,32	0,40	0,29	0,39	0,22	0,45	0,37
55	0,39	0,29	0,37	0,24	0,36	0,20	0,42	0,32
59	0.35	0,24	0,32	0,20	0,31	0,13	0,36	0,22
63	0,31	0,22	0,25	0,17	0,29	0,11	0,32	0,20

Ekspermentlərin nəticələri onu göstərir ki, dekelin materialının bərkliyi artdiqca çapın kontrastı azalır. Bu onunla izah olunur ki, dekel materialının bərkliyinin artması çap kontakt zonasmda təzyiqin artmasına səbəb olur. Bu da öz növbəsində boyanm normadan artıq verilməsinə və rastr təsvirlərinin yayılmasına səbəb olur. Yayılma kontrastın azalmasına səbəb olur.

Tədqiqatların nəticələri göstərmişdir ki, dekel materialının bərkliyi Şorun A şkalası üzrə HSA = 48-63 vahid intervalında dəyişdikdə Şirmer əmsalı K : mavi rəng (C) bölməsində ofset kağızı üçün k = 0,33 - 0,22 , təbaşirli parlaq kağız üçün k = 0,43 - 0,31 ; qırmız rəng (M) bölməsində ofset kağızı üçün k = 0,29 - 0,17 , təbaşirli parlaq kağız üçün k= 0,41 - 0,25 ; sarı rəng (Y) bölməsində ofset kağızı üçün k = 0,27 - 0,11 , təbaşirli parlaq kağız üçün k = 0,41 - 0,29 ; qara rəng (K) bölməsində ofset kağızı üçün k - 0,38 - 0,20 , təbaşirli parlaq kağız üçün k = 0,49 - 0,32 hədlərində dəyişmişdir.

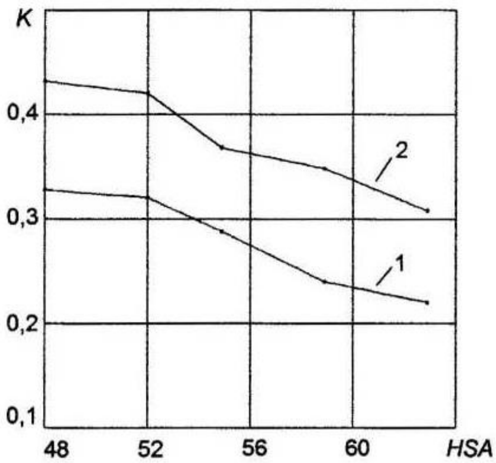

a

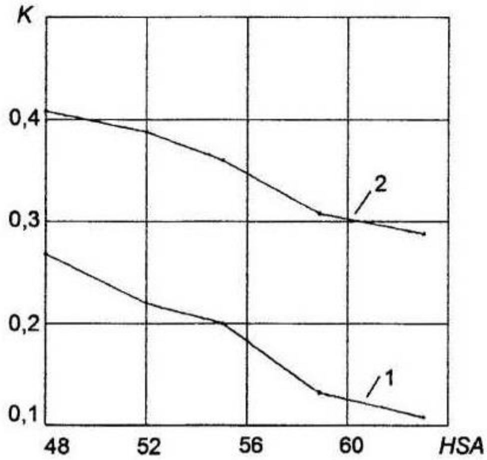

c

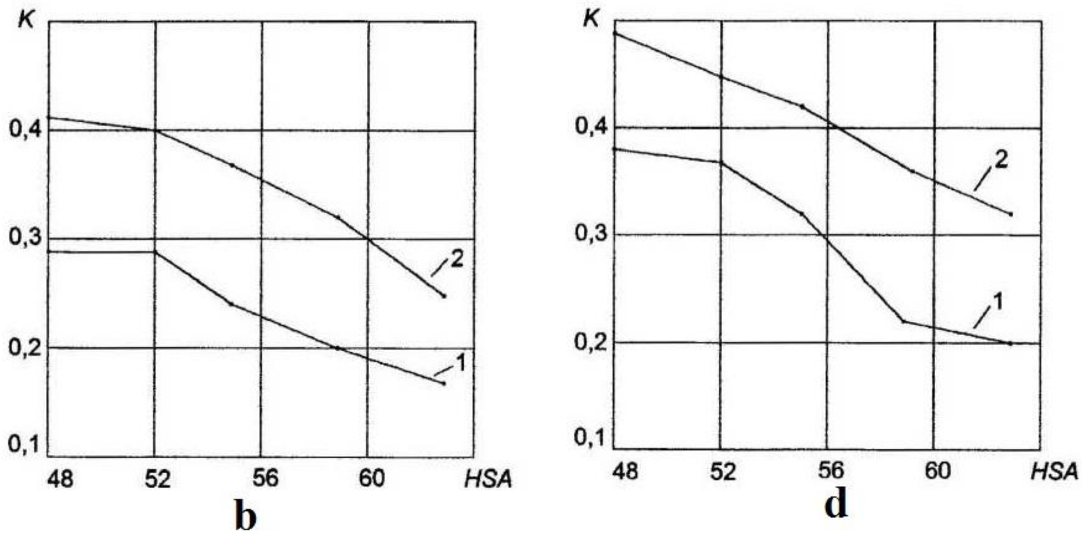

Şəkil 1. Şirmer əmsalının dekeiin bərkliyindən HSA asılılığı
1- ofset kağızı; 2-təbaşirli parlaq kağız
Optik sıxlığı 75 % olan rastrlı sahələr üçün, a-mavi (C), b-qırmızı (moruğu) (M), c-sarı (Y), ç-qara (K)
Çap sürəti- V=3,0 m/s; texnoloji təzyiq -p =0,65MPa;
kağızın çəkisi -ofset kağızı- nv=80 q/m^2, təbaşirli parlaq kağız -m$_t$=135 q/m^2;
forma səthinin kələ - kötürlüyü - R$_{max}$= 21mkm.

Ekspermentlərin nəticələrindən göründüyü kimi dekel materialının bərkliyi (HSA) artdıqca çapın kontrastı azalmışdır. Bu onunla izah olunur ki, dekel materialının bərkliyi HSA 48 vahid olduqda ottisk üzərinə daha çox boya qatı ötürülmüş və bərklik artdıqca boya qatında boyanın miqdarı stabilləşmişdir. Dekel materialının bərkliyi HSA 63 vahidə yüksəldikdə ottisk üzərinə ötürülən boyanın miqdarı azalmış və nəticədə təsvirlər solğun alınmışdır. Bu da kontrastın azalmasına səbəb olmuşdur.

Eksperimentlərin nəticələrindən göründüyü kimi triada rənglərinin ottisklərinin kontrastı demək olar ki, ejmi qanunauyğunluqla dəyişir.

Dekel maerialının bərkliyinin artması Şirmer əmsalmm azalmasma səbəb olur.

Bu baxımdan çap prosesində dekel materialının bərkliyindən asılı olaraq çap tə2yiqinin optimal qiymətdə nizamlanması tələb olunur.

Nəticələr: Aparılmış eksperimental tədqiqatlar dekel materialının bərkliyinin artmasının çap kontrastının azalmasma səbəb olduğunu təsdiq etməyə imkan verir. Bu azalma həmçinin kölgəliyin artması və ottisklərin keyfiyyətinin azalmasma səbəb olur.

Ədəbiyyat

1. Розум О.Ф. Управление тиражестойкоетыо печатных форм. - К.: Техника, 1990-128с.
2. Методы контроля градационной передачи при печати. [Электронный ресурс] - Режим доступа: Журнал КомпьюАрт №2, 2008. www.compuart.ru/article/aspx?-id18697 iid=867
3. Технологический контроль цветовых показателей. [Электронный ресурс] - Режим доступа: https:/www.google.az/webhp?Courceid=chrome putyato.ru /Tech/ print – 23 htm
4. С. Якуцевич, И. Назар, Э. Лазаренко. Качество рулонной офсетной газетной печати на бумаге с различными содержанием макулатуры.// Друкарство- 2004-№5- 33 -38 [Электронный ресурс] - Режим доступа: druk.kpi.ua/ files/publications/ 7166-4_5-04 pdf
5. Измерение цвета в полиграфии.
6. Гудилин Д. Денситометрия в офсетной печати. Журнал КомпьюАрт. №1 -2003 [Электронный ресурс] - Режим доступа: www.compuart.ru/ article/aspx? Id=8351.

Proceedings of the International Symposium of Mechanism and Machine Science, 2017
AzC IFToMM – Azerbaijan Technical University
11-14 September 2017, Baku, Azerbaijan

Topics 3. Dynamics of machines

About application of methods of direct linearization for calculation of interaction of nonlinear oscillatory systems with energy sources

A.A.Alifov
Doctor Technical Science, Professor.
Blagonravov Mechanical Engineering Research Institute of RAS, Moscow, Russia
E-mail: a.alifov@yandex.ru

Abstract.
Use of methods of direct linearization for calculation of the nonlinear oscillatory systems interacting with energy sources of limited power is described. As application of procedure the compelled fluctuations of nonlinear system with limited excitement are considered.
Keywords: method, direct linearization, oscillatory system, interaction, energy source.

1. Introduction

Now the question of economy of energy has moved to the forefront, including in all branches of equipment, at design and calculation of various cars, mechanisms, devices, etc. In this context the theory of oscillatory systems with limited excitement (or interactions of oscillatory systems with energy sources of limited power) which basis was the known physical effect of – Sommerfeld's effect found by A.Sommerfeld at the beginning of the last century (1902) in the analysis of controllability of electric motors deserves attention. Systematic studying of this effect was carried out by V.O.Kononenko whose result was his fundamental monograph which has appeared in 1964 [1]. Development and a condition of this theory has found further in books [2-5, 21] and a set of articles.

In the theory of oscillatory systems with limited excitement the main method of the analysis is the method of averaging of nonlinear mechanics which use is connected by considerable labor and time expenditure depending on a type of the nonlinear characteristic. Such expenses are inherent also in another, described in many works (for example, [2,6-9]), to the known methods of nonlinear mechanics: consecutive approximations, harmonious linearization, power balance, etc. The method of direct linearization (MDL) described in the monograph [11] and a number of articles [12-20] which became further improvement of the method [2,9] offered in 1952 G.Panovko essentially differs from these methods. Indisputable advantage of MDL to carrying out calculations of various technical systems in practice is caused by its properties: simplicity of application; lack of labor-consuming and difficult approximations of various orders applied in the known methods of nonlinear mechanics; possibility of receiving final settlement ratios irrespective of a concrete type and degree of nonlinearity; rather small expenses of work and time (is several orders less in comparison with methods of nonlinear mechanics). Comparison of a number of the results received by the known methods of nonlinear mechanics and MDL stated above contains in [11] and some other works given below in the list of references. It is carried out in case of system with an ideal power source and shows their coincidence: qualitative (full) and quantitative (depending on accuracy parameter: from full coincidence to several percent of discrepancy).

In tasks of the theory of oscillatory systems with limited excitement, at least, two equations, one of which describes actually oscillatory system, another - to loudspeaker of a power source as which in the majority of tasks the electromechanical activator [2] is are considered. As the purpose of the real work is procedure of application of MDL in tasks of the theory of oscillatory systems with limited excitement, will consider her on the basis of the one-mass oscillatory system described by the differential equations of a general view

$$\ddot{x}+k x+c x=F(x,\dot{x},\varphi,\dot{\varphi},\ddot{\varphi}), \qquad (1)$$
$$\ddot{\varphi}=M(\dot{\varphi})+H(\varphi,\dot{\varphi},x,\dot{x},\ddot{x}).$$

The first equation in (1) describes the movement of oscillatory system, the second – an energy source (an electric motor rotor). The $F(x,\dot{x},\varphi,\dot{\varphi},\ddot{\varphi})$, $M(\dot{\varphi})$ and $H(\varphi,\dot{\varphi},x,\dot{x},\ddot{x})$ functions generally nonlinear can also have different concrete types. The last of them reflect respectively a driving force of an energy source and loading (including from oscillatory system) on him.

2. Procedure of replacement of the nonlinear characteristic power source of linear

The nonlinear $G(z)$ or $G(z,\dot{z})$ function depending on some variable of z is replaced by a method of direct linearization [11] with linear function

$$G_*(z) = B + kz\,, \qquad (2)$$

where B and k – the linearization coefficients depending on the linearization accuracy parameter method determining accuracy.

The real characteristics of forces which are, as a rule, nonlinear are approximated in practice in most cases by polynomial function which we will write down in a look

$$G(z) = \sum_n b_n z^n\,,\ b_n = const\,, n = 0, 1, 2, 3, 4, \ldots$$

For this function coefficients of linearization are defined according to [11] expressions

$$B = \sum_n b_n B_n\,,\ B_n = N_n \varsigma^n\,,\ n = 0, 2, 4, \ldots\ (n - \text{even}),\ (3)$$

$$k = \sum_n b_n k_n\,,\ k_n = \bar{N}_n \varsigma^n\,,\ n = 1, 3, 5, \ldots\ (n - \text{odd}),$$

$$N_n = (2r+1)/(2r+n+1)\,,$$

$$\bar{N}_n = (2r+3)/(2r+n+2)\,,\ \varsigma = \max|z|\,,$$

r – linearization accuracy parameter.

Polynomial function it is possible to describe also nonlinear characteristic of an energy source

$$M(\dot{\varphi}) = \sum_i \alpha_i \dot{\varphi}^i\,,\ \alpha_i = const\,,\ i = 0, 1, 2, 3, \ldots, \quad (4)$$

which it is replaceable a linear form

$$M_*(\dot{\varphi}) = B_M + k_M \dot{\varphi}\,. \qquad (5)$$

The power source equation taking into account (5) takes a form

$$\ddot{\varphi} = B_M + k_M \dot{\varphi} + H(\varphi, \dot{\varphi}, x, \dot{x}, \ddot{x})\,. \qquad (6)$$

Coefficients of B_M and k_M are defined by expressions of a look (3) on condition of replacement of ς by $\Omega = \max|\dot{\varphi}|$ giving the maximum size of the average value of speed Ω of a power source considered below.

3. About the decision of the linearized system of the equations

Under conditional names of "a linear form" and "replacement of variables with averaging" in work [11] two methods for the decision of the linearized system of the equations are offered. We will consider here only use of a method of replacement of variables with averaging for the energy source equation because for oscillatory system it is described in [11]. In this method ratios are used

$$x = \upsilon p_\circ^{-1} \cos\psi\,,\ \dot{x} = -\upsilon \sin\psi\,,\ \psi = p_\circ t + \xi\,, \qquad (7)$$

from where expression of $\upsilon = a p_\circ$, where a and $p_\circ$ – respectively amplitude and frequency of fluctuations follows.

We will apply procedure of averaging for the period to the equation (6), believing $\dot{\varphi} = \theta$ therefore we have

$$\frac{d\Omega}{dt} = B_M + k_M \Omega + H(\cdots)\,, \qquad (8)$$

$$H(\cdots) = \frac{1}{2\pi} \int_0^{2\pi} H(\varphi, \dot{\varphi}, x, \dot{x}, \ddot{x})\, d\psi\,.$$

The equation (8) allows to define change in time of average value Ω speeds θ of an energy source. From (7) at $\dot{\Omega} = 0$ we will receive the equation determining parameters of stationary movements

$$B_M + k_M \Omega + H(\cdots) = 0\,. \qquad (9)$$

The equation (9) establishes dependence between amplitude and speed of Ω because generally $H(\cdots) \Rightarrow H(a, \Omega)$.

4. Example

System shown in fig.1 which it is representable the equations of a general view can be the example described by the equations of a look (1)

$$m\ddot{x} + F(\dot{x}) + f(x) = mr\dot{\varphi}^2 \cos\varphi + mr\ddot{\varphi} \sin\varphi\,, \qquad (10)$$

$$J\ddot{\varphi} = M(\dot{\varphi}) + m\ddot{x}r \sin\varphi + mgr \sin\varphi\,,$$

where m – the mass of the unbalanced body fixed at r distance from an engine rotor shaft axis with the total moment of inertia of the I rotating parts, $f(x)$ – the nonlinear elastic force of a spring, $F(\dot{x})$ – the nonlinear force of resistance, $M(\dot{\varphi})$ – a difference of the rotating moment of an energy source and the moment of forces of resistance to rotation, $\dot{\varphi}$ – the speed of rotation of the engine.

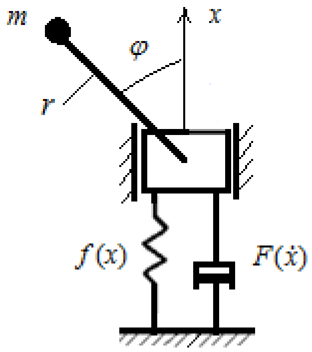

Fig. 1

System presented in fig.1 in case of $f(x) = cx + \gamma x^3$ and $F(\dot{x}) = k\dot{x}$ is considered in work [1] by means of an asymptotic method of averaging.

The nonlinear equations (10) get on the basis of (2) and (4) following linear forms:

$$m\ddot{x} + k_F(\upsilon)\dot{x} + \omega^2(a)x = mr\dot{\varphi}^2\cos\varphi + mr\ddot{\varphi}\sin\varphi, \quad (11)$$

$$J\ddot{\varphi} = B_M(\Omega) + k_M(\Omega)\dot{\varphi} + m\ddot{x}r\sin\varphi + mgr\sin\varphi,$$

where $\omega^2(a)$ and $k_F(\upsilon)$ – coefficients of linearization of nonlinear elastic forces and friction taking into account that at their linearization $\max|x| = a$, $\max|\dot{x}| = \upsilon$.

By a method of replacement of variables with averaging of the solution of the equations (11) it is possible to construct, using ratios of type (7), i.e.

$$y = \upsilon\theta^{-1}\cos\psi, \ \dot{y} = -\upsilon\sin\psi, \quad \psi = \theta t + \xi.$$

On the basis of these ratios we have from (11) equations

$$\frac{d\upsilon}{dt} = \frac{\upsilon}{2m}k_T(\upsilon,\Omega), \ \frac{d\xi}{dt} = \frac{\omega^2 - \Omega^2}{2\Omega}. \quad (12)$$

The second equation (11) according to (8) has an appearance

$$\frac{d\Omega}{dt} = \frac{1}{J}\left[B_{TM}(\upsilon,\Omega) + \Omega\, k_M(\Omega)\right]. \quad (13)$$

From (12) and (13) follow at $\dot{\upsilon} = 0$, $\dot{\xi} = 0$, $\dot{\Omega} = 0$ equations

$$k_T(\upsilon,\Omega) = 0, \ B_{TM}(\upsilon,\Omega) + \Omega k_M(\Omega) = 0, \quad (14)$$

the parameters of stationary movements allowing to define.

References

1. Kononenko V.O. *Kolebatel'nye sistemy s ogranichennym vozbuzhdeniem* [Oscillatory systems with limited excitement]. Moscow, Nauka Publ., 1964. (In Russ.).
2. *Vibracii v tehnike* [Vibrations in equipment]. T.2 / Pod red. I.I.Blehmana. Moscow, Mashinostroenie Publ., 1979. (In Russ.).
3. Ganiev R.F., Koval'chuk P.S. *Dinamika sistem tverdyh i uprugih tel* [Dynamics of systems of solid and elastic bodies]. Moscow, Mashinostroenie Publ., 1980. (In Russ.).
4. Alifov A.A., Frolov K.V. *Vzaimodejstvie nelinejnyh kolebatel'nyh sistem s istochnikami jenergii* [Interaction of nonlinear oscillatory systems with energy sources]. Moscow, Nauka Publ., 1985. (In Russ.).
5. Krasnopol'skaja T.S., Shvec A.Ju. *Reguljarnaja i haoticheskaja dinamika sistem s ogranichennym vozbuzhdeniem* [Regular and chaotic dynamics of systems with limited excitement]. Moscow-Izhevsk, NIC «Reguljarnaja i haoticheskaja dinamika» Publ., Institut komp'juternyh issledovanij, 2008. (In Russ.).
6. Bogoljubov N.N., Mitropol'skij Ju.A. *Asimptoticheskie metody v teorii nelinejnyh kolebanij* [Asymptotic methods in the theory of nonlinear fluctuations]. Moscow, Nauka Publ., 1974. (In Russ.).
7. Butenin N.V., Nejmark Ju.I., Fufaev N.A. *Vvedenie v teoriju nelinejnyh kolebanij* [Introduction to the theory of nonlinear fluctuations]. Moscow, Nauka Publ., 1976. (In Russ.).
8. Hajasi T. *Nelinejnye kolebanija v fizicheskih sistemah* [Nonlinear fluctuations in physical systems]. Moscow, Mir Publ., 1968. (In Russ.).
9. Panovko Ja.G. *Osnovy prikladnoj teorii kolebanij i udara* [Bases of the applied theory of oscillations and blow]. Leningrad, Mashinostroenie Publ., 1976. (In Russ.).
10. Lojcjanskij L.G. *Svobodnye i vynuzhdennye kolebanija pri nalichii kvadratichnogo i promezhutochnogo mezhdu linejnym i kvadratichnym zakonov soprotivlenija* [The free and compelled fluctuations in the presence of square and intermediate between linear and square laws of resistance]. *Izv. AN*

SSSR, OTN, Inzhenernyj sbornik, T.18, 1954. pp.139-148. (In Russ.).
11. Alifov A.A. *Metody prjamoj linearizacii dlja rascheta nelinejnyh sistem* [Methods of direct linearization for calculation of nonlinear systems]. Moscow-Izhevsk, NIC «Reguljarnaja i haoticheskaja dinamika» Publ., 2015. (In Russ.).
12. Alifov A.A. *Dejstvie vibracij na sistemy s nelinejnym treniem* [Action of vibrations on systems with nonlinear friction]. «*Tehnika*», № 4, 2001, pp.47-51. (In Russ.).
13. Alifov A.A. *O nekotoryh metodah rascheta nelinejnyh kolebanij* [About some methods of calculation of nonlinear fluctuations]. *V mire nauchnyh otkrytij*, T.13, №1, 2011, pp.155-159. (In Russ.).
14. Alifov A.A. *Metody rascheta nelinejnyh sistem, osnovannye na metodah prjamoj linearizacii* [The methods of calculation of nonlinear systems based on methods of direct linearization]. *Problemy mashinostroenija i avtomatizacii – Engineering & Automation Problems*. 2011. no. 2, pp.97-99. (In Russ.).
15. Alifov A.A. *Metody rascheta nelinejnyh kolebanij s ispol'zovaniem prjamoj linearizacii nelinejnostej* [Methods of calculation of nonlinear fluctuations with use of direct linearization of not linearities]. Proceedings of the IX Vserossijskoj nauchnoj konferencii «Nelinejnye kolebanija mehanicheskih sistem» / Pod redakciej D.V. Balandina, V.I. Erofeeva, I.S.Pavlova. Nizhnij Novgorod: Izdatel'skij dom «Nash dom», 2012. pp.58-62. (In Russ.).
16. Alifov A.A. *Metod prjamoj linearizacii nelinejnostej smeshannogo tipa dlja rascheta nelinejnyh kolebanij* [Method of direct linearization of not linearities of the mixed type for calculation of nonlinear fluctuations]. Dinamika nelinejnyh diskretnyh jelektrotehnicheskih i jelektronnyh sistem: Proceedings of the 10-j Vseros. nauch.-tehn. konf. Cheboksary: Izd-vo Chuvash. un-ta, 2013. pp.12-14. (In Russ.).
17. Alifov A.A. *Avtokolebanija mehanicheskoj sistemy s udarnym vozdejstviem* [Self-oscillations of mechanical system with shock influence]. Proceedings of the VIII Vseros. nauch. konf. «Nelinejnye kolebanija mehanicheskih sistem». V 2-h tomah. Tom 1 / Pod red. D.V.Balandina, V.I.Erofeeva. Nizhnij Novgorod: Izdatel'skij dom «Dialog Kul'tur». 2008. pp.64-66. (In Russ.).
18. Alifov A.A. About some methods of calculation nonlinear oscillations in machines // Proceedings of the International Symposium of Mechanism and Machine Science, October 5-8, 2010, Izmir, Turkey, 2010, pp.378-381.
19. Alifov A.A. Methods of calculation of the nonlinear systems, based on a straight linearization of nonlinear functions // Dynamical system modelling and stability investigation: Proceedings of the XV International Conference, Kiev, 2011, p.20.
20. Alifov A.A. Methods of direct linearization for calculation of nonlinear oscillations / Engineering & automation problems, 2015, no.2, pp.84-87.
21. A.A.Alifov, K.V.Frolov. Interaction of nonlinear oscillatory systems with energy sources.– Hemisphere Publishing Corporation, Taylor & Francis Group, New York, Washington, Philadelphia, London. 1990, 324 p.

Proceedings of the International Symposium of Mechanism and Machine Science, 2017
AzC IFToMM – Azerbaijan Technical University
11-14 September 2017, Baku, Azerbaijan

The impact of the dynamics of take-up mechanism on the distance between the weft threads in the development of fabric with the variable density of weft

Veliyev Fazil Ali, Jafarov Elman Novruz
Azerbaijan State University of Economics (UNEC)
E-mail: fazil-uzbek@mail.ru

Abstract:
In the commodity is determined by the influence of the dynamics of the regulator to the variable structure of tissues. It is shown that taking into account the compliance of the elements of commodity regulator design results in uneven distances between adjacent weft and smoothing the boundaries between the seal and sparse tissue sections.
Keywords: **weft, warp, vaillant, trademark mechanism, the main regulator, cloth.**

Introduction. A device fitting to the STB type of weaving machine allowing to produce wide range of fabric with variable density in weft has been developed [1]. The principal difference of the device is an additional programme controlled loom motor , abruptly changing the speed of the cross- shaft weaving machine and providing of manufacturing the tighten and loose parts of weft fabric.

Taking into consideration the flexibility of the elements of the construction of take-up mechanism (gears, shafts, etc.), we consider that, fluctuations in the mechanism due to the abrupt change in the angular speed of the cross-shaft leads to irregularity of distances between adjacent weft threads and smoothing of the boundaries between the tightened and loose parts of weft fabric.

Theoretical justification:

Let us estimate the impact of the dynamics of the device on the location of weft threads in the fabric. Imagine a dynamic model of the device in the form of a dual-mass (Fig. 1-a), where the cross section *a* corresponds to a position on the cross- shaft sprocket chain drive connecting the cross shaft with an additional electric loom motor. The driven mass (J_1 and J_2) and stiffness (c_1 and c_2) corresponds to *1* - worm gear of take-up mechanism and 2- take-up roller.

The latter is connected with beam by means of an elastic filling with driven stiffness c_3. The pinning point for the elastic filling systems on the beam is considered fixed/immovable, since it is assumed that the number of pay off the wrap in one turn of the weaving machine corresponds to the amount allocated in the same time for the fabric. In this case, the length of elastic filling system does not change.

Abrupt change of angular speed of the cross-shaft in section *a* allows to consider the system of take-up mechanism in development of fabric with variable density as a kinematically induced system and it considers its movement as a movement of a massless system in adding the forced oscillations/vibrations of the system with the additional fixing at the kinematic excitation point caused by the forces of inertia of the first movement [2]. The dynamic model of the system for determining the forced oscillations (with additionally fixed section *a*) is shown in Fig. 1-*a*.

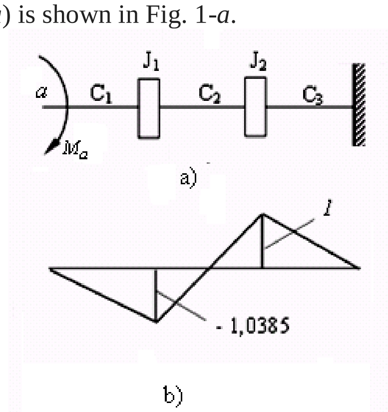

Fig. 1

In determining the forced oscillations of the system with additional fixing in generalized coordinates, the complete displacement of the points of the system can be written as (1):

$$\bar{x}_1=x_1+q_1u_{11}+q_2u_{12}, \qquad (1)$$
$$\bar{x}_2=x_2+q_1u_{21}+q_2u_{22},$$

Where q_i – is the generalized coordinates; u_{ij} – is the corresponding amplitude; x_i – is the point of massless displacement system.

To determine the correlation between the displacement of the motion of a massless system we will use M_a moment in cross-sectional *a* with the displacement of x_a section. Then

$$x_a=M_a/c_1+M_a/c_2+M_a/c_3=M_a(c_2c_2+c_1c_3+c_1c_2)/(c_1c_2c_3)$$
$$x_1=M_a/c_2+M_a/c_3, \quad x_2=M_a/c_3$$

After transformations

$$x_1=x_a(c_1c_2+c_1c_3)/(c_1c_2+c_1c_3+c_2c_3),$$
$$x_2=x_ac_1c_2/(c_1c_2+c_1c_3+c_2c_3)$$

In motion of the system with a fixed section *A* the moments of forces of inertia P are influenced to its mass

$$P_1=-J_1\ddot{x}_a(c_1c_2+c_1c_3)/(c_1c_2+c_1c_3+c_2c_3),$$
$$P_2=-J_2\ddot{x}_ac_1c_2/(c_1c_2+c_1c_3+c_2c_3).$$

The experiments made on the weaving machine and their processing by the method of mathematical statistics indicate that, the angular speed of cross-shaft in the transition from the tightening parts to loose is approximated well by the expression [3]:

$$x_a=\omega(t)=\omega_0+A\,[1-\exp(\alpha t)] \qquad (2)$$

where in ω_0 – is the angular speed of the cross-shaft; A – is the volume of the abrupt action of the angular speed of the cross-shaft , determining the difference between the densities of tightened and loose fabric sections ; α - is an empirical factor depending on the characteristics of the additional engine and design features of the device; t-time.

In our case, α= -0.9. Acceleration of x_a we will find from (2). After substituting in the expression for P_1 and P_2 we will obtain the moments of inertia forces

$$P_1=J_1A\alpha(\exp\alpha t)(c_1c_2+c_1c_3)/c_1c_2+c_1c_3+c_2c_3), \qquad (3)$$
$$P_2=J_2A\,\alpha(\exp\alpha t)c_1c_2/(c_1c_2+c_1c_3+c_2c_3)$$

For the system (3) with a fixed section *a* (Fig. 1-b), mass equations of motion are of

$$J_1\ddot{x}_1+c_1x_1+c_2\,(x_1-x_2)=0 \qquad (4)$$
$$J_2\ddot{x}_2-c_2\,(x_1-x_2)-c_3x_2=0$$

The equations of motion in generalized coordinates have the form

$$\ddot{q}_1+p_1^2\,q_1=Q_1/M_1,\ \ddot{q}_2+p_2^2\,q_2=Q_2/M_2$$

and after substituting in them the generalized forces $\sum_{i=1}^{n} P_iu_{ik}$
and the generalized mass and $M_k=\sum_{i=1}^{n} m_iu^2_{ik}$ taking into account the permanent and found natural frequencies values

$$\ddot{q}_1+0{,}755\bullet10^6q_1=0{,}507A\exp(-0{,}9\,t) \qquad (5)$$
$$\ddot{q}_2+0{,}274\bullet10^6q_2=-1{,}389A\exp(-0{,}9\,t).$$

The initial conditions, appropriate to the time of transition from the development of tightened to the loose parts:

$$x_{10}=M_T/c_1,\quad \dot{x}_{10}=\omega_0: \qquad (6)$$
$$x_{20}=M_T/c_1+m_t/c_2,\quad \dot{x}_{20}=\omega_0:$$

For density of the loose and tightened fabric parts respectively 20 and 30 threads/cm and the speed of the weaving machine of 240 turns in one minute we have ω_0=24 c^{-1},A=12 c^{-1}. The experimental moment of M_t of a tension of fabric on the take-up roller equals to 100 N m.

Since we are interested in movements on the take-up roller, we will use the second equation from (1). Substituting in it the expression for the generalized coordinates found from (5) taking into account (6) - and neglecting insignificant terms, we obtain

$$\bar{x}_2=8{,}85\cdot10^{-3}\,n-4{,}5\,[\,1-\exp(-0{,}9\,n)\,] \qquad (7)$$

where replacement of $t=n\cdot T$ has been made (n-is a number of a turn after transition to development of the loose parts, T – is time of one cycle.

Distances between the adjacent weft thread are characterized by angles of rotation of a take-up roller in the next cycles. The formula (7) gives a total angle of rotation of a take-up roller for *n* turns and allows to determine easily the required sizes as a difference of value x_2 for *n* and *(n-l*) of turns.

Example:

The experimentally determined stiffness and inertial characteristics are having the values: $J_1=2\cdot10^{-2}$ and $J_2=5{,}4\cdot10^{-3}$ kq·м; $C_1=1.12\cdot10^4$ and $C_2=0{,}2\cdot10^4$ and C_3=40 Nм. Taking into consideration these values on the equation (4) the natural frequencies are calculated; $P_1=0{,}869\cdot10^3$ and $P_2=0{,}523\cdot10^3$, c^{-1}. The correlation between the amplitudes: $u_{11}=-1{,}0385\ u_{21}$, $u_{12}=0{,}26\ u_{22}$. The forms of vibrations are shown in Fig. 1-*b*.

CONCLUSIONS

1. Has been developed the analytical method of an assessment of impact of dynamics of the take-up mechanism on change of distance between weft threads at production of fabrics of variable density on a weft.

2. Taking into account the forces of inertia and elasticity of links of the take-up mechanism has been obtained the analytical expression (7), for definition of an angle of rotation of a take-up roller depending on consecutive number of a turn of the main shaft after changing the density of the developed part.

References.

1. A. c. 124-9081 USSR. Weaving machine/F. A. Veliyev. –Published 1986

2 Automatic power supply of weaving machine with basis and weft threads. – M.: Light industry, 2005.

3. Veliyev F. A. “Technology of textile industry” 1988, № 6, p.59-62.

Proceedings of the International Symposium of Mechanism and Machine Science, 2017
AzC IFToMM – Azerbaijan Technical University
11-14 September 2017, Baku, Azerbaijan

Dual-scheme profiling technique for the liquid rocket engine

Parviz Shahmurad ABDULLAYEV[1*], Musa Khanlar ILYASOV[2], Nijat Parviz ABDULLA[3]
[1,2] National Aviation Academy, Baku, Azerbaijan
E-mail: a_parviz@mail.ru
[3] METU NCC, Ankara, Turkey

Abstract

The paper studies profiling method of supersonic nozzle based on the velocity distribution of the 2D gas flow along the nozzle axis. Wherein, uniform flow on the exit section of the nozzle is required. The equations of gas dynamics are solved with a new equation for velocity distribution along the nozzle axis by applying the method of characteristics, which stipulates the development of dual-scheme profiling technique for the liquid rocket engine (LRE) nozzle.

Keywords: liquid rocket engine, optimal nozzle, supersonic flow, perfect gas, Prandtl Meyer function, method of characteristics, relative error

1. Introduction

The expansion of the space exploration area demands future enlargement in launching rockets of different classes with payloads from hundreds of kilograms to tens and more tons.

The optimization of the nozzle construction is carried out, in order to ensure the maximum possible payload. The main goal of the optimization process is to select the area expansion ratio of the nozzle ($\bar{A} = A_e / A_*$) which will be the most advantageous combination from the position of specific impulse I_{sp} and the weight of the engine structure. Particular attention is paid to the choice of the optimal expansion ratio of the LRE. Thus, for example, gas pressure falling at the nozzle exit section leads to the growth of I_{sp} and increment of the geometric dimensions of supersonic part of the nozzle. Increasing of the mass and dimensions of the nozzle results in a reduction while the maximum possible payload taking out by the rocket. In addition, the nozzle dimensions may enable LRE to be satisfactorily assembled in the tail part of the rocket. The rate of the specific impulse in the vacuum mostly depends on the losses in the nozzle, which is increased by the expansion ratio of nozzles. In this case, the expansion ratio is determined both as the geometry of the nozzle contour (throat and exit areas), and as the ratio of the pressures at the inlet and outlet. Therefore, one of the main research fields is the retrieval of an optimal contour of the subsonic and supersonic parts of the LRE

2.The aim of the paper

The purpose of the paper is to form methodology for the preliminary optimal geometry design of the nozzle contour based on the analysis of the theoretical and experimental research results of rocket engines

3.Brief information on the theoretical foundations of gas flows modeling in nozzles

The flow of gas in the LRE chamber is researched for the purpose of selecting the geometric parameters of jet nozzles, determining their thrust and energy characteristics. By the development of rocket technology, the price of a unit of the engine specific impulse is increasing. Thus, the growth of a specific impulse by only 0.3% may lead to an increase in the payload weight up to 1.5%. Calculations on one-dimensional theory enable the determination of the nozzle impulse accurately to several percent. In this case, calculation inaccuracy of integral characteristics of gas flows in jet nozzles by numerical methods should not exceed 0.1%. Methods which do not meet this accuracy are suitable only for a qualitative description of the flow [1,2].

In addition, defining the target task and the specific flight trajectory of the rocket, taking into account the limitations on the dimensions and mass of the nozzle is very necessary in selecting the optimal nozzle. These constraints lead to a very complicated task of profiling and optimization of the nozzle.

Despite various limitations, the main difficulties in creating the definite methodology for calculating the LRE nozzle are related to:

- changing properties of real gas
- inconstant gas flow in different sections,
- non-stationary nature of the stream of gas flow,
- heterogeneity of gas,
- variability of gas composition,
- friction between gas and nozzle walls,
- heat transfer through the nozzle walls,

- viscosity and friction between gas layers,
- different directions of vectors and values of gas velocities at different points of the considered cross-section of the nozzle, etc.

Therefore, the LRE nozzles contour formation is led by using the solution of gas dynamic equations system - the momentum equation (Euler equation), energy, and continuity. In the absence of irreversible processes, this system for a stationary non-vortex axisymmetric (two-dimensional) flow of an in viscid and non-heat-conducting gas, by a constant level of the heat capacity ratio γ, can be indicated as below [1,2]:

$$(u^2-a^2)\frac{\partial u}{\partial x}+uv\left(\frac{\partial u}{\partial y}+\frac{\partial v}{\partial x}\right)+(v^2-a^2)\frac{\partial v}{\partial y}=a^2\frac{v}{y}, \qquad (1)$$

$$\frac{\partial u}{\partial y}-\frac{\partial v}{\partial x}=0, \qquad (2)$$

where u,v - components of flow velocity W on the coordinate axis x, y; x directed along the nozzle axis, the axis y - perpendicular to it.

The system of differential equations (1-2), depending on the flow velocity, can be of various types: elliptical ($M<1$), parabolic ($M=1$), and hyperbolic ($M>1$). Properly, the numerical methods for this system solving are different. Consequently, the questions of profiling the subsonic and supersonic nozzle parts are usually considered separately, which is another drawback of all modern calculation methods.

The profile of the subsonic part of the nozzle can be calculated by solving the equations system (1-2) within specific boundary conditions. However, the solution to this system is extremely difficult. Therefore, a wide application for profiling the subsonic part of the nozzle obtained empirical equations [1, 2, 12, 13].

Differential equations solution (1-2) by the method of characteristics [1, 2, 14, 15] is the base for creating the theoretical profile of the supersonic nozzle part. In addition, other methods of creating optimal nozzles for rocket engines are quite integrated and implemented in practice [14, 15].

In general, the nozzles obtained on the basis of solution of differential equations system (1-2) are characterized by two parameters: the isentropic expansion rate γ and the number M, i.e. Mach number. Herein the specification of the length or radius of the nozzle outlet section within M and γ explicitly defines contour coordinates from the critical (throat) to the exit section of the nozzle.

4. Research analysis in the field of profiling supersonic nozzles of LRE

Generally, development LRE covers two kinds of nozzles: nozzles with uniform characteristics and nozzles with extreme characteristics [8]. The contour of the supersonic part of the extreme nozzle within the same nozzle area expansion ratio is shorter than the nozzles with uniform characteristics. However, the contour of the supersonic part of the nozzle with a uniform characteristic has the advantage that at the same length it has minimum losses for exhaust gases scattering.

Theoretical basis for profiling the supersonic nozzles of LRE in order to achieve the best combination "specific impulse-structural weight" developed in the middle of the last century [3-5]. It has theoretically been proved that the search of an optimal nozzle contour is a variational problem that reduces to numerical integration of the system of ordinary first-order differential equations. Calculations show that the nozzle of the smallest length is not the best by weight characteristics [5]. In other researches presented formulation of the problem and definition of an extreme nozzle as gaining the greatest thrust at given diameters and length [6]. Theoretical-calculation work has been carried out in the field of influence degree of the basic assumptions used in profiling, and proposed a generalized theory of the design of extreme nozzles [7,8]. The rest research works inform about the comparative theoretical studies of the thrust characteristics of rocket nozzles constructed by various methods. It has been shown that the extremely shortest nozzles with a uniform characteristic hold the smallest losses [9].

However, all the mentioned researches do not allow the formation of the initial shape of the nozzle, which should be optimized from the point of view of LRE energy-mass characteristics ($m_{LRE}\rightarrow m_{LRE.\min}$ and $I_{s.i}\rightarrow I_{s.\max}$). Therefore, the research of gas-dynamic and energy characteristics of nozzles from the area expansion ratio is of great importance, which is closely related to the modeling problem of gas flows in nozzles.

5. Problem formulation and solution in the first approximation

The analysis of the existing researches results shows that the design of the nozzle contour in various formulations does not imply any preliminary correct distribution of the parameters γ and M along the length of the nozzle (on the axis or the contour curve). The solution of equations (1-2) within such problem formulation on nozzle profiling requires large mathematical resources. So, according to the logic and sequence of the performed operations by the thermogasdynamic calculation of the LRE, the values of the gas flow parameters are found step by step. Each subsequent value of any thermogasdynamic parameter is calculated on the its previous value.

Alongside with this, if the required distribution of flow parameters is known at the outlet section of the nozzle under given constraints, the contour providing this distribution of the nozzle is defined by calculation. In this case, the solution of the inverse problem of gas dynamics arises. If in this case one of the parameters defining the task must minimized ($I_{sp.i} \rightarrow I_{sp.\max}$ and $m_{LRE} \rightarrow m_{LRE.\min}$), then the problem refers to the class of extremes. Since the contour of the nozzle is specified before solving the problem by some unknown function, then the problem becomes variational.

Thus, the question is: Is it possible to preset the preliminarily known distribution of some gas flow parameters along the length of the nozzle (on contour curve or on the axis) in the first approximation? Such kind of opportunity would allow the more rational use of computational resources for the purpose of creating an optimal or extreme LRE nozzle.

In order to answer the current question theoretical, computational and experimental research analysis were led in the field of designing the LRE chamber. Review of researches results shows that on average distribution of thermogasdynamic parameters (p , T , W etc.) along the length of the rocket engine chamber (combustion chamber, subsonic and supersonic part of the nozzle) is of a certain character. This circumstance is related with the basic principles of the nozzle theory. Naturally, the distribution of parameters is determined by the complex nature of the entire system of thermogasdynamic processes (see p. 3), proceeding in a rocket engine.

A preliminary analysis of these mentioned researches shows an approximate asymmetric sigmoid velocity distribution of the gas flow along the length of the chamber (along the nozzle axis) of the LRE. This velocity distribution (combustion chamber + subsonic and supersonic part of the nozzle) can be indicated as following functions:

$$y(x) = \frac{1+\alpha+bx}{1+\alpha e^{-kx}}, \qquad (3)$$

$$\text{or} \quad y(x) = d + \frac{a-d}{1+\left(x/c\right)^m}, \qquad (4)$$

where α, a, d, c, k, m - some unknown coefficients, which can be specified on the basis of numerical calculations or experimental data, x-the coordinate of the point under consideration on the nozzle axis. It should be noted that an attempt to describe the velocity distribution of the free gas stream over the sigmoid was considered in [10,11]. Formulas (1) and (2) for the gas velocity can also be represented for relative lengths $\bar{x} = x/L$.

$$w(x) = \frac{1+\alpha+b\bar{x}}{1+\alpha e^{-k\bar{x}}}, \qquad (5)$$

$$\text{or} \quad w(x) = d + \frac{a-d}{1+\left(\bar{x}/c\right)^m}. \qquad (6)$$

The contour of the LRE nozzle is created thereby. Firstly, for each value x or $\bar{x}$ the velocity values $w(x)$ on the nozzle axis are determined starting from the critical (throat) section (or from the outlet section of the nozzle):

$$w(x) = w_e - \frac{w_e - w_0}{1+\left(x/c\right)^m},$$

$$\text{or} \quad w(\bar{x}) = w_e - \frac{w_e - w_0}{1+\left(\bar{x}/c\right)^m}. \qquad (7)$$

where w_0 - the velocity of the gas flow in the minimum (throat) section of the nozzle, w_e - the velocity of the gas flow at the outlet from the nozzle. It should be noted that the choice of speed w_0 depends on the shape of the transition surface through the sound speed, which can be flat or curved. An analysis of the results of the researches shows that in order to design the optimal contours of LRE nozzles, the most suitable preliminary velocity distribution along the axis is (7). Thus, system (1-2) can be supplemented by one more equation:

$$\frac{du}{dx} = \frac{u_e - u_0}{\left(1+\left(\frac{x}{c}\right)^m\right)^2} \cdot \left(\frac{x}{c}\right)^m \cdot \frac{m}{x}, \quad u = w_x$$

By taking into account the above mentioned, let us consider a dual-scheme calculation technique for determining the main parameters of a supersonic 2D flow and nozzle geometry.

First calculation scheme (C1). As it has already been noted, the method of characteristics (MC) is often used to calculate the parameters of the expanding part of the nozzle. For a supersonic irrotational perfect gas, the application of the MC starts on sonic line and specified by the following equations [14,15]:

1) first characteristics lines group (C^+)

$$d(\nu-\theta) = 0, \; dy/dx = tg(\theta+\mu). \qquad (8)$$

2) second characteristics lines group (C^-)

$$d(\nu+\theta) = 0, \; dy/dx = tg(\theta-\mu). \qquad (9)$$

Proceedings of the International Symposium of Mechanism and Machine Science, 2017
AzC IFToMM – Azerbaijan Technical University
11-14 September 2017, Baku, Azerbaijan

where ν - the value of the Prandtl-Mayer function obtained from a given M at the considered point, θ - the local flow angle (the angle of inclination of the velocity $\vec{w}$ with respect to the nozzle axis, μ - the angle between the velocity vectors $\vec{w}$ and the tangent to the characteristic line at the point under consideration. In the real conditions the characteristics are curved. The grid formed by the characteristic curves C^+ and C^- will be accurate when they are very close (Fig.1).

In equations (8) and (9), the Prandtl-Mayer function for the considered points will be determined by the formula [14, 15]:

$$\nu = \nu(M) = \sqrt{\frac{\gamma+1}{\gamma-1}} \cdot \arctan\left(\sqrt{(M^2-1)\frac{\gamma-1}{\gamma+1}}\right) - \arctan(\sqrt{(M^2-1)}) \qquad (10)$$

where γ - the heat capacity ratio, M - the Mach number of the gas flow at mentioned the nozzle point.

Thus, on the characteristic line C^+ (points 1 and 3)

$$\theta_1 - \nu(M_1) = \theta_3 - \nu(M_3), \qquad (11)$$

on the characteristic line C^- (points A and 3)

$$\theta_3 + \nu(M_3) = \theta_A + \nu(M_A). \qquad (12)$$

Then for node 3 with coordinate x_3 we can write (Fig. 2)

$$\theta_3 = \frac{1}{2}\left(\tilde{N}^- + \tilde{N}^+\right), \;\; \nu(M_3) = \frac{1}{2}\left(C^- - C^+\right). \qquad (13)$$

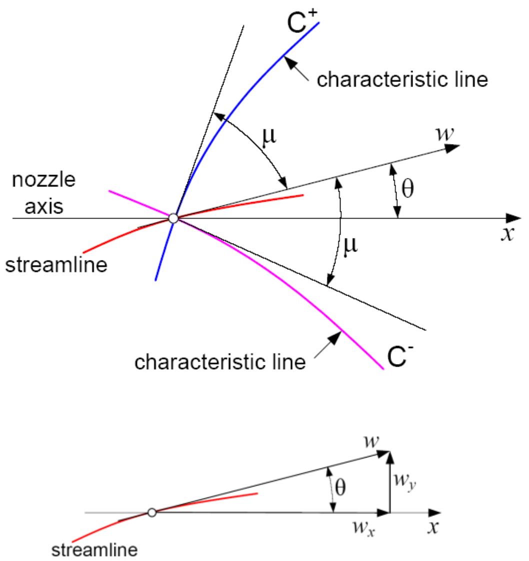

Fig. 1. Geometric representation of the Method of Characteristics

Second calculation scheme (C2). An analysis of the researches shows that the nozzle axis can also be taken as an initial line, by taking into account the equation (7). So the application of the method of characteristics is based on the data obtained from the thermodynamic calculation of the LRE by using a formula (7). Then second calculation scheme C2 is applied in parallel to the C1 calculation scheme.

Thus, on the characteristic line C^+ (points 0 and 2)

$$\theta_0 - \nu(M_0) = \theta_2 - \nu(M_2), \qquad (14)$$

on the characteristic line C^- (points 6 and 2)

$$\theta_6 + \nu(M_6) = \theta_2 + \nu(M_2). \qquad (15)$$

Then for **node 2** with coordinate x_2 we can write (Fig. 2)

$$\theta_2 = \frac{1}{2}\left(C^- + C^+\right), \; \nu(M_2) = \frac{1}{2}\left(C^- - C^+\right), \qquad (16)$$

where

$$M_0 = w_0 / a_{x.0}, \; w_{x.0} = w_0 \cos(\theta_0),$$

$$w_{x.0} = w_e - \frac{w_e - w_0}{1 + (x_0 / c)^m}.$$

It should be noted that the gas velocity in the critical (throat) section of the nozzle (on the intersection of sonic line and nozzle axis) can be taken as an initial. The **calculation scheme C2** is executed both in x and y direction (x axis is the initial line). Determination of a coordinates of any considered point given in [14,15]. The Mach numbers $M(x)$ or $M(\bar{x})$ at the considered initial points (0, 6, 9, etc.) are known from the thermodynamic calculation of the LRE (Fig. 2).

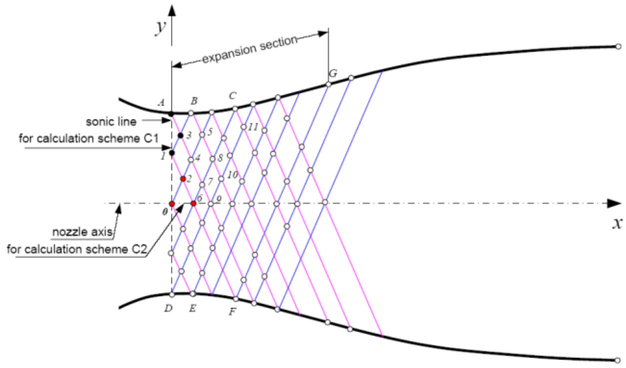

Fig. 2. The calculation scheme (C1+C2) using MC (contour of the nozzle is shown conditionally)

A dual-scheme calculation technique (C1+C2) for determining the main parameters of a supersonic 2D flow and nozzle geometry can be carried out with an unknown or known initial nozzle length L. In the second case, the initial nozzle length after each complete calculation cycle will be verified. The calculation will be repeated with a new value L_i. Accordingly, at the beginning of each calculation cycle, the shape of the distribution $w(x)$ along the nozzle axis will be changed. Therefore, for each new calculation cycle i, the distribution of the parameters values $[M(x)]_i$ and $[a(x)]_i$ given nozzle area expansion ratio $(A_e/A^*)_i = const$ and pressure expansion ratio $\varepsilon_i = (p_c/p_e)_i = const$ will be updated

$$(A_e/A^*)_i = \frac{1}{M_e}\left(\frac{2}{\gamma+1}\left(1+\frac{\gamma-1}{2}M_e^2\right)\right)^{\frac{\gamma+1}{2(\gamma-1)}}$$

or $$(A_e/A^*)_i = \frac{\left(\frac{2}{\gamma+1}\right)^{\frac{1}{\gamma-1}}\sqrt{\frac{\gamma-1}{\gamma+1}}}{(1/\varepsilon_i)^{\frac{1}{\gamma}}\sqrt{1-(1/\varepsilon_i)^{\frac{\gamma-1}{\gamma}}}},$$

where p_c - pressure in the combustion chamber, p_e - pressure on the nozzle exit section. Thus, refinement of the optimal nozzle length L_{opt} and optimal shape of the nozzle contour curve $(NC)_{opt}$ have been carried out. In the other case, the calculation is performed with the condition

$$[\varepsilon = \varepsilon_{opt},\ L_{opt} = const,$$

$$(A_e/A^* = \text{var}) \to (A_e/A^*)_{opt}] \Rightarrow (NC)_{opt}$$

Calculation ends when the condition at fulfillment of conditions

$$F((NC)_{opt}) = \min_{L}\ \max_{I}\ \Phi(I,L),$$

$$\lim\left|(NC)_{opt} - (NC)_{C1+C2}\right| \to \omega,$$

where L - the length of the nozzle supersonic part, I - the specific impulse of the engine, ω - the required value of the error.

6. Conclusion

In the current paper we have proposed a dual-scheme calculation technique for determining an optimum contour of the nozzle using the results of the thermodynamic calculation of the parameter values of the supersonic 2D flow, which is covered the internal curved profile of the LRE nozzle. The method is based on semi empirical formula, which was received based on results analysis of the numerical and experimental researches.

The proposed technique allows performing the thermogasdynamic and geometric calculations of the LRE nozzle with optimum contour by considering the required error.

References

[1]. Alemasov V.E., Dregalin A.F., Tishin A.P., The theory of rocket engines: Textbook for high technical universities (in russian). Moscow: Mashinostroenie, 1989.
[2]. Glushko V.P., Alemasov V.E., Dregalin A.F., Tishin A.P. Thermodynamic and teplophysics properties products of combustion (in russian), Under the editorship of. V.P. Glushko - T.1-10.- M.: AN USSR VI-THREADS, 1976
[3]. Guderley K.G. and Armitage J.V. A general method for the determination of best supersonic rocket nozzles, Symposium on Extremal Problems in Aerodynamics, Seattle, Washington, 1962.
[4]. Guderley K.G., Hantsch E. Beste Formen für achsensymmetrische Überschallschubdüsen, Z. Flugwiss, vol.9,3, 1955.
[5]. Sternin L.E., On the calculation of an axisymmetric jet nozzle of lightest weight, Izv. AN SSSR, Mekhanika i mashinostroenie, no.1, 1959.
[6]. Shmyglevskii Yu. D., Some variational problems of gasdynamics of axisymmetric supersonic flows (in russian), PMM, vol.21, no.2, 1957.
[7]. Sternin L.E. On the applicability of some simplifying assumptions in the profiling of optimal rocket nozzles. Fluid mechanics (Mekhanika zhidkosti i gaza, in russian). №2, 1999. C170 - 174.
[8]. Sternin L.E. Fundamentals of gas dynamics (in russian), M., 1995. 332 p.
[9]. Sternin L.E. Investigation of thrust characteristics of jet nozzles, profiled by different methods. Fluid mechanics (Mekhanika Zhidkosti i Gaza, in russian). 2000. № 1, p.152- 162.
[10]. Walter R. Warren. An Analytical and Experimental Study of Compressible Free Jets. Publ. No.: 23,885, Univ. Microfilms, Inc., 1957.
[11]. James M. Eggers. Velocity profiles and eddy viscosity distributions downstream of a Mach 2.22 nozzle exhausting to quiescent air, Langley Research Center, NASA TN 33-3601, 1966
[12]. Rao G.V.R. Exhaust Nozzle Contour for Optimum Thrust, Marquadt Aircraft Co, Presented at the ARC Semi Annual Meeting, San Fransisco, CA, June 10- 13, 1957.
[13]. Rao G.V.R. Exhaust Nozzle Contour for Optimum Thrust, Jet Propulsion, Vol. 28, No. 6, 1958.
[14]. Anderson Jr. John. Fundamentals of Aerodynamics. McGraw-Hill Book Company, New York, 1988
[15]. Anderson Jr. John. Modern Compressible Flow: With Historical Perspective, McGraw-Hill Book company, New York, 1982

Proceedings of the International Symposium of Mechanism and Machine Science, 2017
AzC IFToMM – Azerbaijan Technical University
11-14 September 2017, Baku, Azerbaijan

Uçan aparatlarda tətbiq edilən pyezoelektrik mikroakselerometrlərin dinamiki həssalığının tədqiqi

Ənvər Tapdıqoğlu HƏZƏRXANOV[1*], Toğrul İsa oğlu KƏRİMLİ[2], Vasif Aydın oğlu NEYMƏTOV[3]
Milli Aviasiya Akademiyası, Bakı, Azərbaycan
25th km, Baku, Azerbaijan
[1*]enver-xan@mail.ru, [2]tkarimli@mail.ru, [3]neymvasif@mail.ru

Xülasə
Məqalədə uçan aparatlarda quraşdırılan mikropyezoelektrik akselerometrlərin idarə edilən pyezotransformator kimi struktur sxeminin parametrlərinin onların dinamik həssaslığı stabil olan işçi tezlik diapazonu ilə təmin edən texniki optimum şərtinə sazlanmasının riyazi ifadələrinin çıxarılışı yerinə yetirlmişdir. Alınmış riyazi ifadələr əsasında keçid prosesinin müddətindən asılı olaraq, hesablanan struktur parametrləri istənilən halda 4-10%-lik ifrat tənzimləməni təmin edir ki, bu da rezonans nöqtəsində amplitudun artımının qarşısını azaltmış olur.
Açar sözlər: pyezoelektrik akselerometr, pyezotransformator, struktur parametrləri, texniki optimum şərti, dinamiki həssaslıq.

1. Giriş

Milli Aviasiya Akademiyasında yerinə yetirilən tədqiqat işlərinin bir hissəsi də uçuş aparatlarının (UA) idarəetmə sistemlərinin (İES) informativlik səviyyəsinin artırılması problemlərinə həsr olunmuşdur. İlkin informasiya mənbəyi kimi özünəməxsus əhəmiyyətə malik olan pyezoelektrik mikroakselerometrlərin (PMA) bərkidəilməsinə olan yüksək tələblərin ödənilməsi məqsədi ilə təklif edilmiş avtomatik tənzimlənən başlanğıc quraşdırma sistemi (ATBQS) təklif edilmiş və bu sistemin idarəetmə alqoritmləri yaradılmış və tənzimləmə məsələləri tədqiq edilmişdir. (Şək.1) [1]. ATBQS-nin çox mühüm və fərqli cəhəti odur ki, bir koordinat üzrə quraşdırılan bir cüt PMA-dan biri tənzimləmə sisteminin tapşırıq qurğusu kimi , digəri isə əks əlaqə bəndi kimi avtomatik olaraq funksiyalaşdırılır. Başqa sözlə, əlavə olaraq tapşırıq və əks əlaqə elementlərinə ehtiyac qalmır. Lakin, PMA-nın özünün ilkin informasiya mənbəyi kimi dinamiki xarakteristikaları da, öz növbəsində, ATBQS-in keyfiyyətli işləməsinə təsdiq göstərən mühüm amillərdən birdir.

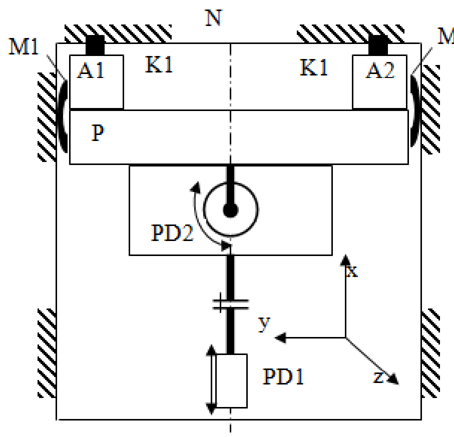

Şək. 1. ATBQS-in tərtibat sxemi A1, A2 – pyezoelektrik akselerometrlər; K1, K2 – akselerometrlərin ətalətli həssas kütlələrinin toxunduğu mexaniki kontaktlar ; M1 M2 – elektromaqnit tormozlar; P –simmeriya oxu boyunca irəliləyən hərəkətli platforma ; PD1- sabit cərəyan mühərrikli izləyici intiqal ; PD2- dönmə stolunun pyezoelektrik mühərriki; N-UA-nın övdəsinə bərkitmə

2. Məqalənin məqsədi

Məqalədə məqsəd, UA-nın müxtəlif təyinatlı idarəetmə-nəzarət sistemlərində tətbiq edilən PMA-nın dinamiki həssaslığınının onlarda tətbiq edilən pyezoelektrik elementlərinin həndəsi ölçülərindən və fiziki-texniki parametrlərindən aslılıq ifadələrini əldə etməkdir.

3. Məsələnini qoyuluşu

İdarə edilən pyezotransformator (PT) rejimində işləyən PMA-nın tipik funksional quruluşuna uyğun olaraq, tərtib edilmiş struktur sxeminə görə (şək.2):

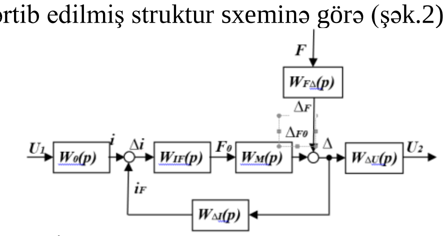

Şək. 2. İdarə edilən PT rejimində işləyən PMA-nınstruktur sxemi

Wo(p) – PT tipli pyezohəssas elementin (PHE) gərginlik-cərəyan çevrilməsi hissəsinin, $W_{IF}(p)$ –PHE-nin cərəyan –qüvvə çevrilməsi hissəsinin, $W_M(p)$ – qüvvə-eninə dalalar çevrilməsi hissəsinin, $W_{\Delta U}(p)$ – PT-li PHE-nin düz pyezoeffek hadisəsi baş verən hissəsinin, $W_{F\Delta}(p)$ – obyektin etdiyi mexaniki çeviricinin, $W_{FI}(p)$ isə çeviricinin təsirindən yaranan mexaniki impedansa sərf olunan gərginlik düşgüsünün ötürmə funksiyalarıdır (ÖF) [2-4]. Struktur sxemində göstərilmiş parametrlər üçün:

$$\begin{cases} U(p) = W_{\Delta U}(p)\Delta(p) \\ \Delta(p) = \Delta_F(p) - \Delta_o(p) \\ \Delta_F(p) = W_{F\Delta}(p)F(p) \\ \Delta_o(p) = W_{IF}(p)W_M(p)\Delta i(p) \\ \Delta i(p) = i_o(p) - i_F(p) \\ i_o(p) = W_O(p)U_O(p) \\ i_F(p) = W_{IF}(p)\Delta(p) \end{cases} \quad (1)$$

tənliklər sistemini yazmaq olar. (1) tənliklər sisteminin həllindən idarə edilən PT rejimində işləyən PHE-li PMA-
nın giriş qidalandırma gərginliyinə görə ÖF:

$$\frac{U(p)}{U_O(p)} = \frac{W_O(p)W_{IF}(p)W_M(p)W_{\Delta U}(p)}{1+W_{FI}(p)W_{IF}(p)W_M(p)}, \quad (2)$$

obyektin təsir qüvvəsinə görə ÖF isə:

$$\frac{U(p)}{F(p)} = \frac{W_F(p)W_{\Delta U}(p)}{1+W_{FI}(p)W_{IF}(p)W_M(p)}. \quad (3)$$

(2) və (3) ifadələrində olan funksional hissələrin ÖF uyğun olaraq:

$$W_O(p) = \frac{1}{T_O p + 1}$$

$$W_{IF}(p) = k_{IF}; W_{FI}(p) = k_{FI}$$

$$W_{\Delta U}(p) = k_{\Delta U}(T_{\Delta U} p + 1)$$

$$W_M(p) = \frac{1}{T_M^2 p^2 + 2\beta_M T_M p + 1}$$

$$W_F(p) = \frac{1}{T_F^2 p^2 + 2\beta_F T_F p + 1}$$

Bu ifadələrdə *To* –PHE-nin gərginlik-cərəyan çevrilməsi hissəsinin zaman sabiti; K_{IF} –PHE-nin cərəyan –qüvvə çevrilməsi hissəsinin küclənmə əmsalı; T_M, β_M - qüvvə-eninə dalalar çevrilməsi hissəsinin mexaniki zaman sabiti və sönmə əmsalı; , $T_{\Delta U}$ – PT-li PHE-nin düz pyezoeffek hadisəsi baş verən hissəsinin zaman sabiti; T_F, β_F - PT-nin generator hissəsinin girişinə dalğa-qüvvə çevrilməsinin mexaniki zaman sabiti və sönmə əmsalıdır.

Struktur sxemində göstərilmiş parametrlər üçün *Wo(p)*, $W_{IF}(p)$, $W_M(p)$, $W_{\Delta U}(p)$, $W_{F\Delta}(p)$, $W_{FI}(p)$ ifadələri nəzərə alındıqdan və sadə riyazi çevrilmələrin yerə yetirilməsindən sonra yazmaq olar ki:

$$W_{UO}(p) = k_{UO}\frac{a_0 p + 1}{b_o p^3 + b_1 p^2 + b_2 p + 1}, \quad (4)$$

$$W_{UF}(p) = k_{UF}\frac{c_0 p^3 + c_1 p^2 + c_2 p + 1}{d_0 p^4 + d_1 p^3 + d_2 p^2 + d_3 p + 1}, \quad (5)$$

burada

$$k_{UO} = k_{UF} = \frac{k_{\Delta U}}{k_{FI}k_{IF} + 1}, a_0 = T_{\Delta U},,$$

$$b_0 = \frac{T_0 T_M^2}{k_{FI}k_{IF} + 1}, b_1 = \frac{T_M^2 + 2\beta_M T_O T_M}{k_{FI}k_{IF} + 1}$$

$$b_2 = \frac{T_O(k_{FI}k_{IF} + 1) + 2\beta_M T_M}{k_{FI}k_{IF} + 1},$$

$$c_0 = T_{\Delta U}T_M^2, c_1 = T_M^2 + 2\beta_M T_{\Delta U}T_M,$$

$$c_2 = T_{\Delta U} + 2\beta_M T_M, d_0 = \frac{T_F^2 T_M^2}{k_{FI}k_{IF} + 1},$$

$$d_1 = \frac{2T_F T_M(\beta_M T_F + \beta_F T_M)}{k_{FI}k_{IF} + 1}$$

$$d_2 = \frac{T_F^2(k_{FI}k_{IF} + 1) + T_M^2 + 4\beta_M\beta_F T_M T_F}{k_{FI}k_{IF} + 1}$$

$$d_3 = \frac{2[\beta_M T_M + \beta_F T_F(k_{FI}k_{IF} + 1)]}{k_{FI}k_{IF} + 1}$$

Tezlik xarakteristikalarından göründüyü kimi PMA-nın istər giriş qidalandırma gərginliyinə görə, istərsə də ölçülən parametrin mexaniki təsirinə görə dinamik xarakteristikaları rezonans təbiətlidir (şək.3).

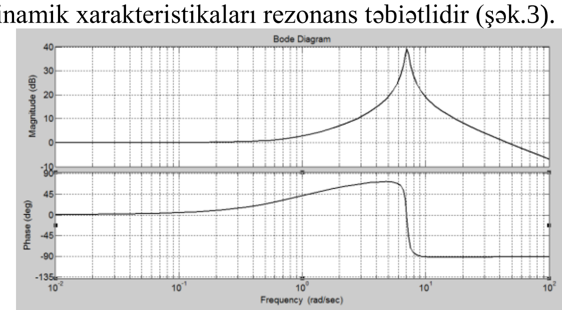

Şək. 3. PHE-li PMA-nın qurulmuş tezlik xarakterristikaları

Rezonans tezliyi ətrafında kiçik stabilləşdirmə zonası var. Buna uyğun olaraq, PMA-nın istər qidalanma gərginliyinə görə, istərsə də həyəcanlandırıcı qüvvəyə görə dinamik həssaslığı yüksək rəqsli göstəricisinə malikdir.

Beləiklə, UA-nın ATBQS-də tətbiq edilən PMA-nı nisbətən geniş tezlik diapazonunda stabil dinamik həssaslıqla təmin etməkdən ötrü keçid prosesinin keyfiyyət göstəriciləri ilə PT-un elektromexaniki parametrlərinin arasında riyazi asılılıqları müəyyən etmək lazımdır. Bu riyazi asılılıqların müəyyən edilməsinin praktik əhəmiyyəti daha böyükdür: belə ki, bu zaman PMA-nın harada və necə tətbiq olunmasından asılı olmayaraq, onun özünün çıxış siqnalının keçid prosesinin tələb olunan keyfiyyət göstəricilərinin ödənilməsini təmin etməyin riyazi şərtləri və ifadələri artıq məlum olacaqdır ki, bu da akselerometrlərin layihələndirilməsi məhrələsində mühüm əhəmiyyətə malikdir.

4. Həlli üsulu

Avtomatlaşdırılmış elektrik intiqallarının tənzimləyicilərinin texniki optimuma sazlanması metodu məlumdur və bu metoda görə texniki optimumu ödəyən keçid prosesi elə bir prosesdir ki, bu zaman tənzimləmə müddəti minimal buraxıla bilər ifrat tənzimləmə faizini ödənilməsi şərti ilə mümkün ola bilən kiçik qiymətə bərabər olmuş olsun [5].

Optimallaşırma hesabatı üsullarından istifadə etməklə nəzəri olaraq, istənilən tərtibli dinamik obyektlər üçün texniki optimum şərtini ödəyən xarakteristik tənliklərin standart forması müəyyən edilmişdir (cədvəl 1).

S. s	XT-nin tərtibi	Nümunəvi xarakteristik tənlik	Tənzimləmə müddəti t_q, san	İfrat tənzimləmə σ,%
1	3	$8T_1^3 p^3 + 8T_1^2 p_1^2 + 4T_1\ p + 1$	$B \cdot T_1$	$4 \div 10$
2	4	$64T_1^4 p^4 + 64T_1^3 p^3 + 32T_1^2 p^2 + +8T_1 p + 1$	$C \cdot T_1$	$4 \div 10$

PHE-li MPÇ-nin (4) və (5) ifadəsi ilə müəyyən olunan girişə və obyektin qüvvəsinə görə ÖF-nin xarakterestik tənliklərin və onların nümunəvi ifadələri uyğun olaraq:

$$\begin{cases} 8T_1^3 p^3 + 8T_1^2 p_1^2 + 4T_1\ p + 1 = 0 \\ b_0 p^3 + b_1 p^2 + b_2 p\ + 1 = 0 \end{cases}, \quad (6)$$

$$\begin{cases} 64T_1^4 p^4 + 64T_1^3 p^3 + 32T_1^2 p^2 + 8T_1 p + 1 = 0 \\ d_0 p^4 + d_1 p^3 + d_2 p^2 + d_3 p + 1 = 0 \end{cases} \quad (7)$$

sistemləri ilə əks oluna bilər. Bu zaman ifrat tənzimləmə $\sigma = 4 \div 10\%$, siqnalın qərarlaşma müddəti isə uyğun olaraq $t_q = B \cdot T_1$, $t_q = C \cdot T_1$ (6) sisteminin ÖF-nin xarakteristik tənliklərinin uyğun əmsallarının qarşılıqlı münasibətindən:

$$\begin{cases} \frac{1}{T_0} + \frac{2\beta_M}{T_M} = \frac{B}{t_q} \\ \frac{2\beta_M}{T_M} + \frac{2\beta_F}{T_F} = \frac{C}{t_q} \\ (1 + k_{FI} k_{IF}) = \frac{\beta_M T_M}{4\frac{t_q}{B} - \beta_F T_F} \end{cases} \quad (8)$$

sistemini almış olaraq. Beləliklə, PMA-nın funksional tərkibinin fiziki parametrlərinin (8) sistemi ilə müəyyən edilən qarşılıqlı münasibəti onun çıxış siqnalının qərarlaşma müddətinin texniki optimuma sazlanmasını təmin etmiş olacaq.

5. Nəticə

Alınmış tənliklər UA-da tətbiq edilən pyezoelektrik mikroakselerometrlərin pyezotransformator rejimində işləməsi zamanı texniki optimuma sazlanmasını və tələb olunan tezlik diapazonunda stabil dinamiki həssaslığa malik olmasını təmin edəcək.

Ədəbiyyat

[1]. Каримли Т.И., Нейматов В.А. Моделирование системы начальной выставки пьезоэлектрических акселерометров. Вестник двигателестроения. Харьков, №2/2016. стр.18-24

[2]. Зикий А.Н. , Зламан П.Н., Власенко Д.В., Гончарова Т.О, Третьяк А.А. Фильтры на поверхностных акустических волнах. Электротехнические и информационные комплексы и системы. № 3, т. 10, 2014. 50-54.

[3]. А.Н.Соловьев, И.Н.Соловьев, А.А.Иванов. Метод увеличения коэффициента трансформации и диапазона рабочих частот пьезоэлектрического трансформатора. Вестник новгородского государственного университета 2012, №67. 33-35

[4] Лавриенко В.В. Пьезоэлектрические трансформа торы. М., Энергия, 1975. 112с.

[5]. Михайлов О.П.. Автоматизированный электропривод станков и промышленных роботов. М., Машиностроение. 1990. 304 с.

Полиноминальное Интерполяционное Сглаживание Крыловых Профилей

Рамиз САДЫХОВ, Фуад МЕЛИКОВ
Национальная Академия Авиации Азербайджана, AZ1045, Баку, пр. Мардакян 30.
E-mail: sadixov@mail.ru, fuadmalikov08@gmail.com

Аннотация: Рассматривается кусочно-полиномиальное сглаживание экспериментальных данных с автоматической стыковкой без учета шумов измерений, на примере интерполяционного сглаживания крыловых профилей.

Ключевые слова: методы интерполяционного профилирования крыловых профилей.

Введение. При сглаживании экспериментальных данных, содержащих области разной степени гладкости, обычно применяемые в подобных случаях регрессионные модели со степенными и ортогональными полиномами не всегда приводят к удовлетворительным результатам. В связи с этим представляет интерес рассматривать кусочно-полиноминальные модели, которые позволяют строить эффективные алгоритмы аппроксимации при наличии областей разной степени гладкости. С указанной целью, исходя из априорных представлений о степени гладкости экспериментальных данных, выбирают элементарный интервал обработки объемом в n точек. В пределах этого интервала сглаживание производят полиномом до четвертой степени [1-5].

Следует иметь в виду, что с увеличением степени аппроксимирующего полинома возрастает случайная ошибка, а методическая ошибка уменьшается. С другой стороны, чем больше интервал сглаживания (а, следовательно, и количество измерений), тем в большей степени можно уменьшать влияние случайных ошибок. Поэтому порядок аппроксимирующего полинома и интервал сглаживания выбирают так, чтобы при проведении операции сглаживания обеспечивался минимум их суммы.

Пусть модель экспериментальных данных элементарного интервала имеет вид:

$$z_y = y + \delta_y \,, \tag{1}$$

где δ_y– аддитивные погрешности измерений с нулевым средним и дисперсией σ^2 .

Определение параметров аппроксимации, начиная со второго интервала, осуществляется с учетом стыковки полиномов по функции, первой, второй и третьей производной. Как показывает опыт практического опробования разработанного на основе метода наименьших квадратов (МНК) алгоритма, оптимальным в смысле результата и затрат машинного времени, при окне аппроксимации от 10 до 30 точек является следующий выбор параметров: степень полинома 3 и число условий 3 – стыковка по функции, первой и второй производным.

Кусочно-полиномиальная интерполяция методом наименьших квадратов. Допустим, что для интерполяции участков траекторных измерений движения летательных аппаратов (ЛА) используется полином третьего порядка, то есть

$$y(x) = a_0 + a_1 x + a_2 x^2 + a_3 x^3. \tag{2}$$

Уравнение измерений выходной координаты Y для этого случая запишется в вид:

$$Z_y = a_0 + a_1 x + a_2 x^2 + a_3 x^3 + \delta_y \,. \tag{3}$$

Тогда модель экспериментального материала для рассматриваемого участка (интервала) можно представить в следующем матричном виде:

$$Z_y = x\Theta + \delta_y \,,$$

где $Z_y = \|z_{1y,}z_{2y}, \dots z_{ny}\|^{T}$ - вектор измерений выходной координаты y; $\Theta = \|a_0, a_1, a_2, a_3, \|^T$ – вектор искомых коэффициентов.

X= $\left\|\begin{matrix} 1\ x_1 & x_1^2 & x_1^3 \\ 1\ x_2 & x_2^2 & x_2^3 \\ \cdot\ \cdot & \cdot & \cdot \\ \vdots\ \vdots & \vdots & \vdots \\ 1\ x_n & x_n^2 & x_n^3 \end{matrix}\right\|$ - структурная матрица; n - количество точек в рассматриваемом интервале.

Обычно для оценки коэффициентов полинома (2) используется МНК следующего вида (4)

$$\hat{\Theta} = (X^T X)^{-1}\left(X^T Z_y\right), \tag{4}$$

$$D_\Theta = (X^T X)^{-1}\sigma^2, \tag{5}$$

где D_Θ - дисперсионная матрица ошибок оценок.

Оценки коэффициентов для первого участка интерполяции получаем по формуле (4). Начиная со второго, компоненты вектора $\hat{\Theta}$ рассчитываются по экспериментальным данным их этого участка, но с учетом параметров, найденных на предыдущем участке. Поэтому каждый последующий участок траектории движения ЛА будем выбирать с перекрытием. При этом целесообразно использовать следующие линейные связи между оцененными параметрами предыдущего участка $\hat{\Theta}_{N-1}$- искомыми $\hat{\Theta}_N$ N - го участка:

$$\mathrm{A}\Theta_{N=}\mathrm{V}, \tag{6}$$

$$A = \begin{bmatrix} 1\ x_e\ x_e^{\ 2} & x_e^3 \\ 0\ 1\ \ 2_{xe} & 3x_e^2 \\ 0\ \ \ 0\ 2 & 6x_e \end{bmatrix}, \tag{7}$$

$$V = \begin{bmatrix} \hat{a}_{ON-1} + \hat{a}_{1N-1}X_e + \hat{a}_{2N-1}X_e^2 + \hat{a}_{3N-1}X_e^3 \\ \hat{a}_{1N-1} + 2\hat{a}_{2N-1}X_e + 3\hat{a}_{3N-1}X_e^2 \\ 2\hat{a}_{2N-1} + 6\hat{a}_{3N-1}X_e \end{bmatrix}, \tag{8}$$

где e= (N-1)(n-L); L - число точек.

Формулы (6)-(8) описывают связи, которые обеспечивают стыковку участков интерполяции по функции первой и второй производным. Если ограничиться только стыковкой по функции, то можно оставит первую строку матрицы A и первую компоненту вектора V, а если только по функции и первой производной, то можно оставить только две первые строки матрицы A и две первых компонента вектора V.

Учитывая равноточность измерений, задачу определения неизвестных коэффициентов модели в этом случае можно сформулировать как задачу на условный экстремум: минимизация квадратичной функции

$$(Z_y - X\Theta)^T\sigma^2 I(Z_y - X\Theta)$$

при ограничивающем условии (6). Здесь I - единичная матрица.

С целью решения таких задач обычно используют метод неопределенных множителей Лагранжа. В результате можно получить следующие выражения для оценивания вектора коэффициентов Θ при наличии линейных связей (6) [6]:

$$\breve{\Theta}^T = \hat{\Theta}^T + (V^T - \hat{\Theta}^T A^T)[A(X^T X)^{-1}A^T]^{-1}\ \ A(X^T X)^{-1}, \tag{9}$$

$$D_{\breve{\Theta}} = D_{\hat{\Theta}} - (X^T X)^{-1}A^T[A(X^T X)^{-1}A^T]^{-1}A(X^T X)^{-1}\sigma^2. \tag{10}$$

Подставляя матрицы A,X и векторы Z и V в формулы (4), (5), (9) и (10), получим оценку вектор коэффициентов для участка траектории движения ЛА с номером N, а также дисперсионную матрицу ошибок оценок.

В результате последовательного применения описанной процедуры с использованием экспериментальных данных получим кусочно-полиномиальную интерполяцию исследуемого участка с автоматической стыковкой.

Результаты обработки с помощью предложенного алгоритма многочисленных экспериментальных данных показывают, что чем больше степень полинома и чем меньше количество условий, тем ближе оказывается интерполяционная кривая к экспериментальным данным. Однако, проводя стыковку только по функции, мы можем получить на интерполированной кривой разрывы первой и второй производных, что особенно нежелательно при оптимальном проектировании крыловых профилей самолетов.

На основе поведенных экспериментальных исследований показано, что оптимальным перекрытием в большинстве случаев является 50% перекрытие.

Интерполирование полиномиальными сплайнами. Помимо кусочно-полиномиальной регрессии существуют полиномиальные сплайны, которые не являются ни аналитическими функциями, ни статистическими моделями.

Сплайны кусочно являются полиномами (на практике наиболее популярны интерполяционные сплайны невысоких нечетных степеней: третьей, пятой) подчиненными условию непрерывности функции и производных (первой наклона и второй кривизны в случае кубических сплайнов) в общих точках соседних участков.

Известно, что кубический сплайн-функцией является такая функция из класса W_2^2 ($W_2^2 -$ класс функций, имеющие суммируемые с квадратом вторые производные), которая принимает в узлах сетки заданное значение и минимизирует функционал,

$$\int_{t_1}^{t_N} [z''(t)]^2\, dt = \min_{w_2^2}$$

то есть имеет минимальную кривизну среди всех непрерывных гладких кривых, соединяющих экспериментальные точки.

При решении задачи сплайновой кусочно – полиномиальной интерполяции замкнутой кривой y (каким является, например, профиль крыла ЛА произвольной формы) воспользуемся ее параметрическими представлением. Пусть кривая y представима конечным числом дискретных точек (произведены точные дискретные измерения) в виде набора периодических кубических сплайнов двух типов.

$$\left((t_j, x_j), (t_j, y_j)\right) = (t_j, z_j), z_j = (x_j, y_j), (j = \overline{1, N}),$$

$$t_j < t_2 <_{\dots}< t_N, t_{N+1} = t_1, X_{N+1} = X_1, Y_{N+1} = Y_1.$$

Тогда восстановление сплайна S(z(t)) , его первой S'(z(t)) и второй S''(z(t)) производных в любой точке z(t)= (x(t), y(t)), где $t \in [0, l]$, $l = \sum_{j=1}^{N} h_j, h_j = |z_j - z_{j-1}|, (j = \overline{1, N})$, осуществляются формулами:

$$S(z(t)) = z_{j-1}(t_j - t)^3/6h_j + z_j^{"}(t - t_{j-1})^3/6h_j + (z_{j-1} - z_{j-1}^{"}h_j^2/6) * \\ * (t_j - t)/h_j + (z_j - z_j^{"}h_j^2/6)(t - t_{j-z})/h_j, \tag{11}$$

$$S^{"}(z(t)) = -z_{j-1}^{"}(t_j - t)^2/2h_j + z_j^{"}(t - t_{j-1})^2/2h_j + (z_j - z_{j-1})/h_j - (z_j^{"} - z_{j-1}^{"})/h_j \tag{12}$$

$$S^{"}(z(t)) = z_{j-1}^{"}(t_j - t)/h_j + z_j^{"}(t - t_{j-1})/h_j\ , \tag{13}$$

где $z_j^{"}$ - вторые производные по сплайну.

Отметим, что формула (11) используется при профилировании крыльев произвольной формы ЛА, движущихся в идеальной невязкой среде, а также для визуализации с высокой точностью на графических устройствах и нашла широкое применение в интерактивных вычислительно-графических системах при построении аэрогидродинамических и газодинамических моделей [3]. Если на каждом из участков h_j профиля Y взять равномерное разбиение с количеством узловых точек $М_j$, то после несложных преобразований получим простые и эффективные с точки зрения реализации на ЭВМ формулы

$$S(z(t)) = -z''_{j-1}\left(\frac{m_j}{M_j}-1\right)\left(\frac{m_j}{M_j}\right)\left(\frac{m_j}{M_j}-2\right) + z''_j\left(\frac{m_j}{M_j}-1\right)\left(\frac{m_j}{M_j}\right)\left(\frac{m_j}{M_j}+1\right) - z_{j-1}\left(\frac{m_j}{M_j}-1\right) + z_j\left(\frac{m_j}{M_j}\right).$$
$$(m_j = \overline{0, M_j}; \ j = \overline{2, N+1}) \tag{14}$$

Аналогично интерпретацию получают формулы (12), (13).

Для нахождения вектора вторых производных по сплайну $Z'' = \|z''_1, z''_2, \dots z''_N\|^{\mathrm{T}}$ Необходимо решить систему уравнений

$$AZ'' = 6B\hat{Z} \tag{15}$$

откуда,

$$Z'' = A^{-1}B\hat{Z} \tag{16}$$

где

$$A = \begin{Vmatrix} 2(h_1+h_2) & h_2 & 0 & \dots & 0 & h_1 \\ h_2 & 2(h_2+h_3)h_3 & \dots & 0 & & 0 \\ \cdot & \cdot & \cdot & & & \cdot \\ h_1 & 0 & 0 & \dots & h_N & 2(h_N+h_1) \end{Vmatrix} \tag{17}$$

$$B = \begin{Vmatrix} h_1^{-1} & -(h_1^{-1}+h_2^{-1}) & h_2^{-1} & \dots & 0 & 0 \\ 0 & h_2^{-1} & -(h_2^{-1}+h_3^{-1}0 & \vdots & 0 & 0 \\ \cdot & \cdot & \cdot & & \cdot & \cdot \\ 0 & 0 & 0 & \dots & -(h_N^{-1}+h_1^{-1}) & h_1^{-1} \end{Vmatrix} \tag{18}$$

$\hat{Z} = \|\hat{Z}_1, \hat{Z}_2 \dots, \hat{Z}_N\|^{\mathrm{T}}$ - вектор измеренных или вычислительных координат точек $\hat{z}_j = (\hat{x}_j, \hat{y}_j), (j = \overline{1, N})$ профиля у.

Матрица А симметричная с трех-диагональным преобладанием и по теореме Гершгорна о локализации собственных значений она положительно определена, следовательно, неособенная. Значит, коэффициенты $z''_1, z''_2, \dots, z''_N$ определяются из (16) однозначно. В связи с чем, сплайн функция S(z(t)) имеет единственное решение. Для решения (15) использовался метод прогонки.

Если уравнение кубического сплайна записать в явном полиномиальном виде.

$$S(z(t)) = a_0 + a_1 t + a_2 t^2 + a_3 t^3 , \tag{19}$$

то коэффициенты a_0, a_1, a_2, a_3,определяющих j-й сплайн (то есть линию, связывающую точки z_j and z_{j+1} , вычисляется следующим образом

$$\begin{gathered} a_0 = z_j; \\ a_1 = z'_j; \\ a_2 = \frac{z''_j}{2} = 3(z_{j+1} - z_j)h_{j+1}^{-2} - 2z'_j h_{j+1}^{-1} - z'_{j+1}h_{j+1}^{-1} \\ a_3 = z'''_j/6 = 2(z_j - z_{j+1})h_{j+1}^{-3} + z'_j h_{j+1}^{-2} + z'_{j+1}h_{j+1}^{-2} \end{gathered} \tag{20}$$

Для нахождения касательных векторов во внутренних точках, в которых наклон линии одинаков по обе стороны сочленения, необходимо решить уравнение

$$A'Z' = 3B'\hat{Z} , \tag{21}$$

Откуда

$$Z' = A'^{-1}3B'\hat{Z}, \tag{22}$$

где $Z' = \|z'_1, z'_2, z'_N\|^{\mathrm{T}}$, - вектор первых производных по сплайну,

$$A' = \begin{Vmatrix} 2(h_1+h_2) & h_1 & 0 & \dots & 0 & h_2 \\ h_3 & 2(h_2+h_3) & h_2 & \vdots & 0 & 0 \\ \cdot & \cdot & \cdot & & 0 & \cdot \\ h_N & 0 & 0 & \dots & h_1 & 2(h_N+h_1) \end{Vmatrix} \tag{23}$$

$$B' = \begin{Vmatrix} h_2 h_1^{-1} & (h_2 h_1^{-1} - h_1 h_2^{-1}) & h_1 h_2 & \dots & 0 & 0 \\ 0 & h_3 h_2^{-1} & (h_3 h_2^{-1} - h_2 h_3^{-1}) & \vdots & 0 & 0 \\ \cdot & \cdot & \cdot & & \cdot & \cdot \\ 0 & 0 & 0 & \dots & (h_1 h_N^{-1} - h_N h_1^{-1}) & h_N h_1^{-1} \end{Vmatrix} \tag{24}$$

Матрица A с трехдиагональным преобладанием положительно определена (по теореме Гершгорна о локализации собственных значений), следовательно, неособенная. Значит, коэффициенты определяются $z_1'', z_2'', \dots, z_N''$ из (22) однозначно. В связи с чем, сплайн-функция S(z(t)) также однозначно восстанавливается по формулам (19), (20) и задача о нахождении кусочно-кубической функции S(z(t)) имеет единственное решение. Для решения (21) использовался метод прогонки. Для вычисления наклонов $z_j', (j = \overline{1,N})$ можно воспользоваться также значениями $z_j'', (j = \overline{1,N})$ найденных из решения (15), используя следующее соотношения.

$$z_j' = -z_j'' h_{j+1}/3 - z_{j+1}'' h_{j+1}/6 + (z_{j+1} - z_j)h_{j+1}^{-1} \tag{25}$$

Отметим, что сплайн-функцию S(z(t)) в отличие от формулы (19) можно восстановить также по следующей формуле (после решения (21)

$$S\big(z(t)\big) = z_{j-1}'(t_j - t)^2(t - t_{j-1})/h_j^2 - z_j'(t - t_{j-1})^2(t_j - t)/h_j^2 + z_{j-1}(t_j - t)^2(2\big(t - t_{j-1}\big) + h_j)/h_j^{-3}$$
$$+z_j(t - t_{j-1})^2(2\big(t_j - t\big) + h_j)/h_j^{-3}$$

Длины дуг (участки профиля лопатки или контура канала охлаждения), их длина (l), ограничиваемая ими площадь (P) и координаты центра ($x_c\ y_c$) определяются следующим образом

$$\int_{t_j}^{t_{j+1}} ((S^{\cdot}\big(x(t)\big))^2 + ((S^{\cdot}\big(x(t)\big))^2)^{\frac{1}{2}} dt, \qquad j = \overline{1,N} \tag{26}$$

$$l = \sum_{j=1}^{N} \int_{t_j}^{t_{j+1}} ((S^{\cdot}\big(x(t)\big))^2 + (\,S^{\cdot}\big(x(t)\big))^2)^{1/2}\, dt, \tag{27}$$

$$P = 1/2 \int_\gamma (S(x(t))\, S^{\cdot}(y(t)) - S^{\cdot}(x(t)) S(y(t)))dt \tag{28}$$

$$x_c = P^{-1} \int_\gamma (S(x(t))\, S\big(y(t)\big) S^{\cdot}\big(x(t)\big)dt,\ y_c = P^{-1} \int_\gamma (S(x(t))\, S\big(y(t)\big) S^{\cdot}\big(y(t)\big)dt \tag{29}$$

Для вычисления интегралов (26), (27), (28), (29) использовалась формула трапеции. Следует отметить, что сплайн – квадратура для периодических сплайнов (замкнутых кривых) является просто формулой трапеции. Однако в случае разомкнутых кривых будем иметь следующую формулу

$$\sum_{j=1}^{N} \int_{t_j}^{t_{j+1}} S\big(z(t)\big)dt = \sum_{j=1}^{N} \frac{z_j + z_{j+1}}{2} h_j - \sum_{j=1}^{N} \frac{z_j'' + z_{j+1}''}{24} h_j^3$$

то есть формула сплайн-квадратуры есть формула трапеций плюс поправочный член, который аппроксимирует ошибку самой формулы трапеции.

Для проверки точности предлагаемых формул были проведены числовые расчеты на персональном компьютере. Рассматривался крыловой профиль, на контуре которого взято равномерное разбиение из 8 точек, координаты первой из которых были (10мм, 0м). Сравнительный анализ проводился с расчетными данными, произведенными по конечно-разностной формуле (КРФ).

$$z_j' = \big(z_j - z_{j-1}\big)h_j^{-1} + \big(z_{j+1} - z_j\big)h_{j+1}^{-1} - (z_{j+1} - z_{j-1})(h_j + h_{j+1})^{-1} \tag{30}$$

Результаты вычислительных экспериментов приведены в таблице 1. В этой таблице вначале приводятся расчетные значения, произведенные с использованием формулы (30), будем обозначать их через КРФ, а затем – расчетные значения, произведенные с использованием сплайнов – (СПЛ). Длина окружности (контура охлаждения канала) вычисленная с использованием КРФ, составляет 61.2288мм, то есть относительная погрешность равна 2.5%. Длина этой же окружности, вычисленная по СПЛ, составляет 62.7936 мм, то есть относительная погрешность равна 0.061%. Площадь круга, вычисленная по КРФ, равнялась 282.843 мм^2, что составляло 9.9% погрешности, а с использованием СПЛ – 313.652 мм^2, то есть 0.17%. Координаты центра круга, вычисленные с использованием СПЛ, равнялись x_c = 0.17501x 10^{-6} и y_c= - 0,45774 x 10^{-5}.

Следует отметить, что в большинстве случаев интерполяционные сплайны дают хорошие результаты в отношении качественного поведения, то есть сохранения монотонности экспериментальных данных, выпуклости и т.д. Однако при больших градиентах в экспериментальных данных на сравнительно редких сетках возможны осцилляции (от них свободны только сплайны первой степени, изображаемые ломанными).

Таблица 1. Результаты вычислительных экспериментов

№	x		y		l	
	КРФ	СПЛ	КРФ	СПЛ	КРФ	СПЛ
1	0.0000	0.0000	0.9238	1.0230	7.6536	7.8492
2	-0.6532	-0.7239	0.6532	0.7239	7.6536	7.8492
3	-0.9238	-1.0230	0.0000	0.0000	7.6536	7.8492
4	-0.6532	-0.7239	-0.6532	-0.7239	7.6536	7.8492
5	0.0000	0.0000	-0.9238	-1.0230	7.6536	7.8492
6	0.6532	0.7239	-0.6532	-0.7239	7.6536	7.8492
7	0.9238	1.0230	0.0000	-0.0000	7.6536	7.8492
8	0.6532	0.7239	0.6532	0.7239	7.6536	7.8492

Для улучшения геометрических свойств кубических сплайнов в их структуру вводят дополнительные параметры, выбором которых можно управлять качественным поведением графиков получаемых кривых (сплайны с натяжением или экспоненциальные, рациональные, сплайны с дополнительными узлами и т.д.)

Задача о построении сплайнов с заданными геометрическими характеристиками была формализована А.И. Гребенниковым, который задачу улучшения геометрических характеристик сплайнов (особенно кубических) назвал задачей изо геометрической аппроксимации. В последующем Ю.А. Флеров стал использовать термин «консервативная интерполяция», который подчеркивает сохранение качественных характеристик экспериментальных данных.

Таким образом решение проблемы идет двумя путями [5]:

- варьируется параметры полиномиального сплайна с целью обеспечения требуемых свойств.
- в структуру кубического сплайна вводятся дополнительные параметры, выбором которых можно управлять качественным поведением графиков получаемых кривых.

Например, для нахождения вторых производных по сплайну $Z^{"} = \left\| z_1^{"}, z_2^{"}, \dots z_N^{"} \right\|^{\mathrm{T}}$ вместо решения системы уравнений (15) необходимо решить следующую систему линейных уравнений

$$h_{j-1}z_{j-1}^{"} + (2+p)\left(h_{j-1}+h_j\right)z_j^{"} + h_j z_{j+1}^{"} = 2(p^2+3p+3)\left(\frac{z_{j+1}}{h_{j+1}} - \frac{z_j - z_{j-1}}{h_j}\right), j = \overline{2, n-1}; p = const$$

Для p=0 получим систему (15), т.е. имеем стандартные кубический сплайн.

Гладкие интерполяционные восполнения. Приведем другой способ гладкого интерполяционного восполнения, например, профилей охлаждаемых лопаток авиационных ГТД, профилей крыльев ЛА произвольной формы или траекторий движения ЛА по точно измеренным или вычисленным значениям координат в конечной системе дискретных точек (смотри первый и второй пункты статьи [1-3]), отличный от метода сплайн-функции также эффективный с точки зрения реализации на компьютерах.

Предположим, что известны значения $\mathrm{z}_1, \mathrm{z}_2, \dots, \mathrm{z}_\mathrm{N}$ в узлах некоторой фиксированной сетки $t_1 < t_2 < \cdots, t_N$, где достаточно велико.

Построим интерполяционную кусочно-полиномиальную функцию класса гладкости $\left(t_j, t_{j+1}\right)$, $\frac{C^S}{(j=1,N-1-s}$ на интервалах. Степень полиномов на интервалах сетки равна 2s+1.

Обозначим P(t) многочлен Лагранжа степени не выше s, совпадающий с заданными значениями в узлах сетки

$$\left.\frac{d^k Q}{dt^k}\right|_{t=t_j} = \left.\frac{d^k p}{dt^k}\right|_{t=t_j}$$

$t_j, t_{j+1}, , \dots t_{j+s}$, а через U(t) – многочлен Лагранжа степени не выше s, принимающий заданные значения в узлах $t_{j+1}, t_{j+2}, , \dots t_{j+1+s}$.. Далее, построим многочлен Q(z(t)) степени не выше 2s+1, который удовлетворяет условиям

$$\left.\frac{d^k Q}{dt^k}\right|_{t=t_{j+1}} = \left.\frac{d^k u}{dt^k}\right|_{t=t_{j+1}}$$

$(k = 0,1,2, \dots, s; j = 1,2, \dots, N-1-s)$

Зафиксируем целое число s<<N. Пусть s=1, тогда многочлен третьей степени запишется в виде

$$Q(z(t))=a_0+a_1t+a_2t^2+a_3t^3 \quad ,$$

а его коэффициенты вычисляются по формулам (выполняются условия гладкости функции и первой производной).

$$a_0 = z_{j,}$$
$$a_1 = \left(z_{j+1} - z_j\right)h_{j+1}^{-1}$$
$$a_2 = -(\left(z_{j+2} - z_{j+1}\right)h_{j+2}^{-1} - \left(z_{j+1} - z_j\right)h_{j+1}^{-1})h_{j+1}^{-1}$$
$$a_3 = ((z_{j+2} - z_{j+1})h_{j+2}^{-1} - \left(z_{j+1} - z_j\right)h_{j+1}^{-1})h_{j+1}^{-1}$$
$$j = 1, N-1-s$$

Если положить s=2 (что соответствует гладкости кубических сплайнов т.е. выполняются условия гладкости функций, первой и второй производной), то будем иметь дело с многочленами пятой степени.

Преимущество такого интерполирования заключается в том, что не нужно решать систему линейных алгебраических уравнений типа (15), (21), хотя степень многочлена выше на два.

Конечно элементное восстановление профилей. Восстанавливается гладкая кривая $Z(t), t \in [t_1, t_N]$ С минимальной кривизной.

$$\int_{t_1}^{t_N} z''\left(t\right)^2 dt = \min_{W_2^2} . \qquad (31)$$

По известным значениям в дискретных точках

$$z(t_i) = z_i, \quad i = \overline{1, N} \qquad (32)$$

Представляется Z (t) в виде линейной комбинации конечного множества базисных функций

$$Z(t) = a_0 + a_1 t + a_2 t^2 + \dots + a_N t^N = C(t)\theta \;, \qquad (33)$$

где $C(t) = \|1, t, t^2, \dots t^N\|$; $\theta = \|a_0, a_2, \dots, a_N\|^{\mathrm{T}}$. Подставляется (33) в (31), (32) и после преобразований получается: минимизировать

$$\tfrac{1}{2}\theta^T H\theta \qquad (34)$$

при ограничениях

$$C\theta = B \qquad (35)$$

где $C = \begin{vmatrix} 1 & t_1 & t_1^2 & \cdots & t_1^N \\ 1 & t_2 & t_2^2 & \cdots & t_2^N \\ 1 & t_N & t_N^2 & \cdots & t_N^N \end{vmatrix}$; $H = 2\int_{t_1}^{1N} C''(t)^T C''(t)dt; B = \|z_1, z_2, \dots, z_N\|^{\mathrm{T}}$.

Решение задачи (34) – (35) находится с помощью множителей Лагранжа: задача без условной оптимизации

$$\tfrac{1}{2}\theta^T H\theta + \boldsymbol{\lambda}(C\theta - B), \qquad (36)$$

где $\boldsymbol{\lambda} = \|\boldsymbol{\lambda_1}, \boldsymbol{\lambda_2}, \dots, \boldsymbol{\lambda_N}\|^{\mathbf{T}}$ **.** В результате, для нахождения неизвестных $\boldsymbol{\lambda}$, $\boldsymbol{\theta}$. Из (36) получается следующая система линейных уравнений.

$$\left\| \begin{matrix} H & C^T \\ C & O \end{matrix} \right\| \left| \begin{matrix} \theta \\ \lambda \end{matrix} \right| = \left| \begin{matrix} O \\ B \end{matrix} \right| \quad (37)$$

Численный пример 1. Пусть функции Z(t) является кубическим полиномом

$$Z(t) = a_0 + a_1 t + a_2 t^2 + a_3 t^3, t \in [0,1]$$

При известных z (0) = 1, z (0.5)=6, z(1)=4. Тогда

$$C = \left\| \begin{matrix} 1 & 0 & 0 & 0 \\ 1 & 1/2 & 1/4 & 1/8 \\ 1 & 1 & 1 & 1 \end{matrix} \right\|$$

$$C^T = \left\| \begin{matrix} 1 & 1 & 1 \\ 0 & 1/2 & 1 \\ 0 & 1/4 & 1 \\ 0 & 1/8 & 1 \end{matrix} \right\|$$

$$H = 2 \left\| \begin{matrix} 0 & 0 & 0 & 0 \\ 0 & 0 & 0 & 0 \\ 0 & 0 & 4 & 6 \\ 0 & 0 & 6 & 12 \end{matrix} \right\|$$

$B = \|1,6,4\|^{T}$. Подставляя значения H, B, C, C^T в (37) получается следующая система уравнений

$$\left\| \begin{matrix} 0 & 0 & 0 & 0 & 1 & 1 & 1 \\ 0 & 0 & 0 & 0 & 0 & 1/2 & 1 \\ 0 & 0 & 0 & 6 & 0 & 1/4 & 1 \\ 0 & 0 & 0 & 12 & 0 & 1/8 & 1 \\ 1 & 0 & 0 & 0 & 0 & 0 & 0 \\ 1 & 1/2 & 1/4 & 1/8 & 0 & 0 & 0 \\ 1 & 1 & 1 & 1 & 0 & 0 & 0 \end{matrix} \right\| \left| \begin{matrix} a_0 \\ a_1 \\ a_2 \\ a_3 \\ \boldsymbol{\lambda}_1 \\ \boldsymbol{\lambda}_2 \\ \boldsymbol{\lambda}_3 \end{matrix} \right| = \left| \begin{matrix} 0 \\ 0 \\ 0 \\ 0 \\ 1 \\ 6 \\ 4 \end{matrix} \right|$$

Решив которую находится $a_0 = 1, a_1 = 17, a_2 = -14, \ a_3 = 0$. Заметим, матрица в уравнении (37) плохо обусловленная, и итерационные методы, используемые для решения больших разреженных систем, отличаются медленной сходимостью. Одно из решений этой проблемы-использование в качестве конечных элементов Вейвлетов [6].

Разработанные алгоритмы реализованы в виде Фортран программ на основе модульного принципа, т.е. в типовом унифицированном виде. Одним из преимуществ этих программ является то, что они не используют библиотечные подпрограммы из системы программного обеспечения конкретного компьютера, а только встроенные элементарные функции алгоритмического языка фортран.

Как показали вычислительные эксперименты, построенные крыловые профиля надежны и имеют практическую значимость в системах профилирования крыла самолета с механизацией.

Литература

[1]. Жданюк Б. Ф. Основы статистической обработки траекторных измерений – М.: Сов. Радио, 1978, 384с.
[2]. Аронов В. И., Жуковский М. И., Журавлев В. А. Профилирование лопаток авиационных газовых турбин/ Под ред. М. И. Жуковского. – М.: Машиностроение, 1975, 192 с.
[3]. Лифанов Н. К. Метод сингулярных интегральных уравнений и числ енный эксперимент в математической физике, аэродинамике, теории
упругости и дифракции волн. – М.: ТОО Янус, 1990, 520с.
[4]. Демиденко Е. З. Линейная и нелинейная регрессия. – М.: Финансы и статистика, 1981, 302с.
[5]. Квасов Б. И. Методы изогеометрической аппроксимации сплайнами. М.: Физматлит, 2006, 360с.
[6]. Стольниц Э., Де Роуз Т., Салезин Д. Вейвлеты в компьютерной графике. Ижевск: НИЦ "Регулярная и хаотическая графика". 2002 г.

Proceedings of the International Symposium of Mechanism and Machine Science, 2017
AzC IFToMM – Azerbaijan Technical University
11-14 September 2017, Baku, Azerbaijan

Резонансные колебания неуравновешенного вертикального гироскопического ротора с нелинейными характеристиками

Жарилкасин ИСКАКОВ

Алматинский Университет Энергетики и Связи, Институт Механики и Машиноведения
Алматы, Казахстан
E-mail: iskakov53@mail.ru

Абстракт
Рассматриваются резонансные колебания вертикального жесткого гироскопического ротора с мягкой нелинейной упругой характеристикой и вязким нелинейным демпфированием, у которого диск имеет перекос и дисбаланс массы. Особое внимание уделено влиянию перекоса диска и дисбаланса массы, нелинейного демпфирования на динамику ротора. Первое из них определяется характером поведения внешнего вынуждающего момента и влияет на амплитуду и фазу колебаний, а второе – реологическими свойствами демпфирующей среды и скоростью вращения вала ротора, влияет не только на амплитудно- и фазово-частотную характеристику, но и на устойчивость движения. Уравнения движения для системы с двумя степенями свободы, записанные в форме Лагранжа, разрешались методом разложения решений в ряд Фурье и методом гармонического баланса. Приближенный критерий устойчивости составлен на основании утверждения того, что вертикальная касательная к резонансной кривой соответствует границе устойчивости. Результаты исследований могут быть важными при разработке методов оптимального управления резонансными колебаниями, для определения оптимальных конструкционных параметров, диапазона рабочих скоростей и методов демпфирования и затухания колебаний ротора в пред проектных работах.
Ключевые слова: гироскопический ротор, дисбаланс массы, перекос диска, резонансные колебания, устойчивость движения, нелинейная характеристика, нелинейное демпфирование.

Введение

Как известно, высокоскоростные роторные машины широко применяются во многих отраслях промышленности (электроэнергетической, электронной и радиотехнической, пищевой, легкой, химической, нефтяной, медицинской, металлургической, космической, ядерной и др.). Высокий коэффициент полезного действия, малый удельный вес и высокая удельная мощность, сравнительно низкие затраты на изготовление и эксплуатацию, а также малая загрязненность окружающей среды ведут к расширению областей применения роторных машин. Следовательно, неудивительно, что роторные машины изучаются давно. Несмотря на это немало проблем, нерешенных, в частности связанных с совместным действием дисбаланса массы и перекоса диска на колебания и устойчивость при учете нелинейных характеристик и нелинейного демпфирования и впоследствии со стабилизацией резонансных нелинейных колебаний роторных машин.

Значительное количество работ посвящено определению положения и ориентации дисбаланса массы и перекоса диска и соответственно методам балансировки, управлению колебаниями ротора. В работах [1, 2] для полного описания динамики консольного ротора с двумя обобщенным дисбалансом внешнее демпфирование учитывалось во всех четырех уравнениях движения. Благодаря чему имели возможность правильно построить амплитудно- и фазово- частотные характеристики ротора, исследовать влияния на них дисбаланса массы и перекоса диска, консольности вала и внешнего сопротивления, сопоставить амплитуды колебаний на критических скоростях. В статье [3] рассматривается случай несимметричного ротора. Совместное влияние перекоса и дисбаланса массы диска приводит к тому, что прецессирующий ротор имеет необычную фазовую характеристику, причем фаза колебаний необязательно должна соответствовать ориентации дисбаланса на малых частотах вращения [4]. Это обстоятельство может существенно изменить методы балансировки ротора. В настоящее время существуют различные методы определения дисбаланса и балансировки. Так, например, в статье [5] предложены акустические методы определения дисбаланса массы ротора. Для определения дисбаланса может быть использован начальный вектор фазы (IPV), но этот метод иногда делает состояние равновесия не определенным. В статье [6] целевое соединение, которое включает в себя величину большой оси и начальный фазовый угол (IPA) орбиты прецессии представлено заменить IPV. Величина и угловое положение дисбаланса массы могут быть определены точно на величину большой оси и IPA, соответственно. В статье [7] предлагается активная схема управления поперечными колебаниями вала ротора из-за дисбаланса. Для этого использует электромагнитный возбудитель, установленный на статоре, в месте, удобном для управления поперечной вибрацией ротора, через воздушный зазор вокруг ротора. В работе [8] предлагается центрифуга с системой автоматического устранения колебаний центрифуги, порожденных ее дисбалансом. Два или более шаров внутри кольца, которые прикреплены к ротору, могут автоматически устранить его вибрации. Шары, которые также называются свободными элементами, смогут изменить свои позиций внутри кольца таким образом, чтобы компенсировать динамические силы. В статье объясняется, что шары занимают конечные положения, когда ротор и шары динамически стабильны. По сравнению с традиционной типа мяча балансировки [8] в статье [9] предлагается более надежный новый дизайн балансировки. В новой конструкции, шарики могут двигаться как радиальные и так и по окружению. Существует не более одного устойчивого равновесная конфигурация, при скорости вращения.

Привлекает внимание работы, посвященные нелинейным колебаниям в физических системах, в том числе роторных. В монографии Хаяси [10] подробно исследованы нелинейные колебания в физических системах с одной степенью свободы. Целью работы [11] является анализ резонансных кривых гармоник более высокого порядка в выражении для решения уравнения колебания с учетом зависимости их амплитуд и фаз от частоты и в предположении о неизменности величин амплитуды вынуждающей силы и коэффициента демпфирования. В работе [12] в отличие от предыдущей изучаются нелинейные резонансные колебания главной и других гармоник при учете силы нелинейного сопротивления. В статье [13] была изучена эффективность пассивных виброизоляторов с линейным затуханием и кубическим нелинейным затуханием в резонансных и нерезонансных областях колебаний. Здесь же приведен отличный обзор об исследованиях линейных и нелинейных виброизолирующих систем. В работе [14] в исследованиях дополнительно учтено влияние кубической нелинейной жесткости материала на производительность изолятора. В работе [15] рассматриваются колебания гибкого ротора на упругих опорах с нелинейной характеристикой, но не изучается взаимодействие с обобщенным дисбалансом диска.

Выше приведенный обзор исследований показывает, что слабо изучено совместное влияние дисбаланса массы и перекоса диска на резонансные колебания, особенно на устойчивость роторных машин при учете нелинейных факторов, имеющихся в реальных конструкциях и ограниченность исследований нелинейных систем с одной степенью свободы. Таким образом, исследования резонансных колебаний и устойчивости роторных машин с перекосом диска и дисбалансом массы с учетом нелинейной упругой характеристики опор и нелинейного вязкого демпфирования, технологии оптимального управления резонансными колебаниями приводящие к созданию новых надежно работающих роторных машин с оптимальными конструкционными параметрами, несомненно, являются актуальными.

Уравнения колебаний ротора с мягкой нелинейной упругой характеристикой и нелинейным сопротивлением

На рис. 1 представлена геометрическая схема ротора. Вал с длиной L установлен вертикально с

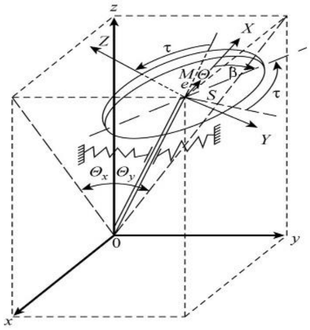

Рис.1. Геометрия ротора

помощью нижней шарнирной и отстоящей от нее на расстояние l_0 верхней упругой опоры. На свободном конце вала закреплен диск, имеющий массу m (веса G), полярный момент инерции I_p и поперечный момент инерции I_T, одинаковый для любого направления. Скорость вращения вала ω настолько большая, что ротор можно рассматривать как гироскоп, неподвижной точкой которого является нижняя опора вала. Положение геометрического центра диска S определяется координатами x, y, а положение вала и в целом ротора в пространстве углами θ_x, θ_y и углом поворота $\varphi = \omega t$. Предполагаем также, что линейный эксцентриситет e лежит на оси SX и отстает от плоскости углового эксцентриситета τ на угол β. Ограничимся малыми отклонениями оси ротора, поэтому будем учитывать в вычислениях только члены, линейные относительно малых величин $e, \tau, \theta_x, \theta_y$.

Верхняя упругая опора гироскопического ротора могут быть выполнены из нелинейных материалов, таких как сырой резины, каучука и других полимеров, широко используемых в качестве демпфера происходящих колебаний. Их выраженные рассеивающие свойства характеризуются нелинейно-вязким демпфированием, и они имеют мягкий или жесткий тип нелинейной упругой характеристики. В гироскопическом роторе коэффициент вязкого затухания μ_{e1} и коэффициент нелинейного члена вязкого затухания μ_{e2}, коэффициентом жесткости k_1 и коэффициентом в нелинейном члене упругой силы k_2.

Уравнения движения вертикального неуравновешенного гироскопического ротора были получены в работе [16]. Введя следующие безразмерные параметры

$$\begin{gathered}\varepsilon = e/L; l = l_0/L; \bar{t} = t\omega_0; \Omega = \omega/\omega_0;\\ \bar{I}_p = I_p/(mL^2); \bar{I}_T = I_T/(mL^2);\\ K_1 = k_1/\left(m\omega_0^2\right); K_2 = k_2 L/\left(m\omega_0^2\right);\\ P = G/\left(mL\omega_0^2\right); \mu_1 = \mu_{e1}/\left(mL^2\omega_0\right);\\ \mu_2 = \mu_{e2}/\left(mL^2\right)\end{gathered} \qquad (1)$$

где $\omega_0 = \sqrt{\left(k_1 l_0^2 - GL\right)/\left[mL^2 - \left(I_p - I_T\right)\right]}$ -критическая скорость бездемпфирной линейной системы, используя обозначения выражений амплитуды

$$M = \sqrt{\left[\left(\Omega^2 + P\right)\varepsilon + H\tau\Omega^2\cos\beta\right]^2 + H\tau^2\Omega^4\sin^2\beta} \qquad (2)$$

и начальной фазы

$$\gamma = \tan{-1}\frac{H\tau\Omega^2\sin\beta}{\left(\Omega^2 + P\right)\varepsilon + H\tau\Omega^2\cos\beta}, \qquad (3)$$

выразив вынуждающий момент с одними гармоническими функциями, можно придать уравнениям движения компактный вид

$$\left(1+\bar{I}_T\right)\theta_x'' + \bar{I}_p\Omega\theta_y' + \mu_1\theta_x' + \mu_2\theta_x'^2 + \left(K_1\ell^2 - P\right)\theta_x + K_2\ell^3\theta_x^2 = M\cos\left(\Omega\bar{t} + \gamma\right), \qquad (4)$$

$$\left(1+\bar{I}_T\right)\theta_y'' - \bar{I}_p\Omega\theta_x' + \mu_1\theta_y' + \mu_2\theta_y'^2 + \left(K_1\ell^2 - P\right)\theta_y + K_2\ell^3\theta_y^2 = M\sin\left(\Omega\bar{t} + \gamma\right), \qquad (5)$$

где $H = I_p - I_T$ - условная толщина диска.

Амплитудно- и фазово-частотные характеристики и устойчивость колебаний на частоте основного резонанса

Аппроксимация решений уравнений (4) и (5) в случае основного резонанса простой гармоникой с частотой колебаний, равной частоте возмущающего момента удовлетворяет

$$\theta_x = A_0 + A\cos(\Omega\bar{t} - \alpha), \qquad (6)$$

$$\theta_y = A_0 + A\sin(\Omega\bar{t} - \alpha). \qquad (7)$$

После применения метода гармонического баланса [10-12] получаем амлитудно- и фазово-частотные зависимости

$$\begin{gathered}\left(K_1 l^2 - P\right)A_0 + K_2 l^3 A_0^2 + \frac{1}{2}\left(\mu_2\Omega^2 + K_2 l^3\right)A^2 = 0\\ \left\{\left[\left(1-H\right)\Omega^2 - \left(K_1 l^2 - P\right) - 2K_2 l^3 A_0\right]^2 + \mu_1^2\Omega^2\right\}A^2 = M^2\end{gathered} \qquad (8)$$

$$tg\alpha = \frac{\left[(1-H)\Omega^2 - (K_1 l^2 - P) - 2K_2 l^3 A_0\right]tg\gamma + \mu_1\Omega}{(1-H)\Omega^2 - (K_1 l^2 - P) - 2K_2 l^3 A_0 - \mu_1\Omega tg\gamma} \qquad (9)$$

При отсутствии нелинейных членов в уравнениях (4) и (5) из выражений (8) и (9) получаться результаты для линейной модели ротора [17].

Амплитудно-частотные опорные кривые обычно описывает соотношение между амплитудой и частотой свободных колебаний системы без демпфирования [18]. Полагая равными нулю выражение *M* обусловленное внешним моментом, и коэффициенты демпфирования μ_1 и μ_2 в уравнениях (8), получаем уравнение опорной кривой для колебаний на частоте основного резонанса

$$A = \sqrt{\left(K_1 l^2 - P\right)^2 - \left(1-H\right)^2\Omega^4}\Big/\left(\sqrt{2}K_2 l^3\right) \qquad (10)$$

Здесь

$$\Omega \le \sqrt{\left(K_1 l^2 - P\right)/\left(1-H\right)}.$$

Из формулы (10) видно, что опорная кривая представляет собой параболу симметричную относительно оси Ω, чем больше величины K_2, тем больше наклона влево, опорной кривой.

$$\begin{gathered}f(\Omega, A) = \{[1-H)\Omega^2 - (K_1 l^2 - P) - 2K_2 l^3 A_0]^2 +\\ +\mu_1^2\Omega^2\}A^2 - M^2 = 0\end{gathered} \qquad (11)$$

где

$$A_0 = [-\left(K_1 l^2 - P\right) + \sqrt{\left(K_1 l^2 - P\right)^2 - 2K_2 l^3\left(\mu_2\Omega^2 + K_2 l^3\right)A^2}\,]/\left(2K_2 l^3\right) \qquad (12)$$

Геометрическое место точек, в которых амплитудные кривые для колебаний основного резонанса имеют вертикальные касательные, определяется уравнением [19]

$$\partial f/\partial A = 0. \qquad (13)$$

Равенство (13) с учетом (11) приводит к уравнению

$$\{[(1-H)\Omega^2-\sqrt{\left(K_1l^2-P\right)^2-2K_2l^3\left(\mu_2\Omega^2+K_2l^3\right)A^2}\,]^2+$$
$$\mu_1^2\Omega^2\}\times\sqrt{\left(K_1l^2-P\right)^2-2K_2l^3\left(\mu_2\Omega^2+K_2l^3\right)A^2}+ \qquad (14)$$
$$+4K_2l^3\left(\mu_2\Omega^2+K_2l^3\right)A[(1-H)\Omega^2-$$
$$-\sqrt{\left(K_1l^2-P\right)^2-2K_2l^3\left(\mu_2\Omega^2+K_2l^3\right)A^2}\,]=0$$

Уравнение (14) описывает граничные кривые области устойчивости для колебаний на частоте основного резонанса. Следовательно, геометрическое место точек, в которых амплитудные кривые имеют вертикальные касательные, определяют границы области устойчивости.

Числовые результаты и оценка влияния параметров

Вычисления по формулам (2) и (3) и решение системы уравнений (8), (9) и (14) производились на компьютере численным методом в системе символьных вычислений «Maple 11» для следующих параметров ротора:

$$H=+0{,}1:\ \varepsilon=0{,}01;\ \tau=0{,}02;\ L=0{,}88;\ \bar{I}_p=0{,}2;$$
$$\bar{I}_T=0{,}1;\ K_1=1{,}19;\ K_2=2{,}19;3{,}19;\ P=0{,}012;$$
$$\mu_1=0;\ \mu_2=0;0{,}5;\ H=-0{,}1:\varepsilon=0{,}01;$$
$$\tau=0{,}02;\ L=0{,}88;\ \bar{I}_p=0{,}1;\ \bar{I}_T=0{,}2;\ K_1=1{,}45;$$
$$K_2=2{,}45;3{,}45;\ P=0{,}014;\ \mu_1=0;\ \mu_2=0;0{,}5.$$

Анализ формулы (2) показывает, что амплитуда вынуждающего момента достигает максимального значения при $\beta=0^0$, H=0,1 ($\beta=180^0$, H=-0,1), минимального значения - при $\beta=180^0$, H=0,1($\beta=0^0$,H=-0,1) и промежуточного значения – при $\beta=\pm90^0$, $H=\pm0{,}1$. Об этом свидетельствуют и графики $M = M(\Omega)$ при различных значениях β и H, представленные на рис. 2 и 3. На рис. 4 и 5, на графиках $\gamma=\gamma(\Omega)$ при $\Omega\to\infty$ начальная фаза вынуждающего момента стремиться к асимптотическому значению: максимальному при $\beta=+90^0$, H=0,1 ($\beta=-90^0$, H=-0,1), минимальному при $\beta=+90^0$, H=-0,1 ($\beta=-90^0$, H=+0,1) и принимает нулевое значение при $\beta=0^0$, 180^0 при любых значениях H.

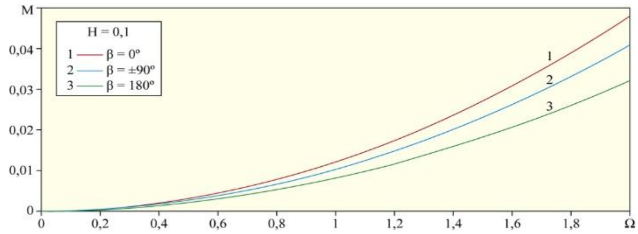

Рис. 2. Зависимость амплитуды вынуждающего момента от частоты вращения. Случай тонкого диска

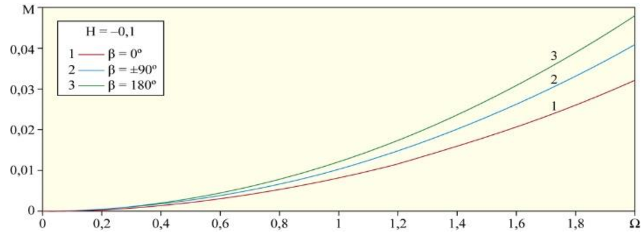

Рис. 3. Зависимость амплитуды вынуждающего момента от частоты вращения. Случай толстого диска

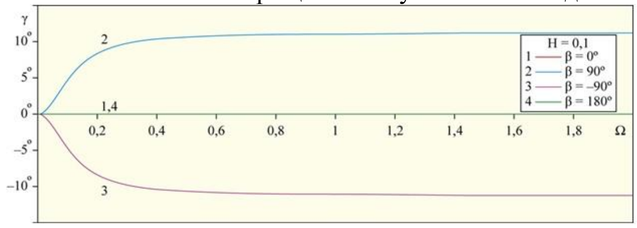

Рис. 4. Зависимость начальной фазы вынуждающего момента от частоты вращения. Случай тонкого диска

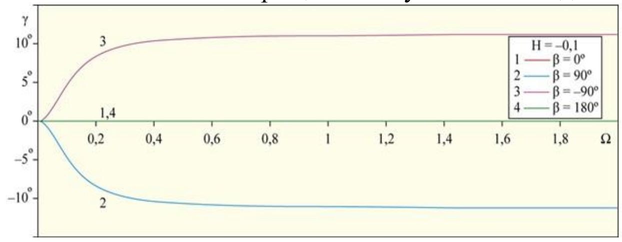

Рис. 5. Зависимость начальной фазы вынуждающего момента от частоты вращения. Случай толстого диска

Зависимости амплитуды A от угла β между линиями дисбаланса массы и максимального перекоса диска (рис. 6 и рис. 8) как в случае линейной модели ротора [17]. Влияние перекоса может приводить либо к увеличению, либо к уменьшению амплитуды колебаний. В случае тонкого диска (H=0,1) при угле $\beta = 0$ линия максимального перекоса совпадает с линией вектора эксцентриситета массы, направления моментов силы тяжести, центробежной силы и гироскопического момента совпадают, вынуждающий момент становиться максимальным (смотри рис. 2) и приводит к усилению эффекта отклонения вала от вертикали.

Зависимости амплитуды A от угла β между линиями дисбаланса массы и максимального перекоса диска (рис. 6 и рис. 8) как в случае линейной модели ротора [17]. Влияние перекоса может приводить либо к увеличению, либо к уменьшению амплитуды колебаний. В случае тонкого диска (H=0,1) при угле $\beta = 0$ линия максимального перекоса совпадает с линией вектора эксцентриситета массы, направления моментов силы тяжести, центробежной силы и гироскопического момента совпадают, вынуждающий момент становиться максимальным (смотри рис. 2) и приводит к усилению эффекта отклонения вала от вертикали.

При угле $\beta = 180^0$ гироскопический момент противоположно направлен суммарному моменту центробежной силы и силы тяжести, вынуждающий момент и амплитуда колебаний оказываются наименьшими (смотри обсуждение формулы (10) и графика на рис 6).

При угле $\beta = \pm 90^0$ возмущающие воздействия перпендикулярны друг другу, и мы получаем промежуточные значения вынуждающего момента и амплитуды колебаний. В случае толстого диска (*H*=-0,1) зависимость амплитуды колебаний *A* от угла β носит теперь противоположный характер ввиду смены знака гироскопического момента (рис. 8). В частотах вращения близких к резонансной частоте наблюдаются признаки скачков амплитуды происходящих в обратном направлении (рис.6, рис.8) [15]. Когда, кривые соответствующие двум значениям амплитуды A основной гармоники ротора соединяются, соответствующие кривые фазово-частотной характеристики замыкаются, а кривая соответствующая оставшемуся третьему значению амплитуды при критической скорости поднимается вверх или опускается вниз, и в дальнейшем стремясь 180^0 либо -180^0 уровню (рис. 7, рис. 9).

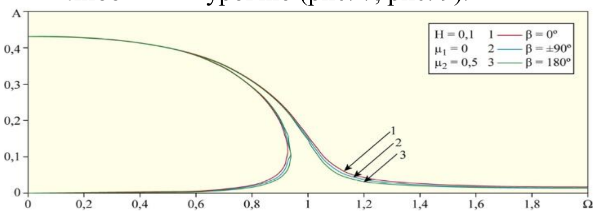

Рис. 6. Влияние угла между ориентациями дисбалансов на амплитудно-частотную характеристику ротора. Случай тонкого диска

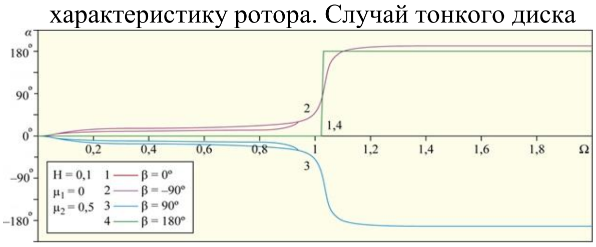

Рис. 7. Влияние угла между ориентациями дисбалансов на фазово-частотную характеристику ротора. Случай тонкого диска

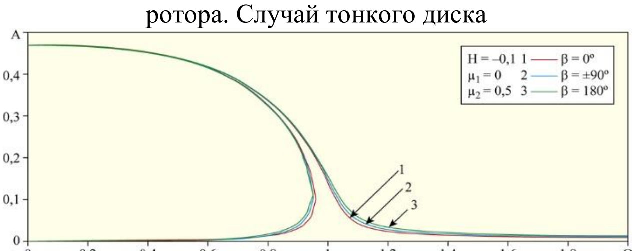

Рис. 8. Влияние угла между ориентациями дисбалансов на амплитудно-частотную характеристику ротора. Случай толстого диска

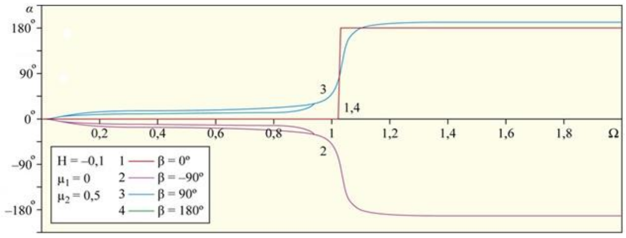

Рис. 9. Влияние угла между ориентациями дисбалансов на фазово-частотную характеристику ротора. Случай толстого диска

В случае $\beta = \pm 90^0$ при изменении толщины диска расположение фазовой частотной характеристики относительно оси абсциссы меняются на обратное. При угле $\beta = 0;180^0$ фазово-частотные характеристики имеют вид как в случае отсутствия демпфирования вообще, хотя коэффициент нелинейного демпфирования μ_2 не равен нулю. Это объясняется с тем, что в выражении $tg\alpha$ (9), слагаемые, содержащие μ_1 и $tg\gamma$, обращаются в нуль, так как значения этих величин равны нулю при угле $\beta = 0;180^0$.

При увеличении коэффициента K_2 нелинейной составляющей упругой силы опоры при постоянном коэффициенте μ_2 нелинейного демпфирования наблюдается картина, показанная на рис. 10 и 11.

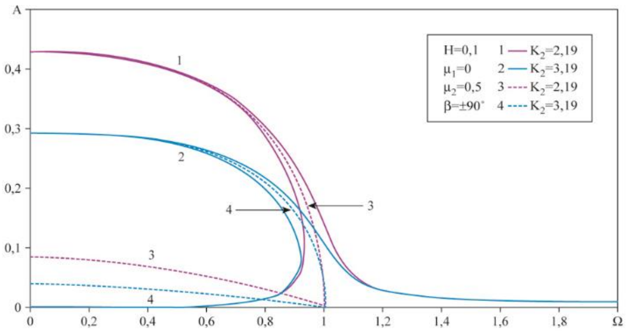

Рис. 10. Влияние коэффициента нелинейной составляющей силы упругости на амплитудно-частотную характеристику и на границы области неустойчивости. Случай тонького диска

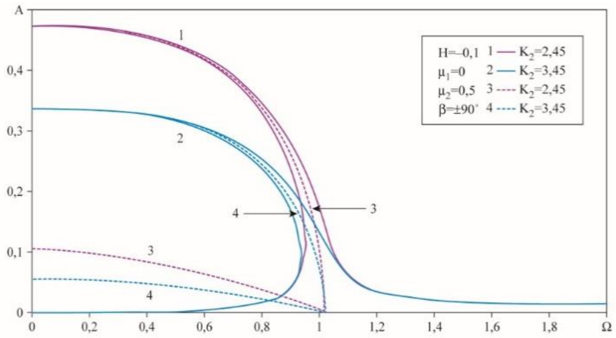

Рис. 11. Влияние коэффициента нелинейной составляющей силы упругости на амплитудно-частотную характеристику и на границы области неустойчивости. Случай толстого диска

Амплитудные кривые изображены сплошными кривыми, а границы между устойчивыми и неустойчивыми областями – пунктирными линиями. Область между этими линиями является областью неустойчивостью. Когда увеличиваем параметр K_2, резонансные кривые затягиваются с конца и наклоняются влево в область низших частот с уменьшением амплитуды. Под влиянием коэффициента K_2 область неустойчивости смещается вниз, верхняя граница больше смешается, чем нижняя. В результате изменяется положение области неустойчивости, а ширина сокращается. Это само собой понятно, что увеличение упругой силы, направленной в положение равновесия, при росте коэффициента K_2 еще больше ограничивает амплитуду колебаний.

На рис. 12 и 13 показаны амплитудно-частотные характеристики и границы области неустойчивости на частоте основного резонанса при различных значениях коэффициента μ_2 нелинейного демпфирования.

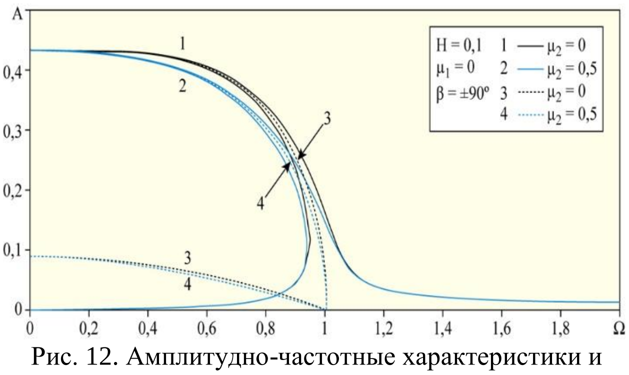

Рис. 12. Амплитудно-частотные характеристики и границы области неустойчивости при различных значениях коэффициента нелинейного демпфирования. Случай тонького диска

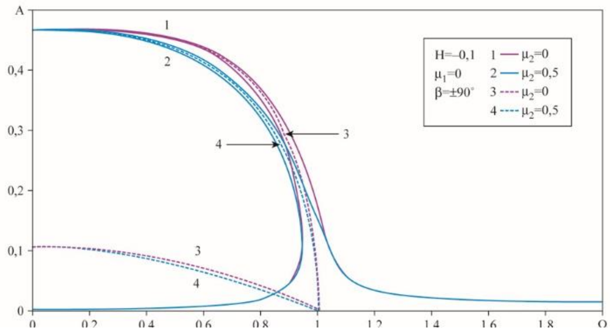

Рис. 13.Амплитудно-частотные характеристики и границы области неустойчивости при различных значениях коэффициента нелинейного демпфирования. Случай толстого диска

Под влиянием коэффициента μ_2 нелинейного демпфирования средняя часть верхних резонансных кривых изгибается, вниз, начиная примерно с особых точек скачков амплитуды. Под действием нелинейного демпфирования средняя часть линии верхней границы смещается вниз значительно больше, чем средняя часть линии нижней границы области неустойчивости, иными словами средняя часть области неустойчивости сужается, что показывает стабилизирующее влияние нелинейного демпфирования. Это доказывает достоверность полученных результатов, прямо противоположных результатам работы [12]. Из-за отсутствия угла β в выражении критерия устойчивости (14) этот угол не влияет на границы устойчивости. Расчеты также показывает, что коэффициент нелинейного демпфирования μ_2 практически не оказывает влияние на фазово-частотные характеристики главного резонанса. Изменение толщины диска ротора влияет на расположение резонансных кривых и на ширину области неустойчивости. Так, например, область неустойчивости для ротора с толстым диском шире чем - для ротора с тонким диском.

Заключение

Исследованы основные резонансные колебания и устойчивость вертикального жесткого гироскопического ротора с мягкой нелинейной упругой характеристикой и нелинейным демпфированием, у которого диск имеет перекос и дисбаланс массы. Обнаружено, что перекос диска влияет на величины амплитуды и фазы вынуждающего момента и соответственно на величины амплитуды и фазы основных резонансных колебаний. Рассмотрены варианты тонкого и толстого диска. Под влиянием нелинейной составляющей упругой силы, как известно резонансные кривые вытягиваются с конца и наклоняются влево, в область низких скоростей вращения, с уменьшением амплитуды, а область неустойчивости смещается вниз, причем верхняя граница больше, чем нижняя граница. Под воздействием нелинейного вязкого демпфирования средняя часть верхних резонансных кривых изгибается, вниз, начиная примерно с особых точек скачков амплитуды. Область неустойчивости смещается, а ее ширина сужается, притом смещение вниз средней части верхней границы больше, чем смещение средней части нижней границы, что доказывает стабилизирующее влияние нелинейного вязкого демпфирования. Формы фазово-частотных характеристик ротора практически остаются неизменными. Изменение толщины диска оказывает влияние на расположение резонансных кривых и на ширину области неустойчивости. Рассмотренную нелинейную модель ротора с двумя степенями свободы можно распространить на модели ротора с четырьмя степенями свободы, так например, на консольный ротор с упругой опорой, на несимметричный ротор с упругими опорами и на другие виды роторов.

Литература

[1]. Zh. Iskakov, *The steady fluctuations of the double-beat cantilever rotor with the skew and disbalance of the disk*, in: Abstracts of the International conference Inverse Problems: Modeling and Simulation. Fethiye – Turkey, pages 77-78, 2008.

[2]. Zh. Iskakov, *Resonance vibrations of unbalanced two-bearing outboard rotor*, in: S.H. Hong, J. Seo, K. Moon (Eds), Advanced Materials, Mechanical and Structural Engineering. Taylor & Francis Group; London, pages 265-270, 2016.

[3]. Zh. Iskakov, & M. Ashirbayev, *Resonant Oscillations of Non-Symmetrical Rotor with Mass Imbalance and Disk Skew*, Applied Mechanics and Materials, Vol. 863, pages 157-162, Trans Tech Publications; Switzerland, 2017

[4]. R.S. Benson, *Steady oscillations of the console rotor with skew and imbalance of a disc*, Design and Manufacturing Engineering 105 (4) pages 35 – 40, 1983.

[5]. B.A. Gordeev, and G.A. Maslov, *Detection of unbalance of rotor with acoustic methods*, in: D.V. Balandin, V.I. Erofeev (Eds), Nonlinear vibrations of mechanical systems 2, Publishing House Dialogue of Cultures; Nizhniy Novgorod, pages 90–95, 2008.

[6]. Y. Liao, and P. Zhang, *Unbalance related rotor precession behavior analysis and modification to the holobalancing metod*, Mechanism and Machine Theory 45 (4), pages 601–610, 2010.

[7]. A.S. Das, and M.C. Nighil, and J.K. Dutt, and H. Irretier, *Vibration control and stability analysis of rotor-shaft system with electromagnetic exciters*, Mechanism and Machine Theory 43 (10), pages 1295-1316, 2008.

[8]. T. Majewski, and D. Szwedowicz, and A. Herrera, *Riquelme*, *Automatic elimination of vibrations for a centrifuge*, Mechanism and Machine Theory 46 (3) pages 344-357, 2011.

[9]. Chung-Jen Lu, and Ming-Cheng Wang, *Stability analysis of a ball–rod–spring automatic balancer*, IJMS 53(10), pages 846-854, 2011.

[10] C. *Hayashi*, *Nonlinear Oscillations in Physical Systems*, Chapters 1, 3 – 6. McGraw – Hill, 1964.

[11] W. Szemplinska-Stupnicka, *Higher harmonic oscillations in heteronymous nonlinear systems with one degree of freedom*, International Journal of Non-Linear Mechanics 3 (1), pages 17-30, 1968.

[12] A.B. Kydyrbekuly, *Vibrations and stability of rotor systems and planar mechanisms with nonlinear elastic characteristics, Dissertation of the doctor of technical sciences*. Mechanics and Engineering Institute; Almaty, 2006.

[13]. Z.K. Peng, and Z.Q Mengand Lang, and W.M. Zhang, and F.L. Chu, *Study of the effects of cubic nonlinear damping on vibration isolations using Harmonic Balance Method*, International Journal of Non-Linear Mechanics 47 (10), pages 1065-1166, 2012.

[14]. C. Ho, and Z.Lang, and S.A. Billings, *The benefits of nonlinear cubic viscous damping on the force transmissibility of a Duffing-type vibration isolator*. In: Proceedings of UKACC International Conference on Control; Cardiff, UK, 2012.

[15]. V.A. Grobov, *Asymptotic methods for calculating the flexural vibrations of turbo machines' shafts*. Academy of Sciences Press of the USSR; Moscow, 1961.

[16]. Zh. Iskakov, *Resonant Oscillations of a Vertical Unbalanced Gyroscopic Rotor with Nonlinear Characteristics*. In: Proceedings of 2015 IFToMM World Congress; Taipei, Taiwan, 2015.

[17] Zh. Iskakov, and A. Kalybaeva, *Vibrations and stability of vertical gyro rotor with warped disk and mass imbalance*, Fundamental and applied problems of science, V. 2, Writings of I International Symposium; Moscow pages 50 – 57, 2010.

[18]. Y.G. Panovko, *Introduction to mechanical vibrations theory*. Science; Moscow, 1971.

[19]. R. Van Dooren, *Combination tones of summed type a non – linear damped vibratory system with two degrees of freedom*, International Journal of Non-Linear Mechanics 6, pages 237-254, 1971.

Proceedings of the International Symposium of Mechanism and Machine Science, 2017
AzC IFToMM – Azerbaijan Technical University
11-14 September 2017, Baku, Azerbaijan

Динамика маятникового виброгасителя крутильных колебаний

Асылбек ДЖОМАРТОВ[1], Амандык ТУЛЕШОВ[2]
[1,2] Институт Механики и Машиноведения им. У.А.Джолдасбекова
Алматы, Казахстан
E-mail: legsert@mail.ru

Абстракт
В работе рассматривается динамика маятникового виброгасителя крутильных колебаний. Маятниковые виброгасители применяются в современных машинах для снижения вибрации. Маятниковый виброгаситель позволяет снизить колебания в широком диапазоне частот. Для моделирования динамики маятникового виброгасителя крутильных колебаний используется программный комплекс SimulationX. Проведен анализ модели упругой трансмиссии с приводом от двигателя внутреннего сгорания с маятниковым виброгасителем на программном комплекс SimulationX.
Ключевые слова: маятник, виброгаситель, динамика, SimulationX.

1. Введение

Машины и механизмы подвергаются воздействию колебаний (вибрации), которые возникают как при работе самой машины, так и при воздействии различных внешних сил. Разработка и исследование различных устройств защиты от вибраций является одной из актуальных задач в данное время. Снижение амплитуды колебаний машины или отдельных ее узлов достигается за счет установки специальных виброгасителей. Установка виброгасителей является наиболее эффективным способом, иногда даже единственно возможным, обеспечивающим необходимое снижение вибраций. Использование виброгасителей может быть предусмотрено не только на стадии проектирования и создания машины, но и в тех случаях, когда вибрации выявлены уже в процессе ее эксплуатации. Принцип работы виброгасителя состоит в том, что, присоединенное определенным способом дополнительное тело (или система тел), своими колебаниями уменьшает колебания узлов машины на частоте (или в каком-то частотном диапазоне) внешнего возбуждения.

2. Центробежный маятниковый виброгаситель крутильных колебаний вала

В современных машинах, для снижения вибрации, часто применяют маятниковые виброгасители. Основное достоинство маятникового виброгасители состоит в широком диапазоне частот гашения колебаний, Расширение диапазона достигается за счет того, что собственная частота маятника в поле центробежных сил пропорциональна скорости вращения [1].

На рис. 1 показана схема центробежного маятникового виброгасителя крутильных колебаний вала, вызываемых гармоническим возбуждением $M = M_0 sin\omega t$. Для гашения колебаний к диску вала на расстоянии r от его оси шарнирно прикреплен маятник с массой m_r, сосредоточенной на конце невесомого стержня длиной l.

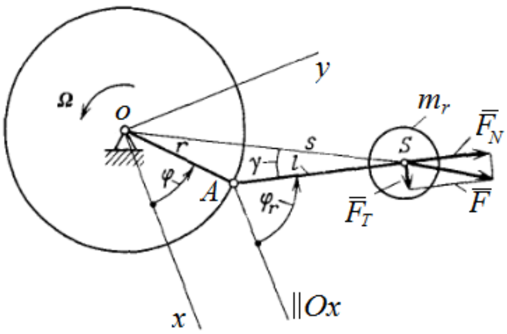

Рис. 1. Схема маятникового гасителя крутильных колебаний вала

Уравнения движения составляем в системе координат Oxy, вращающейся со средней угловой скоростью вала Ω. За обобщенные координаты принимаем угол поворота диска φ, отсчитываемый от оси Ox, и угол качания маятника φ_r отсчитываемый от направления той же оси. При составлении уравнений движения [1] по кинетостатическому методу учитываем силу инерции массы m_r, в абсолютном движении по приближенной формуле $F = m_r s\Omega^2$, где расстояние от центра масс маятника до оси вращения диска. Раскладывая эту силу на две составляющие F_N и F_τ вдоль стержня AS и перпендикулярно к нему, получаем:

$$F_N = m_r\Omega^2 s\, cos\gamma,\ F_\tau = m_r\Omega^2 s\, sin\gamma.$$

Из треугольника OAS находим:

$$s\, cos\,\gamma = l + rcos\,\psi,\ s\, sin\gamma = l + r\, sin\,\psi,$$

где $\psi = \varphi_r - \varphi$. При малых колебаниях маятника, считая $cos\psi = 1, sin\,\psi \approx \psi$, имеем:

$$F_N \approx m_r\Omega^2(l + r),\ F_\tau \approx m_r\Omega^2 r\psi.$$

Уравнение кинетостатического равновесия диска имеет вид

$$J\ddot{\varphi} - F_N r sin\,\psi = M_0 sin\omega t - c\varphi,$$

где J - момент инерции диска, c - коэффициент крутильной жесткости участка вала между двигателем и диском.

Подставляя приближенное значение условие, получаем первое дифференциальное уравнение движения системы

$$J\ddot{\varphi} + c\varphi - m_r\Omega^2 r(l + r)(\varphi_r - \varphi) = M_0\ sin\omega t.$$

При составлении второго дифференциального уравнения пренебрегаем малыми кориолисовыми силами. Силу инерции в переносном движении учитываем по приближенной формуле $F_k \approx m_r r\ddot{\varphi}$, а момент составляющей F_τ относительно точки подвеса маятника равен $m_r\Omega^2 r(\varphi_r - \varphi)l$

$$m_r l^2\ddot{\varphi}_r + \ m_r\,\Omega^2 rl(\varphi_r - \varphi) + m_r\ddot{\varphi} rl = 0.$$

Установившиеся вынужденные колебания с частотой вынуждающей силы описываются решением

$$\varphi = A\, sin\,\omega t,\ \varphi_r = A_r \sin\omega t.$$

Подставляя это решение в систему уравнений движения, получаем два уравнения с двумя неизвестными A и A_r:

$$[c - J\omega^2 + \ m_r\,\Omega^2 r(l + r)]A - m_r\Omega^2 r(l + r) = M_0,$$
$$-m_r rl\,(\Omega^2 + \omega^2)A + m_r l(r\Omega^2 - l\omega^2)A_r = 0.$$

Отсюда

$$A = \frac{M_0}{\Delta} m_r l(r\Omega^2 - l\omega^2), A_r = \frac{M_0}{\Delta} m_r rl(\Omega^2 + \omega^2),$$

где Δ – определитель, который составлен из коэффициентов при A и A_r в системе уравнений движения.

Если $\Delta \neq 0$, то из выражения для амплитуды А можно найти антирезонансную частоту ω_*, при которой $A = 0$

$$\omega_* = \Omega\sqrt{\frac{r}{l}} \quad (1)$$

Следовательно, в центробежном маятниковом виброгасителе в отличие от пружинного виброгасителя антирезонансная частота пропорциональна угловой скорости вращения вала.

Обозначая через n отношение частоты вынуждающей силы ω к средней угловой скорости вала Ω, получаем из (1) условие для выбора параметров виброгасителя

$$\frac{r}{l} = \ n^2 \quad (2)$$

т. е. гашение колебаний, вызываемых n-й гармоникой вынуждающего момента, обеспечивается единой настройкой виброгасителя при любой скорости вращения вала.

При гашении крутильных колебаний для компенсации изгибающего действия составляющей силы F_N устанавливают два маятника в диаметрально противоположных точках диска (рис. 2, а) [1].

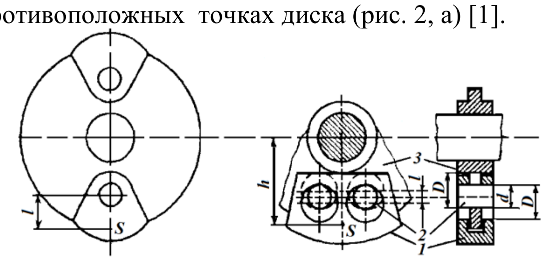

Рис. 2. Конструкции маятникового виброгасителя крутильных колебаний вала

Создаваемый ими эффект снижения колебаний имеет суммарное действие. Однако эта схема конструктивно удобна, как правило, лишь при $n = 1$. С увеличением n длина маятника l существенно уменьшается. При малом l применяется бифилярный подвес (рис. 2, б), при котором в качестве маятника используется противовес 1, укрепленный с помощью роликов 2 на щеке 3 коленчатого вала. Диаметр d роликов меньше, чем диаметр D сверлений в щеке. Указанное крепление обеспечивает поступательное движение противовеса, при котором все его точки движутся по дугам окружностей равных радиусов $l = D - d$. Радиус крепления маятника-противовеса в этом случае $r = h - l$, где h- расстояние от оси вала до центра масс противовеса, и условие (2) для выбора параметров гасителя принимает вид

$$\frac{h - D + d}{D - d} = n^2$$

Массу виброгасителя m_r выбирают из условия, чтобы при допустимых амплитудах качания создаваемый им момент разнялся n -й гармонике вынуждающего момента.

3. Моделирование маятникового виброгасителя крутильных колебаний

Для моделирования работы маятникового виброгасителя крутильных колебаний используем программный комплекс SimulationX . SimulationX – это междисциплинарный программный комплекс для моделирования физико-технических объектов и систем, который разработан фирмой ITI GmbH, Дрезден [2]. Ученые и инженеры, работающие в промышленности и сфере образования, используют этот инструмент для разработки, моделирования, симулирования, анализа и виртуального тестирования сложных мехатронных систем.

Мы будем использовать модель «Маятниковый гаситель» (Pendulum Absorber) на программном комплексе SimulationX. Это модель маятникового виброгасителя, которая используются в приводах машин. Маятниковый виброгаситель является эффективными и адаптивным средством для устранения опасных резонансов во вращающихся валах, в которых частоты возбуждения пропорциональны скорости вращения. На рис. 3 показана схема маятникового виброгасителя.

Модель учитывает момент инерции диска и массу маятника. Сила тяжести действует в направлении оси y маятника. Модель может учитывать переменную длину маятника (параметр **lP**). Модель учитывает трение во вращательной паре крепления маятника.

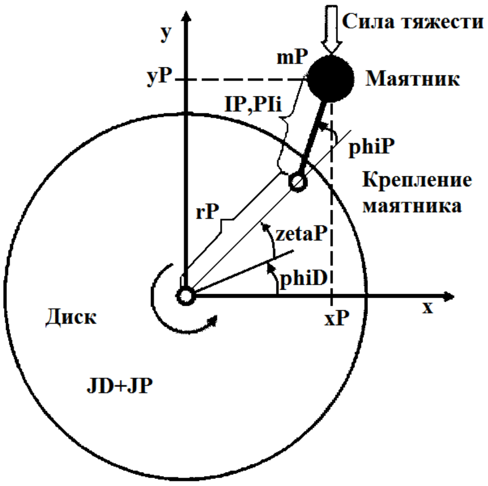

Рис. 3. Схема маятникового виброгасителя

*Входные параметры модели***:** Длина маятника **lP**, радиус маятника **rP** (рис.3) могут быть постоянными или переменными величинами. **zetaP** - угол крепления маятника при сборке. По умолчанию он равен нулю. В случае установки более чем одного маятника на диске или вале, например для гашения более чем одного резонанса, маятники устанавливаются под разными углами, что может быть учтено в модели. Масса маятника **mP .** Момент инерции маятника **JP**. Диск моделируется элементом инерции библиотеки механики вращательных тел. Момент инерции этого элемента представляет собой сумму дискового момента инерции **JD** и момента инерции маятника **JP**. Начальный угол диска **phiD0** и начальная скорость диска **omD0.** Коэффициент трения покоя маятника **mu0**, коэффициент трения скольжения маятника **mu**. Диаметр оси вращения маятника **dPin.**

Выходные параметры модели: **phiP** - угловое перемещение маятника**, omP** - угловая скорость маятника**, alpP** - угловое ускорение маятника, **xP** - перемещение маятника по оси X**, yP** - перемещение маятника по оси У **, vxP** - скорость маятника по оси X**, vyP** - скорость маятника по оси У**, lPi** - текущая длина маятника, **TaD** – крутящий момент диска, **phiD -** угловое перемещение диска, **omD –** угловая скорость диска, **alpD -** угловое ускорение диска, **FxD –** реакция в опоре диска по оси X, **FyD - –** реакция в опоре диска по оси У, **Pk –** кинетическая энергия, **Pl** – потери энергии от трения.

3.1 Модель упругой трансмиссии с приводом от двигателя внутреннего сгорания с маятниковым виброгасителем.

На рис. 4 а, б показаны две модели упругой трансмиссии с приводом от двигателя внутреннего сгорания. Модель упругой трансмиссии с приводом от двигателя внутреннего сгорания, показанная на рис. 4б оснащена маятниковым виброгасителем. Собственная частота упругой трансмиссии равна 58 Гц, и при достижении двигателем 1740 оборотов в минуту, появляются резонансные колебания, вызванные второй гармоникой крутящего момента двигателя внутреннего сгорания.

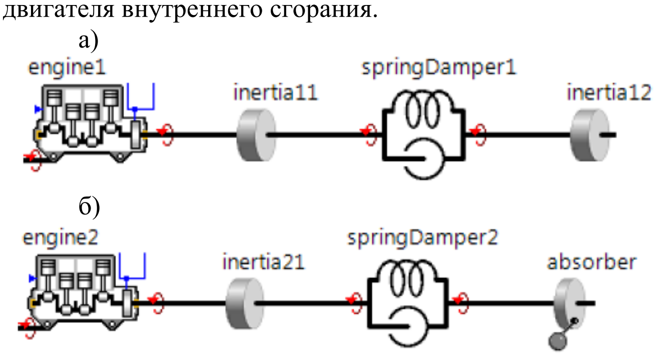

Рис. 4. Модели упругой трансмиссии с приводом от двигателя внутреннего сгорания: а) обычная, б) с маятниковым виброгасителем

Входные параметры модели упругой трансмиссии с приводом от двигателя внутреннего сгорания: мощность 4-х цилиндрового дизельного двигателя **Pn** = 44 квт, номинальные обороты двигателя **omn** = 5000 об/мин, момент инерции двигателя **J**=0.1 $\text{кг}\cdot\text{м}^2$, момент инерции трансмиссии **J21**= 0.2 $\text{кг}\cdot\text{м}^2$, коэффициент жесткости трансмиссии **к**=10^4 нм/рад, коэффициент диссипации трансмиссии **в**=1 $\text{н}\cdot\text{м}\cdot$ с/рад, масса маятника **mP**= 1 кг, момент инерции маятника **JP**=0 $\text{кг}\cdot\text{м}^2$, момент инерции диска **JD**=0,1 $\text{кг}\cdot\text{м}^2$, длина маятника **lP**=20 мм, радиус маятника

rP=80 мм, угол крепления маятника при сборке **zetaP**=0 рад.

Результаты моделирования. Собственная частота трансмиссии равна 58 гц. Маятниковый виброгаситель был настроен для гашения резонанса трансмиссии вызванного второй гармоникой крутящего момента двигателя внутреннего сгорания. Как видно из диаграммы Кемпбела (рис. 5) резонанс, вызываемый второй гармоникой крутящего момента двигателя внутреннего сгорания, происходит при числе оборотов двигателя 1740 об/мин.

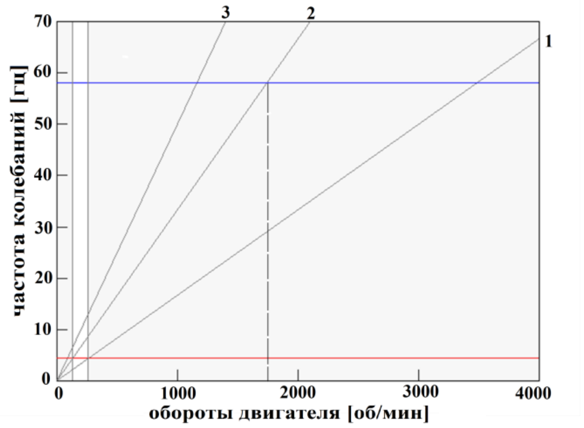

Рис. 5. Диаграмма Кемпбела трансмиссии

Рис. 6. Крутящий момент трансмиссии

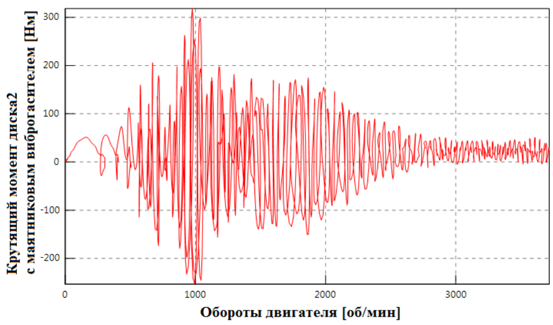

Рис. 7. Крутящий момент трансмиссии с маятниковым виброгасителем

Как видно из рис.6 максимальная амплитуда крутящего момента равна 486 Нм при числе оборотов двигателя 1900 об/мин. На рис. 7 показан график крутящего момента трансмиссии с маятниковым виброгасителем. В результате применения маятникового виброгасителя амплитуда крутящего момента трансмиссии снижена до 175 Нм при числе оборотов двигателя 1900 об/мин.

Выводы

Модель «Маятниковый гаситель» (Pendulum Absorber) на программном комплексе SimulationX может применяться, как в учебном процессе, так и при исследовании существующих трансмиссий двигателей внутреннего сгорания и проектировании новых. Программный комплекс SimulationX позволяет применять модель «Маятниковый гаситель» (Pendulum Absorber) при моделировании динамики широкого класса электро-механических систем

Литература

[1]. Н.И. Левитский, Колебания в механизмах. М.: Наука, 1988.

[2]. Web, http://www.simulationx.com/.

Proceedings of the International Symposium of Mechanism and Machine Science, 2017
AzC IFToMM – Azerbaijan Technical University
11-14 September 2017, Baku, Azerbaijan

Исследование влияние параметров четырехзаходного роторного тканеформирующего механизма на процесс непрерывного ткачества

Фарзалиев Мазахир Гамза оглы, Садирли Садраддин Мовлан оглы
Азербайджанский Государственный Экономический Университет (UNEC)

Аннотация.
В настоящее время текстильную промышленность внедряется ткацкие многозевные машины вырабатывающий ткань непрерывном способом. Основным механизмом ткацкой многозевной машины является тканеформирующий механизм (ТФМ). Для увеличения производительности ткацких многозвенных машин нами предложен четырехзаходный роторный ТФМ. В представленной работе исследован влияние параметров четырехзаходного роторного ТФМ на процессе непрерывного тканеформирования.

Для решения поставленной задачи в работе разработан динамической модель поперечных колебаний передней ветви зева и определены частоты этих колебаний при выработке различных ассортиментов ткани. Получены зависимость для определения частоты контакта зубьев прибойной пластины с опушкой ткани. Дается методика обеспечения не резонансного режима работы машины.

Ключевые слова: прибойная пластина, основные нити, поперечные колебания, частота контакта зубьев, номер нити, натяжения нити.

Введение

Принципиальная схема и конструкция ТФМ определяет конструкции ткацкой многозевной машины, ее эффективность и технико-экономических показателей.

Анализ процесса непрерывного тканенформирования показывает, что на выработке качественной ткани существенно влияние оказывает совокупность основных конструктивных и технологических параметров ТФМ. В период взаимодействия зубьев прибойных пластин с основными и уточными нитями приводит к колебаниям основных нитей и изменяется их натяжения.

В представленной работе исследован поперечные колебания передней ветви зева основных нитей. Исходя из условия обеспечения на резонансного режима перемещения и прибоя уточной нити к опушке ткани определен технологические параметры вырабатываемой ткани и натяжения основных нитей.

Постановка задачи. В настоящее время нами предложена конструкция прибойной пластины на периферии которых имеется четыре комплекта одноименных зубьев. При сборке на валу ТФМ каждая прибойная пластина смещена относительно предыдущей на определений угол . При этом одноименные зубья прибойных пластин образуют четырехзаходную винтовую линию. Контакт каждого зуба прибойной пластины с уточной нитью и опушкой ткани приводит к возмущению упругой системы заправки и основных нитей.

Величина углов образующих зубьев, углов между зубьями и углов смещения прибойных пластин относительно предыдущего определяется из условия обеспечения выработки качественной ткани. Эти же углы должны обеспечит не резонансный режим работы машины.

Метод решения. Экспериментальные исследования (1) показали, что в период времени , соответствующей контакту зубьев прибойной пластины с уточной нитью и опушкой ткани натяжения основных нитей изменяется на 10 – 15 %

Поэтому при исследовании поперечных колебаний основных нитей их натяжения можно считать постоянной величиной и равной $T_0 = T_P = 0{,}3$Н

Проведенными исследованиями [2] установлено, что поперечные колебания передней и задней части ветвей зева можно рассматривать отдельно.

Исследованиями (1)установлено, что поперечные колебания основных нитей зависит от условия закрепления их концов.

Динамический модель передней ветви зева основы принимаем как нить защемленный в конце А и закрепленной в конце В (рис. 1).

Уравнение движения нити имеет вид [1, 2]

$$\frac{\partial^2 y}{\partial t^2} + 2h\frac{\partial y}{\partial t} = a^2 \frac{\partial^2 y}{dx^2} , \qquad (1)$$

где $a=\sqrt{\frac{f_p T_p}{\mu_0}} = \sqrt{\frac{T_p}{\mu_p}}$ скорость распространения поперечных вал в нити.

Для слабо растянутых нитей т.е. для нити упругой по Гуку,

$$\partial T \leq 1 , f \approx 1, \mu_0 \approx \mu_0 \approx \mu$$

Если пренебречь сопротивлением движению ,то уравнение(1) принимает вид:

$$\frac{\partial^2 y}{\partial t^2} = a^2 \frac{\partial^2 y}{dx^2} \quad . \qquad (2)$$

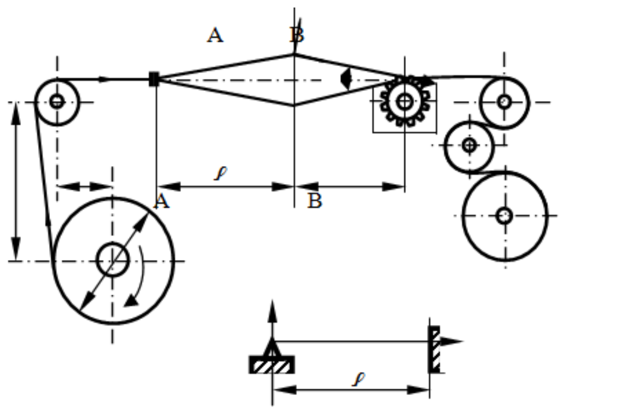

Рис. 1. Расчетная схема поперечных колебаний основных нитей

Это уравнение является волновое уравнения.

При защемленных и закрепленных концах нити задача сводится к решению уравнения (2), при грешных условиях:

$$y/_{x=0} = 0; \qquad y/_{x=\ell} = 0 \qquad (3)$$

где ℓ= AB

и начальных условиях:

$$y/_{t=0} = y_0(x)\frac{\partial y}{\partial t}/_{t=0} = y_0(x) \qquad (4)$$

По методу Фурье частные решения уравнения (2) разыскивается в виде:

$$y(x,t)=y_1(x),y_2(t) \qquad (5)$$

где $y_1(x)$ и $y_2(t)$ соответственно функции только одного переменного. В результате решения уравнений с учетом граничных и начальных условий определяется собственные функции $y_{1к}(x)$,определяющие форму колебаний и функцию $y_{2к}(t)$ и решение задачи дается рядом

$$y(x,t)=\sum_{к=1}^{\infty}\left(a_k \cos\frac{k\pi a}{\ell}t + b_k\frac{k\pi a}{\ell}t\right) sin\frac{k\pi x}{\ell} \qquad (6)$$

где

$$\left.\begin{aligned} a_к &= \frac{2}{\ell}\int_0^{\ell} y_0(x) sin\frac{k\pi x}{\ell}dx \\ a_к &= \frac{2}{\ell}\int_0^{\ell} y_0(x) sin\frac{k\pi x}{\ell}dx \end{aligned}\right\} \qquad (7)$$

Круговая частота собственных колебаний определяется по формуле [2]

$$P_к= \frac{k\pi a}{\ell} = \frac{k\pi}{\ell}\sqrt{\frac{f_p T_p}{\mu_0}} = \frac{k\pi}{\ell}\sqrt{f_p T_p N_g} \quad , \qquad (8)$$

где N метрический номер нити

Частота, контакта каждого зуба пластины и одноименных зубьев каждой соседней пластины с опушкой ткани определяется следующей зависимостью.

$$t_u=\frac{60\varphi_1}{360n}\ cek$$

$$P_b=\frac{\pi}{t_u} \qquad (9)$$

где n частота вращения вала ТФМ,φ_1- угол при определении частота контакта каждого зуба пластины принимаемой равным углу между зубьями не периферии прибойной пластины, а при определении частоты контакта одноименных зубьев каждой соседней применяемой равным углу смещения одноименных зубьев пластины относительно друг-друга.

Результаты решения и их оценка. Для ткацкой многозевной машины типа ТММ параметры заправка следующая (рис.1) ℓ=105mm, ℓ_1=354,2mm .

Величина углов образующие зубья и между зубьями соответственно, ровно $\varphi_{1ком} = \varphi_{2ком} = \varphi_{3ком} = \varphi_{4ком} = \varphi_5$, $\varphi_{1к} = \varphi_1 + \varphi_{12} + \varphi_2 + \varphi_{23} + \varphi_3$, где $\varphi_{1к}, \varphi_{2к}, \varphi_{3к}$ и $\varphi_{4к}$ углы на которым расположены комплект зубья на периферии прибойной пластины; φ_1 - величина угла образующий первый зуб на каждом комплекте; φ_{12} величина угла между первым и вторым зубом на каждом комплекте, φ_2 величина угла образующий второй зуб на каждом комплекте, φ_{23} -величина угла между вторым и третьем зубом на каждом комплекте, φ_3 величина угла образующий третий зуб на каждом комплекте.

Величина этих углов определяется из условия обеспечения выработки качественный ткани непрерывным способом.

Технологической характеристикой ткацкой многозевной машины типа ТММ предусмотрено выработка ткани плотностью в нитях на 10 см по основе максимально до 320, по утку максимально до 300 нити. Толщина перерабатываемой пряжи текс(номер) по основе изменяет в пределах от 100 до 15,4(10÷65) а по утку также в пределах от 100 до 15,4(10÷65).

Исследованиями установлено что, для обеспечения выработки качественной ткани предусмотренной технологической характеристикой ткацкой многозевной машины в конструкции четырехзаходного роторного ТФМ, величина углов образующих зубья и углов между зубьями на периферии прибойной пластины изменяется в следующих пределах: $\varphi_1=16\div20^0$; $\varphi_{12}=8\div4^0$; $\varphi_1=11\div8^0$; $\varphi_{23}=6\div10^0$ и $\varphi_3=4\div2^0$. Максимальный угол смещения прибойных пластин относительно предыдущей составляет $\psi=2^0$ Максимальная частота вращения вала ТФМ равно n =500 $мин^{-1}$

Подставляя значения параметров в формулах (8),(9) определяем частоты собственных поперечных колебаний передней ветви зева и частоты контакта зубьев прибойной пластины с опушкой ткани. Частота вращения вала ТФМ принять ровным n =500 мин$^{-1}$.

Заключение

Анализ также показывает что при значении углов между зубьями и смещении прибойных пластин относительно друг друга равным $\varphi_{11}=6^0$ при использовании пряжи с номером N=10 и натяжении нити равным Т=20,30,40,50 частота собственных колебаний передней ветви зева основы ближе к частота прибоя уточной нити к опушке ткани. При таких значениях параметров возможны резонансный режим работы и увеличение обрывности основных нитей.

Исследование показывает что при значении углов между зубьями и смещении прибойных пластин относительно друг друга равным $\varphi_{11}=8^0$ и при использованы пряжи с номером N= 10 и натяжения нити равным Т=20 могут возникнут резонансный режим работы и увеличения обрывности основных нитей.

Установлено что, резонансный режим работы машины и увеличения обрывности основных нитей могут возникать при значений угла между зубьями и смещения их относительно друг друга равным $\varphi_{12}=4^0$ и использовании пряжи с номером N=20 и натяжении нити равным Т=30,40,50 а также при значении угла равным $\varphi_{12}=6^0$ и натяжении равным Т=20 гр и при значении угла равным $\varphi_{12}=8^0$ и натяжении равным Т=20гр.

Анализом также установлено что при значении угла равным $\varphi_{12}=4^0$ и использовании нити с номером N=30 , и натяжения нити равным Т=20гр,30гр, а также с номерами нити равным N 40,50 натяжении равным Т=20гр возможны возникновения резонансного режима работы и увеличения обрывности основных нитей.

Анализ структуры формула(8) и (9) показывает что, все параметры входящих в эти формулы кроме натяжения нити основы Т устанавливается заранее из условие обеспечения качественной ткани непрерывным способом соответствующий вырабатываемого ассортимента ткани. Изменение значения этих параметров приводит к изменению выбранного ассортимента вырабатываемой ткани непрерывным способом.

Как видно технологические параметры толщина пряжи основы и конструктивные параметры ТФМ угол между зубьями на периферии прибойной пластины и угол смешения их относительно друг-друга для выработки конкретного ассортимента ткани являются постоянными величинами.

Поэтому обеспечения не резонансного режима работы машины изменением технологического параметра толщины основных нитей и конструктивных параметров ТФМ угол между зубьями и угол смещения их относительно друг друга становится не возможным.

Исследования показывает, что уменьшение частоты вращения вала ТФМ приводит к уменьшению производительности а увеличения к увеличению обрывности основных нитей снижение к.п.в. так что в обоих случаях приводит к снижению технико-экономических показателей ткацкий многозевный машины.

По этому при выработке конкретного ассортимента ткани непрерывном способом не целесообразно изменения частоты вращения вала ТФМ и должен оставаться постоянной величиной.

Анализ показывает что технологический параметр натяжения основных нитей не завысить от конкретного ассортимента вырабатываемой ткани и устанавливается на ткацкой машине во время выработки ткани.

Поэтому для обеспечения не резонансного режимы работы машин и уменьшения обрывности основных нитей целесообразно изменяет натяжения основных нитей в конструктивно заправочной линии в процессе выработки ткани непрерывным способом на ткацкой многозевной машине типа ТММ.

Выводы. 1.Исследованием установлено, что в процессе тканеформирования на ткацкой многозевной машине типа ТММ передняя ветвь зева основы совершает поперечные колебания. Частота колебаний передней ветви зева зависит от технологических параметров вырабатываемого ассортимента ткани и конструктивных и кинематических параметров ТФМ.

2.Исследование показали что для обеспечения не резонансного режима работы машины в процессе непрерывного тканеформирования целесообразно использовать изменения натяжения Т основных нитей в КЗЛ в процессе ткачество.

Литература

1.Фарзалиев. М.Г. Разработка методов расчета и проектирования тканеформирующего механизма и исследование процесса прокладки уточной нити в волнообразных зевах основы широких многозевных ткацких машин. Санкт Петербург. 1990.Докторская диссертация.

2.Якубовский Ю.В., Живов В.С., Корытисский Я.И., Мигушов И.И. Основы механики нити. М., Легкая индустрия, 2003, 280 с. 3. 3.

3.Рахматуллин Х.А., Демьянов ЮА. Прочность при интенсивных нагрузках. М., ГИФМЛ, 2001, 410 с.

Topics 4. Transport vehicles

Напряженно - деформированное состояние тормозного барабана автомобиля при критическом тепловом состоянии

Аскер Габиб оглы Тагизаде, Шамиль Гилал оглы Гейдаров
Азербайджанский Технический Университет, Баку
Email: asger-tagizade@rambler.ru

Аннотация. Рассматривается задача о термоупругом состоянии тормозного барабана при критическом состоянии тормозной системы автомобиля, когда на контактной поверхности достигнута предельно допустимая температура для материала барабана или же для материала фрикционной накладки.

Ключевые слова: барабан, накладка, напряжение, термоупругий.

Термоупругое напряженное состояние в барабане в момент торможения в системе подвижных координат *xoy*, вращающихся вместе с барабаном и неподвижных относительно него, можно рассматривать как в равновесии под действием объемных сил инерции и вызванных действием неравномерного поля температур

$$X = \rho_0\omega^2 x - \frac{\alpha E}{1-2\mu}\frac{\partial T}{\partial x}, \quad Y = \rho_0\omega^2 y - \frac{\alpha E}{1-2\mu}\frac{\partial T}{\partial y}, \qquad (1)$$

где ρ_0- плотность материала барабана, α – коэффициент линейного температурного расширения.

Для определения напряженного состояния тормозного барабана имеем [1; 2] уравнения равновесия

$$\frac{\partial \sigma_x}{\partial x} + \frac{\partial \tau_{xy}}{\partial y} + X = 0,$$
$$\frac{\partial \tau_{xy}}{\partial x} + \frac{\partial \sigma_y}{\partial y} + Y = 0, \qquad (2)$$

закон Гука, условия совместности деформаций и геометрические соотношения между перемещениями и деформациями.

Считаем, что внутренний контур барабана близок к круговому. Отнесем барабан к полярной системе координат $r\theta$, выбрав начало координат в центре концентрических окружностей L_0 и L_1 с радиусами $R_б$ и R.

Рассмотрим некоторую реализацию шероховатой поверхности барабана. Представим границу внутреннего контура L_0' в виде

$$\rho = R_б + (\theta), \quad \delta(\theta) + \varepsilon H(\theta), \qquad (3)$$

где ε – малый параметр, равный $R_{max}/R_б$, R_{max}- наибольшая высота микронеровности профиля.

Пусть $t = T - T_c$ избыточная температура.

Температуру в барабане ищем в виде разложения по малому параметру

$$t = t^{(0)} + \varepsilon t^{(1)} + \varepsilon^2 t^{(2)} + \cdots \qquad (4)$$

в котором пренебрегаем членами, содержащими малый параметр ε в степени выше первой. Здесь $t^{(0)}$, $t^{(1)}$, $t^{(2)}$- соответственно температуры нулевого, первого и второго приближения. Каждое из приближений удовлетворяет дифференциальному уравнению теплопроводности.

Граничные условия задачи термоупругости для барабана имеют вид:

на внутренней поверхности барабана при $r = R_б$

$$\sigma_n = -g(\theta), \; \tau_{nt} = -f\, g(\theta) \qquad (5)$$

на контактной площадке

$\sigma_n = 0, \tau_{nt} = 0$ вне площадки контакта

на внешней поверхности барабана при $r = R$

$$\sigma_r = 0, \quad \tau_{r\theta} = 0. \qquad (6)$$

Решение задачи термоупругости представим в виде суммы (принцип суперпозиции)

$$\sigma_r = \sigma_r^{(u)} + \sigma_r^{(T)}, \; \sigma_\theta = \sigma_\theta^{(u)} + \sigma_\theta^{(T)}, \; \tau_{r\theta} = \tau_{r\theta}^{(u)} + \tau_{r\theta}^{(T)}, \qquad (7)$$

где первые слагаемые $\sigma_r^{(u)}$, $\sigma_\theta^{(u)}, \tau_{r\theta}^{(u)}$ есть решение изотермической задачи теории упругости при граничных условиях (5) и (6), а вторые слагаемые $\sigma_r^{(T)}, \sigma_\theta^{(u)}, \tau_{r\theta}^{(T)}$ есть решение термоупругой задачи для барабана, на границе которого отсутствуют внешние усилия

$$\sigma_n^{(T)} = 0, \; \tau_{nt}^{(T)} = 0, \text{ при } r = \rho$$
$$\sigma_r^{(T)} = 0, \; \tau_{r\theta}^{(T)} = 0, \text{ при } r = R \qquad (8)$$

Для решения краевой задачи (8) необходимо знание распределения температуры в барабане.

Напряжения и перемещения ищем в виде разложений по малому параметру.

Краевые условия примут вид

для нулевого приближения

$$\sigma_r^{(0)} = 0, \quad \tau_{r\theta}^{(0)} = 0 \quad \text{при } r = R_б$$
$$\sigma_r^{(0)} = 0, \quad \tau_{r\theta}^{(0)} = 0 \quad \text{при } r = R \qquad (9)$$

для первого приближения

$$\sigma_r^{(1)} = N, \quad \tau_{r\theta}^{(1)} = T \quad \text{при } \boldsymbol{r} = R_б$$
$$\sigma_r^{(1)} = 0, \quad \tau_{r\theta}^{(1)} = 0 \quad \text{при } r = R \qquad (10)$$

Для получения решения задачи термоупругости для сечения барабана единичной высоты в каждом приближении используем термоупругий потенциал перемещений $\Phi(r, \theta)$

$$u_r = \frac{\partial \Phi}{\partial r}, \quad u_\theta = \frac{1}{r}\frac{\partial \Phi}{\partial \theta} \qquad (11)$$

где u_r и u_θ – соответственно радиальная и окружная компоненты вектора перемещения.

В рассматриваемой задаче термоупругий потенциал перемещений в нулевом приближении определяется дифференциальным уравнением

$$\Delta\Phi^{(0)} = \frac{1+\mu}{1-\mu}\alpha t^{(0)}. \qquad (12)$$

Температурная функция $t^{(0)}(r,\theta)$ берется в виде ряда Фурье. Выбираем решение уравнения (12) для температурного потенциала в следующем виде

$$\Phi^{(0)}(r,\theta) = \sum_{n=0}^{\infty}[\Phi_n^{(0)}(r)\cos n\theta + +\Phi_n^{*(0)}\sin n\theta]. \qquad (13)$$

Подставляя (13) в дифференциальное (12), получим для определения функции $\Phi_n^{(0)}(r)$ (n=1,2,...) обыкновенное дифференциальное уравнение второго порядка

$$\frac{d^2\Phi_n^{(0)}}{dr^2}+\frac{1}{r}\frac{d\Phi_n^{(0)}}{dr}-\frac{n^2}{r^2}d\Phi_n^{(0)}=\frac{1+\mu}{1-\mu}\alpha F_n^{(0)} \qquad (14)$$

Частное решение уравнения (14) ищем [5] методом вариации постоянных

$$\Phi_0^{(0)}=\frac{1+\mu}{1-\mu}\alpha\,[-\ln r\int_{R_б}^{к}\rho F_0^{(0)}(\rho)d(\rho)++\int_r^R\rho F_0^{(0)}\ln\rho d\rho]$$

$$\Phi_n^{(0)}=\frac{1+\mu}{1-\mu}\frac{\alpha}{2n}[r^n\int_r^R F_n^{(0)}(\rho)\rho^{1-n}d\rho+$$

$$+r^{-n}\int_{R_б}^r F_n^{(0)}(\rho)\rho^{1-n}d\rho]. \qquad (15)$$

Аналогичное решение получим для функции $\Phi_n^{*(0)}(r)$ (n=1,2,…)

$$\Phi_n^{*(0)}=\frac{1+\mu}{1-\mu}\frac{\alpha}{2n}[r^n\int_r^R B_n^{(0)}(\rho)\rho^{1-n}d\rho++r^{-n}\int_{R_б}^r B_n^{(0)}(\rho)\rho^{1-n}d\rho] \qquad (16)$$

С помощью полученных формул (13), (15), (16) вычисляем соотвутствующие напряжения $\bar\sigma_r^{(0)}, \bar\sigma_\theta^{(0)}, \bar\tau_{r\theta}^{(0)}$. Эти напряжения не удовлетворяют граничным условиям (9) термоупругого состояния. Поэтому необходимо найти второе напряженное состояние $\bar{\bar\sigma}_r^{(0)}$, $\bar{\bar\sigma}_\theta^{(0)}$ и $\bar{\bar\tau}_{r\theta}^{(0)}$, такое,что

$$\sigma_r^{(0)}=\bar\sigma_r^{(0)}+\bar{\bar\sigma}_r^{(0)}=0,$$
$$\tau_{r\theta}^{(0)}=\bar\tau_{r\theta}^{(0)}+\bar{\bar\tau}_{r\theta}^{(0)} \quad \text{при } r=R_б \qquad (17)$$
$$\sigma_r^{(0)}=\bar\sigma_r^{(0)}+\bar{\bar\sigma}_r^{(0)}=0,$$
$$\tau_{r\theta}^{(0)}=\bar\tau_{r\theta}^{(0)}+\bar{\bar\tau}_{r\theta}^{(0)} \quad \text{при } r=R$$

Решая обычную задачу теории упругости (17) находим

$$\bar{\bar\sigma}_r^{(0)}=\Omega_r^\theta,\quad \bar{\bar\sigma}_\theta^{(0)}=\Omega_\theta^{(0)},\quad \bar{\bar\tau}_{r\theta}^{(0)}=\Omega_{r\theta}^{(0)} \qquad (18)$$

С помощью формул (17) находим температурные напряжения в барабане при нулевом приближении. Теперь переходим к построению перемещений в первом приближении. Термоупругий потенциал перемещений в первом приближении определяется решением следующего дифференциального уравнения

$$\Delta\Phi^{(1)}=\frac{1+\mu}{1-\mu}\alpha t^{(1)} \qquad (19)$$

Температурная функция $t^{(1)}(r,\theta)$ берется в виде ряда Фурье

$$t^{(1)}(r,\theta)=\sum_n^\infty[F_n^{(1)}(r)\cos n\theta++B_n^{(1)}(r)\sin n\theta] \qquad (20)$$

Выбираем решение уравнения (20) для термоупругого потенциала в следующем виде

$$\Phi^{(1)}=\sum_{n=0}^\infty[(r)\cos n\theta++\Phi_n^{*(1)}(r)\sin n\theta] \qquad (21)$$

Для функций $\Phi_n^{(1)}(r)$ и $\Phi_n^{*(1)}(r)$ находим $\frac{d^2\Phi_n^{(1)}}{dr^2}+\frac{1}{r}\frac{d\Phi_n^{(1)}}{dr}-\frac{n^2}{r^2}\frac{d\Phi_n^{(1)}}{dr^2}=\frac{1+\mu}{1-\mu}\alpha F_n^{(1)}$ $\quad \frac{d^2\Phi_n^{*(1)}}{dr^2}+\frac{1}{r}\frac{d\Phi_n^{*(1)}}{dr}-\frac{n^2}{r^2}\frac{d\Phi_n^{*(1)}}{dr^2}=\frac{1+\mu}{1-\mu}\alpha B_n^{(1)}$ (22)

Дальнейший ход решения аналогичен нахождения решения в нулевом приближении с очевидными изменениями.

Приведем решение уравнений (22)

$$\Phi_0^{(1)}=\frac{1+\mu}{1-\mu}\alpha\,[-\ln r\int_{R_б}^r F_0^{(1)}(\rho)\rho d\rho+$$
$$+\int_r^R\rho F_0^{(1)}(\rho)\ln\rho d\rho$$

$$\Phi_n^{(1)}=-\frac{1+\mu}{1-\mu}\frac{\alpha}{2n}[r^n\int_r^R F_n^{(1)}(\rho)\rho^{1-n}d\rho++r^{-n}\int_{R_б}^r F_n^{(1)}(\rho)\rho^{1-n}d\rho]$$

$$\Phi_n^{*(1)}=-\frac{1+\mu}{1-\mu}\frac{\alpha}{2n}[r^n\int_r^R B_n^{(1)}(\rho)\rho^{1-n}d\rho+$$
$$+r^{-n}\int_{R_б}^r B_n^{(1)}(\rho)\rho^{1-n}d\rho]$$

Повторяя весь процесс нахождения решения задачи находим сначала напряжения $\bar\sigma_r^{(1)}, \bar\sigma_\theta^{(1)}, \bar\tau_{r\theta}^{(1)}$. Затем ищем второе напряженное состояние этого приближения $\bar{\bar\sigma}_r^{(1)}, \bar{\bar\sigma}_\theta^{(1)}, \bar{\bar\tau}_{r\theta}^{(1)}$ удовлетворяя краевым условиям

$$\bar{\bar\sigma}_r^{(1)}=N-\bar\sigma_r^{(1)},\quad \bar{\bar\tau}_{r\theta}^{(1)}=T-\bar\tau_{r\theta}^{(1)} \quad \text{при } r=R_б$$
$$\bar{\bar\sigma}_r^{(1)}=-\bar\sigma_r^{(1)},\quad \bar{\bar\tau}_{r\theta}^{(1)}=-\bar\tau_{r\theta}^{(1)} \quad \text{при } r=R \qquad (23)$$

Решая краевую задачу (23) определяем температурные напряжения в первом приближении

$$\sigma_r^{(1)}=\bar\sigma_r^{(1)}+\bar{\bar\sigma}_r^{(1)},\quad \sigma_\theta^{(1)}=\bar\sigma_\theta^{(1)}++\bar{\bar\sigma}_\theta^{(1)},\quad \tau_{r\theta}^{(1)}=\bar\tau_{r\theta}^{(1)}+\bar{\bar\tau}_{r\theta}^{(1)} \qquad (24)$$

Изложенный способ позволяет определить температурные напряжения в тормозном барабане в процессе торможения автомобиля при критическом тепловом состоянии системы. Для оценки прочности определяем нормальное тангенциальное напряжение на контактной поверхности $r=\rho(\theta)$

$$\sigma_*=\sigma_\theta^{(0)}|_{r=R_б}+\frac{\partial\sigma_\theta^{(0)}}{\partial r}|_{r=R_б}\varepsilon H(\theta)++\varepsilon\sigma_\theta^{(1)}|_{r=R_б}, \qquad (25)$$

которое представляет собой функцию полярного угла θ.

При выполнении условия прочности

$$\sigma_{*max}=\sigma_o \qquad (26)$$

Будет появляться остаточные деформации, если σ_o есть предел текучести материала тормозного барабана. Если σ_o представляет собой предел хрупкой прочности материала выполнение условия (26) означает нарушение сплошности материала барабана.

Расчеты показывают, что из-за высоких температур на поверхности барабана возникают напряжения, которые превышают напряжения от силовой нагрузки.

Необходимо на стадии проектирования путем конструкторско – технологических решений добиваться выполнения условий

$$T<T_*,\quad \sigma_{*max}<\sigma_0 \qquad (27)$$

В результате удовлетворения неравенств (27) определяем области допустимых значений параметров тормозной системы барабанных колодочных механизмов.

Литература

1.Суслов А.Г., Технологическое обеспечение контактной жесткости сое динений. М.,Наука, 1977, 100 с.

2.Сухов С.А.,Роль шероховатости в процессе трения. Трение и износ в машинах. Изд-во АН СССР, 1959, №4, с.27-34.

Proceedings of the International Symposium of Mechanism and Machine Science, 2017
AzC IFToMM – Azerbaijan Technical University
11-14 September 2017, Baku, Azerbaijan

Взаимодействие жестких включений и трещин со связями между берегами в концевых зонах при продольном сдвиге тела с периодической структурой

Ф.Ф.Гасанов

Азербайджанский Технический Университет,
Азербайджан, г.Баку, пр. Г.Джавид
E-mail: gff74@mail.ru

Abstract
An isotropic medium with a periodic structure under longitudinal shear is considered. A model for the destruction of composite materials with a periodic structure is proposed, based on the investigation of the zone of the fracture process, near the top of the crack. The presence of bonds between the shores of the crack in the end zone is modeled by applying to the crack surfaces the cohesion forces caused by the presence of bonds.
Ключевые слова: изотропная среда, жесткие включения, периодическая система круговых отверстий, трещины со связями между берегами в концевых зонах, силы сцепления, продольный сдвиг.

Введение

На стадии проектирования новых машин и конструкций необходимо учитывать случаи, когда в отдельных деталях машин и конструкций могут возникнуть трещины. Это особенно часто проявляется в деталях новой техники, в которых наибольшее применение находят высокопрочные конструкционные материалы, имеющие периодическую структуру (композиты), и склонные к хрупкому разрушению. Достаточно полное представление о характерном распределении напряжений в микроструктуре линейно армированных материалов, можно получить, изучая распределение напряжений при сдвиге. Решение этой задачи открывает новые возможности прогнозирования механических свойств композитных материалов по данным исходным характеристикам для составляющих компонентов и виду микроструктуры.

Постановка задачи

В структурно-неоднородных материалах при наличии вблизи трещины зон с нарушенной структурой в процесс разрушения вовлекается значительная часть трещины. В таких случаях область разрушения можно рассмотреть как некоторую концевую зону на продолжении трещины с материалом с частично нарушенными межчастичными связями. Принято, что берега трещины в концевых зонах взаимодействуют причем силы этого взаимодействия, называемые силами сцепления, распределены таким образом, что вершина трещины является особой точкой напряженно-деформированного состояния.

Рассматривается плоская задача теории упругости для изотропной среды с периодической системой круговых отверстий, заполненных абсолютно жесткими включениями, спаянными вдоль обвода, и ослабленной прямолинейными трещинами со связями между берегами в концевых зонах коллинеарных оси абсцисс (рис 1).

Изотропная среда ослаблена периодической системой круговых отверстий, имеющих радиус λ (x<1) и центры в точках $P_m = m\omega$ (m=0, ±1, ±2, ...), ω=2 Круговые отверстия среды заполнены абсолютно жесткими включениями, спаянными вдоль обводы. Среда (связующее) ослаблена периодической системой прямолинейных трещин со связями между берегами вдоль оси абсцисс. Берега трещин вне концевых зон свободы от внешних нагрузок. На составное тело (композит) действуют напряжения $\tau_y = \tau_y^\infty$, τ_x=0 (продольный сдвиг на бесконечности).

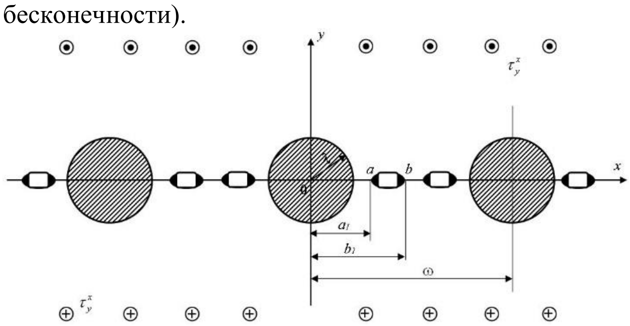

Рис. 1. Расчетная схема задачи

По мере возрастания внешней нагрузки τ_y^∞ на продолжении трещины будут возникать области предразрушения (концевые зоны). Используется модель трещины со связями между берегами в концевых зонах [1-3]. Концевые зоны трещин моделируются областями с ослабленными межчастичными связями в материале связующего. Взаимодействие берегов концевых зон моделируется путем введения между берегами связей с заданной диаграммой деформирования. В исследуемом случае, когда длина концевой зоны трещины не является малой по сравнению с размером трещины, методы оценки сопротивления материала разрушению, основанные на рассмотрение трещины с малой концевой зоной, неприменимы. В таких случаях нужно моделирование напряженно-деформированного состояния в концевой зоне трещины проводить с учетом деформационных характеристик связей и применения двухпараметрического критерия [2] разрушения, описывающего как развитие вершины трещины, так и изменения размера концевой зоны трещины при ее росте.

Когда процессы деформирования и разрушения к концевых зоны трещин включают несколько физических механизмов, как например, композиционных материалах, то в этих случаях эффективным является использование модели концевой зоны с сингулярностью напряженного состояния в вершине трещины. Для однородных материалов такая модель трещины рассмотрена в статьях [2, 4-8] и дано развитие [9, 10] для трещин с концевой зоной на границе раздела материалов с различными свойствами.

Анализ предельного равновесия трещин в композитах с периодической структурой в рамках предлагаемой модели концевой зоны при продольном сдвиге проводится на основе нелокального критерия разрушения с силовыми условием продвижения вершины трещины и деформационными условием для определения продвижения края концевой зоны трещины.

При действии внешней нагрузки τ_y^∞ на составную среду в связях, соединяющих берега концевых зон ($a_1+m\omega$, $a+m\omega$) и ($b+m\omega$, $b_1+m\omega$) будут возникать касательные напряжения $q_y(x)$ эти касательные напряжения неизвестны и подлежат определению.

Краевые условия задачи имеют вид

w=0 на контурах круговых отверстий

τ_y=0 на свободных берегах трещины (1)

$\tau_y=q_y(x)$ на берегах концевых трещин

Основные соотношения рассматриваемой задачи механики разрушения необходимо дополнить уравнением, связывающим сдвиг берегов концевых зон и усилия в связях. Без потери общности это уравнение представим в виде

$$w^+(x,0)-w^-(x,0)=C\big(x,q_y(x)\big)q_y(x), \qquad (2)$$

где функция $C\big(x,q_y(x)\big)$ представляет собой эффективную податливость связей; $\left(w^+-w^-\right)$ – сдвиг берегов концевых зон трещины.

Используя представление напряжений и перемещений через одну аналитическую функцию [11]

$$\tau_x-i\tau_y=f'(z),\quad w=\frac{1}{\mu}\operatorname{Re} f(z),\quad z=x+iy,$$

где μ – постоянная материала среды; $i=\sqrt{-1}$, краевые условия рассматриваемой задачи запишем в виде

$f(\tau)+\overline{f(\tau)}=0$ на контурах круговых отверстий, (3)

$f'(t)-\overline{f(t)}=f_x(t)$, (4)

где $\tau=\lambda e^{i\theta}+m\omega$ (m=0, ±1, ±2, …); t – аффикс точек берегов трещин с концевыми зонами;

$$f_x(t)=\begin{cases}0 & \text{на свободных берегах трещин,}\\ -2iq_y(t) & \text{на берегах концевых трещин}\end{cases}$$

На основании симметрии граничных условий и геометрии области D, занятой материалом связующего, напряжения являются периодическими функциями с периодом ω.

Метод решения задачи

Решение граничный задачи (3)-(4) ищем в следующем виде

$$f(z)=f_1(z)+f_2(z), \qquad (5)$$

$$f_1'(z)=F_1(z)=\tau_y^\infty+\sum_{k=0}^{\infty}\alpha_{2k+2}\frac{\lambda^{2k+2}\rho^{(2k)}(z)}{(2k+1)!}, \qquad (6)$$

$$f_{21}'(z)=F_2(z)=\frac{1}{i\omega}\int_L g(t)ctg\frac{\pi}{\omega}(t-z)dt. \qquad (7)$$

Здесь интеграл в формуле (7) берется по отрезку $L=\{[-a_1,-b_1]\cup[a_1,b_1]\}$; $g(t)$ – искомая функция, характеризующая сдвиг берегов трещины с концевыми зонами:

$$g(x)=\frac{\mu}{2}\frac{d}{dx}\left[w^+(x,0)-w^-(x,0)\right] \text{ на } L \qquad (8)$$

$$\rho(z)=\left(\frac{\pi}{\omega}\right)^2\left[\frac{1}{\sin^2\frac{\pi z}{\omega}}-\frac{1}{3}\right].$$

Неизвестная функция $g(t)$ и искомые коэффициенты α_{2k} пока неизвестны и подлежат определению из граничных условий (3)-(4).

К основным представлениям решения задачи (5)-(8) необходимо добавить дополнительные равенства,

$$\int_{-a_1}^{-b_1}g(t)dt=0,\quad \int_{a_1}^{b_1}g(t)dt=0, \qquad (9)$$

обеспечивающие однозначность перемещений при обходя контура трещины с концевыми зонами.

Для составления уравнений относительно коэффициентов α_{2k} функции $F_1(z)$ преобразуем граничные условие (3) к следующему виду

$$F_1(\tau)+\overline{F_1(\tau)}=F_0(\tau), \qquad (10)$$

где $F_0(\tau)=-F_2(\tau)-\overline{F_2(\tau)}$.

Для решения граничной задачи (10) используем метод степенных рядов. Относительно функции $F_0(\tau)$ считаем, что она разлагается на контуре $|\tau|=\lambda$ в тригонометрический ряд Фурье. Подставив левую часть граничного условия (10) вместо $F_1(\tau)$, $\overline{F_1(\tau)}$ их разложения в ряды Лорана в окрестности нулевой точки $z=0$, а в правую часть (10) вместо функции $F_0(\tau)$ ряд Фурье и приравнивая коэффициенты при одинаковых степенях $\exp(i\theta)$ в обеих частях, получим бесконечную систему алгебраических уравнений относительно коэффициентов α_{2k}:

$$\sum_{k=0}^{\infty}\alpha_{2k+2}\lambda^{2k+2}r_{0,k}+\tau_y^{\infty}=\frac{A_0}{2},$$
$$\sum_{k=0}^{\infty}\alpha_{2k+2}\lambda^{2k+2}r_{j,k}\lambda^{2j}+\alpha_{2j}=A_{2j} \qquad (11)$$

где $A_{2k}=-\dfrac{1}{i\omega}\displaystyle\int_L g(t)f_{2k}(t)dt,$

$$f_{2k}(t)=\frac{\lambda^{2k}}{(2k)!}\gamma^{(2k)}(t)-\frac{\lambda^{2k+2}}{(2k+1)!}\gamma^{(2k+2)}(t), \qquad \gamma=ctg\frac{\pi}{\omega}t,$$

$$r_{j,k}=\frac{(2j+2k+1)!}{(2j)!(2k+1)!2^{2j+2k+2}}, \qquad r_{0,0}=0, \quad g_j=2\sum_{m=1}^{\infty}\frac{1}{m^{2j}}.$$

Удовлетворяя граничному условию на берегах L для определения неизвестной функции $g(x)$, получаем сингулярное интегральное уравнение:

$$\frac{1}{\omega}\int_L g(t)ctg\frac{\pi}{\omega}(t-z)dt-\operatorname{Im}F_1(x)=F_x^*(x) \text{ на } L \qquad (12)$$

$$F_x^*(t)=\begin{cases}0 & \text{на свободных берегах трещин,}\\ 2q_y(x) & \text{на берегах концевых зон трещин}\end{cases}$$

Полученная система алгебраических уравнений (11) совместно с сингулярные интегральным уравнением (12) дает возможность найти искомую функцию $g(x)$ и коэффициенты α_{2k}. Используя в основной полосе периодов разложение функции $ctg\dfrac{\pi}{\omega}z$, а также замену переменных, после некоторых преобразований сингулярное интегральное уравнение (12) приводится к стандартному виду:

$$\frac{1}{\pi}\int_{-1}^{1}\frac{p(\tau)d\tau}{\tau-\eta}+\frac{1}{\pi}\int_{-1}^{1}p(\tau)B(\tau,\eta)d\tau-\operatorname{Im}F_1(\eta)=F_2^*(\eta) \qquad (13)$$

Здесь $\quad B(\tau,\eta)=-\dfrac{1-\lambda_1^2}{2}\displaystyle\sum_{j=0}^{\infty}B_{j+1}\left(\frac{b_1}{2}\right)^{2j+2}\cdot u_0^jA_j^*,$

$$A_j^*=\left[(2j+1)+\frac{(2j+1)(2j)(2j-1)}{1\cdot2\cdot3}\left(\frac{u}{u_0}\right)+\ldots+\right.$$
$$\left.+\frac{(2j+1)(2j)(2j-1)\ldots[(2j+1)-(2j+1-1)]}{1\cdot2\cdot\ldots\cdot(2j+1)}\left(\frac{u}{u_0}\right)^j\right]$$

$$\lambda_1=\frac{a_1}{b_1}, \quad p(\tau)=g(\tau), \quad u=\frac{1-\lambda_1^2}{2}(\tau+1)+\lambda_1^2,$$
$$u_0=\frac{1-\lambda_1^2}{2}(\eta+1)+\lambda_1^2.$$

Решение сингулярного интегрального уравнения (13) ищем в виде [12-14]:

$$p(\eta=\frac{g_0(\eta)}{\sqrt{1-\eta^2}}), \qquad (14)$$

где функция $g_0(\eta)$ непрерывна по Гельдеру на [-1, 1], причем она заменяется [12-14] интерполяционным многочленом Лагранжа, построенного по Чебышевским узлам.

Используя квадратурные формулы Гаусса-Чебышева, после некоторых преобразований сингулярное интегральное уравнение с дополнительным равенством (9) сводится к конечной алгебраической системе уравнений:

$$\sum_{k=1}^{n}a_{m,k}g_k^0-\frac{1}{2}Im\,F_1(\eta_m)=\frac{1}{2}F_2^*(\eta_m) \qquad (15)$$
$$(m=1,2,\ldots,M-1)$$

$$\sum_{k=1}^{M}\frac{g_k^0}{\sqrt{\frac{1}{2}(1-\lambda_1^2)(\tau_k+1)+\lambda_1^2}}=0.$$

Здесь

$$a_{m,k}=\frac{1}{2M}\left[\frac{1}{\sin\theta_m}ctg\frac{\theta_m+(-1)^{|m-k|}\theta_k}{2}+B(\tau_k,\eta_m)\right],$$

$$\eta_m=\cos\theta_m, \qquad \theta_m=\frac{2m-1}{2M}\pi$$

$$(m=1,2,\ldots,M), \tau_m=\eta_m$$

В правую часть полученной системы (15) входят неизвестные значения напряженней $q_y(\eta_m)$ в узловых точках принадлежащих концевым зонам трещин.

Неизвестные напряжения в связях $q_y(\eta_m)$, возникающие на берегах концевых зон

$(a_1+m\omega, a+m\omega)$ и $(b+m\omega, b_1+m\omega)$, находятся из дополнительного условия (2). С помощью построенного решения, дополнительное уравнение (2) представим в виде

$$\frac{d}{2x}\left[C(x,q_y(x))\,q_y(x)\right]=\frac{2}{\mu}g(x) \qquad (16)$$

Требуя выполнения условию (16) в узловых точках, принадлежащих концевым зонам (a_1, a) и (b, b_1) в основной полосе периодов получим еще систему из M_1 уравнений для нахождения приближенных значений $q_y(\eta_{m_1})$ (m_1=1, 2, …, M_1). При этом использовали метод конечных разностей.

В случае нелинейного закона деформирована связей для нахождения касательных усилий в концевых зонах использовали итерационный алгоритм, подобный методу упругих решений [15]. Принималось, что закон деформирования межчастичных связей в концевых зонах линейный при $(w^+ \pm w^-)\le w_*$.

Первый шаг итерационного процесса расчета состоит в решении системы уравнений для линейно-упругих связей. Следующие итерации выполняются только в том случае, если на части концевой зоны имеет место неравенство $(w^+ \pm w^-)> w_*$. Для таких итераций решается система уравнений в каждом приближении для квазихрупких связей с изменяющейся вдоль берегов концевой зоны и зависящей от величины напряжений в связях эффективной податливости, которая вычислены на предыдущем шаге расчета. Процесс последовательных приближений прекращается, когда касательные напряжения вдоль каждой концевой зоны, полученные на двух последовательных итерациях практически не различаются. Расчет эффективной податливости проводили подобно нахождению секущего модуля в методе переменных параметров упругости [16].

Нелинейная часть кривой деформирования связей аппроксимировалась билинейной зависимостью, восходящий участок которой соответствовал деформированию связей $(0<(w^+ \pm w^-)\le w_*)$ с их максимальным усилием связей. При $(w^+ \pm w^-)> w_*$ закон деформирования описывался нелинейной зависимостью, определяемой точками (w_*, τ_*) и (δ_{IIIc}, τ_c), причем при $\tau_c \ge \tau_*$ имело место возрастающая линейная зависимость (линейное упрочнение, соответствующее упругопластической деформации связей).

После решения алгебраических систем коэффициенты интенсивности напряжений K_{III} находились на основании соотношений

$$K_{III}^{a_1}=\sqrt{\frac{\pi b_1(1-\lambda_1^2)}{\lambda_1}}\,\frac{1}{2M}\sum_{k=1}^{M}(-1)^{k+M}g_k^0 tg\frac{\theta_k}{2},$$
$$K_{III}^{b_1}=\sqrt{\pi b_1(1-\lambda_1^2)}\,\frac{1}{2M}\sum_{k=1}^{M}(-1)^{k}g_k^0 ctg\frac{\theta_k}{2} \qquad (17)$$

Анализ предельного состояния

Для анализа предельного равновесия трещин продольного сдвига с концевыми зонами необходимы два условия (двухпараметрический критерий) разрушения.

Первый критерий это условие разрыва связей на краю концевой зоны.

В качестве первого условия разрушения использовали силовой критерий Ирвина. Состоянию предельного равновесия вершины трещины соответствует выполнения условия

$$K_{III}=K_{IIIc} \qquad (18)$$

где K_{IIIc} – постоянная материала, определяемая опытным путем.

В качестве второго условия разрушения использовали критерий критического сдвига трещины и полагали, что предельный сдвиг связей на краю концевой зоны ($x_*=a$, $x_*=b$) происходит при выполнение условия

$$V(x_*)=w^+(x_*,0)-w^-(x_*,0)=\delta_{IIIc}, \qquad (19)$$

где δ_{IIIc} – трещиностойкость материалы.

Решение системы полученных алгебраических уравнений позволяет (при заданных характеристиках связей и длине трещин) найти критическую внешнюю нагрузку τ_y^∞ и предельный сдвиг берегов концевых зон в состоянии предельного равновесия трещин. Для заданных размеров трещин и концевых зон, используя предельные значения K_{IIIc} и δ_{IIIc} можно выделить следующие режимы равновесия и роста трещин при монотонном нагружении.

Если выполняются условия

$$K_{III}\ge K_{IIIc},\ V(x_*)<\delta_{IIIc},$$

то происходит продвижение вершины трещины с одновременным увеличением длины концевой зоны без разрыва связей. Этот этап роста трещин продольного сдвига можно рассматривать, как процесс приспособляемости к заданному уровню внешних нагрузок. Рост вершины трещины с одновременный разрушением связей на краю концевой зоны происходить при выполнении условий

$$K_{III}\ge K_{IIIc},\ V(x_*)\ge \delta_{IIIc}.$$

При выполнении условий

$$K_{III}<K_{IIIc},\ V(x_*)\ge \delta_{IIIc}$$

происходит разрушение связей без продвижения вершины.

Трещины, а размер концевой зоны уменьшается, стремясь к критическому значению для данного уровня нагрузки. При выполнении условий

$K_{III} < K_{IIIc}, V(x_*) < \delta_{IIIc},$

положение вершины трещины и концевой зоны не будут изменяться.

Численными расчетами найдены касательные напряжения в связях и сдвиг противоположных берегов концевых зон трещин от внешнего параметра нагружения τ_y^∞. Расчеты показывают, что при линейном законе деформирования связей напряжения в связях всегда имеют максимальные значения на краю концевой зоны. Аналогичная картина наблюдается и для величины сдвига берегов трещины, т.е. сдвиг берегов трещины на краю концевой зоны имеет максимум при линейном и нелинейном законах деформирования. При этом с увеличением относительной податливости связей возрастает сдвиг берегов трещины.

Таким образом, совместное решение полученной алгебраической системы и условий (18)-(19) дает возможность найти критическую величину внешней нагрузки, при которых происходит рост трещины.

Заключение

Модель трещины с концевыми зонами со связями между берегами позволяет исследовать основные закономерности распределения напряжений в связях при различных законах деформирования, проводить анализ предельного равновесия составного тела (композита) с учетом деформационного и силового условий разрушения, а также оценивать критическую внешнюю нагрузку и трещиностойкость материала.

Список литературы

[3]. The special issue: Cohesive models // Eng. Fraet. Mech., 2003, vol. 70, No 14, p. 174, -1987
[4]. Гаджиев В.Д., Мирсалимов В.М. Предельно-равновесное состояние детали типа втулки контактной пары при наличии трещин со связями между берегами // Оптимальное проектирование механических систем. Баку: Элм, 1999. с. 50-63.
[5]. Mirsalomov V.M. and Hasanov F.F. Solution of the periodic problem of propagation of cohesive cracks under longitudinal shear // Material science, vol. 49, No5, p. 631-636.
[6]. Rose L.R.F. Crack reinforcement by distributed // J. Mech. and Phys. solids. 1987, vol. 35, No4, p. 383-405.
[7]. Budiansky B., Cui Y.L. On the tensile strength of a fiber reinforced ceramic composite containing a crack like flam // J. Mech. and Phys. solids. 1994, vol. 42, No1, p. 341-363.
[8]. Мирсалимов В.М., Рустамов Б.Э. Локальное разрушение горящего твердого ракетного топлива // Изв. вузов. Авиационная техника. 2010, №3, с. 11-15.
[9]. Мир-Салим-Заде М.В. Рост когезионной трещины в стрингерной пластине // Строительная механика инженерных конструкций и сооружений. 2013, №4, с.16-22.
[10]. Mirsalimov V.M. and Mustafayev A.B. Inhibition of a curvilinear bridged crack by induced thermoelastic stress field // J. of Thermal Stresses. 2016, vol. 39, No10, p. 1301-1319.
[11]. Гольдштейн Р.В., Перельмутер М.Н. Трещина на границе соединения материалов со связями между берегами // Изв. РАН. МТТ, 2001, №1, с. 94-11.
[12]. Греков М.А., Морозов Н.Ф. О равновесных трещинах в композитах, армированных одноправленными волокнами// Прикла. мат. и мех., 2006, т. 70, вып. 6, с. 1054-1066.
[13]. Мирсалимов В.М. Разрушение упругих и упругопластических тел с трещинами. Баку, Элм, 1984, -124с.
[14]. Панасюк В.В., Саврук М.П., Дацышин А.П. Распределение напряжений около трещин в пластинах и оболочках. Киев, Наукова думка, 1976, 443 с.
[15]. Мирсалимов В.М. Неодномерные упругопластические задачи. М.: Наука**,** 1987, 256.
[16]. Ladopoulos E.G. Singular integral equations: Linear and non-linear theory and its applications in Science and Engineering. Berlin, Springer-Verlag. 2000. -556 p.
[17]. Ильюшин А.А. Пластичность. Упругопластические деформации. М.:, Л.:, Гостехиздат, 1948, 376 с.
[18]. Биргер И.А. Общие алгоритмы решения задач теории упругости, пластичности и ползучести. // Успехи механики деформируемых сред. М.: Наука, 1975, с. 51-73.

Proceedings of the International Symposium of Mechanism and Machine Science, 2017
AzC IFToMM – Azerbaijan Technical University
11-14 September 2017, Baku, Azerbaijan

Halqavaqri lövhənin yükgötürmə qabiliyyəti haqqında

A.Ə.Cahangirov
Azərbaycan Texniki Universiteti
Az 1073, Bakı, H.Cavid prospekti 25
E-mail: al-akif@mail.ru

Xülasə
Məqalədə səthi üzrə paylanmış yükün təsirinə məruz qalmış həlqəvi kompozit lövhənin yükgötürmə qabiliyyətinin təyini məsələsinə baxılır. Məsələnin riyazi qoyuluşu verilir, axtarılan funksiyaların sinfi təyin edilir, həmçinin sərhəd şərtləri və əyici momentlərin və əyinti sürətlərinin kəsilməzlik şərtləri yazılır. Məsələnin mexaniki qoyulundan istifadə etməklə dairəvi lövhə halında lövhənin mərkəzi üçün və axma altıbucaqlısının şaquli tərəfləri üçün şərtlər yazılır. Axma altıbucaqlısının tərəflərinin tənlikləri momentlərlə ifadə olunur və sonra assosiyə olunmuş axma qanunundan istifadə etməklə bu tənliklər əyinti sürətlərinə nəzərən adi diferensial tənliklərə gətirilir. Axma altıbucaqlısının şaquli tərəflərinin oynaqlı olması şərtindən istifadə etməklə lövhə üçün kompoziti təşkil edən materialların bütün xassələrindən asılı olan limit yük təyin edilir.

Açar sözlə: həddi yük, üçlaylı lifli kompozit, ideal plastik model, əyiji momentlər, əyilmənin deformasiya sürəti.

Giriş. Son yarım əsrdə kompozit materiallar sənaye və texnologiyada daha geniş sahələrə tətbiq olunmağa başlamışlar. Kompozit material dedikdə iki və daha çox materialın istifadəsi ilə ağıllı qaydalar və hesabatlar əsasında hazırlanan, yüngül çəkiyə və tələb olunan möhkəmlik, sərtlik və termik xassələrə malik olan materiallar nəzərdə tutulur. Kompozit konstruksiyaların həddi yükünün təyini riyazi cəhətdən çox mürəkkəb məsələlərdən biridir. Əvvəlcə bütövlükdə kompozitin plastik axma şərtlərini qurmaq, sonpa isə bu şərtləri konkret məsələlərin həllinə tətbiq etmək lazımdır. Bu məqalədə adı çəkilən məsələlərin qoyuluşu və bəzi xassələri haqqında danışılacaqdır. Konkret məsələlərin dəqiq analitik həlləri ədəbiyyat siyahısındakı məqalələrdə təfsilatı ilə verilmişdir [1-5].

1. Məsələnin qoyuluşu.

Halqavari lövhənin yükgötürmə qabiliyyətinin təyini haqqında məsələnin qoyuluşuna baxaq: z oxu aşağıya yönəlməklə R,φ,z silindrik koordinat sisteminin

$$A \le R \le B,\ -\frac{H}{2} \le z \le \frac{H}{2},\ 0 \le \varphi \le 2\pi$$

oblastında verilmiş halqavari kompozit lövhənin P intensivlikli aşağıya yönəlmiş oxasimmetrik yükün təsiri altında plastik əyilməsi (dartılmasız) məsələsini öyrənək. Lövhənin H qalınlığını sabit hesab edirik. Konstruksiyanın yükgötürmə qabiliyyəti tükənir ifadəsi - onun xarici qüvvələrin artımına müqavimət göstərə bilmədiyini ifadə edir. Yükləmə artırılaraq limit yükə çatana qədər lövhə mütləq bərk cisim kimi deformasiyaya uğramır, limit yükə çatdıqda isə lövhənin müqaviməti anidən itir və o plastik maye kimi axmağa başlayır. Məqsəd lövhənin yükgötürmə qabiliyyəti adlanan bu limit yükü tapmaqdan ibarətdir. Bunun üçün lövhənin əyici momentlərlə ifadə edilən müvazinətinin diferensial tənliyi yazılır və ya ölçüsüz kəmiyyətlərlə

$$(rm_1)' - m_2 = -T^{ar} + Ta \qquad \left(T^{ar} = \int_a^r p(\eta)\eta\, d\eta,\ p = P/\sigma_0\right) \tag{1}$$

burada ştrix r - ə görə törəməni göstərir, T – isə lövhənin daxili konturu üzərində (halqavari lövhələr üçün) vahid uzunluğa düşən naməlum dayaq reaksiyasıdır. Dairəvi lövhələr üçün T sıfırdır.

Müvazinət tənliyi aşağıdakı sərhəd şərtləri daxilində həll edilir:

1) sərbəst sərhəddə: $m_1 = 0$;

2) şarnirli dayaqlanmış sərhəddə:

$$m_1 = 0,\quad w = 0; \tag{2}$$

3) bağlanmış sərhəddə: $w = 0$ və, ya $\dfrac{dw}{dr} = 0$, ya da

$$m_1 = m_{01}.$$

(1) tənliyi iki m_1 və m_2 naməlum funksiyalarının təyini üçün bir tənlikdir. Bu kəmiyyətlər arasında ikinci tənlik axma şərtləri ilə verilir. Məlum olduğu kimi, axma altıbucaqkısının daxilində deformasiya yoxdur (elastikdir, ancaq ideal sərt plastiklik nəzəriyyəsinə görə bu halda deformasiya sıfır hesab edilir), üzərində plastik axma şərtləri ödənir, kənarına isə çıxıla bilməz, çünki material möhkəmlənməyəndir.

Lövhənin yükgötürmə qabiliyyətini (limit yükü) təyin etmək üçün əvvəlcə axma altıbucaqlısının tərəflərinin elə ardıcıllığı seçilir ki, bu ardıcıllığın başlanğıc və son nöqtələrində lövhənin konturları üzərindəki momentlərlə yazılan şərtlər ödənsin. Ardıcıllıq üzrə istiqamət isə məsələnin qoyuluşuna uyğun şəkildə momentlərin işarələrinin analizi ilə müəyyən edilir. Qeyd edək ki, alt təbəqələr dartılanda, üst təbəqələr isə sıxılanda $m_r > 0$ olur. Lövhənin səthi altıbucaqlının götürülən tərəflərinin sayı qədər konsentrik halqavari oblastlara (plastik axma rejimlərinə) bölünür. Bu oblastların tənlikləri kəsilməzlik şərtlərindən tapılır.

Beləliklə, verilən kompozit lövhənin yükgötürmə qabiliyyətin təyin etmək üçün aşağıdakı riyazi məsələni həll etmək lazımdır. $p = p(r)$ yükünün elə ən böyük qiymətini tapmaq lazımdır ki, buunun üçün tapıla bilən $m_r(r)$ radial, $m_\theta(r)$ tangensial momentləri və $w(r)$ əyilmə sürəti funksiyaları $a \le r \le b$ intervalında aşağıdakı şərtləri ödəyirlər:

1) m_r, m_θ və w funksiyaları uyğun olaraq C^1, C^0 və C^2 – dən olan hissə-hissə kəsilməz funksiyalardır:

2) m_r və m_θ müvazinətin (1) diferensial tənliyini ödəyirlər; dairəvi lövhənin mərkəzində $m_r = m_\theta$;

3) koordinatları m_r, m_θ olan ümumiləşmiş gərginliklər nöqtəsi axma altıbucaqlısının içərisində və ya üzərində ola bilər. Birinci halda axma sürətləri sıfır olur ($w = 0$), ikinci halda isə əyrilik sürətləri ilə ümumiləşmiş gərginliklər arasında assosiasiya olunmuş axma qanunu ödənir, yəni $(\dot{\chi}_1, \dot{\chi}_2)$ plastik əyinti sürətləri vektoru m_r, m_θ müstəvisində axma altıbucaqlısının təpə nöqtələrindən [6-9] başqa hər bir nöqtəsində ona perpendikulyardır;

4) əyrilik sürətinin dw/dr törəməsi yalnız şarnir çevrələri üzərində, yəni $|m_r| = m_{01}$ olduqda kəsilən olur;

5) sərbəst sərhəddə: $m_1 = 0$; şarnirli dayaqlanmış sərhəddə $m_1 = 0$, $w = 0$; bağlanmış sərhəddə isə $w = 0$ və, ya $\frac{dw}{dr} = 0$, ya da $m_1 = m_{01}$ şərtləri ödənir.

w əyinti sürətinin təyini üçün assosiasiya olunmuş axma qanunundan

$$\dot{\chi}_i = \lambda_p \frac{\partial f_p}{\partial m_i} \qquad (i = 1, 2; \quad p = 1, 2, ..., 6)$$

istifadə etməklə xətti differensial tənliklər alırıq, burada f_p – axma şərtlərinin tənlikləridir, λ_p - mənfi olmayan kəmiyyətlər,

$$\dot{\chi}_1 = -\frac{d^2 w}{dr^2}, \qquad \dot{\chi}_2 = -\frac{1}{r}\frac{dw}{dr}, \tag{3}$$

isə lövhənin orta səthinin əyinti sürətləridir. Assosiasiya olunmuş axma qanununda əyinti sürətləri vektorunun $m_1 m_2$ müstəvisində axma altıbucaqlısının normalı istiqamətində yönəldiyi ifadə edilmişdir .

m_1, m_2 baş momentlərinin işarələrindən asılı olaraq plastik axınlar müxtəlif istiqamətlərdə inkişaf edir. Sadəlik üçün axma altıbucaqlıslnın tərəflərinin tənliklərindən istifadə edək [1-5], onları aşağıdakı kimi yaza bilərik:

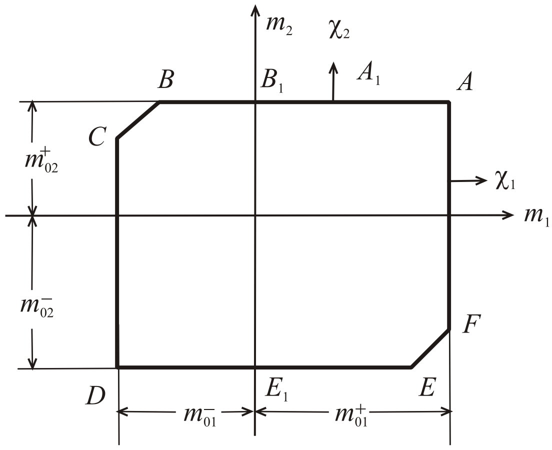

Şəkil. Axma altıbucaqlısı

a) $f_1 = m_2 - \alpha m_1 - \beta_1 = 0$, əgər $m_1 \ge 0$, $m_2 \le 0$ (EF rejimi);

b) $f_2 = m_2 - \alpha m_1 - \beta_2 = 0$, əgər $m_2 \ge 0$, $m_1 \le 0$ (BC rejimi);

c) $f_3 = m_1 - m_{01}^+ = 0$ (AF rejimi);

d) $f_4 = m_1 + m_{01}^- = 0$ (CD rejimi);

e) $f_5 = m_2 - m_{02}^+ = 0$ (AB rejimi);

f) $f_6 = m_2 + m_{02}^- = 0$ (DE rejimi).

Beləliklə, altı hamar axma şərtləri alırıq, yəni $f_p = 0$, $p = \overline{1, 6}$.

Əgər sərhəddə momentlərin (ümumiləşmiş gərginliklərin) qiymətləri verilərsə, onda diferensial müvazinət tənliyi ilə birlikdə m_1, m_2 ümumiləşmiş gərginlik vəziyyətinin deformasiya sürətlərindən asılı olmayan təyini üçün tam tənliklər sistemi alırıq.

w əyinti sürətini təyin etmək üçün assosiyə olunmuş axma qanunundan istifadə etməklə xətti diferenial tənlikləri tapırıq.

$$\dot{\chi}_1 = -\frac{d^2 w}{dr^2}, \qquad \dot{\chi}_2 = -\frac{1}{r}\frac{dw}{dr},$$

Lövhənin orta səthinin əyrilik sürətləridir, həmçinin assosiyə olunmuş axma qanununu yazırıq:

$$\dot{\chi}_i = \lambda_p \frac{\partial f_p}{\partial m_i} \qquad (i = 1, 2; \quad p = 1, 2, ..., 6)$$

burada hissə-hissə hamar f_p axma funksiyaları *a*)-*f*) tənlikləri ilə verilir, λ_p isə mənfi olmayan kəmiyyətlərdir. Beləliklə, əyrilik sürəti vektoru m_1, m_2 müstəvisində axma altıbucaqlısının normalıdır. Onda assosiyə olunmuş axma qanunu m_1, m_2 ümumiləşmiş kəmiyyətləri və χ_1, χ_2 əyrilik sürətləri arasındakı asılılıq üçün də doğrudur.

Deformasiya sürətinin komponentləri aşağıdakı məlum münasibətlərlə təyin edilir:

$$\xi_r = z\chi_1, \qquad \xi_\theta = z\chi_2.$$

Aydındır ki, deformasiya sürətlərinin ξ_r / ξ_θ nisbəti lövhə müstəvisinin normalı istiqaməti üzrə sabitdir.

a) tənliyinə (EF) əsasən alırıq:

$$\frac{\partial f_1}{\partial m_1} = -\alpha, \qquad \frac{\partial f_2}{\partial m_2} = 1,$$

və uyğun olaraq

$$\dot\chi_1 = -\lambda_1\alpha, \qquad \dot\chi_2 = \lambda_1,$$

yəni $\dot\chi_1 + \alpha\dot\chi_2 = 0$ və lövhənin *w* əyinti sürəti ikinci tərtib xətti bircins diferensial tənliyi ödəyir:

$$\frac{d^2w}{dr^2} + \frac{\alpha}{r}\frac{dw}{dr} = 0.$$

Analoji nəticələr BC rejimi üçün də doğrudur. Doğrudan da, *b)* tənliyinə əsasən alırıq:

$$\frac{\partial f_2}{\partial m_1} = -\alpha, \qquad \frac{\partial f_2}{\partial m_2} = 1,$$

və uyğun olaraq

$$\dot\chi_1 = -\lambda_2\alpha, \qquad \dot\chi_2 = \lambda_2,$$

yəni $\dot\chi_1 + \alpha\dot\chi_2 = 0$ və yenə də aşağıdakı diferensial tənliyi almış oluruq:

$$\frac{d^2w}{dr^2} + \frac{\alpha}{r}\frac{dw}{dr} = 0.$$

Uyğun şəkildə digər rejimlərə də baxılır.

2. Mərkəzi layı liflərlə armirlənmiş və sərbəst dayaqlanmış dairəvi üçlaylı kompozit lövhənin yükgötürmə qabiliyyətinin təyini

Üst səthində müntəzəm paylanmış aşağı yönələn *P* yükünün təsirinə məruz qalan *R* radiuslu sərbəst dayanmış dairəvi kompozit lövhəyə baxaq.

Sərbəst dayanmış sərhəddə radial əyici momentin və əyintinin sıfıra bərabər olması şərti ödənməlidir:

$$m_1 = 0, \qquad w = 0.$$

Lövhənin $r = 0$ mərkəzində isə məsələnin simmetrikliyinə görə $m_1 = m_2 = m_0$ şərti ödənir.

Analiz göstərir ki, lövhənin plastikliyi axma altıbucaqlısında $A_1B_1^{'}\left(m_2 = m_0, 0 \le m_1 \le m_0\right)$ rejiminə uyğun gəlir, burada $A_1\left(m_1 = m_2 = m_0\right)$ nöqtəsi mərkəzə, $B_1^{'}\left(m_1 = 0, m_2 = m_0\right)$ nöqtəsi isə lövhənin sərhədinə uyğundur.

(1) tənliyini aşağıdakı şəklə gətirək:

$$\frac{d}{d\xi}\left(\xi m_1\right) - m_2 = -2p\xi.$$

$m_2 = m_0, 0 \le m_1 \le m_0$ olduqda bu tənliyin həlli

$$m_1 = m_0 - \frac{2}{3}p\xi^2 + \frac{C}{\xi},$$

olar, buada *C* ixtiyari inteqrallama sabitidir. Həllin $\xi = 0$ olduqda məhdud olması üçün $C = 0$ qəbul edək. Beləliklə,

$$m_1 = m_0 - \frac{2}{3}p\xi^2.$$

$\xi = \rho$ xarici konturunda $m_1 = 0$ sərhəd şərtindən istifadə etməklə, alarıq:

$$m_0 = \frac{2}{3}p\rho^2.$$

Bu zaman (1) tənliyinin sərhəd şərtlərini ödəyən həlli aşağıdakı kimi yazılır:

$$m_1 = \frac{2}{3}p\left(\rho^2 - \xi^2\right), \qquad (4)$$

p limit yükü isə

$$p = \frac{3}{2}\frac{m_0}{\rho^2}, \qquad (5)$$

bərabərliyindən təyin edilir, burada [1-11]

$$m_0 = \frac{2k}{1+k} + 4s_0\left[\left(1+\mu\right)d + \frac{1-\mu}{2\left(1+k\right)}\right] - \frac{2\left(1-\mu\right)^2}{1+k}s_0^2 +$$

$$+4q_0\frac{1+\nu k}{1+k} - \frac{2\left(1-\nu\right)^2}{1+k}q_0^2 - \frac{4\left(1-\mu\right)\left(1-\nu\right)}{1+k}s_0q_0$$

(5) düsturlarından göründüyü kimi limit yük lövhənin radiusunun kvadratı ilə tərs və m_0 axma həddi ilə düz mütənasibdir. Öz növbəsində, m_0 axma həddi s_0 və q_0 kəmiyyətlərilə düz mütənasibdir. s_0 və q_0 kəmiyyətlərinin kvadratları, həmçinin onların hasili (bu hasil liflərin və örtük təbəqələrin materiallarının dartılma və sıxılmada fərqli müqavimətləri hesabına yaranır) m_0 axma həddini azaldır. Əgər $\mu = 1$ və

$\nu = 1$ olarsa, onda

$$m_0 = \frac{2k}{1+k} + 8s_0 d + 4q_0 .$$

Buradan görünür ki, armirləyici liflər və örtük təbəqələr m_0 axma həddini artırır, d=0,5 və k=1 olduqda m_0 özünün

$$m_0 = 1 + 4(s_0 + q_0) .$$

olan ən böyük qiymətini alır. s_0=q_0=0 olduqda m_0=1 olur və (5) Treskanın tədqiq etdiyi həlli təyin edir [1-5].

İndi isə əyinti sürətlərinin kinematik mümkün sahələrini təyin edək. $\dot{\chi}_i = \lambda \frac{\partial f}{\partial m_i}\ (i = 1, 2)$ assosiyə olunmuş axma qanunundan istifadə edək, burada λ – müsbət əmsal, f – axma altıbucaqlısının uyğun tərəfi ilə təyin olunan axma şərtidir. A_1B_1 rejiminin (şəkil) tənliyi $f = m_2 - \overline{m}_s = 0$ olur və buna əsasən

$$\frac{\partial f}{\partial m_1} = 0, \qquad \frac{\partial f}{\partial m_2} = 1$$

təyin edirik.

Göründüyü kimi axma yalnız ikinci baş istiqamətdə inkişaf edir və uyğun olaraq

$$\chi_1 = 0, \qquad \chi_2 = \lambda \ge 0 .$$

Beləliklə, $0 \le \xi \le \rho$ olduqda $w'' = 0,\ w' < 0$ olur. $\chi_1 = 0$ olduğundan, w əyinti sürəti

$$\frac{d^2 w}{d\xi^2} = 0 ,$$

diferensial tənliyindən təyin olunur və radiusa nəzərən $w = c_1 r + c_2$ şəklində xətti funksiyadır. $w(0)\le\infty$, $w(\rho)=0$ sərhəd şərtlərini nəzərə alsaq

$$w = w_0 \left(1 - \frac{\xi}{\rho}\right), \quad 0 \le \xi \le \rho ,$$

alırıq, burada w_0 – əyinti sürəti olub $\xi = 0$ olduqda qeyri-müəyyən qalır. Göründüyü kimi ideal plastik deformasiya halında lövhə düz konus şəklini alır.

3. Əyici momentlər sahəsinin təyini

Naməlum $\xi = \rho_1$ sərhədli hər hansı mərkəzi oblastında konturu üzrə bağlanmış lövhələrin plastikliyi sərbəst dayanmış lövhələrdəki kimi olacaq, lakin kontura bitişik həlqəvi oblastda radial Əyici moment mənfi olacaq. Mərkəzi hissədə $(0 \le \xi \le \rho_1)$ A_1B_1 rejimi, burada $m_2 = m_0,\ m_0 - A_0 \le m_1 \le m_0$, həlqəvi oblastda isə $(\rho_1 \le \xi \le \rho)$ - B_1C_1 rejimi ödənir, burada $m_2 - m_1 = A_0$, belə ki,

$$A_0 = 2\left\{\frac{1-k}{1+k}\left[s_0(1-\mu) + q_0(1-\nu)\right] + \frac{k}{1+k} + \right.$$
$$\left. + 4s_0(1+\mu)d + 2q_0(1+\nu)\right\}$$

$$m_0 = \frac{2k}{1+k} + 4s_0\left[(1+\mu)d + \frac{1-\mu}{2(1+k)}\right] - \frac{2(1-\mu)^2}{1+k}s_0^2 +$$
$$+ 4q_0\frac{1+\nu k}{1+k} - \frac{2(1-\nu)^2}{1+k}q_0^2 - \frac{4(1-\mu)(1-\nu)}{1+k}s_0 q_0$$

$\mu = \nu = 1$ olduqda alırıq:

$$m_0 = \frac{2k}{1+k} + 8s_0 d + 4q_0 ,$$

$$A_0 = \frac{2k}{1+k} + 16s_0 d + 8q_0 . \tag{6}$$

Göründüyü kimi $A_0 > m_0$. Uyğun oblastlarda müvazinət tənlikləri aşağıdakı kimi olacaq:

$$\frac{dm_1}{d\xi} + \frac{m_1 - m_0}{\xi} = -2p\xi, \quad 0 \le \xi \le \rho_1, \tag{7}$$

$$\frac{dm_1}{d\xi} - \frac{A_0}{\xi} = -2p\xi, \quad \rho_1 \le \xi \le \rho . \tag{8}$$

(7) tənliyini

$$\frac{d}{d\xi}(\xi m_1) - m_2 = -2p\xi .$$

şəklinə gətirək. Bu tənliyin həlli

$$m_1 = m_0 - \frac{2}{3}p\xi^2 + \frac{C}{\xi}$$

funksiyasıdır, burada S – inteqrallama sabitidir. $\xi = 0$ olduqda həllin məhdud olması üçün $C = 0$ götürmək lazımdır. Beləliklə,

$$m_1 = m_0 - \frac{2}{3} p\xi^2 .$$

İkinci tənliyin həlli ilə

$$m_1 = A_0 \ln \xi - p\xi^2 + C$$

funksiyasıdır. C sabitini $\xi = \rho$ sərhəddində $m_1 = -m_0$ şərtindən təyin edərək son nəticə olaraq həlli aşağıdakı kimi yaza bilərik:

$$m_1 = \begin{cases} m_0 - \frac{2}{3} p\xi^2, & 0 \le \xi \le \rho_1, \\ -m_0 + A_0 \ln \frac{\xi}{\rho} + p\left(\rho^2 - \xi^2\right), & \rho_1 \le \xi \le \rho \end{cases}$$

$\xi = \rho_1$ çevrəsində lövhə B_1 rejimi ilə xarakterizə olunur, burada sağdan $m_2 = m_0$ şərti, soldan isə $m_1 = m_0 - A_0$ şərti ödənir, yəni B_1 nöqtəsi $m_1 m_2$ baş Əyici momentlər müstəvisində yerləşir və $B_1\left(m_0 - A_0, m_0\right)$ koordinatına malikdir. m_1 -in sağdan kəsilməzliyini ödəyərək,

$$m_2 - m_1 = m_0 - m_1 = A_0 ,$$

$$m_0 - A_0 = m_1 = m_0 - \frac{2}{3} p\rho_1^2$$

yazaq və sonuncu bərabərliklərdən

$$2p\rho_1^2 = 3A_0 .$$

təyin edək.

B_1 rejimindən solda kəsilməzlik şərtindən isə alarıq:

$$p\left(\rho^2 - \rho_1^2\right) + A_0\left(1 - \ln \frac{\rho}{\rho_1}\right) = 2m_0$$

Birinci tənlikdən limit yük təyin edilir:

$$p = \frac{3A_0}{2\rho_1^2} .$$

Bu ifadəni əvvəlki bərabərlikdə yerinə yazsaq, mərkəzi və həlqəvi deformasiya oblastlarını ayıran naməlum ρ_1 radiusunu tapmış olarıq:

$$3\rho^2 = \rho_1^2\left(1 + \frac{4m_0}{A_0} + 2\ln \frac{\rho}{\rho_1}\right).$$

$\mu = \nu = k = 1$ olduqda $A_0 = 1 + 16ds_0 + 8q_0$, $m_0 = 1 + 8s_0 d + 4q_0$ alırıq və uyğun həllər aşağıdakı şəkildə olur:

$$p = \frac{3}{2\rho_1^2}\left(1 + 16ds_0 + 8q_0\right),$$

$$3\rho^2 = \rho_1^2\left(1 + \frac{4 + 32ds_0 + 16q_0}{1 + 16ds_0 + 8q_0} + 2\ln \frac{\rho}{\rho_1}\right).$$

Göründüyü kimi limit yük armirləyən liflərin, həm də qoruyucu təbəqələrin hesabına kifayət qədər artır. Bundan əlavə, armirləyən liflər layının orta səthdən olan d məsafəsi artıqda da limit yükün qiyməti artır. Bu kəmiyyətlər həm də deformasiya oblastları arasındakı radiuslara təsir edir.

$k = 1,\ s_0 = q_0 = 0$ olduqda Treskanın lövhə üçün çox məlum həlli alınır:

$$2p\rho_1^2 = 3,3\rho^2 = \rho_1^2\left(5 + 2\ln \frac{\rho}{\rho_1}\right).$$

İndi isə axma başlayan anda, yerdəyişmələr hələ çox kiçik ikən, lövhənin həndəsi ölçülərinin dəyişməsi isə əhəmiyyətsiz dərəcədə olduqda əyinti sürətlərinin kinematik mümkün sahələrini təyin edək. Lövhənin axma halına keçmiş hər bir elementi sərt elementlərlə bağlıdır. Buna görə də ayrı-ayrı elementlərin deformasiya sürətləri arasındakı münasibətlər bir-biri ilə əlaqəlidir və bu da sürətlərin qeyri-müəyyən vuruq dəqiqliyi ilə tapılmasına gətirib çıxarır. $\chi_i = \lambda_i \frac{\partial f_i}{\partial m_i}\ (i = 1, 2)$ baş istiqamətlərində assosiyə olunmuş axma qanunundan istifadə edək, burada λ – müsbət əmsal, f – axma altıbucaqlısının uyğun tərəfi ilə təyin olunan axma şərtidir. $A_1 B_1$ rejiminin tənliyi $f = m_2 - \bar{m}_s = 0$ olur və buna əsasən

$$\frac{\partial f}{\partial m_1} = 0, \qquad \frac{\partial f}{\partial m_2} = 1$$

təyin edirik.

Göründüyü kimi axma yalnız ikinci baş istiqamətdə inkişaf edir və uyğun olaraq

$$\chi_1 = 0, \qquad \chi_2 = \lambda \ge 0 .$$

Beləliklə, $0 \le \xi \le \rho$ olduqda $w'' = 0,\ w' < 0$ olur. $\chi_1 = 0$ olduğundan, w əyinti sürəti

$$\frac{d^2 w}{d\xi^2} = 0 ,$$

diferensial tənliyindən təyin olunur və radiusa nəzərən $w = c_1 r + c_2$ şəklində xətti funksiyadır.

BC rejimi üçün də analoji nəticələr doğrudur. Doğrudan da, *b*) tənliyinə əsasən

$$\frac{\partial f_2}{\partial m_1} = -\alpha, \qquad \frac{\partial f_2}{\partial m_2} = 1,$$

və uyğun olaraq

$$\dot{\chi}_1 = -\lambda_2 \alpha, \qquad \dot{\chi}_2 = \lambda_2,$$

alarıq, yəni $\dot{\chi}_1 + \alpha \dot{\chi}_2 = 0$ və aşağıdakı diferensial tənliyi alırıq:

$$\frac{d^2 w}{d\xi^2} + \frac{\alpha}{\xi}\frac{dw}{d\xi} = 0 \cdot$$

$dw/d\xi = u$ işarə edərək sonuncu tənliyi

$$\frac{du}{d\xi} + \frac{\alpha}{\xi} u = 0$$

şəklində yaza bilərik. Bu tənliyi həlli $u = C_3 \xi^{-\alpha}$ kimidir. Onda $dw/d\xi = C_3 \xi^{-\alpha}$ tənliyinin ümumi həlli

$$w = C_3 \frac{\xi^{1-\alpha}}{1-\alpha} + C_4,$$

funksiyası olar, burada C_3 və C_4 ixtiyari inteqrallama sabitləridir ki, onları $\xi = \rho_1$ çevrəsində kəsilməzlik şərtindən və $\xi = \rho$ konturunda sərhəd şərtlərindən təyin edəcəyik. Kontur üzrə əyintinin sıfıra bərabər olması şərtindən $C_4 = -C_3 \dfrac{\rho^{1-\alpha}}{1-\alpha}$ alarıq. Onda əyinti aşağıdakı düsturla təyin edilir:

$$w = C_3 \left(\frac{\xi^{1-\alpha} - \rho^{1-\alpha}}{1-\alpha} \right), \qquad \rho_1 \le \xi \le \rho$$

Çevrə üzərində əyintinin kəsilməzliyi şərti

$$C_1 \rho_1 + C_2 = C_3 \left(\frac{\rho_1^{1-\alpha} - \rho^{1-\alpha}}{1-\alpha} \right),$$

şəklində yazılır, $\xi = \rho_1$ çevrəsində əyintinin birinci tərtib törəməsinin kəsilməzlik şərtindən isə $C_1 = C_3 \rho_1^{-\alpha}$ olduğu alınır.

Sonuncu iki tənlikdən alırıq:

$$C_2 = C_3 \frac{\alpha \rho_1^{1-\alpha} - \rho^{1-\alpha}}{1-\alpha}.$$

Sabitlərin alınmış qiymətlərini nəzərə alsaq, oblastlarda əyintinin ifadəsi aşağıdakı kimi yazıla bilər:

$$w = \begin{cases} w_0 \left[\rho_1^{-\alpha} \xi + \dfrac{\alpha \rho_1^{1-\alpha} - \rho^{1-\alpha}}{1-\alpha} \right], & 0 \le \xi \le \rho_1, \\ \dfrac{w_0}{1-\alpha} \left(\xi^{1-\alpha} - \rho^{1-\alpha} \right), & \rho_1 \le \xi \le \rho \end{cases}$$

burada w_0 – lövhənin $\xi = 0$ mərkəzində əyinti sürəti olub, naməlum qalır.

Göründüyü kimi plastik vəziyyətdə mərkəzi oblastda lövhə düz dairəvi konus şəklini alır, bu oblastdan arxada isə konik səthin şəkli çətinləşir.

Ədəbiyyat

1 Джагангиров А.А. Несущая способность армированной волокнами круглой трехслойной композитной пластинки защемленной по контуру. EKO, 2012. “Ekoenergetika” texniki jurnalı, №4, Bakı, 2012, s.74-80.

2 Джагангиров А.А. Несущая способность армированной волокнами свободно опертой круглой трехслойной композитной пластинки. Научные Труды-Фундаментальные Науки, 2013 №1, т. XII (45), 50- 54.

3 Джагангиров А.А. Несущая способность кольцевой трехслойной волокнистой композитной пластинки, свободно опертой по внутренней и защемленной по внешней кромкам. «Механика композитных материалов и конструкций», Москва, том 21, №1, 2015, с. 35-46.

4 Джагангиров А.А. Несущая способность трехслойной волокнистой композитной кольцевой пластинки, защемленной по кромкам. Механика композитных материалов, №2, 2016, с. 101-114.

5 Джагангиров А.А. Предельная нагрузка трехслойной волокнистой кольцевой пластинки защемленной по внутренней и свободно опертой по внешней кромкам. Проблемы прочности.Т.47, №3, с.481-487. Киев

6 Гопкинс Г., Прагер В. Динамика пластической круглой пластинки //Механика, 1955, №3, с. 112-122.

7 Григорьев А.С. О несущей способности кольцевых пластин //Инж. Сбр., 1953, т. XVI.

8 Mroz Z., Shamiev F.G. Simplified yield conditions for fibre-reinforced plates and shells //Arch. Inz. Lad., 1979, vol. 25, №3, p. 463 - 476.

9 Немировский Ю.В., Романова Т.П. Несущая способность ледяных пластин криволинейной формы, усиленных жесткой вставкой. Прикладная механика и техническая физика, 2013, №4, С. 141 – 149.

Proceedings of the International Symposium of Mechanism and Machine Science, 2017
AzC IFToMM – Azerbaijan Technical University
11-14 September 2017, Baku, Azerbaijan

Proqramla idarə olunan avadanlıqların tətbiqi ilə avtomatik xətlərdə hazırlanacaq detalların təsnifat siniflərinin işlənməsi

F.Q.Əmirov
Azərbaycan Texniki Universiteti

Xülasə: Detalların ölçüləri onların hazırlanmasında iştirak edən avadanlığın xarakteristikasının təyin edilməsində mühüm rol oynayır və detalların emal prosesinə kifayət qədər ciddi təsir göstərir. Eyni zamanda ölçülərinə görə detalların təsnifatı, onların həndəsi modelləşdirilməsi və tam hazırlanma prosesi üçün koordinat sisteminin qurulması üsuluna baxılmışdır.

Açar sözlər: sazlanabilən avtomat xətt, rəqəmli proqramla idarəetmə, texnoloji proses, detalın konstruksiyası və ölçüləri, həndəsi parametrlər.

Giriş.

Avtomat dəzgah sistemi (ADS) kompleksində metalkəsən avadanlıqlar çoxçeşidli istehsalın tələbatlarına daha çox cavab verir [1-3, 8-11]. Eyni zamanda, aparılan işlərin tətbiqi təcrübəsi göstərir ki, bunların çoxu iqtisadi cəhətdən əlverişli deyildir. Lakin bu sahədə kifayət qədər səmərəli istifadə olunma misalları da göstərmək olar. ADS-in aşağı səmərəliliyinin səbəbləri odur ki, milli maşınqayırma sənayesində uyğun infrastruktur və inzibati-texniki şərtlər yaradılmamışdır.

Bu gün ən aktual problem xarakterli məsələ tələb edilən avtomatlaşdırma səviyyəli çoxçeşidli dəzgah sisteminin yaradılmasıdır. Çoxçeşidli istehsalın səmərəliliyinin yüksəldilməsi onun prinsiplərinə cavab verən istehsalın təşkili və idarəetmə tələblərinə uyğun olmasıdır.

Texnoloji proseslərin layihələndirilməsi zamanı çoxçeşidli istehsal üçün dəzgah sistemlərindən istifadədə modul texnologiyaları prinsipi xüsusi əhəmiyyət kəsb edir [4-11]. Modul texnologiyasının mahiyyəti odur ki, məhdud çeşidli modullar ailəsindən modullar çoxluğu seçilə bilər Hər bir modulda bir neçə tipik texnoloji proses işlənə bilir ki, bu zaman detalın materialının tərkibinin müxtəlifliyi, ölçüləri, dəqiqlik və təmizlik tələbləri, səthin keyfiyyəti və bir çox digər parametrləri nəzərə alınır.

Modul və qrup texnologiyalarının birləşdirilməsi, texnoloji avadanlığın ayrı-ayrı qovşaqlarının icra edilməsi əsasında dəzgah sisteminin yaradılmasına şərait yaradır Bu əməliyyatlar nəticəsində elə modul tipləri yaradılır ki, modul tipləri sistemi tətbiq edilməklə bütün maşınqayırma kompleksində tipik detalların istehsalını təşkil etməyə imkan yaranır.

İşin məqsədi: Texnoloji proseslərin ümumi layihələndirmə prinsiplərinin işlənilməsi və əsaslandırılması, detalların təsnifatı və tipik texnoloji proseslər ümumi maşınqayırma texnologiyası nəzəriyyəsinin inkişafında vacib məsələlərdən biridir. Eyni zamanda, avtomatik xətlərdə (AX) detalların hazırlanması üçün tipik texnoloji proseslər işlənilmişdir.

Təsnifat dedikdə, detalların konstruksiyası, ölçüləri və onların hazırlanma prosesinin texnologiyasına görə ümumi hesab edilən müəyyən qrup və sinif halında birləşməsi başa düşülür.

Detalların tipikliyi dedikdə, sazlanabilən avtomatlaşdırılmış axın xətlərində (SAX) hazırlanacaq detalların optimal texnoloji proseslərinin işlənməsi üçün əsas sayılan və həmin sinfi əhatə edən bütün detalların hazırlığı və prinsipial texnoloji marşrut üzrə keçidlərə uyğun detalların səthlərinin emalı prosesi başa düşülür.

Detalların hazırlanması üçün texnoloji proseslərin işlənməsində həlledici qərarlar aşağıdakı faktorlarla xarakterizə edilir: detalların konstruksiyası, səthlərin həndəsi ölçüləri və onların dəqiqlik parametrləri, detalların ölçülərinə görə parametrlərin qarşılıqlı yerləşməsi, buraxılış həcmi və hazırlanma dəqiqliyi [1,2,7-11]. Qeyd edilənlərdən başqa, detalların pəstahlarının alınması üsulları da böyük əhəmiyyət kəsb edir.

Məsələnin həlli:

Beləliklə, detalların tipik hazırlanma texnologiyasını təyin edən əsas faktorlar kimi detalların ölçüləri, onların buraxılış həcmi, pəstahların alınması üsulları, detalların forması (konstruksiyası) və hazırlanma dəqiqliyi qəbul olunmalıdır. Bu faktorların detalların hazırlanma texnoloji prosesinə təsirini araşdıraq.

Detalların ölçüləri bir çox hallarda onların hazırlanmasında iştirak edən avadanlığın xarakteristikasının təyin edilməsində mühüm rol oynayır və detalların emal prosesinə kifayət qədər ciddi təsir göstərir. Müxtəlif ölçülü, lakin eyni formaya malik detalların səthləri eyni kinematikaya malikdir. Lakin ölçülərdə kifayət qədər fərqlər olarsa, detalların səthlərinin forma kinematikası bir-birindən fərqlənə bilər [1, 2, 9-11].

Məsələn, iri və çox da böyük olmayan gövdə tipli detalları hazırlayarkən onun avadanlığı və formasının kinematikası öz aralarında kifayət qədər fərqlənir. Ölçüləri 300x400x825 mm (şək. 1) olan birsıralı altı silindrli mühərrik blokunu emal edərkən nəhəng frezləmə, yonma, aqreqat və digər dəzgahlar tələb edilir [11].

Çox da böyük olmayan gövdə tip detallar (su nasosunun gövdəsi, şək. 2) çoxşpindelli torna-karusel və ya çoxkəskili revolver və çox da böyük olmayan burğulama dəzgahlarında tam hazırlanır. Frezləmə ilə birlikdə səthlər hamarlanır və təmizlənir. Kifayət qədər kiçik ölçülü və çəkili detalların istehsalı istisna olmaqla, bütün gövdə tipli detalların mexaniki emalında bazalaşdırma üsulları və əməliyyatlar ardıcıllığı eynidir.

Qeyd edək ki, emal edilən detalların qabarit ölçüləri AX-ın nəqledici, yükləyici və boşaldıcı qurğularının konstruksiyasına ciddi sürətdə təsir edir.

Şək. 1. Mühərrikin silindr bloku

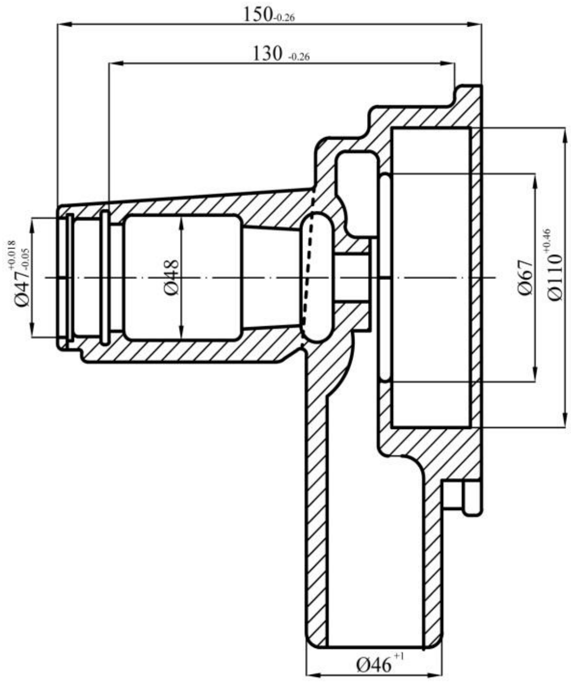

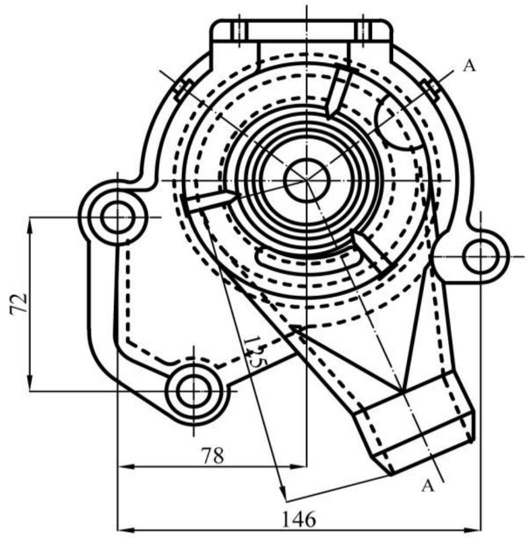

Şək. 2. Su nasosunun gövdəsi

Detalların buraxılış həcmi bir əməliyyatda həyata keçirilən texnoloji keçidlərin əvəz edilməsi səviyyəsinə də təsir göstərir. Bu isə, istifadə edilən avadanlığın texnoloji imkanlarını təyin edir və beləliklə, detalların hazırlanmasının texnoloji prosesinə və mürəkkəblik dərəcəsinə təsir göstərir. Detalların mexaniki emalının əmək sərfinin təyinində onların hazırlanma üsulları ciddi rol oynayır.

Avtomatlaşdırılmış axın xəttinin köməyi ilə istehsalda tipik texnoloji prosesləri yerinə yetirmək üçün mütləq şəkildə bir neçə pəstahalma üsullarından tam şəkildə imtina etmək lazımdır. Çünki müasir maşınqayırmanın inkişaf səviyyəsi nöqteyi nəzərdən bu iş həm iqtisadi, həm də texniki cəhətdən məqsədəuyğun sayılmır.

Detalların texnoloji prosesinin hazırlanmasının aparıcı faktoru onların konstruktiv quruluşudur. Eyni zamanda müxtəlif xarici formalara malik detallar, həmişə onların hazırlanmasında müxtəlif texnoloji prosesləri tələb edir. Gövdə tip detalların, kronşteynlərin və dayaqların xarici formalarının müxtəlifliyinə baxmayaraq, onlar təfsilatlı hazırlanan texnologiyalara malik olurlar.
Əməliyyatlararası nəqletmə zamanı detalların forması onların pəstahlarının bazalaşdırma sxemlərinə ciddi sürətdə təsir göstərir ki, bu da sonradan istifadə ediləcək yükləmə-boşaltma qurğularının kinematik sxemlərində və konstruksiyasında özünü göstərir. Əsas əməliyyatların

ardıcıllığını dəyişmədən yüksək dəqiqlik və təmizlik əldə etmək üçün bir çox əlavə əməliyyatlar aparılır. Əlavə əməliyyatlar nəticəsində mexaniki emalda əmək tutumu artsa da, hazırlanan detalların mexaniki emalı texnoloji proseslərinə uyğun olaraq onların dəqiqlik sinfinin artırılmasına imkan yaranır. Porşen barmaqları və resorlar üçün texnoloji proseslərin keyfiyyətli hazırlanması cədvəl 1 -də göstərilmişdir (şək. 3) [11].

Cədvəl 1. Porşen barmaqları və resorların xarici silindrik səthlərinin emalının müqayisəsi

Resor tipli barmaq: d=22mm, l=112mm, diametral müsaidə T=45mkm, kələkötürlük R_a=1,25	Porşen tipli barmaq: d=22mm, l=76mm, diametral müsaidə T=2,5 mkm, kələkötürlük R_a =0,16
T=80 mkm müsaidə ilə xarici diametrin yonma və ya sürtmə ilə emalı HRC56…62 bərklik təmin edilməklə materialın termiki emalla möhkəmləndirilməsi Mərkəzsiz-pardaxlama dəzgahında xarici silindrik səthin pardaxlanması. Emal payı Δd=0,3 mm, müsaidə T=45mkm, kələkötürlük R_a =0,63	T=80 mkm müsaidə ilə xarici diametrin yonma və ya sürtmə emalı HRC56…62 bərklik təmin edilməklə materialın termiki emalla möhkəmləndirilməsi Mərkəzsiz-pardaxlama dəzgahında xarici silindrik səthin kobud pardaxlanması. Emal payı Δd =0,3 mm, müsaidə T=30 mkm, kələkötürlük R_a =1,25 Mərkəzsiz-pardaxlama dəzgahında xarici silindrik səthin təmiz pardaxlanması. Emal payı Δd =0,15 mm, müsaidə T=15 mkm, kələkötürlük R_a =0,32 Mərkəzsiz-cilalama dəzgahında xarici silindrik səthin təmiz cilalanması. Emal payı Δd =20 mkm, müsaidə T=10 mkm, kələkötürlük R_a =0,080

Analoji fərqi müstəvi və fasonlu səthlərin, yuvaların daha dəqiq emalı prosesində müşahidə etmək olar. Beləliklə, analoji texnoloji proseslərdə iştirak edən, dəqiqliyinə və ayrı-ayrı səthlərin cilalanma səviyyəsinə görə fərqlənən uyğun tipli detallar üçün yeni texnoloji proses yaratmaq lazım deyildir. Sadəcə olaraq tipik texnoloji prosesə tamamlayıcı texnoloji keçidlər əlavə etmək lazımdır. İstehsalda sazlanabilən texnoloji avadanlıqlar müxtəlif emal üsulları şəraitində emal üsullarının ardıcıllığını təmin etməli və universallıq baxımından texnolojiliyi tam əhatə etməlidir. Bu nöqteyi-nəzərdən hal-hazırda istehsal olunan və rəqəmli proqramla idarə olunan torna qruplu emal mərkəzləri təkrar sazlanabilən olduğu üçün, bir əməliyyatda bir yerləşdirmədə müxtəlif formalara malik pəstah səthlərini emal edə bilir. Başqa sözlə desək, müasir texnoloji avadanlığın elə bir unikal imkanı vardır ki, onlar eyni əməliyyatda çoxmövqeli və çoxşpindelli avtomatlara məxsus həcmdə işlər görə bilərlər.

Axın prinsipli istehsalın təşkilində istifadə edilən detalların hazırlanmasında onların forma və təyinatının identikliyini (oxşarlığını) nəzərə alaraq professor F.S. Demyanyuk tərəfindən çəkisi 100 kq-a qədər olan orta ölçülü maşın detallarının altı sinfə bölünməsi təklif edilmişdir [6,11]. Bunlar gövdə tipli detallar, dairəvi çubuqlar, silindrlər, disklər, dairəvi olmayan çubuqlar və bərkidici detallardır.

Gövdə tipli detallar, ayrıca sinfə aid edilmişdir. Belə ki, bu geniş istifadə edilən detallar qrupuna aiddir. Xarici formalarının müxtəlifliyinə baxmayaraq, bütün gövdə tipli detalları analoji proseslər əsasında hazırlanmaq olar. Oxşar proseslər əsasında dabanları, dayaqları, lövhələri və bucaqlıqları hazırlamaq olar. Bunlar da təsnifat cədvəlinə görə gövdə detallar ailəsinə daxildir.

Təsnifat cədvəlində "Dairəvi çubuqlar" sinfinə adi vallar, oxlar, çəkiclər, dairəvi dayaqlar, düz və yumruqvari vallar, kənarları çıxıntılı dişli çarxlı vallar aiddir. Onların da xarici görünüşlərinin müxtəlifliyinə baxmayaraq, eyni hazırlanma proseslərinə malikdirlər. "Dairəvi çubuqlar" sinifli detallar "Vallar" adı ilə müqayisədə daha ümumi olan çox sayda detallar sinfini əhatə edir. Çünki "pərlər" sinfi dedikdə yalnız fırlanma hərəkətli yaylar nəzərdə tutulur.

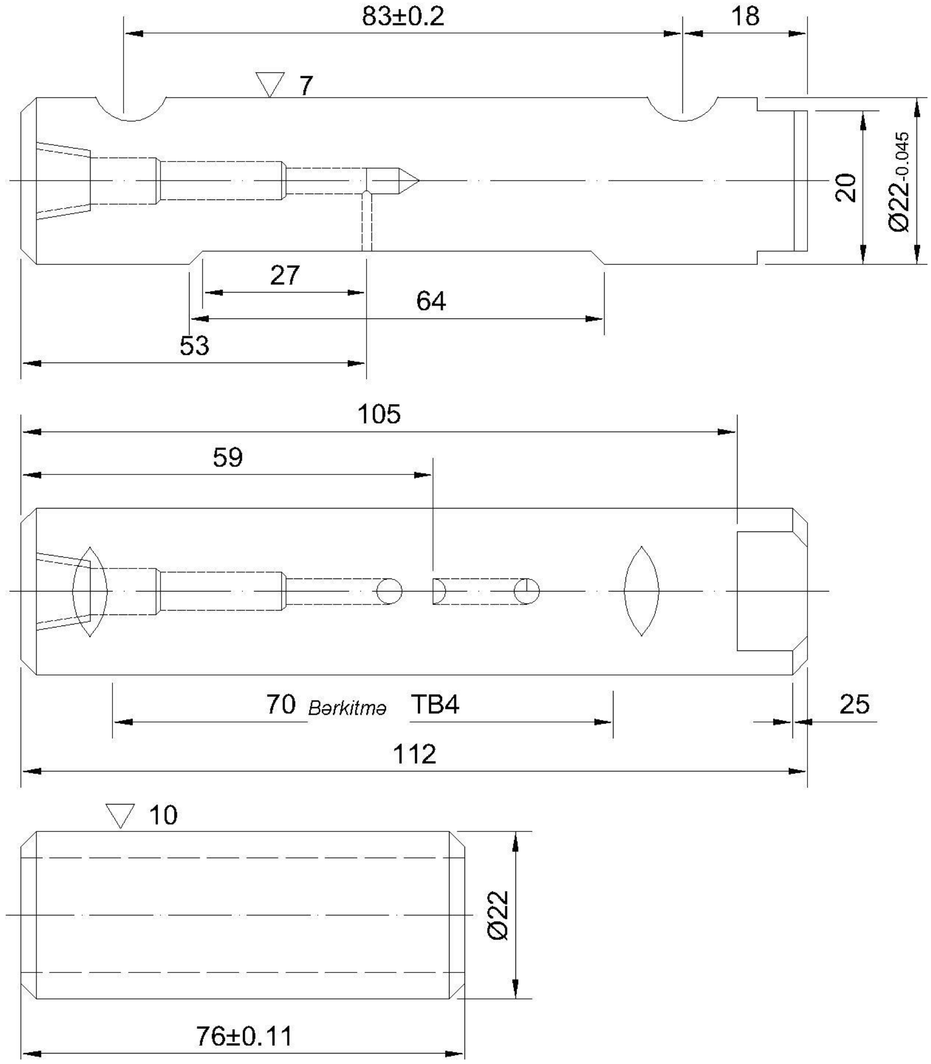

Şək. 3. Barmaq: a) ön resor; b) porşen

"Silindrlər" adlanan detallar sinfinə nəinki oymaqlar, hətta oymaqlara oxşar barabanlar, porşenlər, toplar və s. daxildir.

"Disklər" sinfinə daxil olan detallar dedikdə, diskin xarici diametrinin yarısına bərabər olan hündürlüklü fırlanan səthlər nəzərdə tutulur.

"Dairəvi olmayan çubuqlar" sinfinə müxtəlif tipli dəstəklərdən başqa, qısaldılmış formalı digər dairəvi olmayan detallar aiddir.

"Bərkidici detallar" sinfinə boltlar, qaykalar, işgillər, sancaqlar, vintlər və s. daxildir.

Lakin bu təsnifat RPİ dəzgahlarında detalların emal xüsusiyyətini nəzərə almır. RPİ dəzgahlarının idarəetmə proqramına daxil edilən detallar konstuktor sxemləri əsasında hazırlanmış detalların səthlərinin həndəsi ölçülərinə nəzərən seçilir. Əgər detalların həndəsi modellərini texnoloji baza əsasında qurmaq mümkün olarsa, onda artıq əvvəlcədən detalların konstruktor və texnoloji bazalarını eyniləşdirməklə yol veriləcək xətaları aradan qaldırmaq olar. Yuxarıda deyilənlərdən belə nəticə çıxır ki, rəqəmli proqramla idarə edilən avadanlıqlardan istifadə etməklə ADS qurduqda mütləq hazırlanacaq detalların sinfini bazalaşdırma nəzəriyyəsinin koordinatlar sistemini nəzərə almaqla tərtib etmək lazımdır.

Bunun üçün ölçülərinə görə detalların təsnifatı, onların həndəsi modelləşdirilməsi və tam hazırlanma prosesi üçün koordinat sisteminin qurulması üsuluna əsaslanmaq lazımdır.

Detalların təklif edilən təsnifatının əsasını üç təyinedici faktor təşkil etməlidir: detalların ölçüləri, həndəsi modelləşdirmə üçün koordinat sisteminin qurulma üsulu və onların emal prosesi. Detalların pəstahının alınma üsulunu və onların buraxılış həcmini tipik texnoloji proseslərin yaradılması zamanı nəzərə almaq lazımdır.

Qeyd edək ki, mövcüd təcrübəyə əsasən bütün maşın detallarının ölçülərinə görə qruplara bölünməsi əsasında təsnifat hazırlamaq üçün orta ölçülü bütün maşın detallarını dörd qrupa bölmək qərara alınmışdır: böyük, orta, böyük olmayan və kiçik ölçülü detallar.

Detalların ölçülərinə görə bölünməsi müvafiq dəzgahların tipik ölçülərinə görə bölünməsinə uyğundur:

- böyük ölçülü detallar dedikdə, bütün növ böyük ölçülü dəzgahlarda emal edilə bilən detallar nəzərdə tutulur;
- orta ölçülü detallar dedikdə, orta ölçülü dəzgahlarda emal edilə bilən detallar nəzərdə tutulur;
- nisbətən kiçik ölçülü detallar dedikdə, kiçik modelli dəzgahlarda emal edilə bilən detallar nəzərdə tutulur və s.

Dörd qrupun hər birinə aid olan detalların təsnifat cədvəlinə müxtəlif detalları daxil etmək olar. Məsələn, böyük ölçülü detallar sinfinə gövdə detallar, böyük ölçülü vallar, dişli çarxlar, silindrlər, nazimçarx və s. daxil edilə bilər.

Yuxarıda qeyd edildi ki, rəqəmli proqramla idarə edilən avadanlıqdan istifadə edilərsə, detalların düzülüşünün koordinat sisteminin qurulma üsulu kifayət qədər əhəmiyyət kəsb edir. Başqa sözlə koordinat oxlarının və ya koordinat müstəvilərinin ölçülərinin təyini üçün detalın hansı səthlərindən istifadə edilməsi praktik əhəmiyyət kəsb edir. Ona görə də, detalların səthlərinin ölçülərinin baza vəziyyətini bilməklə qurulmuş koordinat sistemində, detalların işçi cizgilərinə əsasən bütün detalların böyük həcmli həndəsi modelini qurmaq olar.

Avtomatik axın tipli istehsalda onlar xüsusi tərtibatların köməyi ilə emal edilir. Onda təsnifat cədvəlinə daxil olan müxtəlif tipli detalları böyük, orta, nisbətən böyük və kiçik ölçülü olmaqla 4 sinfə bölmək olar. Buradan çıxan nəticə ondan ibarətdir ki, hər bir detalı öz ölçüsünə uyğun yeni təsnifat cədvəlinə daxil etmək lazımdır.

Detalların təsnifata bölünməsindən əsas məqsəd eyni tipli avadanlıqlarda onların emal olunmasını nəzərdə tutmaqdır.

Beləliklə, detalların yeni təsnifat cədvəlinin tərtibi iki əsas prinsipə əsaslanmalıdır: qrupun və sinfin ölçülərinə görə maşın detallarının bölünməsi. Detallar ölçülərinə, eyni sinfə məxsusluğuna, eyni hazırlanma və koordinat sistemində həndəsi ölçülərinin təsvir olunma üsuluna görə bölünürlər.

Əgər göstərilən faktorlar əsasında təsnifat cədvəli tərtib edilərsə, bu cədvəldə dörd ölçüyə və dörd sinfə məxsus detallar yerləşdirsək, onda bu cədvəl orta ölçülü maşın və mexanizmlərə tələb edilən bir çox detalların adlarını özündə əks etdirəcəkdir. Orta ölçülü maşın və mexanizmlərin çoxlu sayda detallarını tətbiq etdikdən sonra dörd ölçüyə və dörd qrupa malik detallar üçün təsnifat cədvəli işlənilmişdir. Bu təsnifata 13 qrupa məxsus detallar (cədvəl 2) daxildir. Bütün bərkidici detallar "xırda detallar" qrupuna daxil edilmişdir.

Müxtəlif həndəsi formalı gövdə tip detallar silindrik formadan başqa əsas etibarı ilə birinci sinif detallar ailəsinə daxildir.

Cədvəl 2. Detalların təsnifat cədvəli

Siniflər	Detalların ölçü qrupları	
Detalların sinifləri	Qabarit ölçüləri və çəkisi L, b, h (mm) G-(кq)	Detalların həndəsi ölçüləri
1	2	3
1-ci sinif	İri (böyük) *L>700 mm* *b>0,3 l* *G>40 kq*	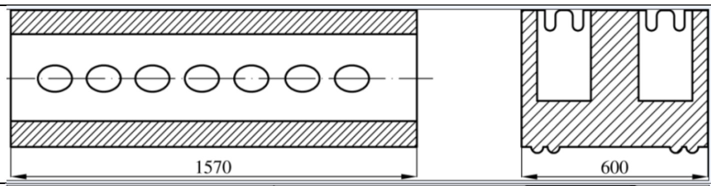
	Orta *L=360÷700 mm* *b>0,3 l* *G=10÷40 кq*	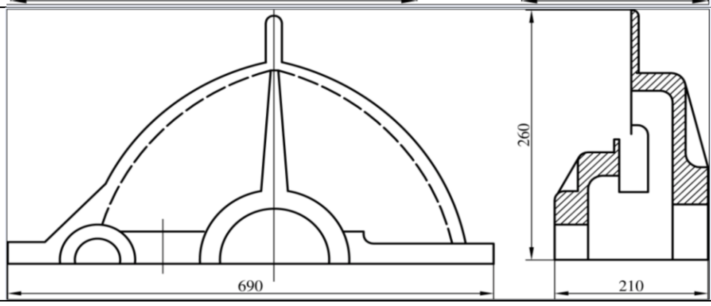

1-ci sinif	böyük olmayan *l=150÷370 mm* *b>0,3 l* *G=3÷10 кq*	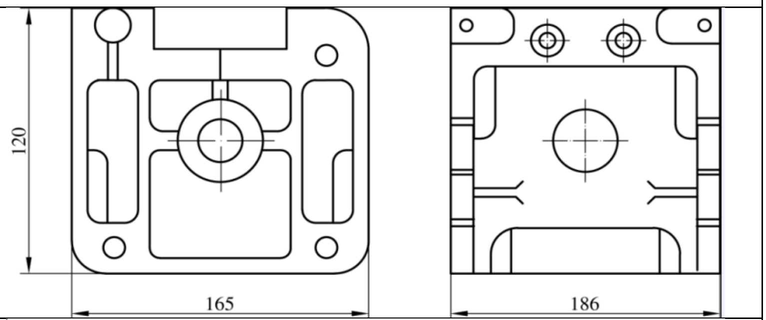
	Kiçik *l<150 mm* *b>0,3 l* *G<2 kq*	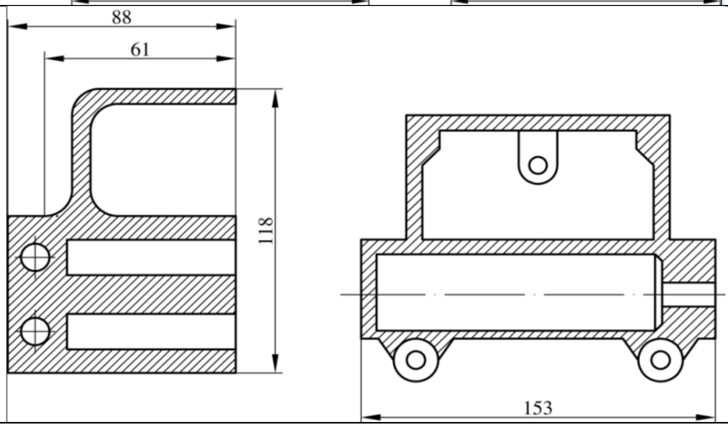

1	2	3
2-ci sinif	İri (böyük) *l>800 mm* *d<0,5 l* *G=10÷100 кq*	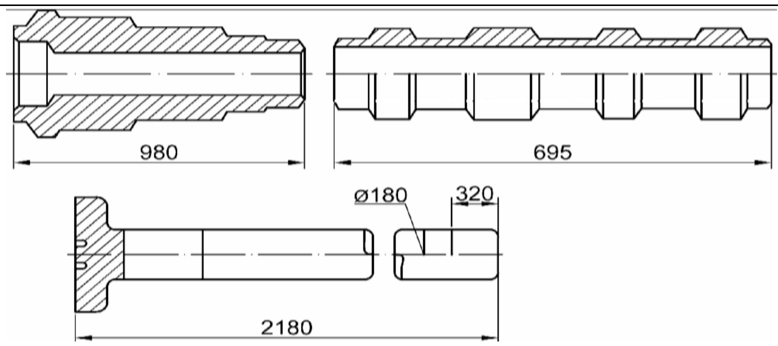
2-ci sinif	Orta *l=250-800 mm* *d<0,5 l* *G=3÷10 кq*	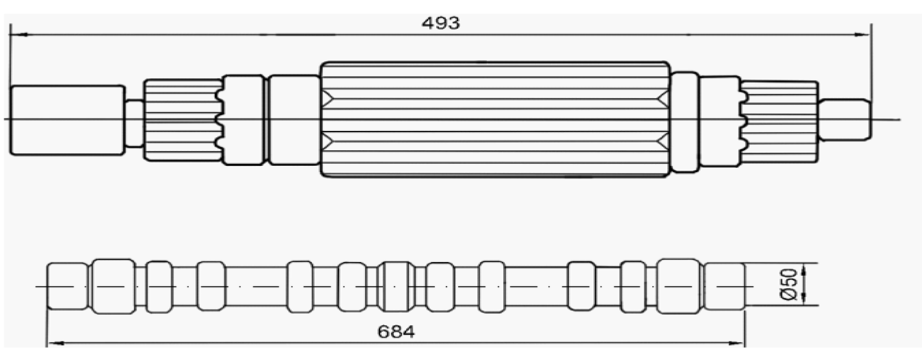

2-ci sinif	Böyük olmayan *l=100-250 mm* *d<0,5 l* *G=3÷.0.8 kq*	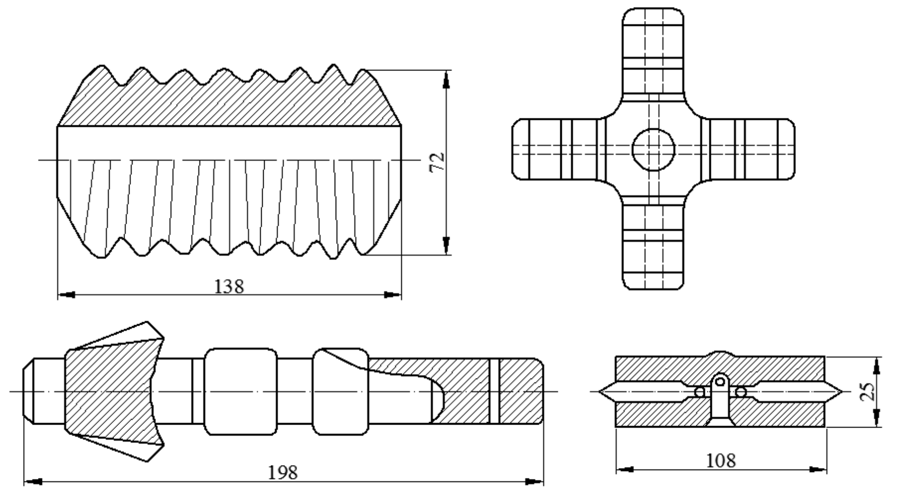
2-ci sinif	Kiçik *l<100 mm* *d<0,5 l* *G=0.8 кq*	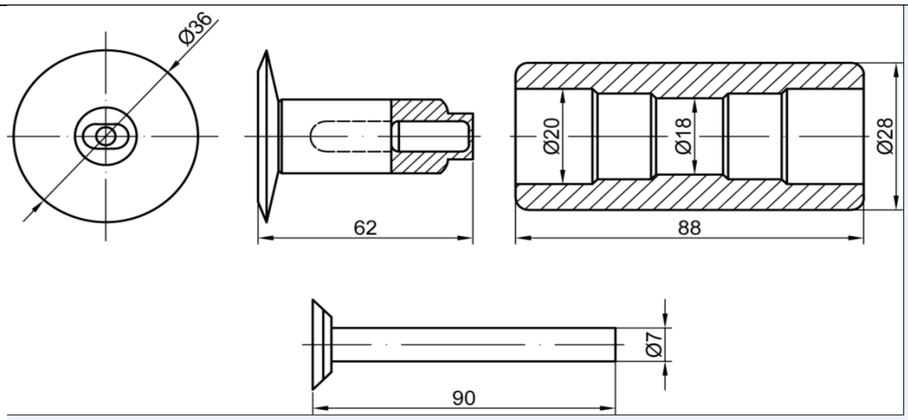
3-cü sinif	İri (böyük) *l>800 mm* *b və h<0.5l* *G>20 kq*	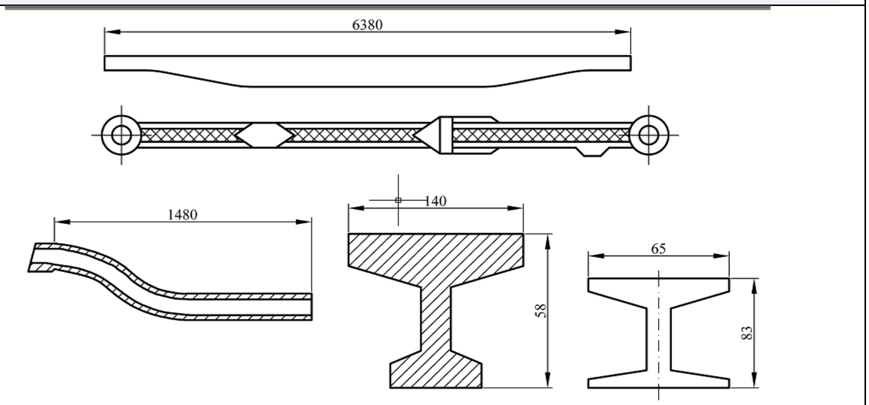

	Orta *l=300-800 mm* *b və h<0.5l* *G=3-20 кq*	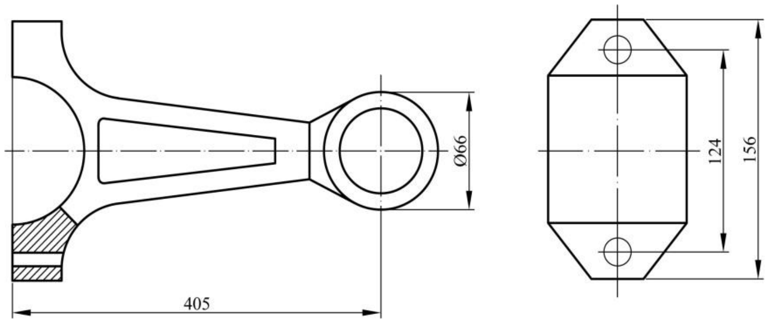
3-cü sinif	Böyük olmayan *l=150-300 mm* *b və h<0.5l* *G=1-3кq*	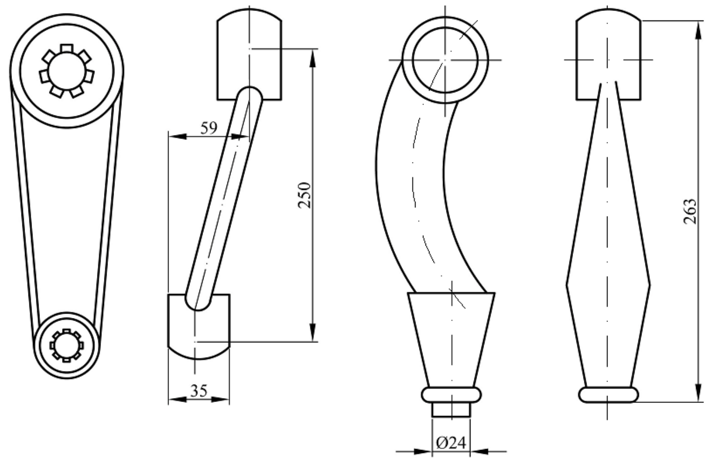
	Kiçik *l<150 mm* *d<0,5 l* *G=10 кq*	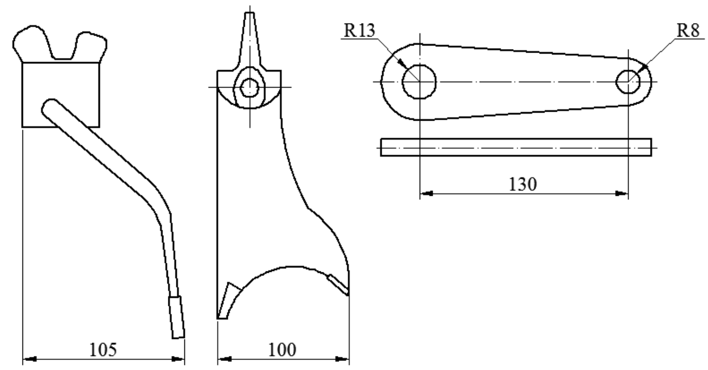
	İri (böyük)	_____
	Orta	_____
	Böyük olmayan	_____

4-cü sinif	Kiçik *l<150 mm* *d<50 mml* *GБO=8 кq*	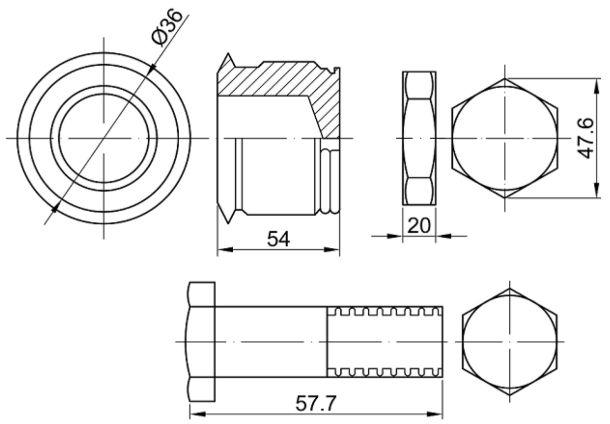

Tərtib edilən təsnifat cədvəli maşınqayırma sənayesinin müxtəlif sahələrində istifadə edilən tipik texnoloji proseslərin ümumi sxemini yaratmağa imkan verəcəkdir. Bu halda maşınqayırmanın hər bir sahəsi üçün texnoloji proseslərin dəqiqləşdirilməsi aparılmalıdır. Aydındır ki, maşınqayırmanın müxtəlif sahələrindən asılı olmayaraq texnoloji proseslərin qurulması prinsipi vahid olmalıdır.

Nəticə:

Aparılmış tədqiqatlar texnoloji proseslərin müxtəlif mərhələlərində pəstahların bazalaşdırılması və hazırlanan detalların həndəsi modelləri ilə əlaqələri, eyni zamanda istifadə edilən müasir texnoloji avadanlığın texnoloji imkanlarını nəzərə almaqla göstərmişdir ki, bütün detallar qabarit ölçülərinə görə 3 sinfə və 4 qrupa bölünə bilər.

Ədəbiyyat

1. Амиров Ф.Г. Повышение эффективности и обеспечение надежности автоматических линий. Вестник машиностроения, 2004, №5, с. 77-78.

2. Амиров Ф.Г. Общие положения создания переналаживаемых автоматических станочных систем. Москва: Машиностроение, Сборка в машиностроении, приборостроении, 2011, №7, с. 44-47.

3. Владзиевский А П., Белоусов А.П. Основы автоматизации и механизации технологических процессов в машиностроении.М.:Высшая школа,1966, 382.

4. Дащенко А.И., Белоусов А.П. Проектирование автоматических линий. М.: Высшая школа, 1983, 328 с.

5. Дымшиц Е.С. Разработка методов расчета надежности автоматических линий по заданным значениям надежности их элементов. М.: ЭНИМС, отчет по теме, этап 3, 1964, 1952 с.

6. Демьянюк Ф.С. Технологические основы поточно автоматизированного производства. М.: Высшая школа, 1968, 700 с.

7. Эрпшер Ю.Б. Надежность и структура автоматических станочный линий. М.: Машиностроение, М.: 1962,179 с.

8. Макаров И.М. Системные принципы создания гибких автоматизированный производств. - М.: Высшая школа, 1986. – 176 с.

9. Султан-заде Н.М. Метод оптимизации структурной компоновки автоматических линий. // Сб.: Системы управления станками и автоматическими линиями, М.: ВЗМИ, 1982. с. 9-13.

10. Султан-заде Н.М. Тимковский В.Г. Метод оптимизации структуру однопоточных автоматических линий. // Сб.: Системы управления станками и автоматицескими линиями, М.: ВЗМИ, 1983, с. 93-96.

11. Султан-заде Н.М., Амиров Ф.Г. Классификация деталей для изготовления их на переналаживаемых автоматических линиях с испольъзованием обрабатывающих центров с числовым программным управлением // Научные известия Сумгаитского государственного университета, 2012, №2 . с. 106-113.

Proceedings of the International Symposium of Mechanism and Machine Science, 2017
AzC IFToMM – Azerbaijan Technical University
11-14 September 2017, Baku, Azerbaijan

Hərəkətdə olan avtomobilin dayanıqlığına onun ağırlıq mərkəzinin koordinatlarının təsiri

[1]Həsənov Şahin Hümmət oğlu, [2]Əliyev Əlləz Hacıəhməd oğlu*
[1,2]Azərbaycan Texniki Universiteti
[1]shahin-hasanov@hotmail.com, [2]allaz_aliev@mail.ru*

Abstract

When the car is moving, it is influenced by different forces. In some cases, violation of the stability of the vehicle because of these forces causes his overthrow or shift.

Considering this, issue of determination of critical speed of losing the stability or overturning of the vehicle according to displacement of the vertical and horizontal plane of coordinates of center of gravity of car in the vehicle's loaded and unloaded condition has been solved.

Keywords: Stability of the car, overturning, center of gravity.

Giriş. Avtomobilin hərəkəti vaxtı, hərəkət şəraitindən asılı olaraq, ona qiymətcə dəyişə bilən və istiqaməti müxtəlif olan bir çox qüvvələr təsir edir. Bəzi hallarda bu qüvvələrin təsiri avtomobilin dayanıqlığının pozulmasına səbəb olur. Bir çox hallarda isə avtomobilin dayanıqlığının pozulması qarşısı alınmaz qəzalara səbəb olur [2].

Avtomobilin dayanıqlığının araşdırılması onun ağırlıq mərkəzinin koordinatlarını (a, b, h_g) müəyyən etmədən mümkün deyildir. Avtomobilin ağırlıq mərkəzi, onun yüklü və ya yüksüz olmasından, yükün fiziki xususiyyətlərindən, onun avtomobilin kuzasında yerləşdirilməsindən və eləcə də hərəkət şəraitindən (yolun uzununa və eninə mailliyi, yandan küləyin olması, dönmə radiusu və s.) asılı olaraq dəyişir.

Yüklü və yüksüz avtomobilin ağırlıq mərkəzinin koordinatlarının təyini. Avtomobilin ağırlıq mərkəzinin üfüqi müstəvi üzrə yerini, cox mürəkkəb olmayan avadanlıq istifadə etmədən, tərəzi vasitəsi ilə, arxa körpüyə düşən çəkini (G_2) müəyyən etməklə, təyin etmək olar. Əğər avto-mobilin öz çəkisini (yüksüz çəkisini) G_a və bazasını uzunluğunu L qəbul etsək, ağırlıq mərkəzinin qabaq oxdan olan məsafəsi aşağıdakı kimi müəyyən etmək olar:

$$a = \frac{G_2 L}{G_a}. \tag{1}$$

Ağırlıq mərkəzinin arxa körpüdən olan məsafəsi isə aşağıdakı kimi olacaqdır:

$$b = L - a. \tag{2}$$

Avtomobilin ağırlıq mərkəzinin şaquli müstəvidə yerini təyin etmək üçün onun arxa körpüsünü yer səthindən müəyyən h_1 hündürlüyə qaldırmaqla, qabaq oxa düşən çəkinin (G_1) müəyyən edilməsi ilə təyin etmək mümkündür:

$$h_g = h_2 + \frac{(G_a - G_1)L\sqrt{L^2 - (h_1 - h_2)^2}}{G_a(h_1 - h_2)}, \tag{3}$$

burada G_a- avtomobilin öz cəkisi; G_1 - qabaq oxa düşən cəki; L - avtomobilin bazası; h_1 - arxa körpünün yer səthindən hündürlüyü; h_2 - qabaq təkərin mərkəzinin hündürlüyüdür.

Yüklə yüklənmiş avtomobilin ağırlıq mərkəzinin şaquli ox üzrə hündürlüyü yükün və avtomobilin ağırlıq mərkəzinə əsasən, aşagıdakı kimi təyin edilir [1]:

$$h_a = \frac{G_a h_g + G_y h_y}{G_a + G_y}, \tag{4}$$

burada G_y - avtomobildəki yükün çəkisi; h_g - yüksüz halda avtomobilin ağırlıq mərkəzinin hündürlüyü; h_y - avtomobildəki yükün ağırlıq mərkəzinin hündürlüyüdür.

Onu da qeyd etmək lazımdır ki, avtomobilə yüklənmiş yük eyni tərkibli oldugu halda, onun ağırlıq mərkəzi yük həcminin ağırlıq mərkəzi kimi qəbul edilməlidir. Müxtəlif formaya və tərkibə malik olan yüklərdə isə hər yükün ağırlıq mərkəzi ayrılıqda müəyyən edilib, ümumi ağırlıq mərkəzi hesablanmalıdır.

Avtomobilin hərəkəti zamanı uzununa dayanıqlığın pozulması halı nadir hallarda baş verən hadisələrdən olduğundan (avtomobilin bazasının uzunluğu koleyasının enindən böyük olduğu üçün) məqalədə yalnız eninə dayanıqlığın pozula biləcəyi hallara baxılmışdır.

Müxtəlif qüvvələrin avtomobilin eninə dayanıqlığına təsirinin müəyyən edilməsi. Avtomobilin və yükün ağırlıq mərkəzləri şaquli bir ox üzərində yerləşdiyi halda eninə mailliyi α olan yol şəraitində R dönmə radiusu üzrə hərəkət zamanı, ona maillik istiqamətində yan külək qüvvəsi təsir etdiyi şəraitdə, qüvvələr sxemi şəkil 1-də verilmişdir.

Sxemə əsasən avtomobilin yan tərəfə sürüşməsinin başlayacağı anı sistemin müvazinət şərtindən istifadə edərək aşagıdakı kimi yazmaq olar:

$$P_k \cos\alpha + G_y \sin\alpha + G_a \sin\alpha - P_y \cos\alpha - P_a \cos\alpha = \varphi\,(P_k \sin\alpha + P_y \sin\alpha + G_y \cos\alpha + P_a \sin\alpha + G_a \cos\alpha). \quad (5)$$

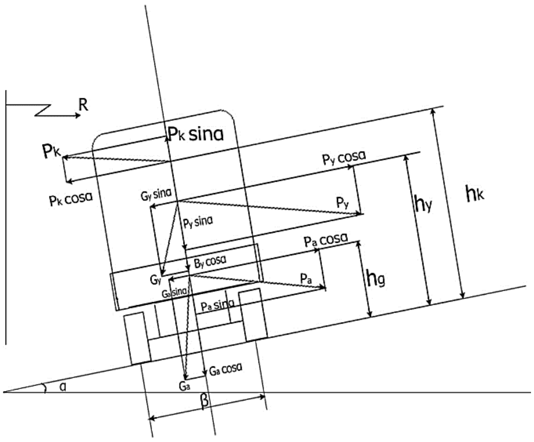

Şək. 1. Hərəkət vaxtı avtomobilə təsir edən qüvvələr

Burada mərkəzdənqaçma ətalət qüvvələrinin qiymətlərini aşağıdakı kimi hesablamaq olar:

$$P_a = \frac{G_a V^2}{127R}\ ,\ P_y = \frac{G_y V^2}{127R} \quad (6)$$

Avtomobilin eninə sürüşməsinin kritik sürətinin təyini. (5) və (6) düsturlarından istifadə etməklə, müəyyən sadələşdirmələr apardıqdan sonra, sürüşmənin başlayacağı an üçün aşağıdakı düsturu alırıq:

$$V_{sur} = \sqrt{\frac{127R((G_a + G_y)(\tan\alpha - \varphi) + P_k(1 + \varphi\tan\alpha))}{(G_a + G_y)(1 + \varphi\tan\alpha)}} \quad (7)$$

Qeyd etmək lazımdır ki, hesablama zamanı kökaltı ifadənin cavabı mənfi qiymət ala bilər. Bu halda kökaltı ifadənin mütləq qiymətini götürmək və sürüşmənin maillik istqamətində baş verəcəyini qəbul etmək lazımdır.

Avtomobilin yana aşmasının kritik sürətlərinin təyini. Avtomobilin yan tərəfə aşmasını müəyyən etmək üçün sağ təkərin yolla ğörüşmə nöqtəsinə (mailliyin əksi istiqamətində) nəzərən moment almaq lazımdır.

Avtomobilin aşmasının başlanğıc halında (sol təkər yol səthindən ayrıldığı üçün) təkərə təsir edən qüvvə və reaksiyalar sıfıra bərabər qəbul edilməlidir. Onda sürüşmənin müvazinət şərtinə əsasən, avtomobilin aşmaya başlayacağı hal üçün aşağıdakı bərabərliyi yazmaq olar:

$$G_a \sin\alpha\, h_g - P_a \cos\alpha\, h_g + G_y \sin\alpha\, h_y - P_y \cos\alpha\, h_y + \frac{B}{2}(G_a \cos\alpha + P_a \sin\alpha) + \frac{B}{2}(G_y \cos\alpha + P_y \sin\alpha) + P_k \cos\alpha\, h_k - P_k \sin\alpha\, \frac{B}{2} = 0. \quad (8)$$

Burada da (6) düsturlarını nəzərə alıb, sadə cevirmələr apardıqdan sonra, avtomobilin aşması üçün kritik hərəkət sürətini təyin etmək üçün aşağıdakı düsturdan istifadə etmək olar:

$$V_a = \sqrt{\frac{127R(G_a(2h_g \tan\alpha + B) + G_y(2h_y \tan\alpha + B) + P_k(2h_k - B\tan\alpha)}{G_a(2h_g - B\tan\alpha) + G_y(2h_y - B\tan\alpha)}} \quad (9)$$

burada P_k - küləyin təsir qüvvəsi; h_k - küləyin təsir qüvvəsinin yelkən mərkəzinin hündürlüyü; R - dönmə radiusu; B - avtomobilin koleyası; α - yolun eninə maillik bucağıdır.

Avtomobilə yüklənmiş yükün ağırlıq mərkəzinin koordinatları dəyişdiyindən ümumi avtomobilin ağırlıq mərkəzinin də koordinatları dəyişəcəkdir. Özü də bu dəyişiklik şaquli müstəvidə baş verdiyi kimi, üfüqi müstəvidə də baş verə bilər.

Tərtib edilmiş sxemlər əsasında, sistemin müvazinət şərtindən istifadə edərək, avtomobilin aşmasınının baş verə biləcəyi kritik hərəkət sürəti üçün aşağıdakı düsturlar alınmışdır.

1. Avtomobilə yüklənmiş yükün ağırlıq mərkəzinin koordinatlarının şaquli müstəvidə yerini dəyişdiyi hal üçün onun aşmasınının baş verə biləcəyi kritik hərəkət sürəti:

$$V_1 = \sqrt{\frac{127R(G_a(h_g \tan\alpha + \frac{B}{2}) + G_y(h_x \tan\alpha + \frac{B}{2}) + P_k(h_k - \frac{B}{2}\tan\alpha)}{G_a(h_g - \frac{B}{2}\tan\alpha) + G_y(h_x - \frac{B}{2}\tan\alpha)}} \quad (10)$$

burada h_x - yükün şaquli müstəvi üzrə ağırlıq mərkəzinin hündürlüyüdür.

2. Avtomobilə yüklənmiş yükün ağırlıq mərkəzinin koordinatlarının üfüqi müstəvidə yerini dəyişdiyi hal üçün aşmanin kritik hərəkət sürəti:

$$V_2 = \sqrt{\frac{127R(G_a(h_g \tan\alpha + \frac{B}{2}) + G_y(h_y \tan\alpha + h_z) + P_k(h_k - \frac{B}{2}\tan\alpha)}{G_a(h_g - \frac{B}{2}\tan\alpha) + G_y(h_y - h_z \tan\alpha)}} \quad (11)$$

burada h_z - aşma nöqtəsindən üfüqi müstəvi üzrə ağırlıq mərkəzinə qədər olan məsafədir.

Ədəbiyyat

1. Б.Е.Боровский. Безопасность движения автомобиль-ного транспорта. – Л.: Лениздат, 1984, 304 стр.
2. Ə.H.Əliyev. Müxtəlif istismar şəraitlərində avtomo-billərin dəyanətliliyinin kompleks tədqiqi. Gəncə, 2007, 22 s.

Proceedings of the International Symposium of Mechanism and Machine Science, 2017
AzC IFToMM – Azerbaijan Technical University
11-14 September 2017, Baku, Azerbaijan

Yüklərin və konteynerlərin daşımaya qəbul olunmasının planlaşdılırılması

Heybətulla Əhmədov[1]*, Nicat Zöhrabov[2]
[1*]Azərbaycan Texniki Universiteti
H.Cavid prospekti 25, AZ 1073, Bakı, Azərbaycan
Email: heybet-ahmedov@mail.ru
[2] nidjatzoxrabov@mail.ru

Xülasə. Məqalədə idarəetmə obyektlərini-xırda göndərişləri,konteyner göndərişlərini, komplektləşdirilmiş konteyner göndərişlərini konteyner qatarlarını vahid texnoloji prosesdə əlaqələndirməyə imkan verən təqvim üzrə kompleks planlaşdırlma metodikası tədqiq olunmuşdur. Təqvim üzrə kompleks planlaşdırılma müştəriyə öz kriterilərinə görə daha effektiv hesab etdiyi ehtiyatlardan asılı olan daşıma sxemini seçmək imkan verir. Bu cür planlaşdırmanın əsasını konteyner terminalında konteynerlərin təqvim üzrə qəbul planı təşkil edir, yəni konteyner şirkətləri logistik zəncirlər və onların seçim imkanı hesabına müştəriləri razı salmaq üçün bilavasitə təsir göstərir. Gələcək perspektivdə konteyner şirkəti yığma konteyner göstərişi-konteyner göndərişi- hər vaqona konteynerlər komplekti-kompleksdə konteyner qatarı zəncirinə baxacaq.Bu cür yanaşma konteyner şirkətində daxil olan konteyner axınlarını artırmağa imkan yaradır.

Açar sözlər: konteyner, konteyner daşımaları, konteyner şirkəti, konteyner terminalı, anbar, təqvim üzrə planlaşdırılma.

1. Giriş. Təqvim üzrə planlaşdırılma məsələlərini cədvəl nəzəriyyəsində, [1-3] işlərdəki metodikalar isə yığma yüklərin konsolidasiya olunmuş anbarlara və konteynerlərin konteyner terminallarına təqvim üzrə qəbulunun təşkilində istifadə etmək olar. Eyni zamanda təqvim üzrə planlaşdırılmaya mövcud yanaşmalar yük göndərənə göndərmə üçün təqdim olunan yükün göndəriş növünü təyin etməyə, konteyner şirkətləri və ekspeditorların müxtəlif növ göndərişləri təqvim üzrə qəbulunu kompleks planlaşdırılmasına və onların daha effektiv idarə edilməsi hesabına yük bazasını artırmağa imkan vermir.

Hər vaqon üçün konteyner komplektinin birbaşa daşımalara görə və birbaşa yığma konteyner göndərişinin seçim imkanı, sutka ərzində konteyner terminalına daxil olan konteynerlərlə və konsolidasiya olunmuş anbarların xırda göndərişlərinin $\bar{q}_i$ müqayisəsindən təyin olunur. Konteyner məntəqələrinə və konsolidasiya olunmuş anbarlara daxil olan ümumi konteyner axını $\sum q_i^{kont}$ və yük axının $\sum q_i^{yük}$, onların qəbulunun nizamlanması zamanı bərabər ölçülü qəbul etmək olar [4]. Vaxta və istiqamətə görə konteyner və yük axının transformasiya etdikdə bəzi istiqamətlər üzrə q_i^{kont} və $q_i^{yük}$ orta sutkalıq axını artırmaq, konteyner terminalında birbaşa konteyner komplektlərinin və konsolidasiya olunmuş anbarlarda birbaşa yığma konteyner göndərişlərini daha çox formalaşdırmaq olar. Bunun üçün müəyyən zaman periodunda axın maksimum qiyməti almalı digər vaxtlarda isə sıfra yaxınlaşmalıdır.

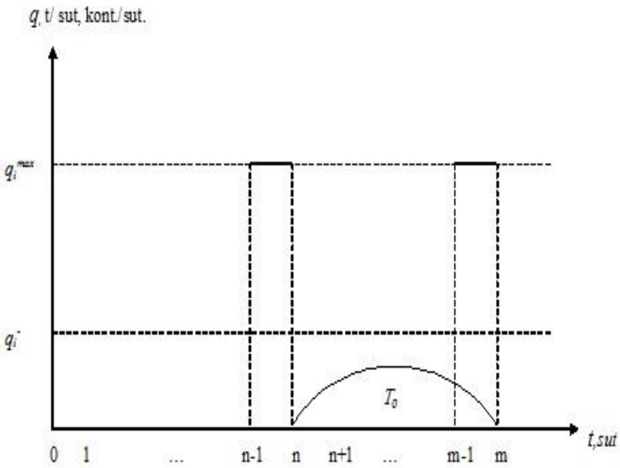

Şəkil 1. Daxil olan axının vaxta görə bölüşdürülməsi

Daxil olan axını elə çevirmək olar ki, $q_i^{\max}$ axınının maksimum gücü T_0 intervalının son sutkalarına uyğun olsun. Onda

$$q_i^{\max\ yük} \geq P_i^{YKG} \text{ və } q_i^{\max\ kont} \geq P_i^{KKG}$$

axınlarının müxtəlif istiqamətlər üzrə ayırmaq imkanı əldə etmiş oluruq. Bununla belə ayrılmış axının orta sutkalıq gücü əvvəlki kimi olacaq,

$$q_i^{-} = \frac{q_i^{\max}}{T_0}. \qquad (1)$$

Təqvim üzrə qəbul vaxta görə xırda göndərişləri və konteynerləri cəmləşdirərək birbaşa daşımaların payını artırmağa, anbarda yük çeşidləmə əməliyyatlarının azaltmağa, konteyner terminalında konteynerlərin və konsolidasiya olunmuş anbarlarda yüklərin toplanması vaxtını azaltmağa imkan verir. Lakin təqvim üzrə qəbul müştəri üçün mənfi effekt verir. Ekspeditorlar logistik zəncirin hesablanmasında bir qayda olaraq sxemləri onların anbarlara, konteyner terminallarına daxil olunmasına görə müqayisə edirlər. Lakin yükgöndərənin anbarında toplanan gizli toplanmış yük böyük əhəmiyyət kəsb edir. Həmin yükün təqvim üzrə qəbulu onun əhəmiyyətini bir azda artırır. Bu yükgöndərənə göstərilən xidmət keyfiyyətinin azalmasına gətirib çıxarır və bəzi hallarda müştərilər tərəfindən alternativ nəqliyyat növlərinin axtarışına səbəb olur.

Bizim fikrimizcə, müştərilər üçün mənfi nəticəni təqvim üzrə kompleks planlaşdırılma aradan qaldırar. Bu da yükgöndərənlər, ekspeditorlar və konteyner terminallarının əməkdaşlığı hesabına mümkündür.
Konteyner terminalında təyinatlar üzrə konteynerlərin qəbulunun təqvim üzrə planlaşdırılması tətbiq olunmuşdur ki, hər vaqona konteynerlər komplektinin toplanma vaxtını $T_{top}^{\kappa\kappa g}$ azaltmaq və avtomobildən vaqona yüklərin birbaşa ötürülməsinin payını artırmaq olsun. Konteynerlər komplektinin konteyner terminalında və konsolidasiya olunmuş anbarlarda olduğu istiqamətlər üzrə yığma konteyner göndərişinin toplanma vaxtının azalması məqsədilə yüklərin təqvim üzrə qəbulu tətbiq olunmuşdur. Bu çoxsəviyyəli təqvim planını nəzərə alaraq (konteyner qatarının formalaşmasının təqvim planı tam yerinə düşər) yükgöndərən xırda göndərişləri konsolidasiya olunmuş anbarlara təqdim etmək üçün və ya konteyner terminalı üçün öz konteyner göndərişini formalaşdırmaq üçün toplamaq qərarına gəlir. Bununla da yük vahidinin nəqliyyat xərcləri və müvafiq səviyyəli göndərişlərin toplanma xərcləri dəyişir. Konsolidasiya olunmuş anbarda təqvim qəbulu intervalına görə formalaşan i istiqamətinin xırda göndərişlərinin çəkisi m_i^{xg} aşağıdakı təşkilediciləri var:

$$m_i^{xg} = q_i^{yük} * T_{top}^{xg}, \qquad (2)$$

Q_i^{xg} yük vahidinin daşınma qiyməti göndərişin çəkisindən asılı olaraq ekspeditor xidmətlərinə görə mövcud tariflərlə müəyyən olunur.
Konteyner terminalında təqvim üzrə qəbul intervalına görə formalaşan i təyinatının konteyner göndərişinin çəkisi:

$$m_i^{kg} = q_i^{yük} * T_{top}^{\kappa g}, \qquad (3)$$

$Q_i^{\kappa g}$ yük vahidinin daşınma qiyməti konteynerdəki yükün çəkisindən asılı olaraq, yükgöndərən üçün konteynerlərin daşınmasının mövcud tarifləri ilə təyin olunur.

Konteyner göndərişinin toplanmasında zaman periodu $T_{top}^{\kappa g\,\min}$ mövcuddur ki, bu müddətdə nəqliyyat xərcləri $Q_i^{kg} > Q_i^{xg}$ olur. $T_{top}^{kg\,\min}$ bitdikdən sonra xərclər $Q_i^{kg} = Q_i^{xg}$. Bu anın başlanğıcından bir qayda olaraq, konteyner terminalında konteyner göndərişlərinin təqvim üzrə qəbulu üst – üstə düşmür. Bu andan sonra $T_{top}^{KGgöz}$

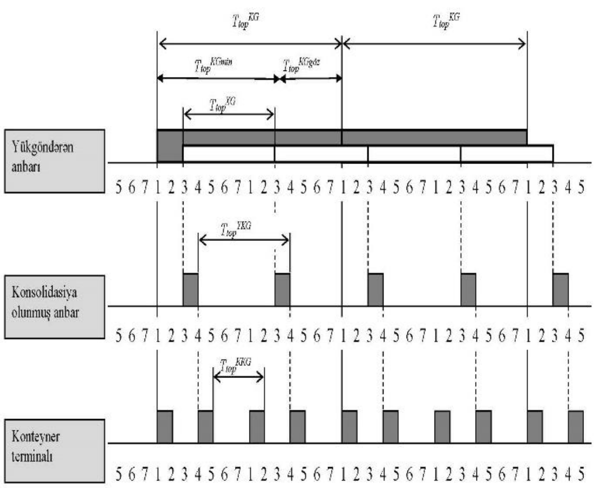

Şəkil 2. Konteynerə yararlı yüklərin qəbulunun təqvim üzrə kompleks planlaşdırılması

qəbul gününün gözləmə periodu başlayır. Bu periodda konteyner göndərişinin toplanması davam edir və yükün konteynerlə daşınması xərci yığma konteynerdə daşınma xərcinə nisbətən daha tez azalır $Q_i^{kg} < Q_i^{xg}$.

$T_{top}^{KGgöz}$ periodunda elə bir hal mümkündür ki, bir konteynerin yükgötürmə qabiliyyətindən artıq yük yığılır və əvvəlki konteyner göndərilməmiş növbəti göndəriş üçün toplanma başlayır. Bunun nəticəsində konteyner göndərişlərinin daşınma xərclərini azaltmaq mümkün olur, lakin bunun əvəzinə X_{anb}^{yg} yükgöndərənin anbarında xərclər artır.

Təqvim üzrə kompleks planlaşdırılma müştəriyə öz kriterilərinə görə daha effektiv hesab etdiyi ehtiyatlardan asılı olan daşıma sxemini seçmək imkan verir. Bu cür planlaşdırmanın əsasını konteyner terminalında konteynerlərin təqvim üzrə qəbul planı təşkil edir, yəni konteyner şirkətləri logistik zəncirlər və onların seçim imkanı hesabına müştəriləri razı salmaq üçün bilavasitə təsir göstərir. Gələcək perspektivdə konteyner şirkəti yığma konteyner göstərişi – konteyner göndərişi- hər vaqona konteynerlər komplekti – kompleksdə konteyner qatarı zəncirinə baxacaq.

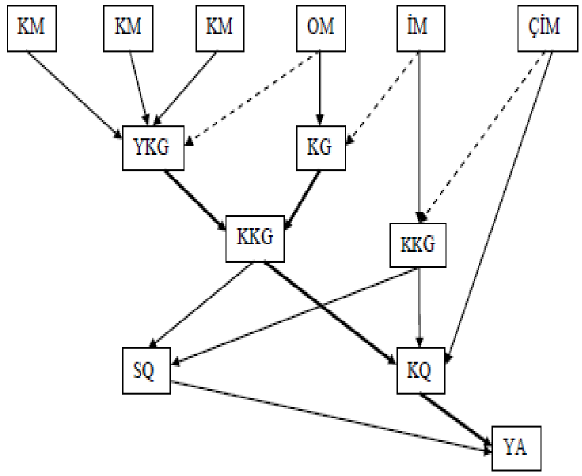

Şəkil 3. Müştərilər və mümkün daşıma növləri

Şərti işarələr: KM – kiçik müştəri; OM – orta müştəri; KK – iri müştəri; ÇİM – çox iri müştəri; YKG – yığma konteyner göndərişi; KG – konteyner göndərişi; KKG – komplektləşdirilmiş konteyner göndərişi; SQ – QTP-yə əsasən tərtib olunmuş sahə qatarı; KQ – konteyner qatarı ; YA -yükalan
istifadə olunan daşıma forması
perspektivdə daşıma forması
qarşılıqlı əlaqənin yüksək forması

Nəticə. Şəxsi xərclərini azaltmaq üçün konteyner şirkəti öz müştəri bazasını birləşdirməklə bərabər ekspeditor xidmətlərindən istifadə edən müştəriləri də birləşdirməli və bununla konteyner kompleksinə daxil olan konteyner axınların artması birbaşa daşımaların payını artırmağa imkan verir. Yükgöndərənlərlə ekspeditorların bu cür qarşılıqlı əlaqəsi realizə olunmuş misal şəkil 4–də verilmişdir.

Təklif olunan təqvim üzrə kompleks planllaşdırılmış qarşılıqlı əlaqə konteynerlərin dəqiq vaxtında çatdırılmasında mühüm addımdır.

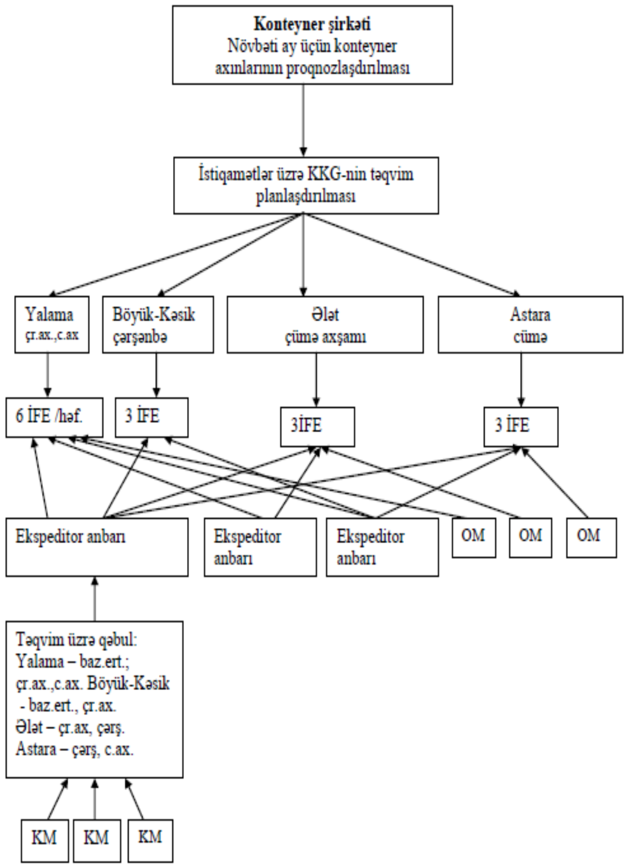

Şəkil 4. Konteyner şirkətində konteynerlərin təqvim üzrə kompleks qəbulunun təşkilinə misal

Ədəbiyyat

[1]. Балалаев А.С. Календарное планирование погрузки по назначениям плана формирования сортировочной станции. М.: Вестник ВНИИЖТ. 1977, № 6, с. 55-57.
[2]. Капитонов А.Е. Организация контейнерных перевозок на основе принципов логистики. диссер. канд. техн. наук. М.: 2001, 190 с.
[3]. Кузнецова А.Н. Разработка методики расчета оптимального плана формирования вагонов с контейнерами. диссер. канд. техн. наук. М.: 2003, 206с.
[4]. Осьминин А.Т. Организации контейнерных перевозок – продуктовый подход. М.: РЖД-Партнер. 2010 № 1-2, с. 51-53.

Proceedings of the International Symposium of Mechanism and Machine Science, 2017
AzC IFToMM – Azerbaijan Technical University
11-14 September 2017, Baku, Azerbaijan

Kompressor qurğularında titrəyişlər (vibrasiya), bunun səbəbləri və minimuma endirilməsi

Mehtiyev Rəşad Murad oğlu
Azərbaycan Texniki Universiteti,
Maşın və mexanizmlər nəzərittəsi kafedrası
E-mail: dr.reshad.mehdiyev@gmail.com

Xülasə. Bu məqalədə vibrasiya haqqında məlumat verilir,onun təhlükəliliyi məsələlərinə toxunulur. Mövcud problemlərdən, səbəblərindən bəhs edilir. Vibrasiya parametrləri izah edilir. Titrəyişlərin insan orqanizminə və avadanlığa zərəri barədə danışılır. Kompressorlarda vibroakustik sınaqların tədqiqatlarının nəticələri təhlil edilir. Kompressor aqreqatının detallarında vibrosürətin orta kvadratik həddinin nominal qiymətləri göstərilir.

Açar sözlər: vibrasiya, porşenli kompressor, AQDKS, vibroyerdəyişmə, vibrosürət, vibrotəcil, tezlik, rəqslər fazası, amplituda, amplituda spektri, təzyiqin pulsasiyası, dinamiki təsirlər, ətalət qüvvəsi, qüvvə momentləri, harmonik təhlil, rezonans rejimi, vibrodempfirləmə.

Azərbaycan dilinə tərcümədə titrəyiş anlamına gələn vibrasiya (latındilindəki "vibratio" sözündən götürülmüşdür) - cisimlərin mexaniki rəqsidir. Titrəyişin yaranması vaxtaşırı baş verən mürəkkəb texnoloji proseslərin gedişində baş verir. Lakin titrəyişlərin təbii mənbələri də mövcuddur. Belə ki, zəlzələlər, vulkan püskürmələri, qasırğalı küləklər və s. buna misal ola bilər. Titrəyişin süni mənbəyi isə istehsalat obyektlərində müxtəlif mexanizmlər, texnoloji avadanlıqlar, mexaniki qurğular və s. ola bilər. Dünyanınhər bir yerində istehsalat obyektlərində texnoloji proseslər zamanı tez-tez dəyişən parametrlərin (təzyiq,temperatur, sürət, sərf, tezlik və s.) təsirini nəzərə alaraq titrəyişlərin qarşısının alınması üçün mütəmati işlər görülür.

Bir sıra təhlükə potensiallı obyektlərdə olduğ kimi avtomobillərə qaz doldurma kompressor stansiyalarında da (AQDKS) əsas texnoloji avadanlıqlar sırasında duran kompressor qurğularının elementlərinə aid olan aparat və boru kəmərlərində titrəyişlərin müəyyən edilmiş normadan yüksək olması olduqca təhlükəli haldır. Bu əksər detalların yeyilməsinə və dağılmasına, avadanlıqların bünövrələrinin və boruların dayaqlarının çökməsinə, arakəsmələrdə çatlar yaranmasına, fləns birləşmələrində, fitinqlərdə kipliyin pozulmasına, qaynaqtikişlərinin çatlamasına, armaturların sınmasına və s.təhlükəli hallara səbəb ola bilir.

Kompressor qurğularında titrəyişlərin əsas mənbələri maşının hərəkət edən hissələrinin kütləsinin qeyri-tarazlığı, boru xətlərində qaz axınlarının qeyri-bərabərliyi, güclü küləklərin tikinti konstruksiyalarına və texnoloji avadanlıqlara təsiri, həmçinin seysmik hadisələrdir. Bütün bunlarla yanaşı kompressor qurğularının quraşdırılması zamanı özüllərin düzgün qurulmaması, layihə tapşırıqlarına və quraşdırma üzrə mövcud qaydalara riayət edilməməsi də son nəticədə güclü titrəyişlərin yaranmasına səbəb olur. Istismar prosesində kompressorun özünün, həmçinin onun boru kəmərləri sisteminin və sistemlə əlaqəli aparatların dinamik dözümlülüyünü təmin etmək çox zəruridir. Bu isə kompressorlarda vaxtaşırı vibroakustik sınaqların və texniki vəziyyətin vibrodiaqnostikasının aparılması sayəsində mümkündür.

Kompressor qurğularının titrəyiş vəziyyətini qiymətləndirərkən vibroyerdəyişmə, vibrosürət, vibrotəcil, tezlik, rəqslər fazasıvə digər parametrlərdən istifadə edilir. Vibroyerdəyişmə qurğunun sisteminə daxil olan obyekt və elementlərin nisbi yerdəyişmələrini yaxud deformasiyasını müəyyən etmək baxımından maraqlıdır. Vibrosürətin tapılması titrəyişlərin insan orqanizminə təsirinin qiymətləndirilməsi üçün gərəklidir, belə ki, vibrosürət güc impulsunu və kinetik enerjini müəyyənləşdirir. Vibrotəcildən ətalət (sükunət) qüvvəsinin amplitudasının (rəqslərin tarazlıq vəziyyə-tindən maksimum yaxud minimum uzaqlaşdığı məsafə) oyanmış təsir güclərinin də əlavə edilməsi ilə kvazistatik sxem üzrə daxili qüvvələrinin təyin edilməsində istifadə olunur.

Titrəyişlərin intensivliyinin qiymətləndirilməsinin daha əlverişli normativ kriteriyası vibrosürətdir. Belə ki, titrəyişin yol verilə bilən təsiri həddində tezliyin artması ilə vibroyerdəyişmə mütənasib olaraq artır, vibrotəcil isə tezliklərin geniş spektri üçün dəyişməz qalır. Həm də tətbiq olunan ölçü cihazlarının etibarlılığı nöqteyi nəzərindən vibrosürət optimal parametr sayılır. Kompressorda titrəyişlərin səciyyələndirilməsi üçün əsasən sürət, kontur, rejim, vaxt miqdarı və yağlanma kimi xarakteristikalar təhlil edilir.

Bu məlumatların verilməsindən məqsəd hazırda geniş miqyasda tətbiq edilməyə başlamış sıxılmış metan qazının alınmasında əsas texnoloji avadanlıq olan kompressor qurğularının səmərəli, fasiləsiz və təhlükəsiz işinin təmin edilməsində əngəl ola bilən titrəyişlərin daim normal səviyyədə saxlanması üçün görülməli olan tədbirlər barədə əlaqədar müəssisələrə tövsiyyələr verməkdir. Bu istiqamətdə araşdırmalarımızı davam etdiririk. Sənaye sahələrində istismar olunan avadanlıq və qurğularda titrəyişlər zərərli və faydalı olmaqla iki yerə bölünürlər. Müxtəlif texnoloji əməliyyatları aparmaq, tikinti işlərində istifadə olunan maşın və mexanizmlərdə zəruri və faydalı olan titrəyişləri yaratmaq üçün vibratorlardan istifadə edilir. Müxtəlif təyinatlı mühərriklər, qurğular, turbinlər, nəqliyyat vasitələri və s. istismarı zamanı yaranan titrəyişlər onların iş rejiminin pozulmasına səbəb ola bildiyi üçün zərərli titrəyişlər hesab edilir.

Titrəyişlərin insan orqanizminə təsiri də müxtəlidir, belə ki, bütün orqanizmə təsir göstərirsə ümumi, orqanizmin bir hissəsinə təsir göstərirsə lokal vibrasiya adlandırılır. Titrəyişlərin bioloji təsiri onun tezliyindən asılıdır. Tezliyi 15 Hs -dək olan rəqslər vestibülyator aparata təsir göstərir. 25 Hs-dək olan rəqslər ayrı-ayrı təkanlar şəklində olub, sümüklərdə və oynaqlarda dəyişikliklər əmələ gətirir. 50 Hs-dən 250 Hs- dək olan rəqslər isə sinir sisteminə təsir edir, damarların spazmasına, vibrasiya xəstəliyinə səbəb olur. Göründüyü kimi həm avadanlıqların istismar müddətinin uzadılması, qəzalarsız və fasiləsiz işin təmin edilməsi ilə yanaşı, insan sağlamlığına təhlükə yaradan bir amil kimi titrəyişlərin səbəblərinin öyrənilməsinə, avadanlıqlarda diaqnostik təhlillər aparmaqla titrəyişlərin minimuma yaxud normal həddə endirilməsinə xüsusi diqqət yetirilməlidir.

Tədqiqatlarımız əsasən hazırda geniş tətbiq olunmağa başlanmış vertikal silindrli porşenli çoxpilləli kompresor qurğuları üzərində aparıldığından titrəyişlər haqqında bütün rəy və təkliflərimiz də adı çəkilən kompressor qurğularına istiqamətlənmişdir. Bunun üçün kompressor qurğusunda vibroakustik sınaqlar aparılmış və vibroölçmə cihazlarının və istehsalçı zavodun qurğuda quraşdırdığı vibroölçü cihazlarının göstəricilərinin vaxtaşırı izlənməsinin nəticələrindən istifadə edilmişdir. Sınaqlar zamanı kompressorun gövdəsinin və yastıqlarının, əlaqələndirici boru xətlərinin və pillələrarası aparatların titrəyişləri tədqiq olunur. Ölçmələr üçün vibroyerdəyişmənin, vibrosürətin, vibrotəcilin maksimal təsir etdiyi nöqtələr seçilmişdir.

Nöqtələrin sayı kompressorun konstruktiv icrası və onunla əlaqəli boru xətləri kommunikasiyasının konfiqurasiyası ilə müəyyən edilir. Müayinə olunan obyektdə titrəyişlər (rəqslər) bir biri ilə qarşılıqlı perpendikulyar üç istiqamətdə : OX, OY və OZ (OX - kompressorun oxuna paralel, üfüqi istiqamətdə; OY - OX oxuna perpendikulyar, üfüqi istiqamətdə; OZ - şaquli istiqamətdə) üzrə ölçülür.

Konkret olaraq ölçü aparatlarının seçilməsi titrəyişlərin parametrlərinin tipindən və ölçülmə diapazonundan asılıdır. Bu zaman aşağıdakı tələbləri də nəzərə almaq lazımdır:

- bütün ölçü quruluşlarının pasportları və formulyarları olmalıdır;
- amplituda və amplituda -tezlik xarakteristikaları bütün işçi diapazonda xətti olmalıdır:
- hər bir sınaqdan əvvəl bütün vibrodəyişdiricilər amplituda və amplituda - tezlik xarakteristikalarını qurmaqla vibrostenddə ölçü sxeması ilə birlikdə dərəcələnməlidirlər.

Vibrodəyişdiricilərin kütləsi tədqiq olunan qovşağın yaxud detalın kütləsinin 5%-dən artıq olmamalıdır. Vibrodəyişdiricilərin ölçülən obyektə bərkidilmə (vintlə, xomutla, yapışqanla, maqnitlə) sərtliyi vibrodəyişdiricidən və bərkidici quruluşdan ibarət sistemin özünün tezliyinin ölçülən titrəyişin tezliyindən 2- 3dəfə artıq olmasını təmin etməlidir. Obyekt və vibrodəyişdiricini bərkitmə quruluşu arasında elastik araqatının qoyulmasına yol verilmir.

Məsələnin mürəkkəbliyindən asılı olaraq titrəyiş prosesinin qismən yaxud ümumi təhlili aparılır. Qismən təhlil vibrosürətin vibroyerdəyişməyə yaxud vibrotəcilə çevrilməsindən və rəqslərin amplitud spektrinin alınmasından ibarət olub sınaqlar dövründə aparılır. Titrəyiş prosesinin ümumu təhlilinə vibroyerdəyişmənin, vibrosürətin və vibrotəcilin amplitudasının; tezlik və amplituda spektrlərinin; harmonik tərkiblərin faza bucaqlarının; titrəyişin pik və orta qiymətlərinin; vibrosürətin orta kvadratik qiymətinin təyini daxildir. Həddən artıq titrəyişlərə məruz qalan nöqtələrdə titrəyişin spektral təhlili yüksək tezlikli rəqslərin spektrdə üstünlük təşkil etdiyi geniş zolaqlı titrəyişlər barədə düzgün nəticəyə gəlməyə imkan verir.

Tədqiqatlar zamanı titrəyiş və təzyiqin pulsasiyası (döyünməsi) zamanı porşenli kompressorların daşıyıcılıq qabiliyyətinin (möhkəmliyinin) və istismar müddətinin uzadılmasının resursları barədə nəticəyə gəlmək mümkündür. Kompressor qurğularında qurulmuş aralıq aparatlar, tutumlar və onlarla əlaqələndirilmiş boru xətləri titrəyişlərin və təzyiq pulsasiyasının təsirinə daim məruz qaldığından bunların metalında yorğunluq zədələnmələrinin artmasına və qəfil dayanmalara, yorğunluq çatlamalarından dağılma halları riskinin artmasına səbəb olur.

Kompressor qurğusunda porşenin irəli-geri hərəkəti nəticəsində dinamiki təsirlərin qeyri-stasionarlığı yaranır bu isə titrəyiş (vibrasiya) vəziyyətinin yaranması ilə səciyyələndirilir. Bu zaman aşağıda göstərilən hallar əlavə vibrasiya mənbələrinin əmələ gəlməsinə səbəb olur:

- fırlanan F_r və irəli hərəkətdə olan kütlələrin F_s ətalətindən yaranan qeyri- taraz qüvvələr;
- fırlanan və irəli hərəkət edən kütlələrin M_i ətalətinin qüvvələr momenti;
- ləngər momenti - M_l ;

- dirsəkli valın hərlənmə rəqsləri;
- silindrlərdə və pillələrarası kommunikasiyalarda qazın təzyiqinin pulsasiyası;
- silindr - porşen qrupuna və klapanlara daxil olan elementlərin hərəkət mexanizmlərinin zərbələri.

Təcrübə yolu ilə çoxsaylı amillərin təsirinin öyrənilməsi ayrı-ayrı parametrlərin qarşılıqlı əlaqəli hərəkətlərinin aşkar edilməsinə imkan vermir. Bu məsələnin mahiyyətcə həlli kompressor qurğusunun işinin riyazi modelləşdirilməsi ilə asanlaşdırılır.

Porşenli kompressorların diaqnostikasının xarakterik diqqət çəkən tərəflərindən biri də nasazlıqlar nəticəsində ortaya çıxan silkələnmələr, kütlələrin qeyri-tarazlığından yaranan ümumu titrəyiş halı ilə üst-üstə düşmür. Bu isə iki cür yanaşmanın zəruriliyini ortaya qoyur:

1. kompressorun qeyri- tarazlığından yaranan titrəyişlərin vahid tam halda təhlili;
2. kompressorun qovşaqlarının qüsurlardan yaranan titrəyişlərinin təhlili.

Bu göstərilən yanaşma hallarının hər biri üçün obyektin işinin riyazi modeli işlənib hazırlanmalıdır.

Kompressor qurğularında titrəyişləri öyrənərkən qeyri-tarazlığın təhlili üçünkompressorun konstruksiyası da az əhəmiyyət kəsb etmir. Silindrlərinin sayı və yerləşmə sxemi, intiqalının gücü, dirsəkli valın fırlanma sürəti müxtəlif olan müxtəlif tipli kompressorlarda aparılan tədqiqatlar da bunu təsdiq edir. Biz nəzəri və eksperimental tədqiqatları CUBOGAS (İtaliya) tipli, 4BVTN/3 markalı, üç pilləli, məhsuldarlığı 2500 m^3 /saat, son sıxma təzyiqi 250 bar (25,0 MPa), elektrik mühərrikinin gücü 450 kW, fırlanma tezliyi dövr/dəqiqə olan kompressor qurğusunda aparara bunların nəticələrinə dair məlumatları nəzərinizə çatdıracağıq. Bu kompressorlar Azərbaycan Respublikası, Bakı şəhəri, Zığ - Hövsan yolunun sol tərəfində yerləşən, "SOCAR-CNG" MMC -yə məxsus avtomobillərə qaz doldurma kompressor stansiyasında (AQDKS) quraşdırılmış və istismar olunmaqdadır. Porşenli kompressorda titrəyişlərin ölçüldüyü nəzarət nöqtələrinin sxemi aşağıda verilir.

Kompressor mexanizminin hərəkətinin iş dövründə ətalət qüvvəsinin və qüvvə momentlərinin hesabatı kinetostatik metoddan istifadə etməklə aparılır. Alınmış asılılıqların harmonik təhlili əsas həmahəngliyə (harmonikaya) aşağıdakı cədvəldə göstərilmiş bu və ya digər faktorun təsirini müəyyən etməyə imkan verir.

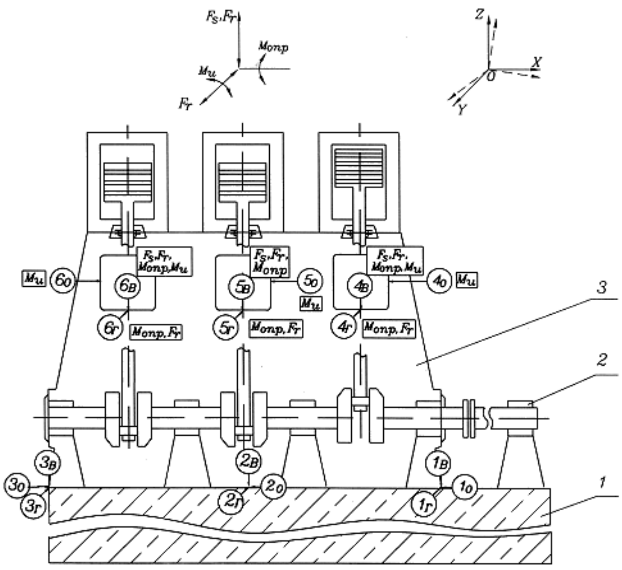

Şəkil 1.

1 - 6 - nəzarət nöqtələri (NN)
1 - bünövrə (özül)
2 - elektrik mühərriki
3 - kompressorun dəzgah çatısı

Cədvəl 1. Titrəyiş spektrinin aşağı tezlikli təhlili

Nəzarət nöqtəsi	Titrəyişin ölçülmə istiqaməti	Təsir edən amillər (faktorlar)	Harmonika (həmahənglik)	Qeydlər
4, 6	Şaquli (Ş) Horizontal (H) Ox üzrə (O)	F_r , F_s M_i $M_{ləng}$ $M_{ləng}$ F_r	I , II I , II I.....VI I.....VI I I , II	Boş-boşuna rejim.III harmonika Boş-boşuna rejim. III harmonika

		M_i		
5	Şaquli (Ş) Horizontal (H) Ox üzrə (O)	F_r , F_s $M_{ləng}$ F_r $M_{ləng}$ M_i	I , II I.....VI I I.....VI I , II	Boş-boşuna rejim. III harmo-nika Boş-boşuna rejim.III harmo-nika
1, 3	Şaquli (Ş) Horizontal (H) Ox üzrə (O)	F_r , F_s $(M_i)^1$ F_r $(M_i)^1$	I , II I , II I I , II	
2	Şaquli (Ş) Horizontal (H) Ox üzrə (O)	F_r , F_s F_r -	I , II I -	

Nəticələr göstərir ki, qeyri-taraz qüvvələrin və momentlərin II harmonikası şatunun məhdud uzunluğu nəticəsində əmələ gəlir. Ləngər momentində bu faktor III harmonikada nəzərə alınır. Kompressorun qeyri - tarazlığının tədqiqatları həm iş və həm də boş- boşuna rejimlərdə aparılmışdır. Bu zaman müəyyən olunmuşdur ki, axırıncı halda ləngər momenti $M_{ləng}$ əsasən III harmonika ilə səciyyələndirilir yaxud xarakterizə edilir. Titrəyişin müxtəlif mənbələrinin təsiri kompressorun dəzgah çatısının özüllə birlikdə mürəkkəb tərpənmə hərəkətinə gətirib çıxarır. Şəkil 1- də qeyri-taraz qüvvələrin və momentlərin təsir istiqamətləri göstərilmişdir. Qeyd etmək lazımdır ki, ətalət qüvvəsinin qeyri - taraz momentlərinin təsirindən titrəyişlərin amplitudası datçikin özülün bünövrəsinin səviyyəsindən yerləşmə hündürlüyü artdıqca yüksəlir : $M_i > (M_i)^1$. Buna görə də onlara dəzgah çatısının pəncərələrində (NN 4 -6) nəzarət etmək tövsiyyə edilir. Əksinə momentlərin zərərli təsirindən qurtarmaq məqsədilə, ətalət qüvvəsini qiymətləndirmək üçün ölçmələri mümkün olduqca özülün bünövrəsinə yaxın orta nöqtədə (NN -2) aparmaq lazımdır. Aşağıda verilmiş cədvəldə (cədvəl 2) kompressorun vibrosürətinin orta kvadratik qiymətləri (OKQ) verilmişdir. Bu cədvəldən görünür ki, kənar nöqtələrdə (NN 4 - 6) şaquli titrəyişin qiyməti demək olar ki, eynidir və orta nöqtədən (NN -5) xeyli çoxdur. Bu onunla izah edilir ki, M_i (ətalət qüvvəsi)-nin təsiri altında kompressorun dəzgah çatısı özüllə birlikdə XOZ müstəvisindəki (şəkil 1) orta nöqtəyə nisbətən yırğalanma hərəkətləri edir. Üfüqi istiqamətdə NN 4- 6 -da titrəyişin II və III harmonikaya qədər xarakterik artımı müşahidə edilir ki, bu da qismən ləngər momentinin $M_{ləng}$ təsiri ilə baş verir. Beləliklə, kompressorun kontur xarakteristi-kasının təhlili onun qeyri -tarazlıq dərəcəsini və titrəyişin əsas mənbəyini təyin etməyə, habelə onun azaldılması üzrə tövsiyyələrin işlənməsinə imkan verir.

Kompressorun müxtəlif nöqtələrində titrəyişlərin amplitudasının hesabatı məxsusi tezliklər, sərtlik xarakteristikaları və özülün həndəsi parametrləri, həmçinin suxurun xassələri nəzərə alınmaqla aparılmalıdır. Porşenli kompressorların digər özəlliyi dövri yüklənmələrin dəyişməsi şəraitində hərəkətdə olan mexanizm qovşaqlarının öz funksiyasını yerinə yetirməsidir. Bu onlarda zərbələrin yaranmasına səbəb olur. Müştərək zərbələrin sürətinin və hər bir qoşulma üçün zərbə impulsların baş verməsinin müddətinin hesabatı onlrın vibroakustik siqnalda ayırd etməyə imkan verir.

Cədvəl 2. Kompressor dəzgahının pəncərələrində vibrosürətin orta kvadratik qiymətinin (OKQ) nominal qiymətləri, mm/san

Nəzarət nöqtəsi	Titrəyişin ölçülmə isriqaməti	Harmonika				
		1	2	3	4	5
4	Ş	0,15	0,06	0,037	0,01	0,02
	Ü	0,03	0,07	0,04	0,06	0,04
	O	0,39	0,16	0,046	0,07	0,04
5	Ş	0, 018	0,028	0,04	0,01 3	0,014
	Ü	0,02	0,08	0,09	0,08	0,05
	O	0,35	0,17	0,05	0,07	0,04
6	Ş	0,13	0,063	0,044	0,03 7	0,005 6
	Ü	0,02	0, 07	0,1	0,08	0,05
	O	0, 35	0, 16	0,04	0, 06	0, 04

Nəticə etibarı ilə hərəkət edən birləşmələrdə ara məsafəsini nəzərə almaqla porşenli kompressorun hərəkət mexanizminin dinamik təhlil edilməsi qarşıya qoyulmuşdur. Bu məsələ ilə yəni mexanizmlərin ara məsafə ilə dinamikasının tədqiqi ilə bir çox alimlər XX əsrin ikinci yarısında məşğul olmuşlar. Lakin aparılmış tədqiqat metodları ayrı-ayrı bəndlərin (təmasda olan və sərbəst hərəkət edən detalların toqquşmaya qədər) bütün növ hərəkətlərinin dinamikasını tam təsvir etməyə imkan verməmişdir. Buna görə də məsələnin həlli Laqranj tənliyinin köməyi ilə həll edilmişdir:

$$\frac{d\partial T}{dt\partial qj} - \frac{\partial T}{\partial qj} = Q_j + Q_j^R \quad (j = 1, 2, \ldots r),$$

$$Q_j^R = \sum_{a=1}^{s} \lambda\, a \frac{\partial fa}{\partial qj},$$

burada λa- a rabitəsinin reaksiyasını xarakterizə edən vurğu; T - mexaniki sistemin kinetik enerjisi (kompressorun hərəkət mexanizminin), Q_j^R və Q_j - uyğun olaraq reaktiv və aktiv qüvvələrin məcmusu; f_a - a rabitəsinin detalların təmas hərəkətinin tənliyi; r- ümumiləşdirilmiş koordinatların sayıdır.

Bununla belə ümumiləşdirilmiş koordinatlar kimi (q_j) bir-birinə bağlanmış detalların ara məsafəsi sahəsindəki nisbi hərəkətinə və dirsəkli valın dönmə bucağına baxılmışdır. Ara məsafələri "porşen - silindr", " kreyskopf başmağı - istiqamətləndirici" qovşaqlarında, həmçinin kreyskopfla şatun sürüşmə yastıqları arasında nəzərə alınmışdır. Tənliyə reaktiv hərəkəti təşkil edən Q_j^R -nin daxil edilməsi eyni bir asılılığın köməyi ilə mexanizmin vibrozərbə rejimində bütün iş dövrünü təsvir etməyə imkan verir. Işlənmiş riyazi model artıq reallaşdırılmış və onun köməyi ilə müxtəlif tipli porşenli kompressorların kinematik və dinamik parametrləri tədqiq olunmuşdur. Hesabatların nəticələrinin təhlili göstərdi ki, bütün tədqiq olunan qovşaqlarda zərbələr əsasən hərəkətsiz vəziyyətdə olan hissələrdə özünü büruzə verir. Riyazi modelin adekvatlığını yoxlamaq məqsədi ilə sürtünmə qovşaqlarının müvafiq yeyilmə (köhnəlmə) vəziyyətlərində kompressorun vibroakustik eksperimental tədqiqatları aparılmışdır. Alınmış nəticələr təsdiq edir ki, vibrosiqnalın və onun statistik funksiyalarının vaxt etibarı ilə reallaşmasında impulsların vəziyyəti, şatun yastıqlarında, kreyskopf qovşağında və silindr-porşen qrupunda zərbələrin əmələ gəlməsinin hesabat yolu ilə təyin edilmiş vaxtla uyğundur.

Amplituda spektrində informativ diaqnostikanın əlamətlərini üzə çıxarmaq üçün, modelləşdirmənin nəticələri üzrə zərbələşmə qüvvəsinin spektri müəyyən edilmişdir :

$$P\,(k) = \frac{2\tau PmaxT}{\pi} \cdot \frac{\cos(\frac{k\pi r}{T})}{(T)2-4\,K2\cdot\tau 2} \qquad (k = 0, 1,2, \ldots, \infty)$$

burada T- zərbənin getmə dövrü; P_{max} - zərbənin maksimal gücü; t - zərbələşmə vaxtı; k - harmonikanın nömrəsidir.

Harmonika nömrəsindən tezliyə keçid formulu belədir:

$$\omega = k / T \quad \text{(Hers)}.$$

Vibrasiya ilə mübarizə metodları kompressor qurğularının və aqreqatlarının istehsalat şəraitində titrəyişləri təsvir edən tənliklərin təhlilinə əsaslanaraq həyata keçirilir. Təhlilin sadəliyi üçün belə hesab edək ki, bu sistemə sinusoidal qanun üzrə ölçüsü müxtəlif olan qüvvələr təsir edir. Onda bu sistemin titrəyişlər tənliyi bu şəkildə olacaqdır:

$$mX_{vt} + \mu X_{vs} + qX = F_m\,\mathcal{E}$$

burada m - sistemin kütləsi; q - sistemin sərtlik əmsalı; X - vibrodəyişmənin cari qiyməti; X_{vs} - vibrosürətin cari qiyməti; X_{vt} - vibrotəcilin cari qiyməti; F_m - məcbur edən qüvvənin amplitudası; Ɛ - məcbur edən qüvvənin bucaq tezliyidir.

Bu tənliyin ümumi həlli düsturu iki toplanandan ibarətdir: birinci toplanan sistemin sərbəst titrəyişlərinə uyğundur və bu halda sistemdə sürtünmə olduğundan sönüb gedir, ikinci toplanan isə məcburi yaranmış titrəyişlərə uyğundur. Vibrodəyişmələri kompleks şəkildə ifadə edərək, X_{vs} və X_{vt} - nin müvafiq qiymətlərini yuxarıdakı formulada yerinə qoyaraq vibrosürətin amplitudası və məcbur edən qüvvə arasında qarşılıqlı nisbəti tapırıq:

$$V_m = \frac{Fm}{\sqrt{\mu 2+(m\varepsilon-\frac{q}{\varepsilon})2}}.$$

Bu ifadənin məxrəci məcbur edən dəyişən qüvvəyə sistemin göstərdiyi müqaviməti xarakterizə edir və titrəyiş sisteminin tam mexaniki impedansı adlanır. μ kəmiyyəti bu müqavimətin aktiv, ($m\mathcal{E}$ - $\frac{q}{\varepsilon}$) isə reaktiv hissəsini təşkil edir. Sonuncu iki müqavimətdən - elastik ($\frac{q}{\varepsilon}$) və inersiya (ətalət) -$m\mathcal{E}$ ibarətdir.

Reaktiv müqavimət rezonans zamanı sıfra bərabərdir, $\mathcal{E} = \mathcal{E}_0 = \sqrt{q/m}$ tezliyinə uyğundur. Bununla da sistem məcbur edən qüvvəyə yalnız sistemin aktiv itkilərinin hesabına müqavimət göstərir. Bu rejimdə titrəyişlərin amplitudası kəskin artır.Beləliklə tənliklərin həllinin təhlilindən belə nəticə çıxır ki, maşın və avadanlıqların, o cümlədən kompressor qurğularının titrəyişləri ilə əsas mübarizə metodlarına aşağıdakılar daxildir:

1) Yarandığı (oyandığı) mənbəyə təsir etməklə titrəyişlərin azaldılması (oyanmaya məcbur edən qüvvələrin azaldılması ilə);
2) Titrəyən sistemin kütləsinin, yaxud sərtliliyinin səmərəli seçilməsi yolu ilə rezonans rejimindən qurtarmaqla;
3) Vibrozəiflətmə (vibrodempfirləmə) - titrəyən konstruktiv elementlərin rezonansa yaxın tezliklərdə titrəmələri zamanı dissipativ qüvvələrin artırılması yolu ilə;
4) Dinamiki vibrosöndürmə - müdafiə olunan obyektə titrəmələrin genişlənməsinə imkan verməyən sisremlərin qoşulması;
5) Vibroudulma - konstruksiyada daxili sürtünmə proseslərinin gücləndirilməsi yolu ilə titrəyişlərin azaldılması; bu zaman vibroenerji geriyə dönmədən istilik enerjisinə çevrilir;
6) Vibroizolyasiya - titrəyiş mənbəyi ilə müdafiə olunan obyekt arasında elastik quruluşun-vibroizolyatorun qoyulması.

Ədəbiyyat

1. Методические рекомендации по проведению виброакустических испытаний центробежных компрессоров. Черкассы: НИИТЭХИМ 1985 г.
2. Правила устройства и безопасной эксплуатации поршневых компрессоров работающих на взрывоопасных и токсичных газах
3. З.З. Рахмилевич. Компрессорные установки. "Химия" 1989 г.
4. Краткий справочник по охране и гигиене труда. Баку 1996 г.
5. Ф.Г. Гайнуллин, А.И. Гриценко и др. Природный газ как моторное топливо на транспорте. Москва, Недра 1986 г.
6. Научно-технические проблемы обеспечения автотранспорта сжатым природным газом в качестве моторного топлива, 1982 г. ВНИИГАЗ.
7. AZS 859- 2015 (İSO/DİS 16923.2:2015) "Təbii qaz yanacaq doldurma məntəqələri - sıxılmış təbii qazla (STQ) işləyən nəqliyyat vasitələrinin yanacaq doldurma məntəqələri". Bakı 2015 - ci il.
8. Пластинин П.И. "Теория и расчет поршневых компрессоров". Агропромиздат 1987 г.
9. Нормы вибрации. Оценка интенсивности вибрации газоперекачивающих агрегатов в условиях эксплуатации на компрессорных Министерства Газовой промышленности. Мингазпром 1985 г.
10. Бернадский С.А. "Снижение вибрации и шума поршневых компрессоров". Судостроение 1990 г.

Proceedings of the International Symposium of Mechanism and Machine Science, 2017
AzC IFToMM – Azerbaijan Technical University
11-14 September 2017, Baku, Azerbaijan

Porşenli kompressorların porşen-silindr qruplarının işi zamanı titrəyişlərin öyrənilməsi üçün tövsiyə edilən riyazi modellər və hesablama alqoritmləri

Mehtiyev Rəşad Murad oğlu
Azərbaycan Texniki Universiteti,
“Maşın və mexanizmlər nəzəriyyəsi” kafedrası
E-mail : dr.reshad.mehdiyev@gmail.com

Xülasə: Bu məqalədə porşenli kompressorların porşen-silindr qruplarının işi zamanı titrəyişlərin öyrənilməsi və bu məqsədlə riyazi modellərdən və hesablama alqoritmlərindən istifadə edilməsi üzrə tövsiyyələr yer almışdır. Vibrodiaqnostikanın aparılması, işçi mühitin təzyiqinin pulsasiyası tezliyinin hesablanması və bunların nəticələrinin müqayisəli təhlili izah edilmişdir. Silindr-porşen qrupunun şərti kinematik sxemləri vasitəsi ilə bir sıra vacib parametrlərin təyin edilməsi üzrə tədqiqatlara yer verilmişdir. Alqoritmlərin blok - sxemləri üzrə ölçülmüş əsas parametrlərin müqayisəsi və təhlili porşen-şatun qrupunun xarakterik xüsusiyyətlərini araşdırmağa imkan verməsi barədə müvafiq qeydlər edilmişdir. İşlənmiş model və alqoritmlərin proqramla-rının reallaşdırılmasının bu gün üçün aktual olan vibrasiya problemlərinin həllində xüsusi yer tutması məqalədə öz əksini tapmışdır.

Açar sözlər: **porşen-silindr qrupu, riyazi modellər və hesablama alqoritmləri, kinematik təhlil, oppozit yerləşmə, bucaqari yerləşmə, L-şəkilli yerləşmə.**

Porşenli kompressor aqreqatları (PKA) texniki qurğular sinfinə daxil olmaqla neft-qaz sənayesində, o cümlədən avtomobillərə qaz doldurma kompressor stansiyalarında (AQDKS) istifadə olunarkən istismarın səmərəliliyini və təhlükəsizliyini müəyyən edir. PKA-nın istismarının etibarlılığını azaldan başlıca amil onun konstruktiv elementlərinin yüksək titrəyişidir (vibrasiya). Bunlara porşenli kompressordan əlavə əlaqələndirici boru xətləri, separatorlar, soyuducular, istidəyişdiricilər, qoruyucu və açıcı-bağlayıcı armaturlar və s. elementlər də aiddir. Vibrasiyaya ən çox əlaqələndirici boru xətləri məruz qalır. Yüksək vibrasiyanın yaranmasının əsas səbəblərindən biri kompressorların silindrlərindəki metan qazının girişi və çıxışının dövriliyi ilə əlaqədar yaranan işçi mühitin təzyiqinin pulsasiyasıdır (təzyiqin qalxıb-enməsi). Bu zaman ən təhlükəli hal kompressorun rezonans şəraitində işləməsidir. Göstərilən halda təzyiqin pulsasiyası və onun harmonikliyinin riyazi qiyməti PKA-nın elementlərinin xüsusi tezliklərinə yaxın olur. Rezonans effektini azaltmaq üçün kompressor aqreqatının elementlərinin, o cümlədən əlaqələndirici boruların titrəyişlərinin rezonans tezliklərinə sazlanması üzrə texniki-quraşdırma tədbirləri işlənir və həyata keçirilir. Titrəyişlərin təhrik edicisi kimi qaz axınının turbulentliyi də ola bilir ki, bu da kompressor qurğusunun əlaqələndirici borularının, armaturlarının, boru əyrilərinin (otvod), keçidlərinin, diafraqmaların, fitinqlərin yaratdığı yerli müqavimət nəticəsində baş verir. Pulsasiyanın və yüksək vibrasiyanın olması təkcə əlavə maliyyə vəsaitinin xərclənməsi ilə bitmir, həm də bu mühüm texnoloji avadanlığın istismarının etibarlılığına və təhlükəsizliyinə mənfi təsir göstərir. Rezonans şəraitində kompressor avadanlıqlarının istismarı ağır nəticələr verə biləcək qəzalara səbəb ola bilər. Titrəyiş mənbələrinin vaxtında aşkar edilməsi və aradan qaldırılması üçün AQDKS-də sistematik olaraq aşağıdakı tədbirlər görülür:

- vibrodiaqnostikanın aparılması;
- işçi mühitin təzyiqinin pulsasiyasının tezliyinin hesablanması;
- virodiaqnostikanın nəticələrinin işçi mühitin pulsasiyası tezliyinin hesablanmasının nəticələri ilə müqayisəli təhlili.

Əgər göstərilən tədbirlər yüksək vibrasiyanın mənbəyini aşkar etməyə imkan vermirsə, onda yerli müqavimətlər tərəfindən təhrik edilən (oyandırılan) pulsasiyanın tezliyinin hesabatı yerinə yetirilir və həmin hasabatın nəticələrinin vibrodiaqnostikanın nəticələri ilə analoji müqayisəsi aparılır. İndi biz işçi mühitin təzyiqinin pulsasiyasının tezliyi üzrə yüksək vibrasiya mənbəyinin aşkar edilməsi üsulunu nəzərdən keçirək. Məqsədəuyğun variant kimi, bu tədqiqatın aparılması üçün qaz mühitinin təzyiqinin rezonans pulsasiya tezliyinin axtarışının avtomatlaşdırılmasına imkan verən rirazi modellərin və hesablama alqoritmlərinin işlənməsi qarşıya qoyulmuşdur. Porşenli kompressorun silindr -porşen qrupunun fəaliyyətinin kinematik təhlili göstərir ki, işçi mühitin təzyiqinin təhrikedici tezliyini kompressorun dirsəkli valınım bir dövrü ərzində bir pillənin porşeninin törətdiyi (yaratdığı) sıxılmış qazın çıxması dövrlərinin köməyi ilə hesablamaq mümkündür. Silindr-porşen qrupu dedikdə, bu halda onun işini sürgüqolu-şatun mexanizminin elementləri ilə (porşen, kreyskopf, şatun, sürgüqolu) təmin edən silindr başa düşülməlidir. Silindr - porşen qrupunun şərti kinematik sxemi 1-ci şəkildə verilir. Sxemdə götərilən porşenin hərəkətinin yuxarı "ölü" nöqtəsi "b" -ci silindrin adi işinin sıxılmış qazı buraxma momentinə uyğundur; porşenin hərəkətinin aşağı "ölü" nöqtəsi "b"-ci silindrin adi işinin sorma momentinə uyğundur. İkili hərəkət prinsipli silindrlər üçün sorulma və qazın sıxılıb buraxılması porşenin həm düzünə (birbaşa) və həm də əks (geriyə) hərəkəti zamanı eyni vaxtda həyata keçirilir. Kinematik sxemin təhlili zamanı sürgüqolunun fırlanması saat əqrəbinin əksi istiqamətində qəbul edilmişdir. Bir pilləyə işləyən bir neçə silindr-porşen qrupunun funksional fəaliyyətinin təhlili göstərir ki, pillədə işçi mühitin pulsasiyasının (təzyiqin enib-qalxması) oyadıcı tezliyi aşağıdakı faktorlardan asılıdır:

- n - porşenli kompressorun dirsəkli valının dövrlərinin tezliyi;
- cil_p - porşenli kompressorun "p"-ci pilləsinə işləyən silindrlərin miqdarı;
- $\mu_{s\ b,p}$ - b-ci və əsas (baza) silindrlərinin oxları arasındakı bucaq, burada b - kompressorun silindrinin nömrəsi, b=1, cil; cil - kompressorun silindrlərinin ümumi miqdarı;
- $\mu_{ş\ b,p}$ - b-ci porşenin və əsas (baza) silindrlərinin arasındakı bucaq.

Burada əsas silindr üçün $\mu_{s\ b,p}$ və $\mu_{şb,p}$ bucaqlarının riyazi qiyməti sıfra bərabər olmalıdır - $\mu_{s\ b,p}=0$ və $\mu_{ş\ b,p}=0$. Porşenli kompressorların icra olunma bazasının təcrübədə rast gəlinən müxtəlifliyi səbəbindən (oppozit, Г - şəkilli, П - şəkilli, V - şəkilli, yelpic şəkilli, şaquli- üfqi) riyazi modellər dirsəkli valın silindrlərinin və sürgüqollarının ixtiyari yerləşmiş bucaqları üçün işlənmişdir ($\mu_{s\ b,\ p} \neq 0$, $\mu_{ş\ b,p} \neq 0$). Porşenli kompressorun porşeninin düzünə (birbaşa) gedişi zamanı sıxılmış metanın ötürülməsi dövrlərinin silindr-porşen qrupunun riyazi model (1) ifadəsində göstərilmişdir; ikili təsirli silindr üçün porşenin əks hərəkəti zamanı sıxılmış metanın kənarlaşdırılması (ötürülməsi) dövrü (2) ifadəsi ilə göstərilmişdir.

$$\{t_{çıx\_düzb,p}\}=\begin{cases}\dfrac{360-(\mu_{sb,p2}-\mu_{şb,p2})}{n360}, \mu_{şb,p2} \le \mu_{sb,p2} \\ \dfrac{\mu_{şb,p2}-\mu_{sb,p2}}{n360}, \mu_{sb,p2} < \mu_{şb,p2} \le 360\end{cases} \quad (1)$$

$$\{t_{çıx\_düzb,p}\}=\begin{cases}t_{çıx\_düzb,p}-\dfrac{1}{2n}, t_{çıx\_düzb,p} \ge \dfrac{1}{2n}; \\ t_{çıx\_düzb,p}+\dfrac{1}{2n}, t_{çıx\_düzb,p} < \dfrac{1}{2n}\end{cases}. \quad (2)$$

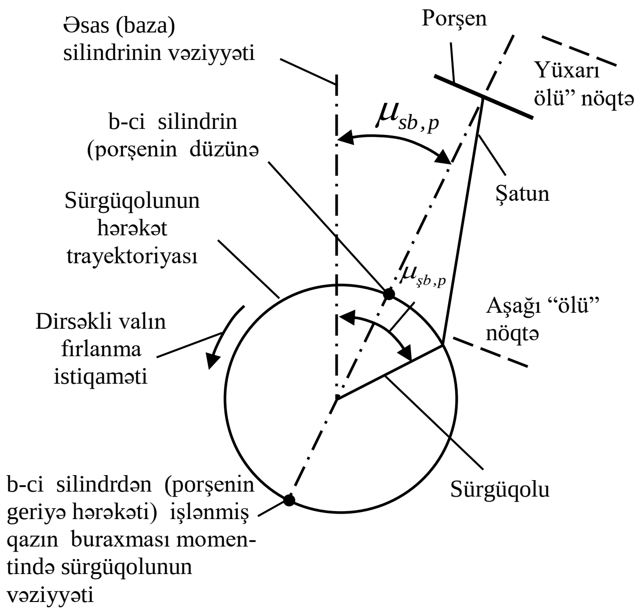

Şəkil 1. "b" -ci silindr üçün silindr-porşen qrupunun kinematik sxemi

Cədvəl 1. Porşenli kompressorun konstruktiv əsasının (bazasının) istisna təşkil edən halları

Sıra №	**Məhdudiyyətlər**	**Konstruktiv əsas (baza)**
1	$\mu_{s\ b,p} = 0$; $\mu_{ş\ b,p} \neq 0$	Silindrlərin, sürgüqollarının boyuncuqlarının ixtiyari vəziyyətdə olan bucaqları ilə sırada yerləşməsi
2	$\mu_{s\ b,p1}=0$, p1= 1,3,5...; $\mu_{s\ b,p2}$ =180, p2= 2,4,6...; $\mu_{ş\ b,p1} \neq 0$, $\mu_{ş\ b,p2} \neq 0$	Silindrlərin, sürgüqollarının boyuncuqlarının ixtiyari vəziyyətdə olan bucaqları ilə oppozit yerləşməsi
3	$\mu_{s\ b,p1}=0$, p1= 1,3,5...; $\mu_{s\ b,p2}$ =45, p2= 2,4,6...; $\mu_{ş\ b,p1} \neq 0$, $\mu_{ş\ b,p2} \neq 0$	Silindrlərin, sürgüqollarının boyuncuqlarının ixtiyari vəziyyətdə olan bucaqları ilə bucaqvari yerləşməsi
4	$\mu_{s\ b,p1}=0$, p1= 1,3,5...; $\mu_{s\ b,p2}=90$, p2= 2,4,6...; $\mu_{ş\ b,p1} \neq 0$, $\mu_{ş\ b,p2} \neq 0$	Silindrlərin, sürgüqollarının boyuncuqlarının ixtiyari vəziyyətdə olan bucaqları ilə L-şəkilli yerləşməsi
5	$\mu_{s\ b,p1}=0$, p1= 1,3,5...; $\mu_{s\ b,p2}=270$, p2= 2,4,6...; $\mu_{ş\ b,p1} \neq 0$, $\mu_{ş\ b,p2} \neq 0$	Silindrlərin, sürgüqollarının boyuncuqlarının ixtiyari vəziyyətdə olan bucaqları ilə L-şəkilli yerləşməsi

Adi hərəkətli silindrlərdə modelin riyazi təsviri (1) ifadəsi ilə məhdudlaşacaqdır; ikili təsirli silindrlərdə isə modelin riyazi təsviri (2) ifadəsi nəzərə alınmaqla aşağıdakı şəkildə olacaqdır:

$$\{t_{çıx\ b,p}\}=\{t_{çıx\_düz\ b,p}\} \cup \{t_{çıx\_əks\ b,p}\}. \qquad (3)$$

Kinematik sxemin (şəkil 1) təhlilinin köməyi ilə alınmış silindr-porşen qrupunun (1)-(3) ifadələri şəklində olan riyazi modellər özlərində sürgüqolunun yerləşmə bucağını, dirsəkli valın dövrlər tezliyini saxlayırlar və onunla fərqlənirlər ki, istənilən əsasda (bazada) icra olunmuş istər adi, istərsə də ikili təsirli bütün silindrlərində sıxılmış qazın çıxması momentini məxsusi işlənib hazırlanmış alqoritmlərin köməyi ilə hesablamağa imkan verir.

Şəkil 2-də (1)-(3) ifadələrindən istifadə edərək silindrlərdən sıxılmış metanın çıxarılması momentlərinin (alqoritm 1) hesablanması alqoritminin blok-sxemi verilmişdir.

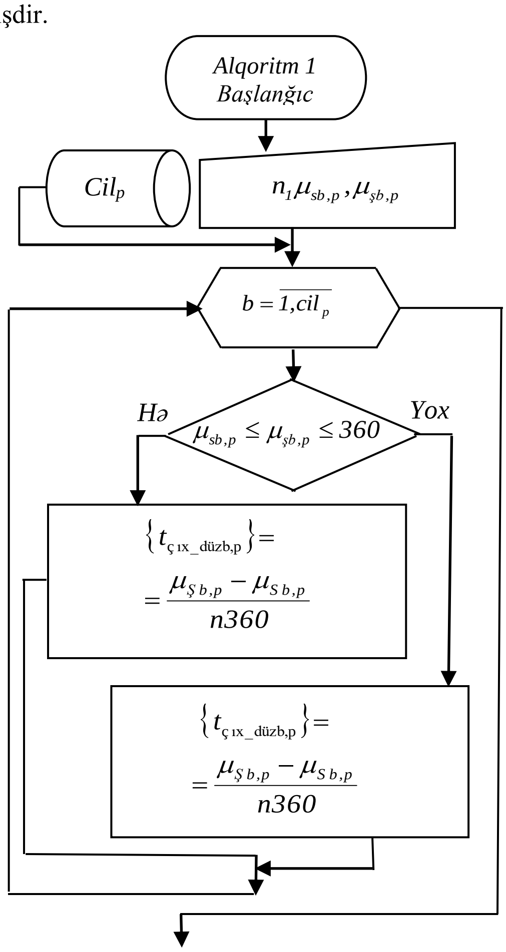

Blok-sxemin davamı

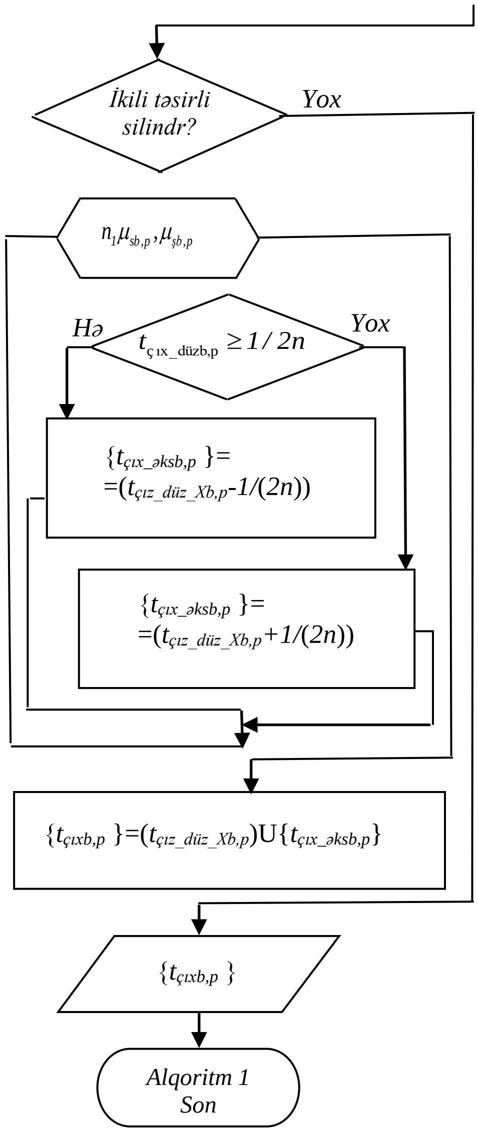

Şək. 2 . Silindrlərin sıxılmış metanı kənaretmə momentlərinin hesablanması alqoritminin blok - sxemi

Yuxarıda qeyd edilmiş modellərdən və alqoritm 1-dən istifadə edərək hesablanmış sıxılmış qazın çıxarılması dövrlərinin riyazi qiymətləri üzrə, (4) və (5) ifadələrinin köməkliyi ilə işçi mühitin təzyiqinin təhrikedici (oyandırıcı) pulsasiyasının tezliyini hesablamaq olar:

$$n_{çıx\ f,p} = 1 / | t_{çıx\ b,p} - t_{çıx\ b-1,p} | ; \qquad (4)$$

$$n_{çıx\ f,p} = 1/ t_{çıx\ b,p} , \qquad (5)$$

burada f -porşenli kompressor aqreqatının p -ci pilləsi üçün tezliyin nömrəsidir, f= 1,N_n ; N_n - nəzərə alınan tezliklərin ümumi miqdarıdır.

(4)-(5) ifadələrinin tətbiq olunduğu adi təsirli silindrlərin istifadəsi zamanı işçi mühitin təzyiqinin

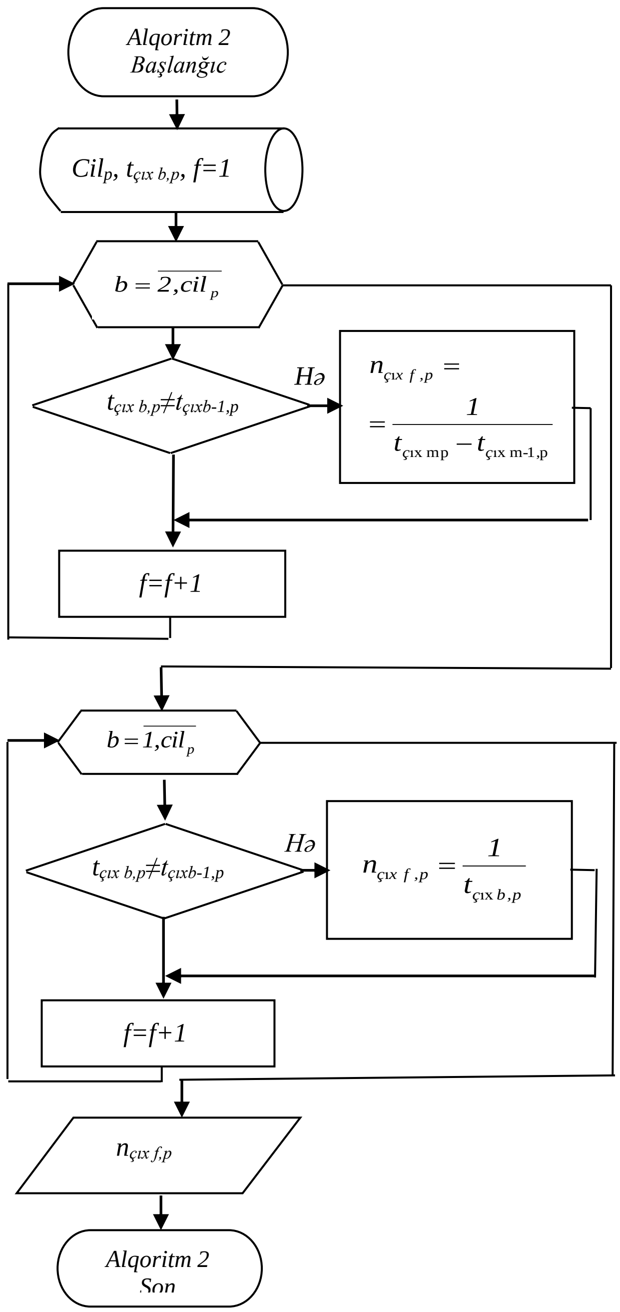

Şəkil 3. İşçi mühitin təzyiqinin pulsasiyasının (enib-qalxmasının) tezliyinin hesablanması alqoritminin blok-sxemi (silindrlərin adi işi halında)

pulsasiyasının tezliyinin hesablanması alqoritminin (alqoritm 2) blok - sxemi 3- cü şəkildə verimişdir.

Mexaniki sistemin təhrikedici tezlikləri və işçi mühitin təzyiqinin enib - qalxmasi (pulsasiyası) tezliklərinin vibrodiaqnostikasının aparılmasının nəticəsində alınmış məlumatların tutuşdurulması müvafiq olaraq (6) və (7) ifadələrinin köməyi ilə həyata keçirilir:

$$n_{çıx\ f,p} + \Delta min \leq n_{ölçi} + \Delta max, \qquad (6)$$

$$g.n_{çıx\ f,p} + \Delta min \leq n_{ölç\ i} \leq g.n_{çıx\ f,p} + \Delta max, \qquad (7)$$

burada $n_{çıx\ f,p}$ - alqoritm 2 - nin (şəkil 3) işinin nəticəsi olan təhrikedici tezliklərin hesablanmış massivi; $n_{ölç\ i}$ - ölçülmüş tezliklərin massivi;

i =1, $N_{ölç}$ (ölçülmüş tezliklərin miqdarı) - bu vibromonitorinq sisteminin köməyi ilə sənaye təhlükəsizliyinin ekspertizasının keçirilməsi nəticəsində alınmışdır. $\Delta min, \Delta max$ - hesablanmış və ölçülmüş tezliklər arasındakı müqayisənin minimal və maksimal fərqləridir və bunlar üst -üstə düşən xassəyə malik kimi qəbul edilir (riyazi qiymətləri vibrasiyasını ölçən cihazın ölçü xətalarından asılı olaraq və vibrasiyanın məlumatlarının ilkin işlənməsi metodikası ilə tapılır; ümumi halda bu qiymətlər istifadəçi tərəfindən müəyyənləşdirilir), Δmin <0, Δ max > 0, *hers*;

i - harmonikasının ölçülmüş tezliklərlə müqayisə olunduğu təhrikedici (oyandırıcı) tezliyin nömrəsi;

g - təhrikedici tezliklərin harmonikalarının bütün nömrələrinin massivi,

g=2, g 1; g 1 - istifadəçi tərəfindən tapşırılan baxılacaq harmonikaların miqdarı.

Hesablanmış təhrikedici və üstünlük təşkil edən ölçülmüş tezliklərin müqayisəsinin alqoritminin blok - sxemi (alqoritm 3) 4- cü şəkildə verilmişdir. Göstərilən alqoritmin işi Δmin və Δmax verilmiş riyazi qiymətləri nəzərə alınmaqla ölçülən tezliklərin $n_{ölç\ i}$ massivinin hər bir elementinin təhrikedici tezliklərinin $n_{çıx\ f,p}$ massivinin hər bir elementi ilə ardıcıl müqayisə etməklə tamamlanır. Əgər (6) qeyri- bərabərliyi yerinə yetirilirsə ölçülən tezlik $n_{ölç\ i}$, təhrikedici tezliklə $n_{çıx\ f,p}$ üst-üstə düşmüş hesab edilir.

(6) qeyri-bərabərliyini ödəyən ölçülən tezliklər K_i massivini təşkil edir və bu alqoritm 3-nün işinin nəticəsi kimi qəbul edilir.

Təhrikedici tezliklərin harmonikası və tezliklərin vibrodiaqnostikasının nəticələri üzrə alınmış məsələlərin müqayisəsinin həlli üçün işlənmiş alqoritm 4-ün blok-sxemi 5-ci şəkildə təqdim olunur. Göstərilən alqoritmin işi müqayisənin minimal və maksimal sərhədlərinin riyazi qiymətlərini nəzərə almaqla ölçülən tezliklərin $n_{ölçi}$ massivinin lementlərinin təhrikedici tezliklərinin g.$n_{çıx\ f,p}$ harmonikliyi massivlərinin elementləri ilə ardıcıl müqayisəsindən ibarətdir. Əgər (7) ifadəsi yerinə yetirilirsə ölçülən tezlik $n_{ölçi}$ təhrikedici tezliyin g.-ci harmonikası ilə üst-üstə düşmüş hesab edilir. (7) ifadəsini təmin edən ölçülən tezliklər alqoritmin birinci hissəsinin işinin nəticəsi olan ikiölçülü $K_{g,\,i}$ massivini əmələ gətirir. g indeksi ölçülən i-ci tezliyin riyazi qiyməti ilə üst-üstə düşən (uyğun gələn) təhrikedici tezliyin j-ci harmoni-kasının nömrəsinin işarəsidir.

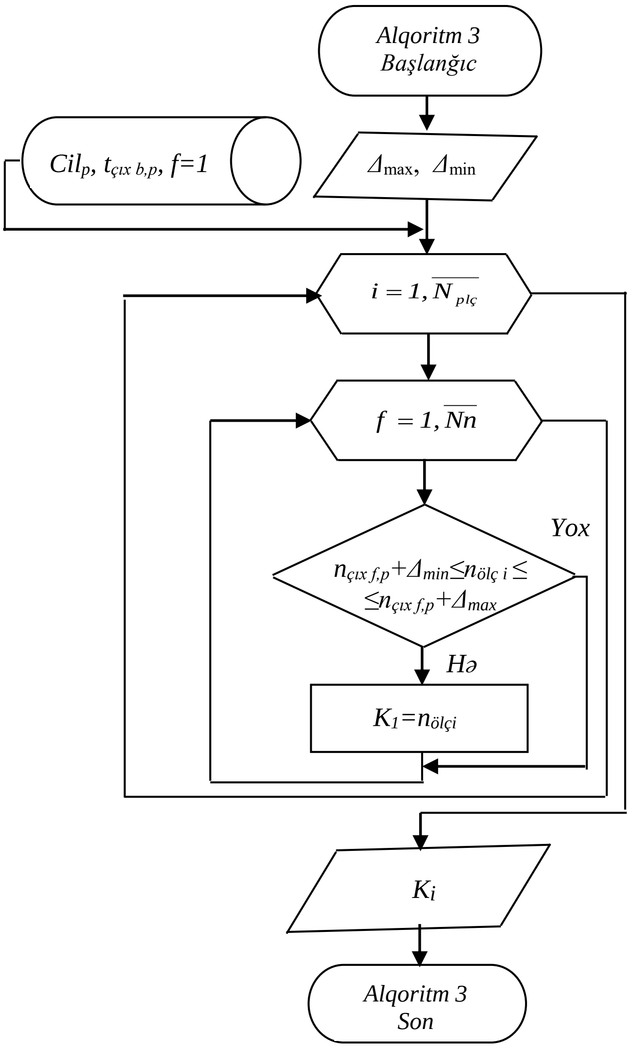

Şəkil 4. Hesablanmış təhrikedici və üstünlük təşkil edən ölçülmüş tezliklərin müqayisəsinin alqoritminin blok-sxemi

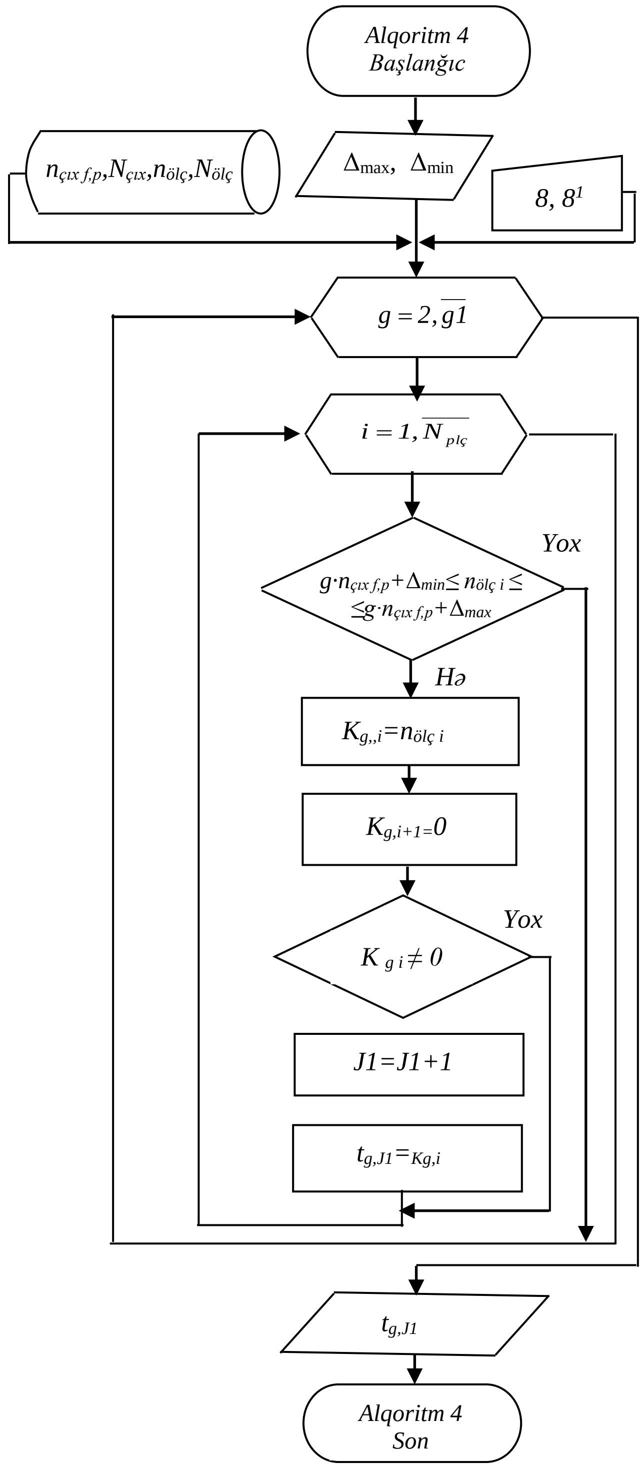

Şəkil 5. Alqoritm 4-ün blok sxemi

Beləliklə, işlənmiş 3 və 4 alqoritmləri porşenli kompressor aqreqatının elementlərinin titrəyişlərinin rezonans tezliklərini aşkar etməyə imkan verir və porşenli kompressor aqreqatının konstruktiv elementlərinin titrəyişlərinin eksperiment yolu ilə ölçülmüş tezliklərinin işçi mühitin təzyiqinin pulsasiyası və onun harmonikasının tezliyi ilə müqayisəsinin axtarışı üsulundan fərqlənir. Bu isə porşenli kompressor aqreqatının elementlərinin titrəyişlərinin rezonans tezliklərini aşkar etməyə imkan verməklə yanaşı, alınmış məlumatları titrəyişlərin rezonans tezliyinə boru kəmərlərinin sazlanmasına texniki quraşdırma həllərinin işlənməsində istifadə edilir.

Belə hesab etmək olar ki, işlənmiş model və alqoritmlərin proqramlarının reallaşdırılması AQDKS-də porşenli kompressor aqreqatlarının istismar təhlükəsizliyinin artırılmasına kömək edəcək və porşenli kompressor aqreqatlarının elementlərinin həddən artıq vibrasiyasının aşkar edilməsinin həllində öz müsbət təsirini göstərəcəkdir.

Ədəbiyyat

1. Клюев И.К., Писаревский В.М., Математическая модель процесса взаимодействия работы цилиндра поршневого компрессора. Машиностроение, 1984 г.
2. Компьютерное моделирование течения сжимаемых газов через сложные технологические трубопроводы. О.Б.Бутусов, В.П.Мешалкин и др. Химическая промышленность 1998 г.
3. Пластинин П.И., Поршневые компрессоры. Теория и расчет. Москва, Колос, 2006.
4. Мошев Е.Р., Ромашкин М.А., Модели и алгоритмы расчета устройств для гашения пульсаций газообразной среды в трубопроводных системах. Прикладная информатика, 2014, №2
5. Френкель М.И., Поршневые компрессоры. Теория, конструкция и основы проектирования. Изд. Машиностроение, 1969 г.
6. Рахмилевич З.З. Компрессорные установки. Москва, Химия, 1989 г.
7. Владиславлев А.П., Козобков А.А., Малышев В.А. Трубопроводы поршневых компрессорных машин. Машиностроение, 1972 г.
8. Поршневые компрессоры: учебное пособие для студентов (под общей редакцией Б.С. Фотина). Машиностроение, 1987 г.
9. Методические рекомендации по снижению вибрации межступенчатых коммуникаций поршневых компрессоров (НИИ технико-экономических исследований химической промышленности).

www.aztu.edu.az

H.Javid ave 25, Baku, Azerbaijan, AZ1073, Azerbaijan Technical University